

SYNTHESIS, STUDY, AND APPLICATIONS OF HIGHLY FLUORINATED
COPPER PYRAZOLATE COMPLEXES OF SMALL ALKENE, ALKYNES
AND CARBON MONOXIDE

by

DEVABORNINY PARASAR

Presented to the Faculty of the Graduate School of
The University of Texas at Arlington in Partial Fulfillment
of the Requirements
for the Degree of

DOCTOR OF PHILOSOPHY

THE UNIVERSITY OF TEXAS AT ARLINGTON

August 2020

Copyright © by Devaborniny Parasar 2020
All Rights Reserved



Acknowledgements

I would like to express my sincere gratitude to my advisor Dr. Rasika Dias for his guidance and support throughout my graduate career. His help, insights, patience, advice and motivation has immensely enriched my research experience. I would also like to thank and acknowledge my dissertation committee members Dr. Robin Macaluso, Dr. Kwangho Nam and and Dr. Frederick MacDonnell for providing insightful suggestions.

I am extremely grateful to the members of Dias's research group, both past and present, for being such wonderful friends and colleagues, and also for all their help and support throughout my graduate studies- Dr. Guocang Wang, Dr. Shawn G. Ridlen, Dr. Tharun T. Ponduru, Jaspreet S. Lakhi, Anurag Noonikara-Poyil, Monika R. Patterson, Adway O. Zacharias and Brandon Watson. I would especially like to convey my sincerest regards to Dr. Naleen B. Jayaratna for his mentorship and guidance during my early days at Dias's lab. I would like to offer my thanks to all the faculty members and the staff of the Department of Chemistry and Biochemistry, and all my collaborators. A special thanks to Dr. Brian Edwards, and Dr. Roy McDougald for all their technical support, without whom my research work would not have been possible.

Most importantly, I would like to thank my beloved parents, Mr. Dilip Kumar Sarmah and Mrs. Bondita Goswami Sarmah for all their support and

encouragement, and for having enough faith in me to let me come so far away from home and fulfill my dreams.

I would also like to acknowledge the Department of Chemistry and Biochemistry of the University of Texas at Arlington and Robert A. Welch Foundation for the financial support.

29 June, 2020

Abstract

SYNTHESIS, STUDY, AND APPLICATIONS OF HIGHLY FLUORINATED COPPER PYRAZOLATE COMPLEXES OF SMALL ALKENE, ALKYNES AND CARBON MONOXIDE

Devaborniny Parasar, PhD

The University of Texas at Arlington, 2020

Supervising Professor: H.V. Rasika Dias

Trinuclear copper pyrazolate complexes (copper trimers) function as excellent precursors to synthesize multinuclear complexes of copper. Using highly fluorinated pyrazolates as supporting ligands, we have successfully synthesized and isolated several unique complexes of copper with alkene (e.g., ethylene), alkynes (e.g., 3-hexyne, butyne, acetylene, etc.) and carbon monoxide from the copper trimers. Synthetic details, solid-state structures, and physico-chemical properties of a series of multinuclear complexes have been studied.

Chapter 2 of this research work focuses on the olefin/paraffin separation technology. For this we have successfully synthesized a novel, highly fluorinated copper pyrazolate complex, that undergoes remarkable structural rearrangement forming a dinuclear species, $[(3,4,5-(CF_3)_3Pz)Cu(H_2C=CH_2)]_2$, when exposed to

ethylene. We have discussed in detail the benefit of this transformation, and how it can be efficiently used for separation of olefins from a mixture of gases.

Chapter 3 covers the synthesis, study of photophysical properties and computational analysis of di- and tetranuclear complexes of copper with internal alkynes. This class of molecules show interesting photoluminescence at different temperatures, and in different solvents. Copper trimer also acts as a powerful catalyst for alkyne transformations as evident from its ability to catalyze the alkyne C(sp)-H bond for carboxylation with CO₂, azide-alkyne cycloaddition and hydrothiolation. The reaction intermediates for these catalytic reactions were isolated and investigated in chapter 3.

Chapter 4 describes the carbonyl chemistry of multinuclear copper pyrazolates and the effects of additional donors such as chloride, bromide, and [3,5-(CF₃)₂Pz]⁻ ions on the stability of the resulting copper(I) carbonyl adducts. Accordingly, {[3,5-(CF₃)₂Pz]Cu(CO)}₂, {[4-Cl-3,5-(CF₃)₂Pz]Cu(CO)}₂, {[3,4,5-(CF₃)₃Pz]Cu(CO)}₂, [NEt₄][{[3,5-(CF₃)₂Pz]Cu(CO)}₄(μ₄-Br)], [NEt₄][{3,5-(CF₃)₂Pz}₃Cu₂(CO)₂], [NEt₄][{[4-Cl-3,5-(CF₃)₂Pz]Cu(CO)}₄(μ₄-Br)], [NEt₄][{[4-Cl-3,5-(CF₃)₂Pz]Cu(CO)}₄(μ₄-Cl)] and [{[4-Cl-3,5-(CF₃)₂Pz]Cu(CO)}₂(μ₂-CH₃CN)] were synthesized and characterized. Theoretical calculations were also performed to study the bonding energy of the synthesized complexes.

Table of Contents

Acknowledgements.....	ii
Abstract.....	iv
List of Illustrations.....	viii
List of Tables.....	xiv
Chapter 1 Introduction.....	1
1.1 Pyrazole ligand.....	1
1.2 Copper pyrazolates.....	4
Chapter 2 Selective adsorption of ethylene using copper(I) pyrazolate complex.....	9
2.1 Abstract.....	10
2.2 Introduction.....	105
2.3 Results and discussions.....	105
2.4 Summary.....	40
Chapter 3 Chemistry and applications of copper-alkyne complexes.....	42
3.1 Copper(I)-alkyne complexes of fluorinated pyrazolate: Synthesis, photophysical properties, and computational analysis.....	42
3.1.1 Abstract.....	43
3.1.2 Introduction.....	44
3.1.3 Results and discussion.....	48
Synthesis and structure.....	48
Computational analysis of structure and bonding.....	60
Photophysical studies.....	66
Computational analysis of photophysics.....	75
3.1.4 Summary.....	183
3.2 Chemistry and transformations of acetylene and terminal alkyne complexes of copper(I).....	89

3.2.1 Abstract	90
3.2.2 Introduction.....	91
3.2.3 Results and discussion	94
Coordination chemistry of copper pyrazolates with acetylene	94
Coordination chemistry of copper pyrazolates with terminal alkynes ..	107
Copper(I) pyrazolates in alkyne transformation.....	114
Carboxylation of terminal alkynes	115
Azide-alkyne cycloaddition.....	117
Hydrothiolation of alkynes	183
3.2.4 Summary	105
Chapter 4 Chemistry of binary copper (I) pyrazolates with carbon monoxide...	105
4.1 Abstract	145
4.2 Introduction.....	145
4.3 Results and discussion	145
4.4 Summary	183
Chapter 5 Experimental section	105
5.1 Instrumentation	145
5.2 Experimental section of chapter 2.....	145
5.3 Experimental section of chapter 3 Part 3.1	145
Experimental section of chapter 3 Part 3.2	1450
5.4 Experimental section of chapter 4.....	205
Appendix A Spectroscopic data for Chapter 2	212
Appendix B Spectroscopic data for Chapter 3 Part 3.1	228
Spectroscopic data for Chapter 3 Part 3.2.....	247
Appendix C Spectroscopic data for Chapter 4.....	296
References.....	323
Biographical information	344

List of Illustrations

1.1 Pyrazole ligand.....	2
1.2 Coordination modes of the pyrazole ligand	54
1.3 Trinuclear copper (I) pyrazolate complex, {[3,5-(CF ₃) ₂ Pz]Cu} ₃	54
1.4 Dewar-Chatt-Duncanson (DCD) Model.	54
2.1 Structures of [(3,4,5-(CF ₃) ₃ Pz)Cu] ₃ , [Cu₃] and [(3,4,5-(CF ₃) ₃ Pz)Cu(C ₂ H ₄) ₂], [Cu₂•(C₂H₄)₂]......	12
2.2 Molecular structures of [(3,4,5-(CF ₃) ₃ Pz)Cu] ₃ , [Cu₃] and illustration showing packing of four molecules of [Cu₃]	13
2.3 Molecular structures of [(3,4,5-(CF ₃) ₃ Pz)Cu(C ₂ H ₄) ₂], [Cu₂•(C₂H₄)₂]; a view showing boat shaped Cu ₂ N ₄ core of [Cu₂•(C₂H₄)₂].	14
2.4 Raman data for [Cu₃] (red) and [Cu₂•(C₂H₄)₂] (blue) generated from exposure to ethylene in solution.	155
2.5 Structural representation of equilibrium equation of ethylene binding.....	1057
2.6 Van't Hoff plot for [Cu₃] binding of ethylene in CDCl ₃ solution	105
2.7 ¹ H NMR spectra of [Cu₂•(C₂H₄)₂] at various temperatures	20
2.8 ¹⁹ F NMR spectra of [Cu₂•(C₂H₄)₂] at various temperatures.....	21
2.9 TGA data for [Cu₂•(C₂H₄)₂] (blue) and [Cu₃] (red) using the mass at 125 °C as the reference for the relative mass calculation.....	22
2.10 DSC cooling data for [Cu₃]	105
2.11 DSC heating data for [Cu₂•(C₂H₄)₂], which converts to [Cu₃] during the first cycle	105
2.12 DSC heating data for [Cu₃],.....	105
2.13 Raman data for [Cu₃] (red), [Cu₂•(C₂H₄)] (blue) generated from exposure to ethylene in solution, and [Cu₃] (green) produced by placing [Cu₂•(C₂H₄)] under vacuum at 60 °C.....	105

2.14 Comparison of experimental PXRD patterns of [Cu₃] prepared from solution (blue) and [Cu₃] prepared by placing solid [Cu₂•(C₂H₄)₂] under vacuum at 60 °C for 6 hours (olive green)	145
2.15 Comparison of experimental PXRD patterns of [Cu₃] (red), [Cu₂•(C₂H₄)₂] produced via the solution method (olive green), and [Cu₂•(C₂H₄)₂] produced by treating [Cu₃] with ethylene gas in the solid state (blue).....	29
2.16 Ethylene adsorption (solid symbols) and desorption (hollow symbols) isotherms of [Cu₃] at 20, 50 and 70 °C.....	145
2.17 The Claussius-Clapeyron plot derived from the pressure where the step is observed in adsorption isotherms measured at 20, 50 and 70 °C	32
2.18 Ethylene adsorption isotherms of [Cu₃] at 20, 50 and 70 °C past the ‘step’ associated with phase change and chemisorption.	35
2.19 The ethene uptake of [Cu₃] over five sorption/desorption cycles. The time axis has been truncated at 120 min for consistency	39
3.1 Diagram showing the structures of Cu ₂ (μ-[3,5-(CF ₃) ₂ Pz]) ₂ (EtC≡CEt) ₂ (1), Cu ₄ (μ-[3,5-(CF ₃) ₂ Pz]) ₄ (μ-EtC≡CEt) ₂ (2), Cu ₄ (μ-[3,5-(CF ₃) ₂ Pz]) ₄ (μ-MeC≡CMe) ₂ (3), Cu ₂ (μ-CF ₃ CO ₂) ₂ (EtC≡CEt) ₂ (4), Cu ₄ (μ-CF ₃ CO ₂) ₄ (μ-EtC≡CEt) ₂ (5).	47
3.2 Synthetic routes to di- and tetra-nuclear complexes complexes Cu ₂ (μ-[3,5-(CF ₃) ₂ Pz]) ₂ (EtC≡CEt) ₂ (1), Cu ₄ (μ-[3,5-(CF ₃) ₂ Pz]) ₄ (μ-EtC≡CEt) ₂ (2), and Cu ₄ (μ-[3,5-(CF ₃) ₂ Pz]) ₄ (μ-MeC≡CMe) ₂ (3) from tri-nuclear {[3,5-(CF ₃) ₂ Pz]Cu} ₃	49
3.3 Molecular structure of Cu ₂ (μ-[3,5-(CF ₃) ₂ Pz]) ₂ (EtC≡CEt) ₂ (1).....	51
3.4 Molecular structure of Cu ₄ (μ-[3,5-(CF ₃) ₂ Pz]) ₄ (μ-EtC≡CEt) ₂ (2).....	53
3.5 Molecular structure of Cu ₄ (μ-[3,5-(CF ₃) ₂ Pz]) ₄ (μ-MeC≡CMe) ₂ (3)	105
3.6 Molecular structure of Cu ₄ (μ-CF ₃ CO ₂) ₄ (μ-EtC≡CEt) ₂ (5)	58
3.7 Molecular structure of Cu ₂ (μ-CF ₃ CO ₂) ₂ (EtC≡CEt) ₂ (4).....	59

3.8 Calculated geometries of (a) free 3-hexyne, (b) free 2-butyne, (c) $\text{Cu}_2(\mu\text{-[3,5-(CF}_3)_2\text{Pz]})_2(\text{EtC}\equiv\text{CEt})_2$ (1), (d) $\text{Cu}_4(\mu\text{-[3,5-(CF}_3)_2\text{Pz]})_4(\mu\text{-EtC}\equiv\text{CEt})_2$ (2) and (e) $\text{Cu}_4(\mu\text{-[3,5-(CF}_3)_2\text{Pz]})_4(\mu\text{-MeC}\equiv\text{CMe})_2$ (3).....	61
3.9 Photoluminescence spectra for a solid powder sample of $\text{Cu}_2(\mu\text{-[3,5-(CF}_3)_2\text{Pz]})_2(\text{EtC}\equiv\text{CEt})_2$ (1), at 298 K (top) and 77 K (bottom). Excitation and emission wavelengths used in the emission and excitation spectra, respectively, are labeled. A photograph is shown as an inset for colorless crystals packed in Suprasil quartz tubes while being exposed to UV light at room temperature.....	69
3.10 Photoluminescence spectra for a solid powder sample of $\text{Cu}_4(\mu\text{-[3,5-(CF}_3)_2\text{Pz]})_4(\mu\text{-EtC}\equiv\text{CEt})_2$ (2), at 298 K (top) and 77 K (bottom). A photograph is shown as an inset for colorless crystals packed in Suprasil quartz tubes while being exposed to UV light at room temperature.....	70
3.11 Photoluminescence spectra for a solid powder sample of $\text{Cu}_4(\mu\text{-[3,5-(CF}_3)_2\text{Pz]})_4(\mu\text{-MeC}\equiv\text{CMe})_2$ (3), at 298 K (top) and 77 K (bottom). A photograph is shown as an inset for colorless crystals packed in Suprasil quartz tubes while being exposed to UV light at room temperature.....	71
3.12 Photoluminescence spectra for frozen solution of $\text{Cu}_2(\mu\text{-[3,5-(CF}_3)_2\text{Pz]})_2(\text{EtC}\equiv\text{CEt})_2$ (1) in benzene (conc. = 1×10^{-3} M). Photograph is shown as inset for frozen solution in Suprasil quartz tube while being exposed to UV light at a liquid-nitrogen bath (77 K).	72
3.13 Photoluminescence spectra for frozen solution of $\text{Cu}_4(\mu\text{-[3,5-(CF}_3)_2\text{Pz]})_4(\mu\text{-EtC}\equiv\text{CEt})_2$ (2) in benzene (conc. = 1×10^{-3} M). Photograph is shown as inset for frozen solution in Suprasil quartz tube while being exposed to UV light at a liquid-nitrogen bath (77 K).....	73
3.14 Photoluminescence spectra for frozen solution of $\text{Cu}_4(\mu\text{-[3,5-(CF}_3)_2\text{Pz]})_4(\mu\text{-MeC}\equiv\text{CMe})_2$ (3) in benzene (conc. = 1×10^{-3} M). Photograph is shown as inset for	

frozen solution in Suprasil quartz tube while being exposed to UV light at a liquid-nitrogen bath (77 K).....	74
3.15 Isodensity surface plots (isodensity value = 0.043) of the frontier orbitals that contribute to the most intense TDDFT peaks of (a) $\text{Cu}_2(\mu\text{-[3,5-(CF}_3)_2\text{Pz]})_2(\text{EtC}\equiv\text{CEt})_2$ (1), (b) $\text{Cu}_4(\mu\text{-[3,5-(CF}_3)_2\text{Pz]})_4(\mu\text{-EtC}\equiv\text{CEt})_2$ (2), and (c) $\text{Cu}_4(\mu\text{-[3,5-(CF}_3)_2\text{Pz]})_4(\mu\text{-MeC}\equiv\text{CMe})_2$ (3)..	76
3.16 Energy levels (eV) of the dinuclear and tetranuclear complexes 1-3 .	77
3.17 (a) Experimental absorption spectra of dichloromethane solution of 1 – 5 . Calculated electronic spectrum with spin-allowed (singlet-to-singlet, $S_0 \rightarrow S_n$) excitation energies (vertical lines) and oscillator strengths for the complex 1, 2 , and 3 in dichloromethane solvent, are depicted in (b), (c), and (d), respectively.....	81
3.18 Singlet (S_0) and triplet (T_1) optimized geometries. Singlet and triplet $\text{C}\equiv\text{C}\dots\text{C}\equiv\text{C}$ dihedral angles of samples.....	83
3.19 Diagram showing the structures of $\{\mu\text{-[3,5-(CF}_3)_2\text{Pz]Cu}\}_3$ (1), $\text{Cu}_2(\mu\text{-[3,5-(CF}_3)_2\text{Pz]})_2(\text{EtC}\equiv\text{CEt})_2$ (2), and $\text{Cu}_4(\mu\text{-[3,5-(CF}_3)_2\text{Pz]})_4(\mu\text{-EtC}\equiv\text{CEt})_2$ (3)	93
3.20 Synthetic routes to di- and tetra-nuclear complexes complexes $\text{Cu}_2(\mu\text{-[3,5-(CF}_3)_2\text{Pz]})_2(\text{HC}\equiv\text{CH})_2$ (5) and $\text{Cu}_4(\mu\text{-[3,5-(CF}_3)_2\text{Pz]})_4(\mu\text{-HC}\equiv\text{CH})_2$ (4) from trinuclear $\{\mu\text{-[3,5-(CF}_3)_2\text{Pz]Cu}\}_3$	94
3.21 Structures and synthetic routes to tetra-nuclear complexes $\text{Cu}_4(\mu\text{-[3,5-(CF}_3)_2\text{Pz]})_4(\mu\text{-HC}\equiv\text{CH})_2$ (4), $\text{Cu}_4(\mu\text{-[4-Br-3,5-(CF}_3)_2\text{Pz]})_4(\mu\text{-HC}\equiv\text{CH})_2$ (6), $\text{Cu}_4(\mu\text{-[4-Cl-3,5-(CF}_3)_2\text{Pz]})_4(\mu\text{-HC}\equiv\text{CH})_2$ (7) and di-nuclear complexes and $\text{Cu}_2(\mu\text{-[3,5-(CF}_3)_2\text{Pz]})_2(\text{HC}\equiv\text{CH})_2$ (5) and $\text{Cu}_2(\mu\text{-[4-Br-3,5-(CF}_3)_2\text{Pz]})_2(\text{HC}\equiv\text{CH})_2$ (8) from trinuclear copper(I) pyrazolates and acetylene	95
3.22 Molecular structure of $\text{Cu}_4(\mu\text{-[3,5-(CF}_3)_2\text{Pz]})_4(\mu\text{-HC}\equiv\text{CH})_2$ (4)	97
3.23 ^1H NMR spectra of $\text{Cu}_2(\mu\text{-[3,5-(CF}_3)_2\text{Pz]})_2(\text{HC}\equiv\text{CH})_2$ (5) (in CD_2Cl_2) in the presence of excess acetylene at various temperatures.	99
3.24 Molecular structure of $\text{Cu}_2(\mu\text{-[4-Br-3,5-(CF}_3)_2\text{Pz]})_2(\text{HC}\equiv\text{CH})_2$ (8)	101

3.25 Raman spectra showing the conversion of $\text{Cu}_2(\mu\text{-[4-Br-3,5-(CF}_3)_2\text{Pz]})_2(\text{HC}\equiv\text{CH})_2$ (8) to $\text{Cu}_4(\mu\text{-[4-Br-3,5-(CF}_3)_2\text{Pz]})_4(\mu\text{-HC}\equiv\text{CH})_2$ (6) with time at room temperature and in open air	102
3.26 ^1H NMR spectra of $\text{Cu}_2(\mu\text{-[4-Br-3,5-(CF}_3)_2\text{Pz]})_2(\text{HC}\equiv\text{CH})_2$ (8) (in CD_2Cl_2) in presence of excess acetylene at various temperatures.	104
3.27 Synthetic routes to di-nuclear complexes $\text{Cu}_2(\mu\text{-[3,5-(CF}_3)_2\text{Pz]})_2(\text{HC}\equiv\text{CPh})_2$ (9) and $\text{Cu}_2(\mu\text{-[3,5-(CF}_3)_2\text{Pz]})_2(\text{HC}\equiv\text{C(CH}_2)_5\text{C}\equiv\text{CH})$ (10) from tri-nuclear $\{[\text{3,5-(CF}_3)_2\text{Pz]Cu}\}_3$ and the corresponding alkyne.	108
3.28 Molecular structure of $\text{Cu}_2(\mu\text{-[3,5-(CF}_3)_2\text{Pz]})_2(\text{HC}\equiv\text{CPh})_2$ (9).....	109
3.29 Molecular structure of $\text{Cu}_2(\mu\text{-[3,5-(CF}_3)_2\text{Pz]})_2(\text{HC}\equiv\text{C(CH}_2)_5\text{C}\equiv\text{CH})$ (10)..	110
3.30 Synthetic routes to $\text{Cu}_4(\mu\text{-[3,5-(CF}_3)_2\text{Pz]})_4(\text{HC}\equiv\text{C(CH}_2)_4\text{C}\equiv\text{CH})_2$ (11) and $\text{Cu}_4(\mu\text{-[3,5-(CF}_3)_2\text{Pz]})_4(\text{C}_2\text{H}_5\text{C}\equiv\text{C(CH}_2)_4\text{C}\equiv\text{CC}_2\text{H}_5)_2$ (12) from tri-nuclear $\{[\text{3,5-(CF}_3)_2\text{Pz]Cu}\}_3$ and the corresponding alkyne.....	111
3.31 Molecular structures of $\text{Cu}_4(\mu\text{-[3,5-(CF}_3)_2\text{Pz]})_4(\text{HC}\equiv\text{C(CH}_2)_4\text{C}\equiv\text{CH})_2$ (11) (top) and $\text{Cu}_4(\mu\text{-[3,5-(CF}_3)_2\text{Pz]})_4(\text{C}_2\text{H}_5\text{C}\equiv\text{C(CH}_2)_4\text{C}\equiv\text{CC}_2\text{H}_5)_2$ (12) (bottom)....	112
3.32 The $\{\mu\text{-[3,5-(CF}_3)_2\text{Pz]Cu}\}_3$ catalyzed carboxylation of terminal alkynes...	116
3.33 The $\{\mu\text{-[3,5-(CF}_3)_2\text{Pz]Cu}\}_3$ catalyzed alkyne-azide cycloaddition involving acetylene or various terminal alkynes as the alkyne source and p-tolylazide.....	118
3.34 The $\{\mu\text{-[3,5-(CF}_3)_2\text{Pz]Cu}\}_3$ catalyzed hydrothiolation of terminal alkynes.....	121
4.1 Structures of $[\text{HB(3,5-(CF}_3)_2\text{Pz)}_3]\text{CuCO}$ (1)	127
4.2 Structurally characterized $[\text{Cu(CO)\{2-(3(5)-Pz),6-(CH}_3)\text{py}\}}]_3$ and $(\text{py})\text{Cu[3,5-(MeCO}_2)_2\text{Pz]}_2\text{Cu(CO)(py)}$, and the proposed structure of $[\text{Cu}_4(\text{dmnpz})_6(\text{CO})_4]^{2-}$ based on solution data.....	129
4.3 Synthetic route to $\{[\text{3,5-(CF}_3)_2\text{Pz]Cu(CO)}\}_2$ (5), $\{[\text{4-Cl-3,5-(CF}_3)_2\text{Pz]Cu(CO)}\}_2$ (6), $\{[\text{3,4,5-(CF}_3)_3\text{Pz]Cu(CO)}\}_2$ (7) from $\{[\text{3,5-(CF}_3)_2\text{Pz]Cu}\}_3$ (2), $\{[\text{4-Cl-3,5-(CF}_3)_2\text{Pz]Cu}\}_3$ (3), and $\{[\text{3,4,5-(CF}_3)_3\text{Pz]Cu}\}_3$ (4).	131

4.4 Molecular structure of $\{[3,5-(\text{CF}_3)_2\text{Pz}]\text{Cu}(\text{CO})\}_2$ (5).....	133
4.5 Molecular structure of $\{[3,4,5-(\text{CF}_3)_3\text{Pz}]\text{Cu}(\text{CO})\}_2$ (7).....	137
4.6 NOCV-EDA analysis of the Cu-CO interaction in $\{[3,5-(\text{CF}_3)_2\text{Pz}]\text{Cu}(\text{CO})\}_2$ (5)	140
4.7 Synthetic route to $[\text{NEt}_4][\{[3,5-(\text{CF}_3)_2\text{Pz}]\text{Cu}(\text{CO})\}_4(\mu_4\text{-Br})]$ (8) and $[\text{NEt}_4]\{[3,5-(\text{CF}_3)_2\text{Pz}]\}_3\text{Cu}_2(\text{CO})_2$ (9) from $\{[3,5-(\text{CF}_3)_2\text{Pz}]\text{Cu}\}_3$ (2).....	143
4.8 Molecular structure of $[\text{NEt}_4][\{[3,5-(\text{CF}_3)_2\text{Pz}]\text{Cu}(\text{CO})\}_4(\mu_4\text{-Br})]$ (8)	144
4.9 Molecular structure of $[\text{NEt}_4]\{[3,5-(\text{CF}_3)_2\text{Pz}]\}_3\text{Cu}_2(\text{CO})_2$ (9).....	148
4.10 Synthetic route to $[\text{NEt}_4][\{[4\text{-Cl-3,5-(CF}_3)_2\text{Pz}]\text{Cu}(\text{CO})\}_4(\mu_4\text{-Br})]$ (10) and $[\text{NEt}_4][\{[4\text{-Cl-3,5-(CF}_3)_2\text{Pz}]\text{Cu}(\text{CO})\}_4(\mu_4\text{-Cl})]$ (11) from $[\{[4\text{-Cl-3,5-}$ $(\text{CF}_3)_2\text{Pz}]\text{Cu}\}_3$ (3).....	150
4.11 Molecular structure of $[\text{NEt}_4][\{[4\text{-Cl-3,5-(CF}_3)_2\text{Pz}]\text{Cu}(\text{CO})\}_4(\mu_4\text{-Br})]$ (10).....	152
4.12 Molecular structure of $[\text{NEt}_4][\{[4\text{-Cl-3,5-(CF}_3)_2\text{Pz}]\text{Cu}(\text{CO})\}_4(\mu_4\text{-Cl})]$ (11).....	153
4.13 Molecular structure of $[\{[4\text{-Cl-3,5-(CF}_3)_2\text{Pz}]\text{Cu}(\text{CO})\}_2(\mu_2\text{-CH}_3\text{CN})]$ (12)	154
4.14 NOCV-EDA analysis of the Cu-CO interaction in 8 and 9.....	156
4.15 Correlation between \bar{v}_{CO} vs ΔE_{orb} (blue), and \bar{v}_{CO} vs ΔE_{int} (red), along all the calculated series, denoting a better correlation in the former relationship	159

List of Tables

2.1 ^1H and ^{19}F NMR data for $[\text{Cu}_3]$ binding of ethylene in CDCl_3 solution.	18
2.2 Heat of equilibrium for $[\text{Cu}_3]$ binding of ethylene in CDCl_3 solution	19
2.3 Ethylene loading of $[\text{Cu}_3]$ with pressure..	31
2.4 Isotherm data for the phase change of $[\text{Cu}_3]$ to $[\text{Cu}_2\cdot(\text{C}_2\text{H}_4)_2]$ under increasing ethylene pressure.....	32
2.5 Data from fitting the Claussius-Clapeyron equation to the phase change of $[\text{Cu}_3]$ to $[\text{Cu}_2\cdot(\text{C}_2\text{H}_4)_2]$ under increasing ethylene pressure	33
2.6 Isotherm data for $[\text{Cu}_3]$ binding of ethylene in the solid-state under 100.7 kPa of ethylene.....	34
2.7 Heat of equilibrium for $[\text{Cu}_3]$ binding of ethylene in the solid-state under 100.7 kPa of ethylene.....	35
2.8 Model parameters for $[\text{Cu}_3]$ binding of ethylene in the solid-state under generated from isotherm data above an ethylene pressure of 60 kPa	36
2.9 Aggregated ethylene chemisorption/desorption energies of the reversible $[\text{Cu}_3]$ to $[\text{Cu}_2\cdot(\text{C}_2\text{H}_4)_2]$ transformation, as determined by various experimental techniques	37
3.1 Selected bond distances (\AA) for $\text{Cu}_2(\mu\text{-}[3,5\text{-}(\text{CF}_3)_2\text{Pz}])_2(\text{EtC}\equiv\text{CEt})_2$ (1), $\text{Cu}_4(\mu\text{-}[3,5\text{-}(\text{CF}_3)_2\text{Pz}])_4(\mu\text{-EtC}\equiv\text{CEt})_2$ (2), $\text{Cu}_4(\mu\text{-}[3,5\text{-}(\text{CF}_3)_2\text{Pz}])_4(\mu\text{-MeC}\equiv\text{CMe})_2$ (3), and $\text{Cu}_4(\mu\text{-CF}_3\text{CO}_2)_4(\mu\text{-EtC}\equiv\text{CEt})_2$ (5).....	54
3.2 Selected bond angles ($^\circ$) for $\text{Cu}_2(\mu\text{-}[3,5\text{-}(\text{CF}_3)_2\text{Pz}])_2(\text{EtC}\equiv\text{CEt})_2$ (1), $\text{Cu}_4(\mu\text{-}[3,5\text{-}(\text{CF}_3)_2\text{Pz}])_4(\mu\text{-EtC}\equiv\text{CEt})_2$ (2), $\text{Cu}_4(\mu\text{-}[3,5\text{-}(\text{CF}_3)_2\text{Pz}])_4(\mu\text{-MeC}\equiv\text{CMe})_2$ (3), and $\text{Cu}_4(\mu\text{-CF}_3\text{CO}_2)_4(\mu\text{-EtC}\equiv\text{CEt})_2$ (5).....	55
3.3 Raman bands $\bar{\nu}_{\text{C}=\text{C}}$ of sample 1 , 2 , 3 , and free alkynes	63

3.4 NBO orbital descriptions for the C≡C of the adducts, Cu ₂ (μ-[3,5-(CF ₃) ₂ Pz]) ₂ (EtC≡CEt) ₂ (1) and Cu ₄ (μ-[3,5-(CF ₃) ₂ Pz]) ₄ (μ-EtC≡CEt) ₂ (2).....	65
3.5 Summary of photophysical parameters for all five complexes in this study for the solid state: Cu ₂ (μ-[3,5-(CF ₃) ₂ Pz]) ₂ (EtC≡CEt) ₂ (1), Cu ₄ (μ-[3,5-(CF ₃) ₂ Pz]) ₄ (μ-EtC≡CEt) ₂ (2), Cu ₄ (μ-[3,5-(CF ₃) ₂ Pz]) ₄ (μ-MeC≡CMe) ₂ (3), Cu ₂ (μ-CF ₃ CO ₂) ₂ (EtC≡CEt) ₂ (4) and Cu ₄ (μ-CF ₃ CO ₂) ₄ (μ-EtC≡CEt) ₂ (5).....	66
3.6 Summary of photophysical parameters for complexes 1-3 in frozen solutions (glassy benzene matrix) at 77 K.....	75
3.7 Computed excitation energies (eV) and oscillator strengths (<i>f</i>) for the optical transitions with <i>f</i> > 0.025 of the dinuclear complex Cu ₂ (μ-[3,5-(CF ₃) ₂ Pz]) ₂ (EtC≡CEt) ₂ (1) in the gas phase in terms of molecular orbitals involved in the excitations with percentages larger than 12%.....	78
3.8 Computed excitation energies (eV) and oscillator strengths (<i>f</i>) for the optical transitions with <i>f</i> > 0.01 of the 3-hexyne ligated tetranuclear complex Cu ₄ (μ-[3,5-(CF ₃) ₂ Pz]) ₄ (μ-EtC≡CEt) ₂ (2) in the gas phase in terms of molecular orbitals involved in the excitations with percentages larger than 12%.....	79
3.9 DFT-computed Cu-Cu distances, alkyne dihedral angles τ (C≡C...C≡C), and phosphorescence wavelengths (λ _{em}) for models of 1-3	84
3.10 DFT-computed excitation and emission wavelengths for complexes 1-3 upon varying the dihedral angles in the S ₀ ground and T ₁ excited states and their correlation with experimental photophysical data	85
3.11 Selected bond distances (Å) and angles (°) for Cu ₂ (μ-[3,5-(CF ₃) ₂ Pz]) ₂ (EtC≡CEt) ₂ (2), Cu ₄ (μ-[3,5-(CF ₃) ₂ Pz]) ₄ (μ-EtC≡CEt) ₂ (3), Cu ₄ (μ-[3,5-(CF ₃) ₂ Pz]) ₄ (μ-HC≡CH) ₂ (4), Cu ₂ (μ-[4-Br-3,5-(CF ₃) ₂ Pz]) ₂ (HC≡CH) ₂ (8), Cu ₂ (μ-[3,5-(CF ₃) ₂ Pz]) ₂ (HC≡CPh) ₂ (9), Cu ₂ (μ-[3,5-(CF ₃) ₂ Pz]) ₂ (HC≡C(CH ₂) ₅ C≡CH) (10), Cu ₄ (μ-[3,5-(CF ₃) ₂ Pz]) ₄ (HC≡C(CH ₂) ₄ C≡CH) ₂ (11), and Cu ₄ (μ-[3,5-(CF ₃) ₂ Pz]) ₄ (C ₂ H ₅ C≡C(CH ₂) ₄ C≡CC ₂ H ₅) ₂ (12)	105

3.12 Carboxylation of terminal alkynes using $\{\mu\text{-}[3,5\text{-(CF}_3)_2\text{Pz}]\text{Cu}\}_3$ (2 mol%) as the catalyst	116
3.13 Hydrothiolation of terminal alkynes using $\{\mu\text{-}[3,5\text{-(CF}_3)_2\text{Pz}]\text{Cu}\}_3$ (1 mol %) as the catalyst.....	121
4.1 Calculated bonding interaction energies (ΔE_{int}) and its derived terms ($\Delta E_{\text{Pauli}} + \Delta E_{\text{Estat}} + \Delta E_{\text{orb}} + \Delta E_{\text{disp}}$), along with their percent contribution	138
4.2 Selected bond distances (Å), bond angles (°) and CO stretching frequency (cm^{-1}) for $[\text{NEt}_4][\{[3,5\text{-(CF}_3)_2\text{Pz}]\text{Cu(CO)}\}_4(\mu_4\text{-Br})]$ (8), $[\text{NEt}_4][\{[3,5\text{-(CF}_3)_2\text{Pz}]\}_3\text{Cu}_2(\text{CO})_2]$ (9), $[\text{NEt}_4][\{[4\text{-Cl-}3,5\text{-(CF}_3)_2\text{Pz}]\text{Cu(CO)}\}_4(\mu_4\text{-Br})]$ (10) and $[\text{NEt}_4][\{[4\text{-Cl-}3,5\text{-(CF}_3)_2\text{Pz}]\text{Cu(CO)}\}_4(\mu_4\text{-Cl})]$ (11). X = Br or Cl	144
4.3 Vibrational and structural data for the calculated systems at the ZORA TZ2P/BP86-D3 level of theory.....	160

Chapter 1

Introduction

The choice of a bridging ligand is very important in the formation of a coordination complex. Our research work is based on the pyrazole ligand system. We are interested in this ligand system in particular because of its versatile and rich coordination chemistry, and also due to its ability to provide precise control of the environment at the metal centers via changes to the pyrazolyl ring substituents. This simple ligand system has been widely used in inorganic, bioinorganic, and organometallic chemistry.^{1,2} In this chapter, we will provide a brief introduction to the pyrazole ligand, the chemistry of coinage metal complexes supported by highly fluorinated pyrazole ligand, and its applications in various fields.

1.1 Pyrazole ligand

Pyrazoles are five-membered heterocyclic rings consisting of three carbon and two adjacent nitrogen atoms. These are well-known nitrogen donors and can behave as either monodentate or bidentate ligands after deprotonation of the N1-H group (Figure 1.1). One of the very attractive features of this ligand system is the ease of tunability. It is possible to change the electronic and the steric properties of the pyrazole by simply incorporating appropriate substituents in the 3-, 4- or 5-positions of the pyrazolyl moiety. The tunable nature at three possible sites is one of the major reasons for the widespread use of pyrazole ligand among chemists.

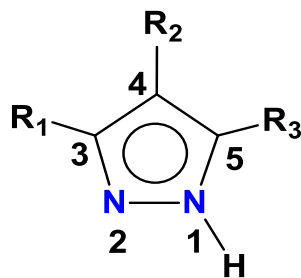


Figure 1.1 Pyrazole ligand

Pyrazoles upon deprotonation become pyrazolate ions, which can then coordinate to metal in several different ways including as a bridging ligand using both nitrogen donor sites. It has been used as ligand for most metals of the periodic table.³ One of the main research focuses in our laboratory is the synthesis and study of coinage metal complexes, and pyrazole plays an important role as a ligand in coinage metal chemistry. These ligands can strongly bind to coinage metal ions which are Cu(I), Ag(I), and Au(I) in neutral monodentate, anionic monodentate or *exo/endo*-bidentate fashion (Figure 1.2).⁴ Depending upon the reaction conditions and nature of substituents on the pyrazole ring, the complexes adopt various conformation ranging from monomers, dimers, trimers, tetramers, hexamers to polymers. The degree of aggregation can be controlled by tuning the substituents on the 3-, 4- and 5- positions of the pyrazole ring as well as the reaction conditions. For example, $[\text{Cu}(\text{Pz})]_n$ ^{3,4} is polymeric whereas $\{[3,5-(\text{CF}_3)_2\text{Pz}]\text{Ag}\}_3$,⁷ $\{[3,5-(t\text{-Bu})_2\text{Pz}]\text{Au}\}_4$,⁸ $\{[3,5-(\text{Ph})_2\text{Pz}]\text{Au}\}_6$ ⁹ adopt trimeric, tetrameric and hexameric structures respectively. The bridging mode of pyrazoles provides ligand assistance

to the metal center to be in close proximity to each other.¹⁰ However, in this study, we have focused only on the *exo*-bidentate mode of coordination as it allows the formation of multinuclear coinage metal complexes.

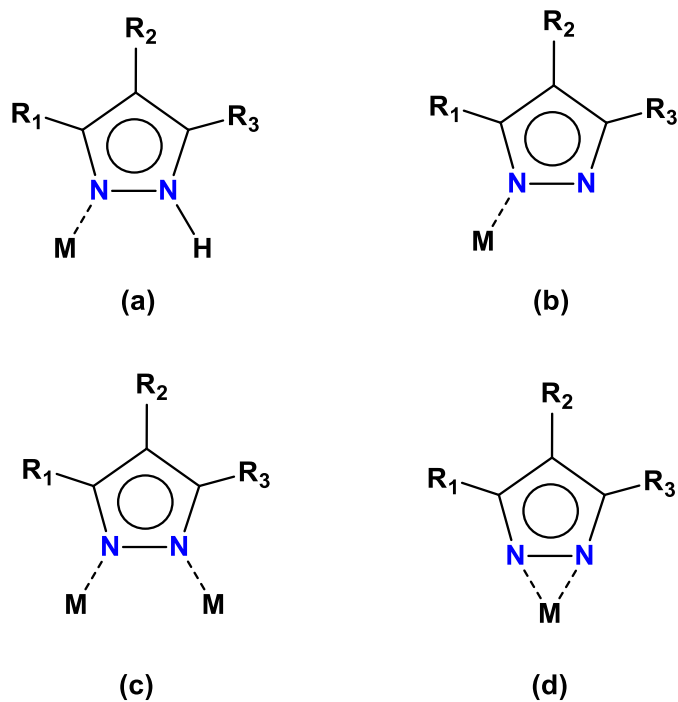


Figure 1.2 Coordination modes of the pyrazole ligand (a) neutral monodentate, (b) anionic monodentate, (c) *exo*-bidentate and (d) *endo*-bidentate

Search of the literature shows that most work with pyrazolate ligands has been limited to parent ligand, [Pz⁻], electron-rich alkyl (e.g., [3,5-(CH₃)₂Pz]⁻) or aryl-substituted (e.g., [3,5(Ph)₂Pz]⁻) pyrazolate ligands, and relatively very little is known about those with fluorine-containing substituents.⁷ It is well known that the presence of the C-F bond in an organic framework can significantly modify its

physico-chemical profile.¹¹ Thus, introduction of fluorinated substituents on the pyrazole ring makes it more electron-deficient, and also imparts interesting characteristics to the complexes to which they are attached, such as high oxidative resistance, relative inertness, fluorocarbon solubility,^{10,11} thermal stability, higher volatility, longer shelf life compared to their non-fluorinated analogs, and most importantly remarkable photophysical properties.¹⁴⁻¹⁶ Among the several pyrazolates used in our laboratory, $[3,5-(CF_3)_2Pz]^-$ is the most extensively studied. For our study we have dealt with many fluorinated pyrazole ligands, with CF_3 group on the 3- and 5- position and other substituents including H, CF_3 , Cl and Br on the 4- position of the pyrazolyl moiety.

1.2 Copper pyrazolates

As mentioned earlier, one of the main research areas in our laboratory is focused on the synthesis and study of coinage metal (Cu, Ag and Au) complexes of pyrazole ligand. We are interested in the copper pyrazolates in particular. Several copper pyrazolates were reported in the literature, with structures ranging from trimers to polymers with *exo*-bidentate co-ordination of the pyrazole ligand to the copper centers. For instance, several trimeric copper(I) pyrazolates such as $\{[3,5-(Me)_2Pz]Cu\}_3$,¹⁷ $\{[3,5-(Me)_2,4-(NO_2)Pz]Cu\}_3$,⁶ tetrameric copper(I) pyrazolates such as $[3-(i-Pr),5-(t-Bu)Pz]Cu\}_4$, $\{[3,5-(dcsb)_2Pz]Cu\}_4$ (dcsb = dicarbo-*sec*-butoxy)^{16,17} and the polymeric $[Cu(Pz)]_n$ ^{3,4}. However, in contrast to

these non-fluorinated analogs, copper complexes of fluorinated pyrazolates are surprisingly rare.³

In 2000, our group introduced a convenient synthetic route to synthesize a copper(I) complex containing a highly fluorinated pyrazolate, $\{[3,5-(\text{CF}_3)_2\text{Pz}]\text{Cu}\}_3$ ⁷ (Figure 1.3). This complex adopts a triangular conformation, containing a planar nine-membered metallo-cycle. Using a similar approach, synthetic routes for several other fluorinated trinuclear copper(I) pyrazolate

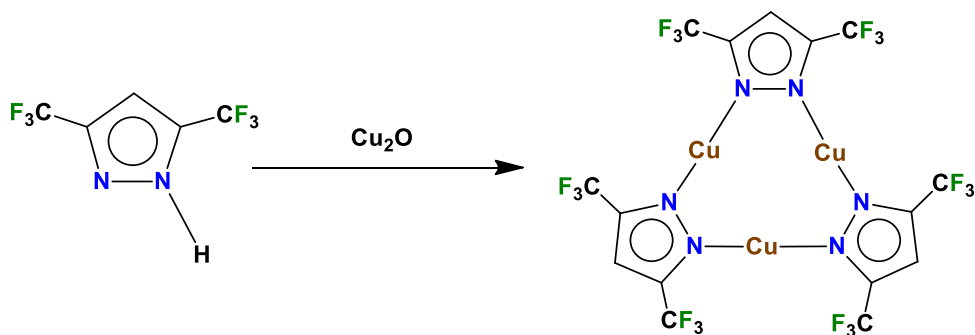


Figure 1.3. Trinuclear copper(I) pyrazolate complex, $\{[3,5-(\text{CF}_3)_2\text{Pz}]\text{Cu}\}_3$

complexes were reported by our group, those are, $\{[3-(\text{CF}_3)\text{Pz}]\text{Cu}\}_3$,¹⁵ $\{[3-(\text{CF}_3),5-(\text{Me})\text{Pz}]\text{Cu}\}_3$,¹⁵ $\{[3-(\text{CF}_3),5-(\text{Ph})\text{Pz}]\text{Cu}\}_3$,¹⁵ $\{[4-\text{Br},3,5-(\text{CF}_3)_2\text{Pz}]\text{Cu}\}_3$ ²⁰ and $\{[4-\text{Cl},3,5-(\text{CF}_3)_2\text{Pz}]\text{Cu}\}_3$ ²⁰. Photophysical properties,^{13,19,20} metallophilic bonding interactions,^{15,23,24} π -acceptor/ σ -donor interactions^{23,25,26} and dissociation-aggregation behavior^{27,28} of such complexes are of significant interest.

Previous studies done in our group show that most of these trinuclear copper(I) pyrazolates exhibit bright photoluminescence under UV light in the solid

state as well as in solution. This photoluminescence can be fine and coarse-tuned to multiple bright visible colors by varying the solvent, concentration, temperature, and excitation wavelength. For example, solid $\{[3,5-(\text{CF}_3)_2\text{Pz}]\text{Cu}\}_3$ exhibits bright orange color under UV light at room temperature, which changes to bright red at 110 K.¹⁵ This photoluminescent property makes the monovalent copper complexes containing fluorinated ligands potential candidates for emitting materials to be used in molecular light-emitting devices (MOLEDs) with predictable emission colors.

Another interesting factor that governs the trinuclear copper(I) complexes is their π -acceptor/ σ -donor nature. These electron-deficient complexes have an affinity for electron-rich environment. In the presence of a donor ligand (carbon, nitrogen, phosphorus or π -base) trimeric complexes readily react them. Thus, $\{[3,5-(\text{CF}_3)_2\text{Pz}]\text{Cu}\}_3$ also functions as excellent precursors to obtain various multinuclear complexes e.g., $\{[3,5-(\text{CF}_3)_2\text{Pz}]\text{Cu}(\text{PPh}_3)\}_2$,²⁹ $\{[3,5-(\text{CF}_3)_2\text{Pz}]\text{Cu}(2,4,6\text{-collidine})\}_2$,¹⁰, $\{[3,5-(\text{CF}_3)_2\text{Pz}]\text{Cu}(\text{Me}_2\text{bipy})\}_2$,³⁰ $\{[3,5-(\text{CF}_3)_2\text{Pz}]\text{Cu}(\text{Me}_2\text{phen})\}_2$,³⁰ $\{[3,5-(\text{CF}_3)_2\text{Pz}]\text{Cu}\}_3(\text{Naphthyridine})$,³⁰ $\{[3,5-(\text{CF}_3)_2\text{Pz}]_2\text{Cu}_2(\text{pyridazine})\}_2$,³⁰ $\{[3,5-(\text{CF}_3)_2\text{Pz}]\text{Cu}\}_3(\text{benzo}(c)\text{cinnoline})$ ³⁰. Moreover, it is also possible to tailor the desired product by simply tweaking the ratio of the reagents in the reaction mixture. For instance, $\{[3,5-(\text{CF}_3)_2\text{Pz}]\text{Cu}\}_3$ and bis(diphenylphosphino)methane (dppm) in 1:1.5 ratio forms a trinuclear cluster complex, $[\{3,5-(\text{CF}_3)_2\text{PzCu}\}_3((\text{PPh}_2)_2\text{CH}_2)]$ and in 1:3 molar ratio forms a dinuclear complex, $[\{3,5-(\text{CF}_3)_2\text{Pz}\}\text{Cu}\{(\text{PPh}_2)_2\text{CH}_2\}]_2$.^{31,32}

Considering all these fascinating properties of trinuclear copper(I) pyrazolates, we proposed to synthesize and isolate several unique complexes of copper with alkene, alkynes and carbon monoxide from the copper trimers, and study their coordination chemistry. The alkene and alkynes we utilized for this study are ethylene, 2-butyne, 3-hexyne, acetylene, phenylacetylene, 1,8-Nonadiyne, 1,7-Octadiyne and 3,9-Dodecadiyne. These ligands coordinate to the metal center based on the concept of the Dewar-Chatt-Duncanson Model (Figure 1.4).

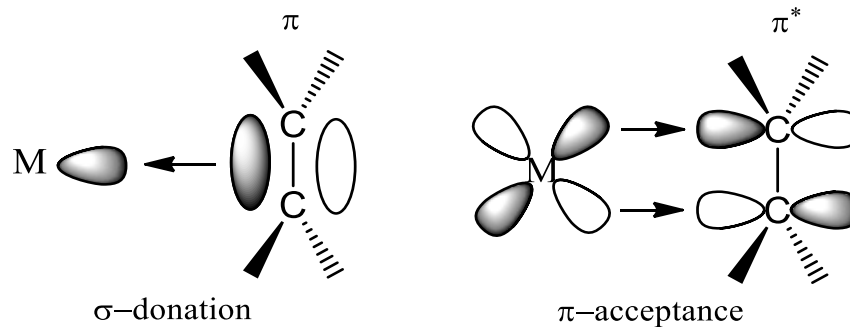


Figure 1.4 Dewar-Chatt-Duncanson (DCD) Model.

The synthesized complexes are employed for different applications including olefin/paraffin separation, small-molecule sensing based on photoluminescence and catalytic alkyne transformations. With alkenes, copper trimer undergoes very beneficial bonding and structural transformation phenomenon. As discussed in chapter 2, detailed study of these properties showed that these synthesized copper complexes can be effectively used for efficient

olefin/paraffin separation technology. We have also synthesized several multinuclear copper-alkyne complexes supported by highly fluorinated pyrazolate ligands, using 3-hexyne and 2-butyne. These complexes show fascinating photoluminescence property, which is studied in detail in chapter 3. Also described in chapter 3 is the synthesis and isolation of another group of copper-alkyne complexes. These are the copper pyrazolate complexes with acetylene and terminal alkynes. Some of these are utilized as reaction intermediates in catalytic alkyne transformation. Chapter 4 covers the synthesis and isolation of several rare multinuclear copper-CO complexes. Chapter 5 is devoted to the experimental details (and some additional information) of the complexes synthesized throughout the research work, Appendix A-C includes the spectroscopic data i.e. NMR, IR and Raman data of chapter 2, 3 and 4 respectively. Further details about the research work can be found in the related chapters herein.

Chapter 2

Selective adsorption of ethylene using copper(I) pyrazolate complex

Naleen B. Jayaratna, Matthew G. Cowan, Devaborniny Parasar, Hans H. Funke,
Joseph Reibenspies, Pavel K. Mykhailiuk, Oleksii Artamonov, Richard D. Noble,

H. V. Rasika Dias

(Part of this work has been published in *Angew. Chem. Int. Ed.* 2018, 57, 16442 –
16446)

Reproduced from references³³ with permission from the © 2018 Wiley-VCH
Verlag GmbH & Co. KGaA, Weinheim

2.1 Abstract

The trinuclear copper(I) pyrazolate complex [**Cu**₃] rearranges to the dinuclear analogue [**Cu**₂•(C₂H₄)₂] when exposed to ethylene gas. Remarkably, the [**Cu**₃]↔[**Cu**₂•(C₂H₄)₂] rearrangement occurs reversibly in the solid state. Furthermore, this transformation emulates solution chemistry. The bond-making and breaking processes associated with the rearrangement in the solid-state results in an observed heat of adsorption ($-13 \pm 1 \text{ kJ mol}^{-1}$ per Cu–C₂H₄ interaction) significantly lower than other Cu–C₂H₄ interactions ($\geq -24 \text{ kJ mol}^{-1}$). The low overall heat of adsorption, ‘step’ isotherms, high ethylene capacity (2.76 mmol g⁻¹; 7.6 wt % at 293 K), and high ethylene/ethane selectivity (136:1 at 293 K) make [**Cu**₃] an interesting basis for the rational design of materials for low-energy ethylene/ethane separations.

2.2 Introduction

Ethylene and propylene gases are the most-produced organic chemicals in the world, with their purification costs accounting for ca. 0.3% of the world’s total energy consumption.³⁴ The high energy costs are driven by the use of cryogenic distillation, which could be supplemented or replaced by lower-energy process such as membrane separation³⁵⁻³⁷ or swing adsorption.³⁸⁻⁴⁰ In the recent times there has been considerable interest in developing materials for both technologies.⁴¹⁻⁴⁶

Adsorbent materials show either kinetic or thermodynamic selectivity for adsorbing components of a gas mixture, and are used in pressure (PSA) and temperature swing adsorption (TSA) processes to produce high-purity gases. Key parameters for adsorbent materials include heat of adsorption, working-capacity, selectivity, sorption kinetics, and tolerance to contaminants.⁴⁷

Heat of adsorption directly affects the heating and cooling energy required to control adsorbent temperature during PSA cycles and control the swing energy required for a TSA process. In 2014, a solid to liquid phase change ($\Delta H_{\text{melt}} < 19.9$ kJ mol⁻¹) was combined with CO₂ chemisorption (ca. -52 kJ mol⁻¹) and noted for significantly reducing of the overall heat of adsorption.⁴⁸ A process design taking advantage of the lower overall heat of adsorption showed 55% energy savings compared to standard monoethanolamine (MEA) scrubbing technology.⁴⁹ In 2015, the idea was applied to the well-known phenomena of ‘gate-opening’ phase changes in metal-organic frameworks,⁵⁰ termed ‘intrinsic heat management’, and shown to reduce energy released by methane adsorption by 28% compared to a calculated ‘rigid’ analogue.⁵¹

During the investigation of adsorbents for ethylene/ethane separations, we discovered that exposing the highly fluorinated copper(I) complex [(3,4,5-(CF₃)₃Pz)Cu]₃ ([**Cu**₃], 3,4,5-(CF₃)₃Pz = 3,4,5-tris(trifluoromethyl)pyrazolyl) to ethylene gas drives a reversible solid-state transformation to [(3,4,5-(CF₃)₃Pz)Cu(C₂H₄)]₂ ([**Cu**₂•(C₂H₄)₂]). Herein we discuss the benefits of this

transformation on gas uptake properties relevant to swing adsorption processes, and suggest that using endothermic structural rearrangements to balance the heat of adsorption could produce net adiabatic or endothermic adsorbent materials.

2.3 Results

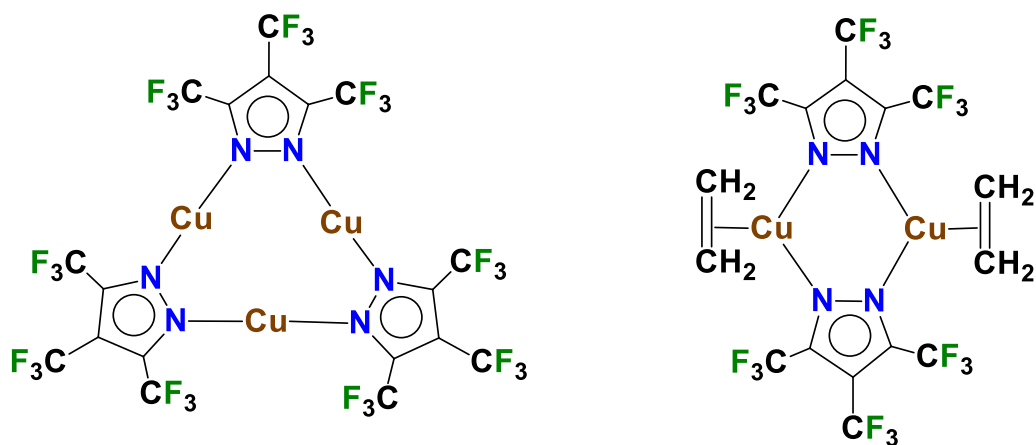


Figure 2.1 Structures of $[(3,4,5-(CF_3)_3Pz)Cu]_3$, $[Cu_3]$ (left) and $[(3,4,5-(CF_3)_3Pz)Cu(C_2H_4)]_2$, $[Cu_2 \cdot (C_2H_4)_2]$ (right).

The copper(I) complex $[Cu_3]$ (Figure 2.1) is an air stable white solid prepared by reacting copper(I) oxide with 3,4,5- $(CF_3)_3PzH$ ⁵² in a solvent free process, followed by extraction with dichloromethane. Copper(I) complexes are often sensitive to oxygen and moisture, however the very high fluorine content (51% mass content or the 50% atom count) of $[Cu_3]$ appears to make the compound hydrophobic and resistant to oxidation. $[Cu_3]$ was characterized by ¹⁹F and ¹³C NMR and Raman spectroscopy, and by single crystal and powder XRD (SCXRD

and PXRD). Crystals suitable for X ray structure determination were obtained via evaporation of a CS₂ solution.

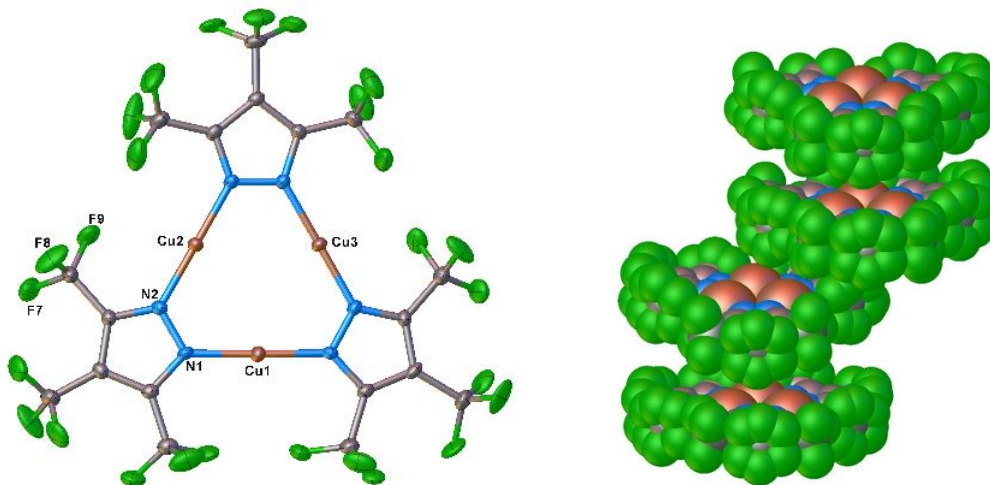


Figure 2.2 Molecular structures of [(3,4,5-(CF₃)₃Pz)Cu]₃, [**Cu₃**] (top) and illustration showing packing of four molecules of [**Cu₃**] (bottom).

The molecular structure of [**Cu₃**] is illustrated in Figure 2.2. The [**Cu₃**] core consists of three copper atoms bridged by three pyrazolyl groups, forming a planar nine membered Cu₃N₆ ring as observed in copper pyrazolates such as [(3,5-(CF₃)₂Pz)Cu]₃. However, in contrast to [(3,5-(CF₃)₂Pz)Cu]₃ which forms columnar structures of zigzag Cu₃N₆ rings and somewhat close inter-trimer Cu•••Cu contacts,^{15,23,53} [**Cu₃**] crystallizes as discrete molecules with no inter-trimer Cu atoms at a close distance (the closest inter-trimer Cu•••Cu distance is at 5.17 Å, which is much longer than the van der Waals separation of copper atoms, 2.80 Å). There are however somewhat close inter-molecular Cu•••F contacts (closest at 3.06

Å) found in $[\mathbf{Cu}_3]$ (sum of Bondi's van der Waals radii of copper and fluorine is 2.87 Å).

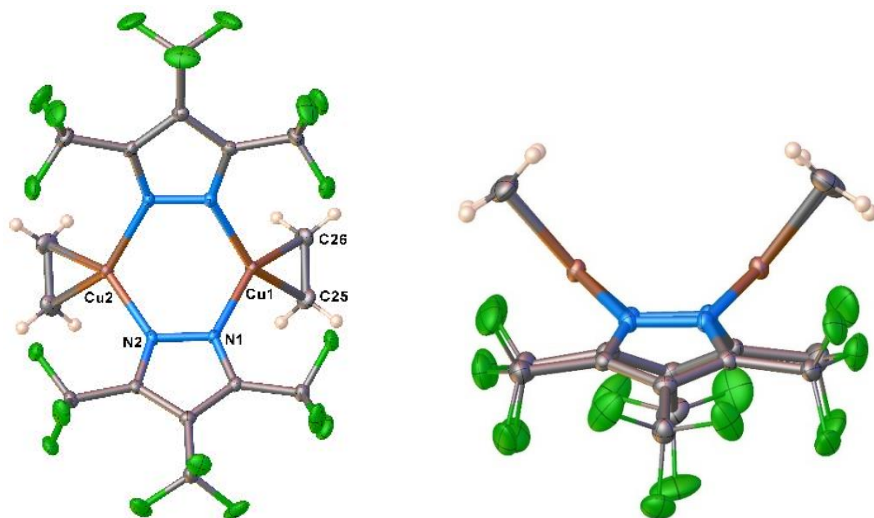


Figure 2.3 Molecular structures of $[(3,4,5-(\text{CF}_3)_3\text{Pz})\text{Cu}(\text{C}_2\text{H}_4)]_2$, $[\mathbf{Cu}_2\bullet(\text{C}_2\text{H}_4)_2]$; a view showing boat shaped Cu_2N_4 core of $[\mathbf{Cu}_2\bullet(\text{C}_2\text{H}_4)_2]$.

$[\mathbf{Cu}_3]$ upon reaction with ethylene gives $[\mathbf{Cu}_2\bullet(\text{C}_2\text{H}_4)_2]$ (Figure 2.1). Crystals of the dinuclear copper(I)-ethylene complex $[\mathbf{Cu}_2\bullet(\text{C}_2\text{H}_4)_2]$ were prepared by treating a dichloromethane solution of $[\mathbf{Cu}_3]$ with ethylene gas, and SCXRD revealed the structural transformation and coordination of ethylene (Figure 2.3). $[\mathbf{Cu}_2\bullet(\text{C}_2\text{H}_4)_2]$ molecules are dinuclear species with a boat shaped Cu_2N_4 metallacycles. The X-ray crystal structures of $[\mathbf{Cu}_3]$ and $[\mathbf{Cu}_2\bullet(\text{C}_2\text{H}_4)_2]$ show that they are dense solids with no internal pore volume. Copper atoms adopt trigonal planar geometry, and ethylene moieties coordinate to the copper ion in a typical η^2 fashion. The coordination of ethylene was also directly observed by Raman

spectroscopy (Figures 2.4). Signals corresponding to coordinated ethylene are prominently observed at 1544, 1280 and 960 cm^{-1} (spectrum in blue color).⁵⁴ Fine structure between 1100-1200 cm^{-1} also changes considerably from $[\text{Cu}_3]$ (red) to $[\text{Cu}_2\cdot(\text{C}_2\text{H}_4)_2]$ (blue) upon ethylene coordination.

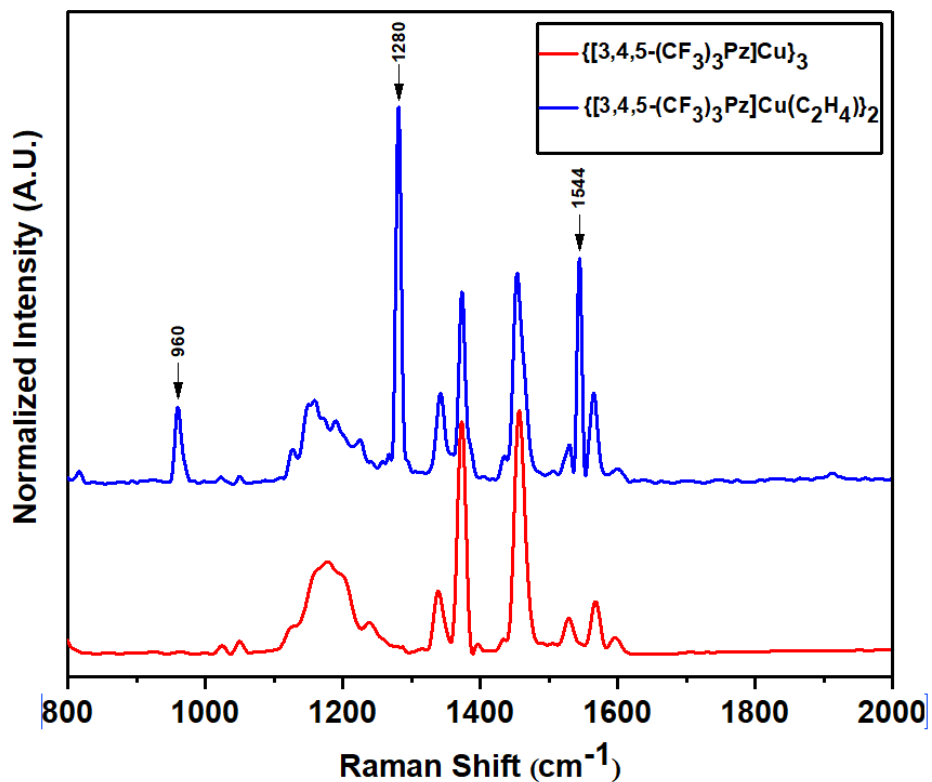


Figure 2.4 Raman data for $[\text{Cu}_3]$ (red) and $[\text{Cu}_2\cdot(\text{C}_2\text{H}_4)_2]$ (blue) generated from exposure to ethylene in solution.

¹H and ¹⁹F NMR spectra of $[\text{Cu}_2\cdot(\text{C}_2\text{H}_4)_2]$ in CDCl_3 at room temperature indicate that in addition to $[\text{Cu}_2\cdot(\text{C}_2\text{H}_4)_2]$, free ethylene and $[\text{Cu}_3]$ are also present

in solution, suggesting partial dissociation of the copper-ethylene adduct forming its precursors. Proton signals due to free and copper bound ethylene appear as separate but broad signals indicating an exchange process on the NMR time scale. A variable temperature NMR study was performed to determine the equilibrium energy involved in ethylene binding in solution. This study was based on relative concentrations of C_2H_4 , $[\text{Cu}_2\cdot(\text{C}_2\text{H}_4)_2]$, and $[\text{Cu}_3]$ in CDCl_3 solution at temperatures between 35 and -30 °C. The concentrations of each species were related through ^1H and ^{19}F NMR (Figure 2.7 and 2.8), i.e. ^1H quantifies the ratio of $[\text{Cu}_2\cdot(\text{C}_2\text{H}_4)_2]$ and free C_2H_4 , and ^{19}F NMR quantifies the ratio of $[\text{Cu}_2\cdot(\text{C}_2\text{H}_4)_2]$ and $[\text{Cu}_3]$, as given in Table 2.1. Peak integrals were combined with the equilibrium expression (Equation 1 and Figure 2.5). The heat of reaction was estimated using Van't Hoff analysis (Equation 2 and Figure 2.6) which gave an $\text{Cu}-\text{C}_2\text{H}_4$ binding energy of $-28.5 \text{ kJ}\cdot\text{mol}^{-1}$ (Table 2.2), a significantly smaller value than the $-41 \text{ kJ}\cdot\text{mol}^{-1}$ reported for ligand exchange in a CuI di-imine complex.⁵⁵ We attribute the difference in ethylene coordination energies to energies associated with accompanying transformation of trinuclear $[\text{Cu}_3]$ to dinuclear $[\text{Cu}_2\cdot(\text{C}_2\text{H}_4)_2]$ species. Likewise, the entropy change is ca. half ($-96 \text{ J mol}^{-1} \text{ K}^{-1}$ vs. $-200 \text{ J mol}^{-1} \text{ K}^{-1}$). It makes sense to correlate these observations to the structure rearrangement of $[\text{Cu}_3]$ to $[\text{Cu}_2\cdot(\text{C}_2\text{H}_4)_2]$.

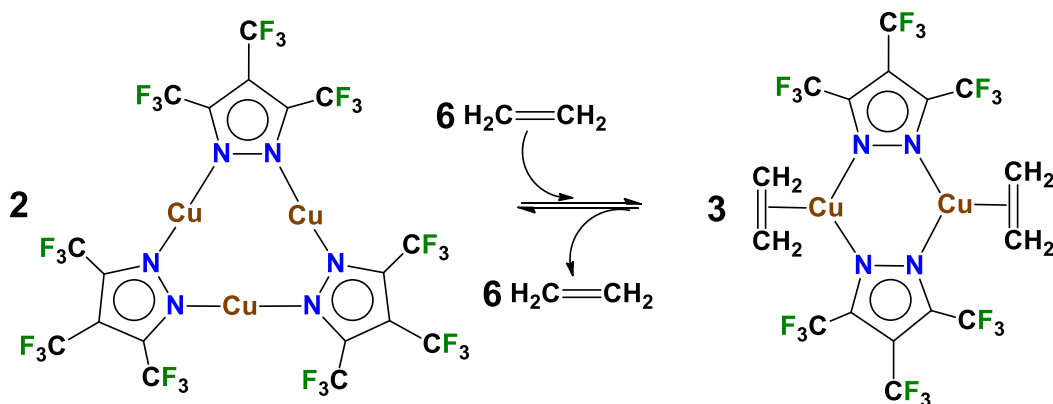
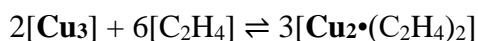


Figure 2.5 Structural representation of equilibrium equation of ethylene binding.



$$K = \frac{[\text{Cu}_2 \cdot (\text{C}_2\text{H}_4)_2]^3}{[\text{Cu}_3]^2 [\text{C}_2\text{H}_4]^6} \quad \text{eq. 1}$$

Equation 1

Equilibrium equation used for binding of ethylene in CDCl_3 solution.

$$\ln(K) = \frac{-\Delta H}{RT} + \frac{\Delta S}{R} \quad \text{eq. 2}$$

Equation. 2

Equation used for the Van't Hoff analysis where K = the equilibrium constant for the reversible reaction shown above; ΔH = change in enthalpy (J mol^{-1}); ΔS = change in entropy ($\text{J mol}^{-1} \text{K}^{-1}$); R = the gas constant ($\text{J mol}^{-1} \text{K}^{-1}$); T = temperature (K).

Table 2.1 ^1H and ^{19}F NMR data for $[\text{Cu}_3]$ binding of ethylene in CDCl_3 solution.

Temperature (K)	^1H NMR Integrals		^{19}F NMR Intergrals		K	ln(K)	1/T
	Ethylene	$[\text{Cu}_2\cdot(\text{C}_2\text{H}_4)_2]$	$[\text{Cu}_2\cdot(\text{C}_2\text{H}_4)_2]$	$[\text{Cu}_3]$			
243	0.12	1	1	0.64	817622	13.6	0.00411
263	0.19	1	1	0.82	31612	10.4	0.00380
283	0.4	1	1	1.26	154	5.04	0.00353
294	0.9	1	1	1.33	1.07	0.0618	0.00340
308	1.5	1	1	2.37	0.0156	-4.16	0.00325

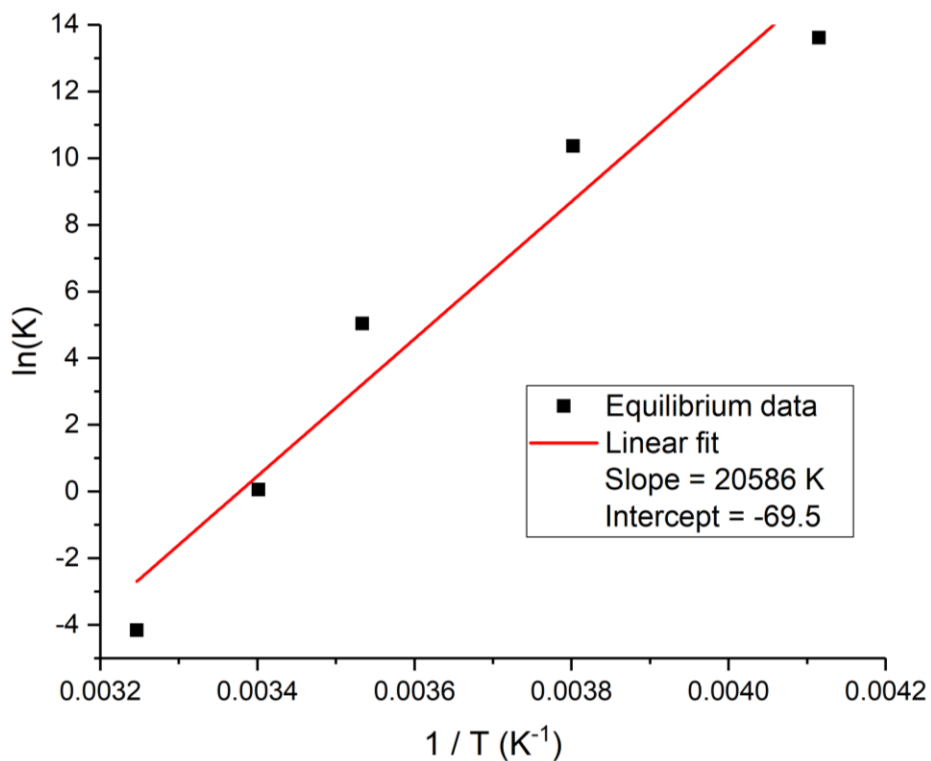


Figure 2.6 Van't Hoff plot for [Cu₃] binding of ethylene in CDCl₃ solution.

Table 2.2 Heat of equilibrium for [Cu₃] binding of ethylene in CDCl₃ solution.

	ΔH (kJ mol ⁻¹)	ΔS (J mol ⁻¹ K ⁻¹)
Overall equilibrium	-171±45	-578±1
Per [Cu₃] unit	-86±24	-289±1
Per Cu–C₂H₄ interaction	-28±8	-96±1

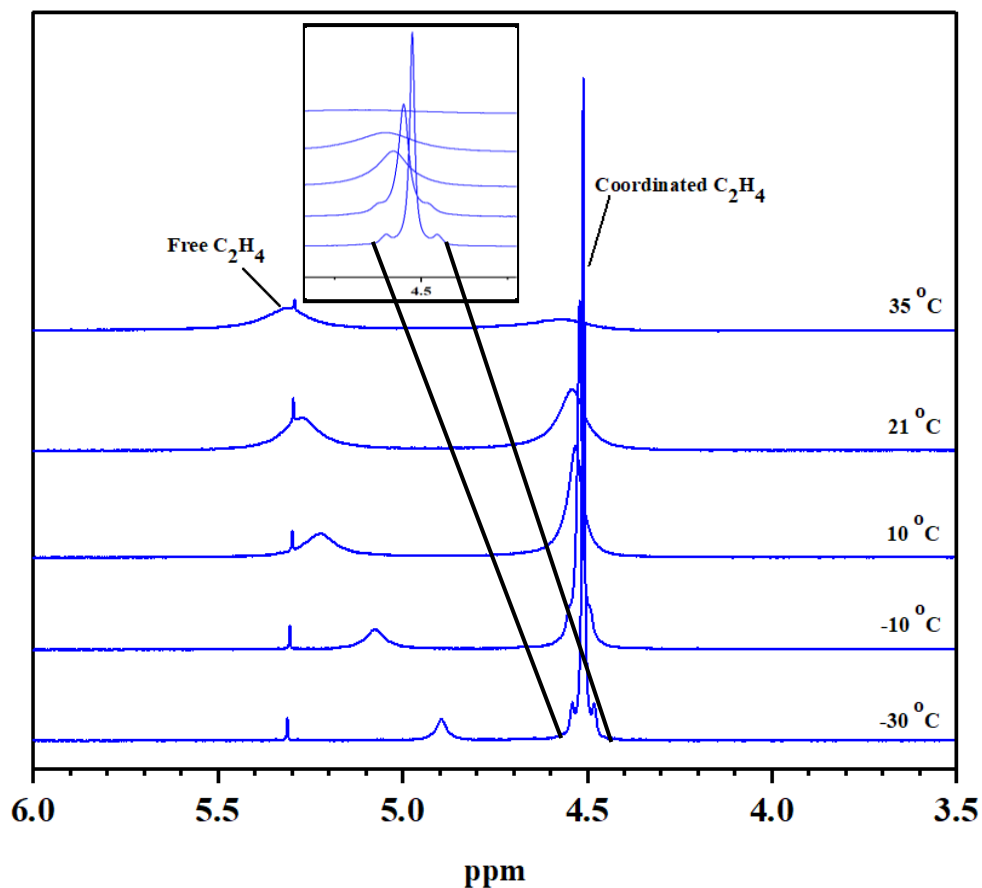


Figure 2.7 ^1H NMR spectra of $[\text{Cu}_2\bullet(\text{C}_2\text{H}_4)_2]$ at various temperatures. This spectrum also shows presence of free ethylene resulting from the disproportionation of $[\text{Cu}_2\bullet(\text{C}_2\text{H}_4)_2]$ to $[\text{Cu}_3]$ and free ethylene. Peak at 4.51 ppm ($-30\text{ }^\circ\text{C}$) is the signal corresponding to coordinated ethylene while 4.89 ppm peak is the signal of free ethylene in equilibrium with $[\text{Cu}_2\bullet(\text{C}_2\text{H}_4)_2]$ and $[\text{Cu}_3]$.

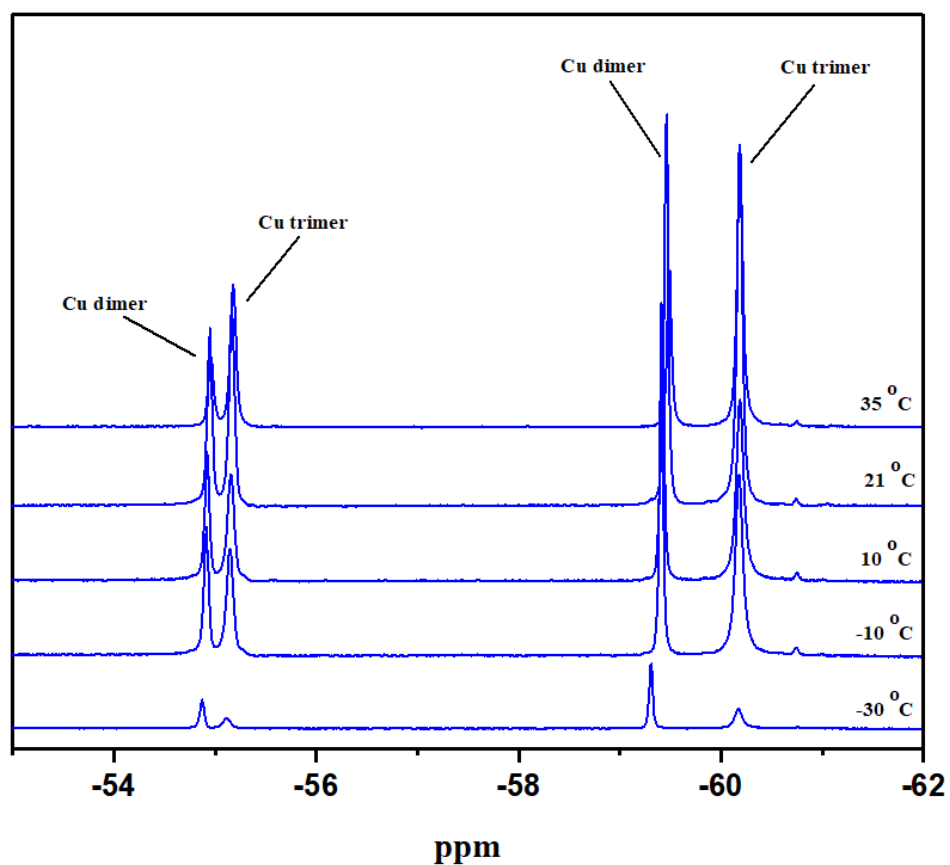


Figure 2.8 ^{19}F NMR spectra of $[\text{Cu}_2\bullet(\text{C}_2\text{H}_4)_2]$ at various temperatures. This spectrum also shows presence of $[\text{Cu}_3]$ (labelled as Cu trimer) resulting from the disproportionation of $[\text{Cu}_2\bullet(\text{C}_2\text{H}_4)_2]$ to $[\text{Cu}_3]$ and free ethylene. Peaks at -54.87 and -59.31 ppm (-30 °C) are the signals corresponding to $[\text{Cu}_2\bullet(\text{C}_2\text{H}_4)_2]$ while peaks at -55.11 and -60.17 ppm correspond to $[\text{Cu}_3]$.

Remarkably, the dinuclear $[\text{Cu}_2\bullet(\text{C}_2\text{H}_4)_2]$ complex could also be prepared in the solid-state by treating solid $[\text{Cu}_3]$ with ethylene gas (discussed in details later, shown in Figure 2.15). Furthermore, it is possible to remove ethylene from solid

$[\text{Cu}_2\cdot(\text{C}_2\text{H}_4)_2]$ to re-generate $[\text{Cu}_3]$ using temperature, as demonstrated by thermal gravimetric analysis (TGA, Figure 2.9) and differential scanning calorimetry (DSC). The TGA results show that $[\text{Cu}_2\cdot(\text{C}_2\text{H}_4)_2]$ starts losing ethylene molecule (loses 2 moles of ethylene) beginning at approximately 50°C , and rate of ethylene loss increases with the increase in temperature finally leaving only $[\text{Cu}_3]$.

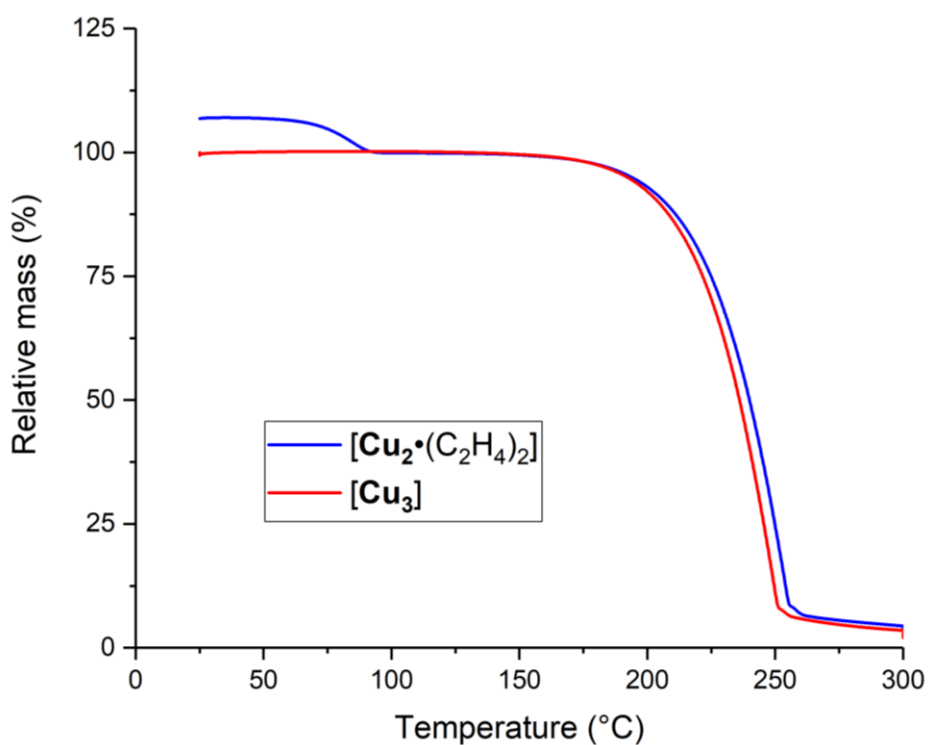


Figure 2.9 TGA data for $[\text{Cu}_2\cdot(\text{C}_2\text{H}_4)_2]$ (blue) and $[\text{Cu}_3]$ (red) using the mass at 125°C as the reference for the relative mass calculation.

DSC was used to investigate the energies involved in the ethylene desorption process and its associated phase change. The melt and solidification energy of $[\text{Cu}_3]$ is $23.8\text{--}24.3\text{ kJ mol}^{-1}$ (Figure 2.10). The DSC scan of $[\text{Cu}_2\cdot(\text{C}_2\text{H}_4)_2]$

reveals that several endothermic processes takes place at 100-130 °C (Figure 2.11) with total energy of 60.9 kJ mol^{-1} ($20.4+28.3+10.4+1.8 = 60.9 \text{ kJ mol}^{-1}$; associated with the combination of melting and ethylene desorption). Subtracting the average [Cu₃] melt energy of 24.5 kJ mol^{-1} (24.3, 23.8, 26.0, 23.9 kJ mol^{-1} ; average melt 24.5 kJ mol^{-1}), Figure 2.10, 2.11 and 2.12, from the desorption process gives an ethylene desorption energy of 36.4 kJ mol^{-1} per [Cu₃] unit (i.e., approximately equal to the -38 kJ mol^{-1} heat of adsorption determined from the ethylene adsorption isotherms), which is equivalent to a heat of adsorption of $-13.1 \text{ kJ mol}^{-1}$ per Cu–C₂H₄ interaction (considering that [Cu₃] absorbs 2.76 moles of ethylene in the solid state). The lowest measured Cu–C₂H₄ interactions we have identified from the literature is -24 kJ mol^{-1} .⁵⁶ The second DSC cycle of the same sample shows no further gas desorption, indicating complete conversion of [Cu₂•(C₂H₄)₂] to [Cu₃] (i.e. release of all adsorbed ethylene). This overcomes the slow desorption kinetics observed for pressure swing and positions [Cu₃] as a potential adsorbent for a TSA process.

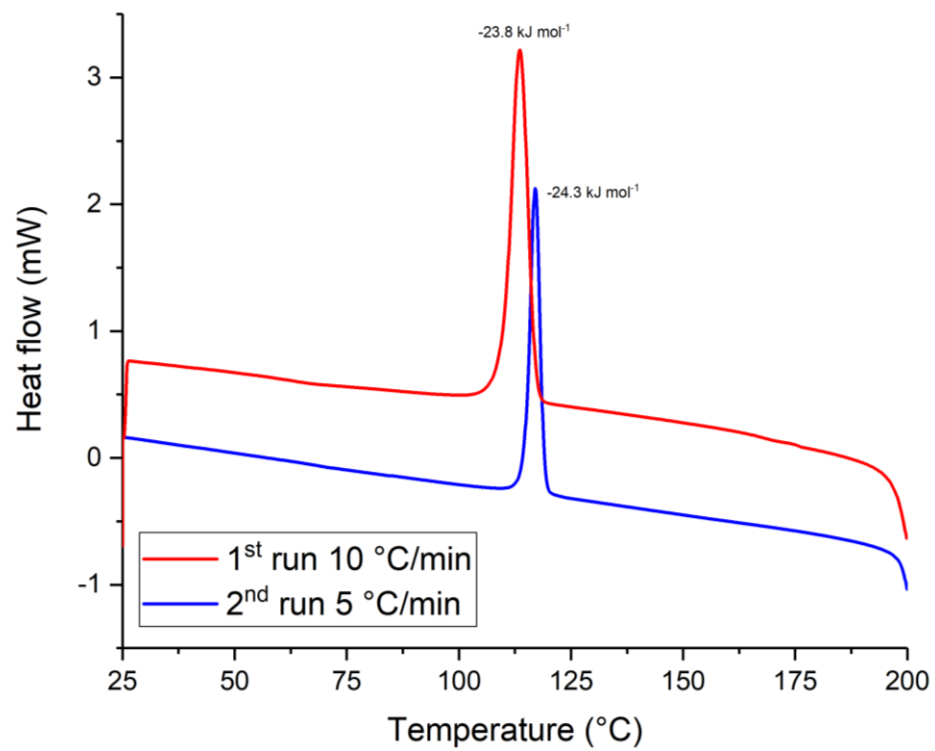


Figure 2.10 DSC cooling data for [Cu₃]. Note: mol⁻¹ refers to mole of [Cu₃].

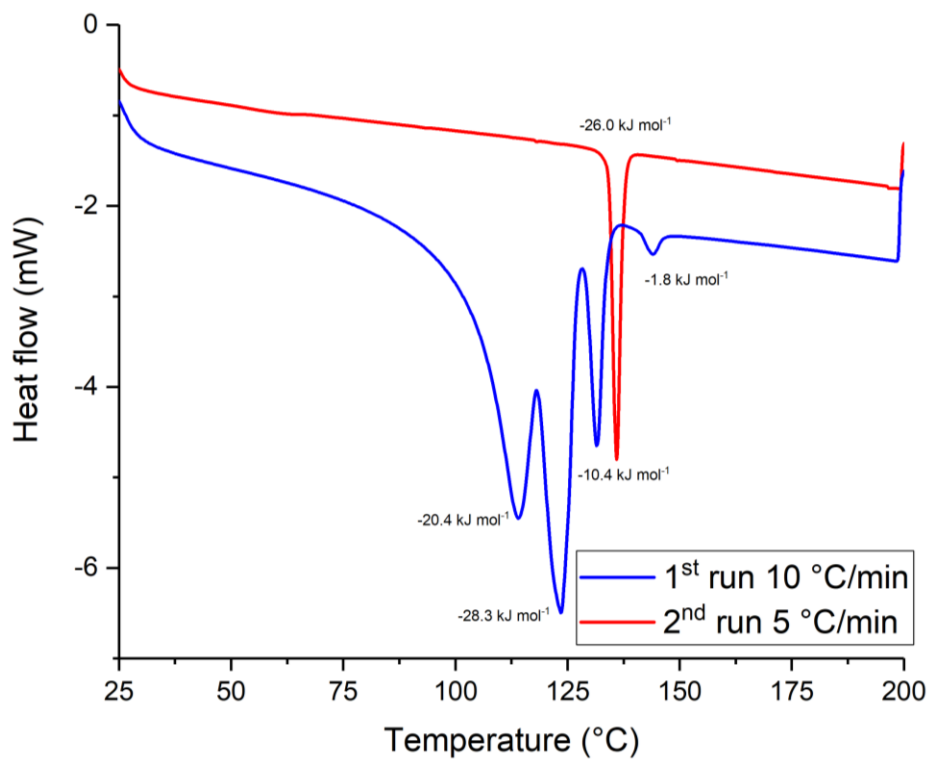


Figure 2.11 DSC heating data for $[\text{Cu}_2\bullet(\text{C}_2\text{H}_4)_2]$, which converts to $[\text{Cu}_3]$ during the first cycle. Note: mol^{-1} refers to mole of $[\text{Cu}_3]$ equivalents.

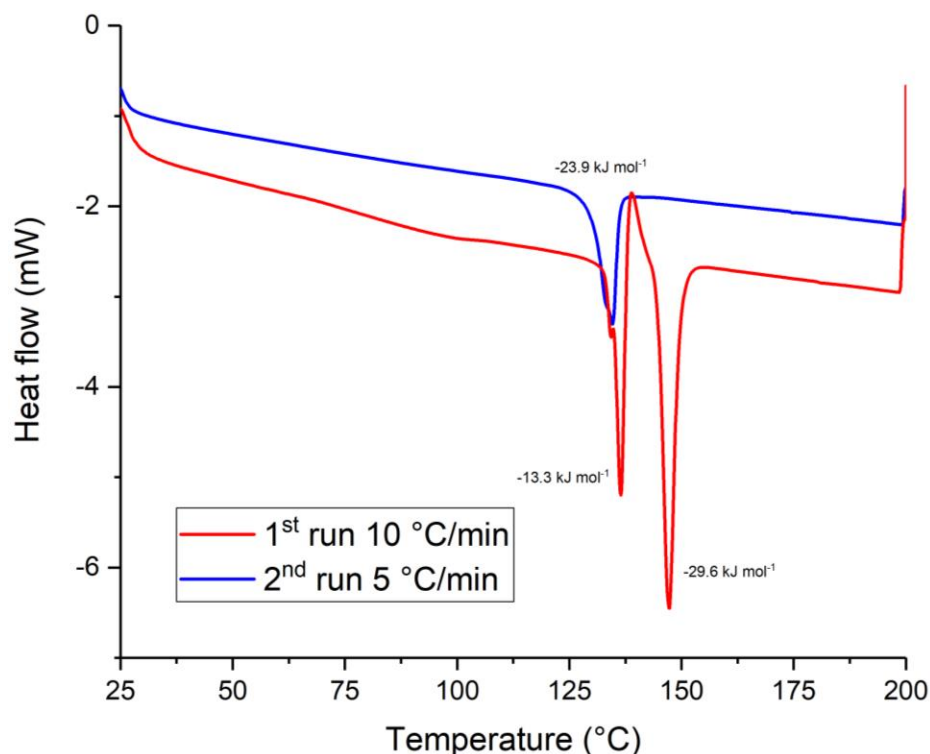


Figure 2.12 DSC heating data for [Cu₃], note: the first cycle includes energy from unifying distinct crystal populations within the sample.⁵⁷ Note: mol⁻¹ refers to mole of [Cu₃].

It is also possible to remove ethylene from solid [Cu₂•(C₂H₄)₂] to regenerate [Cu₃] using vacuum as demonstrated through Raman spectroscopy (Figure 2.13) and repeated gas adsorption isotherms (Figure 2.16, discussed in details later). As discussed earlier, signals corresponding to coordinated ethylene are observed at 1544, 1280, 960 cm⁻¹, and in between 1100-1200 cm⁻¹ (depicted in blue in Figure 2.13). Upon exposure to vacuum at 60 °C these peaks disappear, and the sample returns to the previous state, [Cu₃] (depicted in green in Figure 2.13).

These results demonstrate the reversible transitions between $[\text{Cu}_3]$ and $[\text{Cu}_2\cdot(\text{C}_2\text{H}_4)_2]$.

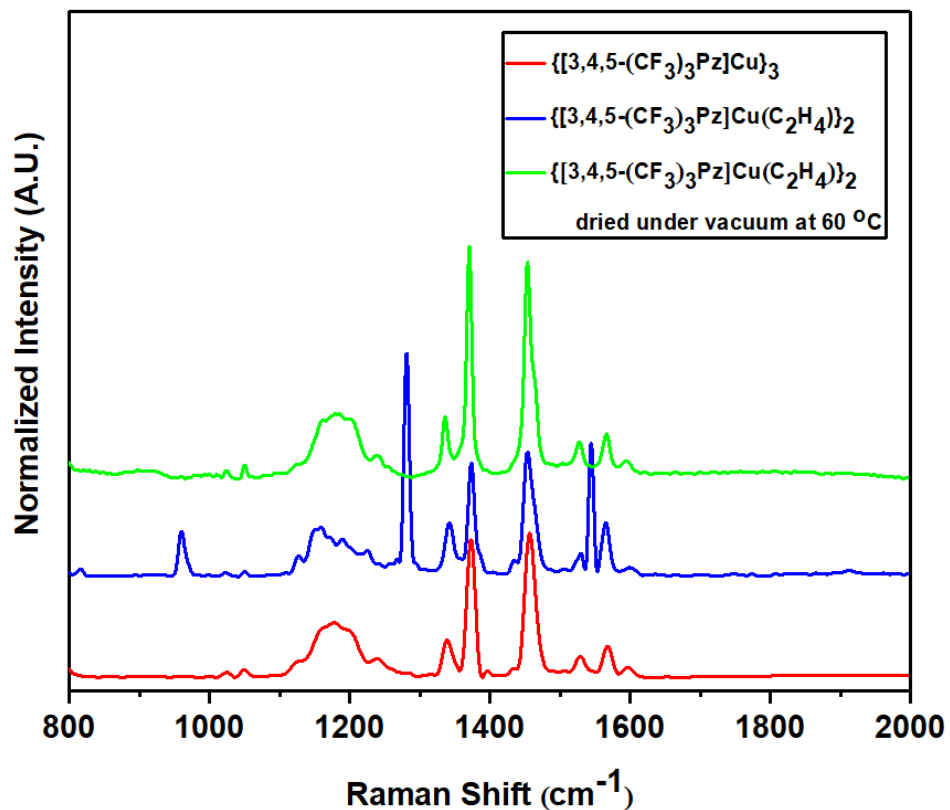


Figure 2.13 Raman data for $[\text{Cu}_3]$ (red), $[\text{Cu}_2\cdot(\text{C}_2\text{H}_4)]$ (blue) generated from exposure to ethylene in solution, and $[\text{Cu}_3]$ (green) produced by placing $[\text{Cu}_2\cdot(\text{C}_2\text{H}_4)]$ under vacuum at 60 °C.

This unprecedented, fully reversible and major solid-state structural rearrangement of $[\text{Cu}_3] \leftrightarrow [\text{Cu}_2\cdot(\text{C}_2\text{H}_4)_2]$ was confirmed through comparison of experimental and simulated PXRD (Figure 2.14 and 2.15, discussed in detail in

Section 5.2.2 of chapter 5). These “Teflon lined” adducts contain heavily fluorinated peripheries and weakly coordinating pyrazolates.⁵⁸ Materials containing C-F bonds are known to have low intermolecular dispersion interactions^{59,60} and produce porous materials that undergo small structural changes in response to increasing pressure.^{61,62} It is possible that the high degree of fluorination of [**Cu**₃] provides a local “fluorocarbon” medium and weak Cu-N interactions to facilitate this interesting solid-state transformation.

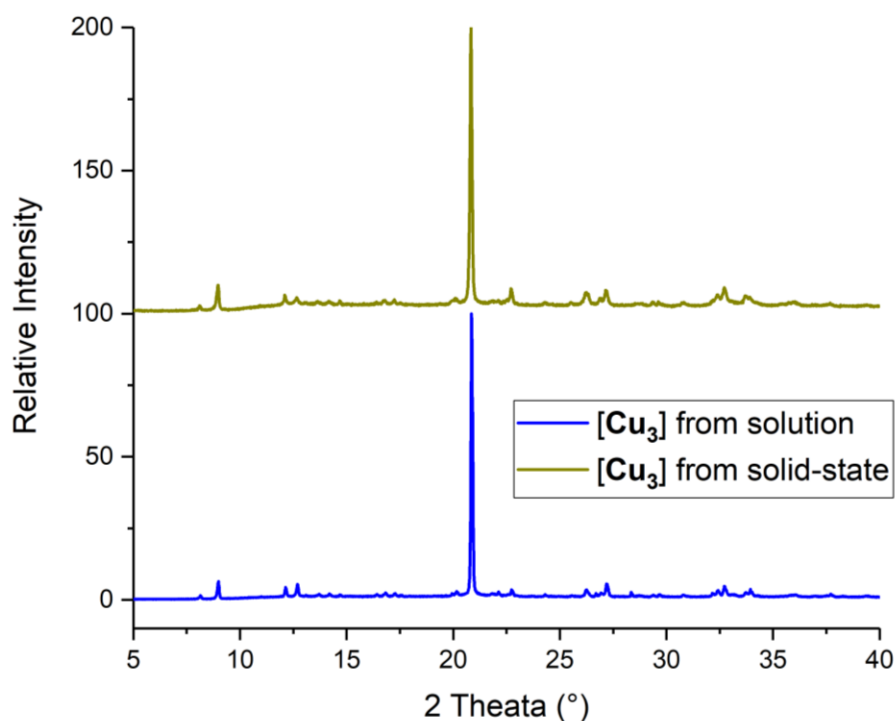


Figure 2.14 Comparison of experimental PXRD patterns of [**Cu**₃] prepared from solution (blue) and [**Cu**₃] prepared by placing solid [**Cu**₂•(C₂H₄)₂] under vacuum at 60 °C for 6 hours (olive green).

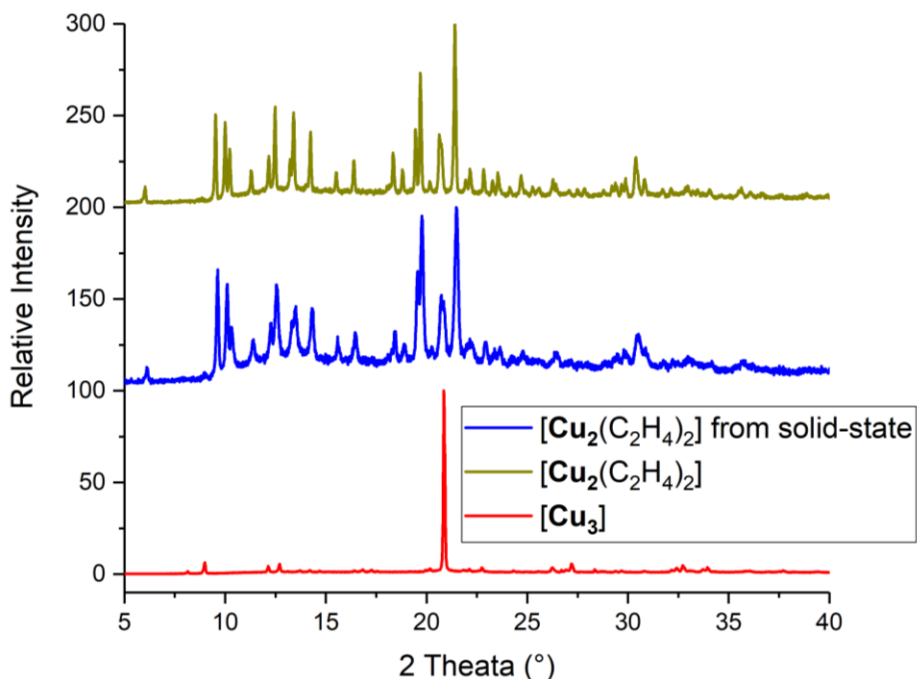


Figure 2.15 Comparison of experimental PXRD patterns of $[\text{Cu}_3]$ (red), $[\text{Cu}_2 \cdot (\text{C}_2\text{H}_4)_2]$ produced via the solution method (olive green), and $[\text{Cu}_2 \cdot (\text{C}_2\text{H}_4)_2]$ produced by treating $[\text{Cu}_3]$ with ethylene gas in the solid state (blue). In the latter case, less than 1% of $[\text{Cu}_3]$ remains.

The ethylene and ethane adsorption properties of $[\text{Cu}_3]$ were measured using variable temperature (20, 50 and 70 °C) single-gas adsorption isotherm (Figure 2.16). The isotherm show that most loading occurs at a step pressure that increases with increasing temperature.⁶³ This shape of adsorption of isotherm has significant potential for use in pressure or temperature swing process, because the pressure or temperature would only need to be changed by a small amount to bind/release almost the full capacity of the adsorbent.^{64,65} Similar adsorption

isotherms have been observed for phase change sorption processes in porous solids,⁶⁶⁻⁶⁸ H₂ and N₂ clathrate formation,^{69,70} cooperative insertion of CO₂,⁶⁵ and the chemisorption of ethylene in small molecule adsorbents.⁷¹ For [Cu₃], the step appears correlated to the phase change associated with the rearrangement from [Cu₃] to [Cu₂•(C₂H₄)₂].

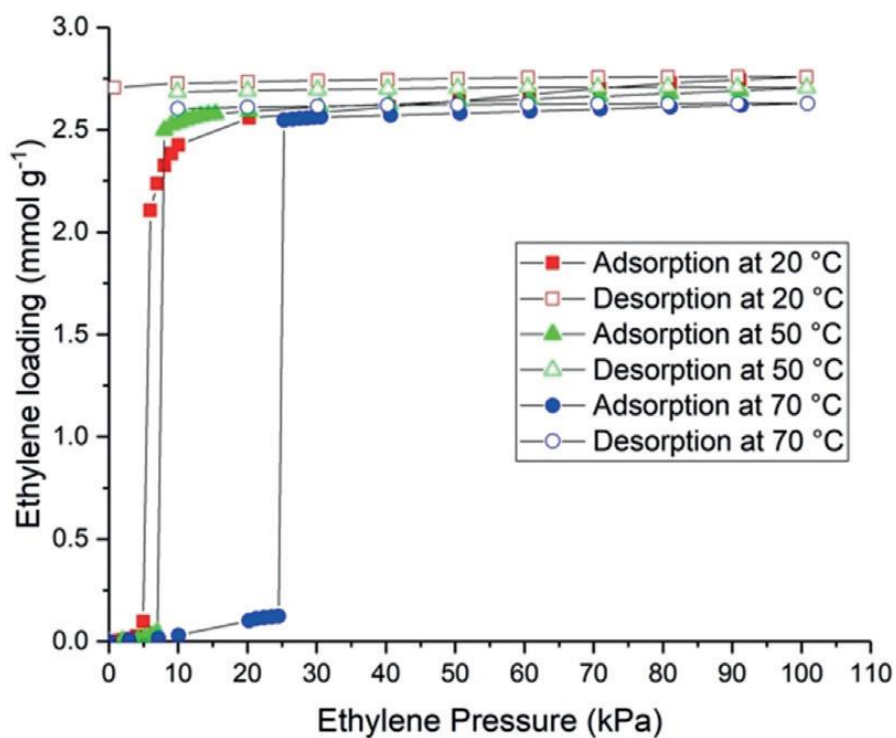


Figure 2.16 Left: Ethylene adsorption (solid symbols) and desorption (hollow symbols) isotherms of [Cu₃] at 20, 50 and 70 °C.

Table 2.3 Ethylene loading of [Cu₃] with pressure.

Temperature (K)	Ethylene loading at 100 kPa (mmol g ⁻¹)	'Step' pressure (kPa)	'Step Loading' (mmol g ⁻¹)
293	2.76	6.0	2.11
323	2.70	8.0	2.50
343	2.63	25.3	2.55

Claussius-Clapeyron analysis of isotherms and models: The Claussius-Clapeyron equation was used to estimate the adsorption energy associated at the 'step' using variable pressure and variable temperature data. Results show that the 'step' has an enthalpy of -38 kJ mol⁻¹ per [Cu₃] and -13 ± 1 kJ mol⁻¹ per Cu ion. This adsorption 'step' appears to occur at the same pressure for all copper binding sites in the sample, resulting in occupancy of all available copper binding sites to ethylene gas.

$$P_{step}(T) = P_{step,T_0} \left(\frac{\Delta H}{R} \right) \left(\frac{1}{T_0} - \frac{1}{T} \right)$$

$$\ln \left(\frac{P_{step}}{P_{step,T_0}} \right) = \left(\frac{-\Delta H}{R} \right) \left(\frac{1}{T_0} - \frac{1}{T} \right) \quad eq. 3$$

Equation 3

Equation used for the Claussius-Clapeyron analysis where P_{step} = the ethylene partial pressure at the step; P_{step,T₀} = the ethylene partial pressure at the step at 293 K; ΔH = change in enthalpy (J·mol⁻¹); R = 8.314 (J·mol⁻¹·K⁻¹) the gas constant; T₀ = 293 K; T = temperature (K).

Table 2.4 Isotherm data for the phase change of [Cu₃] to [Cu₂•(C₂H₄)₂] under increasing ethylene pressure.

Temperature (K)	1/T ₀ - 1/T	'Step' pressure (kPa)	P/P ₀	ln(P/P ₀)
293	0	2.44	1	0
323	3.17 x 10 ⁻⁴	8.02	3.3	1.19
323	3.17 x 10 ⁻⁴	8.85	3.6	1.23
343	4.98 x 10 ⁻⁴	20.6	8.4	2.13
343	4.98 x 10 ⁻⁴	53.5	9.6	2.27
343	4.98 x 10 ⁻⁴	25.3	10.3	2.34

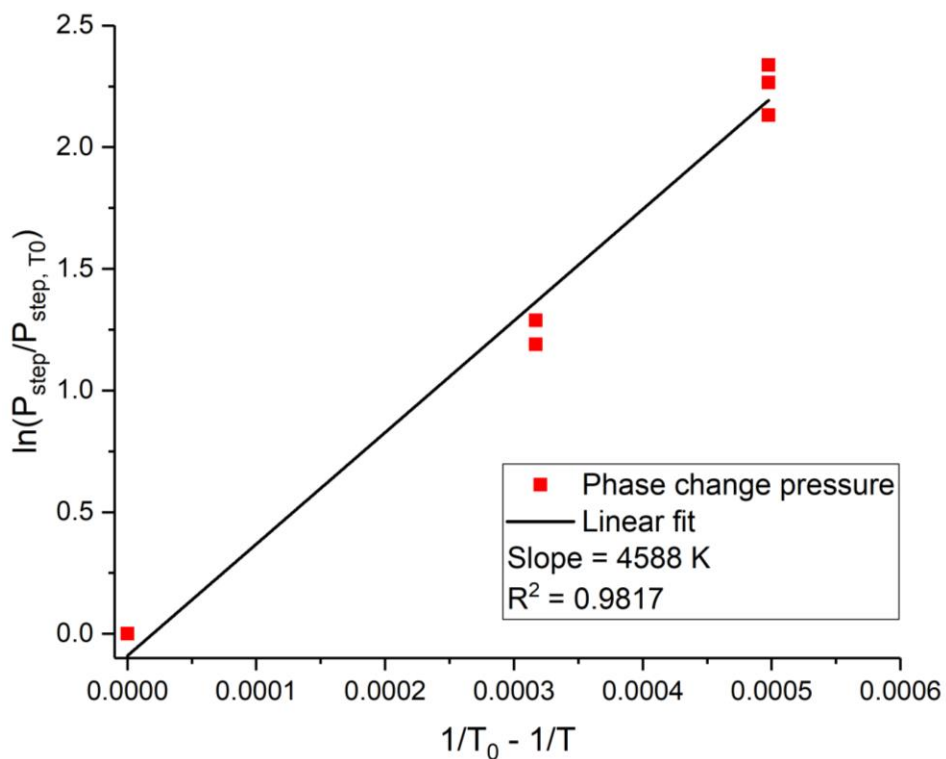


Figure 2.17 The Clausius-Clapeyron plot derived from the pressure where the step is observed in adsorption isotherms measured at 20, 50 and 70 °C.

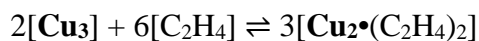
Table 2.5 Data from fitting the Claussius-Clapeyron equation to the phase change of [Cu₃] to [Cu₂•(C₂H₄)₂] under increasing ethylene pressure.

Data Source	Slope	R ²	$\Delta H_{\text{ethylene}/[\text{Cu}_3]}$ (kJ mol ⁻¹)	$\Delta H_{\text{ethylene}/\text{Cu}}$ (kJ mol ⁻¹)
Step pressures	4588	0.9817	-38	-13± 1

Van't Hoff analysis and Langmuir modelling of ethylene adsorption after 'step':

Above the 'step', Van't Hoff analysis of the isotherms gives a chemisorption energy of only -3 kJ mol⁻¹ per Cu ion, reflective of either only surface adsorption, or a balance between endothermic phase change and exothermic chemisorption processes.

The steepness of the 'step' increases with temperature, making the Langmuir behaviour difficult to capture. Applying the Langmuir isotherm model to data around the 'step' pressure produced effective results for the data collected at 25 and 50 °C when isotherms with a resolution of 2 kPa were collected. However, the data at 70 °C did not follow the same trend and the model clearly does not capture the underlying physical phenomena. Van't Hoff analysis of the Langmuir model for the 25 and 50 °C isotherms produces a heat of adsorption of -32 kJ mol⁻¹. However, due to the lack of accuracy we believe that Claussius-Clapeyron analysis of the step pressure (which has shown to correlate directly to heat of adsorption in small molecule adsorbents with step isotherms)⁷¹ is a more accurate reflection of the heat of adsorption.



$$K = \frac{[\text{Cu}_2 \cdot (\text{C}_2\text{H}_4)_2]^3}{[\text{Cu}_3]^2 [\text{C}_2\text{H}_4]^6} \quad \text{eq. 1}$$

Equation 1

Equilibrium equation used for binding of ethylene in CDCl_3 solution.

$$\ln(K) = \frac{-\Delta H}{RT} + \frac{\Delta S}{R} \quad \text{eq. 2}$$

Equation 2

Equation used for the Van't Hoff analysis where K = the equilibrium constant for the reversible reaction shown above; ΔH = change in enthalpy (J mol^{-1}); ΔS = change in entropy (J mol^{-1}); R = the gas constant ($\text{J mol}^{-1} \text{K}^{-1}$); T = temperature (K).

Table 2.6 Isotherm data for $[\text{Cu}_3]$ binding of ethylene in the solid-state under 100.7 kPa of ethylene

Temperature (K)	$[\text{Ethylene}]^6$	$[\text{Cu}_2 \cdot (\text{C}_2\text{H}_4)_2]^3 / [\text{Cu}_2 \cdot (\text{C}_2\text{H}_4)_2]^2$	K	$\ln(K)$	1/T
294	0.966	432	448	6.10	0.00340
232	0.966	264	273	5.61	0.00310
343	0.966	149	153	5.03	0.00291

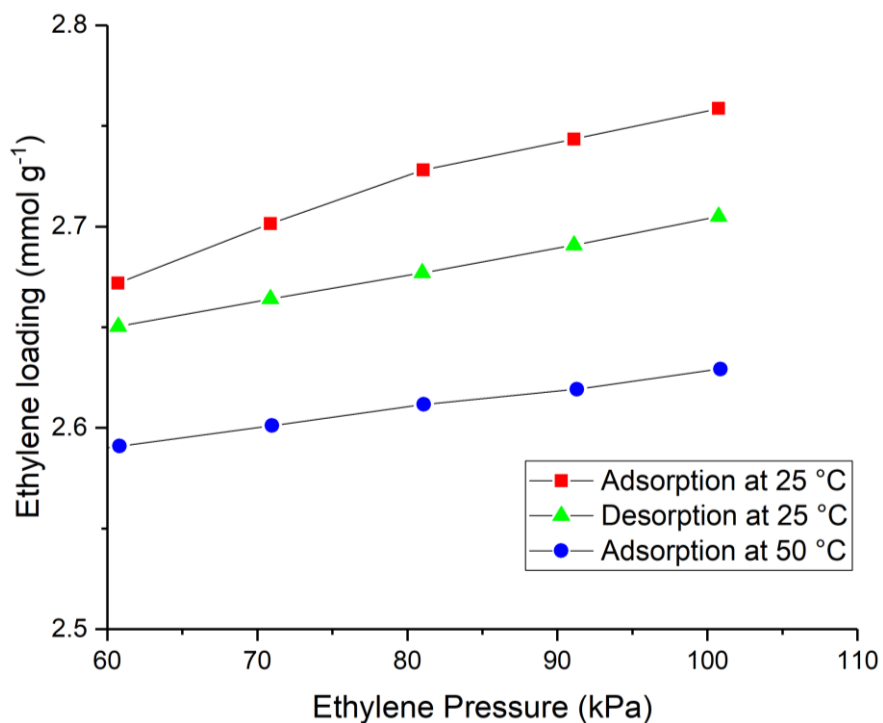


Figure 2.18 Ethylene adsorption isotherms of [Cu₃] at 20, 50 and 70 °C past the ‘step’ associated with phase change and chemisorption.

Table 2.7 Heat of equilibrium for [Cu₃] binding of ethylene in the solid-state under 100.7 kPa of ethylene.

	ΔH (kJ mol ⁻¹)	ΔS (J mol ⁻¹ K ⁻¹)
Overall equilibrium	-17.8±1	-8±1
Per [Cu₃] unit	-8.9±1	-4±1
Per Cu – C₂H₄ interaction	-3.0±1	-2±1

$$\text{Loading of ethylene} = \frac{\alpha \cdot P \cdot N}{\alpha \cdot P + 1} \quad \text{eq. 4}$$

Equation 4

Equation used for the Langmuir modelling where α = the equilibrium constant for the adsorption site; P = pressure of ethylene (kPa); N = number of adsorption sites present.

Table 2.8 Model parameters for $[\text{Cu}_3]$ binding of ethylene in the solid-state under generated from isotherm data above an ethylene pressure of 60 kPa.

Temperature (K)	' α ' from model	'N' from model	K	$\ln(\alpha)$	1/T
294	19.4	2.76	448	2.96	0.00340
232	31.8	2.69	273	3.46	0.00310
343	44.7	2.64	153	3.80	0.00291

The aggregated data for the overall energy of ethylene chemisorption during the $[\text{Cu}_3]$ to $[\text{Cu}_2\cdot(\text{C}_2\text{H}_4)_2]$ transformation are internally consistent at ca. -13 ± 1 kJ mol^{-1} per copper(I) ion (Table 2.9). This value is significantly lower than ethylene adsorption/chemisorption measured for other copper(I) complexes, which ranges from -24 kJ mol^{-1} to -55 kJ mol^{-1} (Median -36 kJ mol^{-1} ; Section 5.2.7, Table 5.1 of chapter 5). The difference can be attributed to the phase change energy associated with the physical constraints of the solid-state $[\text{Cu}_3]$ to $[\text{Cu}_2\cdot(\text{C}_2\text{H}_4)_2]$ transformation. Indeed, the solution-state binding energy of $-28 \pm 8 \text{ kJ mol}^{-1}$ per copper-ethylene interaction captures the same bond-making and bond-breaking processes of the $[\text{Cu}_3]$ to $[\text{Cu}_2\cdot(\text{C}_2\text{H}_4)_2]$ transformation, suggesting that

overcoming the intermolecular crystal lattice interactions (e.g., C-F•••F-C, Cu•••F contacts) pose a further endothermic barrier to the structural rearrangement.

Table 2.9 Aggregated ethylene chemisorption/desorption energies of the reversible [Cu₃] to [Cu₂•(C₂H₄)₂] transformation, as determined by various experimental techniques.

Energies associated with ethylene chemisorption	(kJ mol⁻¹)
DSC	
Overall per [Cu ₃] unit	60.9
Average [Cu ₃] melt energy	24.5
Per Cu–C ₂ H ₄ interaction	13.1
Adsorption Isotherms	
Ethylene adsorption ‘step’ per [Cu ₃] unit	-38 ± 2
‘Step’ energy per Cu•••C ₂ H ₄ interaction	-13 ± 1
After ‘step’ adsorption per [Cu ₃] unit	-8.9
After ‘step’ adsorption per Cu•••C ₂ H ₄ interaction	-3
Solution State (NMR)	
Overall equilibrium	-171 ± 45
Per [Cu ₃] unit	-86 ± 24
Per Cu–C ₂ H ₄ interaction	-28 ± 8

The rate of ethylene chemisorption by [**Cu₃**] was measured using a dead-end adsorption apparatus (discussed in detail in Section 5.2.4 of Chapter 5). The initial chemisorption (1 min) is rapid at 0.22-0.27 mol_{ethylene}mol_{complex}⁻¹ min⁻¹ but decreases significantly to 8 x 10⁻³ mol_{ethylene} mol_{complex}⁻¹ min⁻¹ for approximately 40 minutes and continues to decline over time (Figure 2.19). These results are similar to those observed for ethylene chemisorption on small molecule silver(I) complexes, where the majority of chemisorption occurs within the first minute.⁷¹ The decrease in uptake rate over time is potentially linked to the low surface area of the [**Cu₃**] complex (0.66 m²g⁻¹) and could be explained by transport of ethylene through the interior of the [**Cu₃**] particles being further hindered by the kinetics of the solid-state structural transition of [**Cu₃**] to [**Cu₂**•(C₂H₄)₂]. The ethylene capacity of [**Cu₃**] after 120 minutes is 31%, similar to the results obtained for [Ag^I(6,6'-dimethyl-2,2'-bipyridine)][BF₄] (34%), which had close contacts between silver(I) ions, and much lower than [Ag^I(6,6'-dimethyl-2,2'-bipyridine)][OTf] (84%), which did not have close contacts between silver(I) ions.⁷¹ It is inferred from breakthrough curve measurements that the adsorption rate of ethylene in porous solids (surface areas >100 m² g⁻¹) is much faster than in these discrete molecules (<10 m² g⁻¹).

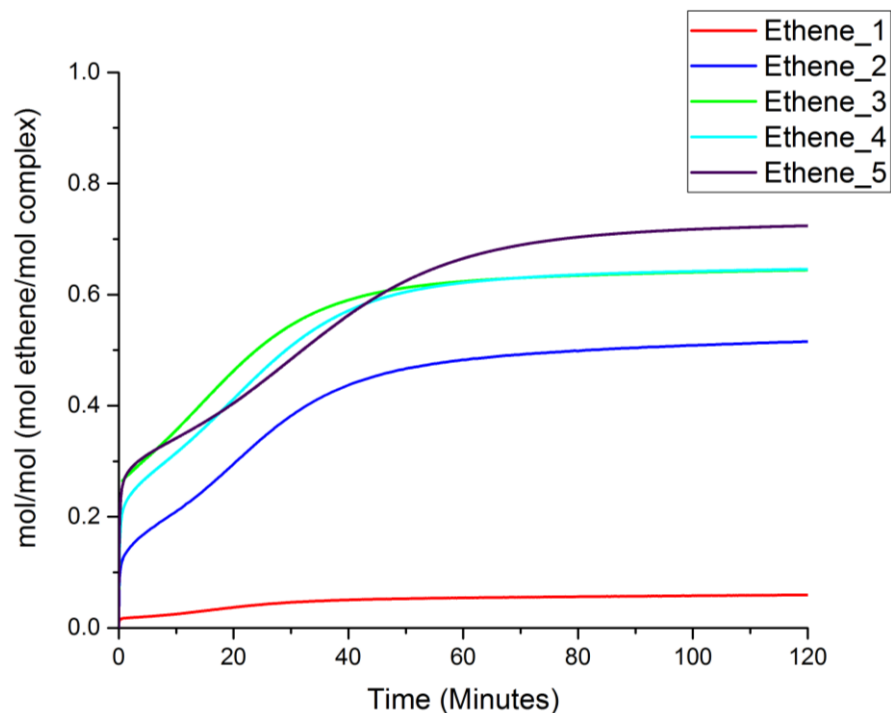


Figure 2.19 The ethene uptake of $[\text{Cu}_3]$ over five sorption/desorption cycles. The time axis has been truncated at 120 min for consistency

Acetylene adsorption is a known issue for the industrial processing of raw olefin mixtures.⁷² Therefore to probe the effects of acetylene on $[\text{Cu}_3]$, seven alternate 120 minute acetylene/ethylene adsorption cycles were measured using a dead-end adsorption apparatus (discussed in detail in Section 5.2.5 of chapter 5). The acetylene capacity remained consistent (0.37 mmol g^{-1}) over the cycles, but the ethylene capacity decreased significantly from (0.44 to 0.13 mmol g^{-1}). PXRD data (Figure 5.9 in Chapter 5) showed a significant loss of order and patterns unrelated to either $[\text{Cu}_3]$ or $[\text{Cu}_2 \cdot (\text{C}_2\text{H}_4)_2]$, leading to the inference that the structure of the

complex was permanently degraded by exposure to acetylene. Note however that industrially, adsorbents or membrane systems employed to remove acetylene from ethylene/ethane feed sent to cryogenic distillation. Therefore scope exists for the use of [**Cu₃**] in a hybrid process.

Ideal ethylene/ethane selectivity determined from the equilibrium loadings at 1 atm was 131:1 (70 °C) and 136:1 (20 °C). These selectivities are higher than observed for chemisorption on porous solids (3.6 to 27 ethylene/ethane) (Section 5.2.7, Table 5.2 of chapter 5), which suffer from high non-specific surface areas, but are lower than for other silver(I)-based small-molecule systems (390:1).⁷¹ Because ethane cannot chemisorb to the copper(I) ion like ethylene can, mixed gas studies would likely be reflective of the ideal selectivity.

2.4 Summary

In summary, the trinuclear copper(I) complex [**Cu₃**] undergoes a remarkable structural rearrangement to the dinuclear analogue [**Cu₂•(C₂H₄)₂**] upon exposure to ethylene in the solid-state, which emulates chemistry observed in solution. A combination of adsorption isotherms, SCXRD, PXRD, variable temperature ¹H and ¹⁹F NMR, DSC, Raman and infrared spectroscopy, and TGA have been used to demonstrate that the solid-state transformation is reversible and effectively reduces the heat of adsorption to only -13 ± 1 kJ mol⁻¹ per Cu–C₂H₄ interaction, 42% lower than values reported for other copper(I) ethylene

interactions ($\geq -24 \text{ kJmol}^{-1}$). Ethylene chemisorption occurred in step-shaped isotherms, as has been observed for other small molecule chemisorbents, with high ideal selectivity of 136:1 ethylene:ethane. These properties highlight the value of combining a structural rearrangement phase change with gas sorption to achieve low net heats of adsorption while retaining high selectivity.

Chapter 3

Chemistry and applications of Copper-alkyne complexes

Part 3.1 Copper(I)-alkyne complexes of fluorinated pyrazolate: Synthesis, photophysical properties, and computational analysis

Devaborniny Parasar, Ruaa M. Almotawa, Naleen B. Jayaratna, Yavuz S. Ceylan,
Thomas R. Cundari, Mohammad A. Omary, and H. V. Rasika Dias

(Part of this work has been published in *Organometallics* 2018, 37, 4105–4118)

Reproduced from references⁷³ with permission from the © 2018 American
Chemical Society

3.1.1 Abstract

This work describes the reaction of a cyclic trinuclear complex {[3,5-(CF₃)₂Pz]Cu}₃ with internal alkynes to construct di- and tetra-nuclear copper(I) complexes with short cuprophilic contacts, and the study of their intriguing bonding and photophysical properties, both experimentally and theoretically. For comparison, we have also investigated the related copper(I) trifluoroacetate 3-hexyne complexes so as to deduce and isolate the role played by the supporting pyrazolate ligand on the luminescence of these and related complexes. Some adducts reported herein feature bridging (i.e., μ₂-η²,η²-) alkyne coordination modes, which is rare for copper(I)-alkyne complexes documented in the literature. Raman data show red shifts in the average $\bar{\nu}_{\text{C}\equiv\text{C}}$ stretching frequency from 2260 cm⁻¹ in free 3-hexyne to 2050 cm⁻¹ in the terminal η²-/2e-donor alkyne adduct Cu₂(μ-[3,5-(CF₃)₂Pz])₂(EtC≡CEt)₂ (**1**) and, more drastically, to 1874 cm⁻¹ in the bridged μ₂-η²,η²-/4e-donor adduct Cu₄(μ-[3,5-(CF₃)₂Pz])₄(μ-EtC≡CEt)₂ (**2**). The tetra-nuclear 2-butyne adduct Cu₄(μ-[3,5-(CF₃)₂Pz])₄(μ-MeC≡CMe)₂ (**3**) also shows a large reduction in $\bar{\nu}_{\text{C}\equiv\text{C}}$ relative to that of free 2-butyne. The effects of strengthened copper-alkyne interactions in the bridging relative to terminal alkynes are also reflected in the C-C≡C bending back angles. Photophysical studies in the solid state revealed the significance of the pyrazolate supporting ligand to bestow bright photoluminescence, which was found only for the pyrazolate-supported

compounds **1-3** but not the trifluoroacetate copper alkyne complexes $\text{Cu}_2(\mu\text{-CF}_3\text{CO}_2)_2(\text{EtC}\equiv\text{CEt})_2$ (**4**) and $\text{Cu}_4(\mu\text{-CF}_3\text{CO}_2)_4(\mu\text{-EtC}\equiv\text{CEt})_2$ (**5**). The orange phosphorescence with $\sim 50 \mu\text{s}$ lifetime at room temperature in **1-3** thermochromically changes to generate additional green/yellow bands at cryogenic temperatures due to suppression of internal conversion from the respective $T_2 \rightarrow T_1$ states in each solid, whereas solvent effects lead to additional blue-shifted bands in glassy solvent media. Computational analysis explains the bonding and spectral results and suggests that the major excited-state distortion is due to significant ($\geq 20^\circ$) rotation of the alkyne ligands on Cu(I) in the di- or tetra-nuclear adducts, as opposed to excimeric contraction of cuprophilic Cu(I)•••Cu(I) distances. X-ray crystallographic data of **1-3** and **5** are also presented.

3.1.2 Introduction

Homoleptic pyrazolates of copper(I) have attracted significant interest due to their diverse structures, chemistry and fascinating photophysical properties.^{3, 15,74-79} Among the several structural types, trinuclear adducts are the most common. The copper(I) adduct $\{[3,5\text{-(CF}_3)_2\text{Pz}]\text{Cu}\}_3$ represents the most celebrated example reported by members of this team a few years ago.^{7,15,23,53,80,81} It exhibits bright phosphorescent emissions both in the solid state and in solution under UV excitation that can be easily fine- and coarse-tuned to multiple visible colors by varying the solvent, copper adduct concentration, temperature, excitation

wavelength, and/or medium rigidity.^{15,23,53} Detailed studies on solid $\{[3,5-(\text{CF}_3)_2\text{Pz}]\text{Cu}\}_3$ samples suggest that these emissions originate from an excited state that modifies the inter-trimer closed-shell cuprophilic interactions in the ground state to become covalent in the phosphorescent Cu-Cu centered excimer.^{23,80-83} The mixed Cu-Au metal systems derived from $\{[3,5-(\text{CF}_3)_2\text{Pz}]\text{Cu}\}_3$ and trinuclear gold(I) imidazolate complexes show near-unity photoluminescence quantum yields.⁸⁴ Various other trinuclear copper pyrazolate adducts are also known for their interesting chemistry and remarkable photophysical features, including some showing luminescence responses due to mechanical action and pressure changes, acid-base chemistry, and volatile organic chemical detection.^{20,26,74,75,81,85-102}

Trinuclear copper(I) pyrazolates also serve as good precursors to obtain various mixed ligand complexes of copper with different nuclearities. For example, solid samples of dinuclear $\text{Cu}_2(\mu-[3,5-(\text{CF}_3)_2\text{Pz}])_2(2,4,6\text{-collidine})_2$ obtained from $\{[3,5-(\text{CF}_3)_2\text{Pz}]\text{Cu}\}_3$ and 2,4,6-collidine show ligand based blue emissions that are different from the orange emissions of the precursor $\{[3,5-(\text{CF}_3)_2\text{Pz}]\text{Cu}\}_3$.¹⁰ The copper(I) adduct reacts with pyridazine, affording a tetranuclear species with a cage type skeleton.³⁰ The trinuclear $\{[3,5-(\text{CF}_3)_2\text{Pz}]\text{Cu}\}_3$ also reacts with $\text{Me}_3\text{SiC}\equiv\text{CSiMe}_3$, affording dinuclear $\text{Cu}_2(\mu-[3,5-(\text{CF}_3)_2\text{Pz}])_2(\text{Me}_3\text{SiC}\equiv\text{CSiMe}_3)_2$, an excellent volatile chemical vapor deposition (CVD) precursor for copper.⁹⁵

Herein we describe the reaction of trinuclear $\{[3,5-(\text{CF}_3)_2\text{Pz}]\text{Cu}\}_3$ with internal alkynes to construct di- and tetra-nuclear copper(I) complexes with short

cuprophilic contacts, and a detailed photophysical and computational study of the resulting molecules. We have also included the related copper(I) trifluoroacetate 3-hexyne complexes¹⁰³ for comparison to probe the effect of pyrazole ligand support on luminescence. Some of the copper(I) adducts reported here feature bridging alkyne ligands (i.e., μ_2 - η^2, η^2 -alkynes). Although copper complexes of alkynes are of significant interest as models for reaction intermediates due to their relevance in catalysis (e.g., click chemistry, cyclopropanation),¹⁰⁴⁻¹¹⁰ and as precursors in CVD applications,^{111,112} the vast majority of the well-characterized copper-alkynes in the literature have only 2e-donor, η^2 -alkynes moieties.^{109,112-116} Examples of copper(I) complexes of bridging alkynes are limited¹¹⁷ and reports involving internal alkyne ligands include $\text{Cu}_2(\text{tropocoronand})(\mu\text{-RC}\equiv\text{CR})$ ($\text{R} = \text{MeCO}_2, \text{EtCO}_2, \text{Ph}$),^{118,119} $\text{Cu}_4(\mu\text{-CF}_3\text{CO}_2)_4(\mu\text{-EtC}\equiv\text{CEt})_2$ ^{103,120} $[\text{Cu}_2\text{Cl}\{\text{bis}[1\text{-bis}(2\text{-pyridylmethyl}),1\text{-pyridyl}]\text{butyne}\}][\text{CuCl}_2]$,¹²¹ $\text{Cu}_4(\mu\text{-2-XC}_6\text{H}_4\text{CO}_2)_4(\mu\text{-RC}\equiv\text{CR})_2$ ($\text{X} = \text{Cl}, \text{Br}$; ¹²¹ $\text{R}=\text{EtCO}_2$),¹²² $\text{Cu}_4(\mu\text{-MeCO}_2)_4(\mu\text{-3,3,6,6-Me}_4\text{-1-thia-4-cycloheptyne})_2$,¹²³ $\text{Bis}[(\mu\text{-RC}\equiv\text{CR})\text{copper(I)}]\text{oxalate}$ ($\text{R} = \text{Et}, \text{Me}_3\text{Si}, \text{Me}_3\text{Si}^n\text{Bu}$)¹²⁴ and $\text{Cu}_2[\text{HC}\{\text{MeCN}(\text{CH}_2\text{Ph})\}_2](\mu\text{-PhC}\equiv\text{CPh})$.¹²⁵

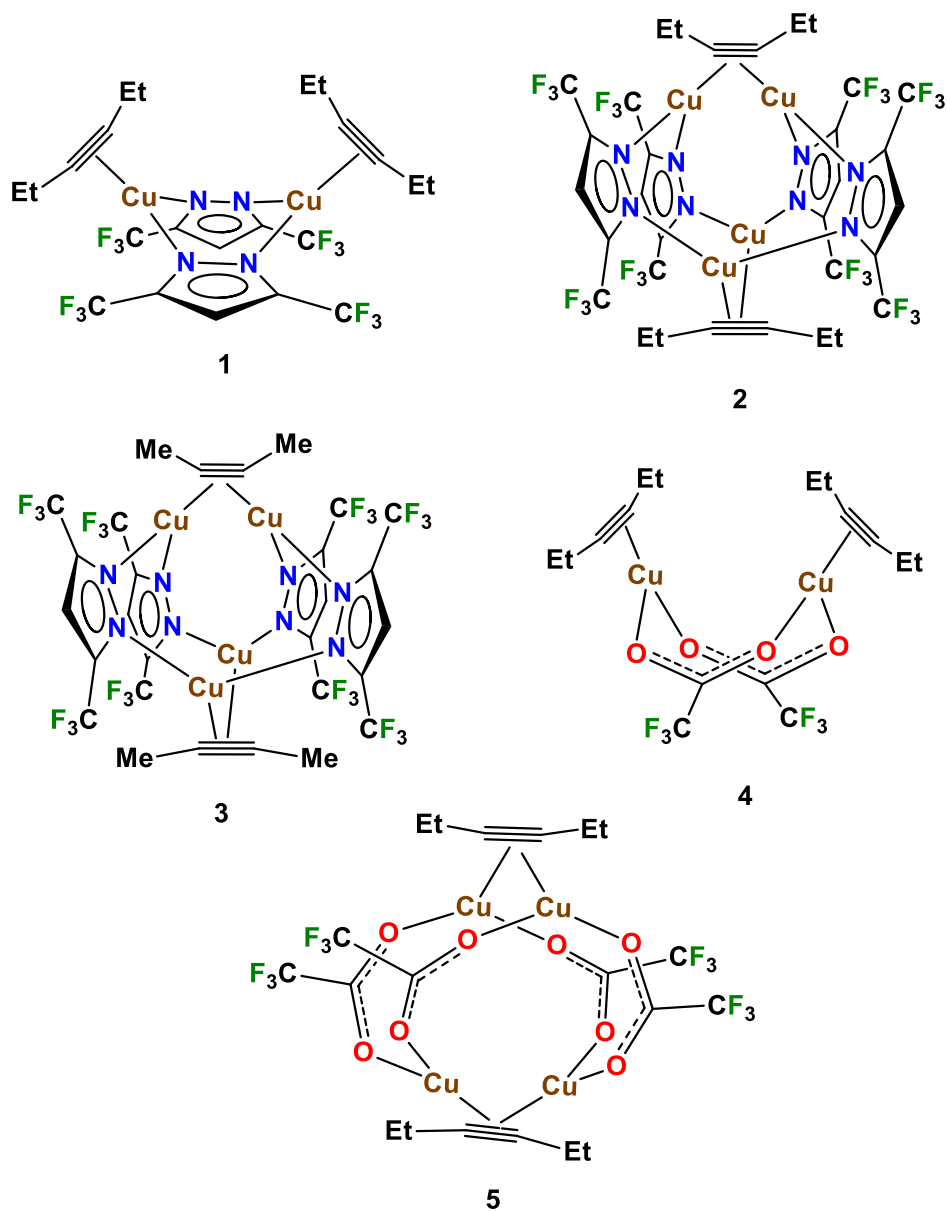


Figure 3.1 Diagram showing the structures of $\text{Cu}_2(\mu\text{-}[3,5\text{-}(\text{CF}_3)_2\text{Pz}])_2(\text{EtC}\equiv\text{CEt})_2$ (1), $\text{Cu}_4(\mu\text{-}[3,5\text{-}(\text{CF}_3)_2\text{Pz}])_4(\mu\text{-EtC}\equiv\text{CEt})_2$ (2), $\text{Cu}_4(\mu\text{-}[3,5\text{-}(\text{CF}_3)_2\text{Pz}])_4(\mu\text{-MeC}\equiv\text{CMe})_2$ (3), $\text{Cu}_2(\mu\text{-CF}_3\text{CO}_2)_2(\text{EtC}\equiv\text{CEt})_2$ (4), $\text{Cu}_4(\mu\text{-CF}_3\text{CO}_2)_4(\mu\text{-EtC}\equiv\text{CEt})_2$ (5).

3.1.3 Results and Discussion

Synthesis and structures :

The highly fluorinated $\{[3,5-(\text{CF}_3)_2\text{Pz}]\text{Cu}\}_3$ reacts readily with 3-hexyne in a 1:3 molar ratio, affording $\text{Cu}_2(\mu-[3,5-(\text{CF}_3)_2\text{Pz}])_2(\text{EtC}\equiv\text{CEt})_2$ (**1**) in ~95% yield (Figure 3.2). The synthesis of $\text{Cu}_2(\mu-[3,5-(\text{CF}_3)_2\text{Pz}])_2(\text{EtC}\equiv\text{CEt})_2$ using a mixture of 3,5-(CF_3)₂PzH, Cu_2O and 3-hexyne has been noted in a patent on CVD precursors of copper, but only thermal analysis data were presented.⁹⁵ The Raman spectrum of solid **1** shows that the $\bar{\nu}_{\text{C}\equiv\text{C}}$ vibrations of the copper-bound 3-hexynes are shifted by about $\sim 210\text{ cm}^{-1}$ to lower energy compared to the free 3-hexyne (average $\bar{\nu}_{\text{C}\equiv\text{C}}$ stretching frequency values of **1** and free $\text{EtC}\equiv\text{CEt}$ are 2050 and 2260 cm^{-1} , respectively).^{124,126,127} Such a shift is typical for η^2 -bound Cu(I)-alkynes. For example, $[\text{N}\{(\text{C}_3\text{F}_7)\text{C}(\text{Dipp})\text{N}\}_2]\text{Cu}(\text{EtC}\equiv\text{CEt})$ and $\text{Cu}_2(\mu-\text{O}_4\text{C}_2)(\text{EtC}\equiv\text{CEt})_2$ involving Cu(I)-3-hexyne moieties are known, and they display a reduction of similar magnitude in the $\bar{\nu}_{\text{C}\equiv\text{C}}$ value upon coordination to copper(I).^{124,126} The room temperature ^1H and ^{13}C NMR data of **1** in CDCl_3 , however, show only a small shift of ethyl proton and acetylenic carbon resonances relative to the corresponding resonances of the free 3-hexyne, suggesting the presence of weak copper-alkyne interaction in solution (e.g., acetylenic resonances of **1** and free 3-hexyne are observed at δ 82.5 and 81.0 ppm, respectively). For comparison, the corresponding carbon resonances of $[\text{N}\{(\text{C}_3\text{F}_7)\text{C}(\text{Dipp})\text{N}\}_2]\text{Cu}(\text{EtC}\equiv\text{CEt})$ and $\text{Cu}_2(\mu-$

$\text{O}_4\text{C}_2)(\text{EtC}\equiv\text{CEt})_2$ have been observed at more downfield regions, i.e., δ 98.2 and 87.6 ppm, respectively.^{124,126}

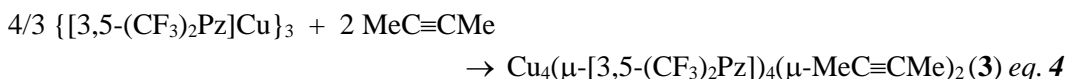
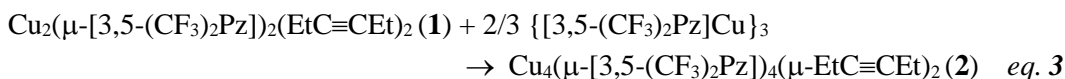
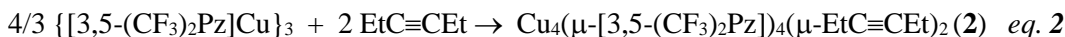
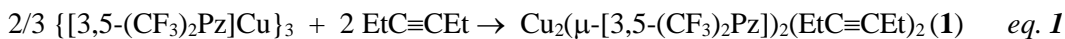


Figure 3.2 Synthetic routes to di- and tetra-nuclear complexes $\text{Cu}_2(\mu-[3,5-(\text{CF}_3)_2\text{Pz}])_2(\text{EtC}\equiv\text{CEt})_2$ (**1**), $\text{Cu}_4(\mu-[3,5-(\text{CF}_3)_2\text{Pz}])_4(\mu-\text{EtC}\equiv\text{CEt})_2$ (**2**), and $\text{Cu}_4(\mu-[3,5-(\text{CF}_3)_2\text{Pz}])_4(\mu-\text{MeC}\equiv\text{CMe})_2$ (**3**) from tri-nuclear $\{[3,5-(\text{CF}_3)_2\text{Pz}]\text{Cu}\}_3$.

Interestingly, the reaction of $\{[3,5-(\text{CF}_3)_2\text{Pz}]\text{Cu}\}_3$ with 3-hexyne in a 2:3 molar ratio affords a different product in 84% yield, which was identified by several methods as $\text{Cu}_4(\mu-[3,5-(\text{CF}_3)_2\text{Pz}])_4(\mu-\text{EtC}\equiv\text{CEt})_2$ (**2**) (Figure 3.2). It is a copper(I) pyrazolate with a bridging alkyne moiety. The $\bar{\nu}_{\text{C}\equiv\text{C}}$ band of solid **2** in the Raman spectrum was observed at 1874 cm^{-1} , representing a significant red shift relative to the corresponding stretching frequency of the free 3-hexyne, and also relative to that of **1**. Such a large red shift in $\bar{\nu}_{\text{C}\equiv\text{C}}$ is consistent with the $\mu_2-\eta^2, \eta^2$ -alkyne bonding mode, where the alkyne interacts with two copper sites. The acetylenic

carbon NMR resonance shows a downfield shift from that of **1** and was observed at δ 84.8 ppm as a broad resonance. It is possible to convert tetranuclear **2** to dinuclear **1** by treating it with 3-hexyne in a 1:2 molar ratio. In a similar fashion, **2** can be generated from **1** by reacting it with the appropriate molar quantity of $\{[3,5-(\text{CF}_3)_2\text{Pz}]\text{Cu}\}_3$. These transformations can be verified using NMR and Raman spectroscopy.

The copper-alkyne adducts $\text{Cu}_2(\mu\text{-}[3,5-(\text{CF}_3)_2\text{Pz}])_2(\text{EtC}\equiv\text{CEt})_2$ (**1**) and $\text{Cu}_4(\mu\text{-}[3,5-(\text{CF}_3)_2\text{Pz}])_4(\mu\text{-EtC}\equiv\text{CEt})_2$ (**2**) have been characterized by X-ray crystallography. Figure 3.3 shows the molecular structure of **1**. Selected bond distances and angles are given in Tables 3.1 and 3.2. Compound **1** is a dinuclear copper complex with trigonal planar copper(I) sites. The Cu_2N_4 core adopts a boat conformation. The $\text{EtC}\equiv\text{CEt}$ coordinates to Cu(I) centers in a typical η^2 -fashion. The alkyne $\text{C}\equiv\text{C}$ bond distance in **1** shows marginal elongation relative to typical alkyne $\text{C}\equiv\text{C}$ bond lengths 1.202(5) Å (e.g., 1.2022(15) Å in $t\text{BuC}\equiv\text{C}t\text{Bu}$).¹²⁸ The $\text{C}\equiv\text{C}$ bond angle (av. 161.2°) however exhibits notable deviation from linearity. Compound **1** also shows a close intramolecular $\text{Cu}\cdots\text{Cu}$ contact at 3.0514(3) Å but it is longer than the sum of van der Waals radii of two copper atoms based on Bondi (2.80 Å).¹²⁹ Recent work by Alvarez,^{130,131} Batsanov, and others,¹³² however, point to the presence of van der Waals interactions at even longer distances than those suggested by Bondi's radii (e.g., van der Waals radii sum proposed by Alvarez for

Cu-Cu = 4.76 Å). It is also interesting to note that the related $\text{Cu}_2(\mu\text{-}[3,5\text{-}(\text{CF}_3)_2\text{Pz}])_2(2,4,6\text{-collidine})_2$ has a planar Cu_2N_4 core (in contrast to the boat conformation in **1**) and a much larger intramolecular $\text{Cu}\cdots\text{Cu}$ separation of 3.3940(9) Å.¹⁰ These results also point to the flexibility of Cu_2N_4 core resulting in different degrees of $\text{Cu}\cdots\text{Cu}$ interactions.

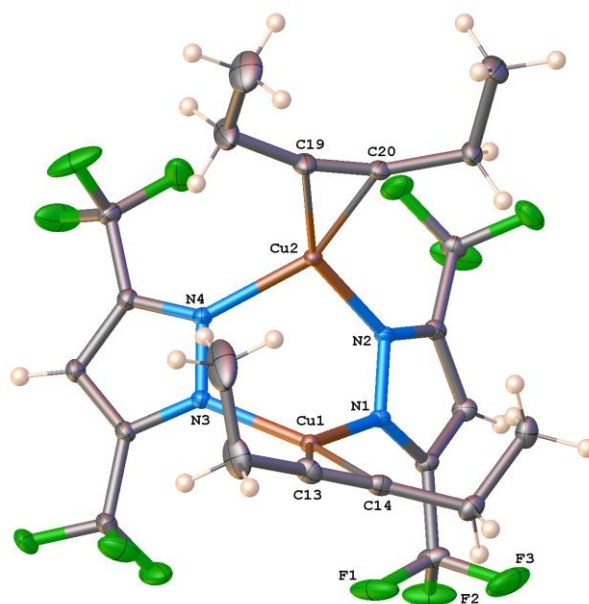


Figure 3.3 Molecular structure of $\text{Cu}_2(\mu\text{-}[3,5\text{-}(\text{CF}_3)_2\text{Pz}])_2(\text{EtC}\equiv\text{CEt})_2$ (**1**).

The X-ray crystal structure of $\text{Cu}_4(\mu\text{-}[3,5\text{-}(\text{CF}_3)_2\text{Pz}])_4(\mu\text{-EtC}\equiv\text{CEt})_2$ (**2**) is illustrated in Figure 3.4. It is a tetranuclear copper(I) complex with trigonal planar copper sites. The Cu_4N_8 core sits on a 2-fold rotation axis. The $\text{EtC}\equiv\text{CEt}$ groups act as bridging ligands to Cu(I) in a $\mu_2\text{-}\eta^2, \eta^2\text{-alkyne}$ bonding mode. The alkyne $\text{C}\equiv\text{C}$ bond distances of **2** (both at 1.265(2) Å) demonstrate significant elongation

relative to the corresponding bond lengths in **1**, which has a non-bridging alkyne. The average C-C≡C bend back angle of **2** also displays an additional 6° increase. These metrical parameters of the alkyne moieties point to significant weakening of the C≡C bond and are consistent with the aforementioned Raman and ¹³C NMR spectroscopic data. Compound **2** also exhibits several close intramolecular Cu•••Cu contact with the shortest separation at 2.6463(2) Å, which is well within even the most conservative Bondi van der Waals separation of 2.80 Å.¹²⁹ Indeed, this lies in the vicinity of bond distances recently scrutinized by Otten et al. to be covalent as opposed to cuprophilic.¹³³ However, we suspect the situation herein to be more similar to the “control” cases in that work whereby the short Cu(I)-Cu(I) distances are brought about by the ligand bite size as opposed to covalency, akin to Cotton’s classic work on bis(formamidinate) dinuclear adducts,¹³⁴ as the situation does not warrant inter-shell mixing of 4s⁰/4p⁰ orbitals with 3d¹⁰ orbitals that is required for covalency.

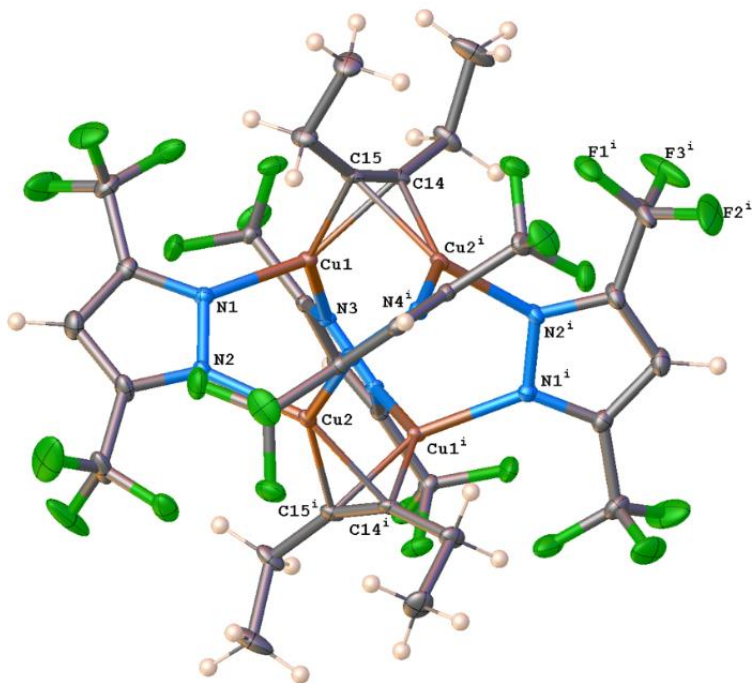


Figure 3.4 Molecular structure of $\text{Cu}_4(\mu\text{-}[3,5\text{-}(\text{CF}_3)_2\text{Pz}])_4(\mu\text{-EtC}\equiv\text{CEt})_2$ (**2**) and additional two view showing the Cu_4N_8 core .

Table 3.1 Selected bond distances (Å) for $\text{Cu}_2(\mu\text{-[3,5-(CF}_3)_2\text{Pz]})_2(\text{EtC}\equiv\text{CEt})_2$ (**1**), $\text{Cu}_4(\mu\text{-[3,5-(CF}_3)_2\text{Pz]})_4(\mu\text{-EtC}\equiv\text{CEt})_2$ (**2**), $\text{Cu}_4(\mu\text{-[3,5-(CF}_3)_2\text{Pz]})_4(\mu\text{-MeC}\equiv\text{CMe})_2$ (**3**), and $\text{Cu}_4(\mu\text{-CF}_3\text{CO}_2)_4(\mu\text{-EtC}\equiv\text{CEt})_2$ (**5**).

Parameter\Complex	1	2	3	5
Cu-C	1.9844(18)	2.0264(13)	2.0242(11)	1.973(2)
	1.9766(17)	2.0049(13)	2.0132(11)	2.002(2)
	1.9741(18)	2.0078(14)	2.0164(11)	1.979(2)
	1.9758(16)	2.0246(14)	2.0186(11)	2.009(2)
		2.0264(13)	2.0242(11)	1.985(2)
		2.0049(13)	2.0132(11)	2.003(2)
		2.0078(14)	2.0164(11)	2.001(2)
		2.0246(14)	2.0186(11)	2.005(2)
av. Cu-C	1.978	2.016	2.018	1.995
C≡C	1.225(3)	1.265(2)	1.275(2)	1.279(3)
	1.228(3)	1.265(2)	1.275(2)	1.272(3)
av. C≡C	1.227	1.265	1.275	1.276
Shortest Cu•••Cu	3.0514(3)	2.6463(2)	2.6642(3)	2.8382(4)
Cu-X*	1.9750(14)	1.9774(11)	1.9751(10)	1.9602(17)
	1.9921(14)	1.9813(12)	1.9743(10)	1.9530(17)
	1.9873(14)	1.9717(13)	1.9707(11)	1.9806(17)
	1.9850(14)	1.9815(11)	1.9724(10)	1.9539(16)
		1.9774(11)	1.9751(10)	1.9592(16)
		1.9813(12)	1.9743(10)	1.9570(17)
		1.9717(13)	1.9707(11)	1.9557(17)
		1.9815(11)	1.9724(10)	1.9712(17)

*: X = N or O

Table 3.2 Selected bond angles (°) for $\text{Cu}_2(\mu\text{-}[3,5\text{-}(\text{CF}_3)_2\text{Pz}])_2(\text{EtC}\equiv\text{CEt})_2$ (**1**), $\text{Cu}_4(\mu\text{-}[3,5\text{-}(\text{CF}_3)_2\text{Pz}])_4(\mu\text{-EtC}\equiv\text{CEt})_2$ (**2**), $\text{Cu}_4(\mu\text{-}[3,5\text{-}(\text{CF}_3)_2\text{Pz}])_4(\mu\text{-MeC}\equiv\text{CMe})_2$ (**3**), and $\text{Cu}_4(\mu\text{-CF}_3\text{CO}_2)_4(\mu\text{-EtC}\equiv\text{CEt})_2$ (**5**)

Parameter\Complex	1	2	3	5
C-Cu-C	36.03(8)	36.57(6)	36.81(6)	37.59(9)
	36.22(7)	36.56(6)	36.83(6)	37.26(10)
		36.57(6)	36.81(6)	37.41(9)
		36.56(6)	36.83(6)	37.09(10)
C-C≡C	161.5(2)	154.43(14)	158.23(7)	155.1(2)
	161.72(18)	155.97(13)	158.51(7)	154.0(2)
	161.19(19)	154.43(14)	158.23(7)	156.2(2)
	160.30(18)	155.97(13)	158.51(7)	153.7(2)
Av. C-C≡C	161.2	155.2	158.4	154.7
X-Cu-X*	96.62(6)	108.93(5)	110.53(4)	94.29(8)
	98.35(6)	109.04(5)	110.32(5)	92.81(7)
		108.93(5)	110.53(4)	97.32(8)
		109.04(5)	110.32(5)	97.09(7)

*: X = N or O

The reaction between $\{[3,5\text{-}(\text{CF}_3)_2\text{Pz}]\text{Cu}\}_3$ and 2-butyne leads to the formation of tetranuclear $\text{Cu}_4(\mu\text{-}[3,5\text{-}(\text{CF}_3)_2\text{Pz}])_4(\mu\text{-MeC}\equiv\text{CMe})_2$ (**3**) (Figure 3.2). Unlike **1** and **2**, changes in the stoichiometric ratio of the precursors have no effect

upon the product formation of **3**. We could not isolate the dinuclear copper species even in the presence of excess 2-butyne, indicating that there is a significant driving force for the formation of tetranuclear **3** in solution at room temperature. The less crowded alkyne moiety perhaps facilitates cluster formation. The $\bar{\nu}_{\text{C}\equiv\text{C}}$ band in the Raman spectrum was observed at 1886 cm^{-1} , which represents a 348 cm^{-1} red shift vs the corresponding signal reported for the free 2-butyne (2234 cm^{-1}).¹³⁵ This indicates significant weakening of the C \equiv C bond, as a result of simultaneous coordination to two copper(I) sites.

The X-ray crystal structure of **3** is illustrated in Figure 3.5. This molecule also sits on a 2-fold rotation axis. It features a Cu_4N_8 core and $\mu_2\text{-}\eta^2,\eta^2$ -bonded alkyne groups. The alkyne C \equiv C bond distances of **3** (both at $1.275(2)\text{ \AA}$) show significant elongation relative to the corresponding bond lengths in **1**, but similar to that observed in **2**. The alkyne moieties of **3** also exhibit substantial deviation of linearity (bending backwards) as evident from the average C-C \equiv C angle of 158.4° . These parameters are consistent with the Raman spectroscopic data and indicate a significant effect on the C \equiv C bond order, as a result of each alkyne acting as a formal $4e^-$ donor to two copper(I) sites. The Cu-C bond distances of **1** (av. 1.978 \AA) also differ from the corresponding distances in **2** and **3** (av. 2.016 and 2.018 \AA , respectively). The Cu-C bond distances in the bridging alkyne species **2** and **3** are shorter than the Cu-C distance in **1**, perhaps as a result of increased coordination

number at carbon sites. The Cu-N distances, in contrast, are not significantly different in **1–3**. As in **2**, compound **3** also shows several close intramolecular Cu•••Cu contacts with the shortest separation at 2.6642(2) Å, akin to the situation discussed above for **2** in relation to the literature cuprophilic vs covalent bonding.

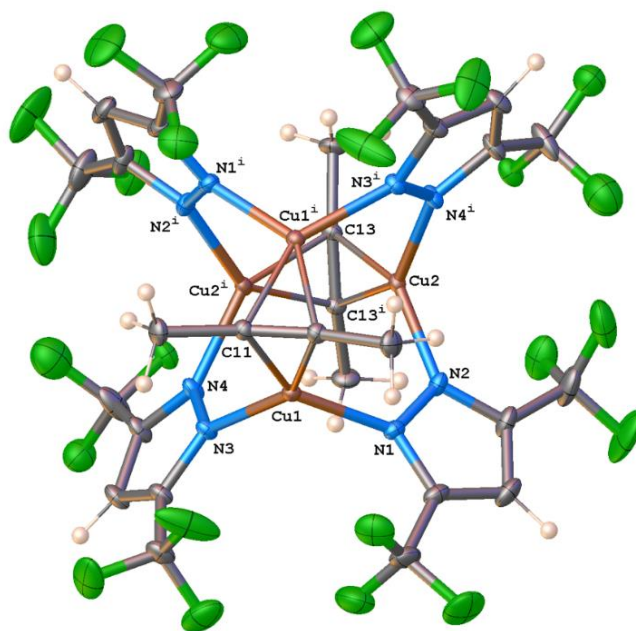


Figure 3.5 Molecular structure of $\text{Cu}_4(\mu\text{-}[3,5\text{-}(\text{CF}_3)_2\text{Pz}])_4(\mu\text{-MeC}\equiv\text{CMe})_2$ (**3**).

We have also synthesized di- and tetra-nuclear copper 3-hexyne complexes $\text{Cu}_2(\mu\text{-CF}_3\text{CO}_2)_2(\text{EtC}\equiv\text{CEt})_2$ (**4**) and $\text{Cu}_4(\mu\text{-CF}_3\text{CO}_2)_4(\mu\text{-EtC}\equiv\text{CEt})_2$ (**5**) involving trifluoroacetate ligand support (instead of pyrazolate) for comparison.^{103,120} These complexes also offer a platform to investigate the effects of pyrazolyl groups and Cu•••Cu contacts on the corresponding photophysical properties. These molecules were reported by Reger et al. but their photophysical properties have not been

probed. The X-ray structure of **5** has been reported and showed close Cu•••Cu contacts.¹²⁰ During our studies on this tetranuclear copper complex, we also found a different polymorph (Figure 3.6). It shows a closest intra-molecular Cu•••Cu contact at 2.8382(4) Å, which is longer than those found in **2** and **3** (Table 3.1), but similar to those in the previous report (2.820 and 2.799 Å).¹²⁰ We also managed to crystallize Cu₂(μ-CF₃CO₂)₂(EtC≡CEt)₂ (**4**) and obtain X-ray structural data (Figure 3.7). Although dinuclear nature (with a Cu•••Cu contact at 2.97 Å) and atom connectivity are clear from the

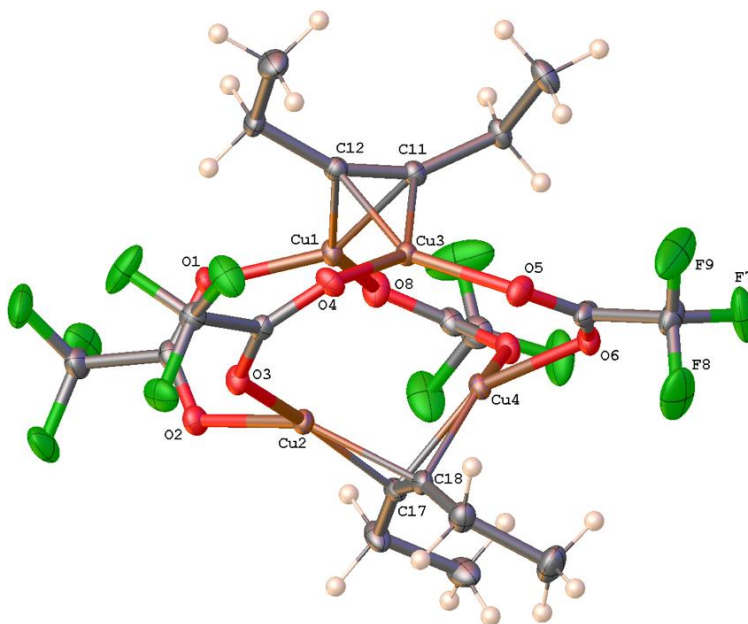


Figure 3.6 Molecular structure of Cu₄(μ-CF₃CO₂)₄(μ-EtC≡CEt)₂ (**5**)

structure, it is unfortunately not suitable for detailed analysis of metrical parameters due to weakly diffracting nature of crystals and poor data quality. Overall, the

structural data of these pyrazolate and acetate supported copper-alkyne complexes show that copper atoms exhibit strong cuprophilic interactions in the ground state, which are conducive to be strengthened in the excited state if the transition were metal-centered to form a phosphorescent excimer,⁸¹ which computational analyses (*vide infra*) disprove.

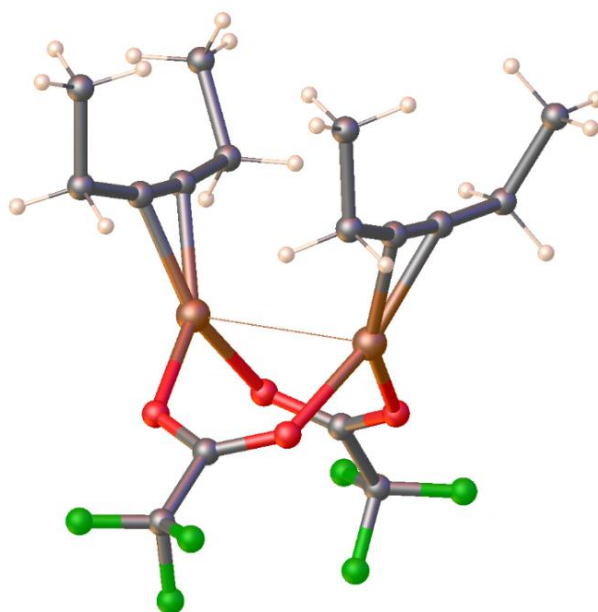


Figure 3.7 Molecular structure of $\text{Cu}_2(\mu\text{-CF}_3\text{CO}_2)_2(\text{EtC}\equiv\text{CEt})_2$ (**4**)

Computational analysis of structure and bonding:

We have performed a detailed computational study of $\text{Cu}_2(\mu\text{-}[3,5\text{-}(\text{CF}_3)_2\text{Pz}])_2(\text{EtC}\equiv\text{CEt})_2$ (**1**), $\text{Cu}_4(\mu\text{-}[3,5\text{-}(\text{CF}_3)_2\text{Pz}])_4(\mu\text{-EtC}\equiv\text{CEt})_2$ (**2**), and $\text{Cu}_4(\mu\text{-}[3,5\text{-}(\text{CF}_3)_2\text{Pz}])_4(\mu\text{-MeC}\equiv\text{CMe})_2$ (**3**) to investigate the effect of copper on the alkynes and to understand the bonding and photoluminescence of these adducts. The computational level of theory (BP86/6-311+G(d)) reproduced experimental structural and spectroscopic trends for the Cu_2 complex **1** relative to the Cu_4 complex **2**, and the 2-butyne ligated Cu_4 complex **3**. Experimental $\text{Cu}\cdots\text{Cu}$ distances of the complexes are reported as 3.05, 2.65, and 2.66 Å for complex **1**, **2**, and **3**, respectively. Similarly, DFT calculations predicted $\text{Cu}\cdots\text{Cu}$ distances of these same complexes are 3.16, 2.67, and 2.67 Å, respectively. The rest of the computationally-predicted bonding parameters and structures are reported in Figure 3.8. Note that the structures of $\text{Cu}_2(\mu\text{-CF}_3\text{CO}_2)_2(\text{EtC}\equiv\text{CEt})_2$ (**4**) and $\text{Cu}_4(\mu\text{-CF}_3\text{CO}_2)_4(\mu\text{-EtC}\equiv\text{CEt})_2$ (**5**) are not discussed here because of their non-photoluminescent behavior (*vide infra*). According to the Dewar-Chatt-Duncanson (DCD) model,¹³⁶⁻¹³⁸ σ -donation from π_{CC} of an alkyne ligand to a Cu orbital and π -backbonding from a Cu-based orbital to the π^*_{CC} orbital of alkyne would each cause the $\text{C}\equiv\text{C}$ bond to be elongated versus the free alkyne, as well as bend the $\text{C-C}\equiv\text{C}$ angle away from linearity.

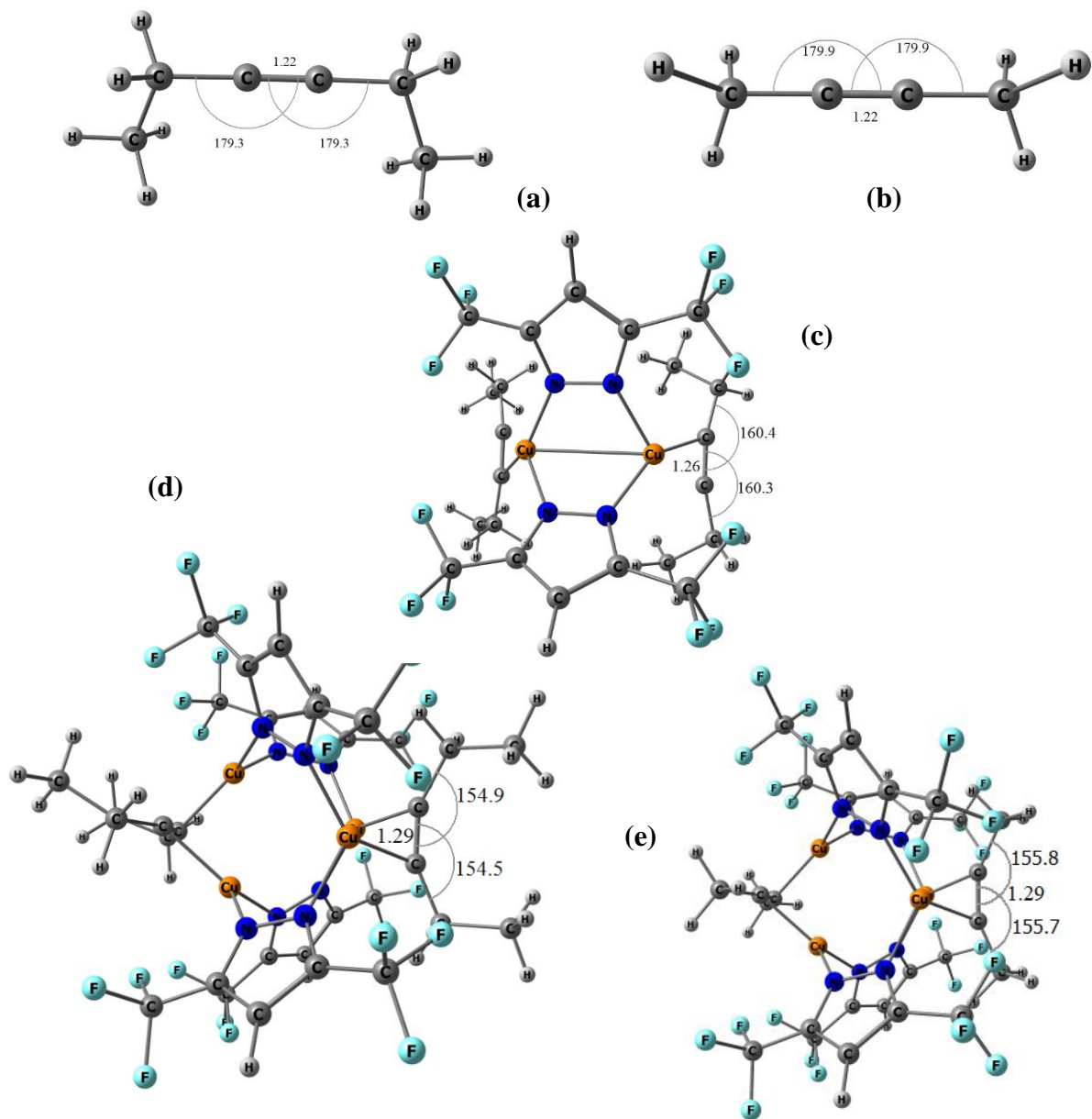


Figure 3.8 Calculated geometries of (a) free 3-hexyne, (b) free 2-butyne, (c) $\text{Cu}_2(\mu\text{-[3,5-(CF}_3)_2\text{Pz]})_2(\text{EtC}\equiv\text{CEt})_2$ (**1**), (d) $\text{Cu}_4(\mu\text{-[3,5-(CF}_3)_2\text{Pz]})_4(\mu\text{-EtC}\equiv\text{CEt})_2$ (**2**) and (e) $\text{Cu}_4(\mu\text{-[3,5-(CF}_3)_2\text{Pz]})_4(\mu\text{-MeC}\equiv\text{CMe})_2$ (**3**). Bond lengths in Å, and angles in

degrees. Note that both alkyne ligands within a particular complex are nearly identical in **c**, **d** and **e**.

DFT predicted the average C≡C distance of 3-hexyne in $\text{Cu}_2(\mu\text{-}[3,5\text{-}(\text{CF}_3)_2\text{Pz}])_2(\text{EtC}\equiv\text{CEt})_2$ (**1**) and $\text{Cu}_4(\mu\text{-}[3,5\text{-}(\text{CF}_3)_2\text{Pz}])_4(\mu\text{-EtC}\equiv\text{CEt})_2$ (**2**) as 1.26 and 1.29 Å, respectively (representing 0.03 Å elongation as a result of the coordination of two Cu atoms rather than one to the alkyne). Calculations also predicted an average C≡C distance of 1.28 Å for $\text{Cu}_4(\mu\text{-}[3,5\text{-}(\text{CF}_3)_2\text{Pz}])_4(\mu\text{-MeC}\equiv\text{CMe})_2$ (**3**). These results show that compared to the DFT-predicted free 3-hexyne and 2-butyne C≡C distances of 1.22 Å the corresponding alkyne distances in **1**, **2**, and **3** were elongated by 0.04, 0.07, and 0.06 Å, respectively. Computational results thus mirror experiment (Table 3.1) in terms of the elongation of 3-hexyne C≡C bonds upon going from the dinuclear adduct with η^2 -alkyne to the tetranuclear species with $\mu_2\text{-}\eta^2, \eta^2$ -alkyne, and for both alkynes in terms of CC triple bond elongation upon coordination to copper(I).

The optimized C-C≡C bond angles of 3-hexyne in **2** and **1** are $154.7 \pm 0.2^\circ$ and $160.4 \pm 0.1^\circ$, respectively (Figure 3.8, which agree well with the experimental values of 155.2° and 161.2° , respectively (Table 3.2)). Thus, on the basis of the DCD model, one may propose that the CC triple bond of the alkyne moiety in **2** either (i) donates more electrons to copper(I) relative to **1**, (ii) participates more significantly in π -backbonding, or (iii) both of these effects are operative. For the

tetranuclear **3**, the optimized C-C≡C bond angle of 2-butyne is $155.7 \pm 0.1^\circ$. We suggest from the calculated data that the CC triple bond of the alkyne moiety in **2** and **3** are similar with respect to the Dewar-Chatt-Duncanson bonding model.

Another indicator of the Cu/alkyne interaction is the stretching frequency, $\bar{\nu}_{\text{C}\equiv\text{C}}$. The Raman bands corresponding to $\bar{\nu}_{\text{C}\equiv\text{C}}$ of **1** have been observed at 2033 and 2066 cm^{-1} (average 2050 cm^{-1}), while the corresponding bands for **2** and **3** appear at 1874 and 1886 cm^{-1} , respectively. Similarly, the BP86/6-311+G(d) treatment predicted that $\bar{\nu}_{\text{C}\equiv\text{C}}$ values in **1**, **2** and **3** are 2058, 1889, and 1914 cm^{-1} , respectively. As with the bond length/angle differences discussed above, this difference is consistent with either less electron donation from C≡C to the Cu metal and/or less π -backbonding from Cu to C≡C for **1** relative to **2**. Moreover, the DFT-predicted Raman bands $\bar{\nu}_{\text{C}\equiv\text{C}}$ of sample **1**, **2**, **3**, and free alkynes correspond reasonably well with experimental Raman bands, Table 3.3. Computational and experimental Raman spectra of the complexes and free alkynes are reported in Appendix A

Table 3.3 Raman bands $\bar{\nu}_{\text{C}\equiv\text{C}}$ of sample **1**, **2**, **3**, and free alkynes

Complex	DFT $\bar{\nu}_{\text{C}\equiv\text{C}}$ (cm^{-1})	Experimental $\bar{\nu}_{\text{C}\equiv\text{C}}$ (cm^{-1})
1	2066	2033 and 2066
2	1891	1874
3	1913	1886
Free 3-Hexyne	2270	2232, 2247 and 2299
Free 2-Butyne	2285	2234

The NBO method was used to analyze the bond order of the CC bond in the two copper(I) adducts of 3-hexyne, $\text{Cu}_2(\mu\text{-[3,5-(CF}_3)_2\text{Pz]})_2(\text{EtC}\equiv\text{CEt})_2$ (**1**) and $\text{Cu}_4(\mu\text{-[3,5-(CF}_3)_2\text{Pz]})_4(\mu\text{-EtC}\equiv\text{CEt})_2$ (**2**). According to NBO, one σ and two π bonds define the $\text{C}\equiv\text{C}$ bond of the alkyne; given in Table 3.4. However, different natural bond occupancies exist for **1** versus **2**. The sum of the NBO electron occupancies for the $\text{C}\equiv\text{C}$ bonding orbitals of **1** and **2** are thus $5.751e^-$ and $5.671e^-$, respectively. Electron occupancies of the $\text{Cu}_2(\mu\text{-[3,5-(CF}_3)_2\text{Pz]})_2(\text{EtC}\equiv\text{CEt})_2$ (**1**) and $\text{Cu}_4(\mu\text{-[3,5-(CF}_3)_2\text{Pz]})_4(\mu\text{-EtC}\equiv\text{CEt})_2$ (**2**) for the corresponding anti-bonding NBOs are $0.365e^-$ and $0.553e^-$, for **1** and **2**, respectively. Therefore, based on the DCD model, it is suggested that both increased σ -donation from 3-hexyne and increased π -backbonding to the π^*_{CC} of 3-hexyne in **2** versus **1** leads to greater elongation of $\text{C}\equiv\text{C}$ bonds in the alkyne adduct for the $\text{Cu}_4(\mu\text{-[3,5-(CF}_3)_2\text{Pz]})_4(\mu\text{-EtC}\equiv\text{CEt})_2$ (**2**), the more bent the $\text{C-C}\equiv\text{C}$ bond angle, and the more red-shifted the $\text{C}\equiv\text{C}$ stretching frequency. Furthermore, the NBO analysis suggests that the π -backbonding effects are more substantial than those for σ -donation in discriminating between the Cu_2 and Cu_4 complexes. NBO analysis was also carried out to investigate the bonding character between $\text{Cu}\cdots\text{Cu}$ bonds for all complexes studied. The NBO method did not find any covalent bonding interactions, thus we conclude that these interactions are very weak or dispersion (cuprophilic) in nature.

Table 3.4 NBO orbital descriptions for the C≡C of the adducts, Cu₂(μ-[3,5-(CF₃)₂Pz])₂(EtC≡CEt)₂ (**1**) and Cu₄(μ-[3,5-(CF₃)₂Pz])₄(μ-EtC≡CEt)₂ (**2**).

Cu₂(μ-[3,5-(CF₃)₂Pz])₂(EtC≡CEt)₂ (**1**)

Description	Occp.	% C	% C	% orbitals
C-C σ bond	1.976	50	50	44% s +56% p
C-C π ₁ bond	1.946	50	50	100% p
C-C π ₂ bond	1.829	50	50	7% s +93% p
C-C σ* bond	0.029	50	50	44% s +56%
C-C π ₁ * bond	0.080	50	50	100% p
C-C π ₂ * bond	0.256	50	50	7% s +93% p
∑ e ⁻ occp.	5.751			
∑ e ⁻ occp.*	0.365			

Cu₄(μ-[3,5-(CF₃)₂Pz])₄(μ-EtC≡CEt)₂ (**2**)

Description	Occp.	% C	% C	% orbitals
C-C σ bond	1.964	50	50	39% s +61% p
C-C π ₁ bond	1.934	50	50	100% p
C-C π ₂ bond	1.773	50	50	11% s +89% p
C-C σ* bond	0.034	50	50	39% s +61% p
C-C π ₁ * bond	0.199	50	50	100% p
C-C π ₂ * bond	0.320	50	50	11% s +89% p
∑ e ⁻ occp.	5.671			
∑ e ⁻ occp.*	0.553			

* = Antibonding

Photophysical studies:

We have investigated the photophysical properties of these di- and tetranuclear copper(I) alkyne complexes **1-5** and found that the pyrazolate-supported compounds **1-3** are brightly luminescent molecules under UV light at ambient temperature. The trifluoroacetate copper alkyne complexes **4** and **5**, however, do not exhibit detectable luminescence at such temperatures. Details are summarized in Table 3.5. Figures 3.9, 3.10 and 3.11 illustrates the electronic absorption and photoluminescence spectra. This points to the importance of pyrazolyl moieties for the luminescence in these copper-alkyne complexes.

Table 3.5 Summary of photophysical parameters for all five complexes in this study for the solid state: $\text{Cu}_2(\mu\text{-}[3,5\text{-}(\text{CF}_3)_2\text{Pz}])_2(\text{EtC}\equiv\text{CEt})_2$ (**1**), $\text{Cu}_4(\mu\text{-}[3,5\text{-}(\text{CF}_3)_2\text{Pz}])_4(\mu\text{-EtC}\equiv\text{CEt})_2$ (**2**), $\text{Cu}_4(\mu\text{-}[3,5\text{-}(\text{CF}_3)_2\text{Pz}])_4(\mu\text{-MeC}\equiv\text{CMe})_2$ (**3**), $\text{Cu}_2(\mu\text{-CF}_3\text{CO}_2)_2(\text{EtC}\equiv\text{CEt})_2$ (**4**) and $\text{Cu}_4(\mu\text{-CF}_3\text{CO}_2)_4(\mu\text{-EtC}\equiv\text{CEt})_2$ (**5**).

Complex /Temp	ϵ ($\text{M}^{-1} \text{cm}^{-1}$)	λ_{exc} (max) (nm)		λ_{em} (max) (nm)		τ (μs)	
	298 K	298 K	77 K	298 K	77 K	298 K	77 K
1	1.3×10^4	280	270, 305	650	575, 675	38.11	60.38
2	1.0×10^5	280	270, 300	650	575, 675	40.97	59.94
3	1.1×10^5	280	270, 300	650	580, 665	44.05	56.98
4	8.1×10^3	N/A	N/A	N/A	N/A	N/A	N/A
5	1.8×10^4	N/A	N/A	N/A	N/A	N/A	N/A

ϵ = extinction coefficient at 298 nm for dilute (ca. 1×10^{-5} M) solutions. τ = photoluminescence lifetime at the characteristic λ_{\max} . Some entries are designated with “N/A” for “not applicable” because no emission was detectable.

The spectral profiles show overall similar results for solid powder samples of **1**, **2** and **3** at room temperature and at 77 K. At 298 K, complexes **1-3** show a single emission in the orange region with a peak maximum at 650 nm as a broad, unstructured band, and a single excitation feature centered at 280 nm. The emission peaks are assigned to ($T_1 \rightarrow S_0$) phosphorescence, evidenced by phosphorescence decay lifetimes of 40-44 μs . The spin-forbidden excitation, ($S_0 \rightarrow T_1$), is similar to the weak lowest-energy solution absorption maxima at $\lambda_{\max} \leq 300$ nm (Table 3.5, Figure 3.9, 3.10 and 3.11). This assignment affords a huge Stokes' shift of 20,300 cm^{-1} , suggesting very large excited state distortion. The photoluminescence spectra at 77 K of the three complexes show multiple emission bands depending on the temperature and excitation wavelengths. The difference between the excitations band intensities at $\lambda_{\text{exc}} \sim 320$ nm vs. 270 nm points at the contribution of spin-forbidden ($S_0 \rightarrow T_1$) and spin-allowed ($S_0 \rightarrow S_1$) transitions, respectively. The 298 K lower-energy emission ($\lambda_{\max} = 650$ nm, $T_1 \rightarrow S_0$) displays thermal broadening at 77 K and another higher-energy band appears at $\lambda_{\max} = 580$ nm, assignable to $T_2 \rightarrow S_0$ phosphorescence given its lifetime is also in the μs regime. No T_2 band at room temperature appears, as can be attributed to the presence of an internal conversion

process to the T_1 state.²³ However, additional observations for frozen solutions, data in Table 3.6, Figures 3.12, 3.13 and 3.14, show solvent-dependent emission and display a blue shift with ($\lambda_{\text{max/em}} = 470$ nm and $\lambda_{\text{max/exc}} \sim 265, 300$ nm for **1**; $\lambda_{\text{max/em}} = 560$ nm and $\lambda_{\text{max/exc}} \sim 280$ nm for both **2** and **3** in benzene (conc. 1×10^{-3} M)). The lower-energy electronic transition in the more polar solvent suggests a more polar excited state vs the ground state. This is consistent with the LMCT/LMMCT assignments to the initial excited state in Cu(I) pyrazolate clusters.^{23,80-83} Modification of the excited state assignment by intermolecular interactions in such literature precedents is, however, unlikely because of the absence of long-range cuprophilic interactions or other interaction types known to significantly affect photophysical transition energies - based on the crystallographic data above that do not show such interactions in **1-3**. Finally, we wish to comment that one cannot completely rule out delayed fluorescence from a higher-lying singlet (e.g., S_2) but the scan calculations we have performed for the $T_1 \rightarrow S_0$ transition (*vide infra*) have been sufficient in describing the excited state structure consistent with the experimental photophysics data in this section. Nevertheless, the presence or absence of thermally-activated delayed fluorescence (TADF) akin to that invoked in some literature precedents for this phenomenon in other molecular systems,¹³⁹⁻¹⁴¹ including Cu(I) complexes,^{140,141} warrants additional experimental/computational investigations that can distinguish TADF from the present phosphorescence assignment from partially-distorted T_1 and T_2 states.

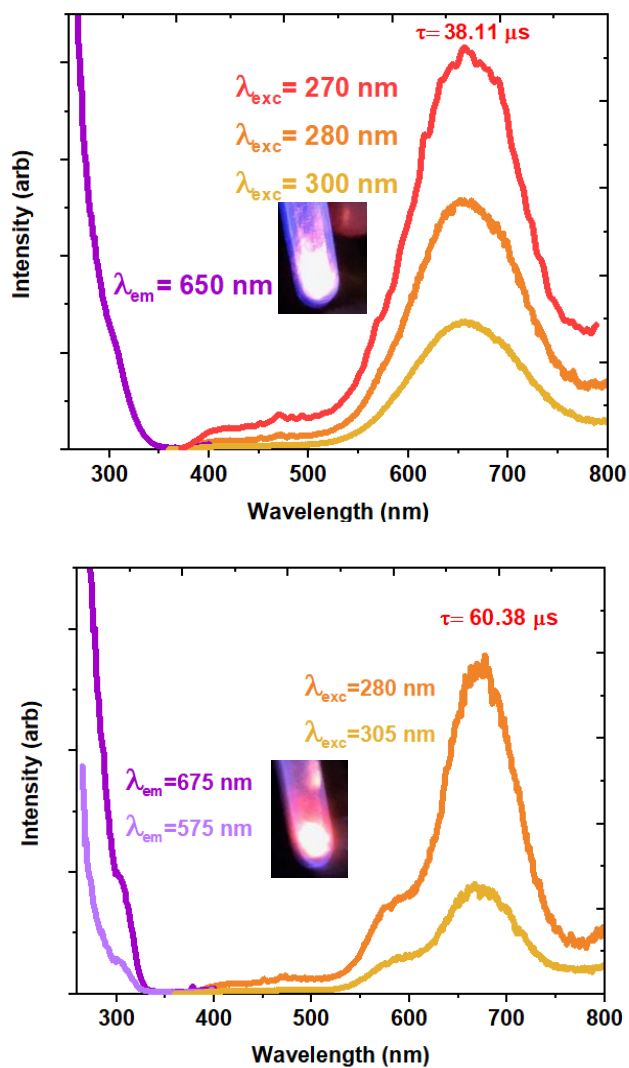


Figure 3.9 Photoluminescence spectra for a solid powder sample of $\text{Cu}_2(\mu\text{-}[3,5\text{-}(\text{CF}_3)_2\text{Pz}])_2(\text{EtC}\equiv\text{CEt})_2$ (**1**), at 298 K (top) and 77 K (bottom). Lifetimes are noted and have errors of $< 5\%$. Excitation and emission wavelengths used in the emission and excitation spectra, respectively, are labeled. A photograph is shown as an inset for colorless crystals packed in Suprasil quartz tubes while being exposed to UV light at room temperature.

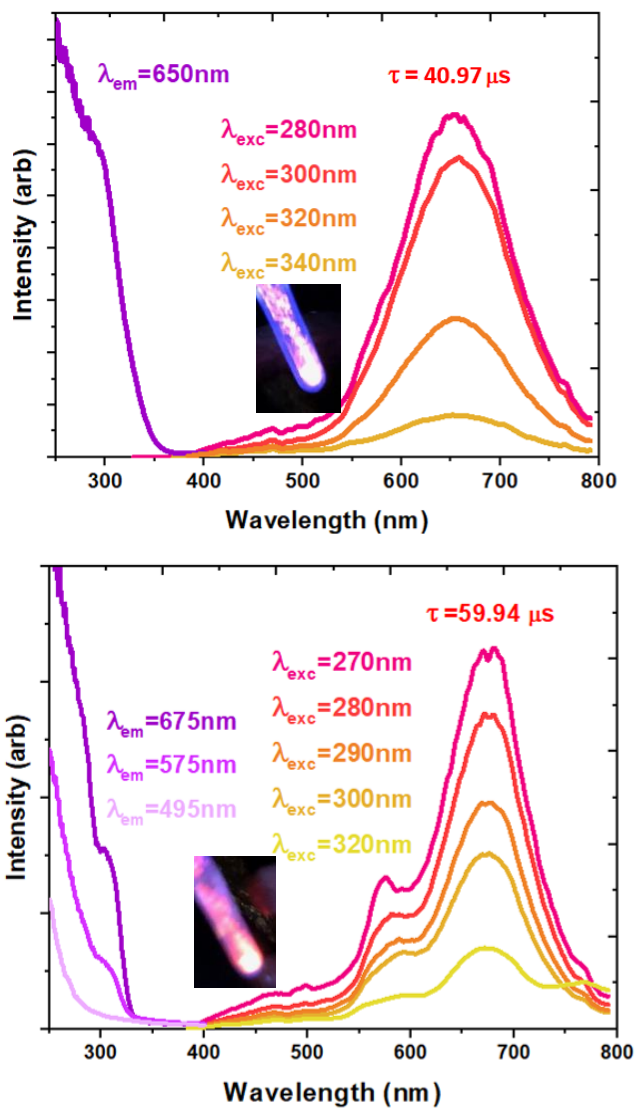


Figure 3.10 Photoluminescence spectra for a solid powder sample of $\text{Cu}_4(\mu\text{-}[3,5\text{-}(\text{CF}_3)_2\text{Pz}])_4(\mu\text{-EtC}\equiv\text{CEt})_2$ (**2**), at 298 K (top) and 77 K (bottom). Excitation and emission wavelengths used in the emission and excitation spectra, respectively, are labeled. A photograph is shown as an inset for colorless crystals packed in Suprasil quartz tubes while being exposed to UV light at room temperature.

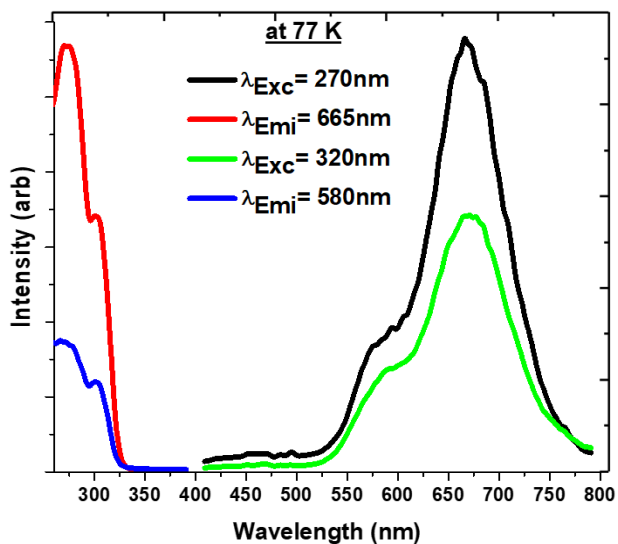
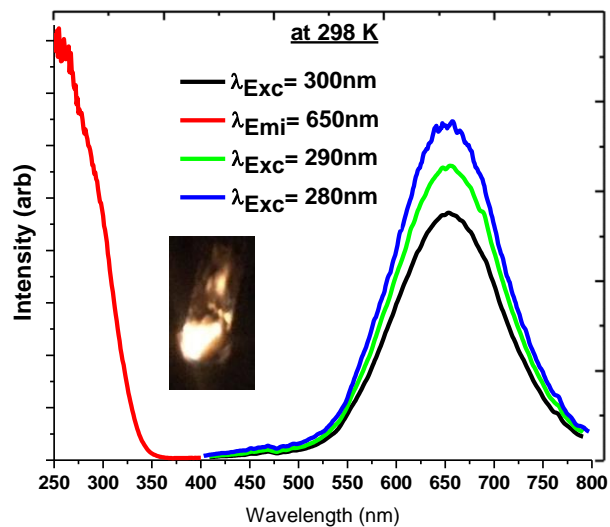


Figure 3.11 Photoluminescence spectra for a solid powder sample of $\text{Cu}_4(\mu\text{-}[3,5\text{-}(\text{CF}_3)_2\text{Pz}])_4(\mu\text{-MetC}\equiv\text{CMe})_2$ (**3**), at 298 K (top) and 77 K (bottom). Excitation and emission wavelengths used in the emission and excitation spectra, respectively, are labeled. A photograph is shown as an inset for colorless crystals packed in Suprasil quartz tubes while being exposed to UV light at room temperature.

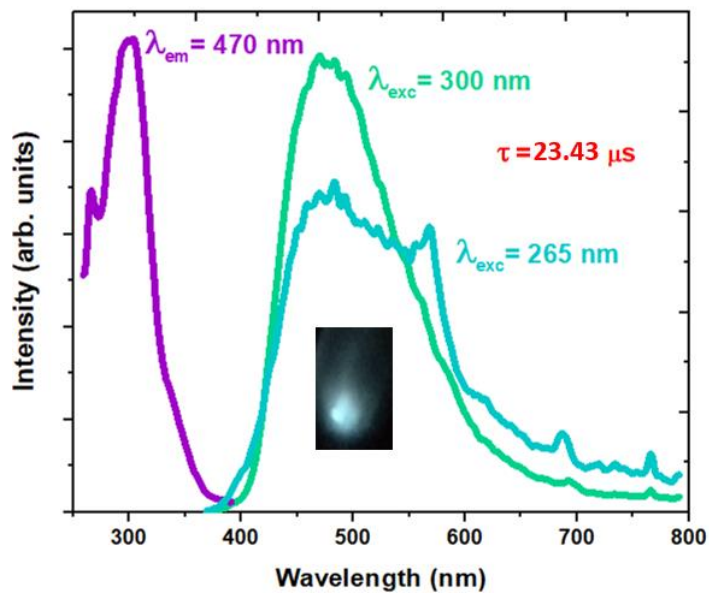


Figure 3.12 Photoluminescence spectra for frozen solution of $\text{Cu}_2(\mu\text{-}[3,5\text{-}(\text{CF}_3)_2\text{Pz}])_2(\text{EtC}\equiv\text{CEt})_2$ (**1**) in benzene (conc. = 1×10^{-3} M). Lifetimes are noted and have errors of $< 5\%$. Excitation and emission wavelengths used in the emission and excitation spectra, respectively, are labeled. Photograph is shown as inset for frozen solution in Suprasil quartz tube while being exposed to UV light at a liquid-nitrogen bath (77 K).

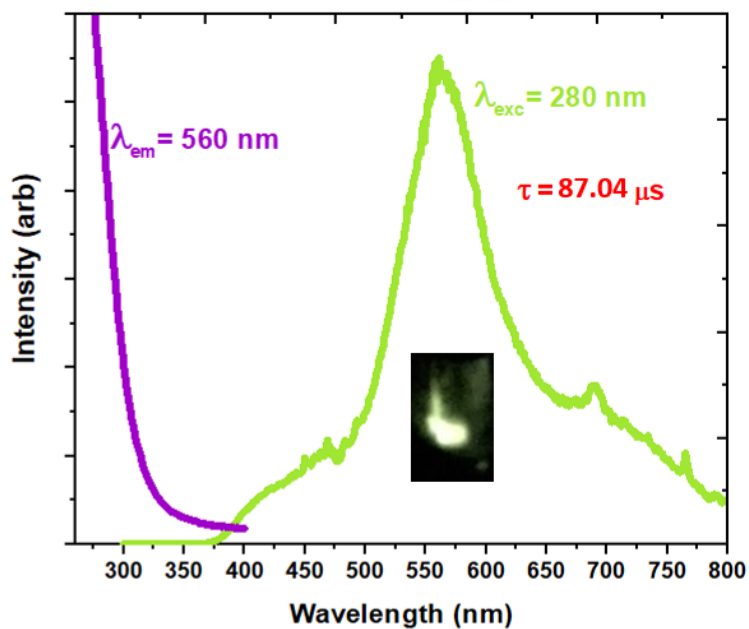


Figure 3.13 Photoluminescence spectra for frozen solution of $\text{Cu}_4(\mu\text{-}[3,5\text{-}(\text{CF}_3)_2\text{Pz}])_4(\mu\text{-EtC}\equiv\text{CEt})_2$ (**2**) in benzene (conc. = 1×10^{-3} M). Lifetime is noted and have error of < 5%. Excitation and emission wavelengths used in the emission and excitation spectra, respectively, are labeled. Photograph is shown as inset for frozen solution in Suprasil quartz tube while being exposed to UV light at a liquid-nitrogen bath (77 K).

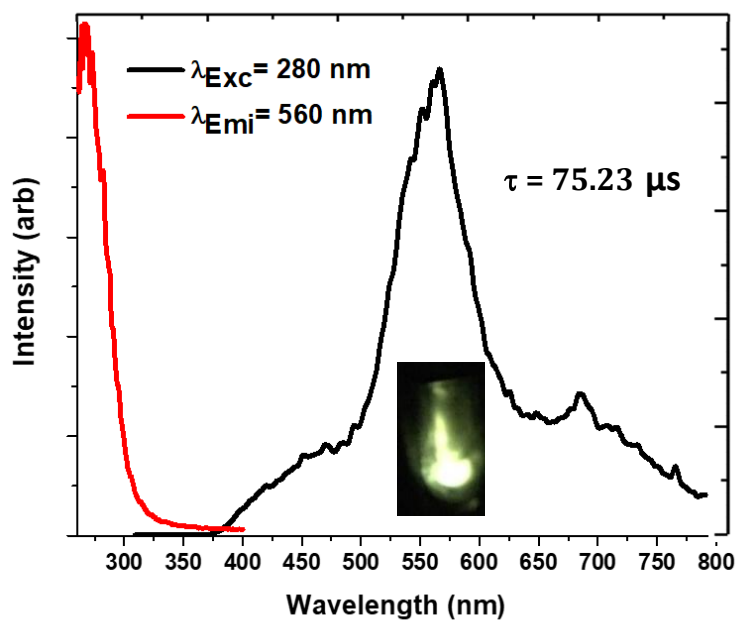


Figure 3.14 Photoluminescence spectra for frozen solution of $\text{Cu}_4(\mu\text{-}[3,5\text{-}(\text{CF}_3)_2\text{Pz}])_4(\mu\text{-MeC}\equiv\text{CMe})_2$ (**3**) in benzene (conc. = 1×10^{-3} M). Lifetime is noted and have error of $< 5\%$. Excitation and emission wavelengths used in the emission and excitation spectra, respectively, are labeled. Photograph is shown as inset for frozen solution in Suprasil quartz tube while being exposed to UV light at a liquid-nitrogen bath (77 K).

Table 3.6 Summary of photophysical parameters for complexes **1-3** in frozen solutions (glassy benzene matrix) at 77 K

Complex	$\lambda_{\text{exc (max)}} \text{ (nm)}$	$\lambda_{\text{em (max)}} \text{ (nm)}$	$\tau \text{ (\mu s)}$
1	265, 300	470	23.43
2	280	560	87.04
3	280	560	75.23

Computational analysis of photophysics:

To gain further insights on the excited state structure and photophysical transition band assignment, we have carried out pertinent DFT/TD-DFT simulations for the model complexes $\text{Cu}_2(\mu\text{-}[3,5\text{-}(\text{CF}_3)_2\text{Pz}]_2)(\text{EtC}\equiv\text{CEt})_2$ (**1**), $\text{Cu}_4(\mu\text{-}[3,5\text{-}(\text{CF}_3)_2\text{Pz}]_4)(\mu\text{-EtC}\equiv\text{CEt})_2$ (**2**) and $\text{Cu}_4(\mu\text{-}[3,5\text{-}(\text{CF}_3)_2\text{Pz}]_4)(\mu\text{-MeC}\equiv\text{CMe})_2$ (**3**). These models represent individual molecules for the solid-state structures of crystalline **1-3**, respectively, without explicitly accounting for intermolecular interactions. Moreover, experimental absorption spectra of complexes **1-3** were compared with TD-DFT simulations. The four sub-sections described below summarize the simulation results.

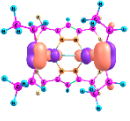
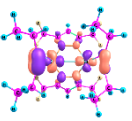
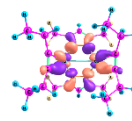
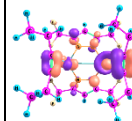
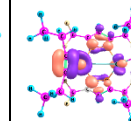
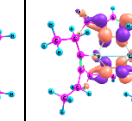
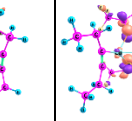
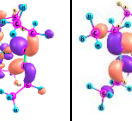
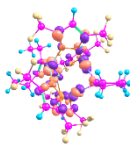
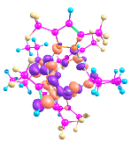
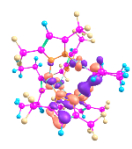
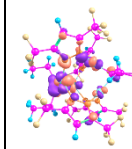
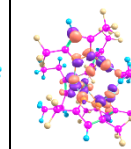
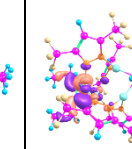
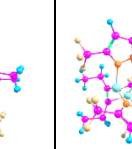
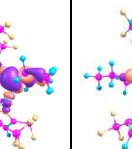
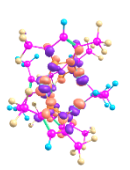

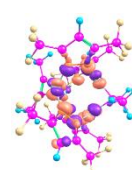
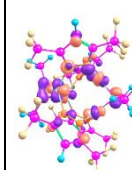
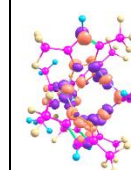
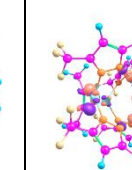
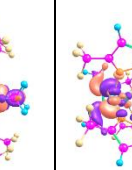
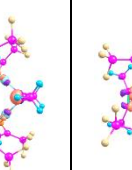
a								
	HOMO-4 (160)	HOMO-3 (161)	HOMO-2 (162)	HOMO-1 (163)	HOMO (164)	LUMO (165)	LUMO+1 (166)	LUMO+2 (167)
b								
	HOMO-4 (278)	HOMO-3 (279)	HOMO-2 (280)	HOMO-1 (281)	HOMO (282)	LUMO (283)	LUMO+1 (284)	LUMO+2 (285)
c								
	HOMO-6 (260)	HOMO-4 (262)	HOMO-3 (263)	HOMO-1 (265)	HOMO (266)	LUMO (267)	LUMO+1 (268)	LUMO+2 (269)

Figure 3.15 Isodensity surface plots (isodensity value = 0.043) of the frontier orbitals that contribute to the most intense TDDFT peaks of (a) $\text{Cu}_2(\mu\text{-}[3,5\text{-}(\text{CF}_3)_2\text{Pz}])_2(\text{EtC}\equiv\text{CEt})_2$ (**1**), (b) $\text{Cu}_4(\mu\text{-}[3,5\text{-}(\text{CF}_3)_2\text{Pz}])_4(\mu\text{-EtC}\equiv\text{CEt})_2$ (**2**), and (c) $\text{Cu}_4(\mu\text{-}[3,5\text{-}(\text{CF}_3)_2\text{Pz}])_4(\mu\text{-MeC}\equiv\text{CMe})_2$ (**3**).

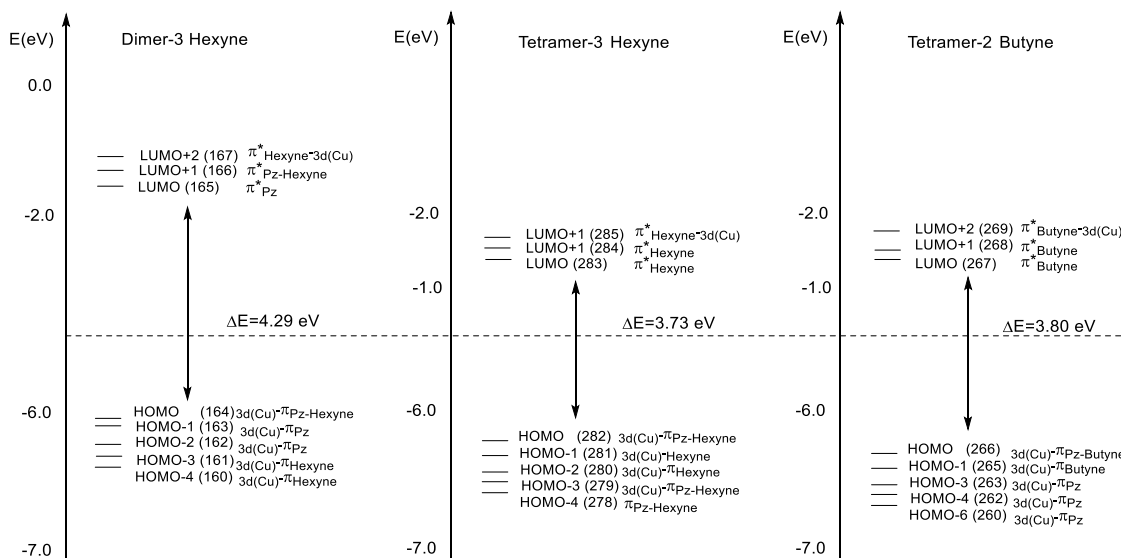


Figure 3.16 Energy levels (eV) of the dinuclear and tetranuclear complexes **1-3**.

Orbitals that did not significantly contribute to UV-vis band are not shown.

(a) *UV/Vis spectra for 1*: Based on the calculations, for the dinuclear complex of **1**, the three most intense spin-allowed ($S_0 \rightarrow S_n$) transitions computed have oscillator strength (f) magnitudes of 0.050, 0.038, and 0.028 for the bands with $\lambda_{\text{max/abs}} = 263$, 280 and 272 nm, respectively. Specifically, the most intense transition for **1** at 263 nm ($f = 0.050$) has a metal-ligand to ligand charge transfer (ML \rightarrow LCT) character that mainly originates from a 3d(Cu)- π_{hexyne} HOMO-3(161) to the $\pi^*_{\text{Pz}}-\pi^*_{\text{hexyne}}$ LUMO+1(166), as given in Figure 3.15, 3.16 and Table 3.7. This was followed by quasi-degenerate M&L-LCT transitions of similar intensity ($f = 0.038$ and 0.028) found at 280 and 272 nm whose final states are a π^*_{Pz} orbital LUMO(165), delocalized over the pyrazolate (Pz) ligands, with larger contributions arising from

the $3d(\text{Cu})-\pi_{\text{hexyne}}-\pi_{\text{Pz}}$ HOMO(164) and $3d(\text{Cu})-\pi_{\text{hexyne}}$ HOMO-3(161). The experimental excitation maximum is 280 nm, which is closer to the computed second most intense excitation value (280 nm).

Table 3.7 Computed excitation energies (eV) and oscillator strengths (f) for the optical transitions with $f > 0.025$ of the dinuclear complex $\text{Cu}_2(\mu\text{-}[3,5\text{-}(\text{CF}_3)_2\text{Pz}])_2(\text{EtC}\equiv\text{CEt})_2$ (**1**) in the gas phase in terms of molecular orbitals involved in the excitations with percentages larger than 12%.

nm	f	Type	
BP86/6-311+G(d) (Dimer)			
263	0.050	M&L LCT	$49\%(t_{2g}\text{Cu}-\pi_{\text{Hexyne}})_{161} \rightarrow (\pi_{\text{Pz}}^*-\pi_{\text{Hexyne}}^*)_{166} + 15\%(t_{2g}\text{Cu}-\pi_{\text{Hexyne}})_{160} \rightarrow (\pi_{\text{Hexyne}}^*)_{167}$
280	0.038	M&L LCT	$57\%(t_{2g}\text{Cu}-\pi_{\text{Pz}}-\pi_{\text{Hexyne}})_{164} \rightarrow (\pi_{\text{Pz}}^*)_{165} + 22\%(t_{2g}\text{Cu}-\pi_{\text{Hexyne}})_{163} \rightarrow (\pi_{\text{Pz}}^*)_{165}$
272	0.028	M&L LCT	$67\%(t_{2g}\text{Cu}-\pi_{\text{Hexyne}})_{161} \rightarrow (\pi_{\text{Pz}}^*)_{165} + 12\%(t_{2g}\text{Cu}-\pi_{\text{Pz}})_{162} \rightarrow (\pi_{\text{Pz}}^*-\pi_{\text{Hexyne}}^*)_{166}$

In parentheses we report the character of the orbitals involved in the transition; orbital numbering is the same of Fig. 3 for gas.

(b) *UV/Vis spectra for 2*: According to TD-DFT, for the 3-hexyne ligated tetranuclear complex model of **2** in the gas phase, the three most intense transitions are in the 314–305 nm range with $f > 0.01$. In particular, the most intense transition for the complex was at 305 nm ($f = 0.018$). This transition has an ML→MLCT character, whereby metal-ligand mixing takes place in both the filled source and virtual destination orbitals. Specifically, the transition originates from the $3d(\text{Cu})-\pi_{\text{hexyne}}$ HOMO-1(281) \rightarrow $3d(\text{Cu})-\pi_{\text{hexyne}}^*$ LUMO+2(285) with a substantial contribution from the $\pi_{\text{Pz}}-\pi_{\text{hexyne}}$ HOMO-4 (278) \rightarrow π_{hexyne}^* LUMO+1(284) (12 %)

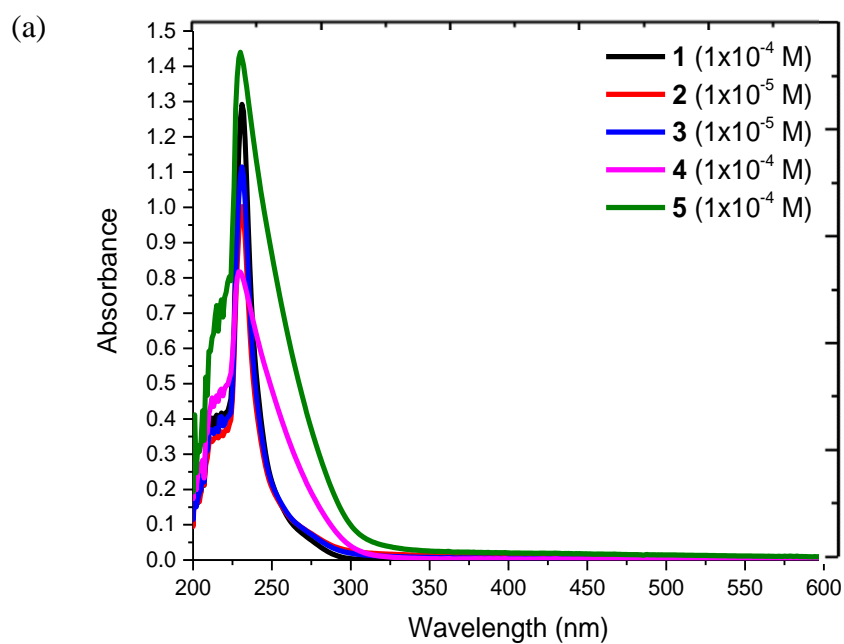
transitions, Figure 3.15, 3.16 and Table 3.8. This most intense calculated transition agrees well with the experimental excitation value of 280 nm. The second most intense transition has an LLCT assignment, being of $\pi_{\text{hexyne}}-\pi_{\text{Pz}}$ HOMO-4(278) $\rightarrow \pi^*_{\text{hexyne}}$ LUMO(283) character. The third most intense transition has an ML \rightarrow LCT assignment, attributed to a $3d(\text{Cu})-\pi_{\text{hexyne-Pz}}$ HOMO-3(279) $\rightarrow \pi^*_{\text{hexyne}}$ LUMO+1(284) transition, with considerable contribution from $3d(\text{Cu})-\pi_{\text{hexyne}}$ HOMO-2(280) $\rightarrow \pi^*_{\text{hexyne}}$ LUMO+1(284).

Table 3.8 Computed excitation energies (eV) and oscillator strengths (f) for the optical transitions with $f > 0.01$ of the 3-hexyne ligated tetranuclear complex $\text{Cu}_4(\mu\text{-}[3,5\text{-}(\text{CF}_3)_2\text{Pz}])_4(\mu\text{-EtC}\equiv\text{CEt})_2$ (**2**) in the gas phase in terms of molecular orbitals involved in the excitations with percentages larger than 12%.

nm	f	Type	
BP86/6-311+G(d) (3-Hexyne ligated tetramer)			
305	0.018	M&L M&LCT	81%($t_{2g}\text{Cu}-\pi_{\text{Hexyne}}$) $_{281} \rightarrow (t_{2g}\text{Cu}-\pi^*_{\text{Hexyne}})$ $_{285}$; 12%($\pi_{\text{Pz}}-\pi_{\text{Hexyne}}$) $_{278} \rightarrow (\pi^*_{\text{Hexyne}})$ $_{284}$
309	0.017	LLCT	86%($\pi_{\text{Pz}}-\pi_{\text{Hexyne}}$) $_{278} \rightarrow (\pi^*_{\text{Hexyne}})$ $_{284}$
314	0.011	M&L LCT	62%($t_{2g}\text{Cu}-\pi_{\text{Pz}}-\pi_{\text{Hexyne}}$) $_{279} \rightarrow (\pi^*_{\text{Hexyne}})$ $_{284}$; 17%($t_{2g}\text{Cu}-\pi_{\text{Hexyne}}$) $_{280} \rightarrow (\pi^*_{\text{Hexyne}})$ $_{284}$
In parentheses we report the character of the orbitals involved in the transition; orbital numbering is the same of Fig. 3 for gas and Fig. 5 for solvents.			

(c) *UV/Vis spectra of 1-3 in dichloromethane solvent:* Based on the TD-DFT calculations, for the complexes of **1-3**, the average of three most intense spin-allowed ($S_0 \rightarrow S_n$) transitions computed as 276, 308, and 302 nm, respectively, according to the SMD continuum solvation model for CH_2Cl_2 ; SMD = solvent model based on density. The experimental absorption spectra of the complexes of

1-3 in dichloromethane solution were reported to be close to 240 nm. Thus, perturbations of the TD-DFT spectra due to solvent are ≈ 5435 , 9199 and 8554 cm^{-1} , for the complexes **1**, **2**, and **3**, respectively. Detailed TD-DFT results are given in Figure 3.17.



(b)

nm	f	Type
BP86/6-311+G(d) (Dimer)		
265	0.057	
286	0.054	
276	0.043	

In dichloromethane solvent

(c)

m	f	Type
<hr/>		
BP86/LANL2DZ (3-Hexyne ligated tetramer)		
305	0.036	M&L M&LCT
305	0.023	LLCT
315	0.017	M&L LCT

In dichloromethane solvent

(d)

nm	f	Type
<hr/>		
BP86/LANL2DZ (2-Butyne ligated tetramer)		
298	0.069	M&L M&LCT
300	0.036	M&L LCT
308	0.028	M&L LCT

In dichloromethane solvent

Figure 3.17. (a) Experimental absorption spectra of dichloromethane solution of **1** – **5**. Calculated electronic spectrum with spin-allowed (singlet-to-singlet, $S_0 \rightarrow S_n$) excitation energies (vertical lines) and oscillator strengths for the complex **1**, **2**, and **3** in dichloromethane solvent, are depicted in (b), (c), and (d), respectively.

(d) *Emissive states*: Phosphorescence energies for the Cu₂ adduct **1** and Cu₄ adducts **2** and **3** are calculated from the vertical T₁→S₀ transitions; such notation stands for the T₁ (excited state) and S≡T (ground-state singlet spin multiplicity at the excited-state triplet geometry). These are expected in the vicinity of the yellow-orange region of the spectrum based on the experimental values in Table 3.5. Singlet (S₀) and triplet (T₁) optimized geometries are depicted in Figure 3.18. Excited state distortion in T₁ was computed to involve mild changes in the Cu-Cu distance(s) contrasted with a significant change of the dihedral angle formed by the two C≡C bonds, δτ, which afforded 83°, 34° and 28° for **1**, **2** and **3**, respectively (Table 3.9). For the model of **1**, for example, S₀ (179°) → T₁ (96°) and δτ = 83° dihedral angles are obtained.

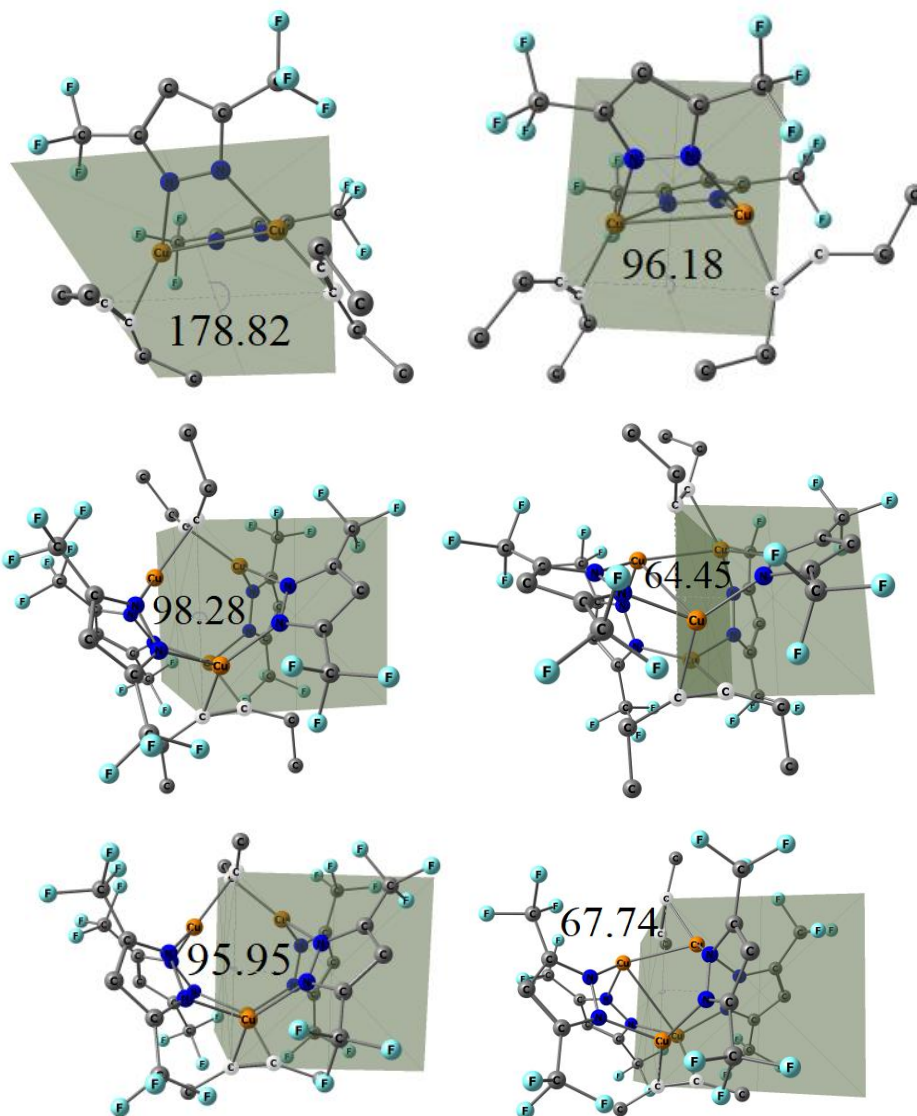


Figure 3.18 Singlet (S_0) and triplet (T_1) optimized geometries. Singlet and triplet $C\equiv C\dots C\equiv C$ dihedral angles of samples. First row: singlet of **1**; triplet of **1**. Second row: singlet of **2**; triplet of **2**. Third row: singlet of **3**; triplet of **3**.

Prior to single-point scan calculations of the $C\equiv C\cdots C\equiv C$ dihedral angles, the DFT-computed emission wavelengths for **1-3** models were computed to be in the near-IR region with too large Stokes' shifts that did not correlate with experimental values even qualitatively. The gas phase models allow for drastic excited-state distortions that are not feasible in the confined crystalline topology of packed molecules, necessitating the pertinent scan calculations we have performed to attain more realistic excited-state structures. The computed phosphorescence transition energies agreed well with experimental trends upon varying the dihedral angle for the T_1 geometries (relaxed scan calculations) of **1**, **2** and **3** by $\sim 20^\circ$ versus the corresponding S_0 ground state $\delta\tau$ value, as given in Tables 3.9 and 3.10.

Table 3.9 DFT-computed Cu-Cu distances, alkyne dihedral angles τ ($C\equiv C\dots C\equiv C$), and phosphorescence wavelengths (λ_{em}) for models of **1-3**^a.

Model	S_0	T_1	S_0	T_1	$\delta\tau$ ($^\circ$)	Scanned	Calc.	Expt.
	Opt.	Opt.						Opt.
	d_{Cu-Cu}	d_{Cu-Cu}	τ ($^\circ$)	τ ($^\circ$)		T_1	λ_{em}	λ_{em}
	(\AA)	(\AA)				$\delta\tau$ ($^\circ$)	(nm)	(nm)
1	3.16	3.19	179 $^\circ$	96 $^\circ$	83 $^\circ$	160 $^\circ$	640	650
2	2.67	2.61	98 $^\circ$	64 $^\circ$	34 $^\circ$	80 $^\circ$	679	650
3	2.67	2.61	96 $^\circ$	68 $^\circ$	28 $^\circ$	80 $^\circ$	685	650

^aBesides fully-optimized τ values in gas phase models, analogous values are given from scan calculations (10° increments) that most-closely approach experimental

solid-state phosphorescence maxima. λ_{em} values are calculated for the $T_1 \rightarrow S_0$ vertical transitions. $\delta\tau$ = difference in τ between fully optimized S_0 and T_1 states.

Table 3.10 DFT-computed excitation and emission wavelengths for complexes **1** - **3** upon varying the dihedral angles in the S_0 ground and T_1 excited states and their correlation with experimental photophysical data.

	Scan $\delta\tau$ ^a	180°	170°	160° [*]	150°	140°	Experimental λ_{max} (nm)
1	λ_{exc} (nm)	289	292	292 [*]	321	346	280
	λ_{em} (nm)	546	619	640 [*]	670	712	650
	Scan $\delta\tau$ ^a	85°	80° [*]	75°	70°	---	---
2	λ_{exc} (nm)	335	338 [*]	344	355	---	280
	λ_{em} (nm)	710	679 [*]	567	560	---	650
	Scan $\delta\tau$ ^a	85°	80° [*]	75°	---	---	---
3	λ_{exc} (nm)	332	336 [*]	343	---	---	280
	λ_{em} (nm)	580	685 [*]	732	---	---	650
	Scan $\delta\tau$ ^a	85°	80° [*]	75°	---	---	---

^aRelaxed scans of the $C \equiv C \dots C \equiv C$ dihedral angle ($\delta\tau$) are performed for the ground singlet and excited triplet state. The asterisks (*) denote the τ for which the computed emission wavelength (in nm) most closely approximates experiment (last column).

The calculations thus suggest that the major excited-state rearrangement (Δq), which involves twists in the alkyne ligands, is less severe in the solid state than in the gas-phase simulations, as manifest by T_1 dihedral angle change vs the S_0 ground state of $\Delta q \sim 20^\circ$ in the solid state for all three complexes vs larger Δq values of 83° , 34° and 28° for gas phase models of **1**, **2** and **3**, respectively. Such a milder change in the solid state is a reasonable contention and not without precedent in d^{10} photophysics.¹⁴²

3.1.4 Summary

Overall, we report convenient routes to the syntheses of di- and tetra-nuclear copper(I) complexes, $\text{Cu}_2(\mu\text{-}[3,5\text{-}(\text{CF}_3)_2\text{Pz}])_2(\text{EtC}\equiv\text{CEt})_2$ (**1**), $\text{Cu}_4(\mu\text{-}[3,5\text{-}(\text{CF}_3)_2\text{Pz}])_4(\mu\text{-EtC}\equiv\text{CEt})_2$ (**2**), $\text{Cu}_4(\mu\text{-}[3,5\text{-}(\text{CF}_3)_2\text{Pz}])_4(\mu\text{-MeC}\equiv\text{CMe})_2$ (**3**) with short cuprophilic contacts using readily available $\{[3,5\text{-}(\text{CF}_3)_2\text{Pz}]\text{Cu}\}_3$ and the corresponding internal alkynes. Control of reaction stoichiometry also allows for conversion of adducts **1** and **2** to/from one another. X-ray crystallographic data confirm the dinuclear nature of **1** and the tetra-nuclear structure of **2** and **3**. Structurally characterized adducts like **2** and **3** with bridging (i.e., $\mu_2\text{-}\eta^2, \eta^2\text{-}$) alkyne ligands are rare in copper chemistry. Raman data show a reduction in $\bar{\nu}_{\text{C}=\text{C}}$ stretching frequency from 2260 cm^{-1} in free 3-hexyne to 2050 cm^{-1} in the terminal $\eta^2\text{-}/2e\text{-donor}$ alkyne adduct **1** and, more drastically, to 1874 cm^{-1} in the bridged

$\mu_2-\eta^2,\eta^2$ -4e-donor adduct **2**, akin to IR $\bar{\nu}_{C\equiv O}$ shifts in terminal and bridging metal carbonyls. The complex **3** also shows a similar trend.

The chosen level of theory (BP86/6-311+G(d)) reproduced experimental trends with respect to the alkyne bond lengths and the geometry for the Cu_2 complex **1** relative to Cu_4 complex **2**, and 2-butyne ligated Cu_4 complex **3**. The $C\equiv C$ bond of **1-3** were predicted to be lengthened versus the relative free alkynes, as well as bending of the $C-C\equiv C$ angle away from linear. Moreover, predicted CC stretching frequencies of the samples were well correlated with experimental data and bonding parameters. Natural bond orbital analysis method was used to analyze the bond order of the CC bond of 3-hexyne adducts **1** and **2**. The analysis indicated that $C\equiv C$ bonding orbitals of **2** has $0.080e^-$ less as compared to the dinuclear species **1**. Moreover, there are 0.188 more electrons in $C\equiv C$ antibonding orbitals for **2** versus **1**. Therefore, based on the DCD model, it is suggested that both increased σ -donation from 3-hexyne to copper and increased π -backbonding from copper to the π^*_{CC} of 3-hexyne in **2** versus **1**. This also explains the greater elongation of $C\equiv C$ bonds, the more bent the $C-C\equiv C$ bond angle, and the more red-shifted the $C\equiv C$ stretching frequency in **2**.

We have also investigated the related copper(I) trifluoroacetate 3-hexyne complexes **4** and **5** to deduce, and isolate the role played by the supporting pyrazolate ligand on the luminescence of complexes like **1-3**. Solid samples of

pyrazolate-supported compounds **1-3** show bright photoluminescence, whereas trifluoroacetate copper alkyne complexes **4** and **5** do not show any luminescence upon UV excitation. Computational analysis of **1-3** suggest that the photo-excitation consists of mixed metal-ligand to ligand and mixed metal-ligand to metal-ligand charge transfer process involving pyrazolate ligands.

Furthermore, the orange phosphorescence with ~ 50 μs lifetime at room temperature in **1-3** thermochromically changes to generate additional green/yellow bands at cryogenic temperatures due to suppression of internal conversion from the respective $T_2 \rightarrow T_1$ states in each solid, whereas solvent effects lead to additional blue-shifted bands in glassy solvent media. Computational analysis suggests that the major excited-state distortion is due to significant ($\geq 20^\circ$) rotation in the alkyne's dihedral angle upon coordination to Cu(I) in the di- or tetra-nuclear adducts, as opposed to excimeric contraction of cuprophilic Cu(I) \cdots Cu(I) distances.

Part 3.2 Chemistry and transformations of acetylene and terminal alkyne

complexes of copper(I)

Devaborniny Parasar, Tharun T. Ponduru, Anurag Noonikara Poyil, Naleen B.

Jayaratna, and H. V. Rasika Dias

(Part of this work has been published in *Dalton Trans.*, 2019, 48, 15782–15794)

Reproduced from references¹⁴³ with permission from the © The Royal Society of
Chemistry 2019

3.2.1 Abstract

Trinuclear $\{\mu\text{-}[3,5\text{-}(\text{CF}_3)_2\text{Pz}]\text{Cu}\}_3$ reacts with acetylene to produce the 2:1 copper(I) acetylene complex, $\text{Cu}_4(\mu\text{-}[3,5\text{-}(\text{CF}_3)_2\text{Pz}])_4(\mu\text{-HC}\equiv\text{CH})_2$. Related $\text{Cu}_4(\mu\text{-}[4\text{-Br-}3,5\text{-}(\text{CF}_3)_2\text{Pz}])_4(\mu\text{-HC}\equiv\text{CH})_2$ and $\text{Cu}_4(\mu\text{-}[4\text{-Cl-}3,5\text{-}(\text{CF}_3)_2\text{Pz}])_4(\mu\text{-HC}\equiv\text{CH})_2$ have also been isolated using the corresponding copper(I) pyrazolate and acetylene. The 1:1 adducts $\text{Cu}_2(\mu\text{-}[3,5\text{-}(\text{CF}_3)_2\text{Pz}])_2(\text{HC}\equiv\text{CH})_2$ and $\text{Cu}_2(\mu\text{-}[4\text{-Br-}3,5\text{-}(\text{CF}_3)_2\text{Pz}])_2(\text{HC}\equiv\text{CH})_2$ are significantly less stable to the acetylene loss and can be observed in solution at low temperatures under excess acetylene. The X-ray crystal structures of 2:1 and 1:1 complexes, $\text{Cu}_4(\mu\text{-}[3,5\text{-}(\text{CF}_3)_2\text{Pz}])_4(\mu\text{-HC}\equiv\text{CH})_2$ and $\text{Cu}_2(\mu\text{-}[4\text{-Br-}3,5\text{-}(\text{CF}_3)_2\text{Pz}])_2(\text{HC}\equiv\text{CH})_2$ are reported. Raman data show a reduction in $\bar{\nu}_{\text{C}\equiv\text{C}}$ stretching frequency by about ~ 340 and ~ 163 cm^{-1} in the 2:1 and 1:1 Cu(I)/acetylene complexes, respectively, from that of the free acetylene. Copper(I) pyrazolate complexes of the terminal alkynes, phenylacetylene, 1,8-nonadiyne, and 1,7-octadiyne are also reported. They form adducts involving one copper atom on each alkyne moiety. The $\{\mu\text{-}[3,5\text{-}(\text{CF}_3)_2\text{Pz}]\text{Cu}\}_3$ is also a very versatile and competent catalyst for alkyne transformations as evident from its ability to catalyze the alkyne C(sp)-H bond carboxylation chemistry with CO_2 , azide-alkyne cycloadditions leading to 1,2,3-triazoles including the use of acetylene itself as a substrate, and thiol addition to phenylacetylene affording vinyl sulfides.

3.2.2 Introduction

Trinuclear copper pyrazolates are of significant interest due to their fascinating photophysical properties and tendency to self-assemble via Cu•••Cu contacts.^{15,21,53,74,75,79,85,88,91,97,99,144-148} For example, the copper complex $\{\mu\text{-}[3,5\text{-}(\text{CF}_3)_2\text{Pz}]\text{Cu}\}_3$ (**1**) exhibits bright orange luminescence, which can be fine- and coarse-tuned to multiple bright visible colors by varying solvents, concentration, temperatures, and excitation wavelength.^{15,53} Dendritic, trinuclear Cu(I) pyrazolate complexes carrying long alkyl chains have been utilized in the fabrication of rewritable phosphorescent paper.⁷⁵ Trinuclear copper pyrazolates also serve as good precursors to produce various mixed ligand complexes or hybrid materials with different nuclearities and/or supramolecular structures.^{6,30,33,85,87,94,96,144,149} For example, dinuclear $\text{Cu}_2(\mu\text{-}[3,5\text{-}(\text{CF}_3)_2\text{Pz}])_2(2,4,6\text{-collidine})_2$ obtained from $\{\mu\text{-}[3,5\text{-}(\text{CF}_3)_2\text{Pz}]\text{Cu}\}_3$ and 2,4,6-collidine show ligand based blue emissions that are different from the orange emissions of the precursor $\{\mu\text{-}[3,5\text{-}(\text{CF}_3)_2\text{Pz}]\text{Cu}\}_3$.¹⁰ Some of these copper complexes such as $\{\mu\text{-}[3,5\text{-}(\text{CF}_3)_2\text{Pz}]\text{Cu}\}_3$ with electron-withdrawing fluoroalkyl groups on the ligand backbones act as π -acidic units, and are known to associate with electron rich arenes (e.g., benzene, mesitylene) and C_{60} leading to 2D- or 3D-stacks.^{87,93,100} In addition, copper pyrazolates also show promise in catalysis,^{19,89,98,150-154} and adsorption and/or separation of small molecules,^{33,145,155,156} but these applications have received relatively less scrutiny.

Copper mediates many important transformations involving alkynes such as hetero atom-hydrogen bond additions, cycloaddition chemistry, cyclopropanation, C_{sp}-H bond functionalizations, and alkyne coupling processes.^{79,104,105,114,157-169} Copper alkyne or alkynide complexes are believed to be key intermediates in most of these reactions. Copper alkynes are also used as precursors for the copper deposition.^{124,170} Despite the importance of copper in alkyne chemistry and the availability of a large number and a diverse group of binary copper(I) pyrazolates, coordination chemistry of copper pyrazolates with alkynes, or the use of copper-pyrazolates as catalysts in alkyne transformations remain virtually unexplored. There was an isolated report in 2002 relevant to this topic concerning the synthesis Cu₂(μ-[3,5-(CF₃)₂Pz])₂(Me₃SiC≡CSiMe₃)₂, as a chemical vapor deposition (CVD) precursor for copper.⁹⁵ As a first part of a detailed investigation into this area, we reported the isolation of di- and tetra-nuclear copper complexes such as **2** and **3** (Figure 3.19) resulting from the reaction between trinuclear {μ-[3,5-(CF₃)₂Pz]Cu}₃ (**1**) and internal-alkynes, together with their structures (including molecules featuring bridged, μ₂-η²,η²-/4e-alkyne donors) and photophysical properties.⁷³ Herein we describe the coordination chemistry of copper(I) pyrazolates with acetylene and terminal-alkynes, as well as the use of {μ-[3,5-(CF₃)₂Pz]Cu}₃ as a catalyst in the carboxylation, azide-cycloaddition and hydrothiolation of alkynes. Recently, a communication appeared on the use of {μ-[3,5-(CF₃)₂Pz]Cu}₃ in click-chemistry, and the isolation of two mixed-valent

copper alkyne complexes (resulting from the partial oxidation of Cu(I) in the precursor).¹⁷¹ Their report complement the azide-alkyne cycloaddition results described herein.

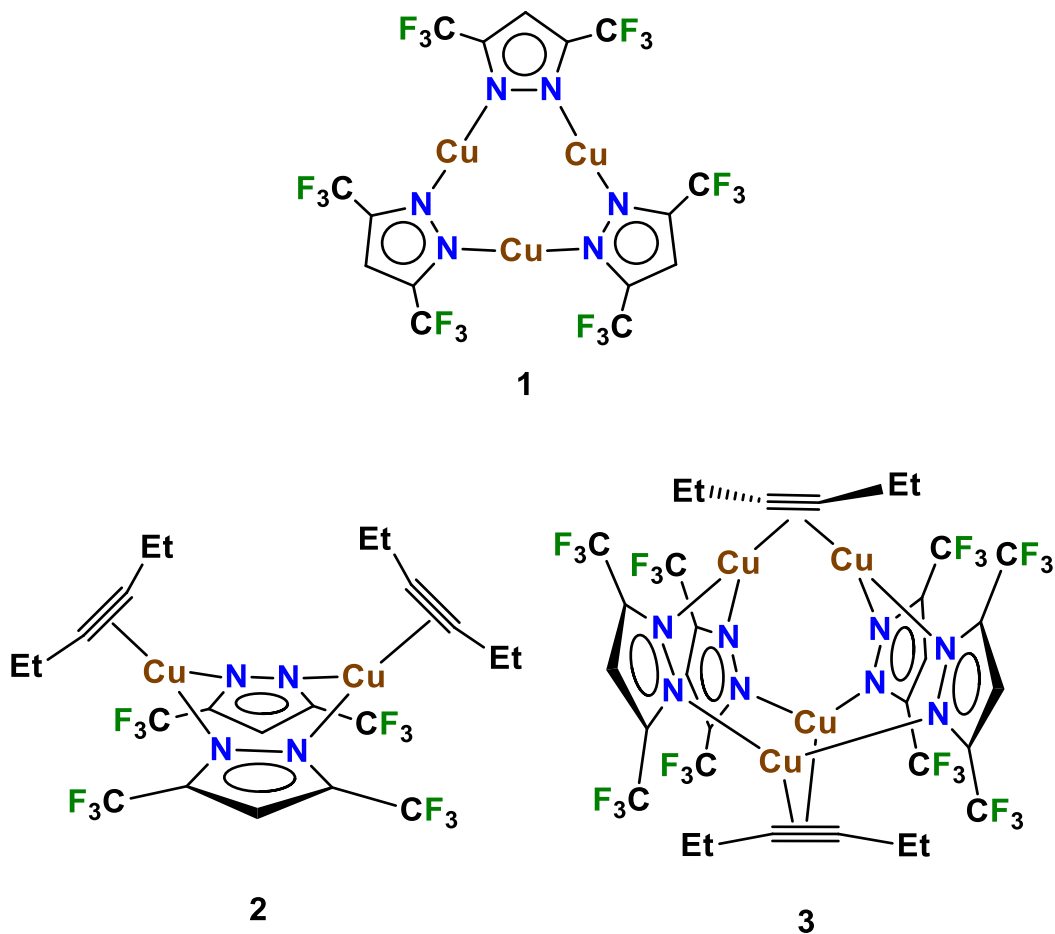


Figure 3.19 Diagram showing the structures of $\{\mu\text{-}[3,5\text{-(CF}_3)_2\text{Pz}]\text{Cu}\}_3$ (**1**), $\text{Cu}_2(\mu\text{-}[3,5\text{-(CF}_3)_2\text{Pz}])_2(\text{EtC}\equiv\text{CEt})_2$ (**2**), and $\text{Cu}_4(\mu\text{-}[3,5\text{-(CF}_3)_2\text{Pz}])_4(\mu\text{-EtC}\equiv\text{CEt})_2$ (**3**)

3.2.3 Results and Discussion

Coordination chemistry of copper pyrazolates with acetylene:

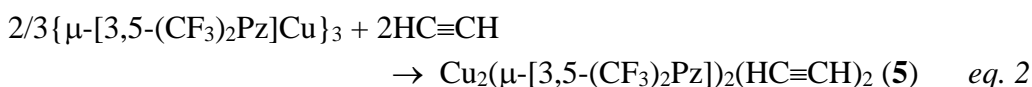
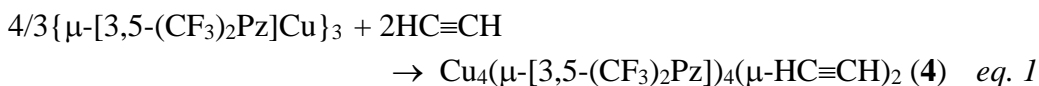


Figure 3.20 Synthetic routes to di- and tetra-nuclear complexes complexes $\text{Cu}_2(\mu\text{-}[3,5\text{-}(\text{CF}_3)_2\text{Pz}])_2(\text{HC}\equiv\text{CH})_2$ (**5**) and $\text{Cu}_4(\mu\text{-}[3,5\text{-}(\text{CF}_3)_2\text{Pz}])_4(\mu\text{-HC}\equiv\text{CH})_2$ (**4**) from trinuclear $\{\mu\text{-}[3,5\text{-}(\text{CF}_3)_2\text{Pz}]\text{Cu}\}_3$

The highly fluorinated $\{\mu\text{-}[3,5\text{-}(\text{CF}_3)_2\text{Pz}]\text{Cu}\}_3$ (**1**) reacts with purified acetylene (~ 1 atm)^{169,172} in CH_2Cl_2 , affording $\text{Cu}_4(\mu\text{-}[3,5\text{-}(\text{CF}_3)_2\text{Pz}])_4(\mu\text{-HC}\equiv\text{CH})_2$ (**4**) as a white, crystalline solid in $>90\%$ yield (Figure 3.20, eq. 1 and Figure 3.21). The room temperature ^1H NMR data of **4** in CDCl_3 displayed the presence of a 2:1 Cu:acetylene complex, and a large, down-field shift of acetylenic proton resonances (observed at δ 6.16 ppm) relative to the corresponding signal of the free acetylene (δ 2.05 ppm). The $\bar{\nu}_{\text{C}\equiv\text{C}}$ band of solid **4** in the Raman spectrum was observed at 1638 cm^{-1} , representing a significant (336 cm^{-1}) red shift relative to the

corresponding stretching frequency of the free acetylene (1974 cm^{-1}).¹⁷³

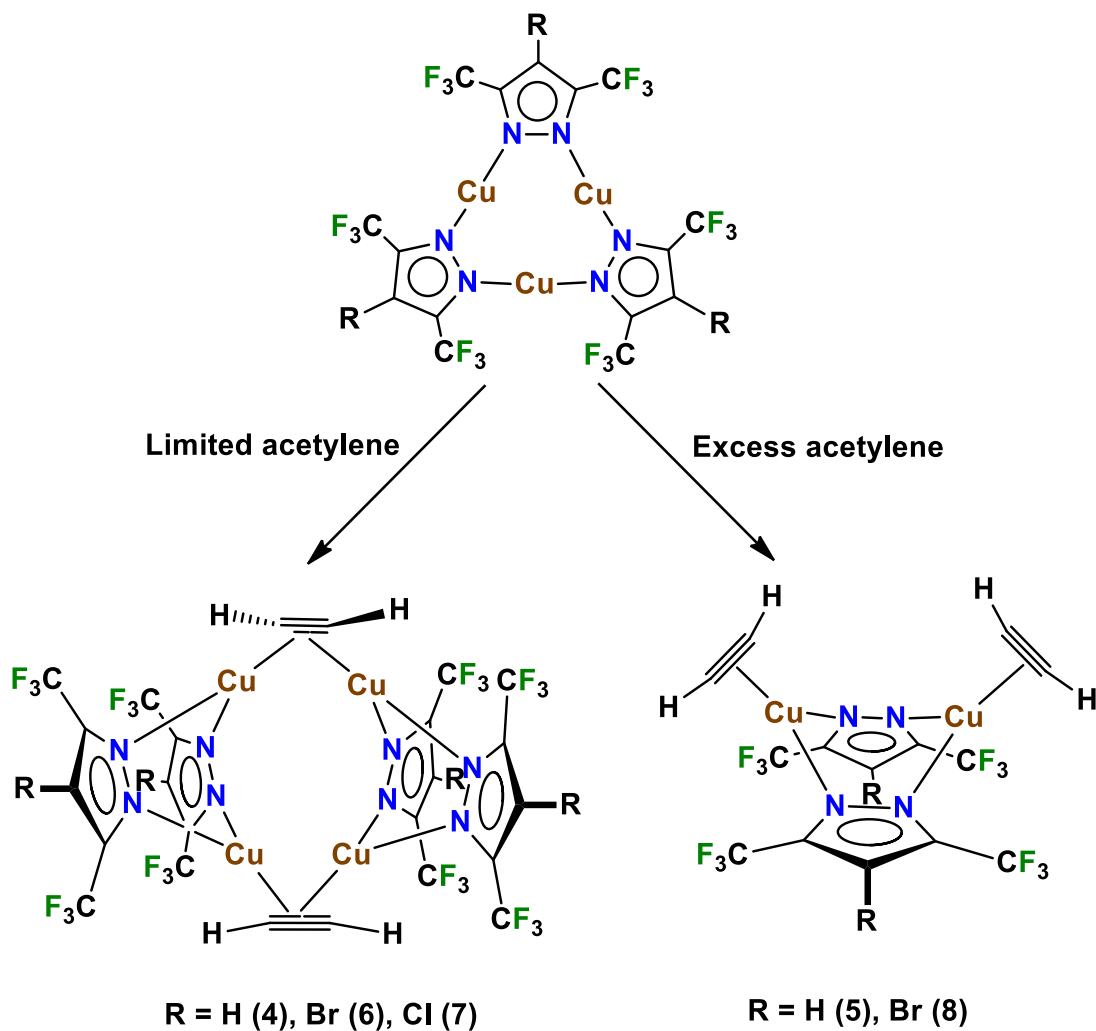


Figure 3.21 Structures and synthetic routes to tetra-nuclear complexes $\text{Cu}_4(\mu\text{-}[3,5\text{-}(\text{CF}_3)_2\text{Pz}])_4(\mu\text{-HC}\equiv\text{CH})_2$ (**4**), $\text{Cu}_4(\mu\text{-}[4\text{-Br-}3,5\text{-}(\text{CF}_3)_2\text{Pz}])_4(\mu\text{-HC}\equiv\text{CH})_2$ (**6**), $\text{Cu}_4(\mu\text{-}[4\text{-Cl-}3,5\text{-}(\text{CF}_3)_2\text{Pz}])_4(\mu\text{-HC}\equiv\text{CH})_2$ (**7**) and di-nuclear complexes and $\text{Cu}_2(\mu\text{-}[3,5\text{-}(\text{CF}_3)_2\text{Pz}])_2(\text{HC}\equiv\text{CH})_2$ (**5**) and $\text{Cu}_2(\mu\text{-}[4\text{-Br-}3,5\text{-}(\text{CF}_3)_2\text{Pz}])_2(\text{HC}\equiv\text{CH})_2$ (**8**) from trinuclear copper(I) pyrazolates and acetylene.

Although there is a long history of copper(I)-acetylene chemistry,^{174,175} copper(I) acetylene complexes with detailed structural and spectroscopic data are surprisingly scarce. This is perhaps due to challenges such as facile loss of coordinated acetylene, copper acetylide formation, and the potential explosion hazard associated with this work.^{168,175,176} Search of Cambridge Structural Database¹¹⁷ revealed eight structurally characterized copper-acetylene complexes. These include, $[\text{Cu}\{\text{NH}(\text{Py})_2\}(\text{HC}\equiv\text{CH})]\text{BF}_4$ and $[\text{Cu}(\text{phen})(\text{HC}\equiv\text{CH})]\text{ClO}_4$ complexes with $\text{Cu}(\eta^2\text{-HC}\equiv\text{CH})$ moieties,¹⁷⁶⁻¹⁷⁸ and polymeric or octanuclear, chloride bridged copper(I) adducts containing $\mu_2\text{-}\eta^2,\eta^2\text{-(HC}\equiv\text{CH)}$ moieties.¹⁷⁹⁻¹⁸¹ Among these, compound $[\text{Cu}\{\text{NH}(\text{Py})_2\}(\text{HC}\equiv\text{CH})]\text{BF}_4$ has ¹H NMR and IR data available for comparison, and displays its acetylenic proton resonance and $\bar{\nu}_{\text{C}\equiv\text{C}}$ band at δ 5.59 ppm and 1795 cm^{-1} , respectively.¹⁷⁷ The $\text{C}\equiv\text{C}$ stretch of $[\text{Cu}(\text{phen})(\text{HC}\equiv\text{CH})]\text{ClO}_4$ has been reported at 1800 cm^{-1} .¹⁷⁸ These two copper adducts featuring η^2 -acetylene moieties show only about 174-179 cm^{-1} lowering of their acetylene $\text{C}\equiv\text{C}$ stretching frequency upon coordination to Cu(I). Both the NMR shifts and $\bar{\nu}_{\text{C}\equiv\text{C}}$ data of the acetylene ligands of $\text{Cu}_4(\mu\text{-}[3,5\text{-}(\text{CF}_3)_2\text{Pz}])_4(\mu\text{-HC}\equiv\text{CH})_2$ (**4**) are however, significantly different from these adducts, and suggest the presence of a $\mu_2\text{-}\eta^2,\eta^2$ -acetylene group rather than the η^2 -acetylene moiety. Note that even larger down field shifts of acetylenic proton resonance¹⁸² and more significant reductions in $\text{C}\equiv\text{C}$ stretching frequency have been reported for

coordinated acetylene (e.g., $\bar{\nu}_{\text{C}\equiv\text{C}}$ band of $\text{Co}_2(\text{CO})_6(\mu\text{-HC}\equiv\text{CH})$ in IR was observed at 1402 cm^{-1} , which is about 570 cm^{-1} lower than that of free acetylene),¹⁸³ but they involve earlier transition metal ions instead of Cu(I).

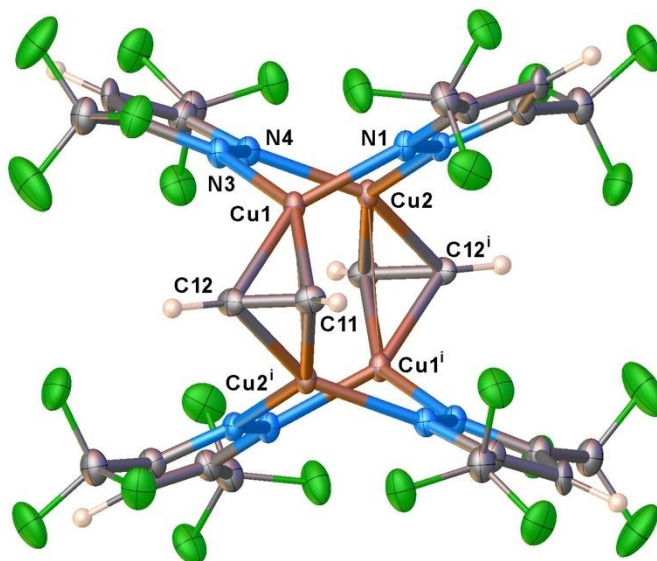


Figure 3.22 Molecular structure of $\text{Cu}_4(\mu\text{-}[3,5\text{-}(\text{CF}_3)_2\text{Pz}])_4(\mu\text{-HC}\equiv\text{CH})_2$ (**4**); ORTEP view with 50% probability ellipsoids are shown. Disordered atoms of the minor occupancy (12%) component have been removed for clarity.

The X-ray crystal structure of $\text{Cu}_4(\mu\text{-}[3,5\text{-}(\text{CF}_3)_2\text{Pz}])_4(\mu\text{-HC}\equiv\text{CH})_2$ (**4**) is illustrated in Figure 3.22. It is a tetranuclear copper(I) complex with trigonal planar copper sites and sits on an inversion center. Unfortunately, this molecule shows positional disorder over two orientations (at 88%:12% occupancy), which was rather challenging initially to recognize, but was resolved satisfactorily. Although metrical parameters (Table 3.11) are not ideal for a detailed analysis due to the

disorder, the basic structural features and atom connectivities are clear and indicate the presence of $\mu_2\text{-}\eta^2,\eta^2\text{-(HC}\equiv\text{CH)}$ moieties, consistent with the spectroscopic data. There are close intramolecular $\text{Cu}\cdots\text{Cu}$ contacts that are within the van der Waals separation of two copper atoms.¹³⁰ It is also interesting to note that during the formation of **4**, copper pyrazolate moieties of $\{\mu\text{-[3,5-(CF}_3)_2\text{Pz]Cu}\}_3$ rearrange to form two separate six-membered, Cu_2N_4 fragments, whereas in $\text{Cu}_4(\mu\text{-[3,5-(CF}_3)_2\text{Pz]})_4(\mu\text{-EtC}\equiv\text{CEt})_2$ (**3**), they form a large 12-membered Cu_4N_8 metallacycle (Figures 3.19 and 3.21).⁷³

We could not isolate the 1:1 complex, $\text{Cu}_2(\mu\text{-[3,5-(CF}_3)_2\text{Pz]})_2(\text{HC}\equiv\text{CH})_2$ (**5**), involving non-bridging acetylene, from solutions containing even large excess of acetylene with $\{\mu\text{-[3,5-(CF}_3)_2\text{Pz]Cu}\}_3$ (Figure 3.20, eq. 2 and Figure 3.21). This is however, not surprising based on the similar findings reported by us and others involving alkynes like 2-butyne with $\{\mu\text{-[3,5-(CF}_3)_2\text{Pz]Cu}\}_3$ or $\text{MeC}\equiv\text{CCO}_2\text{Me}$ with copper(I) trifluoroacetate.^{73,103} Only the tetranuclear copper complexes featuring bridging alkynes have been obtained from these reactions, despite the presence of excess of alkyne. The VT-NMR data of $\{\mu\text{-[3,5-(CF}_3)_2\text{Pz]Cu}\}_3$ in the presence of excess acetylene in CD_2Cl_2 indicated the likely presence of $\text{Cu}_2(\mu\text{-[3,5-(CF}_3)_2\text{Pz]})_2(\text{HC}\equiv\text{CH})_2$ (**5**) in solution, as evident from the appearance of a broad signal at δ 4.86 ppm corresponding to bound acetylene, starting at about -35 °C during the cooling process (Figure 3.23). It is still broad even at -70 °C indicating

the presence of extremely labile copper-bound acetylene group in **5** that rapidly exchanges with free acetylene on the NMR time scale.

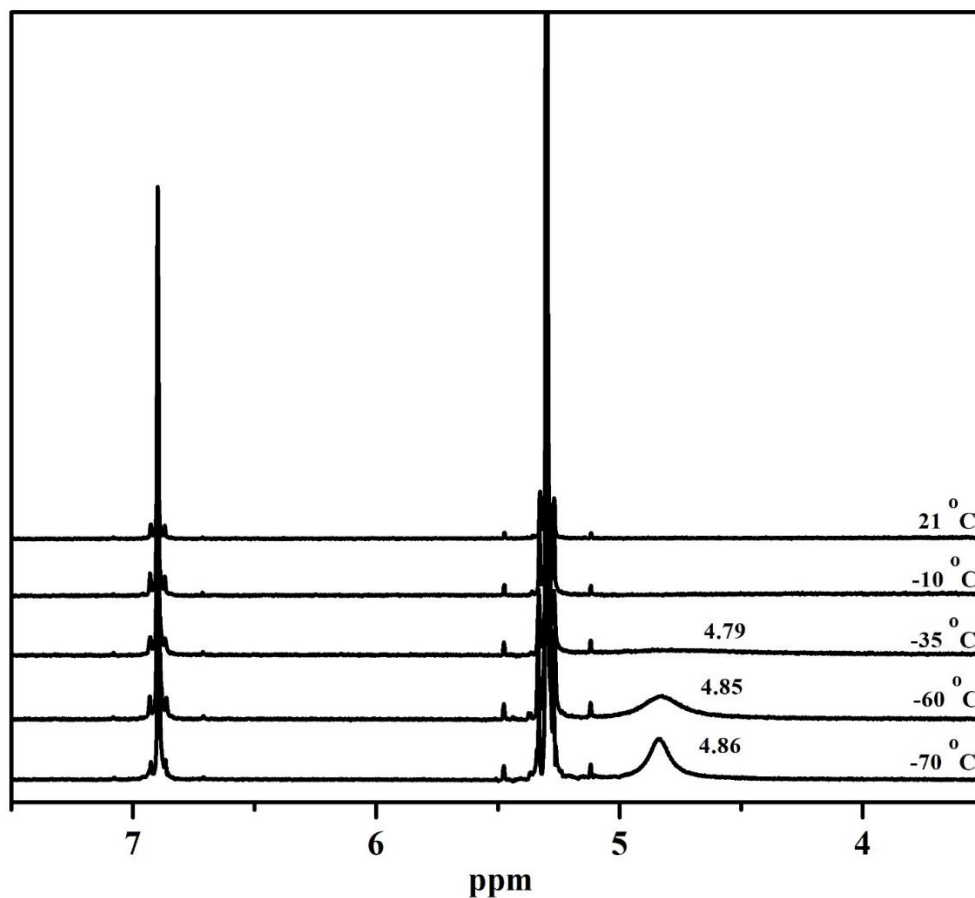


Figure 3.23 ¹H NMR spectra of Cu₂(μ-[3,5-(CF₃)₂Pz])₂(HC≡CH)₂ (**5**) (in CD₂Cl₂) in the presence of excess acetylene at various temperatures. Peak at 4.86 ppm (-70 °C) is the signal corresponding to coordinated acetylene.

The work involving CO and fluorinated copper(I) pyrazolates indicates that more weakly coordinating pyrazolates such as [3,4,5-(CF₃)₃Pz]⁻ offer greater

stability to, and allow relatively easier isolation of the dinuclear Cu-CO adducts such as $\text{Cu}_2(\mu\text{-}[3,4,5\text{-}(\text{CF}_3)_3\text{Pz}])_2(\text{CO})_2$ relative to that of $\text{Cu}_2(\mu\text{-}[3,5\text{-}(\text{CF}_3)_2\text{Pz}])_2(\text{CO})_2$.¹⁴⁹ Accordingly, we also investigated the chemistry of $\{\mu\text{-}[4\text{-Br-}3,5\text{-}(\text{CF}_3)_2\text{Pz}]\text{Cu}\}_3$,²⁰ and $\{\mu\text{-}[4\text{-Cl-}3,5\text{-}(\text{CF}_3)_2\text{Pz}]\text{Cu}\}_3$ ²⁰ with acetylene. The treatment of $\{\mu\text{-}[4\text{-Br-}3,5\text{-}(\text{CF}_3)_2\text{Pz}]\text{Cu}\}_3$ and $\{\mu\text{-}[4\text{-Cl-}3,5\text{-}(\text{CF}_3)_2\text{Pz}]\text{Cu}\}_3$ with acetylene in CH_2Cl_2 followed by the cooling at -20°C afforded white crystalline solids. The ^1H NMR and Raman spectroscopic data of these samples however, indicated the formation of $\text{Cu}_4(\mu\text{-}[4\text{-Br-}3,5\text{-}(\text{CF}_3)_2\text{Pz}])_4(\mu\text{-HC}\equiv\text{CH})_2$ (**6**) and $\text{Cu}_4(\mu\text{-}[4\text{-Cl-}3,5\text{-}(\text{CF}_3)_2\text{Pz}])_4(\mu\text{-HC}\equiv\text{CH})_2$ (**7**) featuring bridging acetylenes, respectively, rather than molecules with 2e-donor, $\eta^2\text{-}(\text{HC}\equiv\text{CH})$ ligands.^{176-178,184} For example, copper-bound acetylene proton signal of **6** and **7** was observed at δ 6.03 and 6.04 ppm, respectively, whereas their C \equiv C stretch in Raman spectra was detected at 1631 and 1632 cm^{-1} , respectively. These values are similar to those observed for the tetranuclear $\text{Cu}_4(\mu\text{-}[3,5\text{-}(\text{CF}_3)_2\text{Pz}])_4(\mu\text{-HC}\equiv\text{CH})_2$ (**4**). The solubility of **6** and **7** in less polar solvents like hexanes are rather limited once the solid is formed. Unfortunately, many attempts to grow acceptable crystals of **6** and **7** for X-ray crystallography failed. Twinning and the formation of badly inter-twined crystals are common. Interestingly, solids obtained from certain batches of $\text{Cu}_4(\mu\text{-}[4\text{-Br-}3,5\text{-}(\text{CF}_3)_2\text{Pz}])_4(\mu\text{-HC}\equiv\text{CH})_2$ (**6**) in CH_2Cl_2 solutions at -20°C indicated the presence of two types of crystals and new band at 1810 and 1811 cm^{-1} in the IR

and Raman spectra, respectively (in addition to the $\bar{\nu}_{\text{C}\equiv\text{C}}$ band due to **6**). These new peaks with relatively small changes in C \equiv C frequency are indicative of a copper-bound, non-bridging acetylene moiety. Indeed, a careful analysis of a needle-shaped crystal fragment (found as a minor product amongst diamond shaped, and often badly twinned crystals) revealed the presence of 1:1 adduct, $\text{Cu}_2(\mu\text{-[4-Br-3,5-(CF}_3)_2\text{Pz]})_2(\text{HC}\equiv\text{CH})_2$ (**8**). It was later obtained as the major product (and as much better-quality single crystals) using toluene as the solvent of crystallization. X-ray crystal structure of this molecule is illustrated in Figure 3.24.

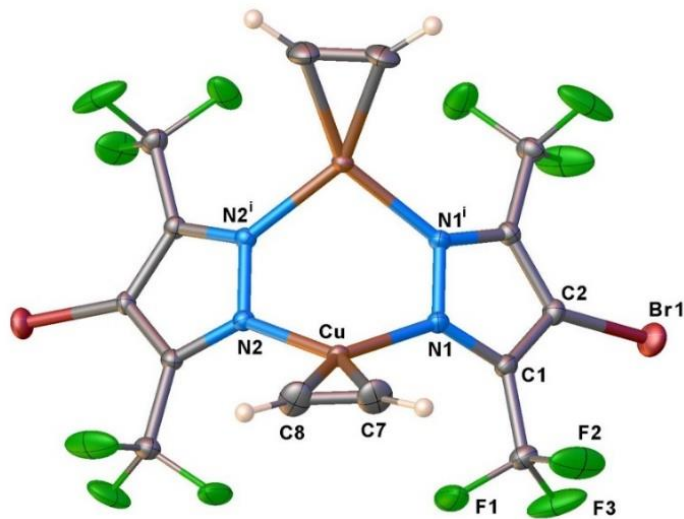


Figure 3.24 Molecular structure of $\text{Cu}_2(\mu\text{-[4-Br-3,5-(CF}_3)_2\text{Pz]})_2(\text{HC}\equiv\text{CH})_2$ (**8**); ORTEP view with 50% probability ellipsoids are shown.

It crystallizes with molecules of toluene in the crystal lattice, and sits on a mirror plane. The copper sites adopt trigonal planar geometry and acetylenes bind to

copper atoms in an η^2 -fashion. The average C \equiv C bond distance of **8** (1.227 Å) is slightly longer than the corresponding distance of free acetylene (1.2033(2) Å).¹⁷³

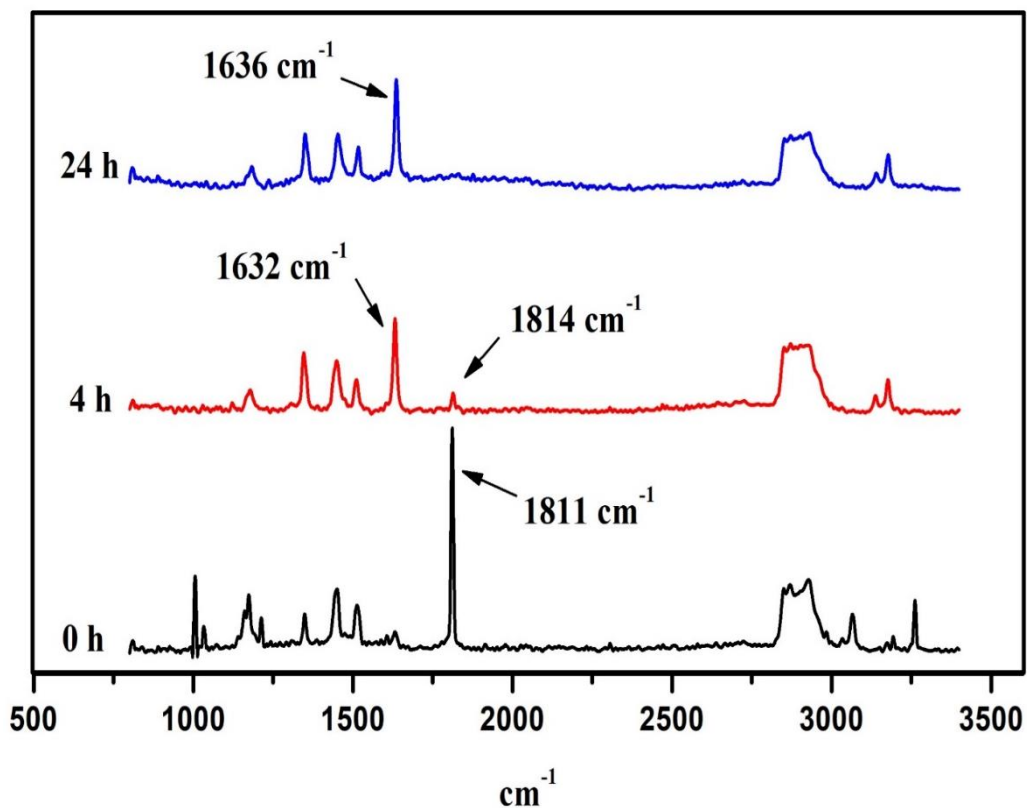


Figure 3.25 Raman spectra showing the conversion of $\text{Cu}_2(\mu\text{-[4-Br-3,5-(CF}_3)_2\text{Pz]})_2(\text{HC}\equiv\text{CH})_2$ (**8**) to $\text{Cu}_4(\mu\text{-[4-Br-3,5-(CF}_3)_2\text{Pz]})_4(\mu\text{-HC}\equiv\text{CH})_2$ (**6**) with time at room temperature, in open air. The peaks at 1811 cm^{-1} and 1636 cm^{-1} correspond to complexes **8** and **6**, respectively. (Note: Oil coated $\text{Cu}_2(\mu\text{-[4-Br-3,5-(CF}_3)_2\text{Pz]})_2(\text{HC}\equiv\text{CH})_2\cdot\text{C}_7\text{H}_8$ crystals were used in this study).

The Raman spectrum of solid samples of **8** displays a strong band at 1811 cm^{-1} , corresponding to the $\bar{\nu}_{\text{C}\equiv\text{C}}$ (Figure 3.25). This represents a 163 cm^{-1} reduction in stretching frequency as a result of copper-coordination, relative to that of the free acetylene.¹⁷³ Solid samples of **8** (even with a thin, hydrocarbon oil coating) lose acetylene upon standing at room temperature in air, as evident from the gradual intensity loss of 1811 cm^{-1} band over several hours, and a complete disappearance within a day. This process accompanies the gradual growth of the 1636 cm^{-1} band, pointing to the formation of a bridged-acetylene species **6**, which is relatively more stable to the loss of acetylene. Notably, we could not observe the NMR signal of the coordinated acetylene in **8** in CD_2Cl_2 at room temperature, as it rapidly loses some of the acetylene during the dissolution (can even observe the release of bubbles when the NMR solvent is added to dissolve the crystals), and establishes a fast equilibrium with the free acetylene on the NMR time scale. We can however observe this resonance at low temperatures in the presence of excess acetylene. The copper bound acetylenic proton signal of **8** was observed as a broad peak at δ 4.75 ppm in CD_2Cl_2 (Figure 3.26). We have not probed the acetylene chemistry of 4-chloro analog $\{\mu\text{-}[4\text{-Cl-}3,5\text{-(CF}_3)_2\text{Pz}]\text{Cu}\}_3$ in greater detail apart from the isolation of **7**, although it could also show similar chemistry as the 4-bromo analog, $\{\mu\text{-}[4\text{-Br-}3,5\text{-(CF}_3)_2\text{Pz}]\text{Cu}\}_3$.

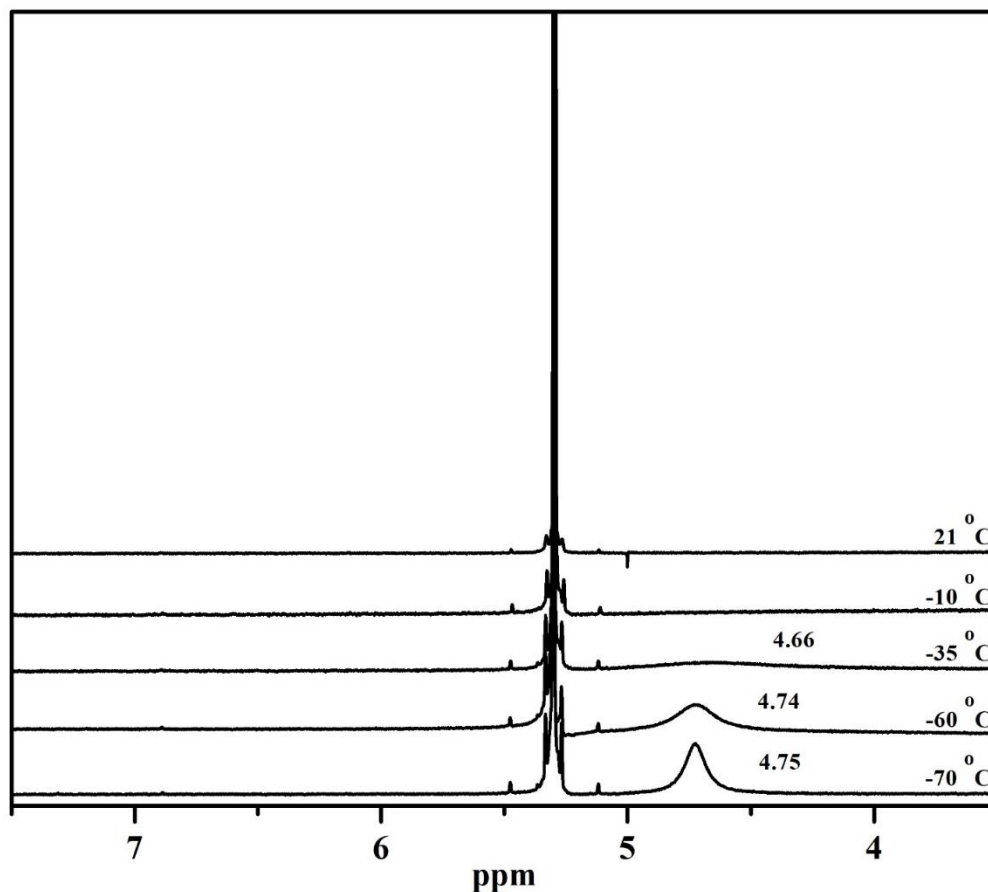


Figure 3.26 ¹H NMR spectra of Cu₂(μ-[4-Br-3,5-(CF₃)₂Pz])₂(HC≡CH)₂ (**8**) (in CD₂Cl₂) in presence of excess acetylene at various temperatures. Peak at 4.75 ppm (-70 °C) is the signal corresponding to coordinated acetylene.

The solutions of **4** (in CH₂Cl₂) is notably sensitive and change color to brown on exposure to air or upon removal of solvent under reduced pressure or if purged with nitrogen. It however, remains stable for a few days under acetylene atmosphere both in solution (in -20 °C freezer) and in solid state but slowly decomposes over time. In contrast, solutions of compounds **6** and **7** are

comparatively stable, and do not show noticeable color changes upon exposure to air or if purged with nitrogen briefly. Both these complexes remain stable for days in solution (in a freezer) and in solid state under an acetylene atmosphere. In the presence of excess acetylene at room temperature, solutions of tetranuclear **4**, **6** and **7** lose the bound acetylene signal in ^1H NMR spectrum indicating fast exchange with free acetylene, and perhaps the formation of 1:1 Cu:alkyne adducts.

Table 3.11 Selected bond distances (Å) and angles ($^\circ$) for $\text{Cu}_2(\mu\text{-}[3,5\text{-}(\text{CF}_3)_2\text{Pz}])_2(\text{EtC}\equiv\text{CEt})_2$ (**2**), $\text{Cu}_4(\mu\text{-}[3,5\text{-}(\text{CF}_3)_2\text{Pz}])_4(\mu\text{-EtC}\equiv\text{CEt})_2$ (**3**), $\text{Cu}_4(\mu\text{-}[3,5\text{-}(\text{CF}_3)_2\text{Pz}])_4(\mu\text{-HC}\equiv\text{CH})_2$ (**4**), $\text{Cu}_2(\mu\text{-}[4\text{-Br-}3,5\text{-}(\text{CF}_3)_2\text{Pz}])_2(\text{HC}\equiv\text{CH})_2$ (**8**), $\text{Cu}_2(\mu\text{-}[3,5\text{-}(\text{CF}_3)_2\text{Pz}])_2(\text{HC}\equiv\text{CPh})_2$ (**9**), $\text{Cu}_2(\mu\text{-}[3,5\text{-}(\text{CF}_3)_2\text{Pz}])_2(\text{HC}\equiv\text{C}(\text{CH}_2)_5\text{C}\equiv\text{CH})$ (**10**), $\text{Cu}_4(\mu\text{-}[3,5\text{-}(\text{CF}_3)_2\text{Pz}])_4(\text{HC}\equiv\text{C}(\text{CH}_2)_4\text{C}\equiv\text{CH})_2$ (**11**), and $\text{Cu}_4(\mu\text{-}[3,5\text{-}(\text{CF}_3)_2\text{Pz}])_4(\text{C}_2\text{H}_5\text{C}\equiv\text{C}(\text{CH}_2)_4\text{C}\equiv\text{CC}_2\text{H}_5)_2$ (**12**).

Parameter\ Complex	3	4*	2	8	9	10	11	12
av. Cu-C(H)C \equiv	-	1.987	-	1.970	1.943	1.955	1.958	-
av. Cu-C(C)C \equiv	2.016	-	1.978	-	1.996	2.008	1.992	1.981
av. C \equiv C	1.265	1.269	1.227	1.227	1.226	1.229	1.220	1.234
av. Cu-N	1.978	1.961	1.985	1.972	1.971	1.978	1.975	1.982
Shortest Cu \cdots Cu	2.646	2.647	3.051	3.200	3.161	3.136	3.128	3.074

av. C-Cu-C	36.57	37.24	36.13	36.28	36.23	36.10	35.97	36.29
av. C-C≡C	155.2	-	161.2	-	161.4	161.1	163.7	162.4
av. N-Cu-N	108.99	103.04	97.49	98.95	100.05	98.13	100.04	97.85
-C≡C- bonding mode	$\mu_2-\eta^2, \eta^2-$	$\mu_2-\eta^2, \eta^2-$	η^2-	η^2-	η^2-	η^2-	η^2-	η^2-
<i>ref</i>	⁷³	This work	⁷³	This work	This work	This work	This work	This work

*Metrical parameters of **4** should be used with due caution considering the disorder.

Only the bond distance/angle values for major occupancy component are provided

for compound **4**.

Coordination chemistry of copper pyrazolates with terminal-alkynes:

We have also explored the chemistry of phenylacetylene and 1,8-nonadiyne with $\{\mu\text{-}[3,5\text{-(CF}_3)_2\text{Pz}]\text{Cu}\}_3$. The treatment of the copper pyrazolate with slight excess of these terminal alkynes in CH_2Cl_2 led to $\text{Cu}_2(\mu\text{-}[3,5\text{-(CF}_3)_2\text{Pz}])_2(\text{HC}\equiv\text{CPh})_2$ (**9**) and $\text{Cu}_2(\mu\text{-}[3,5\text{-(CF}_3)_2\text{Pz}])_2(\text{HC}\equiv\text{C(CH}_2)_5\text{C}\equiv\text{CH})$ (**10**) in high yield (Figure 3.27). They show their $\text{C}\equiv\text{C}$ stretch in Raman at 1932 (average of three bands observed at 1918, 1928, 1950 cm^{-1}) and 1946 cm^{-1} , respectively, indicating the presence of typical, non-bridging, 2e donor, η^2 -alkynes on copper. They represent a ~ 179 and 169 cm^{-1} reduction in stretching frequency upon Cu(I) coordination (free phenylacetylene and 1,8-nonadiyne display their $\text{C}\equiv\text{C}$ stretch in Raman at 2011 and 2015 cm^{-1} , respectively). For comparison, the bis(pyrazolyl)borate complex $[\text{H}_2\text{B(3,5-(CF}_3)_2\text{Pz)}_2]\text{Cu}(\text{HC}\equiv\text{CPh})$ exhibits its $\text{C}\equiv\text{C}$ band at 1927 cm^{-1} ,¹⁸⁵ while the mixed-valent $\text{Cu}\{(\mu\text{-}[3,5\text{-(CF}_3)_2\text{Pz}])_2\text{Cu}(\text{HC}\equiv\text{CPh})\}_2$ and $\text{Cu}\{(\mu\text{-}[3,5\text{-(CF}_3)_2\text{Pz}])_2\text{Cu}(\text{HC}\equiv\text{CC}_6\text{H}_{13})\}_2$ show their $\text{C}\equiv\text{C}$ bands at 1910 and 1945 cm^{-1} ,¹⁷¹ respectively, in their IR spectra. Copper complexes featuring η^2 - and $\mu_2\text{-}\eta^2, \eta^2$ -bound, internal alkyne 3-hexyne, $\text{Cu}_2(\mu\text{-}[3,5\text{-(CF}_3)_2\text{Pz}])_2(\text{EtC}\equiv\text{CEt})_2$ (**2**) and $\text{Cu}_4(\mu\text{-}[3,5\text{-(CF}_3)_2\text{Pz}])_4(\mu\text{-EtC}\equiv\text{CEt})_2$ (**3**), show their $\bar{\nu}_{\text{C}\equiv\text{C}}$ bands in Raman at 2050 and 1874 cm^{-1} , respectively, and about 210 and 386 cm^{-1} red shifts relative to the corresponding stretching frequency of the free $\text{EtC}\equiv\text{CEt}$.⁷³ In addition to these, the search of Cambridge Structural Database

revealed a few more structurally characterized copper-terminal alkyne complexes.

These includes- tris(pyrazolyl)borate complexes $[\text{HB}(3\text{-(Mes)Pz})_3]\text{Cu}(\text{HC}\equiv\text{CPh})$

($\bar{\nu}_{\text{C}\equiv\text{C}} = 1923 \text{ cm}^{-1}$), $[\text{HB}(3\text{-(Mes)Pz})_3]\text{Cu}(\text{HC}\equiv\text{C}_5\text{H}_9)$ ($\bar{\nu}_{\text{C}\equiv\text{C}} = 1957 \text{ cm}^{-1}$), $[\text{HB}(3\text{-(Mes)Pz})_3]\text{Cu}(\text{HC}\equiv\text{CCOOEt})$ ($\bar{\nu}_{\text{C}\equiv\text{C}} = 1901 \text{ cm}^{-1}$) and $[\text{CuCl}(\text{Me}_2\text{C}(\text{OH})\text{C}\equiv\text{CH})]_4$

($\bar{\nu}_{\text{C}\equiv\text{C}} = 1940 \text{ cm}^{-1}$).^{153,154}

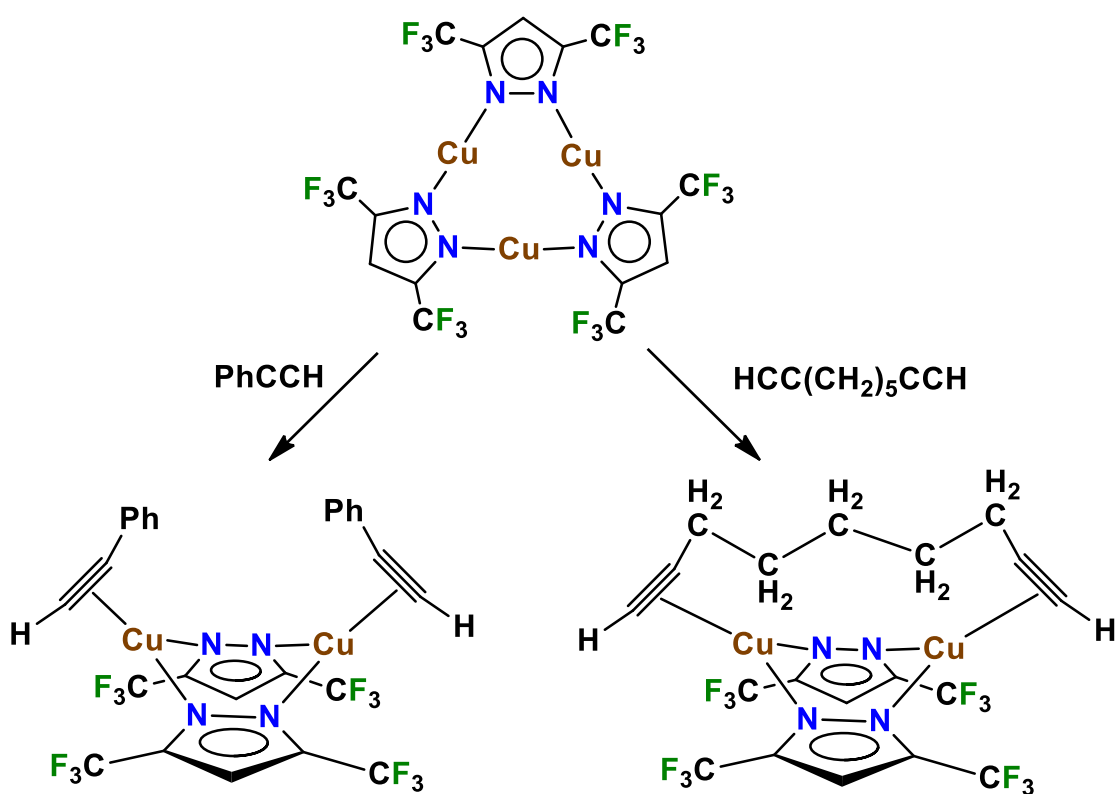


Figure 3.27 Synthetic routes to di-nuclear complexes $\text{Cu}_2(\mu\text{-}[3,5\text{-(CF}_3)_2\text{Pz}]_2)(\text{HC}\equiv\text{CPh})_2$ (**9**) and $\text{Cu}_2(\mu\text{-}[3,5\text{-(CF}_3)_2\text{Pz}]_2)(\text{HC}\equiv\text{C}(\text{CH}_2)_5\text{C}\equiv\text{CH})$ (**10**)

from tri-nuclear $\{[3,5\text{-(CF}_3)_2\text{Pz}]\text{Cu}\}_3$ and the corresponding alkyne.

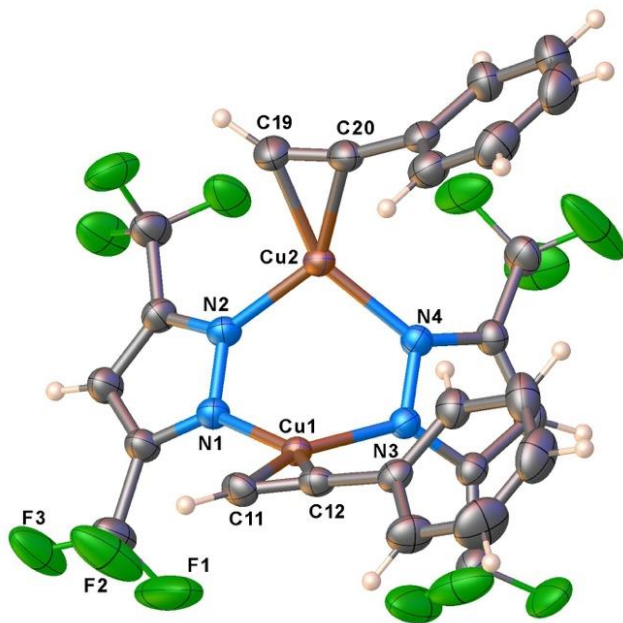


Figure 3.28 Molecular structure of $\text{Cu}_2(\mu\text{-}[3,5\text{-(CF}_3)_2\text{Pz}])_2(\text{HC}\equiv\text{CPh})_2$ (**9**); ORTEP view with 50% probability ellipsoids are shown.

X-ray crystal structures of **9** and **10** confirm the formation of dinuclear species containing alkyne ligands bonded to copper in an η^2 -fashion. Compound $\text{Cu}_2(\mu\text{-}[3,5\text{-(CF}_3)_2\text{Pz}])_2(\text{HC}\equiv\text{CPh})_2$ (**9**) crystallized in the P-1 space group with two chemically similar but crystallographically different molecules in the asymmetric unit. One of these molecules are depicted in Figure 3.28. In these molecules, phenylacetylene ligands orient in a similar fashion with phenyl moieties pointing in the same direction. The Cu_2N_4 metallacycle adopts the familiar boat shape.

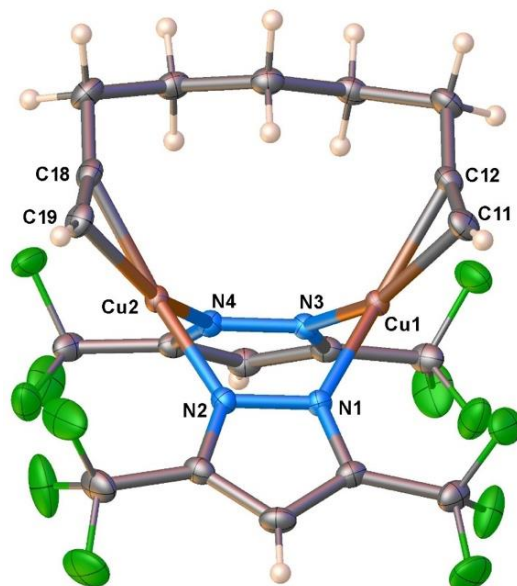


Figure 3.29. Molecular structure of $\text{Cu}_2(\mu\text{-}[3,5\text{-(CF}_3)_2\text{Pz}])_2(\text{HC}\equiv\text{C(CH}_2)_5\text{C}\equiv\text{CH})$ (**10**); ORTEP view with 50% probability ellipsoids are shown.

The X-ray structure of $\text{Cu}_2(\mu\text{-}[3,5\text{-(CF}_3)_2\text{Pz}])_2(\text{HC}\equiv\text{C(CH}_2)_5\text{C}\equiv\text{CH})$ (**10**) is shown in Figure 3.29. The 1,8-nonadiyne serves as an intramolecular bridge for two copper sites of the dinuclear “ $\text{Cu}_2(\mu\text{-}[3,5\text{-(CF}_3)_2\text{Pz}])_2$ ” fragment, and the alkyne groups coordinate to copper atoms in an η^2 -fashion. ^1H NMR resonances corresponding to $\text{H-C}\equiv$ protons of **9** and **10** in CDCl_3 at room temperature appear as broad singlets at δ 3.17 and 4.33 ppm, respectively. The ^{13}C NMR peaks assignable to the $\text{C}\equiv\text{C}$ carbons are also broad suggesting that the alkyne groups in these complexes are rather labile in solution at ambient temperatures.

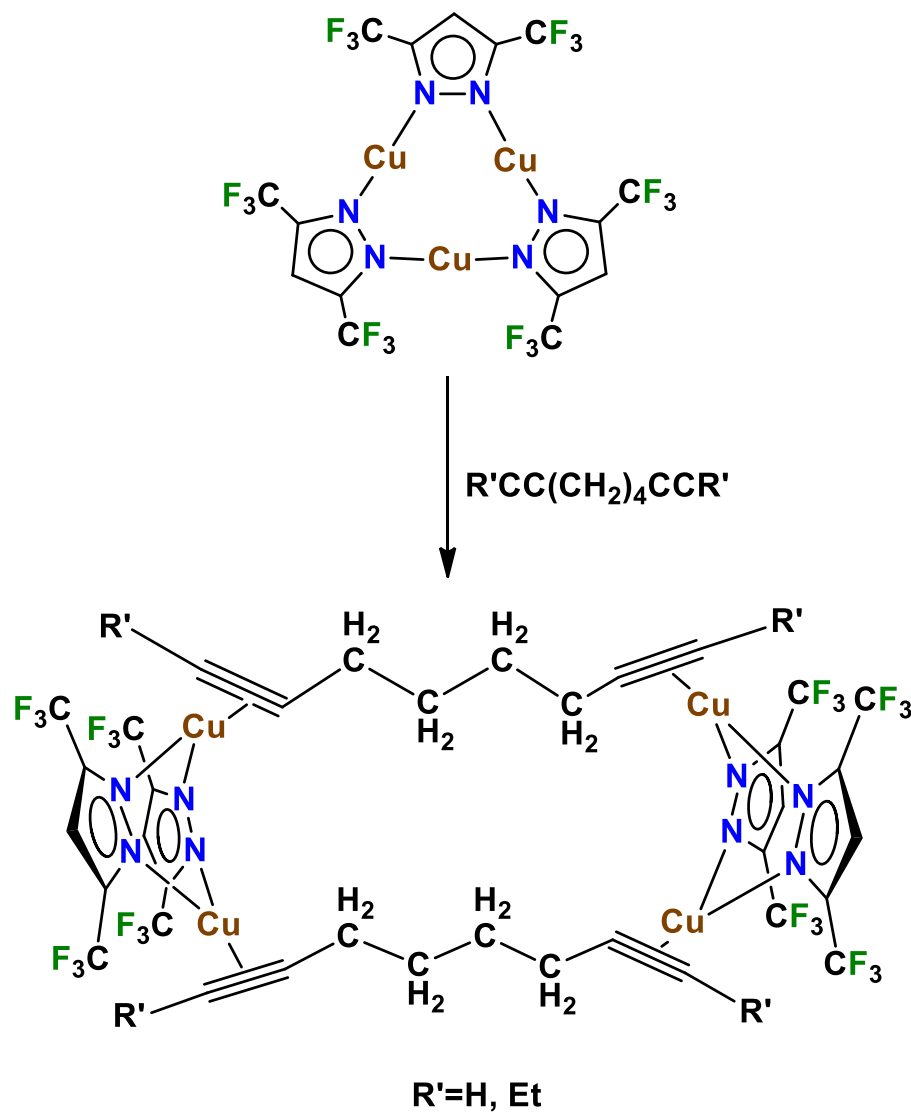


Figure 3.30 Synthetic routes to $\text{Cu}_4(\mu\text{-}[3,5\text{-}(\text{CF}_3)_2\text{Pz}])_4(\text{HC}\equiv\text{C}(\text{CH}_2)_4\text{C}\equiv\text{CH})_2$ (**11**) and $\text{Cu}_4(\mu\text{-}[3,5\text{-}(\text{CF}_3)_2\text{Pz}])_4(\text{C}_2\text{H}_5\text{C}\equiv\text{C}(\text{CH}_2)_4\text{C}\equiv\text{CC}_2\text{H}_5)_2$ (**12**) from tri-nuclear $\{[3,5\text{-}(\text{CF}_3)_2\text{Pz}]\text{Cu}\}_3$ and the corresponding alkyne.

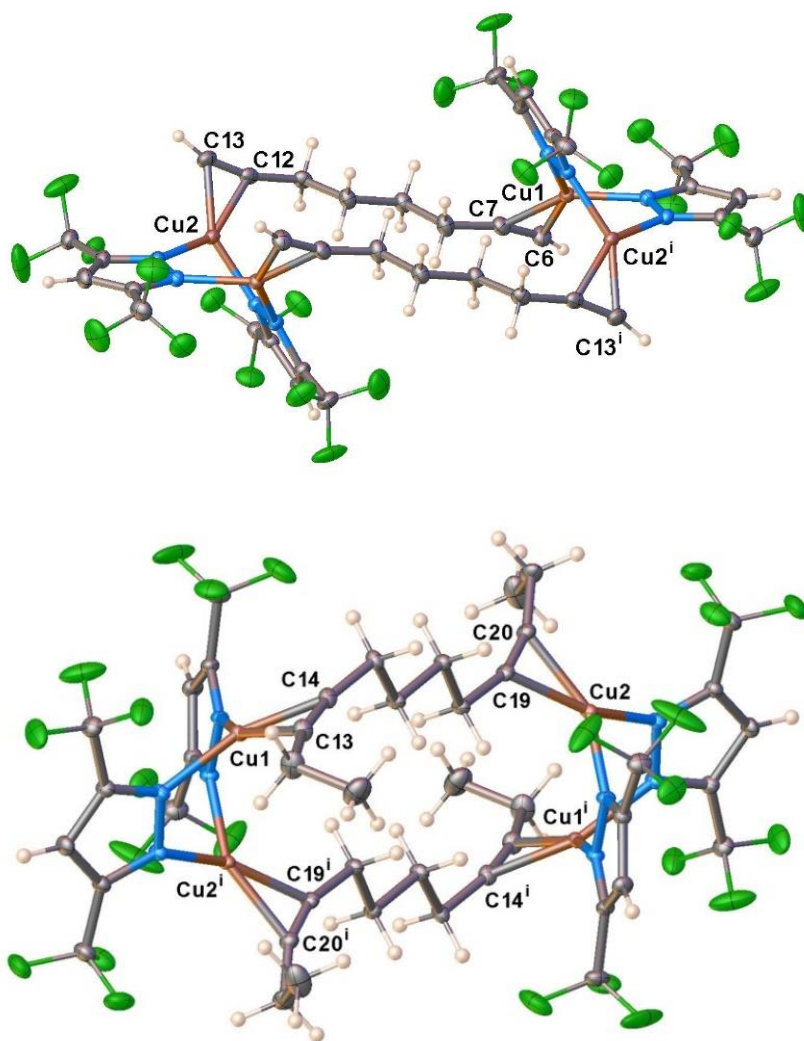


Figure 3.31 Molecular structures of $\text{Cu}_4(\mu\text{-}[3,5\text{-}(\text{CF}_3)_2\text{Pz}])_4(\text{HC}\equiv\text{C}(\text{CH}_2)_4\text{C}\equiv\text{CH})_2$ (**11**) (top) and $\text{Cu}_4(\mu\text{-}[3,5\text{-}(\text{CF}_3)_2\text{Pz}])_4(\text{C}_2\text{H}_5\text{C}\equiv\text{C}(\text{CH}_2)_4\text{C}\equiv\text{CC}_2\text{H}_5)_2$ (**12**) (bottom); ORTEP views with 50% probability ellipsoids are shown.

We have investigated the effect of alkyne moiety linker length on copper-alkyne adduct formation by using a terminal bis-alkyne 1,7-octadiyne, as well as an internal bis-alkyne 3,9-dodecadiyne ligands with $\{\mu\text{-}[3,5\text{-}(\text{CF}_3)_2\text{Pz}]\text{Cu}\}_3$ (Figure 3.30). The X-ray crystal structures of the resulting molecules $\text{Cu}_4(\mu\text{-}[3,5\text{-}(\text{CF}_3)_2\text{Pz}])_4(\text{HC}\equiv\text{C}(\text{CH}_2)_4\text{C}\equiv\text{CH})_2$ (**11**) and $\text{Cu}_4(\mu\text{-}[3,5\text{-}(\text{CF}_3)_2\text{Pz}])_4(\text{C}_2\text{H}_5\text{C}\equiv\text{C}(\text{CH}_2)_4\text{C}\equiv\text{CC}_2\text{H}_5)_2$ (**12**) are illustrated in Figure 3.31. In **11** and **12**, the two alkyne moieties are linked by a four-carbon, $\text{-(CH}_2)_4\text{-}$ linker, and they serve as a bridge to two-separate dinuclear “ $\text{Cu}_2(\mu\text{-}[3,5\text{-}(\text{CF}_3)_2\text{Pz}])_2$ ” fragments. In contrast, the di-alkyne $\text{HC}\equiv\text{C}(\text{CH}_2)_5\text{C}\equiv\text{CH}$ with a five-carbon linker in **10** acts as an intramolecular bridge to a single “ $\text{Cu}_2(\mu\text{-}[3,5\text{-}(\text{CF}_3)_2\text{Pz}])_2$ ” moiety. Thus, it appears that anything shorter than the five-carbon $\text{-(CH}_2)_5\text{-}$ linker in these aliphatic bis-alkyne molecules is not long enough to bridge Cu atoms of dinuclear “ $\text{Cu}_2(\mu\text{-}[3,5\text{-}(\text{CF}_3)_2\text{Pz}])_2$ ” fragments in an intra-dimer fashion.

A comparison of metrical parameters of **3** and **4** containing 4e-donor, $\mu_2\text{-}\eta^2,\eta^2\text{-}$ alkynes to **2**, **8-12** featuring 2e-donor, $\eta^2\text{-}$ alkyne ligands (Table 3.11) show that the former group of molecules have longer C=C bonds, which is expected and consistent with the vibration spectroscopic data.¹⁸⁸ Also, compound **3** shows a greater alkyne bending-back angle (deviation from linearity of the alkyne C-C=C bond angle) as a result of the coordination of two copper atoms compared to those of the **2** and **9-12** that have only one copper atom on each alkyne. The structural

data from **9-11** with terminal alkynes indicate that the Cu-C(H)C≡ bond is significantly shorter than the Cu-C(C)C≡ bond length, which is probably a result of steric effects. The coordinated alkyne groups of **4** and **8-12** are co-planar with respect to the trigonal plane of copper (i.e., N₂CuC₂ atoms are in the same plane). These molecules represent a rare group of structurally characterized, terminal alkyne complexes of copper, derived from binary copper(I) pyrazolates. The mix-valent, $\text{Cu}\{(\mu\text{-}[3,5\text{-}(\text{CF}_3)_2\text{Pz}])_2\text{Cu}(\text{HC}\equiv\text{CPh})\}_2$ and $\text{Cu}\{(\mu\text{-}[3,5\text{-}(\text{CF}_3)_2\text{Pz}])_2\text{Cu}(\text{HC}\equiv\text{CC}_6\text{H}_{13})\}_2$ featuring Cu(I) and Cu(II) sites are the only copper-alkyne-pyrazolates that are somewhat related to **8-11** in the literature.¹⁷¹

Copper(I) pyrazolates in alkyne transformations:

Despite the importance of copper in alkyne chemistry,^{79,104,105,114,157-169} and the ease of synthesis and availability of many copper(I) pyrazolates, they have not been used widely as catalysts in alkyne transformations. We have been working on the chemistry of highly fluorinated copper pyrazolates,^{7,53} and copper-alkyne complexes for a number of years.^{126,185,189,190} Fluorinated copper pyrazolates serve as excellent Lewis acids and bind to molecules with lone pairs (e.g., CO, pyridines) or π -electrons (e.g., alkene, alkynes).^{10,30,73,93,100,144,145} During this work, we noticed that they are also competent catalysts for several processes that transform alkynes. Here we report the use of fluorinated copper pyraolates as a catalyst in the carboxylation, azide-cycloaddition and hydrothiolation of alkynes.

Carboxylation of terminal alkynes:

Incorporation of carbon dioxide into molecules is a significant current interest.^{161,163} One way to achieve this is *via* the insertion of CO₂ into C(sp)-H bonds of terminal alkynes leading to carboxylic acids. Copper is turning out to be an important catalyst in this regard.^{161,163} For example, CuCl with various ligands (e.g., TMEDA) in the presence of K₂CO₃ have been reported to mediate CO₂ insertion to phenylacetylene.¹⁶³ We found that {μ-[3,5-(CF₃)₂Pz]Cu}₃ is also effective in this process. It does not require an external base and the reactions proceed at 1 atm of CO₂ at the room temperature (Figure 3.32, Table 3.12). For example, {μ-[3,5-(CF₃)₂Pz]Cu}₃ at 2 mol% level, catalyzes the reaction between phenylacetylene and CO₂ at room temperature and produces PhC₂CO₂H in 72% isolated yield (entry 1). In these reactions, molecules resulting from an alkyne coupling were also observed as a minor product.

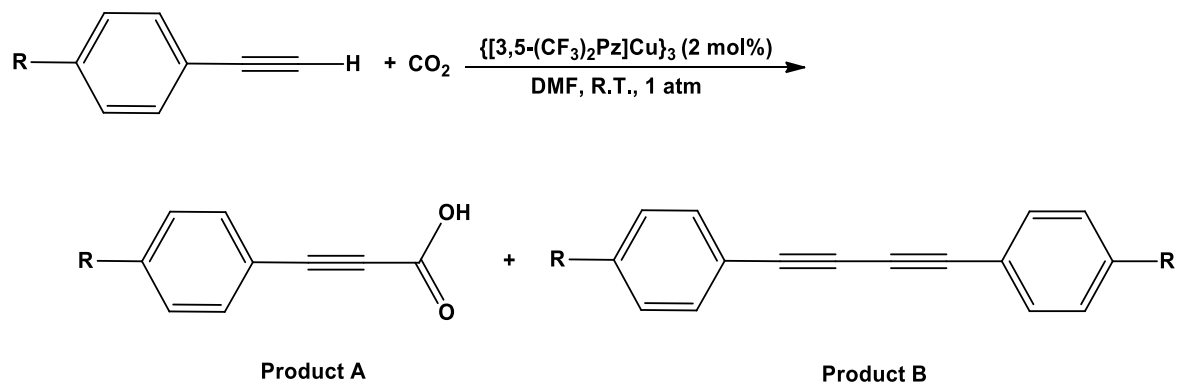


Figure 3.32 The $\{\mu\text{-}[3,5-(\text{CF}_3)_2\text{Pz}]\text{Cu}\}_3$ catalyzed carboxylation of terminal alkynes

Table 3.12 Carboxylation of terminal alkynes using $\{\mu\text{-}[3,5-(\text{CF}_3)_2\text{Pz}]\text{Cu}\}_3$ (2 mol%) as the catalyst.

Entry	R	Time (h)	% Yield (Product A)	% Yield (Product B)
1	H	12	72	10
2	CH ₃	12	80	2
3	Cl	12	64	5

Azide-alkyne cycloaddition:

Copper catalyzed synthesis of 1,2,3-triazoles via the cycloaddition of azides to triple bonds of alkynes is perhaps the most well-known process involving copper and alkynes.^{105,114,191-193} The standard catalytic system uses copper(II) salts such as copper sulfate pentahydrate in the presence of a reducing agent, such as sodium ascorbate.¹⁹² During our work involving copper(I) pyrazolates and alkynes, we discovered that $\{\mu\text{-}[3,5\text{-}(\text{CF}_3)_2\text{Pz}]\text{Cu}\}_3$ is an excellent catalyst for the cycloaddition of azides to terminal alkynes. Furthermore, it also mediates similar chemistry with acetylene,¹⁹⁴ which is rare (Figure 3.33). It is important to note that a report appeared recently on the use of $\{\mu\text{-}[3,5\text{-}(\text{CF}_3)_2\text{Pz}]\text{Cu}\}_3$ in click chemistry with 1-octyne and phenylacetylene with *ortho*-fluorobenzyl azide.¹⁷¹ That work complements the findings reported below involving terminal alkynes.

Specifically, the trinuclear copper(I) pyrazolate $\{\mu\text{-}[3,5\text{-}(\text{CF}_3)_2\text{Pz}]\text{Cu}\}_3$ (1 mol%) catalyzes the cycloaddition of *p*-tolylazide and acetylene (1 atm) to form the desired 1-substituted-1,2,3-triazole in quantitative yield based on the NMR spectroscopic analysis of the product mixture (Figure 3.33). Reaction proceeds in CH_2Cl_2 under mild conditions and no heating or base is required. The reactions ensue equally well with phenylacetylene or 1-octyne as the alkyne source affording the corresponding 1,4-disubstituted 1,2,3-triazole.¹⁹⁵ Mild reaction conditions of the copper pyrazolate catalyzed process and the high yields are noteworthy, as also highlighted by Titov and co-workers.¹⁷¹

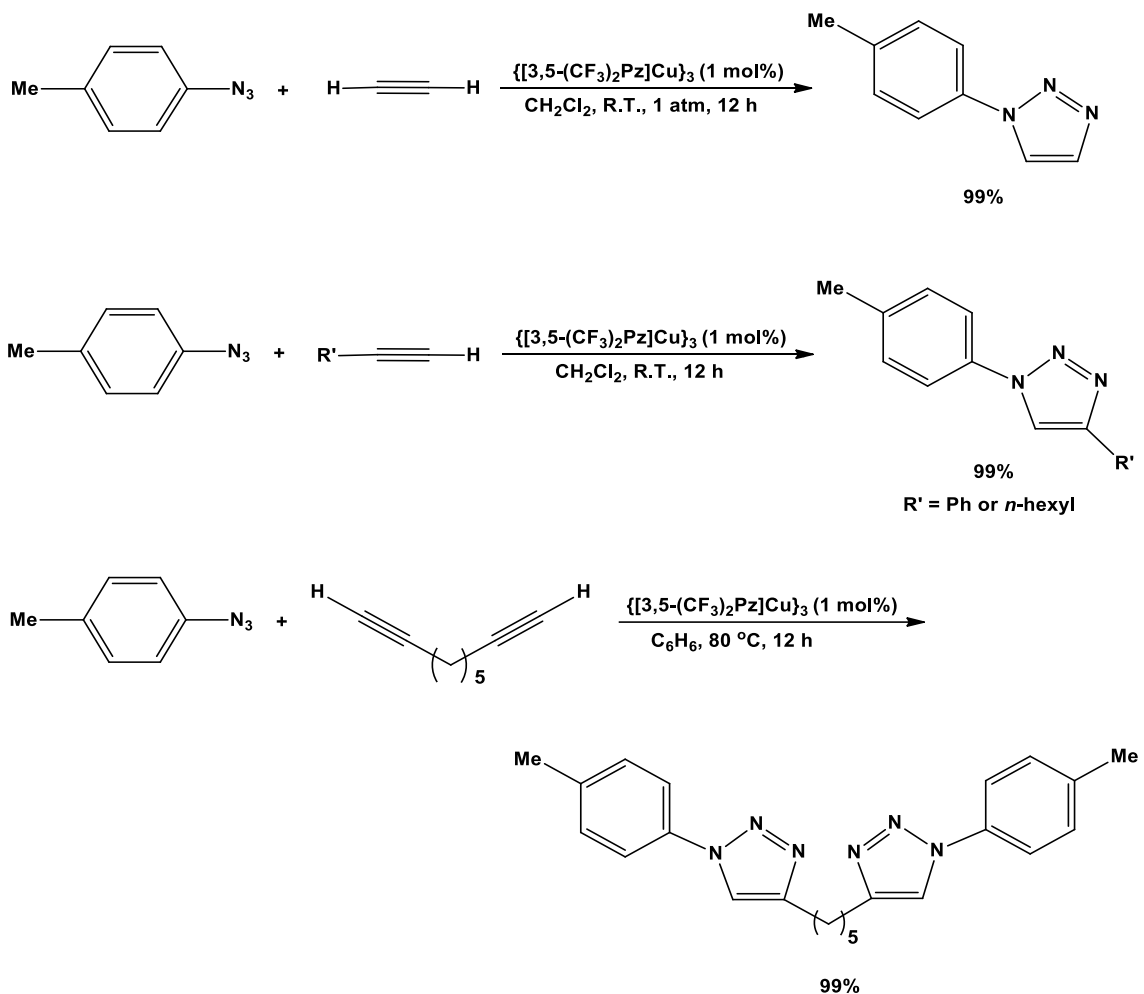


Figure 3.33 The $\{\mu\text{-}[3,5\text{-(CF}_3)_2\text{Pz]Cu}\}_3$ catalyzed alkyne-azide cycloaddition involving acetylene or various terminal alkynes as the alkyne source and *p*-tolylazide

We have also successfully converted 1,8-nonadiyne to the corresponding 1,4-disubstituted 1,2,3-triazole using *p*-tolylazide (Figure 3.33). Although it produces the bis-triazole product in quantitative yield, this reaction required the use

of slightly elevated temperature (80 °C) and benzene as the solvent. The control reaction at this temperature (with no copper catalyst) produces the product in 19% yield. The $\{\mu\text{-}[3,5\text{-(CF}_3)_2\text{Pz}]\text{Cu}\}_3$ catalyzed process at room temperature also gives the product, but in low yield (13%). Overall, this work indicates that the trinuclear copper(I) pyrazolate $\{\mu\text{-}[3,5\text{-(CF}_3)_2\text{Pz}]\text{Cu}\}_3$ can be used as an efficient catalyst to prepare 1-substituted-1,2,3-triazoles and 1,4-disubstituted 1,2,3-triazoles using just the organo azide and an alkyne source. Some of the isolable copper-alkyne complexes described earlier (e.g., Figure 3.21, 3.27, Table 3.11), resulting from the same alkynes and $\{\mu\text{-}[3,5\text{-(CF}_3)_2\text{Pz}]\text{Cu}\}_3$ combination may exist as intermediates in these processes.

Hydrothiolation of alkynes:

Copper also plays an important role as a catalyst in the alkyne hydrothiolation chemistry which leads to an important class of compound, vinyl sulfides.^{157,196-201} We found that $\{\mu\text{-}[3,5\text{-(CF}_3)_2\text{Pz}]\text{Cu}\}_3$ is an effective catalyst in this process involving phenylacetylene and thiophenol (Figure 3.34, Table 3.13). For example, it catalyzes (1 mol%) the addition of thiol group of PhSH to the alkyne moiety of PhCCH at room temperature under CO₂ producing PhCHCHSPh in 70% isolated yield (entry 1). Note that both the E- and Z-isomers are obtained, which is not unusual for a copper catalyzed process.¹⁹⁷ Interestingly, the control reaction

without the catalyst also produces the product,²⁰⁰ albeit in lower yield (e.g., 42% yield (with almost opposite E:Z of 30:70) at room temperature after 3 h under CO₂).

The E/Z stereoselectivity of $\{\mu\text{-}[3,5\text{-(CF}_3)_2\text{Pz}]\text{Cu}\}_3$ catalyzed reaction is somewhat complicated, and dependent on reaction time, reaction temperature and the atmosphere. For example, at 0 °C and after 3 h of reaction time (entry 2), we have observed different stereoselectivities for reactions carried out under CO₂ (E/Z ratio = 26:74) and N₂ atmosphere (E/Z ratio = 10:90). At 90 °C and after 16 h of reaction time, a reversal in product stereoselectivity was observed (E/Z ratio = 78:22) in the reaction performed under CO₂ atmosphere compared to the 3h reaction at 0°C (entries 4 and 2). The change in product ratio was less significant for the reaction carried out under N₂ atmosphere (E/Z ratio = 34:66 vs 10:90). The hydrothiolation chemistry reported by Y. Zhang and coworkers using CuI (5 mol%) catalyst (in DMSO with K₂CO₃ as a base)¹⁹⁷ under similar reaction temperatures and time, also generated very different product ratios under CO₂ and argon (E/Z ratio = 10:90 and 84:16, with 92% and 68% yields, respectively). Note also that the E/Z stereoselectivity is nearly opposite for the two copper catalysts (i.e., E/Z ratio = 10:90 and 78:22 for CuI and $\{\mu\text{-}[3,5\text{-(CF}_3)_2\text{Pz}]\text{Cu}\}_3$ catalyzed reactions, respectively). The isolated product yields of each $\{\mu\text{-}[3,5\text{-(CF}_3)_2\text{Pz}]\text{Cu}\}_3$ catalyzed experiment were relatively low, when the reactions were performed under N₂ instead of CO₂. We have thus far not probed various temperature, solvent, reaction

time effects in detail. This work however, shows that copper pyrazolates are competent catalysts for alkyne hydrothiolations.

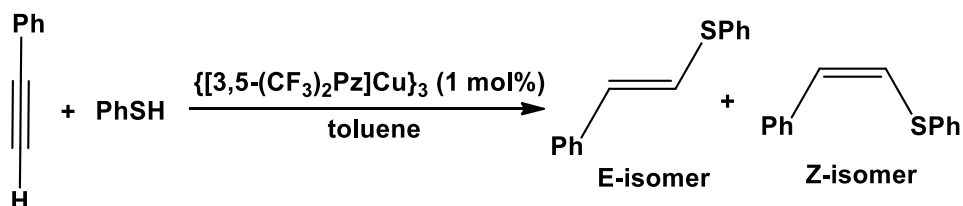


Figure 3.34 The $\{\mu\text{-}[3,5\text{-}(\text{CF}_3)_2\text{Pz}]\text{Cu}\}_3$ catalyzed hydrothiolation of terminal alkynes

Table 3.13 Hydrothiolation of terminal alkynes using $\{\mu\text{-}[3,5\text{-}(\text{CF}_3)_2\text{Pz}]\text{Cu}\}_3$ (1 mol %) as the catalyst. Yields reported are isolated yields (average from two separate experiments). The E/Z ratio was determined by ^1H NMR analysis.

Entry	Temp (°C)	Time (h)	Under CO ₂ (E:Z)	Under N ₂ (E:Z)	Overall % yield under CO ₂	Overall % yield under N ₂
1	RT	3	63:37	50:50	70	56
2	0	3	26:74	10:90	65	48
3	90	3	30:70	56:44	78	62
4	90	16	78:22	34:66	90	81

3.2.4 Summary and Conclusions

Overall, we describe convenient routes to HC≡CH and terminal alkyne (phenylacetylene, 1,8-nonadiyne, 1,7-octadiyne) complexes of copper(I) using readily available, fluorinated copper(I) pyrazolates and the corresponding alkynes. The 2:1 copper:acetylene complexes $\text{Cu}_4(\mu\text{-[3,5-(CF}_3)_2\text{Pz]})_4(\mu\text{-HC}\equiv\text{CH})_2$ (**4**), $\text{Cu}_4(\mu\text{-[4-Br-3,5-(CF}_3)_2\text{Pz]})_4(\mu\text{-HC}\equiv\text{CH})_2$ (**6**), and $\text{Cu}_4(\mu\text{-[4-Cl-3,5-(CF}_3)_2\text{Pz]})_4(\mu\text{-HC}\equiv\text{CH})_2$ (**7**) are easier to isolate and relatively more stable in solid state and solution. They have bridging acetylene ligands as evident from the NMR and Raman spectroscopic data and confirmed for **4** by X-ray crystallography. Low temperature NMR data suggest the existence of 1:1 Cu:alkyne adducts, perhaps of the type $\text{Cu}_2(\mu\text{-[3,5-(CF}_3)_2\text{Pz]})_2(\text{HC}\equiv\text{CH})_2$ (**5**) and $\text{Cu}_2(\mu\text{-[4-Br-3,5-(CF}_3)_2\text{Pz]})_2(\text{HC}\equiv\text{CH})_2$ (**8**) in solutions containing excess acetylene. They are however, extremely labile in solution, and challenging to isolate than **4**, **6**, or **7**. Compound **8** have been isolated in crystalline form, and characterized structurally but it loses acetylene even in the solid state. Raman data show a reduction in $\bar{\nu}_{\text{C}\equiv\text{C}}$ stretching frequency from 1974 cm^{-1} in free acetylene to 1811 cm^{-1} in the $\eta^2\text{-}/2\text{e-}$ donor acetylene adduct **8** and, more drastically, to 1631 cm^{-1} in the bridged $\mu\text{-}\eta^2, \eta^2\text{-}/4\text{e-}$ donor adduct **6**. The terminal alkynes, phenylacetylene, 1,8-nonadiyne, and 1,7-octadiyne easily form their $\eta^2\text{-}/2\text{e-}$ donor alkyne adducts $\text{Cu}_2(\mu\text{-[3,5-(CF}_3)_2\text{Pz]})_2(\text{HC}\equiv\text{CPh})_2$ (**9**), $\text{Cu}_2(\mu\text{-[3,5-(CF}_3)_2\text{Pz]})_2(\text{HC}\equiv\text{C(CH}_2)_5\text{C}\equiv\text{CH})$ (**10**), and

$\text{Cu}_4(\mu\text{-}[3,5\text{-}(\text{CF}_3)_2\text{Pz}])_4(\text{HC}\equiv\text{C}(\text{CH}_2)_4\text{C}\equiv\text{CH})_2$ (**11**) that have 1:1 Cu/alkyne stoichiometry. Isolation of a copper(I)-pyrazolate **12** containing an internal alkyne is also reported. In addition to alkyne coordination, the $\{\mu\text{-}[3,5\text{-}(\text{CF}_3)_2\text{Pz}]\text{Cu}\}_3$ is also a very versatile and competent catalyst for alkyne transformations. We have presented its utility in C(sp)-H bond carboxylation with CO_2 , facile azide-alkyne cycloaddition leading to 1,2,3-triazoles including the rare chemistry involving acetylene itself, and S-H addition to alkyne moiety leading to vinyl sulfides. We are currently, exploring further details on these copper-alkyne chemistry and additional transformations of alkynes mediated by copper. Note that unlike the often used copper halide catalysts, these copper pyrazolates can be more easily fine-tuned sterically and electronically via changes to pyrazolyl ring substituents, which is a useful attribute for homogeneous catalysts.

Chapter 4

Chemistry of binary copper(I) pyrazolates with carbon monoxide

Devaborniny Parasar, Naleen B. Jayaratna, Alvaro Muñoz-Castro, Allison E.

Conway, Pavel K. Mykhailiuk and H. V. Rasika Dias

(Part of this work has been published in *Dalton Trans.*, 2019, 48, 19, 6358–6371)

Reproduced from references¹⁴⁹ with permission from the © The Royal Society of
Chemistry 2019

4.1 Abstract

Syntheses of neutral and anionic, di- and tetra-nuclear copper carbon monoxide complexes using binary copper(I) pyrazolate precursors are reported. The reaction of $\{[3,5-(\text{CF}_3)_2\text{Pz}]\text{Cu}\}_3$ (**2**), $\{[4\text{-Cl-}3,5-(\text{CF}_3)_2\text{Pz}]\text{Cu}\}_3$ (**3**) or $\{[3,4,5-(\text{CF}_3)_3\text{Pz}]\text{Cu}\}_3$ (**4**) with CO in CH_2Cl_2 led to copper carbonyl complexes. They however, lose CO quite easily if not kept under a CO atmosphere. Compounds $\{[3,5-(\text{CF}_3)_3\text{Pz}]\text{Cu}(\text{CO})\}_2$ (**5**) and $\{[3,4,5-(\text{CF}_3)_3\text{Pz}]\text{Cu}(\text{CO})\}_2$ (**7**) were characterized by X-ray crystallography. They are dinuclear species with a Cu_2N_4 core. The reaction of $\{[3,5-(\text{CF}_3)_2\text{Pz}]\text{Cu}\}_3$ with CO in the presence of $[\text{NEt}_4]\text{Br}$ or $[\text{NEt}_4][3,5-(\text{CF}_3)_2\text{Pz}]$ affords relatively more stable $[\text{NEt}_4][\{[3,5-(\text{CF}_3)_2\text{Pz}]\text{Cu}(\text{CO})\}_4(\mu_4\text{-Br})]$ (**8**) and $[\text{NEt}_4][\{[3,5-(\text{CF}_3)_2\text{Pz}\}_3\text{Cu}_2(\text{CO})_2]$ (**9**). The related $[\text{NEt}_4][\{[4\text{-Cl-}3,5-(\text{CF}_3)_2\text{Pz}]\text{Cu}(\text{CO})\}_4(\mu_4\text{-Br})]$ (**10**) and $[\text{NEt}_4][\{[4\text{-Cl-}3,5-(\text{CF}_3)_2\text{Pz}]\text{Cu}(\text{CO})\}_4(\mu_4\text{-Cl})]$ (**11**) can be synthesized using $\{[4\text{-Cl-}3,5-(\text{CF}_3)_2\text{Pz}]\text{Cu}\}_3$, CO and $[\text{NEt}_4]\text{Br}$ or $[\text{NEt}_4]\text{Cl}$. The X-ray structures show that **8**, **10** and **11** are tetranuclear species with terminal Cu-CO groups and quadruply bridging Cl^- and Br^- ions. Compound **9** features an anionic cage of nearly D_{3h} symmetry formed by three bridging $[3,5-(\text{CF}_3)_2\text{Pz}]^-$ ions two terminal Cu-CO moieties. Theoretical calculations show that bonding in these 16- and 18-electron copper complexes follows Dewar–Chatt–Duncanson (DCD) model, where the CO stretching frequencies correlate well to the orbital interaction energy ΔE_{orb} . The major Cu-CO interaction however is electrostatic in nature. Further theoretical

exploration of the role of the substituent at pyrazolyl ring 4-position between -H, -Cl, and -CF₃, shows a slight decrease in covalent character of the Cu-CO interaction and diminished π -back bonding as pyrazolate groups become more weakly donating with added electron withdrawing substituents.

4.2 Introduction

Copper complexes of carbon monoxide are of significant historical, scientific and technological importance.²⁰²⁻²¹¹ In fact, the first reports of CO chemistry with copper can be traced back to 1850s, which concern the absorption of carbon monoxide by hydrochloric acid solutions of copper(I) chloride.²⁰² However, copper carbonyl complexes that can be isolated as analytically pure solids and are stable in the absence of CO came to prominence only after 1969 with the synthesis of molecules such as Cu(CF₃CO₂)CO and [HB(Pz)₃]CuCO.²¹²⁻²¹⁴ Although there are a number of well-defined copper carbonyl adducts in the literature presently,^{203,205} synthesis and the chemistry of such species continue to attract wide interest due to their significance in the purification and separation of CO from gas mixtures using copper (e.g., copper-liquor scrubbing, COSORB process, adsorption processes),²¹⁵⁻²¹⁹ industrially significant reactions of CO involving copper (e.g., oxidation using Hopcalite, Cu(I)/ZnO catalyzed synthesis of methanol from syngas, copper mediated water-gas shift reaction),^{215,220-229} implications in the carbonylation of alkenes, amines, hydrocarbons, and alcohols

facilitated by copper,^{206,230-236} CO reduction with Cu based catalysts,²³⁷ and value as a convenient spectroscopic probe to study copper sites in solid materials, molecules, and metallo-enzymes.^{210,238-255}

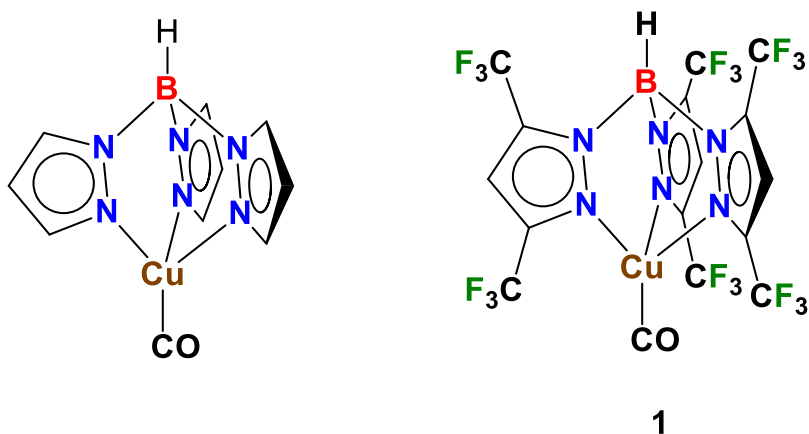


Figure 4.1 Structures of [HB(Pz)₃]CuCO and [HB(3,5-(CF₃)₂Pz)₃]CuCO (**1**)

Carbonyl complexes are particularly useful to gauge the electronic properties of supporting ligands, and to understand the bonding and some chemistry of metal adducts. For example, the CO stretching frequency of [HB(3,5-(CF₃)₂Pz)₃]CuCO (**1**, $\bar{\nu}_{\text{CO}} = 2137 \text{ cm}^{-1}$) is 71 cm^{-1} higher than that of the non-fluorinated analog [HB(3,5-(CH₃)₂Pz)₃]CuCO ($\bar{\nu}_{\text{CO}} = 2066 \text{ cm}^{-1}$), and points to the presence of rather electron deficient copper site in the fluorinated system.^{205,256} [Cu(*trans,trans,trans*-1,5,9-cyclododecatriene)(CO)][SbF₆] with a $\bar{\nu}_{\text{CO}}$ of 2160 cm^{-1} is an example of a non-classical metal carbonyl complex,²⁵⁷ that has a CO stretching frequency higher than that of free CO ($\bar{\nu}_{\text{CO}} = 2143 \text{ cm}^{-1}$).²⁴⁹ Copper and

silver complexes supported by fluorinated tris(pyrazolyl)borate ligands such as $[\text{HB}(3,5\text{-(CF}_3)_2\text{Pz)}_3]^-$ that display very high $\bar{\nu}_{\text{CO}}$ are powerful catalyst for carbene and nitrene transfer reactions.^{205,258-261} The “[HB(4-Br-3,5-(CF₃)₂Pz)₃]M” (M = Cu, Ag) even catalyzes the functionalization of methane via carbene insertion.²⁶²

In this chapter we describe the carbonyl chemistry of binary copper(I) pyrazolates $\{[3,5\text{-(CF}_3)_2\text{Pz}]\text{Cu}\}_3$ (**2**),⁷ $\{[4\text{-Cl-}3,5\text{-(CF}_3)_2\text{Pz}]\text{Cu}\}_3$ (**3**),²⁰ and $\{[3,4,5\text{-(CF}_3)_3\text{Pz}]\text{Cu}\}_3$ (**4**),³³ and the effects of additional donors such as chloride, bromide, and $[3,5\text{-(CF}_3)_2\text{Pz}]^-$ ions on the stability of the resulting copper(I) carbonyl adducts, especially **2** and **3**. It is noteworthy that although a large number of binary copper(I) pyrazolates are known,^{5,74} their coordination chemistry with CO is very limited. Trinuclear $[\text{Cu}(\text{CO})\{2\text{-(}3(5)\text{-Pz)}\}_6(\text{CH}_3\text{py})]_3$ and dinuclear $(\text{py})\text{Cu}[3,5\text{-(MeCO}_2)_2\text{Pz}]_2\text{Cu}(\text{CO})(\text{py})$ represent two rare examples of copper carbonyls derived from binary copper pyrazolates (Figure 4.2).^{263,264} There is also a report of an anionic copper carbonyl complex $[\text{Cu}_4(\text{dmnpz})_6(\text{CO})_4]^{2-}$ (dmnpz = 3,5-dimethyl-4-nitro-pyrazolate, Figure 4.2),⁶ but apart from the IR data, it has not been well characterized due to the highly labile nature of the CO ligand. The ability to coordinate CO at Cu sites of a copper-pyrazolate based metal–organic framework has been reported by Volkmer *et al.*²⁶⁵

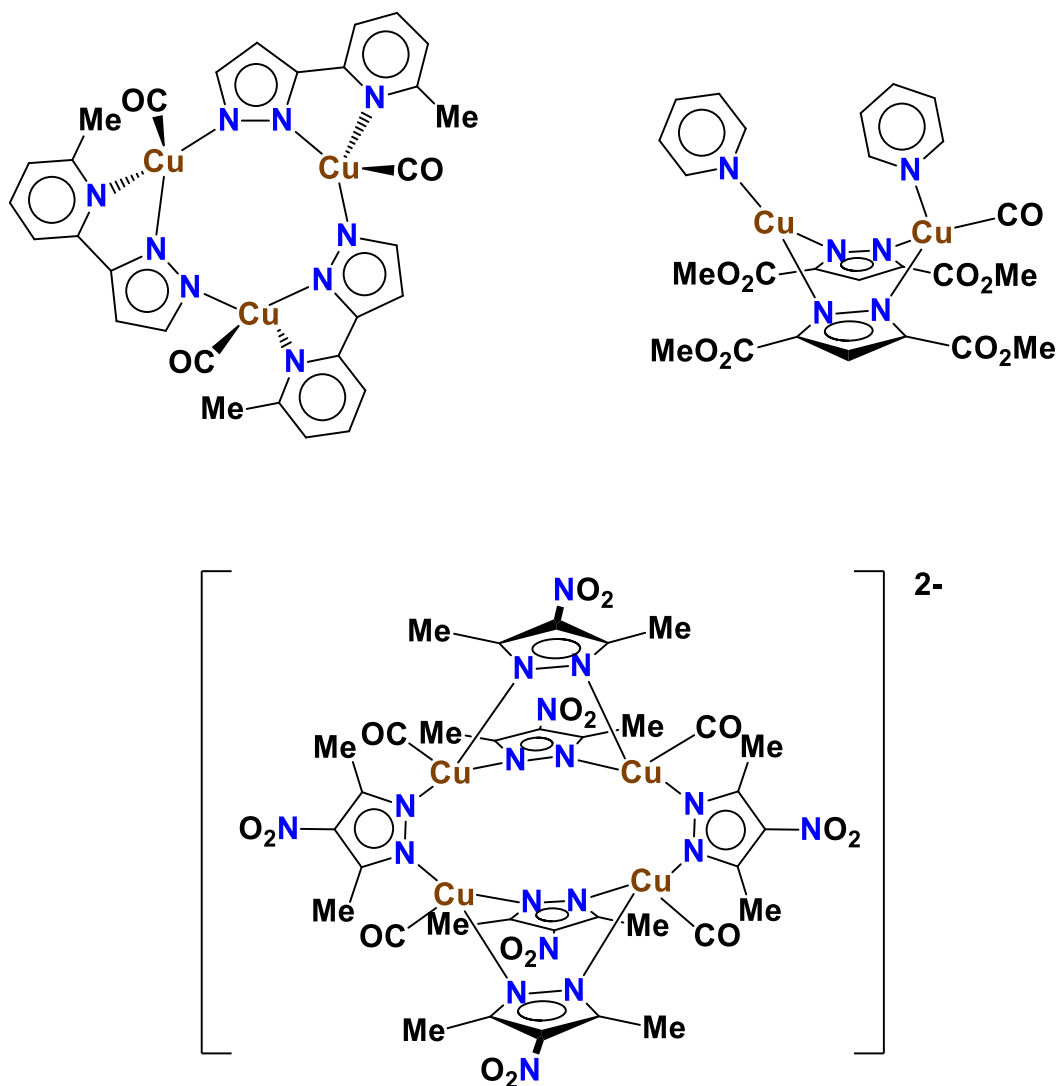


Figure 4.2 Structurally characterized $[\text{Cu}(\text{CO})\{2\text{-}(3(5)\text{-Pz}),6\text{-(CH}_3\text{)py}\}]_3$ and $(\text{py})\text{Cu}[3,5\text{-(MeCO}_2)_2\text{Pz}]_2\text{Cu}(\text{CO})(\text{py})$, and the proposed structure of $[\text{Cu}_4(\text{dmpz})_6(\text{CO})_4]^{2-}$ based on solution data.

4.3 Results and discussion

The trinuclear copper(I) pyrazolates such as $\{[3,5-(\text{CF}_3)_2\text{Pz}]\text{Cu}\}_3$ (**2**) and $\{[3,5-(i\text{-Pr})_2\text{Pz}]\text{Cu}\}_3$ are known for their remarkable photophysical properties.^{15,53} The fluorinated copper pyrazolate $\{[3,5-(\text{CF}_3)_2\text{Pz}]\text{Cu}\}_3$ (**2**) is also an interesting π -acid that forms acid-base adducts with π -bases like benzene and C_{60} and other Lewis bases leading to supramolecular aggregates.^{87,93,100} Chemistry described below with the σ -donor/ π -acceptor carbon monoxide ligand under various conditions illustrates a different facet of this adduct. We have also probed the chemistry of related $\{[4\text{-Cl-}3,5-(\text{CF}_3)_2\text{Pz}]\text{Cu}\}_3$ (**3**)²⁰ and $\{[3,4,5-(\text{CF}_3)_3\text{Pz}]\text{Cu}\}_3$ (**4**)³³ to understand the electronic effects of pyrazolyl ligand supports on bonding and stability of the resulting copper carbonyls.

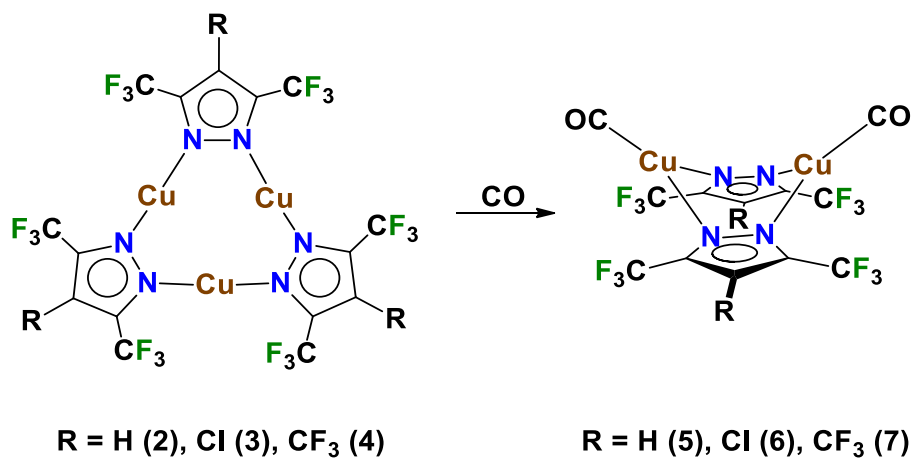


Figure 4.3 Synthetic route to $\{[3,5\text{-(CF}_3)_2\text{Pz}]\text{Cu(CO)}\}_2$ (**5**), $\{[4\text{-Cl-3,5-(CF}_3)_2\text{Pz}]\text{Cu(CO)}\}_2$ (**6**), $\{[3,4,5\text{-(CF}_3)_3\text{Pz}]\text{Cu(CO)}\}_2$ (**7**) from $\{[3,5\text{-(CF}_3)_2\text{Pz}]\text{Cu}\}_3$ (**2**), $\{[4\text{-Cl-3,5-(CF}_3)_2\text{Pz}]\text{Cu}\}_3$ (**3**), and $\{[3,4,5\text{-(CF}_3)_3\text{Pz}]\text{Cu}\}_3$ (**4**)

Concentration of a warm (40-45 °C) dichloromethane solution of $\{[3,5\text{-(CF}_3)_2\text{Pz}]\text{Cu}\}_3$ (**2**) by a slow stream of CO led to the precipitation of a white solid. The IR data of this solid display two strong bands at 2099 and 2108 cm^{-1} in the typical region for terminal CO groups supported by weakly coordinating ligands,^{205,266} indicating the formation of a copper-carbonyl species $\{[3,5\text{-(CF}_3)_2\text{Pz}]\text{Cu(CO)}\}_2$ (**5**) (Figure 4.3). In Nujol, only a single band was observed at 2128 cm^{-1} suggesting some medium effects. Compound **5** loses CO rapidly and reverts back to **2** in the absence of a CO atmosphere. Interestingly, the treatment of **2** in dichloromethane with CO at room temperature did not lead to the formation of a CO complex. It is possible that CO is not nucleophilic enough to break-up the

nine-membered Cu₃N₉ metallacycle in {[3,5-(CF₃)₂Pz]Cu}₃ (**2**) without added heat. In contrast, better nucleophiles such as 2,4,6-collidine and 3-hexyne afford dinuclear products {[3,5-(CF₃)₂Pz]Cu(2,4,6-collidine)}₂ and {[3,5-(CF₃)₂Pz]Cu(EtC≡CEt)}₂ quite easily with **2** at the room temperature.^{30,73} We have also investigated {[3,5-(CF₃)₂Pz]Cu(CO)}₂ (**5**) computationally. The calculated CO frequencies of 2095 and 2101 cm⁻¹ for **5**, which account for both antisymmetric and symmetric $\bar{\nu}_{\text{CO}}$ stretch, are in good agreement with the experimental observations, 2099 and 2108 cm⁻¹.

The ¹³C{¹H} spectrum of {[3,5-(CF₃)₂Pz]Cu(CO)}₂ (**5**) in CD₂Cl₂ saturated with CO at the room temperature displays a signal at δ 172.3 ppm indicating the existence of copper bound CO in solution, and in the expected region for copper carbonyls.^{205,238,253} For comparison, the signal for ¹³CO gas in CD₂Cl₂ was observed relatively upfield at δ 184 ppm. Compound **5** has a rather labile CO, which is lost by bubbling dinitrogen into the CD₂Cl₂ solution or during the removal of solvent using reduced pressure, producing the starting copper complex **2**. ¹⁹F NMR spectrum of {[3,5-(CF₃)₂Pz]Cu(CO)}₂ (**5**) in CD₂Cl₂ shows that it is in an equilibrium with **2** as indicated by two sets of ¹⁹F NMR signals.

The observed **2**↔**5** equilibrium upon CO saturation/removal in dichloromethane solution is further evaluated by the estimated reaction free-energy change at room temperature ($\Delta G^{298\text{K}}$) for the reaction: 2 {[3,5-(CF₃)₂Pz]Cu}₃ + 6 CO → 3 {[3,5-(CF₃)₂Pz]Cu(CO)}₂, which amounts to -17.35 kcal mol⁻¹ (-5.78 kcal

per mol of **5**) suggesting the CO incorporation in **2** to be thermodynamically favorable and dominated by kinetic control. External heat helps overcome activation barrier in the synthesis of **5**.

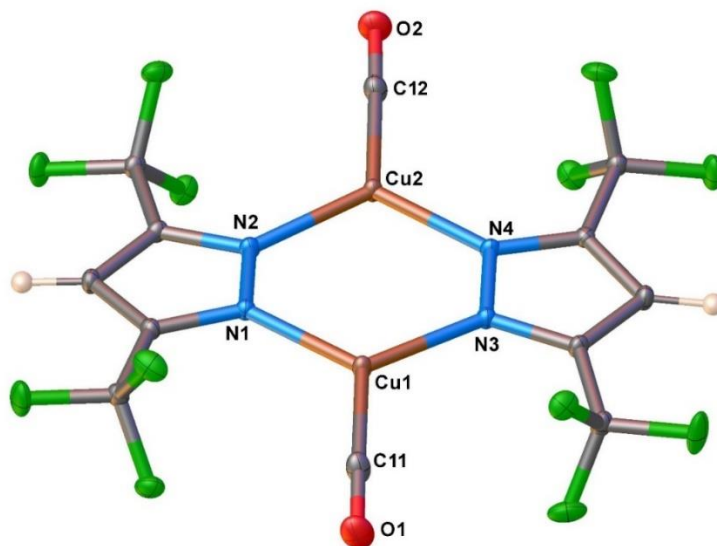


Figure 4.4. Molecular structure of $\{[3,5-(\text{CF}_3)_2\text{Pz}]\text{Cu}(\text{CO})\}_2$ (**5**). Only one of the 1.5 molecules present in the asymmetric unit are shown. Selected, average bond distances (Å) and angles ($^\circ$): Cu-C 1.843, O-C 1.123, N-Cu 1.9709, N-Cu-N 113.71, O-Cu-Cu 177.1, Cu \cdots Cu 3.52

The X-ray crystal structure of **5** is shown in Figure 4.4. Selection and mounting of suitable crystals for data collection is challenging due to rapid CO loss at room temperature, even under Paratone oil. Compound **5** crystallizes in *P*-1 space group with 1.5 molecules in the asymmetric unit. It is a dinuclear species with essentially planar Cu_2N_4 core, with an average Cu \cdots Cu distance of 3.52 Å.

Copper centers are three-coordinate and adopt a trigonal planar geometry. As noted earlier, trinuclear $[\text{Cu}(\text{CO})\{2\text{-(3(5)-Pz),6-(\text{CH}_3)\text{py}}\}]_3$ and dinuclear $(\text{py})\text{Cu}[3,5\text{-(MeCO}_2)_2\text{Pz}]_2\text{Cu}(\text{CO})(\text{py})$ are the only well-authenticated copper carbonyls derived from binary copper pyrazolates in the literature (Figure 4.2) to our knowledge.^{263,264} They both feature four-coordinate copper-carbonyl sites. In contrast, three-coordinate copper complexes with an $\text{N}_2\text{Cu-CO}$ coordination sphere as in **5** are rare. There are only eight such adducts in the Cambridge Structural database.²⁶⁷⁻²⁷⁴ While none of these three-coordinate $\text{N}_2\text{Cu-CO}$ adducts involve pyrazolate ligand supports, a comparison of their Cu-CO distances (which range from 1.749 to 1.818 Å) to that of **5** (av. 1.843 Å) show that that latter has a relatively long Cu-C bond which is at the upper end of this spectrum.

We have also investigated the chemistry of related $\{[4\text{-Cl-3,5-(CF}_3)_2\text{Pz}]\text{Cu}\}_3$ (**3**) and $\{[3,4,5\text{-(CF}_3)_4\text{Pz}]\text{Cu}\}_3$ (**4**) with CO. These molecules possess comparatively more weakly coordinating pyrazolates. As with **2**, it was necessary to heat the solution containing **3** before treating with CO to afford the corresponding copper carbonyl adduct $\{[4\text{-Cl-3,5-(CF}_3)_2\text{Pz}]\text{Cu}(\text{CO})\}_2$ (**6**). In contrast, $\{[3,4,5\text{-(CF}_3)_3\text{Pz}]\text{Cu}(\text{CO})\}_2$ (**7**) can be obtained by treating **4** with CO at room temperature in CH_2Cl_2 . The IR spectra of compounds **6** and **7** show their CO stretching frequencies at 2139 cm^{-1} . In Nujol, compound **6** exhibits a prominent broad band at 2110 cm^{-1} with shoulder bands at 2127 and 2146 cm^{-1} (average signal at 2128 cm^{-1}) while **7** displays $\bar{\nu}_{\text{CO}}$ at 2146 cm^{-1} . The calculated CO frequencies of

6 and **7** are 2099, 2106 and 2102, 2108 cm^{-1} (which account antisymmetric and symmetric $\bar{\nu}_{\text{CO}}$ stretch of each adduct), respectively. These experimental and computed $\bar{\nu}_{\text{CO}}$ values are closer to that of the free CO (2143 cm^{-1}) pointing to the presence of fairly electrophilic copper sites in **6** and **7** with low π -backbonding capabilities. This is not surprising as Cu-CO moieties of **6** and **7** are supported by very weakly donating pyrazolyl ligands decorated with electron withdrawing substituents CF_3 , Cl, CF_3 and CF_3 , CF_3 , CF_3 at the 3, 4, and 5-positions, respectively, while in **5**, pyrazolyl moieties have only CF_3 , H, CF_3 groups on the backbone (Figure 4.3). For comparison, relatively electron rich $(\text{py})\text{Cu}[3,5\text{-}(\text{MeCO}_2)_2\text{Pz}]_2\text{Cu}(\text{CO})(\text{py})$ (Figure 4.2)²⁶⁴ displays its IR band at a significantly lower value of 2073 cm^{-1} . Three-coordinate copper complexes such as $[\text{N}\{(\text{F}_7\text{C}_3)\text{C}(2\text{-F},6\text{-(CF}_3)\text{C}_6\text{H}_3)\text{N}\}_2]\text{Cu}(\text{CO})$ ²⁶⁹ and $[\text{HC}\{(\text{F}_3\text{C})\text{C}(\text{C}_6\text{F}_5)\text{N}\}_2]\text{Cu}(\text{CO})$ ²⁷⁰ supported by heavily fluorinated ligands display $\bar{\nu}_{\text{CO}}$ bands (more like **6** and **7**) at 2128 and 2122, 2135 (two bands for the latter as a result of inter-molecular $\text{F}\cdots\text{CO}$ contacts), respectively. Compound $[\text{Cu}(\textit{trans,trans,trans}\text{-1,5,9-cyclododecatriene})(\text{CO})][\text{SbF}_6]$ with a $\bar{\nu}_{\text{CO}}$ of 2160 cm^{-1} is an example of a non-classical metal carbonyl complex,²⁵⁷ with a $\bar{\nu}_{\text{CO}}$ significantly higher than that of free CO.

Solid samples of **6** and **7** also lose CO quite easily under vacuum or in the absence of CO atmosphere. It is also possible to monitor the diminishing IR signal of $\bar{\nu}_{\text{CO}}$ with time using solid samples on an ATR stage. Compound **7** is the most

thermally stable adduct among **5-7** which shows the slowest rate of CO loss in air. $^{13}\text{C}\{^1\text{H}\}$ spectra of CO saturated solutions of **6** and **7** in CD_2Cl_2 at room temperature display resonances at δ 171.8 and 170.9 ppm corresponding to the copper bound CO in solution, with **7** showing the most upfield shift from the free CO. The calculated ^{13}CO chemical shift of **7** (δ 168.7 ppm) agrees well with the experimental observation.

We have also been able to obtain the X-ray crystal structure of $\{[3,4,5\text{-(CF}_3)_3\text{Pz}]\text{Cu}(\text{CO})\}_2$ (**7**), which is illustrated in Figure 4.5. The molecule **7** sits on a mirror plane containing two C-4 carbons of the pyrazolyl moieties. It is a dinuclear species with a boat-shaped, six-membered Cu_2N_4 core. The corresponding copper ethylene complex $\{[3,4,5\text{-(CF}_3)_3\text{Pz}]\text{Cu}(\text{C}_2\text{H}_4)\}_2$ also has a similar dinuclear structure, but with a much closer intramolecular $\text{Cu}\cdots\text{Cu}$ separation (3.21 Å vs 3.31 Å in **7**). In contrast, **5** and $\{[3,5\text{-(CF}_3)_2\text{Pz}]\text{Cu}(2,4,6\text{-collidine})\}_2$ have planar Cu_2N_4 cores with larger $\text{Cu}\cdots\text{Cu}$ separations (3.52 and 3.39 Å, respectively), which illustrate the conformational flexibility of six-membered Cu_2N_4 frame in these systems. The average Cu-N distance of **7** (1.9897 Å) is slightly longer than the corresponding distance observed for **5** (1.9709 Å), perhaps as a result of the relatively weakly donating nature of the supporting pyrazolate in the former adduct.

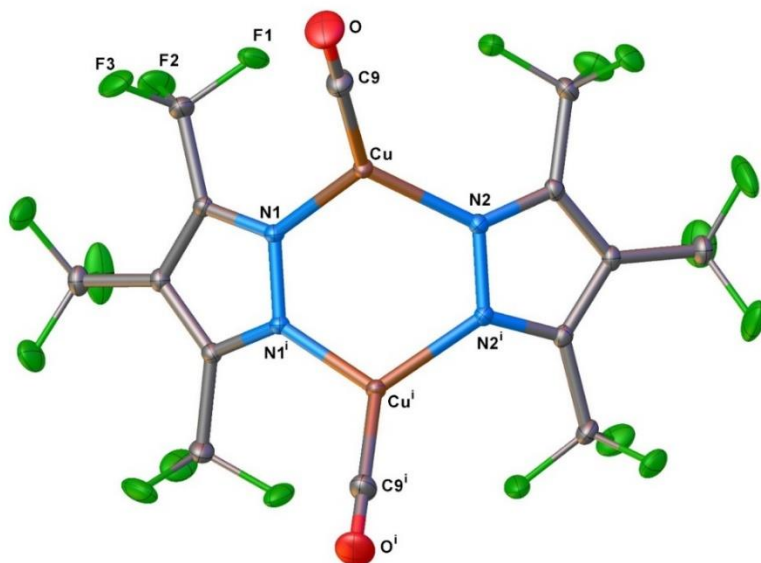


Figure 4.5 Molecular structure of $\{[3,4,5-(\text{CF}_3)_3\text{Pz}]\text{Cu}(\text{CO})\}_2$ (**7**). Selected bond distances (Å) and angles (°): Cu-C9 1.831(2), O-C9 1.123(3), N1-Cu 1.9873(15), N2-Cu 1.9921(15), N1-Cu-N2 102.25(6), C9-Cu-N1 127.13(8), C9-Cu-N2 130.53(8), O-Cu-Cu 179.1(2)

Evaluation of the effects of -H, -Cl and -CF₃, substituent at the 4-position of [3,5-(CF₃)₂Pz]⁻ by computational methods reveal that the Cu-CO bonding energy is more favorable in the following order, -38.53 (**5**) > -37.08 (**6**) > -34.80 (**7**) kcal mol⁻¹, suggesting the strongest bond for the former (Table 4.1). The Cu-CO binding energy (ΔE_{int}) can be further dissected to different, chemically meaningful terms within the Energy Decomposition Analysis (EDA) given by Ziegler and Rauk,²⁷⁵ $\Delta E_{\text{int}} = \Delta E_{\text{Pauli}} + \Delta E_{\text{elstat}} + \Delta E_{\text{orb}} + \Delta E_{\text{disp}}$; where the ΔE_{Pauli} term accounts for the repulsive four-electron/two-orbital interactions, and ΔE_{elstat}

and ΔE_{orb} account for stabilizing terms related to both electrostatic and covalent character of the interaction, respectively.

Table 4.1 Calculated bonding interaction energies (ΔE_{int}) and its derived terms

($\Delta E_{\text{Pauli}} + \Delta E_{\text{Elstat}} + \Delta E_{\text{orb}} + \Delta E_{\text{disp}}$), along with their percent contribution. Values in kcal/mol.

Complexes	ΔE_{Pauli}	ΔE_{Elstat}	%	ΔE_{orb}	%	ΔE_{disp}	%	ΔE_{int}
{[3,5-(CF ₃) ₂ Pz]Cu(CO)} ₂ (5)	113.63	-91.87	60.4	-58.26	38.3	-2.03	1.3	-38.53
{[4-Cl-3,5-(CF ₃) ₂ Pz]Cu(CO)} ₂ (6)	111.11	-88.64	59.8	-57.58	38.9	-1.97	1.3	-37.08
{[3,4,5-(CF ₃) ₃ Pz]Cu(CO)} ₂ (7)	110.10	-88.79	61.3	-53.71	37.1	-2.40	1.7	-34.80
{[3,5-(CF ₃) ₂ Pz] ₃ Cu ₂ (CO) ₂ } ⁻ (9)	133.75	-103.11	60.5	-62.37	36.6	-5.06	3.0	-36.79
{[4-Cl-3,5-(CF ₃) ₂ Pz] ₃ Cu ₂ (CO) ₂ } ⁻	124.01	-96.10	60.4	-57.71	36.3	-5.35	3.4	-35.15
{[3,4,5-(CF ₃) ₃ Pz] ₃ Cu ₂ (CO) ₂ } ⁻	124.10	-95.10	60.7	-56.38	36.0	-5.16	3.3	-32.54
[{[3,5-(CF ₃) ₂ Pz]Cu(CO)} ₄ (μ ₄ -Br)] (8)	121.70	-95.67	60.5	-58.02	36.7	-4.41	2.8	-36.40

$[[\{4\text{-Cl-3,5-}(\text{CF}_3)_2\text{Pz}\}\text{Cu}(\text{CO})\}_4(\mu_4\text{-Br})]^-$ (10)	121.30	-94.81	60.6	-56.87	36.3	-4.80	3.1	-35.18
$[[\{3,4,5\text{-}(\text{CF}_3)_3\text{Pz}\}\text{Cu}(\text{CO})\}_4(\mu_4\text{-Br})]^-$	121.02	-94.38	60.5	-56.54	36.3	-4.99	3.2	-34.89
$[[\{3,5\text{-}(\text{CF}_3)_2\text{Pz}\}\text{Cu}(\text{CO})\}_4(\mu_4\text{-Cl})]^-$	121.14	-95.59	60.4	-58.14	36.7	-4.51	2.9	-37.10
$[[\{4\text{-Cl-3,5-}(\text{CF}_3)_2\text{Pz}\}\text{Cu}(\text{CO})\}_4(\mu_4\text{-Cl})]^-$ (11)	121.86	-95.56	60.4	-57.42	36.3	-5.13	3.2	-36.25
$[[\{3,4,5\text{-}(\text{CF}_3)_3\text{Pz}\}\text{Cu}(\text{CO})\}_4(\mu_4\text{-Cl})]^-$	119.10	-93.79	60.5	-56.16	36.2	-5.12	3.3	-35.97
$[\text{H}_2\text{B}(3,5\text{-}(\text{CF}_3)_2\text{Pz})_2]\text{CuCO}$	107.70	-89.51	61.2	-54.38	37.2	-2.39	1.6	-38.58
$[\text{HB}(3,5\text{-}(\text{CF}_3)_2\text{Pz})_3]\text{CuCO}$ (1)	108.58	-91.10	60.7	-55.00	36.7	-3.96	2.6	-41.48

The EDA analysis of Cu-CO bonding in **5-7** show that the electrostatic character is the most significant term (~60%), followed by the orbital contributions (~38%), and with minor contributions from ΔE_{disp} (~2%). As a comparison, terminal Fe-CO of $\text{Fe}_2(\text{CO})_9$ at a related level of theory exhibits ΔE_{int} value of $-48.7 \text{ kcal mol}^{-1}$,²⁷⁶ and a slightly larger covalent character (~42%, ΔE_{orb}), pointing

relatively lower covalent interactions in d^{10} -Cu(I) system. Among **5**, **6**, and **7**, the most electrostatic interaction (ionic character) is observed for **7** (61.3%, ΔE_{elstat}).

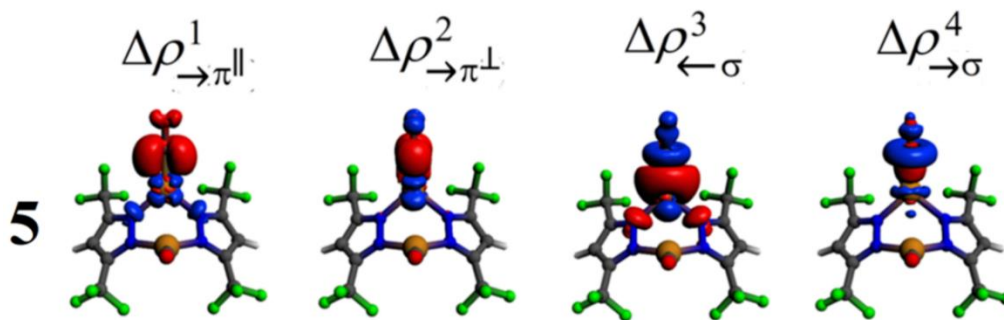


Figure 4.6 NOCV-EDA analysis of the Cu-CO interaction in $\{[3,5\text{-(CF}_3)_2\text{Pz]Cu(CO)}\}_2$ (**5**), accounting for the Dewar–Chatt–Duncanson bonding model, and the nonclassical σ interaction ($\Delta\rho^4_\sigma$). The direction of charge flow in the deformation densities is from red \rightarrow blue.

The orbital interaction term (ΔE_{orb} , covalent character) provides information on synergistic bonding depicted by the Dewar–Chatt–Duncanson (DCD) model. The orbital term for **5** is the strongest in the series ($-58.26 \text{ kcal mol}^{-1}$), followed by **6** ($-57.58 \text{ kcal mol}^{-1}$) and **7** ($-53.71 \text{ kcal mol}^{-1}$). In addition, ΔE_{orb} can be decomposed to individual contributions within the NOCV-EDA framework (Figure 4.6),^{277,278} which accounts for parallel and tangential oriented π -backbonding ($\Delta\rho^1_{\rightarrow\pi^{\parallel}}$ and $\Delta\rho^2_{\rightarrow\pi^{\perp}}$) and σ -donor ($\Delta\rho^3_{\leftarrow\sigma}$) bonding interactions ascribed to the DCD model, with the addition of a nonclassical σ interaction

$(\Delta\rho^4_\sigma)$.²⁷⁶ Such individual bonding interactions are somewhat similar in the 16-electron **5**, **6** and **7** series, where the overall π -backbonding bonding scheme accounts for 56.3% > 54.6% > 53.9% of ΔE_{orb} ($\Delta\rho^1_{\rightarrow\pi\parallel} + \Delta\rho^2_{\rightarrow\pi\perp}$), respectively, while the σ -donor ($\Delta\rho^3_{\leftarrow\sigma}$) component of **5**, **6** and **7** shows the opposite trend, 26.6% < 27.1 % < 28.2 %, respectively. These values suggest that **5** exhibits the largest π -backbonding and lowest σ -donor contribution to the Cu-CO bonding scheme, whereas **7** shows the lowest π -backbonding and largest σ -donor contribution to the Cu-CO coordination. They correlate well with the electron withdrawing capabilities of substituent at the pyrazolyl ring 4-position.

We thought that it may be possible to stabilize labile carbonyl compounds **5** and **6** by blocking the open-coordination sites of these 16-electron copper complexes using Lewis bases leading to 18-electron copper carbonyl sites. In fact, $[\text{Cu}(\text{CO})\{2\text{-}(3(5)\text{-Pz}),6\text{-(CH}_3\text{)py}\}]_3$ and $(\text{py})\text{Cu}[3,5\text{-(MeCO}_2)_2\text{Pz}]_2\text{Cu}(\text{CO})(\text{py})$ have 18-electron Cu-CO sites. Furthermore, the three-coordinate $[\text{H}_2\text{B}(3,5\text{-(CF}_3)_2\text{Pz})_2]\text{CuCO}$ is very labile and readily lose CO while the four-coordinate $[\text{H}_2\text{C}(3,5\text{-(CF}_3)_2\text{Pz})_2]\text{CuCO}(\text{OTf})$ is isolable,²⁷⁹ and the tris(pyrazolyl)borate analog $[\text{HB}(3,5\text{-(CF}_3)_2\text{Pz})_3]\text{CuCO}$ shows a notably high air and thermal stability.²⁵⁶ In this work, we set out to probe the ability of easily available halide ions as stabilizing Lewis bases for **5** and **6** not only because they are less widely explored

(compared for example to N-based donors), but also due the current interest in halide encapsulating molecules.^{280,281}

Indeed, compound **5** encapsulates bromide ions from [NEt₄]Br effectively leading to an interesting and isolable 18-electron species [NEt₄][{[3,5-(CF₃)₂Pz]Cu(CO)}₄(μ₄-Br)] (Figure 4.7, **8**). In this molecule, bromide ion coordinates to the open coordination sites copper without displacing the bound CO. Compound **8** has been synthesized by treating a dichloromethane solution of **2** with CO in the presence [NEt₄]Br, and isolated as an analytically pure solid in 84% yield. It is however, a rather air sensitive solid and decomposes over a period of minutes in air at the room temperature. It can be stored in a freezer under a CO atmosphere for prolonged periods. Compound **8** displays a single strong sharp absorption at 2098 cm⁻¹ in the IR spectrum, which is diagnostic for the presence of a terminal carbonyl group, and suggestive of a symmetric coordination environment. This also indicates the presence of marginally electron rich copper sites in **8** relative to those of **5** ($\bar{\nu}_{\text{CO}} = 2099, 2108 \text{ cm}^{-1}$). This is not surprising as compound **5** is a neutral molecule with two fluorinated pyrazolates on copper, while the compound **8** features Cu-CO sites in a formally anionic fragment and bonded to two pyrazolates and a bromide ion (Figure 4.7).

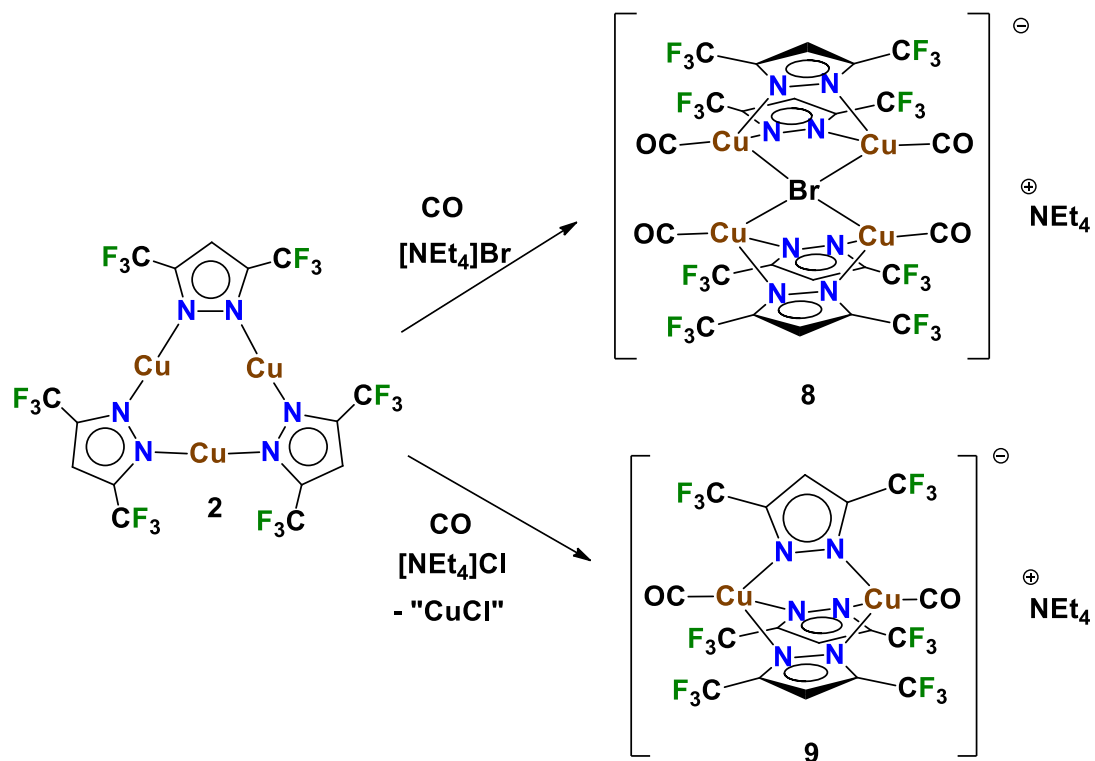


Figure 4.7 Synthetic route to $[\text{NEt}_4][\{[3,5\text{-(CF}_3)_2\text{Pz]Cu(CO)}\}_4(\mu_4\text{-Br})]$ (**8**) and $[\text{NEt}_4][\{[3,5\text{-(CF}_3)_2\text{Pz]}_3\text{Cu}_2(\text{CO})_2\}]$ (**9**) from $\{[3,5\text{-(CF}_3)_2\text{Pz]Cu}\}_3$ (**2**)

The X-ray crystal structure of **8** (Figure 4.8) reveals a tetranuclear copper compound, featuring well separated $[\text{NEt}_4]^+$ cation and $[\{[3,5\text{-(CF}_3)_2\text{Pz]Cu(CO)}\}_4(\mu_4\text{-Br})]^-$ anion. Selected bond distances and angles are given in Table 4.2. The two $\{[3,5\text{-(CF}_3)_2\text{Pz]Cu(CO)}\}_2$ fragments assume a boat-shape, and are held together by a quadruply bridging bromide ion ($\mu_4\text{-Br}$) using all four lone pairs. The geometry at Br may be described as a flattened tetrahedron (Cu-

Br-Cu angles deviate significantly from ideal 109.5° and range from 72.1° to 166.4°).

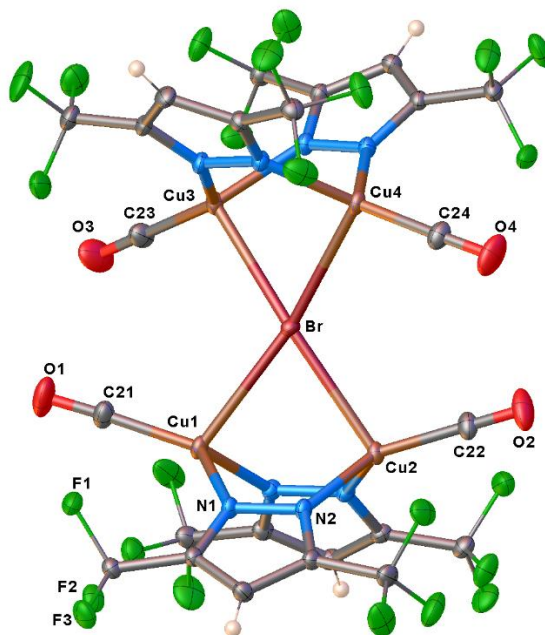


Figure 4.8. Molecular structure of $[\text{NEt}_4][\{[3,5\text{-(CF}_3)_2\text{Pz]Cu(CO)}\}_4(\mu_4\text{-Br})]$ (**8**).

The cation $[\text{NEt}_4]^+$ has been omitted for clarity.

Table 4.2 Selected bond distances (\AA), bond angles ($^\circ$) and CO stretching frequency (cm^{-1}) for $[\text{NEt}_4][\{[3,5\text{-(CF}_3)_2\text{Pz]Cu(CO)}\}_4(\mu_4\text{-Br})]$ (**8**), $[\text{NEt}_4][\{[3,5\text{-(CF}_3)_2\text{Pz]}_3\text{Cu}_2(\text{CO})_2\}]$ (**9**), $[\text{NEt}_4][\{[4\text{-Cl-3,5-(CF}_3)_2\text{Pz]Cu(CO)}\}_4(\mu_4\text{-Br})]$ (**10**) and $[\text{NEt}_4][\{[4\text{-Cl-3,5-(CF}_3)_2\text{Pz]Cu(CO)}\}_4(\mu_4\text{-Cl})]$ (**11**). X = Br or Cl

Parameter \Complex	8	9	10		11
Cu-N	2.0137(11)	2.0452(16)	2.0094(18)	2.018 (2)	2.017(3)
	1.9992(12)	2.0410(16)	2.0204(18)	2.027 (2)	2.029(3)
	2.0004(12)	2.0468(17)	2.0332(17)	2.009(2)	2.030(3)
	1.9988(11)	2.0391(18)	2.0254(17)	2.019(2)	2.019(3)
	2.0024(12)	2.0492(18)	2.0116(19)	2.018(2)	2.015(4)
	1.9941(11)	2.0379(16)	2.0283(18)	2.009(2)	2.029(4)
	2.0075(11)		2.0208(18)	2.027(2)	2.030(4)
	1.9960(11)		2.0083(18)	2.019(2)	2.011(4)
<i>av. Cu-N</i>	<i>2.002</i>	<i>2.043</i>	<i>2.019</i>		<i>2.023</i>
Cu-C	1.8253(15)	1.813(2)	1.819(2)	1.816(3)	1.818(5)
	1.8120(15)	1.814(2)	1.829(2)	1.818(3)	1.808(5)
	1.8148(15)		1.822(3)	1.816(3)	1.820(5)
	1.8166(14)		1.821(2)	1.818(3)	1.826(5)
<i>av. Cu-C</i>	<i>1.817</i>	<i>1.814</i>	<i>1.820</i>		<i>1.818</i>
Cu-X	2.7593(2)		2.5967(4)	2.5731(4)	2.4633(11)
	2.7089(2)		2.5865(4)	2.5731(4)	2.4578(11)
	2.7329(2)		2.6124(4)	2.6059(4)	2.4785(11)
	2.7601(2)		2.6006(4)	2.6059(4)	2.4598(11)
<i>av. Cu-X</i>	<i>2.740</i>		<i>2.595</i>		<i>2.465</i>
Cu-C-O	177.30(16)	178.7(2)	172.8(2)	175.6(2)	174.5(5)
	175.96(14)	179.4(2)	173.0(2)	175.2(3)	174.3(5)
	179.33(17)		174.9(3)	175.2(2)	176.6(5)

	176.10(15)		177.2(3)	175.6(2)	177.6(5)
<i>av. Cu-C-CO</i>	177.2	179.1	174.9		175.8
C≡O stretch	2098	2087	2106		2105

Compounds like **8** with a Cu-CO moiety on an anionic fragment are rare. A survey of structurally characterized molecules with a “Cu-CO” fragment in the Cambridge Structural Database²⁶⁷ shows that they are found usually in neutral molecules (e.g., [HB(3,5-(CF₃)₂Pz)₃]CuCO)²⁵⁶ or cationic species (e.g., [Cu(*trans,trans,trans*-1,5,9-cyclododecatriene)(CO)]⁺).²⁴⁹ Copper carbonyl complexes of quadruply bridging halides are not available for structural data comparison.^{203,267} However, molecules such as [{Cu(tmen)(CO)}₂(μ₂-X)](BPh)₄ (X = Cl, Br, I) with doubly bridging halides are known.²⁰⁸ The average Cu-Br distance of [Cu(tmen)(CO)X](BPh)₄ (2.456 Å) is shorter than the corresponding parameter of **8** (2.740 Å), likely reflecting the μ₂-Br vs μ₄-Br halide bridge (i.e., a result of different coordination numbers).

Solution ¹H, ¹³C{¹H} and ¹⁹F NMR data of **8** in CD₂Cl₂ at room temperature are consistent with the structure depicted in Figure 4.7. In addition to a broad peak at δ -60.7 ppm in the ¹⁹F NMR spectrum which can be assigned to **8**, there is also a small peak at δ -59.6 ppm, indicating that there is minor dissociation of **8** in solution

to $\{[3,5-(\text{CF}_3)_2\text{Pz}]\text{Cu}(\text{CO})\}_2$ and $[\text{NEt}_4]\text{Br}$. The $^{13}\text{C}\{^1\text{H}\}$ resonance of the copper bound CO appears at δ 173.0 ppm, which is in the expected region.^{205,253}

Interestingly, the attempted synthesis of the chloride bridged analog of **8** using $\{[3,5-(\text{CF}_3)_2\text{Pz}]\text{Cu}\}_3$, CO and $[\text{NEt}_4]\text{Cl}$ led to an unexpected product, $[\text{NEt}_4]\{[3,5-(\text{CF}_3)_2\text{Pz}]\}_3\text{Cu}_2(\text{CO})_2$ (**9**, Figure 4.7). This indicates a loss of one equivalent of Cu(I) from $\{[3,5-(\text{CF}_3)_2\text{Pz}]\text{Cu}\}_3$, perhaps as “CuCl”. Indeed, it is possible to synthesize $[\text{NEt}_4][3,5-(\text{CF}_3)_2\text{Pz}]$ from $\{[3,5-(\text{CF}_3)_2\text{Pz}]\text{Cu}\}_3$ and $[\text{NEt}_4]\text{Cl}$ *via* the elimination of “CuCl”. This loss of Cu(I) is somewhat similar to the chemistry observed between $[\text{HB}(3,5-(\text{CF}_3)_2\text{Pz})_3]\text{CuCO}$ and $[\text{NEt}_4]\text{CN}$, which results in the formation of $[\text{NEt}_4][\text{HB}(3,5-(\text{CF}_3)_2\text{Pz})_3]$ with the loss of “CuCN”.²⁸² Compound **9** can also be generated *via* an alternative route using $\{[3,5-(\text{CF}_3)_2\text{Pz}]\text{Cu}\}_3$, CO and $[\text{NEt}_4][3,5-(\text{CF}_3)_2\text{Pz}]$. Here, the pyrazolate anion $[3,5-(\text{CF}_3)_2\text{Pz}]^-$ serves as a capping ligand to **5** generating **9**. It is a much more stable solid in air compared to **8**. The compound **9** displays a strong $\bar{\nu}_{\text{CO}}$ band in the IR at 2087 cm^{-1} . It also indicates the presence of somewhat electron rich copper sites compared to those present in the neutral, dinuclear species **5**. The room temperature ^{19}F NMR spectrum of $[\text{NEt}_4]\{[3,5-(\text{CF}_3)_2\text{Pz}]\}_3\text{Cu}_2(\text{CO})_2$ (**9**) indicated that it also dissociates to a small degree in solution to **5** and presumably $[\text{NEt}_4][3,5-(\text{CF}_3)_2\text{Pz}]$.

A comparison of $[\text{NEt}_4]\{[3,5-(\text{CF}_3)_2\text{Pz}]\}_3\text{Cu}_2(\text{CO})_2$ (**9**, Figure 4.7) to the mono-nuclear species $[\text{HB}(3,5-(\text{CF}_3)_2\text{Pz})_3]\text{CuCO}$ (**1**, Figure 4.1) is also interesting. In these four-coordinate copper adducts, $[\text{Cu}(\text{CO})]^+$ moieties are supported by

$\{(\text{OC})\text{Cu}[3,5\text{-(CF}_3)_2\text{Pz}]_3\}^{2-}$ and $[\text{HB}(3,5\text{-(CF}_3)_2\text{Pz})_3]^-$ groups, respectively. The overall electronic effects due to this change (or the replacement of a $[\text{Cu}(\text{CO})]^+$ fragment of **9** by $[\text{HB}]^{2+}$ group at the distant end of the supporting ligand) on copper sites are very significant as evident from their $\bar{\nu}_{\text{CO}}$ values 2087 vs. 2137 cm^{-1} , respectively. In fact, $[\text{HB}(3,5\text{-(CF}_3)_2\text{Pz})_3]\text{CuCO}$ (**1**) has one of the most Lewis acidic copper centers in a neutral molecule.

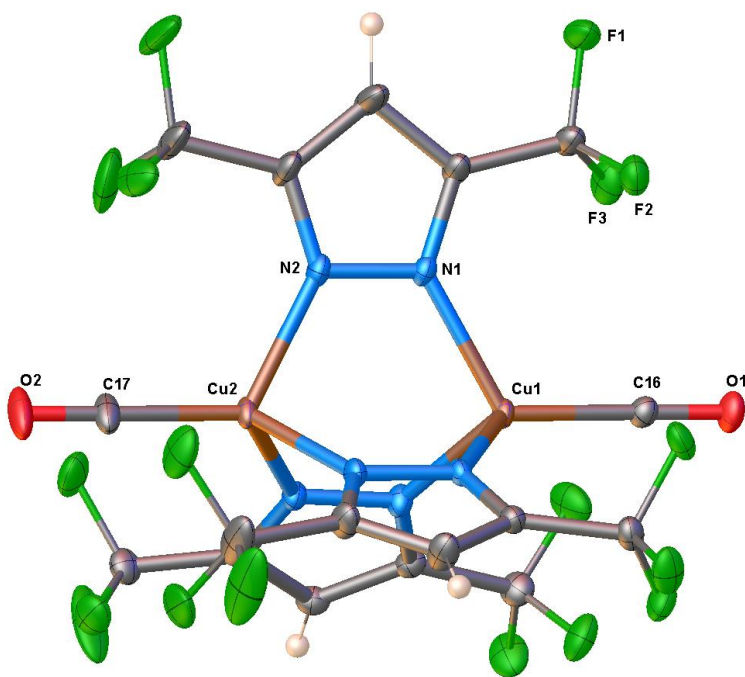


Figure 4.9. Molecular structure of $[\text{NEt}_4]\{[3,5\text{-(CF}_3)_2\text{Pz}]_3\text{Cu}_2(\text{CO})_2\}$ (**9**). The cation $[\text{NEt}_4]^+$ has been omitted for clarity.

X-ray crystal structure of $[\text{NEt}_4]\{[3,5\text{-(CF}_3)_2\text{Pz}]_3\text{Cu}_2(\text{CO})_2\}$ (**9**) is illustrated in Figure 4.9 and selected bond distances and angles are given in Table

4.2. It is a dinuclear copper complex with three bridging pyrazolates. The copper atoms adopt *pseudo*-tetrahedral coordination geometry and the Cu-CO groups are linear. The anionic moiety, $\{[3,5-(\text{CF}_3)_2\text{Pz}]_3\text{Cu}_2(\text{CO})_2\}^-$ displays nearly D_{3h} symmetry. Although, structural data on dinuclear Cu-CO complexes featuring cage structures like **9** are not available for comparison, mono-metallic copper carbonyls with $\text{N}_3\text{Cu-CO}$ coordination sphere such as **1** are quite common.^{205,283,284} A comparison of Cu-N and Cu-C distances of **9** with **1** show that they are very similar (*e.g.*, average Cu-N distances are 2.043 and 2.052 Å, and Cu-CO distances are 1.814 and 1.808 Å, respectively). Thus, unlike the $\bar{\nu}_{\text{CO}}$ values (that show 50 cm^{-1} difference between the two adducts as noted above), these bond distances are rather insensitive to the variations present in neutral mono-nuclear $[\text{HB}(3,5-(\text{CF}_3)_2\text{Pz})_3\text{CuCO}$ (**1**) and the anionic di-nuclear $\{[3,5-(\text{CF}_3)_2\text{Pz}]_3\text{Cu}_2(\text{CO})_2\}^-$.

There is a previous report of a di-anionic copper carbonyl complex resulting from a reaction between $[\text{Cu}_4(\text{dmnpz})_6]^{2-}$ and CO. Based on the IR data (one band at 2050 cm^{-1}), a tetranuclear structure $[\text{Cu}_4(\text{dmnpz})_6(\text{CO})_4]^{2-}$ (dmnpz = 3,5-dimethyl-4-nitro-pyrazolate, Figure 4.2),⁶ has been suggested for this species. However, based on the formation of $\{[3,5-(\text{CF}_3)_2\text{Pz}]_3\text{Cu}_2(\text{CO})_2\}^-$ (**9**), we think that a dinuclear molecule $[\text{Cu}_2(\text{dmnpz})_3(\text{CO})_2]^-$ of the type **9** perhaps the more likely structure of this species.

We have also investigated the chemistry of trinuclear {[4-Cl-3,5-(CF₃)₂Pz]Cu}₃ (**3**)²⁰ with carbon monoxide in the presence of halide ions (Figure 4.10). Note that compared to {[3,5-(CF₃)₂Pz]Cu}₃,⁷ the copper complex **3** has an

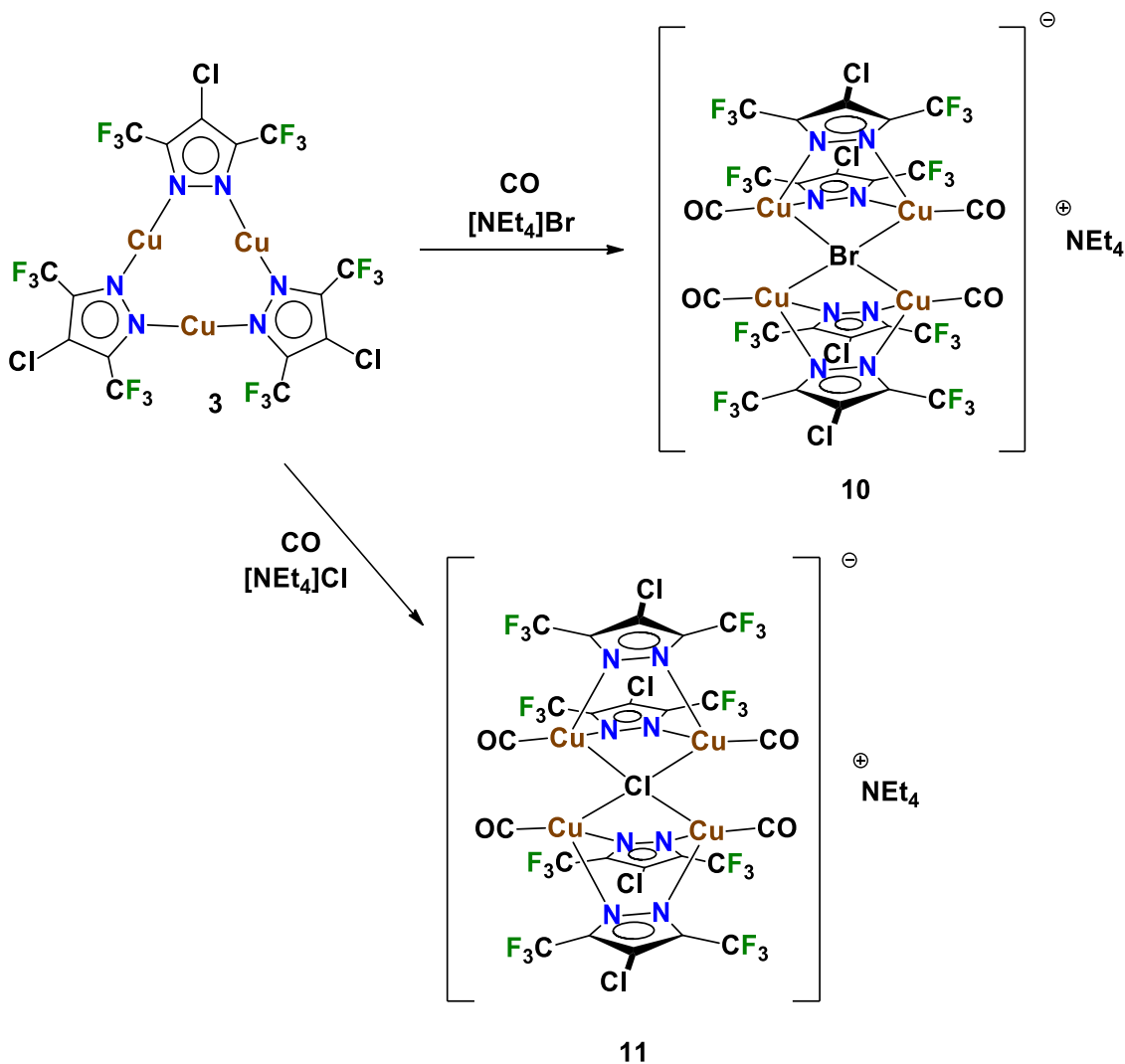


Figure 4.10 Synthetic route to [NEt₄][{[4-Cl-3,5-(CF₃)₂Pz]Cu(CO)}₄(μ₄-Br)] (**10**) and [NEt₄][{[4-Cl-3,5-(CF₃)₂Pz]Cu(CO)}₄(μ₄-Cl)] (**11**) from {[4-Cl-3,5-(CF₃)₂Pz]Cu}₃ (**3**)

even more weakly coordinating pyrazolate with Cl group at the pyrazolyl ring 4-position (instead of a hydrogen atom). The treatment of a concentrated solution of **3** in dichloromethane at ambient temperature with CO in the presence of [NEt₄]Br led to [NEt₄][{[4-Cl-3,5-(CF₃)₂Pz]Cu(CO)}₄(μ₄-Br)] (**10**, Figure 4.10), which is analogous to **8**. It is a moderately air sensitive solid (decomposes over a period of minutes in air) and has been isolated in 87% yield. Compound **10** displays a single strong $\bar{\nu}_{\text{CO}}$ band at 2106 cm⁻¹ in the IR spectrum. This higher CO frequency value relative to that of **8** points to the presence of more electron-deficient Cu sites in **10** (Table 4.2). This is not surprising considering the relatively weakly donating nature of [4-Cl-3,5-(CF₃)₂Pz]⁻ ligand in **10**, which would result in a more electrophilic copper site and a lower degree of Cu→CO backbonding.

X-ray crystal structure of **10** is illustrated in Figure 4.11. Selected bond distances and angles are given in Table 4.2. It adopts a tetranuclear structure, featuring well separated [NEt₄]⁺ cation and [{[4-Cl-3,5-(CF₃)₂Pz]Cu(CO)}₄(μ₄-Br)]⁻ anion. It crystallizes in the *C2/c* space group with 1.5 molecules in the asymmetric unit, in which one sits on a 2-fold rotation axis. In these molecules, the {[4-Cl-3,5-(CF₃)₂Pz]Cu(CO)}₂ fragments adopt a boat-shape, and are held together by a quadruply bridging bromide ion (μ₄-Br). The Br atom adopts a flattened tetrahedral geometry with Cu-Br-Cu angles ranging from 75.5° to 151.3°. A comparison of metrical parameters of **10** to **8** show that Cu-N and Cu-C distances

are practically unaffected by the nature of pyrazolate (Table 4.2). The Cu-Br distances however show a notable difference, where significantly shorter Cu-Br distances (on average, shorter by about 0.145 Å) are observed with **10** involving the more electrophilic copper sites. Solution NMR spectroscopic data of **10** in CD₂Cl₂ at room temperature are consistent with the structure depicted in Figure 4.10 and 4.11. In addition to a broad, very prominent peak at δ -60.2 ppm in the ¹⁹F NMR spectrum, which can be assigned to **10**, there is also a minor signal at δ -62.0 ppm, indicating some dissociation into precursor components.

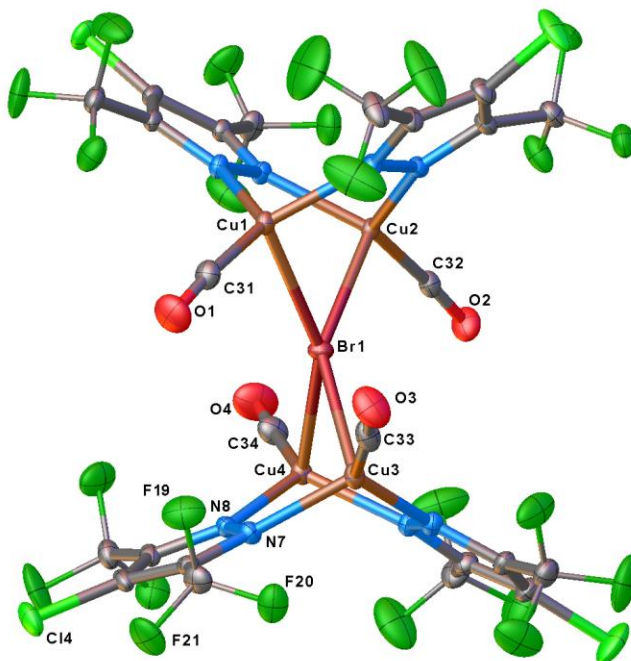


Figure 4.11 Molecular structure of [NET₄][{[4-Cl-3,5-(CF₃)₂Pz]Cu(CO)₄}(μ₄-Br)] (**10**). The cation [NET₄]⁺ has been omitted for clarity.

The reaction of **3** with [NEt₄]Cl salt under CO atmosphere led to the formation of a tetranuclear [NEt₄][{[4-Cl-3,5-(CF₃)₂Pz]Cu(CO)}₄(μ₄-Cl)] (**11**, Figure 4.10), with an isolated yield of 86%. Compound **11** displays a single strong sharp absorption at 2105 cm⁻¹ in the IR spectrum which is within the expected range for terminal metal carbonyls, and also suggests the formation of rather symmetric molecule. The X-ray crystal structure and selected bond distances and angles of **11** is illustrated in Figure 4.12 and Table 4.2 respectively. It forms a tetra-

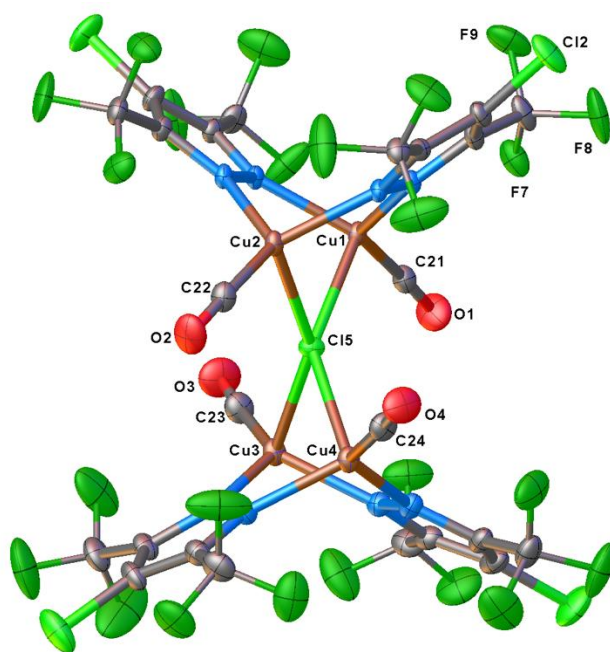


Figure 4.12 Molecular structure of [NEt₄][{[4-Cl-3,5-(CF₃)₂Pz]Cu(CO)}₄(μ₄-Cl)] (**11**). The cation [NEt₄]⁺ has been omitted for clarity.

nuclear copper complex, with two boat-shaped $\{[4\text{-Cl-3,5-(CF}_3)_2\text{Pz]Cu(CO)}\}_2$ fragments held together by a quadruply bridging chloride ion ($\mu_4\text{-Cl}$). The bridging chloride atom adopts a distorted tetrahedral geometry. The average Cu-Cl distance of 2.465 Å in **11** is significantly shorter than the average Cu-Br distances of **8** or **10**, which is reasonable considering the smaller ionic radius of Cl^- . Preliminary studies suggest that it may also be possible to use neutral Lewis bases to stabilize Cu-CO adducts of binary pyrazolates. We successfully isolated one such molecule $\{[4\text{-Cl-3,5-(CF}_3)_2\text{Pz]Cu(CO)}\}_2(\mu_2\text{-CH}_3\text{CN})$ (**12**, Figure 4.13). It has an interesting asymmetrically bonded, bridging acetonitrile ligand.

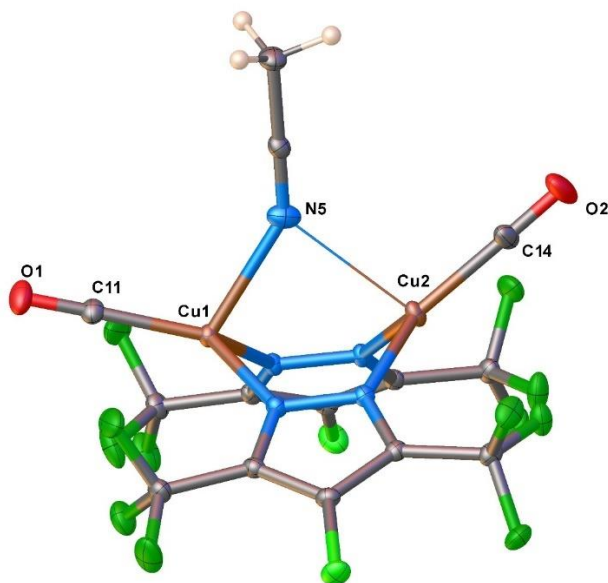


Figure 4.13 Molecular structure of $\{[4\text{-Cl-3,5-(CF}_3)_2\text{Pz]Cu(CO)}\}_2(\mu_2\text{-CH}_3\text{CN})$ (**12**)

In order to gain more insights to the Cu-CO bonding in the 18-electron species **8-11**, theoretical calculations were performed on optimized structures, as well as on several additional but related molecules without constraints (Table 4.3). We will discuss **8** and **9** which contain the supporting ligand [3,5-(CF₃)₂Pz]⁻ separately from **10** and **11** (that have [4-Cl-3,5-(CF₃)₂Pz]⁻ ligand support). The optimized geometries agree well with the X-ray crystallographic findings for **8** and **9**. The calculated CO frequencies of **8** and **9** of 2104 and 2089 cm⁻¹, respectively, are also in good accord with experimental observations (2098 and 2087 cm⁻¹, respectively). The Cu-CO bonding interaction energy (ΔE_{int}) of **8** and **9** amounts to -36.40 and -36.79 kcal mol⁻¹, denoting a similar strength despite of the different $\bar{\nu}_{\text{CO}}$ stretching frequencies. As discussed for M₂(CO)₉ carbonyls (M = Fe, Ru and Os),²⁷⁶ this indicates that the orbital interaction alone do not rule the bond strength.

Further dissection of ΔE_{int} to chemically meaningful terms within the Energy Decomposition Analysis (EDA)²⁷⁵ shows that the nature of Cu-CO interaction in **8** and **9** remains similar to **5** (16-electron system), with a ~60% of electrostatic character, followed by the orbital contribution (~37%), and a small ΔE_{disp} (~3%) contribution. Moreover, the DCD bonding model can be directly related to the orbital interaction accounted by ΔE_{orb} , denoting a trend where larger values of ΔE_{orb} corresponds to lower $\bar{\nu}_{\text{CO}}$ stretching (Figure 4.15). The ΔE_{orb} can be further decomposed to individual contributions within the NOCV-EDA framework (Figure 4.14)^{277,278} as discussed above, with parallel and tangential

oriented π -backbonding ($\Delta\rho^1_{\rightarrow\pi\parallel}$ and $\Delta\rho^2_{\rightarrow\pi\perp}$) and σ -donor ($\Delta\rho^3_{\leftarrow\sigma}$), and a nonclassical σ interaction ($\Delta\rho^4_{\rightarrow\sigma}$).²⁷⁶ These findings in comparison to **5**, **8** and **9**, reveal similar bonding characteristics within the series of 16- and 18-electron Cu centers. The overall π -backbonding bonding in **8** and **9**, accounts for 57.0% and 59.0%, respectively of ΔE_{orb} ($\Delta\rho^1_{\rightarrow\pi\parallel} + \Delta\rho^2_{\rightarrow\pi\perp}$), whereas σ -donor ($\Delta\rho^3_{\leftarrow\sigma}$) component contributes about 26.7% and 26.0%, respectively of ΔE_{orb} , with a contribution of 16.6% and 16.4% from the nonclassical σ interaction ($\Delta\rho^4_{\rightarrow\sigma}$), respectively. Such observation accounts for the lower CO stretching frequency found in **9** in comparison to **8**.

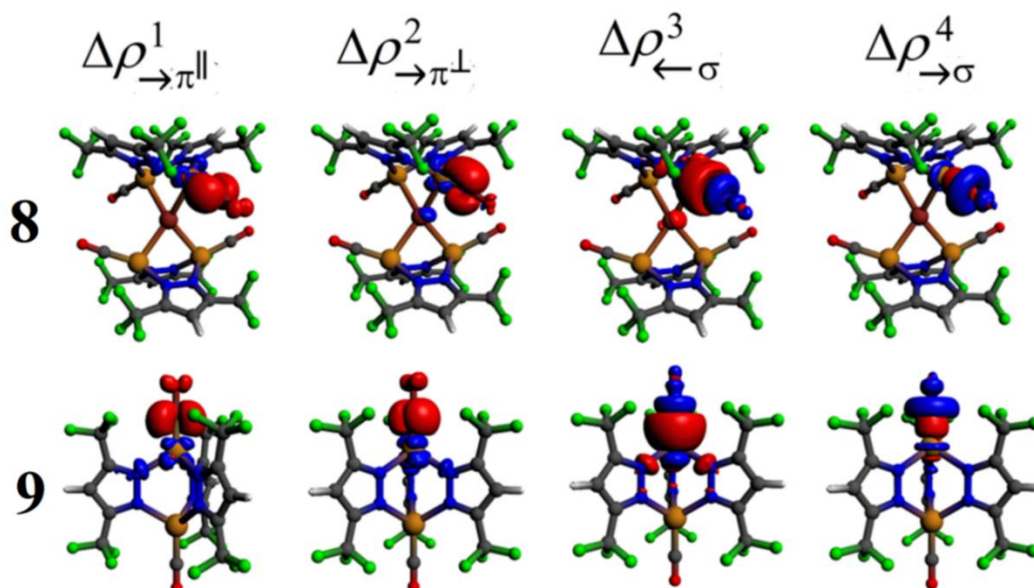


Figure 4.14 NOCV-EDA analysis of the Cu-CO interaction in **8** and **9**, accounting for the Dewar–Chatt–Duncanson bonding model, and the nonclassical σ interaction

($\Delta\rho^4_\sigma$). The direction of charge flow in the deformation densities is from red \rightarrow blue.

The optimized geometries of **10** and **11** agree well with the X-ray crystallographic findings. The calculated CO frequencies of **10** and **11** of 2110 and 2110 cm^{-1} , respectively, are also in good accord with experimental observations (2106 and 2105 cm^{-1} , respectively). The Cu-CO bonding in these adducts are similar to that described for **8** and **9**, with a dominant electrostatic character, followed by the orbital contribution, and a small ΔE_{disp} contribution (Table 4.1).

We have analyzed and compared the Cu-CO bonding in $[\text{NEt}_4]\{[3,5\text{-(CF}_3)_2\text{Pz}]_3\text{Cu}_2(\text{CO})_2\}$ (**9**) and $[\text{HB}(3,5\text{-(CF}_3)_2\text{Pz})_3]\text{CuCO}$ (**1**). Calculations show that the replacement of one of the $[\text{Cu}(\text{CO})]^+$ fragment of **9** by $[\text{HB}]^{2+}$ group leading to **1** results in a shift of CO frequency from 2089 to 2131 cm^{-1} (compared to experimental values 2087 and 2137 cm^{-1} , respectively), which is explained by a significant decrease in ΔE_{orb} from -62.37 to -55.00 kcal mol^{-1} . Similarly, the replacement of a $[\text{Cu}(\text{CO})]^+$ fragment in **5** by $[\text{H}_2\text{B}]^+$ leading to bis(pyrazolyl)borate $[\text{H}_2\text{B}(3,5\text{-(CF}_3)_2\text{Pz})_2]\text{CuCO}$ decreases the orbital interaction term related to the DCD model (ΔE_{orb}) from -58.26 to -54.38 kcal mol^{-1} , which in turn shifts CO to higher stretching frequency from 2095/2101 to 2136 cm^{-1} (experimental values: 2099/2108 vs 2127 cm^{-1}).²⁷⁹

The effect of pyrazolyl ring 4-substituent on anion encapsulating capabilities of molecules such as **5**, **6** and **7** have also been investigated. Calculations show that 4-H, 4-Cl and 4-CF₃ substituents enhance the interaction energy from -91.37 < -95.76 < -102.42 kcal mol⁻¹, respectively, for the series related to **8** (i.e., two molecules of **5**, **6** or **7** encapsulating Br⁻) and -94.65 < -102.63 < -110.32 kcal mol⁻¹, for the series related to **11** (i.e., Cl⁻ anion encapsulation by two molecules of **5**, **6** or **7**). Such results envisage an interesting halide encapsulating properties of **5-7** similar to [Cu₆{3,5-(CF₃)₂Pz}₆(OH)₆] and Ni₂-Capsoplexes.^{280,281} For comparison, anion encapsulation energy (ΔE_{int}) value of -91.37 kcal mol⁻¹ computed for **8** for the binding of a Br⁻ by two molecules of **5** is significantly larger than that found for [*trans*-Cu₆{3,5-(CF₃)₂Pz}₆(OH)₆] interaction with Br⁻ (-69.81 kcal mol⁻¹) at a related level of theory.²⁸⁵ These copper-halide bonding in **8-11** is dominated by electrostatic interactions (e.g., 73.5% of ΔE_{elstat} for **8**).

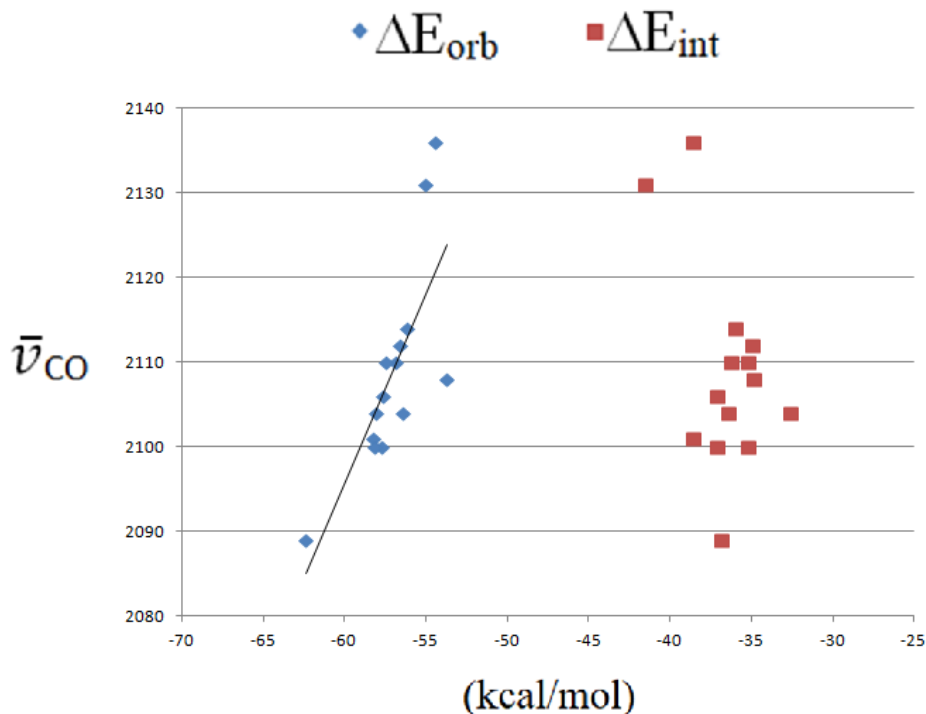


Figure 4.15 Correlation between $\bar{\nu}_{\text{CO}}$ vs ΔE_{orb} (blue), and $\bar{\nu}_{\text{CO}}$ vs ΔE_{int} (red), along all the calculated series, denoting a better correlation in the former relationship.

Further analysis of bonding and CO stretching frequencies of a larger group of 16- and 18-electron copper complexes (Table 4.1 and 4.3) indicate that the Dewar–Chatt–Duncanson (DCD) model, where the CO stretching frequencies correlate well to the orbital interaction energy ΔE_{orb} , but not necessarily to the ΔE_{int} (Figure 4.15). The major Cu-CO interaction however is electrostatic in nature. Theoretical exploration of the role of the substituent at pyrazolyl ring 4-position between -H, -Cl, and -CF₃ in all these complexes shows a slight decrease in

covalent character of the Cu-CO interaction and diminished π -back bonding as pyrazolate groups become more weakly donating with added electron withdrawing substituents.

Table 4.3 Vibrational and structural data for the calculated systems at the ZORA TZ2P/BP86-D3 level of theory. Distances in Angstrom, angles in degrees and $\bar{\nu}_{\text{CO}}$ in cm^{-1} . Experimental results are given in parenthesis.

Parameter\Complex	$\bar{\nu}_{\text{CO}}$	Cu-N	Cu-X	Cu-CO	Cu-C-O
{[3,5-(CF ₃) ₂ Pz]Cu(CO)} ₂ (5)	2095/2101 (2099/2108)	2.064 (1.971)		1.830 (1.843)	172.2 (177.1)
{[4-Cl-3,5-(CF ₃) ₂ Pz]Cu(CO)} ₂ (6)	2099/2106 (2139)	2.078		1.835	168.4
{[3,4,5-(CF ₃) ₃ Pz]Cu(CO)} ₂ (7)	2102/2108 (2139)	2.042 (1.990)		1.853 (1.831)	178.9 (179.1)
{[3,5-(CF ₃) ₂ Pz] ₃ Cu ₂ (CO) ₂ } ⁻ (9)	2089 (2087)	2.101 (2.043)		1.819 (1.813)	180.0 (179.1)
{[4-Cl-3,5-(CF ₃) ₂ Pz] ₃ Cu ₂ (CO) ₂ } ⁻	2100	2.117		1.845	180.0
{[3,4,5-(CF ₃) ₃ Pz] ₃ Cu ₂ (CO) ₂ } ⁻	2104	2.122		1.851	179.8
[{[3,5-(CF ₃) ₂ Pz]Cu(CO)} ₄ (μ -4-Br)] ⁻ (8)	2104 (2098)	2.071 (2.002)	2.661 (2.740)	1.837 (1.817)	177.3 (177.2)

$[\{[4\text{-Cl-3,5-}(\text{CF}_3)_2\text{Pz}]\text{Cu}(\text{CO})\}_4(\mu_4\text{-Br})]^-$ (10)	2110 (2106)	2.088 (2.019)	2.665 (2.595)	1.841 (1.817)	176.5 (174.9)
$[\{[3,4,5\text{-}(\text{CF}_3)_3\text{Pz}]\text{Cu}(\text{CO})\}_4(\mu_4\text{-Br})]^-$	2112	2.073	2.678	1.843	173.9
$[\{[3,5\text{-}(\text{CF}_3)_2\text{Pz}]\text{Cu}(\text{CO})\}_4(\mu_4\text{-Cl})]^-$	2100	2.069	2.537	1.835	176.3
$[\{[4\text{-Cl-3,5-}(\text{CF}_3)_2\text{Pz}]\text{Cu}(\text{CO})\}_4(\mu_4\text{-Cl})]^-$ (11)	2110 (2105)	2.087 (2.023)	2.480 (2.465)	1.837 (1.823)	176.7 (175.8)
$[\{[3,4,5\text{-}(\text{CF}_3)_3\text{Pz}]\text{Cu}(\text{CO})\}_4(\mu_4\text{-Cl})]^-$	2114	2.099	2.484	1.844	176.6
$[\text{H}_2\text{B}(3,5\text{-}(\text{CF}_3)_2\text{Pz})_2]\text{CuCO}$	2136 (2127)	2.024		1.836	177.0
$[\text{HB}(3,5\text{-}(\text{CF}_3)_2\text{Pz})_3]\text{CuCO}$ (1)	2131 (2137)	2.108		1.833	180.0

4.4 Summary

Overall, we describe high yield routes to multi-nuclear copper carbonyl complexes using binary copper pyrazolates, tetraethylammonium chloride or bromide as the halide source, and carbon monoxide. The tetranuclear molecules $[\text{NEt}_4][\{[3,5\text{-(CF}_3)_2\text{Pz]Cu(CO)}\}_4(\mu_4\text{-Br})]$ (**8**), $[\text{NEt}_4][\{[4\text{-Cl-3,5-(CF}_3)_2\text{Pz]Cu(CO)}\}_4(\mu_4\text{-Br})]$ (**10**) and $[\text{NEt}_4][\{[4\text{-Cl-3,5-(CF}_3)_2\text{Pz]Cu(CO)}\}_4(\mu_4\text{-Cl})]$ (**11**) feature quadruply bridging halide ions. Isolation of $\{[3,5\text{-(CF}_3)_2\text{Pz]Cu(CO)}\}_2$ (**5**) or $\{[4\text{-Cl-3,5-(CF}_3)_2\text{Pz]Cu(CO)}\}_2$ (**6**) is significantly more challenging in the absence of halide donors (or capping pyrazolate ions) due to facile CO loss. This type of anion encapsulating chemistry or the presence of Cu-CO in anionic moieties have not been reported in copper-carbonyl chemistry. Compounds $\{[3,5\text{-(CF}_3)_2\text{Pz]Cu(CO)}\}_2$ (**5**) and $\{[3,4,5\text{-(CF}_3)_3\text{Pz]Cu(CO)}\}_2$ (**7**) represent rare, structurally authenticated, three-coordinate copper carbonyl complex based on binary copper pyrazolates. These two adducts also illustrate the flexibility of the six-membered Cu_2N_4 core found in these adducts as they adopt planar or boat conformations. Compounds **6** and **7** display their $\bar{\nu}_{\text{CO}}$ at 2139 cm^{-1} , which is very close to that of the free CO (2143 cm^{-1}). The infrared spectra of **8**, **10** and **11** also show high CO stretching frequencies (although not as high as **6** or **7**) in the range of $2098\text{-}2106\text{ cm}^{-1}$. These adducts feature fairly electrophilic copper sites with relatively low level of Cu \rightarrow CO backbonding. Dinuclear $[\text{NEt}_4][\{[3,5\text{-(CF}_3)_2\text{Pz}]_3\text{Cu}_2(\text{CO})_2\}]$ (**9**) could be viewed as a cage assembly involving $\{[3,5\text{-(CF}_3)_2\text{Pz}]_3\text{Cu}_2(\text{CO})_2\}$

$(\text{CF}_3)_2\text{Pz}]\text{Cu}(\text{CO})\}_2$ and a pyrazolate $[3,5-(\text{CF}_3)_2\text{Pz}]^-$ ion. The formation and the stability of **8** - **11** suggest the possibility of using various other Lewis bases to stabilize Cu-CO adducts of binary pyrazolates. These anionic copper carbonyl moieties could serve as counter ions for more common cationic copper carbonyls. Preliminary studies suggest that it may also be possible to use neutral Lewis bases like acetonitrile to stabilize Cu-CO adducts of binary pyrazolates. One such molecule $[[4\text{-Cl-}3,5\text{-(CF}_3)_2\text{Pz}]\text{Cu}(\text{CO})\}_2(\mu_2\text{-CH}_3\text{CN})]$ (**12**), we managed to isolate. We are presently exploring additional chemistry of binary copper pyrazolates as well as the chemistry involving silver and gold carbonyls.

Chapter 5

Experimental section

5.1 Instrumentation

All manipulations were carried out under an atmosphere of purified nitrogen using standard Schlenk techniques or in a MBraun glove-box equipped with a -25 °C refrigerator. Solvents were purchased from commercial sources, purified prior to use. NMR spectra were recorded at 25 °C on a JEOL Eclipse 500 and JEOL Eclipse 300 spectrometer (¹H, 500.16 MHz and 300.53 MHz; ¹³C, 125.78 MHz, and 75.59 MHz; ¹⁹F, 470.62 MHz, and 282.78 MHz), unless otherwise noted. Proton and carbon chemical shifts are reported in ppm versus Me₄Si. ¹⁹F NMR values were referenced to external CFC₃. Melting points were obtained on a Mel-Temp II apparatus and were not corrected. Elemental analyses were performed using a Perkin-Elmer Model 2400 CHN analyzer. Raman data were collected on a Horiba Jobin Yvon LabRAM Aramin Raman spectrometer with a HeNe laser source of 633 nm. Crystals of the compound under study were placed on a glass slide for Raman analysis. Different experimental settings (laser intensity, level of magnification, time of exposure, number of cycles) were used for each compound in order to obtain the best signal-to-noise ratio. IR data were collected on a Bruker Alpha FTIR spectrometer with an ATR attachment. Gas sorption measurements were performed using an experimental apparatus and method described previously (see Ideal (i.e., Single-Gas) Ethylene/Ethane Uptake Data section for details).^{286,287} The gas sorption measurements were performed at 20 ± 1 °C with a feed pressure of 1.0 ± 0.1 atm. Powder X-ray diffraction (PXRD) spectra were collected using a

Bruker D8 ECO or Inel CPS 120 PXRD system with a monochromated Cu K α radiation source. High-resolution mass spectra (HRMS) were recorded in Electron spray ionization time-of-flight (ESI/TOF) mode. Samples were introduced as solution in dichloromethane. 3,4,5-(CF₃)₃PzH,⁵² {[3,5-(CF₃)₂Pz]Cu}₃ (or { μ -[3,5-(CF₃)₂Pz]Cu}₃),⁷ { μ -[4-Br-3,5-(CF₃)₂Pz]Cu}₃,²⁰ and {[4-Cl-3,5-(CF₃)₂Pz]Cu}₃ (or { μ -[4-Cl-3,5-(CF₃)₂Pz]Cu}₃),²⁰ Cu₂(μ -CF₃CO₂)₂(EtC \equiv CEt)₂¹²⁰ and Cu₄(μ -CF₃CO₂)₄(μ -EtC \equiv CEt)₂¹²⁰ was prepared by reported literature procedures with a slight modifications. p-Tolyl azide was prepared according to literature procedure.²⁸⁸ Acetylene gas, was freed from acetone and purified before use.¹⁷² All other reactants and reagents were purchased from commercial sources.

5.2 Experimental section of chapter 2

[(3,4,5-(CF₃)₃Pz)Cu]₃ ([Cu₃]): Freshly dried 3,4,5-(CF₃)₃PzH (500 mg, 1.83 mmol) and Cu₂O (217 mg, 1.51 mmol) were placed in a Schlenk flask attached to a reflux condenser, slowly heated to 125 °C and kept for 4 h while stirring. A heat gun was used to melt down the pyrazole condensed on the wall of the Schlenk flask, as needed. Excess 3,4,5-(CF₃)₃PzH was removed by sublimation and the product was extracted into dichloromethane and filtered through a bed of Celite. The filtrate was collected and solvent was removed under reduced pressure to obtain [Cu₃] as a white powder. A solution of [Cu₃] in CS₂ was evaporated to dryness to obtain X-ray quality crystals. Yield: 90% (1.36 g, based on Cu₂O). M.p.: 110 °C. Anal. Calc. for C₁₈N₆F₂₇Cu₃: C, 21.54; H, 0.00; N, 8.37. Found: C, 21.23; H, <0.1; N, 8.81. ¹⁹F NMR (CDCl₃): δ (ppm) -55.10 (br s), -60.10 (q, 8.9 Hz). ¹³C{¹H} NMR (CDCl₃): δ (ppm) 111.3 (q, ²J_{C-F} = 40.7 Hz, C-4), 117.8 (q, ¹J_{C-F} = 274.7 Hz, CF₃), 119.1 (q, ¹J_{C-F} = 266.3 Hz, CF₃), 143.3 (q, ²J_{C-F} = 39.5 Hz, C-3/C-5). Raman (neat, cm⁻¹): 3063, 1597, 1568, 1529, 1455, 1373, 1338, 1240, 1178, 1050, 1021. Comparison of PXRD data of bulk material to simulated PXRD pattern based on single crystal X-ray data and the cell dimensions also confirm the identity of the product.

[(3,4,5-(CF₃)₃Pz)Cu(C₂H₄)₂] ([Cu₂•(C₂H₄)₂): [(3,4,5-(CF₃)₃Pz)Cu]₃ (250 mg, 0.25 mmol) was dissolved in 10 mL of CH₂Cl₂, ethylene was bubbled for 10 min. The solution was kept at -5 °C to obtain X-ray quality colorless crystals of [(3,4,5-

$(\text{CF}_3)_3\text{PzCu}(\text{C}_2\text{H}_4)_2$. Yield: 90% (1.36 g, based on Cu_2O). M.p.: 128-130 °C. Raman (neat, cm^{-1}): 3101, 3087, 3062, 2998, 1601, 1565, 1544, 1529, 1454, 1373, 1342, 1280, 1228, 1189, 1159, 1123, 960. ATR-IR (neat, cm^{-1}): 2953, 2924, 2853, 1600, 1559, 1518, 1458, 1429, 1338, 1217, 1129, 1015. Comparison of PXRD data of bulk material to simulated PXRD pattern based on single crystal X-ray data and the cell dimensions confirm the identity of the bulk product. Room temperature NMR data: ^1H NMR (CDCl_3): δ (ppm) 4.54 (br s, C_2H_4 ; resonance due to free ethylene resulting from dissociation from copper also observed at 5.34 (br s)). ^{19}F NMR (CDCl_3): δ (ppm) -54.95 (sept, $J_{\text{F-F}} = 7.2$ Hz), -59.45 (q, $J_{\text{F-F}} = 7.2$ Hz); ($[\text{Cu}_3]$ generated due to ethylene loss from ($[\text{Cu}_2 \bullet (\text{C}_2\text{H}_4)_2]$) also present in the mixture and its signals were observed at -55.15 (br s), -60.17 (d, $J_{\text{F-F}} = 5.3$ Hz)). $^{13}\text{C}\{^1\text{H}\}$ NMR (CDCl_3): (selected peaks) δ (ppm) 85.6 (s, $\text{CH}_2=\text{CH}_2$; free ethylene signal in this mixture was found as a broad peak at δ 115.6). NMR data of ($[\text{Cu}_2 \bullet (\text{C}_2\text{H}_4)_2]$) at -40 °C with added ethylene: ^1H NMR (CDCl_3): δ (ppm) 4.51 (br s). ^{19}F NMR (CDCl_3): δ (ppm) -54.9 (sept, $J_{\text{F-F}} = 6.5$ Hz), -59.3 (q, $J_{\text{F-F}} = 6.5$ Hz). NMR data of ($[\text{Cu}_2 \bullet (\text{C}_2\text{H}_4)_2]$) at -80 °C with excess ethylene: ^1H NMR (CD_2Cl_2): δ (ppm) 4.47 (s). ^{19}F NMR (CDCl_3): δ (ppm) -55.1 (m), -59.6 (m). Drying solid ($[\text{Cu}_2 \bullet (\text{C}_2\text{H}_4)_2]$) under vacuum leads to slow loss of coordinated ethylene (much faster at 60 °C). Solid samples of ($[\text{Cu}_2 \bullet (\text{C}_2\text{H}_4)_2]$) kept at room temperature also lose ethylene slowly over a period of many days.

Single crystal X-ray crystallographic data: A suitable crystal covered with a layer of hydrocarbon/Paratone-N oil was selected and mounted on a Cryo-loop, and immediately placed in the low temperature nitrogen stream. The X-ray intensity data for [**Cu₃**] were measured at 200(2) K on a Bruker D8 Quest with a Photon 100 CMOS detector equipped with an Oxford Cryosystems 700 series cooler, a Triumph monochromator, and a Mo K α fine-focus sealed tube ($\lambda = 0.71073 \text{ \AA}$), whereas data for [**Cu₂**•(C₂H₄)₂] were measured at 100(2) K on the same instrument. Crystals of [**Cu₃**] are rather soft and shatter quite easily at 100 K. Intensity data were processed using the Bruker Apex program suite. Absorption corrections were applied by using SADABS.²⁸⁹ All the calculations for the structure determination were carried out using the SHELXTL package (version 6.14). Initial atomic positions were located by direct methods using SHELXT,²⁹⁰ and the structures of the compounds were refined by the least-squares method using SHELXL²⁹¹ within the Olex2 suite.²⁹² All the non-hydrogen atoms were refined anisotropically. X-ray structural figures were generated using Olex2. Further details are given in cif files. The CCDC [1836466-1836467](https://www.ccdc.cam.ac.uk/conts/retrieving.html) contain the supplementary crystallographic data. These data can be obtained free of charge via <http://www.ccdc.cam.ac.uk/conts/retrieving.html> or from the Cambridge Crystallographic Data Centre (CCDC), 12 Union Road, Cambridge, CB2 1EZ, UK).

[Cu₃] crystallizes in the *P2₁/c* space group with two molecules of [Cu₃] in the asymmetric unit. Most of the fluorine atoms of CF₃ groups show positional disorder which was modelled effectively.

[Cu₂•(C₂H₄)₂] crystallized in space group *P2₁/c* with two independent molecules in the asymmetric unit. The cell dimensions mimic that of Orthorhombic crystal system with the β-angle of essentially 90°. These crystals show twinning by pseudomerohedry, and the use of Twin Law (-1 0 0 0 -1 0 0 0 1) during refinement led to a significant drop in the R-value and improvements in all refinement indicators. All the non-hydrogen atoms were refined anisotropically. Hydrogen atoms of ethylene moieties were located on a difference map and included in the refinement. We have also considered, solved, and refined the structure in the Orthorhombic *Pccn* space group (as suggested by CheckCif as a possibility). However, the final refinement indicators (final *R*₁ was 0.0823 (*I* > 2σ(*I*)) and *wR*₂ was 0.2027 (all data), GooF = 1.462) were poor compared to those of the Monoclinic option (Final *R*₁: 0.0248 (*I* > 2σ(*I*)) and *wR*₂: 0.0587 (all data); GooF = 1.029), and indicate that Monoclinic indeed is the correct choice.

5.2.1 Thermogravimetric analysis (TGA)

Three TGA studies were undertaken on [Cu₂•(C₂H₄)₂] and [Cu₃]. To summarize, the TGA results show that [Cu₂•(C₂H₄)₂] loses 2 moles of ethylene beginning at approximately 50 °C and increasing in rate as the temperature

increases. At a heating rate of 10 °C/min both [$\text{Cu}_2\cdot(\text{C}_2\text{H}_4)_2$] and [Cu_3] sublime at approximately the same rate and temperature. The temperature profile used was 25 °C to 300 °C at 10 °C/min then holding at 300 °C for 30 minutes.

5.2.2 Powder X-ray diffraction data (PXRD)

Powder X-ray diffraction was used to characterize [$\text{Cu}_2\cdot(\text{C}_2\text{H}_4)_2$] and [Cu_3], monitor the transition of solid [Cu_3] to [$\text{Cu}_2\cdot(\text{C}_2\text{H}_4)_2$] following exposure to ethylene gas (confirming that less than 1% [Cu_3] remains based on peak analysis), and that [Cu_3] is re-generated when ethylene is removed from solid samples of [$\text{Cu}_2\cdot(\text{C}_2\text{H}_4)_2$] by application of vacuum at 60 °C for 6 hours.

The general procedure for all experiments is to place the sample in the sample holder of a two circle goniometer, enclosed in a radiation safety enclosure. The X-ray source was a 1kW Cu X-ray tube, maintained at an operating current of 40 kV and 25 mA. The X-ray optics was the standard Bragg-Brentano parafocusing mode with the X-ray diverging from a DS slit (0.6 mm) at the tube to strike the sample and then converging at a position sensitive X-ray Detector (Lynx-Eye, Bruker-AXS). The two-circle 280 mm diameter θ - θ goniometer was computer controlled with independent stepper motors and optical encoders for the θ circle with the smallest angular step size of $0.0001^\circ 2\theta$. The software suit for data collection and evaluation is windows based. Data collection is automated

COMMANDER program by employing a DQL file. Data is analyzed by the program EVA.²⁹³

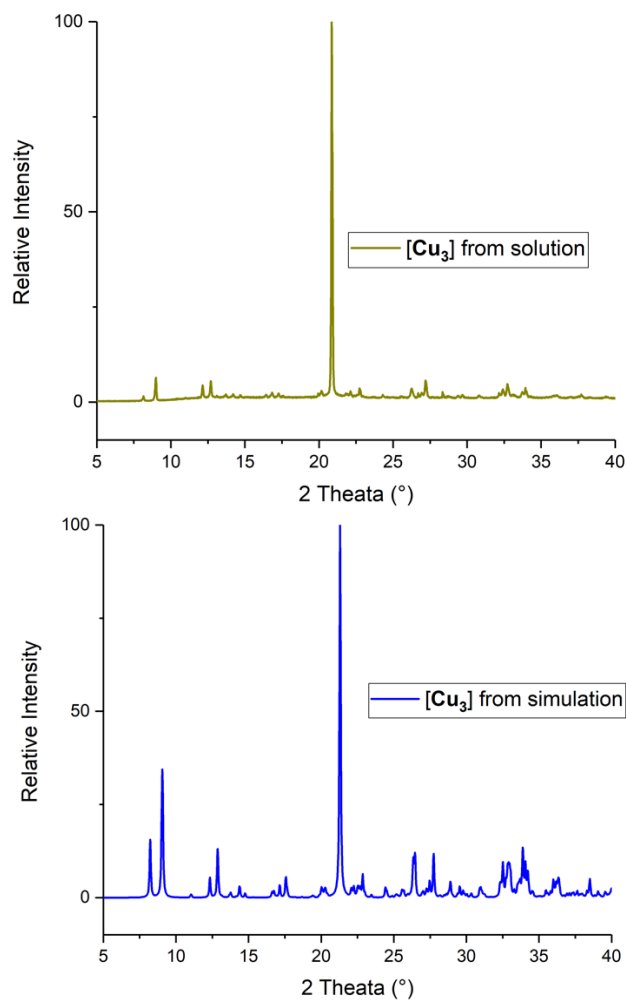


Figure 5.1 Comparison of experimental PXRD (olive, 25 °C) of bulk [Cu₃] and simulated PXRD from single crystal data (blue, -73 °C) for [Cu₃].

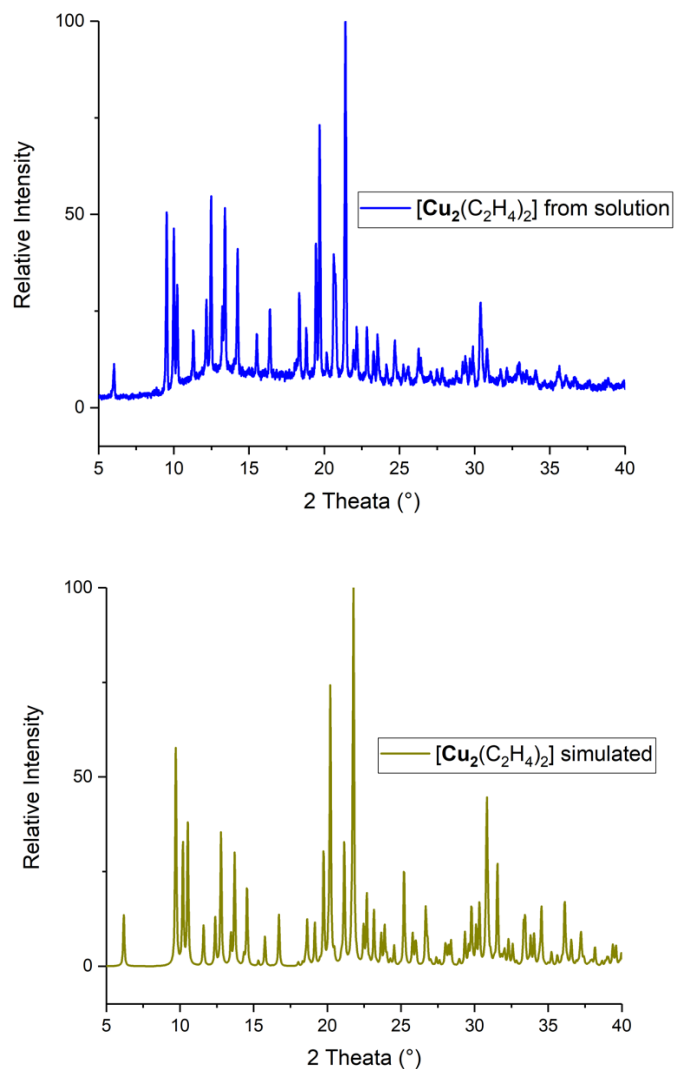


Figure 5.2 Comparison of experimental (blue) and simulated from single crystal data (olive) PXRD patterns for $[\text{Cu}_2 \cdot (\text{C}_2\text{H}_4)_2]$ produced via the solution method.

5.2.3 Ideal (Single-Gas) Ethylene Isotherm Data

The single-gas sorption isotherms of solid $[\text{Cu}_3]$ were measured using a Quantachrome Autosorb AS-1C. Initially, the sample only adsorbed ca. 20% of the

theoretical loading. Repeated cycling at room temperature showed continually increasing amounts of gas adsorption, and the influence of a conditioning process was hypothesized. The sample was then held under 1 bar of ethylene at 70 °C for 3 days. Afterwards, the maximum ethylene loadings at 20, 50 and 70 °C became reproducible.

5.2.4 Measurement of ethylene/ethane adsorption rate using pressure drop method

These experiments were performed to measure the rate at which ethylene was adsorbed into the material. Overall the initial adsorption of ethylene occurs at a rate $> 0.2 \text{ mol mol}^{-1} \text{ min}^{-1}$ for the first minute, slowing to $8 \times 10^{-3} \text{ mol mol}^{-1} \text{ min}^{-1}$ for approximately 40 minutes, and then slowing further. This may represent transitions between rapid adsorption of ethylene onto copper binding sites on the surface of the material, followed by different diffusion regimes within the crystal. Subsequent adsorption/desorption cycles condition the material, increasing the number of copper binding sites initially ‘available’. Note that these experiments are not intended to show equilibrium loadings and are all performed at ambient temperature (21 °C).

The experimental rig used to make these measurements is shown in Figure 5.7. [Cu₃] was ground into a fine powder using a mortar and pestle and placed in the sample chamber. Residual gases were removed from the sample by opening

valves 1 and 2 to dynamic vacuum (<0.1 torr) for 3–24 h. Valve 2 was closed after degassing, and the feed volume filled with approximately 1 bar (14.5 psi) of the gas to be measured. Valve 2 was opened for 1 s, filling the sample chamber with the gas of interest, and the pressure decrease in the sample chamber was measured over time until a constant pressure (P_f) was observed. The pressure difference, corrected for the empty cell, (Equation 1 and 2) was used to calculate the amount of gas adsorbed by the sample in units of mol_{gas} . The amount of gas adsorbed was then normalised by the amount of sample.

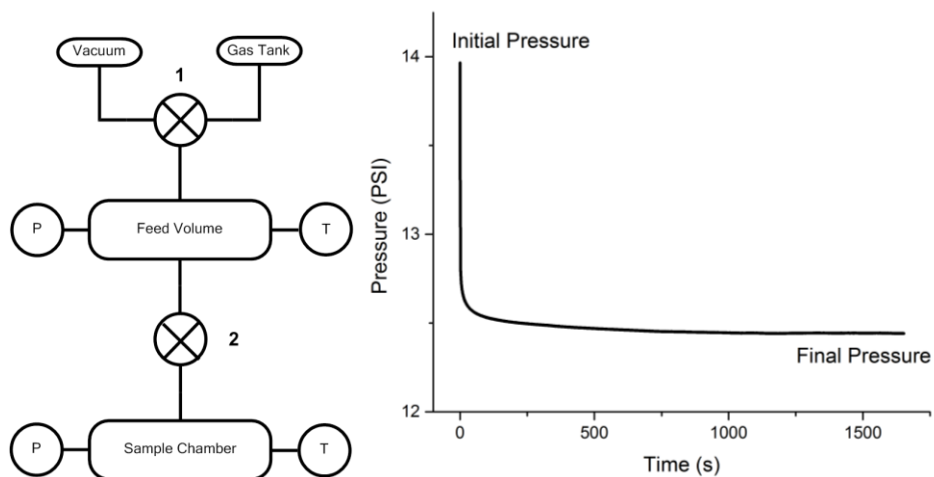


Figure 5.7 Left: The experimental set up for measurement of gas adsorption using the pressure drop method. Where ‘P’ and ‘T’ are pressure and temperature sensors, respectively; circles with crosses denote valves and the volume of the sample chamber is known. Right: An example of the pressure vs. time data obtained from the experiment.

$$\Delta P = P_i - P_f - \Delta P_{Blank}$$

$$\Delta P_{Blank} = P_{i(empty)} - P_{f(empty)} \quad eq. 1$$

Equation 1

P_i = the initial pressure (time zero); P_f = the final pressure (time final).

$$n_{gas} = \frac{\Delta P \cdot V}{R \cdot T} \quad eq.2$$

Equation 2

n_{gas} = moles of gas adsorbed; V = volume of the sample chamber; R = the ideal gas constant; T = temperature of sample chamber.

Table 5.7 Measured ethene uptake capacities of fresh [Cu₃] after 120 min expressed in different sorbent performance terms. Note the equilibrium pressure is around 0.4 atm (41 kPa).

Run	Time (min)	Ethene Uptake (mmol_{ethene}/g_{complex})	Ethene Uptake (cc_{ethene}/g_{complex})	Ethene Uptake (mol_{ethene}/mol_{complex})	% of Full Capacity	Ethene/Ethane Selectivity
1	120	0.06	1.3	0.06	3	6.2
2	120	0.50	11.1	0.50	23	54
3	120	0.62	13.9	0.62	27	67
4	120	0.62	13.9	0.62	27	67
5	120	0.70	15.6	0.70	31	76

Table 5.8 The ethene uptake rates of [Cu₃] measured using the pressure drop method with ca. 1 atm starting feed pressure. The adsorption rate is broken into 3 phases, 0-1 min; 1-40 min; 40-120 min.

Cycle	Average rate (0-1 min) (mol _{ethene} /mol _{complex} /min)	Average rate (1-40 min) (mol _{ethene} /mol _{complex} /min)	Average rate (40-120 min) (mol _{ethene} /mol _{complex} /min)
1	0.02	8 x 10 ⁻⁴	1 x 10 ⁻⁴
2	0.14	8 x 10 ⁻³	1 x 10 ⁻³
3	0.27	8 x 10 ⁻³	7 x 10 ⁻⁴
4	0.22	9 x 10 ⁻³	1 x 10 ⁻³
5	0.26	8 x 10 ⁻³	2 x 10 ⁻³

5.2.5 Measurement of acetylene/ethylene adsorption rate using pressure drop method

Resistance to acetylene is considered an important feature of potential sorbents targeting the application of raw olefin/paraffin separation. This is to avoid formation of explosive copper(I) acetylides. For these reasons, we have established the adsorption behavior with acetylene using the pressure drop method. It appears that acetylene can reversibly adsorb and desorb from [Cu₃], however this results in loss of crystallinity (Figure 5.9) and the adsorption does not appear to be completely reversible, reducing the adsorption capacity of [Cu₃] for ethylene while acetylene capacity remains high.

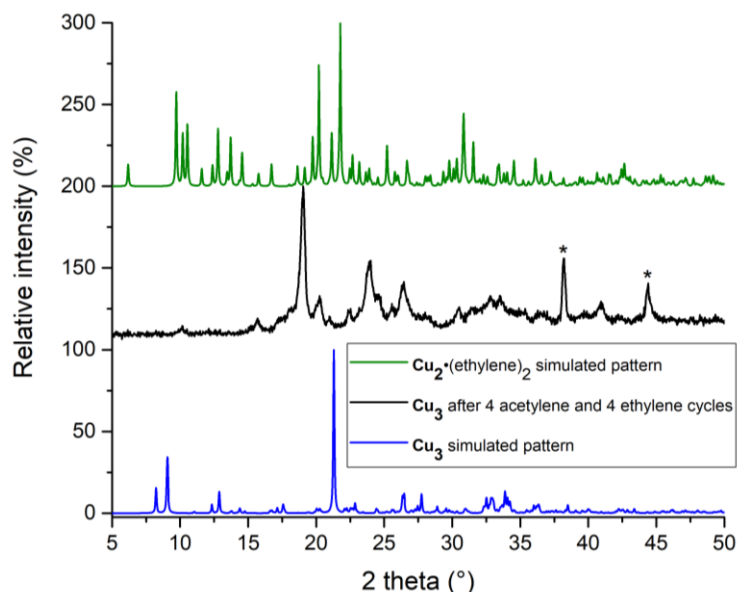


Figure 5.9 The effect of 4 acetylene and 4 ethylene adsorption/desorption cycles on the crystallinity of [Cu₃] as evident from PXRD.

Table 5.9 Measured ethylene and acetylene uptake capacities of complex [Cu₃] after 120 min expressed in different sorbent performance terms. The equilibrium pressure is ca. 0.9 atm (92 kPa). Between each run samples were degassed under dynamic vacuum (<0.1 torr) for 48 hours, with the exception of before runs 4 and 5, where shorter degas times of 2 hours under dynamic vacuum were used.

Cycle	Time (min)	Gas Uptake (mmol _{gas} /g _{complex})	Gas Uptake (cc _{gas} /g _{complex})	Gas Uptake (mol _{gas} /mol _{complex})
1 (C ₂ H ₄)	120	0.44	9.8	0.440
2 (C ₂ H ₂)	120	0.37	8.3	0.373
3 (C ₂ H ₄)	120	0.33	7.4	0.332
4 (C ₂ H ₂)	120*	0.08	1.8	0.081

5 (C₂H₄)	120*	0.03	0.6	0.028
6 (C₂H₂)	120	0.37	8.3	0.375
7 (C₂H₄)	120	0.13	2.9	0.129

Table 5.10 Ethylene and acetylene uptake rates of solid-state material [Cu₃] measured using the pressure drop method with ca. 1 atm starting feed pressure. The adsorption rate is broken into 3 phases, 0-1 min; 1-40 min; 40-120 min.

Cycle	Average rate (0-1 min) (mol_{gas}/mol_{complex}/min)	Average rate (1-40 min) (mol_{gas}/mol_{complex}/min)	Average rate (40-120 min) (mol_{gas}/mol_{complex}/min)
1 (C₂H₄)	0.11	7×10^{-3}	7×10^{-4}
2 (C₂H₂)	0.13	4×10^{-3}	6×10^{-4}
3 (C₂H₄)	0.11	3×10^{-3}	1×10^{-3}
4 (C₂H₂)	0.02	2×10^{-4}	9×10^{-4}
5 (C₂H₄)	0.03	2×10^{-4}	5×10^{-5}
6 (C₂H₂)	0.32	2×10^{-3}	0
7 (C₂H₄)	0.08	2×10^{-3}	2×10^{-4}

5.2.6 Ethane adsorption isotherms

Ethane isotherms at 20 °C, 50 °C and 70 °C were collected after completion of the ethylene isotherms. These show that ethane is not chemically adsorbed into [Cu₃] and does not cause a phase change.

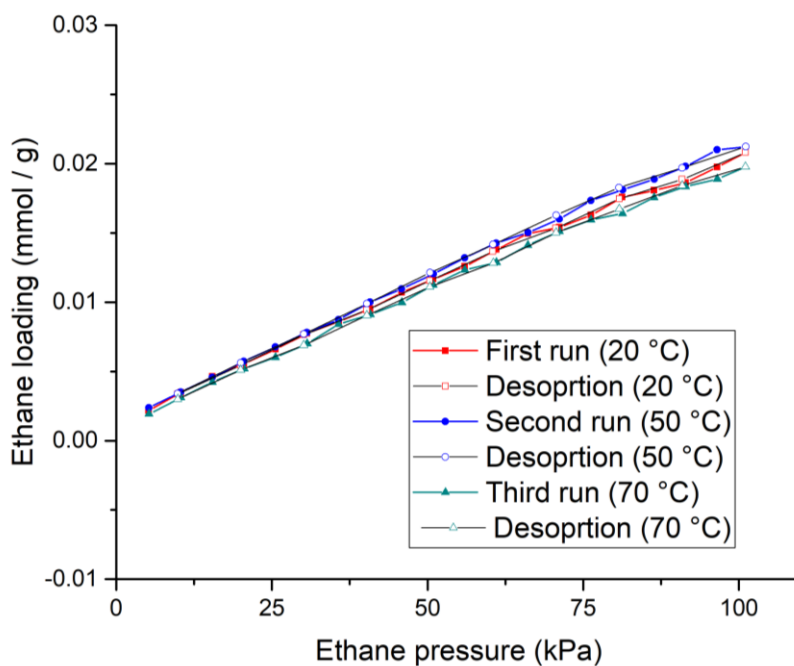


Figure 5.10 Ethane adsorption (solid symbols) and desorption (hollow symbols) isotherms of [Cu₃] at 20, 50 and 70 °C.

5.2.7 Summaries of literature searches

Search for comparable ethylene heat of adsorption on copper: This search was performed as a screen to investigate previous examples of ethylene gas adsorption

into solid copper-based materials in the hope of identifying other examples where ethylene adsorption had caused a significant molecular rearrangement and contextualize the ΔH_{ads} that we observed. Note: there was no discrimination between the different oxidation states of copper.

Our search was performed using the Scifinder database. The ‘research topic’ function was used with the phrase “adsorption of ethylene on copper” which returned 295 references with the concepts “ethylene”, “adsorption”, and “copper” closely associated with one another. It also returned 2240 references where “ethylene”, “adsorption”, and “copper” were present anywhere in the reference, these results were not examined. The set of 295 references was refined by ‘language’ to: ‘English’ (sorry we do not have the ability or resources to interpret non-English works); and refined by ‘document type’ to ‘journal’. Finally, duplicates were removed, leaving 209 references. The abstract of each reference was examined for any indication that ethylene adsorption had been studied and any suggestive papers were examined in detail. In the results obtained (24 papers), all observed gas adsorption was exothermic, i.e. $\Delta H_{\text{ads}} = \text{negative}$. Where available the ΔH_{ads} values have been recorded in Table 5.1. It should be noted however, that most authors simply report ΔH_{ads} as an absolute number which required further examination of the supporting information to confirm that the adsorption capacity of the materials decreased with increasing temperatures.

Table 5.1 Literature examples of ethylene binding on copper and copper containing materials.

Ethylene adsorption energy (kJ mol⁻¹)	Measurement type	Reference
-13.8 (step)	Isotherm	This work
-3 (past 'step')	Isotherm	This work
-13.1	DSC	This work
-28.5	NMR (Solution)	This work
-24	Isotherm	294
-36.1	Isotherm	295
-21.5 , -23.7	Calculation	296
-54.0	Calculation	297
-25	Isotherm	298
-22	Calculation	299
-82, -119	Calculation	300
-34	Isotherm	301
Exothermic	Isotherm	302
-29.1	Isotherm	303
-33.8, -125.4	Calculation	304
-55	Calculation	305
-45.0	Isotherm	306
-88	Isotherm	307
-37.6	Isotherm	308
-26 ± 8	Calculation	309
-55, -180	Desorption	310
-45	Calculation	309
-11.1, -10.9	Desorption	311

-86.8	Calculation	312
-32	Isotherm	313
-36	Desorption	314
Exothermic	Isotherm	315
-42.2	Isotherm	316
-36	Median	
-45	Average	

Comparable ethylene adsorbents:

Table 5.2 Comparison of ethene uptake and ethene/ethane sorption selectivity values of [Cu₃] measured in this study with those reported for other solid-state ethylene/ethane sorbent materials in the literature. This list was adapted from reference.⁷¹

<i>Material</i>	<i>Ethene Uptake (mmol_{ethene} /g_{material})</i>	<i>Temperature (K)</i>	<i>Pressure (atm)</i>	<i>Ethene/Ethane Selectivity</i>	<i>Reference</i>
[Cu ₃]	2.63	343	1	131	This work
[Cu ₃]	2.76	293	1	136	This work
[Ag ^I (2,2'-bipyridine)][BF ₄]	2.38	293	0.9	390	71
[Ag ^I (6,6'-dimethyl-2,2'-bipyridine)][OTf]	2.18	293	0.9	340	71

PAF-1-SO ₃ Ag	4.1	296	1	27 ^a	317
Zeolite 5A	~2.3	303	1	– ^b	318
Zeolite NaX	~4.2	305	1	8 ^a	317,319
CuA ₁₀ B ₁	~1.8	298	0.79	3.8 ^a	317,320
CoMOF-74	–	–	–	6.4 ^a	317,321
MgMOF-74	7.2	296	1	5.6 ^a	317,321
Cu-BTC	7.2	296	1	3.6 ^a	317,321
NOTT-102	5.8	296	1	3.8 ^{a c}	317,321
FeMOF-74	–	318	1	11 ^a	317,322
HOF-4	11.1	296	1	14 ^a	323
Ag(I)/ phenanthroline- based polymer	5.04	293	1 bar	15 ^d	286
[Ag ^I (phen-based ligand) ₂] ₂ OTf	0.20	293	1 bar	13	317

^aCalculated using ideal absorbed solution theory (IAST) for an equimolar amount of ethene and ethane at 296 K and 100 KPa. ^bData not shown. ^cApproximately determined from Figure 3 in Ref.⁷¹. ^dIdeal solubility selectivity.

5.3 Experimental section of chapter 3

3.1 Synthesis of Copper-alkyne pyrazolate complexes

Cu₂(μ-[3,5-(CF₃)₂Pz])₂(EtC≡CEt)₂ (1): 3-Hexyne (76 mg, 0.925 mmol) was added dropwise to a solution of {[3,5-(CF₃)₂Pz]Cu}₃ (250 mg, 0.312 mmol) in dichloromethane (~10 mL) in 3:1 molar ratio. The reaction mixture was stirred for 4 h under nitrogen at the room temperature. The resulting solution was vacuum-dried under reduced pressure for 3 h to obtain Cu₂(μ-[3,5-(CF₃)₂Pz])₂(EtC≡CEt)₂ as a white solid. X-ray quality crystals were grown from dichloromethane at -20 °C. Yield: >95%. M.p.: 84 °C. Anal. Calc.: C, 37.88%; H, 3.18%; N, 8.03%. Found: C, 37.75%; H, 3.17%; N, 7.98%. ¹H NMR (in CDCl₃): δ (ppm) 1.10 (t, *J* = 7.4 Hz, 6H, CH₃), 2.15 (q, *J* = 7.4 Hz, 4H, CH₂), 7.01 (s, H, Pz-H). ¹⁹F NMR (in CDCl₃): δ (ppm) -61.15 (s). ¹³C{¹H} NMR (in CDCl₃): δ (ppm) 13.2 (br s, CH₃), 14.5 (br s, CH₂), 82.5 (br s, C≡C), 104.4 (s, C-4), 120.1 (q, ¹*J*_{C-F} = 269.5 Hz, CF₃), 144.4 (br q, ²*J*_{C-F} = 37.2 Hz, C-3/C-5). Raman (selected peaks, cm⁻¹): 2033 and 2066 (C≡C).

Cu₄(μ-[3,5-(CF₃)₂Pz])₄(μ-EtC≡CEt)₂ (2): 3-Hexyne (38 mg, 0.463 mmol) was added dropwise to a solution of {[3,5-(CF₃)₂Pz]Cu}₃ (250 mg, 0.312 mmol) in dichloromethane (~10 mL) in 3:2 molar ratio. The reaction mixture was stirred for 4 h under nitrogen at the room temperature. The resulting solution was reduced to dryness by evaporation of solvent under a vacuum for 3 h to obtain Cu₄(μ-[3,5-

(CF₃)₂Pz])₄(μ-EtC≡CEt)₂ as a white solid. X-ray quality crystals were grown from dichloromethane at -20 °C. Yield: 84%. M.p.: 90 °C. Anal. Calc.: C, 31.23%; H, 1.97%; N, 9.10%. Found: C, 31.11%; H, 1.93%; N, 9.04%. ¹H NMR (in CDCl₃): δ (ppm) 1.10 (t, J = 7.5 Hz, 6H, CH₃), 2.16 (q, J = 7.5 Hz, 4H, CH₂), 7.01 (s, 2H, Pz-H). ¹⁹F NMR (in CDCl₃): δ (ppm) -61.02 (s). ¹³C{¹H} NMR (in CDCl₃): δ (ppm) 14.1 (br s, CH₃), 14.4 (br s, CH₂), 84.8 (br s, C≡C), 104.3 (s, C-4), 120.1 (q, ¹J_{C-F} = 264.2 Hz, CF₃), 144.4 (br q, ²J_{C-F} = 39.6 Hz, C-3/C-5). Raman (selected peak, cm⁻¹): 1874 (C≡C).

Cu₄(μ-[3,5-(CF₃)₂Pz])₄(μ-MeC≡CMe)₂ (3): 2-Butyne (25 mg, 0.462 mmol) was added dropwise to a solution of {[3,5-(CF₃)₂Pz]Cu}₃ (250 mg, 0.312 mmol) in dichloromethane (~10 mL) in 3:2 molar ratio. The reaction mixture was stirred for 4 h under nitrogen at the room temperature. The resulting solution was vacuum-dried under pressure for 3 h to obtain Cu₄(μ-[3,5-(CF₃)₂Pz])₄(μ-MeC≡CMe)₂ as a white solid. X-ray quality crystals were grown from dichloromethane at -20 °C. Yield: 82%. M.p.: 190 °C. Anal. Calc.: C, 28.63%; H, 1.37%; N, 9.54%. Found: C, 28.68%; H, 1.33%; N, 9.44%. ¹H NMR (in CDCl₃): δ (ppm) 1.76 (br s, 6H, CH₃), 7.03 (s, 2H, Pz-H). ¹⁹F NMR (in CDCl₃): δ (ppm) -61.19 (s). ¹³C{¹H} NMR (in CD₂Cl₂): δ (ppm) 4.4 (br s, CH₃), 77.0 (br s, C≡C), 104.6 (s, C-4), 120.6 (q, ¹J_{C-F} = 264.2 Hz, CF₃), 144.5 (br q, ²J_{C-F} = 39.6 Hz, C-3/C-5). Raman (selected peak, cm⁻¹): 1886 (C≡C).

Cu₂(μ-CF₃CO₂)₂(EtC≡CEt)₂ (4): 3-hexyne (92 mg, 1.124 mmol) was added dropwise to a solution of {[Cu(μ-O₂CCF₃)]₂(C₆H₆)}₂ (250 mg, 0.281 mmol) in benzene (~10-12 mL) in 4:1 molar ratio.^{7,103} The green solution was stirred for 3 h under nitrogen at room temperature. The reaction mixture was reduced to dryness by evaporation of the solvent under reduced vacuum pressure to obtain Cu₂(μ-CF₃CO₂)₂(EtC≡CEt)₂ as green-colored solid. X-ray quality crystals were grown from hexane at -20 °C. Yield: >95%. M.p.: 95 °C. ¹H NMR (in CDCl₃): δ (ppm) 1.19 (t, *J* = 7.5 Hz, 6H, CH₃), 2.38 (br q, *J* = 7.5 Hz, 4H, CH₂). ¹⁹F NMR (in CDCl₃): δ (ppm) -74.26 (s). ¹³C{¹H} NMR (in CDCl₃): δ (ppm) 14.3 (br s, CH₃), 15.9 (br s, CH₂), 88.7 (br s, C≡C), 116.3 (q, ¹*J*_{C-F} = 282.4 Hz, CF₃), 164.1 (br s, CO). Raman (selected peaks, cm⁻¹): 2029 and 2065 (C≡C).

Cu₄(μ-CF₃CO₂)₄(μ-EtC≡CEt)₂ (5): 3-hexyne (46 mg, 0.562 mmol) was added dropwise to a solution of {[Cu(μ-O₂CCF₃)]₂(C₆H₆)}₂ (250 mg, 0.281 mmol) in benzene (~10-12 mL) in 2:1 molar ratio.^{7,103} The light green solution was stirred for 3 h under nitrogen at room temperature. The resulting solution was vacuum dried under reduced pressure for 3 h to obtain Cu₄(μ-CF₃CO₂)₄(μ-EtC≡CEt)₂ as light green-colored solid. X-ray quality crystals were grown from hexane at -20 °C. Yield: 84%. M.p.: 140 °C. ¹H NMR (in CDCl₃): δ (ppm) 1.22 (t, *J* = 6.3 Hz, 6H, CH₃), 2.44 (br q, 4H, CH₂). ¹⁹F NMR (in CDCl₃): δ (ppm) -73.71 (s). ¹³C{¹H} NMR

(in CDCl₃): δ (ppm) 14.3 (br s, CH₃), 16.2 (br s, CH₂), 89.1 (br s, C \equiv C), 116.2 (q, ¹J_{C-F} = 269.5 Hz, CF₃), 164.6 (br s, CO). Raman (selected peak, cm⁻¹): 1844 (C \equiv C).

X-ray crystallographic data: A suitable crystal covered with a layer of hydrocarbon/Paratone-N oil was selected and mounted on a Cryo-loop, and immediately placed in the low temperature nitrogen stream. The X-ray intensity data were measured at 100(2) K on a Bruker D8 Quest with a Photon 100 CMOS detector equipped with an Oxford Cryosystems 700 series cooler, a Triumph monochromator, and a Mo K α fine-focus sealed tube ($\lambda = 0.71073$ Å). Intensity data were processed using the Bruker Apex3 program suite. Absorption corrections were applied by using SADABS. Initial atomic positions were located by direct methods using XT, and the structures of the compounds were refined by the least-squares method using SHELXL^{290,291} within Olex2²⁹² GUI. All the non-hydrogen atoms were refined anisotropically. Hydrogen atoms were included at calculated positions and refined riding on corresponding carbons. X-ray structural figures were generated using Olex2. CCDC [1865182-1865185](#) files contain the additional crystallographic data.

Luminescence Measurements: Steady-state luminescence spectra were acquired with a PTI Quanta Master Model QM-4 scanning spectrofluorometer equipped with a 75 W xenon lamp, emission and excitation monochromators, an excitation correction unit, and a PMT detector. Lifetime data were attained using a xenon flash

lamp as phosphorescence sub-system add-ons to the PTI instrument. Absorption spectra were acquired with a PerkinElmer Lambda 900 double-beam UV/Vis/NIR spectrophotometer for solutions of crystalline samples prepared in ACS-grade acetonitrile using standard 1 cm quartz cuvettes.

Computational Methods: The Gaussian 09³²⁴ package was employed for quantum calculations and DFT was applied to optimize the geometries of the studied complexes. The BP86 functional was used with the 6-311+G(d)^{325,326} basis set for all elements; this level of theory was used in a study of coinage metal-ethylene complexes supported by tris(pyrazolyl)borates,³²⁷ and showed the particular utility of BP86 for coinage metal chemistry.^{328,329} In order to calculate absorption wavelengths, TDDFT³³⁰ computations were carried out with the BP86 functional and augmented 6-311+G(d) basis set with the Gaussian 09 package. DFT was employed to analyze the frontier orbitals with the same functional and basis set. Transition energies calculated at the singlet- and triplet-optimized geometries related with the vertical $T_1 \rightarrow S_0$ ($T_1 \rightarrow S@T$) emission and $S_0 \rightarrow T_1$ ($S_0 \rightarrow T@S$) excitation energies, respectively. The DFT method used in order to carry out these calculations employed the BP86 functional with the 6-311+G(d) basis sets for the Cu metal and main group atoms. Furthermore, natural bond orbital (NBO) analysis was also used to investigate the bonding character between the alkyne and Cu for all complexes studied. Orbitals were plotted with GaussView 5. All systems were

fully optimized to obtain vibrational frequencies in the gas phase, and free energies at 1 atm and 298.15 K.

3.2 Synthesis of Copper pyrazolate complexes with acetylene and terminal alkynes

Cu₄(μ-[3,5-(CF₃)₂Pz])₄(μ-HC≡CH)₂ (4): {μ-[3,5-(CF₃)₂Pz]Cu}₃ (0.25 g, 0.312 mmol) was dissolved in 10 mL of dichloromethane and stirred for ~10 min while bubbling acetylene as a steady stream (1 atm) through the solution. The reaction mixture was concentrated with continuous flow of acetylene and kept at -20 °C to obtain X-ray quality colorless crystals of Cu₄(μ-[3,5-(CF₃)₂Pz])₄(μ-HC≡CH)₂. Yield: >90%. M.p.: 170 °C (decomp.). Anal. calc. C₂₄H₈Cu₄F₂₄N₈·0.4C₁₅H₃Cu₃F₁₈N₆: C, 25.05%; H, 0.64%; N, 10.13%. Found: C, 25.68%; H, 0.74%; N, 10.02%. ¹H NMR (in CDCl₃): δ (ppm) 6.16 (s, 2H, CH), 6.84 (s, 2H, Pz-H). ¹⁹F NMR (in CDCl₃): δ (ppm) -60.1 (s). ¹³C{¹H} NMR (in CDCl₃): δ (ppm) 79.2 (br s, C≡C), 104.8 (s, C-4), 120.7 (q, ¹J_{C-F} = 268.7 Hz, CF₃), 143.0 (br q, ²J_{C-F} = 37.8 Hz, C-3/C-5). Raman (selected peak, cm⁻¹): 1638 (C≡C). Compound 4 lose some acetylene under reduced pressure leading to 1. Signals corresponding to {μ-[3,5-(CF₃)₂Pz]Cu}₃ were also observed in the solutions of resulting material. ¹H NMR (in CDCl₃): δ (ppm) 7.01 (br s, 2H, Pz-H). ¹⁹F NMR (in CDCl₃): δ (ppm) -61.0 (br s).

Cu₂(μ-[3,5-(CF₃)₂Pz])₂(HC≡CH)₂ (5): {μ-[3,5-(CF₃)₂Pz]Cu}₃ (4 mg) was dissolved in 1.5 mL CD₂Cl₂ in a NMR tube and acetylene gas was bubbled for 30 to 60 s. The NMR tube was quickly sealed and the ¹H and ¹⁹F NMR data were collected at different temperatures (21 °C, -10 °C, -35 °C, -60 °C and 70 °C). A broad peak started to appear around 4.8 ppm at -35 °C which is likely the signal from bound acetylene of Cu₂(μ-[3,5-(CF₃)₂Pz])₂(HC≡CH)₂. ¹H NMR (in CD₂Cl₂ at -70 °C): δ (ppm) 6.92 (s, Pz-H), 4.86 (br s, ≡CH). ¹⁹F NMR (in CD₂Cl₂ at -70 °C): δ (ppm) -59.7 (s). We could not isolate this molecule as a solid, as all attempts even in the presence of excess acetylene led to the precipitation of 4.

Cu₄(μ-[4-Br-3,5-(CF₃)₂Pz])₄(μ-HCuCH)₂ (6): {μ-[4-Br-3,5-(CF₃)₂Pz]Cu}₃ (0.25 g, 0.241 mmol) was dissolved in 10 mL of dichloromethane and stirred for ~10 min while bubbling acetylene as a steady stream (1 atm) through the solution. The reaction mixture was concentrated using an acetylene stream and kept at -20 °C to obtain Cu₄(μ-[4-Br-3,5-(CF₃)₂Pz])₄(μ-HCuCH)₂ as a crystalline solid. Yield: 85%. M.p.: 180 °C (decomp.). Anal. calc. C₂₄H₄Br₄Cu₄F₂₄N₈: C, 20.09%; H, 0.28%; N, 7.81%. Found: C, 20.87%; H, 0.31%; N, 8.01%. ¹H NMR (in CDCl₃): δ (ppm) 6.03 (s, 2H, CH). ¹⁹F NMR (in CDCl₃): δ (ppm) -59.5 (s). Solid **6** does not show good solubility in most NMR solvents to collect good ¹³C NMR data. ¹³C{¹H} NMR (in (CD₃)₂CO): δ (ppm) 74.0 (br s, C≡C), 92.8 (s, C-4), 121.7 (br, CF₃), 142.6 (br, C-3/C-5). Raman (selected peak, cm⁻¹): 1631 (C≡C). Also in solution, some Cu₄(μ-

$[4\text{-Br-3,5-(CF}_3)_2\text{Pz}]_4(\mu\text{-HCuCH})_2$ dissociates into $\{\mu\text{-[4-Br-3,5-(CF}_3)_2\text{Pz]Cu}\}_3$ and free acetylene as evident from ^{19}F and ^1H NMR data.

$\text{Cu}_2(\mu\text{-[4-Br-3,5-(CF}_3)_2\text{Pz]})_2(\text{HC}\equiv\text{CH})_2$ (8): $\{\mu\text{-[4-Br-3,5-(CF}_3)_2\text{Pz]Cu}\}_3$ (4 mg) was dissolved in 1.5 mL CD_2Cl_2 in a NMR tube and acetylene gas was bubbled for 30 to 60 s. The NMR tube was quickly sealed and the ^1H and ^{19}F NMR data were collected at different temperatures (21 °C, -10 °C, -35 °C, -60 °C and -70 °C). A broad peak started to appear around 4.7 ppm at -35 °C which is likely the signal from bound acetylene of $\text{Cu}_2(\mu\text{-[4-Br-3,5-(CF}_3)_2\text{Pz]})_2(\text{HC}\equiv\text{CH})_2$. ^1H NMR (in CD_2Cl_2 at -70 °C): δ (ppm) 4.75 (br s, 4H, CH). ^{19}F NMR (in CD_2Cl_2 at -70 °C): δ (ppm) -59.6 (s). X-ray quality crystals of $\text{Cu}_2(\mu\text{-[4-Br-3,5-(CF}_3)_2\text{Pz]})_2(\text{HC}\equiv\text{CH})_2$ was obtained in toluene at -20 °C. For that, 50 mg of $\{\mu\text{-[4-Br-3,5-(CF}_3)_2\text{Pz]Cu}\}_3$ was dissolved in 8 mL of dry dichloromethane in 50 mL Schlenk flask and acetylene gas was bubbled until all dichloromethane was evaporated and white powder was obtained. This white powder was dissolved in 10 mL of dry toluene under acetylene atmosphere and kept at -20 °C refrigerator to obtain colorless crystals. Raman (selected peak, cm^{-1}): 1811 ($\text{C}\equiv\text{C}$). ATR-IR (selected peak, cm^{-1}): 1810. This molecule loses acetylene easily in solution or in the solid.

$\text{Cu}_4(\mu\text{-[4-Cl-3,5-(CF}_3)_2\text{Pz]})_4(\mu\text{-HC}\equiv\text{CH})_2$ (7): $\{\mu\text{-[4-Cl-3,5-(CF}_3)_2\text{Pz]Cu}\}_3$ (0.25 g, 0.276 mmol) was dissolved in 10 mL of dichloromethane, and acetylene was bubbled as a steady stream (1 atm) through the solution for 10 min. The reaction

mixture was concentrated using acetylene stream and kept at -20 °C to obtain $\text{Cu}_4(\mu\text{-[4-Cl-3,5-(CF}_3)_2\text{Pz]})_4(\mu\text{-HC}\equiv\text{CH})_2$ as a white, crystalline solid. Yield: 87%. M.p.: 180 °C (decomp.). Anal. calc. $\text{C}_{24}\text{H}_4\text{Cl}_4\text{Cu}_4\text{F}_{24}\text{N}_8$: C, 22.93%; H, 0.32%; N, 8.92%. Found: C, 22.53%; H, 0.56%; N, 8.45%. ^1H NMR (in CDCl_3): δ (ppm) 6.04 (s, 2H, CH). ^{19}F NMR (in CDCl_3): δ (ppm) -59.6 (s). Solid **7** does not show good solubility in most NMR solvents to collect good ^{13}C NMR data. $^{13}\text{C}\{^1\text{H}\}$ NMR (in $(\text{CD}_3)_2\text{CO}$): δ (ppm) 74.1 (br s, $\text{C}\equiv\text{C}$), 109.6 (s, C-4), 119.4 (br, CF_3), 140.7 (br q, C-3/C-5). Raman (selected peak, cm^{-1}): 1632 ($\text{C}\equiv\text{C}$). Compound **7** tend to lose some acetylene under reduced pressure. Also in solution, some $\text{Cu}_4(\mu\text{-[4-Cl-3,5-(CF}_3)_2\text{Pz]})_4(\mu\text{-HC}\equiv\text{CH})_2$ dissociates into $\{\mu\text{-[4-Cl-3,5-(CF}_3)_2\text{Pz] Cu}\}_3$ and free acetylene as evident from ^{19}F and ^1H NMR data.

$\text{Cu}_2(\mu\text{-[3,5-(CF}_3)_2\text{Pz]})_2(\text{HC}\equiv\text{CPh})_2$ (9**):** Phenylacetylene (0.096 g, 0.936 mmol) was added dropwise to a solution of $\{\mu\text{-[3,5-(CF}_3)_2\text{Pz]Cu}\}_3$ (**1**) (0.25 g, 0.312 mmol) in dichloromethane (~10 mL) at room temperature. The reaction mixture was stirred for 4 h under nitrogen, and the resulting solution was reduced to dryness by evaporation of solvent under vacuum to obtain $\text{Cu}_2(\mu\text{-[3,5-(CF}_3)_2\text{Pz]})_2(\text{HC}\equiv\text{CPh})_2$ as an off-white solid. X-ray quality crystals were grown from dichloromethane at -20 °C. Yield: >90%. M.p.: 55-57 °C. Anal. calc. $\text{C}_{26}\text{H}_{14}\text{Cu}_2\text{F}_{12}\text{N}_4$: C, 42.34%; H, 1.91%; N, 7.60%. Found: C, 42.37%; H, 1.94%; N, 7.69%. ^1H NMR (in CDCl_3): δ (ppm) 3.17 (br s, 2H, CH), 7.01 (s, 2H, Pz-H),

7.32 (m, $J = 6.65$ Hz, 6H, CH), 7.47 (d, $J = 6.85$ Hz, 4H, CH). ^{19}F NMR (in CDCl_3): δ (ppm) -61.0 (s). $^{13}\text{C}\{^1\text{H}\}$ NMR (in CDCl_3): δ (ppm) 77.8 (br s, $\text{C}\equiv\text{C}$), 104.6 (s, C-4), 120.5 (q, $^1J_{\text{C-F}} = 268.3$ Hz, CF_3), 122.4 (s, phenyl-C), 128.8 (s, m-CH), 129.4 (s, p-CH), 132.3 (s, o-CH), 144.4 (br q, $^2J_{\text{C-F}} = 37.2$ Hz, C-3/C-5). The $^{13}\text{C}\{^1\text{H}\}$ NMR peak of the quaternary carbon atom of the triple bond of phenylacetylene broadens into the base line at around 84-85 ppm and as a result, it is difficult to pinpoint its exact position. Raman (selected peaks, cm^{-1}): 1918, 1928 and 1950 ($\text{C}\equiv\text{C}$).

$\text{Cu}_2(\mu\text{-}[3,5\text{-}(\text{CF}_3)_2\text{Pz}])_2(\text{HC}\equiv\text{C}(\text{CH}_2)_5\text{C}\equiv\text{CH})$ (10): $\{\mu\text{-}[3,5\text{-}(\text{CF}_3)_2\text{Pz}]\text{Cu}\}_3$ (0.25 g, 0.312 mmol) was dissolved in the dichloromethane (~ 10 mL) under nitrogen at room temperature. To this solution, 3 equivalents of 1,8-nonadiyne (0.11 g, 0.936 mmol) was slowly added and stirred for ~ 4 h. The solution was then filtered and dried under reduced pressure to obtain crude white $\text{Cu}_2(\mu\text{-}[3,5\text{-}(\text{CF}_3)_2\text{Pz}])_2(\text{HC}\equiv\text{C}(\text{CH}_2)_5\text{C}\equiv\text{CH})$ as solid product. X-ray quality crystals were grown from dichloromethane at -20 °C. Yield: 82%. M.p.: 144 °C. Anal. calc. $\text{C}_{19}\text{H}_{14}\text{Cu}_2\text{F}_{12}\text{N}_4$: C, 34.92%; H, 2.16%; N, 8.57%. Found: C, 34.89%; H, 2.01%; N, 8.56%. ^1H NMR (in CDCl_3): δ (ppm) 1.31 (br s, 4H, CH_2), 1.53 (m, $J = 7.5$ Hz, 2H, CH_2), 2.61 (br s, 4H, CH_2), 4.33 (br s, 2H, CH), 6.81 (s, 2H, Pz-H). ^{19}F NMR (in CDCl_3): δ (ppm) -60.54 (s). $^{13}\text{C}\{^1\text{H}\}$ NMR (in CDCl_3): δ (ppm) 21.7 (br s, alkyne C-3/ C-7), 26.4 (br s, alkyne C-4/C-5/C-6), 75.1 (br s, $\text{C}\equiv\text{C}$), 96.4 (br s, C-

2/C-8), 103.6 (s, C-4), 121.6 (q, $^1J_{C-F} = 268.3$ Hz, CF₃), 142.2 (br q, $^2J_{C-F} = 37.2$ Hz, C-3/C-5). Raman (selected peak, cm⁻¹): 1946 (C≡C).

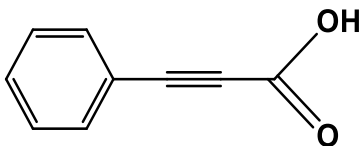
Cu₄(μ-[3,5-(CF₃)₂Pz])₄(HC≡C(CH₂)₄C≡CH)₂ (11): 1,7-Octadiyne (0.080 g, 0.750 mmol) was added dropwise to a solution of {μ-[3,5-(CF₃)₂Pz]Cu}₃ (0.20 g, 0.250 mmol) in dichloromethane (~8 mL) in 3 : 1 molar ratio. The reaction mixture was stirred for ~4 h under nitrogen at room temperature. The resulting mixture was filtered and dried under reduced pressure to obtain Cu₄(μ-[3,5-(CF₃)₂Pz])₄(HC≡C(CH₂)₄C≡CH)₂ as white solid. It was recrystallized from dichloromethane at -20 °C to obtain X-ray quality crystals of Cu₂(μ-[3,5-(CF₃)₂Pz])₂(1,7-octadiyne). Yield: 81%. Raman (selected peak, cm⁻¹): 1952 (C≡C).

Cu₄(μ-[3,5-(CF₃)₂Pz])₄(C₂H₅C≡C(CH₂)₄C≡CC₂H₅)₂ (12): 3,9-Dodecadiyne (0.091 g, 0.561 mmol) was added dropwise to a solution of {μ-[3,5-(CF₃)₂Pz]Cu}₃ (0.15 g, 0.187 mmol) in dichloromethane (~8 mL) in 3 : 1 molar ratio. The reaction mixture was stirred for ~4 h under nitrogen at room temperature. The solution was then filtered and dried under reduced pressure to obtain crude white Cu₄(μ-[3,5-(CF₃)₂Pz])₄(C₂H₅C≡C(CH₂)₄C≡CC₂H₅)₂ as solid product. X-ray quality crystals were grown from dichloromethane at -20 °C. Yield: 78%. M.p.: 118 °C. Anal. calc. C₄₄H₄₀Cu₄F₂₄N₈: C, 37.99%; H, 2.90%; N, 8.06%. Found: C, 37.82%; H, 2.82%; N, 8.15%. ¹H NMR (in CDCl₃): δ (ppm) 1.11 (t, *J* = 7.2 Hz, 6H, CH₃), 1.54 (br s, 4H, CH₂), 1.57 (br s, 4H, CH₂), 2.18 (br s, 4H, CH₂), 7.01 (s, 2H, Pz-H). ¹⁹F NMR

(in CDCl₃): δ (ppm) -60.98 (s). ¹³C{¹H} NMR (in CDCl₃): δ (ppm) 13.1 (br s, CH₃), 14.4 (br s, CH₂), 19.1 (br s, CH₂), 28.3 (br s, CH₂), 80.3 (br s, C \equiv C), 83.2 (br s, C \equiv C), 104.3 (s, C-4), 121.3 (br q, CF₃), 143.9 (br q, C-3/C-5). Raman (selected peaks, cm⁻¹): 2040 and 2070 (C \equiv C).

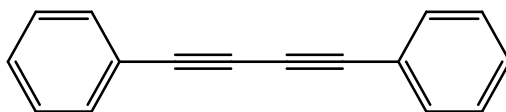
General procedure for carboxylation of terminal alkynes: { μ -[3,5-(CF₃)₂Pz]Cu}₃ (0.036 mmol, 30 mg, 2 mol% based on phenylacetylene) was dissolved in DMF (4 mL) in a reaction vessel. Phenylacetylene (2 mmol, 204 mg) was introduced into the reaction mixture while stirring under CO₂, and stirred for 12 h at room temperature under a CO₂ atmosphere using a balloon. After completion of the reaction, DMF was removed, as much as possible, under reduced pressure and treated with water/CH₂Cl₂ mixture. The product was extracted with dichloromethane (3 \times 5 mL). The leftover aqueous layer was acidified with concentrated HCl to pH = 1 and then extracted with ethyl acetate (3 \times 5 mL) to collect additional product. The organic layers (CH₂Cl₂ and ethyl acetate extracts) were combined, dried with anhydrous Na₂SO₄, filtered and the volatiles were removed in vacuo. The residue was purified by silica gel column chromatography (ethyl acetate/n-hexane gradient), affording the carboxylic acid product as a major product (72% yield) and alkyne coupling product as a minor product (10% yield).^{331,332}

Phenylpropionic acid:¹⁶³ Entry 1- Product A



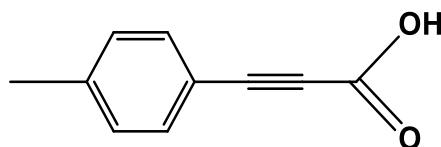
¹H NMR (in (CD₃)₂CO): δ (ppm) 14.14 (br, s, 1H, COOH), 7.60–7.57 (m, 1H, Ar-H), 7.49–7.42 (m, 2H, Ar-H), 7.32 (br, s, 2H, Ar-H).

1,4-diphenyl buta-1,3-diyne:³³³ Entry 1- Product B



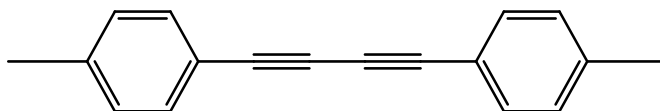
¹H NMR (in CDCl₃): δ (ppm) 7.56-7.51 (m, 4 H), 7.40-7.28 (m, 6 H).

4-Methylphenylpropionic acid:³³¹ Entry 2- Product A



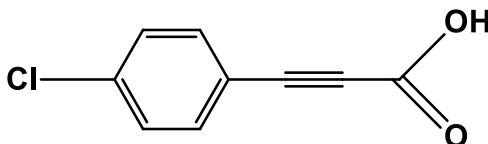
¹H NMR (in CDCl₃): δ (ppm) 10.55 (br s, 1H, COOH) 7.51 (d, *J* = 8.0 Hz, 2H, Ar-H), 7.20 (d, *J* = 8.0 Hz, 2H, Ar-H), 2.39 (s, 3H, CH₃).

1,4-Bis(*p*-methylphenyl)buta-1,3-diyne:³³³ Entry 2- Product B



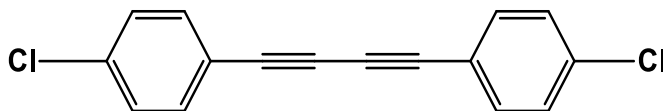
^1H NMR (in CDCl_3): δ (ppm) 7.40 (d, $J = 8.4$ Hz, 4H), 7.12 (d, $J = 8.2$ Hz, 4H), 2.34 (s, 6H).

(4-chlorophenyl)propionic acid:¹⁶³ **Entry 3- Product A**



^1H NMR (in CDCl_3): δ (ppm) 13.64 (br, s, 1H, COOH) 7.61 (d, $J = 5.6$ Hz, 2H, Ar-H), 7.52 (d, $J = 5.6$ Hz, 2H, Ar-H).

1,4-bis(4-chlorophenyl) buta-1,3-diyne:³³⁴ **Entry 2- Product B**



^1H NMR (in CDCl_3): δ (ppm) 7.55-7.47 (m, 4 H), 7.07-7.01 (m, 4 H)

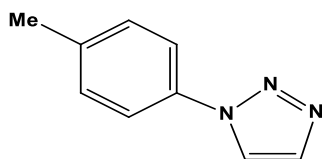
General procedure for alkyne - *p*-tolylazide cycloaddition reaction: $\{\mu\text{-}[3,5\text{-}(\text{CF}_3)_2\text{Pz}]\text{Cu}\}_3$ (0.018 mmol, 15 mg, 1 mol% based on *p*-tolylazide) was dissolved in CH_2Cl_2 (5 mL) under nitrogen atmosphere at room temperature. Acetylene (1 atm, balloon) and *p*-tolylazide (1.5 mmol, 200 mg) were introduced into the reaction mixture under stirring, while slowly closing the nitrogen line. The reaction mixture was stirred at room temperature for 12 h while maintaining the mixture under an acetylene atmosphere (using a balloon). After removal of the solvent under reduced pressure, the crude reaction mixture was analyzed using ^1H NMR, which

indicated the presence of the desired triazole product in 99% yield.³³⁵ Similarly, we have used phenylacetylene or 1-octyne (1.5 mmol, 0.18 mL) as the alkyne source along with *p*-tolylazide, and reacted it with a dichloromethane solution of $\{\mu\text{-}[3,5\text{-}(\text{CF}_3)_2\text{Pz}]\text{Cu}\}_3$ (0.018 mmol, 15 mg, 1 mol% based on alkyne) under nitrogen atmosphere at room temperature. After completion of the reaction, the crude reaction mixture was analyzed using ^1H NMR indicating the formation of desired triazole product in 99% yield.³³⁶ We were also successful in isolating the bis-triazole using the terminal alkyne 1,8-nonadiyne. In this reactions, the alkyne(1.5 mmol) and *p*-tolylazide (1.5 mmol, 400 mg of 1,8-nonadiyne) were added to a solution of $\{\mu\text{-}[3,5\text{-}(\text{CF}_3)_2\text{Pz}]\text{Cu}\}_3$ (0.015 mmol, 12 mg, 1 mol% based on respective alkyne) in benzene (5 mL) under nitrogen and heated to 80 °C with continuous stirring for 12 h. After cooling the mixture to room temperature and removal of the solvent under reduced pressure, the crude reaction mixture was characterized using ^1H NMR. The observed product yield was 99% (the control reaction without the copper catalyst under same conditions gave about 19% of the bis-triazole, and the Cu catalyzed reaction at room temperature in CH_2Cl_2 is slow and gave the bistriazole product in about 13% yield after 12 h).

Entry	Alkyne	Solvent	Reaction Temp (°C)	Reaction Time (h)	% Yield*
1	Acetylene	dichloromethane	RT	12	99
2	Phenylacetylene	dichloromethane	RT	12	99
3	1-Octyne	dichloromethane	RT	12	99
4	1,8-Nonadiyne	benzene	80	12	99

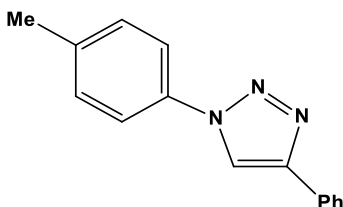
*Calculated NMR yield using 1,3,5-Tris(trifluoromethyl)benzene as internal standard.

1-*p*-Tolyl-1*H*-1,2,3-triazole:³³⁵



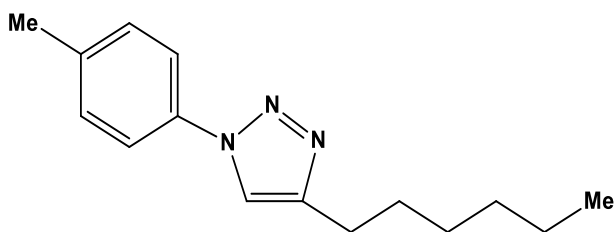
¹H NMR (in CDCl₃): δ (ppm) 2.40 (s, 3H), 7.30 (d, *J* = 7.75 Hz, 2H), 7.60 (d, *J* = 7.70 Hz, 2H), 7.83 (s, 1H), 7.99 (s, 1H) ppm. ¹³C{¹H} NMR (in CDCl₃): δ (ppm) 21.2, 120.7, 122.1, 130.3, 134.5, 134.9, 139.0. HRMS calculated for C₉H₁₀N₃⁺: 160.0870, found: 160.0853.

1-*p*-Tolyl-4-phenyl-1*H*-1,2,3-triazole:³³⁶



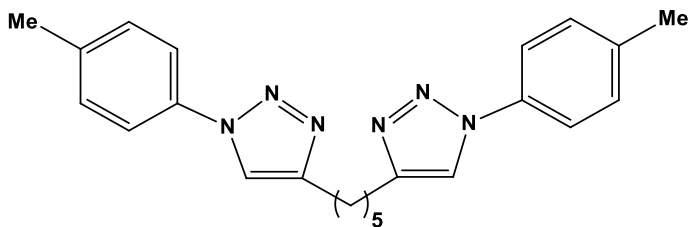
^1H NMR (in CDCl_3): δ (ppm) 2.41 (s, 3H), 7.30-7.36 (m, 3H), 7.44 (t, $J = 6.90$ Hz, 2H), 7.64 (d, $J = 7.45$ Hz, 2H), 7.90 (d, $J = 6.90$ Hz, 2H), 8.15 (s, 1H). $^{13}\text{C}\{^1\text{H}\}$ NMR (in CDCl_3): δ (ppm) 21.2, 117.8, 120.5, 125.9, 128.4, 129.0, 130.3, 134.8, 139.0, 148.3 ppm. HRMS calculated for $\text{C}_{15}\text{H}_{14}\text{N}_3^+$: 236.1183, found: 236.1153.

4-hexyl-1-(*p*-tolyl)-1*H*-1,2,3-triazole:



^1H NMR (in CDCl_3): δ (ppm) 0.85 (t, $J = 6.87$ Hz, 3H), 1.26-1.29 (m, 4H), 1.33-1.37 (m, 2H), 1.65-1.71 (m, 2H), 2.35 (s, 3H), 2.73 (t, $J = 7.45$ Hz, 2H), 7.23 (d, $J = 8.02$ Hz, 2H), 7.55 (d, $J = 8.02$ Hz, 2H), 7.68 (s, 1H) ppm. $^{13}\text{C}\{^1\text{H}\}$ NMR (in CDCl_3): δ (ppm) 14.1, 21.0, 22.6, 25.7, 29.0, 29.4, 31.6, 118.9, 120.2, 130.1, 135.0, 138.4, 149.0 ppm.

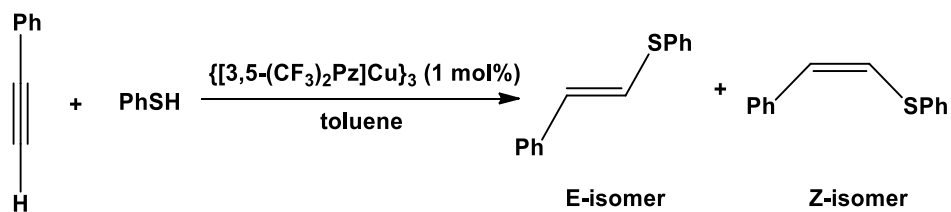
1-*p*-Tolyl-4-(5-(1-*p*-tolyl-1*H*-1,2,3-triazol-4-yl)pentyl)-1*H*-1,2,3-triazole:



^1H NMR (in CDCl_3): δ (ppm) 1.5 (m, $J = 7.20$ Hz, 2H), 1.79 (m, $J = 7.40$ Hz, 2H), 2.39 (s, 3H), 2.80 (m, $J = 7.30$ Hz, 2H), 7.28 (d, $J = 7.45$ Hz, 2H), 7.57 (d, $J =$

8.0 Hz, 2H) ppm. $^{13}\text{C}\{^1\text{H}\}$ NMR (in CDCl_3): δ (ppm) 21.2, 25.5, 28.6, 29.1, 119.1, 120.4, 130.2, 135.0, 138.5, 148.8 ppm. HRMS calculated for $\text{C}_{23}\text{H}_{27}\text{N}_6^+$: 387.2292, found: 387.2242.

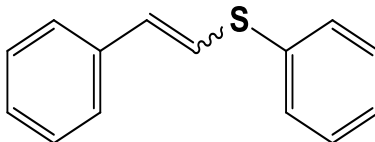
General procedure for hydrothiolation of alkynes: $\{\mu\text{-}[3,5\text{-}(\text{CF}_3)_2\text{Pz}]\text{Cu}\}_3$ (0.01 mmol, 7.99 mg, 1.0 mol% based on phenylacetylene) was dissolved in dry toluene (5 mL) in a reaction vessel. Phenylacetylene (1.0 mmol, 100 mg) was added to it under a CO_2 atmosphere (1 atm, balloon). Then thiophenol (1.1 mmol, 118 mg) was introduced into the reaction mixture under stirring. The resulting mixture was stirred at room temperature for 3 h. After removal of the solvent and all the volatilities (including unreacted starting materials) under reduced pressure, the crude reaction mixture was analyzed using ^1H NMR. The vinyl sulfide products were obtained at a yield of 70% (isolated yield) and an E/Z ratio of 63 : 37 (from NMR peak analysis).¹⁹⁷ The reaction performed under the same conditions, except for the use of N_2 , gave similar products but with different stereoselectivity (E/Z ratio = 50 : 50). These results demonstrate that the stereoselectivity of this Cu(I)-catalyzed alkyne hydrothiolation reaction could be controlled with the presence or absence of the CO_2 atmosphere. We have then performed several experiments by changing the reaction temperature and reaction time.



Entry	Catalyst	Temp (°C)	Time (h)	Under CO ₂ (E:Z)	Under N ₂ (E:Z)	Overall % yield under CO ₂	Overall % yield under N ₂	References
1	$\{[3,5-(\text{CF}_3)_2\text{Pz}]\text{Cu}\}_3$	RT	3	63:37	50:50	70	56	This work
2	No catalyst	RT	3	30:70	70:30	42	37	This work
3	$\{[3,5-(\text{CF}_3)_2\text{Pz}]\text{Cu}\}_3$	0	3	26:74	10:90	65	48	This work
4	$\{[3,5-(\text{CF}_3)_2\text{Pz}]\text{Cu}\}_3$	90	3	30:70	56:44	78	62	This work
5	$\{[3,5-(\text{CF}_3)_2\text{Pz}]\text{Cu}\}_3$	90	16	78:22	34:66	90	81	This work
6 ^a	CuI/K ₂ CO ₃	90	16	10:90	84:16	92	68	¹⁹⁷

^aReaction conditions: phenylacetylene (0.5 mmol), thiophenol (0.75 mmol), CuI (5 mol%), K₂CO₃ (0.6 mmol), H₂O (25 μL) and DMSO (3 mL) .

Phenyl(styryl)sulfane:¹⁹⁷



¹H NMR (in CDCl₃) δ (ppm) 7.56 – 7.22 (m, 20H), 6.90 (d, 1H, $J = 15.0$ Hz), 6.75 (d, 1H, $J = 15.0$ Hz), 6.61 (d, 1H, $J = 10.8$ Hz), 6.52 (d, 1H, $J = 10.8$ Hz).

X-ray crystallographic data: A suitable crystal covered with a layer of hydrocarbon/ Paratone-N oil was selected and mounted on a Cryo-loop, and immediately placed in the low temperature nitrogen stream. The X-ray intensity data were measured at 100(2) K on a Bruker D8 Quest with a Photon 100 CMOS detector equipped with an Oxford Cryosystems 700 series cooler, a Triumph monochromator, and a Mo K α fine-focus sealed tube ($\lambda = 0.71073$ Å). Intensity data were processed using the Bruker Apex3 program suite. Absorption corrections were applied by using SADABS. Initial atomic positions were located by direct methods using XT, and the structures of the compounds were refined by the leastsquares method using SHELXL^{290,291} within Olex2²⁹² GUI. All the non-hydrogen atoms were refined anisotropically. Hydrogen atoms were included at calculated positions and refined riding on corresponding carbons. X-ray structural figures were generated using Olex2. CCDC [1934981–1934986](#) files contain the additional crystallographic data.

5.4 Experimental section of chapter 4

{[3,5-(CF₃)₂Pz]Cu(CO)}₂ (5): {[3,5-(CF₃)₂Pz]Cu}₃ (100 mg, 0.12 mmol) was dissolved in 8 mL of dichloromethane in a Schlenk tube (with a side arm) under nitrogen. The side arm was closed, the solution was slowly warmed to 40-45 °C and allowed to stir at this temperature for ~5 min. The solution was removed from heat, the side arm of the Schlenk tube was opened to nitrogen, and the glass stopper was replaced with a rubber septum. Carbon monoxide (~1 atm) was gently bubbled into the warm solution via a large needle through the rubber septum for ~10 min while the nitrogen flow was slowly decreased. This mixture was then concentrated to ~3 mL by bubbling a slow stream of CO through the solution. The resulting solution was kept at -20 °C overnight to obtain {[3,5-(CF₃)₂Pz]Cu(CO)}₂ as colorless crystals. NMR data were collected with excess CO in the NMR tube. ¹H NMR (in CD₂Cl₂): δ (ppm) 7.05 (s). ¹⁹F NMR (in CD₂Cl₂): δ (ppm) -59.63 (br). ¹³C{¹H} NMR (in CD₂Cl₂): δ (ppm) 104.8 (s), 120.7 (br q, ¹J_{C-F} = 265.5 Hz, CF₃), 144.6 (br q, C-3 & C-5), 172.3 (s, CO). Vacuum drying led to the formation of {[3,5-(CF₃)₂Pz] Cu}₃. ATR-IR (single crystals, selected peaks, cm⁻¹): 2099 and 2108 (C≡O stretch), IR data in Nujol (selected peak, cm⁻¹): 2128 (C≡O stretch).

{{[4-Cl-3,5-(CF₃)₂Pz]Cu(CO)}₂ (6): {[4-Cl-3,5-(CF₃)₂Pz]Cu}₃ (200 mg, 0.221 mmol) was dissolved in 8 mL of dichloromethane and the solution was slowly warmed to ~50 °C. The reaction mixture was removed from heat and carbon monoxide was bubbled through the warm solution for ~10 min, and then concentrated to ~3 mL with a gentle flow of CO. The resulting solution was kept at -20 °C overnight to obtain {[4-Cl-3,5-(CF₃)₂Pz]Cu(CO)}₂ as colorless crystals. NMR data were collected with excess CO in the NMR tube. ¹⁹F NMR (in CD₂Cl₂): δ (ppm) -60.27 (s). ¹³C{¹H} NMR (in CD₂Cl₂): δ (ppm) 109.9 (s), 120.4 (q, ¹J_{C-F} = 270.7 Hz, CF₃), 140.6 (q, ²J_{C-F} = 37.2 Hz, C-3 & C-5), 171.8 (s, CO). ATR-IR (single crystals, selected peak, cm⁻¹): 2139 (C≡O stretch). IR data in Nujol (selected peaks, cm⁻¹): 2110, 2127 (sh), 2146 (sh) (C≡O stretch). The compound lose CO easily preventing the CHN analysis.

{{[3,4,5-(CF₃)₃Pz]Cu(CO)}₂ (7): {[3,4,5-(CF₃)₃Pz]Cu}₃ (100 mg, 0.10 mmol) was dissolved in 8 mL of CH₂Cl₂, carbon monoxide was bubbled for ~10 min. The solution was kept at -20 °C under CO atmosphere to obtain X-ray quality colorless crystals of {[3,4,5-(CF₃)₃Pz]Cu(CO)}₂. Yield: 92% (100 mg, based on {[3,4,5-(CF₃)₃Pz]Cu}₃). NMR data were collected with excess CO in the NMR tube. ¹⁹F NMR (in CD₂Cl₂): δ (ppm) -55.23 (s), -59.38 (s). ¹³C{¹H} NMR (in CD₂Cl₂): δ (ppm) 110.5 (s), 119.9 (q, ¹J_{C-F} = 270.7 Hz, CF₃), 142.9 (br s, C-3 & C-5), 170.9 (s, CO). ATR-IR (single crystals, selected peak, cm⁻¹): 2139 (C≡O stretch). IR data

in Nujol (selected peak, cm^{-1}): 2146 ($\text{C}\equiv\text{O}$ stretch). Vacuum drying led to the formation of $\{[3,4,5\text{-(CF}_3)_3\text{Pz}]\text{Cu}\}_3$.

[NEt₄][{[3,5-(CF₃)₂Pz]Cu(CO)}₄(μ -4-Br)] (8): $\{[3,5\text{-(CF}_3)_2\text{Pz}]\text{Cu}\}_3$ (100 mg, 0.125 mmol) and NEt₄Br (19 mg, 0.093 mmol) were dissolved in dichloromethane (~5 mL) in two different Schlenk flasks. Both the solutions were gently bubbled with CO before mixing together. The solution mixture was then allowed to stir for a few minutes in a CO rich environment and finally concentrated to ~3 mL with a stream of CO. X-ray quality crystal were grown from dichloromethane at -20 °C under CO. Yield: 84% (based on $\{[3,5\text{-(CF}_3)_2\text{Pz}]\text{Cu}\}_3$). Anal. calc. for C₃₂H₂₄BrCu₄F₂₄N₉O₄: C, 27.68%; H, 1.74%; N, 9.08%. Found: C, 27.62%; H, 2.08%; N, 9.01%. ¹H NMR (in CD₂Cl₂): δ (ppm) 1.21 (t, $J = 7.2$ Hz, 12H, CH₃), 3.03 (q, $J = 7.2$ Hz, 8H, CH₂), 6.84 (s, 4H, Pz-H). ¹⁹F NMR (in CD₂Cl₂): δ (ppm) -60.73 (br). ¹³C{¹H} NMR (in CD₂Cl₂): δ (ppm) 7.6 (s, CH₂/CH₃), 103.8 (s, C-4), 121.4 (q, ¹J_{C-F} = 271.5 Hz, CF₃), 142.4 (br q, ²J_{C-F} = 37.2 Hz, C-3 & C-5), 173.0 (s, CO). ATR-IR (single crystals, selected peak, cm^{-1}): 2098 ($\text{C}\equiv\text{O}$ stretch).

[NEt₄][{[3,5-(CF₃)₂Pz]₃Cu₂(CO)₂}] (9): A solution of $\{[3,5\text{-(CF}_3)_2\text{Pz}]\text{Cu}\}_3$ (100 mg, 0.125 mmol) in dichloromethane saturated with CO was slowly added to a CO saturated solution of NEt₄Cl (30 mg, 0.187 mmol) in CH₂Cl₂ (~5 mL). After addition the reaction mixture was stirred for ~10 min resulting in a cloudy solution which was filtered through Celite to yield a colorless filtrate. The filtrate was

collected and concentrated to ~3 mL by gently bubbling with CO. This supersaturated solution was placed under a CO atmosphere and cooled at -20 °C to obtain colorless crystals. Yield: 82% (based on {[3,5-(CF₃)₂Pz]Cu}₃). Anal. calc. for C₂₅H₂₃Cu₂F₁₈N₇O₂: C, 32.55%; H, 2.51%; N, 10.63%. Found: C, 32.43%; H, 2.80%; N, 10.55%. ¹H NMR (in CD₂Cl₂): δ (ppm) 1.20 (t, *J* = 6 Hz, 12H, CH₃), 3.04 (q, 8H, CH₂), 6.80 (s, 3H, Pz-H). ¹⁹F NMR (in CD₂Cl₂): δ (ppm) -60.63 (br). ¹³C{¹H} NMR (in CD₂Cl₂): δ (ppm) 7.7 (s, CH₃), 8.0 (s, CH₂), 103.8 (s, C-4), 121.3 (q, ¹*J*_{C-F} = 271.0 Hz, CF₃), 142.3 (br q, C-3 & C-5), 173.2 (br, CO). ATR-IR (single crystals, selected peak, cm⁻¹): 2087 (C≡O stretch).

Alternative method: [3,5-(CF₃)₂Pz]NEt₄ (32 mg, 0.096 mmol) was dissolved in 12 mL of CH₂Cl₂ with 4 Å molecular sieves and saturated with CO. {[3,5-(CF₃)₂Pz]Cu}₃ (74 mg, 0.092 mmol) was dissolved in 3 mL of CH₂Cl₂, saturated with CO and [3,5-(CF₃)₂Pz]NEt₄ solution was slowly added while gently bubbling CO. The resultant solution was filtered through a bed of Celite, saturated with CO and stored under CO atmosphere to obtain X-ray quality colorless crystals of [NEt₄]{[3,5-(CF₃)₂Pz]₃Cu₂(CO)₂}.

[NEt₄][{[4-Cl-3,5-(CF₃)₂Pz]Cu(CO)}₄(μ₄-Br)] (10): A CO saturated solution of {[4-Cl-3,5-(CF₃)₂Pz]Cu}₃ (250 mg, 0.272 mmol) in dichloromethane (~10 mL) and NEt₄Br (42.8 mg, 0.204 mmol) in dichloromethane (~6 mL) were mixed together and stirred for ~10 min. The reaction mixture was concentrated to ~3 mL

with a stream of CO and cooled to -20 °C to obtain X-ray quality crystals. Yield: 87% (based on {[4-Cl-3,5-(CF₃)₂Pz]Cu}₃). Anal. calc. for C₃₂H₂₀BrCl₄Cu₄F₂₄N₉O₄: C, 25.18%; H, 1.32%; N, 8.26%. Found: C, 25.04%; H, 1.48%; N, 8.36%. ¹H NMR (in CD₂Cl₂): δ 1.29 (t, *J* = 7 Hz, 12H, CH₃), 3.13 (q, *J* = 7 Hz, 8H, CH₂). ¹⁹F NMR (CD₂Cl₂): δ -60.25 (br s). ¹³C{¹H} NMR (in CD₂Cl₂): δ 7.6 (s, CH₂/CH₃), 107.8 (s, C-4), 121.1 (q, ¹*J*_{C-F} = 269.9 Hz, CF₃), 138.4 (br q, ²*J*_{C-F} = 36 Hz, C-3 & C-5), 172.4 (br, CO). ATR-IR (single crystals, selected peak, cm⁻¹): 2106 (C≡O stretch).

[NEt₄][{[4-Cl-3,5-(CF₃)₂Pz]Cu(CO)}₄(μ₄-Cl)] (11): {[4-Cl-3,5-(CF₃)₂Pz]Cu}₃ (250 mg, 0.276 mmol) and NEt₄Cl (33.56 mg, 0.202 mmol) were dissolved in dichloromethane (~5 mL) in two different Schlenk flasks. Both the solutions were gently bubbled with CO before mixing together and then stirred for ~10 min. The reaction mixture was concentrated to ~4 mL with a stream of CO and cooled to -20 °C to obtain X-ray quality crystals. Yield: 86% (based on {[4-Cl-3,5-(CF₃)₂Pz]Cu}₃). Anal. calc. C₃₂H₂₀Cl₅Cu₄F₂₄N₉O₄: C, 25.94%; H, 1.36%; N, 8.51%. Found: C, 25.90%; H, 1.60%; N, 8.49%. ¹H NMR (in CD₂Cl₂): δ (ppm) 1.30 (t, *J* = 7.3 Hz, 12H, CH₃), 3.14 (q, *J* = 7.3 Hz, 8H, CH₂). ¹⁹F NMR (in CD₂Cl₂): δ (ppm) -60.45 (br). ¹³C{¹H} NMR (in CD₂Cl₂): δ (ppm) 8.0 (CH₂/CH₃), 108.4 (C-4), 120.2 (q, ¹*J*_{C-F} = 251.1 Hz, CF₃), 139.2 (br q, ²*J*_{C-F} = 37.2 Hz, C-3 & C-5), 172.6 (br, CO). ATR-IR (single crystals, selected peak, cm⁻¹): 2105 (C≡O stretch).

[[[4-Cl-3,5-(CF₃)₂Pz]Cu(CO)]₂(μ₂-CH₃CN)] (12): This molecule was obtained from a reaction of {[4-Cl-3,5-(CF₃)₂Pz]Cu}₃ with excess CO in dichloromethane containing small amount of acetonitrile. Colorless crystals were obtained at -27 °C. ¹H NMR (CDCl₃): δ (ppm) 2.12 (br s).

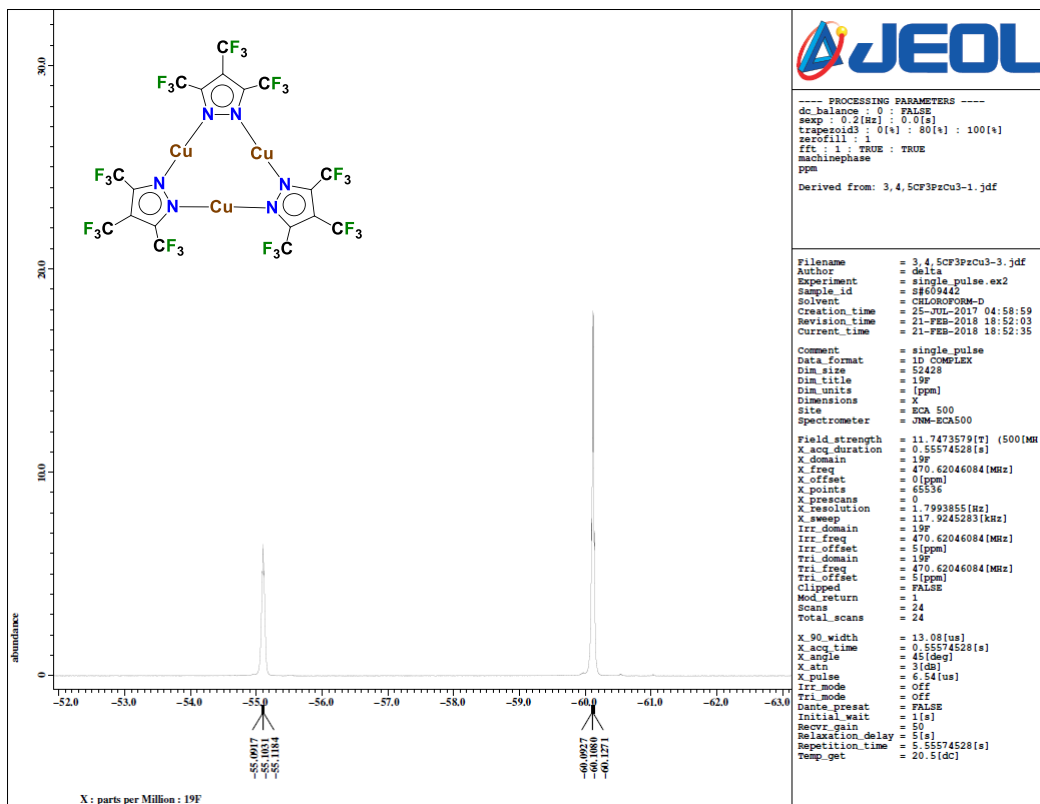
X-ray crystallographic data: A suitable crystal covered with a layer of hydrocarbon/ Paratone-N oil was selected and mounted on a Cryo-loop, and immediately placed in the low temperature nitrogen stream. The X-ray intensity data were measured at 100(2) K on a Bruker D8 Quest with a Photon 100 CMOS detector equipped with an Oxford Cryosystems 700 series cooler, a Triumph monochromator, and a Mo Kα fine-focus sealed tube (λ = 0.71073 Å). Intensity data were processed using the Bruker Apex2 or Apex3 program suite. Absorption corrections were applied by using SADABS. Initial atomic positions were located by direct methods using XT, and the structures of the compounds were refined by the least-squares method using SHELXL^{290,291} within Olex2²⁹² GUI. All the non-hydrogen atoms were refined anisotropically. Hydrogen atoms were included at calculated positions and refined riding on corresponding carbons. X-ray structural figures were generated using Olex2. CCDC [1894966–1894971](#) and [1895213](#) files contain the additional crystallographic data.

Computational details: DFT calculations were carried out using the ADF 2016 code,³³⁷ incorporating scalar corrections *via* the zeroth-order regular approximation

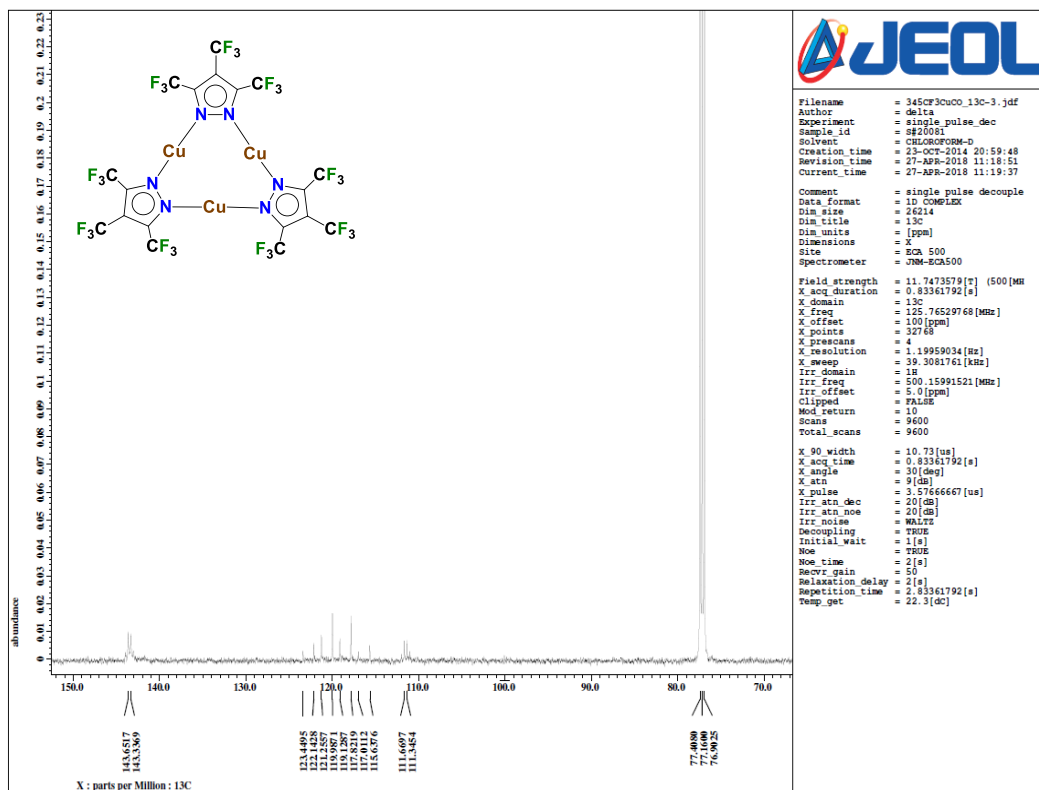
(ZORA) Hamiltonian.³³⁸ All calculations were performed using triple- ξ Slater quality basis set, plus two polarization functions (STO-TZ2P), within the generalized gradient approximation (GGA) according to the Becke–Perdew (BP86) exchange-correlation functional.^{339,340} The pair-wise Grimme correction (D3)³⁴¹ and Becke–Johnson damping functions³⁴² were taken into account for the empirical dispersion correction to DFT (DFT-D), which accounts for the stabilizing dispersion interaction (ΔE_{disp}). To overcome basis set superposition error (BSSE), the counterpoise method was also employed. The frozen core approximation was applied up to the [2p] core electrons for Cu and Cl, [1s] for C, N and O, and [3p] for Br, leaving the remaining electrons to be treated variationally. Geometry optimizations were performed without any symmetry restrain, via the analytical energy gradient method implemented by Versluis and Ziegler³⁴³ followed by the respective vibrational analysis obtained from analytical second derivatives. Calculated ν_{CO} stretching values were referenced to free $\bar{\nu}_{\text{CO}}$ 2143 cm^{-1} . The use of energy decomposition analysis^{277,278} allows to account for the relevant terms contributing to the overall interaction energy, which further provides a rationalization of the inclusion complexes formation. ^{13}C -NMR were obtained at the BP86-D3 optimized geometries by using all electron TZ2P basis set within the OPBE functional, which offers a good performance for NMR properties calculations.³⁴⁴ The calculated ^{13}C chemical shifts were references to tetramethylsilane (TMS).

Appendix A

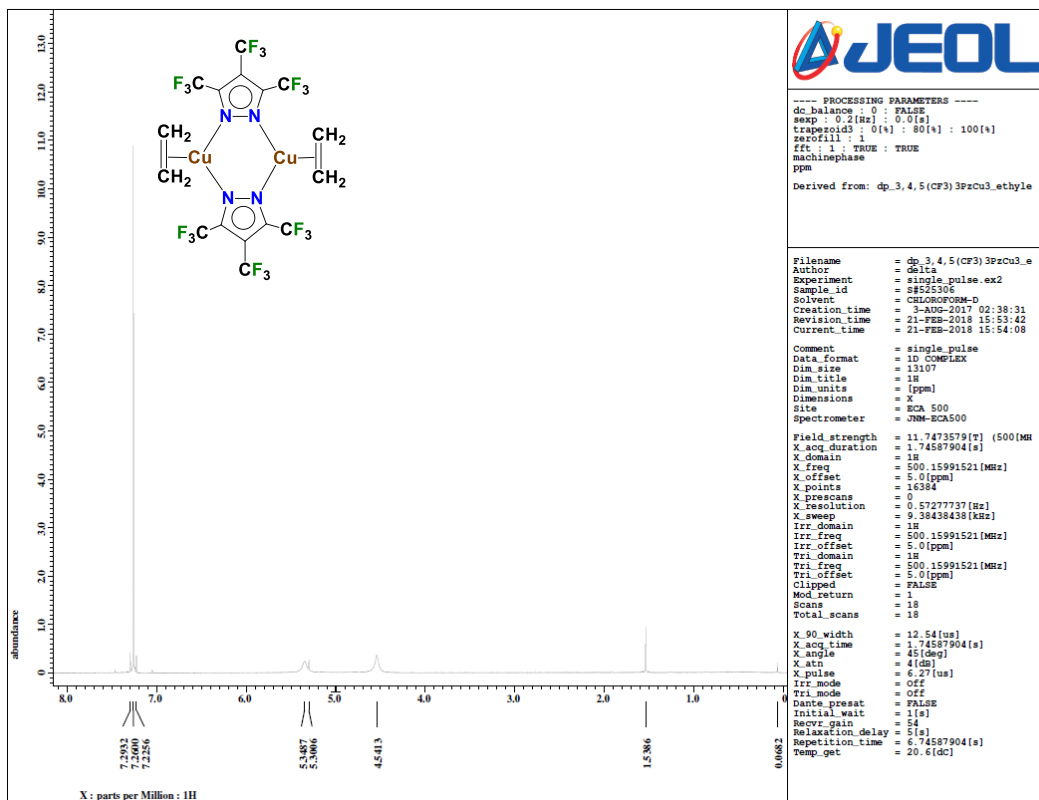
Spectroscopic data of chapter 2



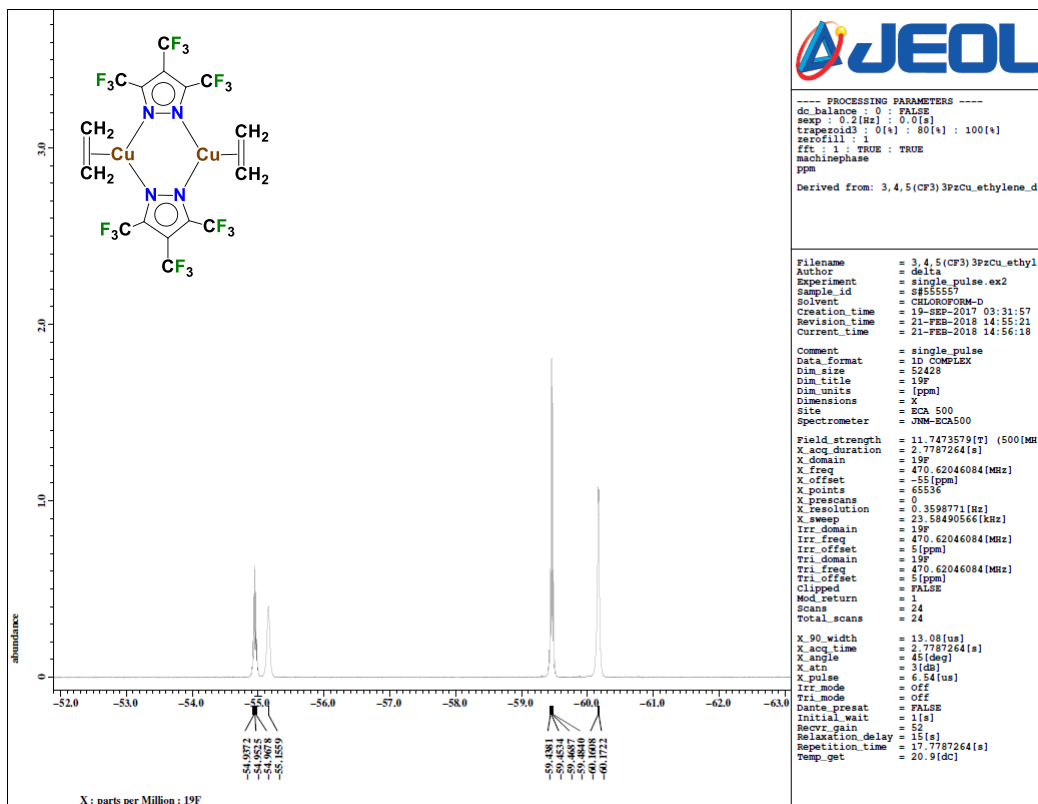
^{19}F NMR spectrum of $[(3,4,5-(CF_3)_3Pz)Cu]_3$ ($[Cu_3]$) in $CDCl_3$ at the room temperature.



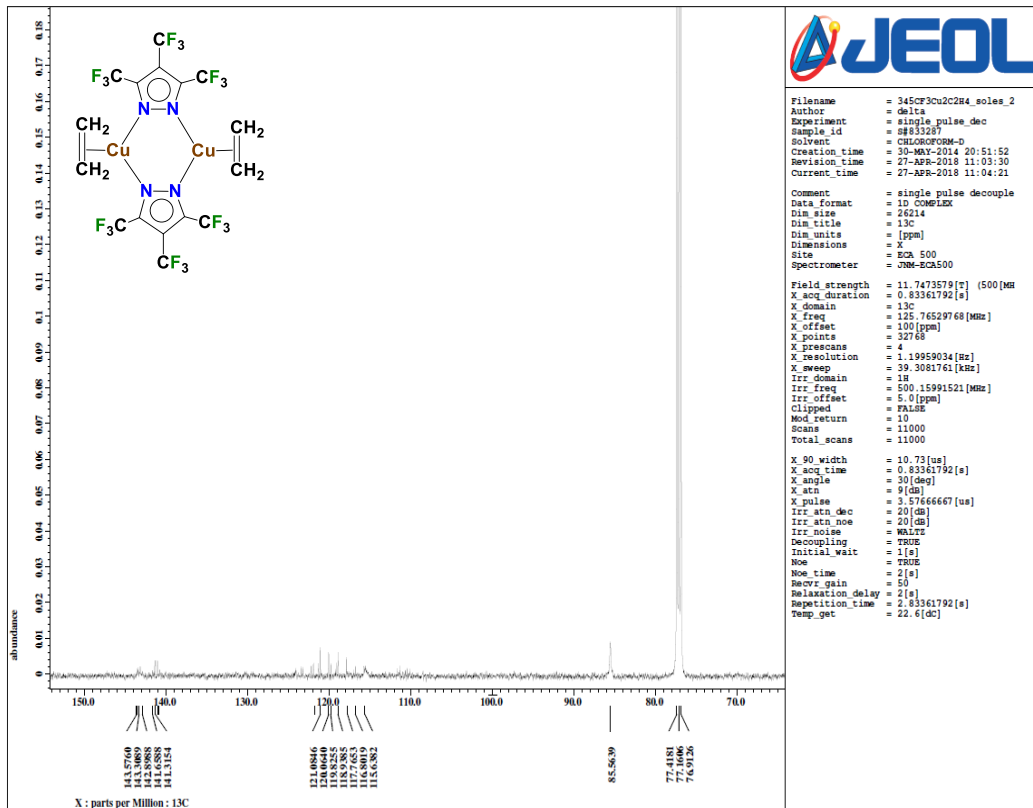
$^{13}\text{C}\{^1\text{H}\}$ NMR spectrum of $[(3,4,5\text{-}(\text{CF}_3)_3\text{Pz})\text{Cu}]_3$ ($[\text{Cu}_3]$) in CDCl_3 at the room temperature.



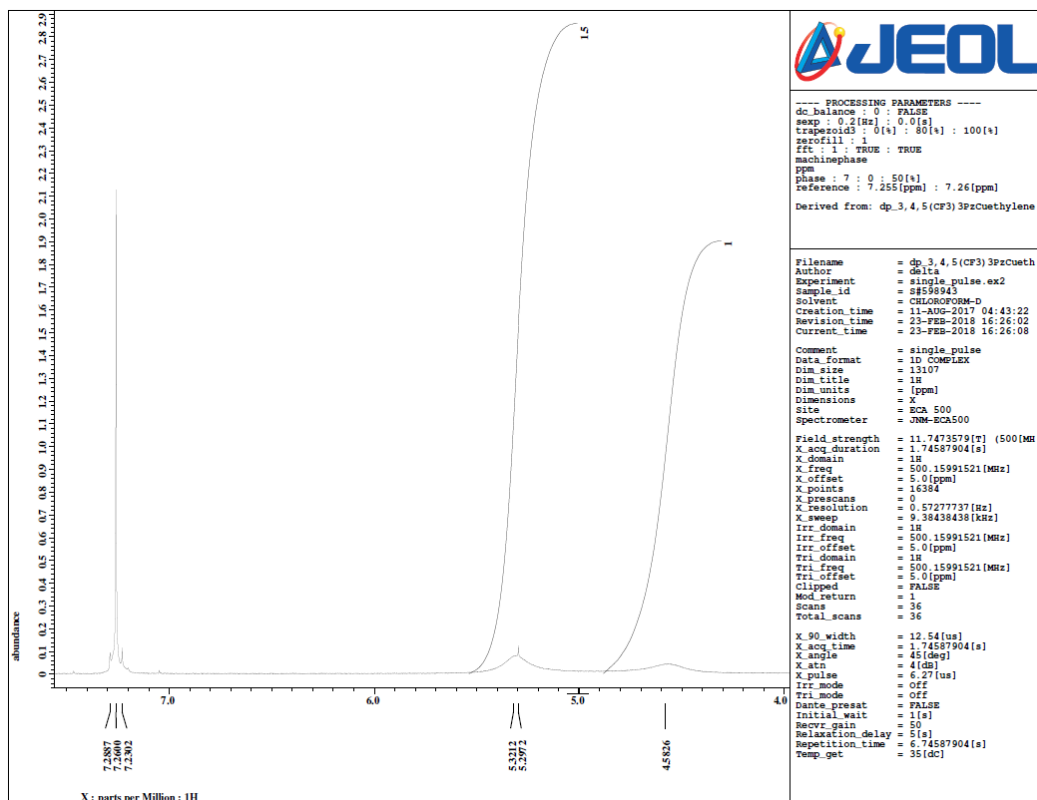
1H NMR spectrum of $[(3,4,5-(CF_3)_3Pz)Cu(C_2H_4)]_2$ ($[Cu_2 \cdot (C_2H_4)_2]$) in $CDCl_3$ at the room temperature. This spectrum also shows presence of free ethylene resulting from the disproportionation of $[Cu_2 \cdot (C_2H_4)_2]$ to $[Cu_3]$ and free ethylene. Peak at 4.54 ppm is the signal corresponding to coordinated ethylene while 5.34 ppm peak is the signal of free ethylene.



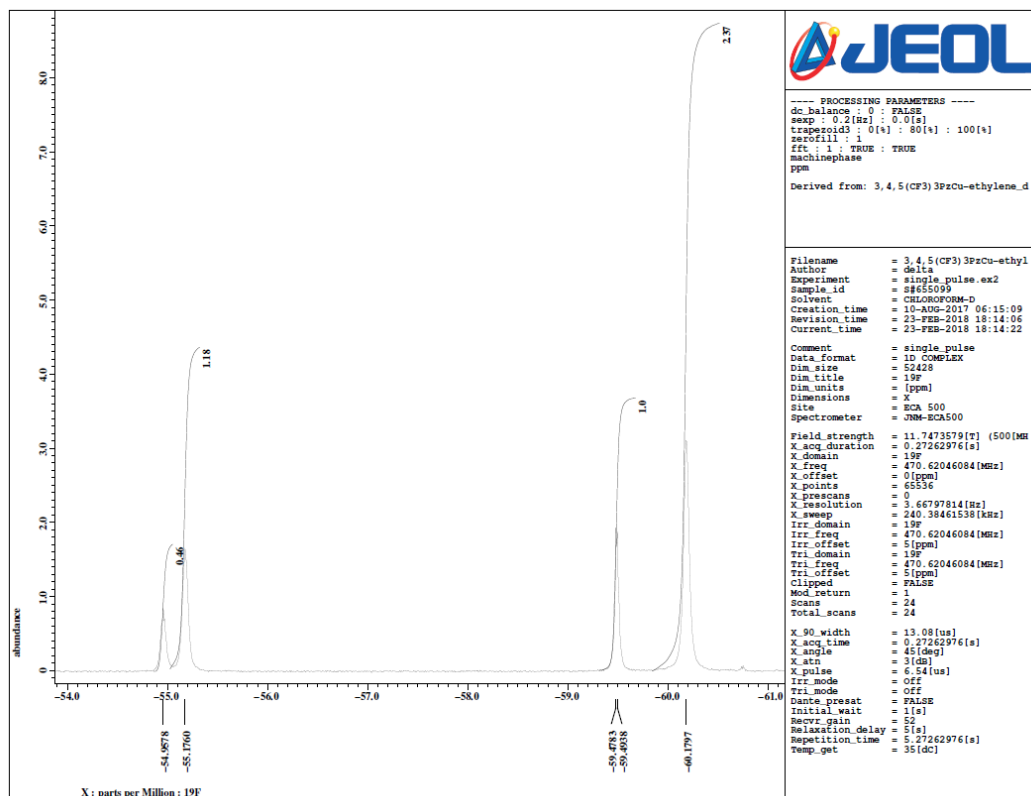
^{19}F NMR spectrum of $[(3,4,5\text{-(CF}_3)_3\text{Pz)Cu(C}_2\text{H}_4)]_2$ ($[\text{Cu}_2\bullet(\text{C}_2\text{H}_4)_2]$) in CDCl_3 at the room temperature. This spectrum also shows presence of $[\text{Cu}_3]$ resulting from the disproportionation of $[\text{Cu}_2\bullet(\text{C}_2\text{H}_4)_2]$ to $[\text{Cu}_3]$ and free ethylene. Peaks at -54.95 ppm and -59.45 ppm are the signals corresponding to $[\text{Cu}_2\bullet(\text{C}_2\text{H}_4)_2]$ while peaks at -55.15 ppm and -60.17 ppm corresponds to $[\text{Cu}_3]$.



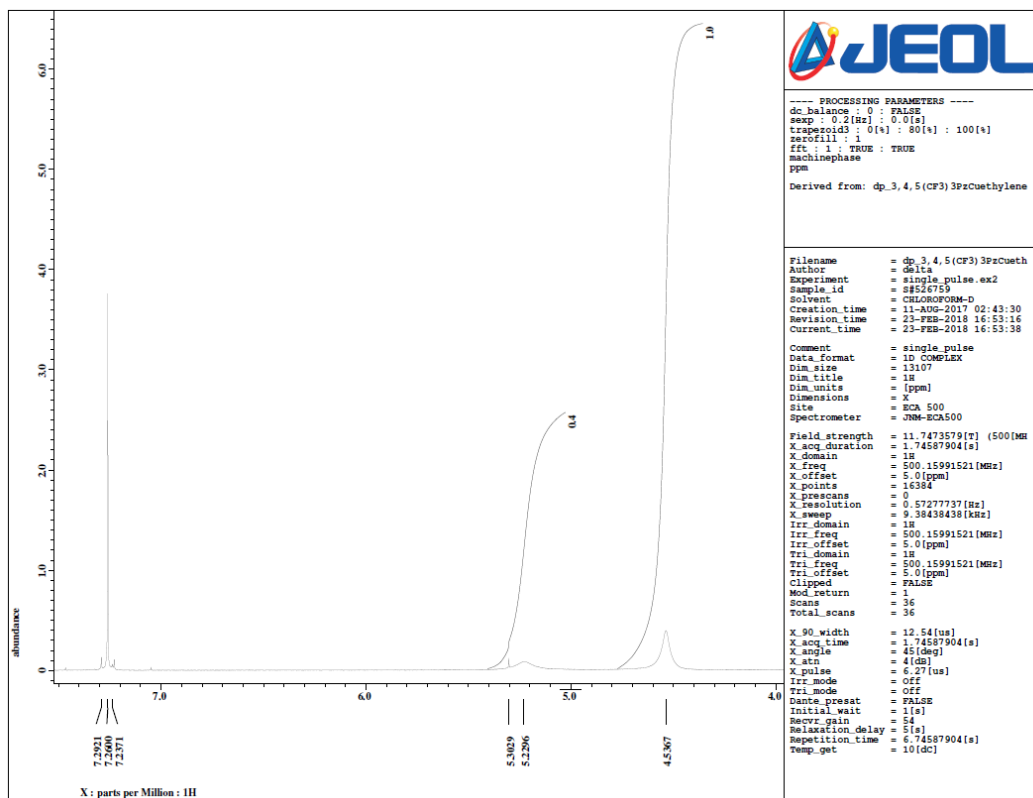
$^{13}\text{C}\{^1\text{H}\}$ NMR spectrum of $[(3,4,5\text{-}(\text{CF}_3)_3\text{Pz})\text{Cu}(\text{C}_2\text{H}_4)_2]$ ($[\text{Cu}_2\bullet(\text{C}_2\text{H}_4)_2]$) in CDCl_3 at the room temperature. This spectrum also shows presence of $[\text{Cu}_3]$ resulting from the disproportionation of $[\text{Cu}_2\bullet(\text{C}_2\text{H}_4)_2]$ to $[\text{Cu}_3]$ and free ethylene.



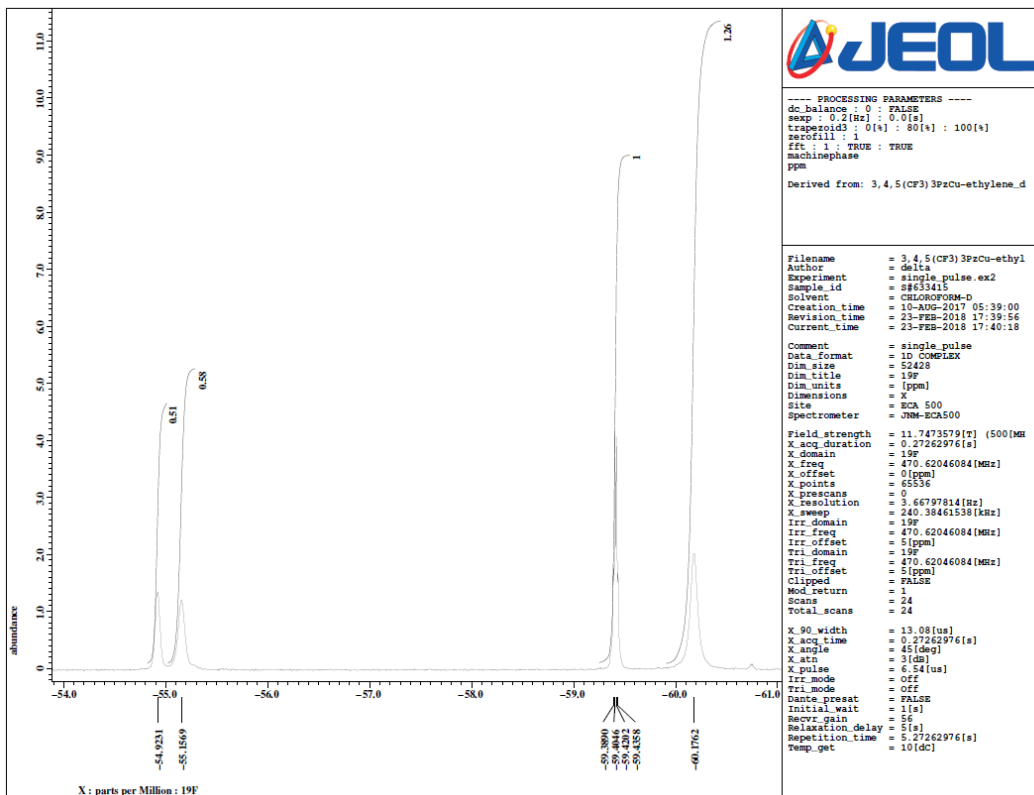
^1H NMR spectrum of $[(3,4,5\text{-(CF}_3)_3\text{Pz)Cu(C}_2\text{H}_4)]_2$ ($[\text{Cu}_2\bullet(\text{C}_2\text{H}_4)_2]$) in CDCl_3 at the $35\text{ }^\circ\text{C}$. At higher temperature the reaction proceeds towards dissociation of $[\text{Cu}_2\bullet(\text{C}_2\text{H}_4)_2]$ to $[\text{Cu}_3]$ and free ethylene. Thus, signal for coordinated ethylene is obtained as a broad peak at 4.58 ppm while signal for free ethylene is obtained as comparatively sharper peak at 5.32 ppm.



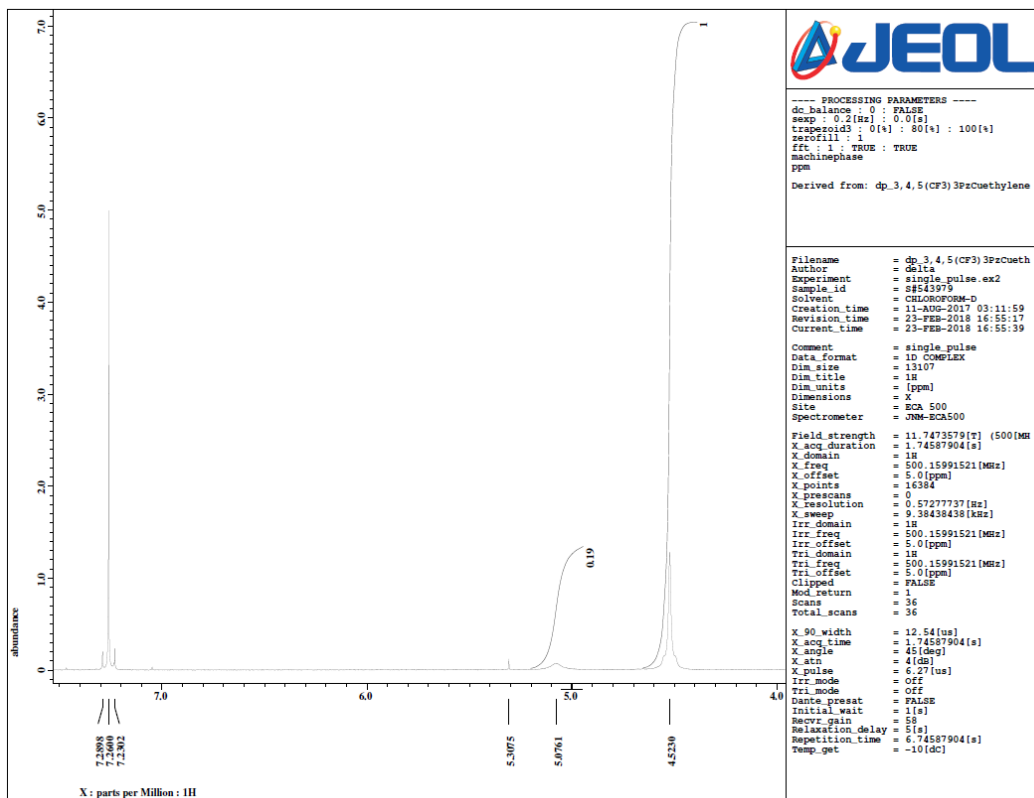
^{19}F NMR spectrum of $[(3,4,5\text{-(CF}_3)_3\text{Pz)Cu(C}_2\text{H}_4)]_2$ ($[\text{Cu}_2\bullet(\text{C}_2\text{H}_4)_2]$) in CDCl_3 at the $35\text{ }^\circ\text{C}$. At higher temperature the reaction proceeds towards dissociation of $[\text{Cu}_2\bullet(\text{C}_2\text{H}_4)_2]$ to $[\text{Cu}_3]$ and free ethylene. Peaks at -54.96 ppm and -59.48 ppm are the signals corresponding to $[\text{Cu}_2\bullet(\text{C}_2\text{H}_4)_2]$ while peaks at -55.18 ppm and -60.18 ppm corresponds to $[\text{Cu}_3]$.



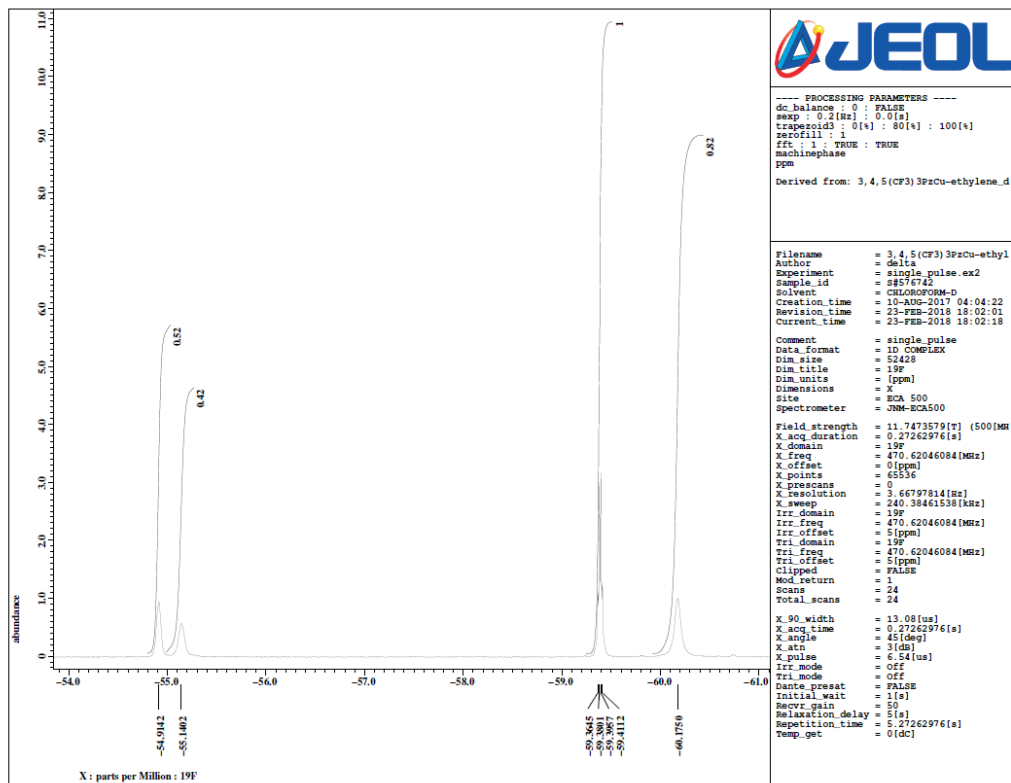
^1H NMR spectrum of $[(3,4,5\text{-}(\text{CF}_3)_3\text{Pz})\text{Cu}(\text{C}_2\text{H}_4)]_2$ ($[\text{Cu}_2\bullet(\text{C}_2\text{H}_4)_2]$) in CDCl_3 at the 10°C . Peak at 4.54 ppm corresponds to coordinated ethylene while 5.23 ppm peak is the signal of free ethylene.



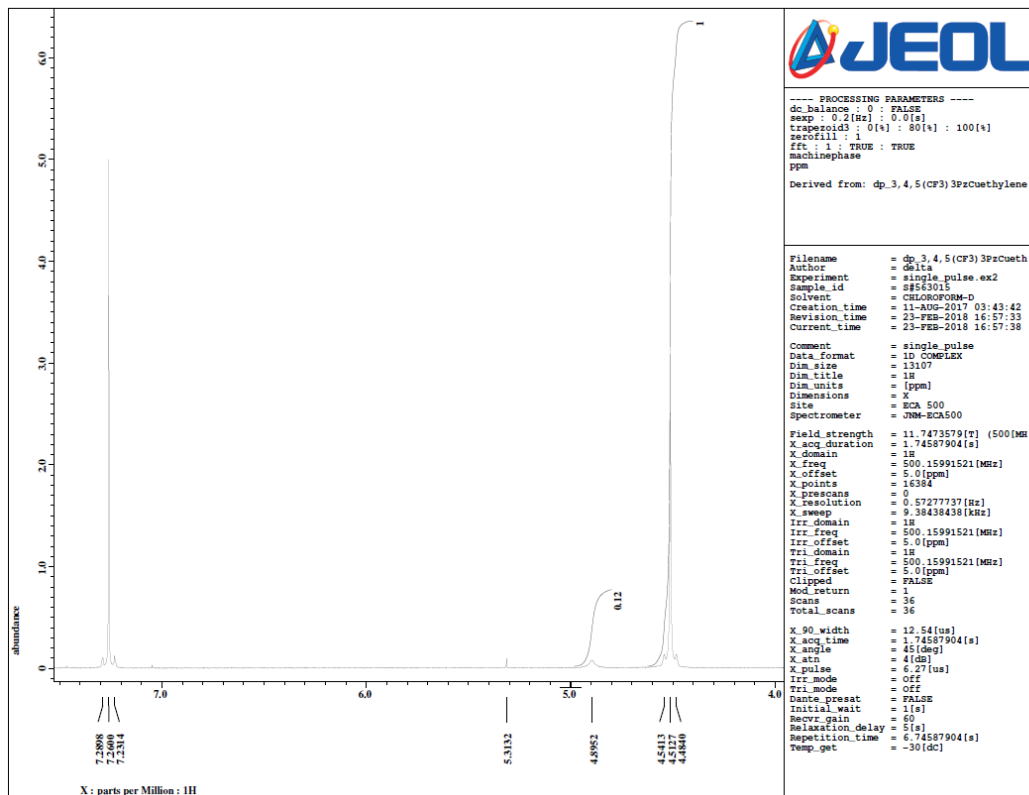
^{19}F NMR spectrum of $[(3,4,5\text{-(CF}_3)_3\text{Pz)Cu(C}_2\text{H}_4)]_2$ ($[\text{Cu}_2\bullet(\text{C}_2\text{H}_4)_2]$) in CDCl_3 at the 10 °C. Peaks at -54.92 ppm and -59.41 ppm are the signals corresponding to $[\text{Cu}_2\bullet(\text{C}_2\text{H}_4)_2]$ while peaks at -55.17 ppm and -60.18 ppm corresponds to $[\text{Cu}_3]$.



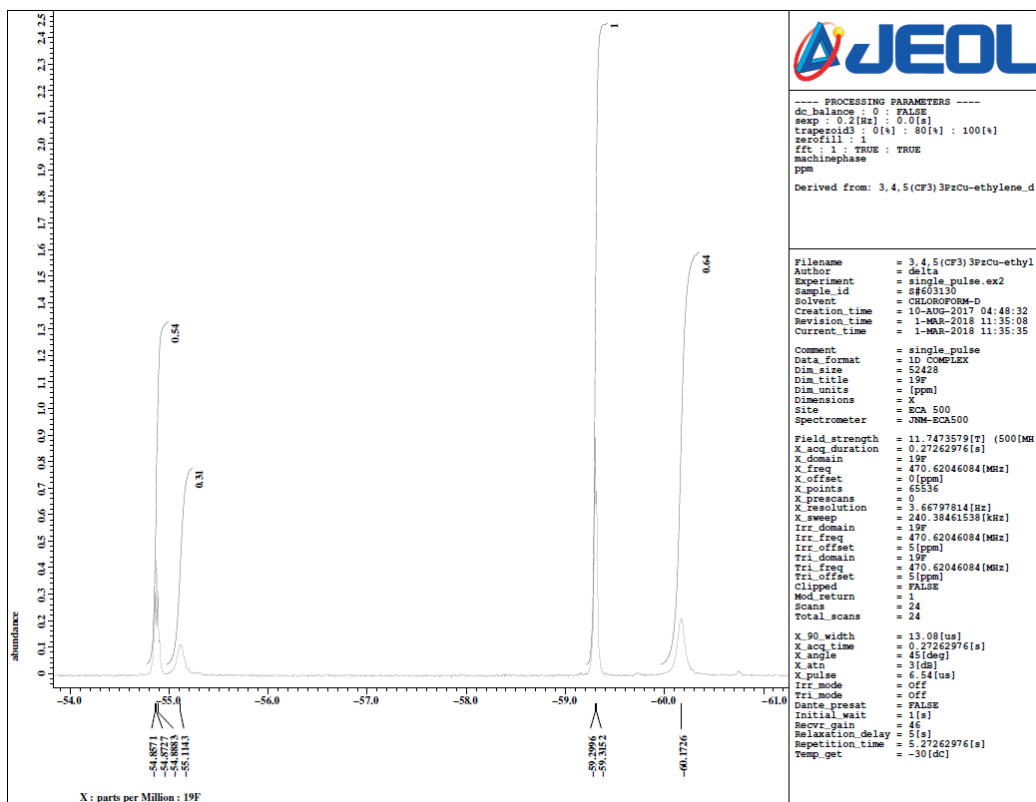
^1H NMR spectrum of $[(3,4,5\text{-(CF}_3)_3\text{Pz)Cu(C}_2\text{H}_4)]_2$ ($[\text{Cu}_2\bullet(\text{C}_2\text{H}_4)_2]$) in CDCl_3 at the $-10\text{ }^\circ\text{C}$. Peak at 4.52 ppm corresponds to coordinated ethylene while 5.08 ppm peak is the signal of free ethylene.



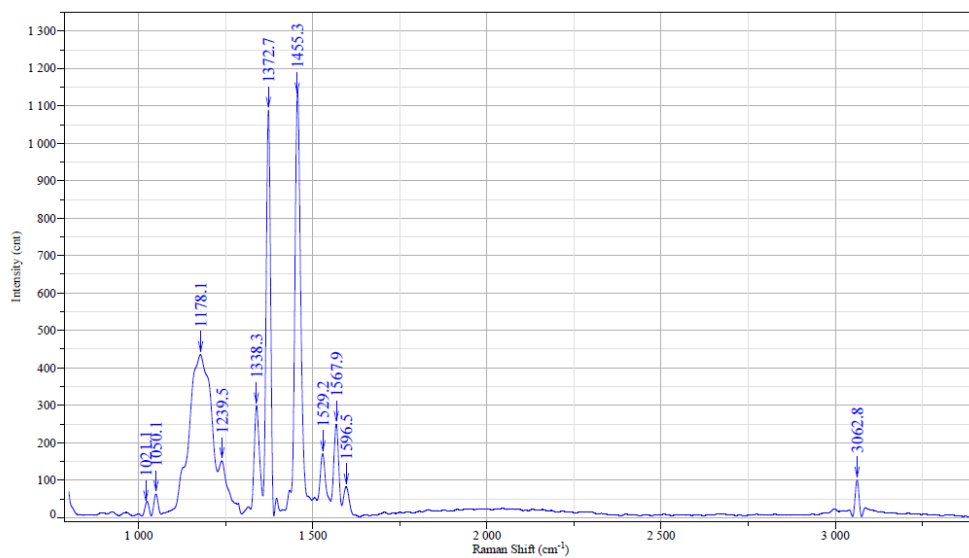
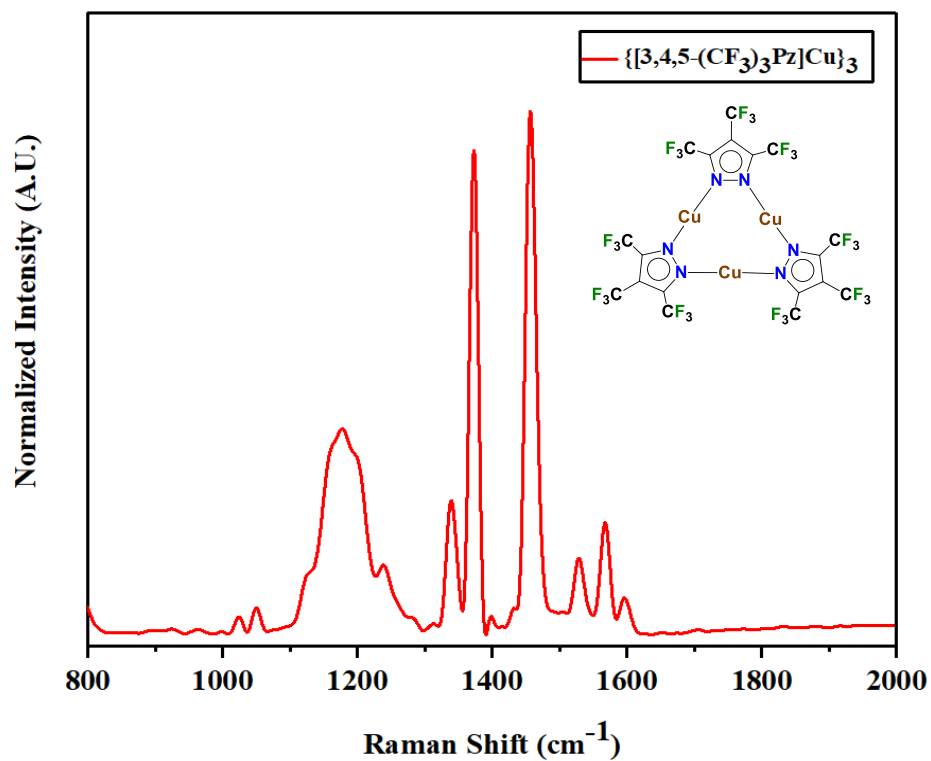
¹⁹F NMR spectrum of [(3,4,5-(CF₃)₃Pz)Cu(C₂H₄)₂] ([Cu₂•(C₂H₄)₂]) in CDCl₃ at the -10 °C. Peaks at -54.91 ppm and -59.39 ppm are the signals corresponding to [Cu₂•(C₂H₄)₂] while peaks at -55.14 ppm and -60.18 ppm corresponds to [Cu₃].



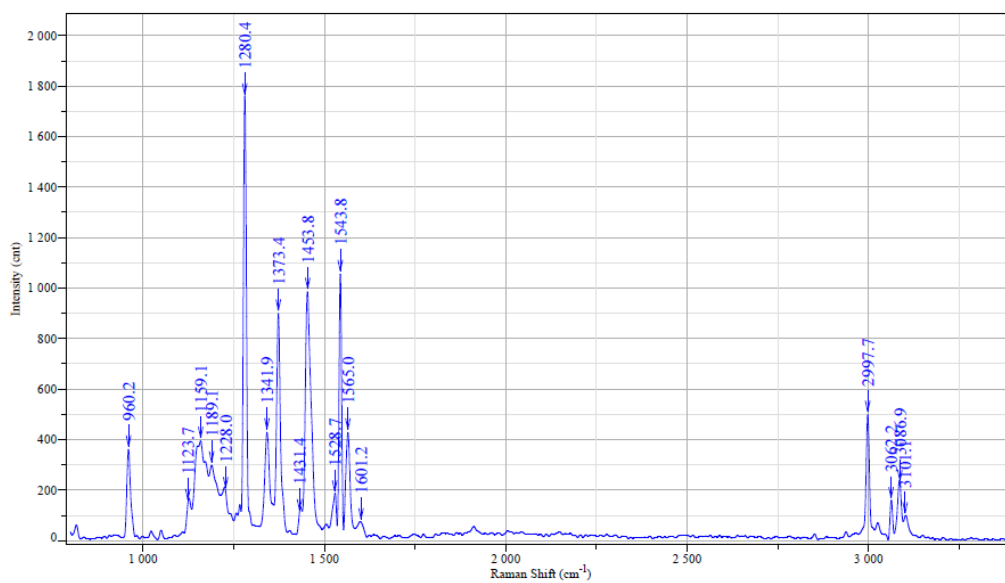
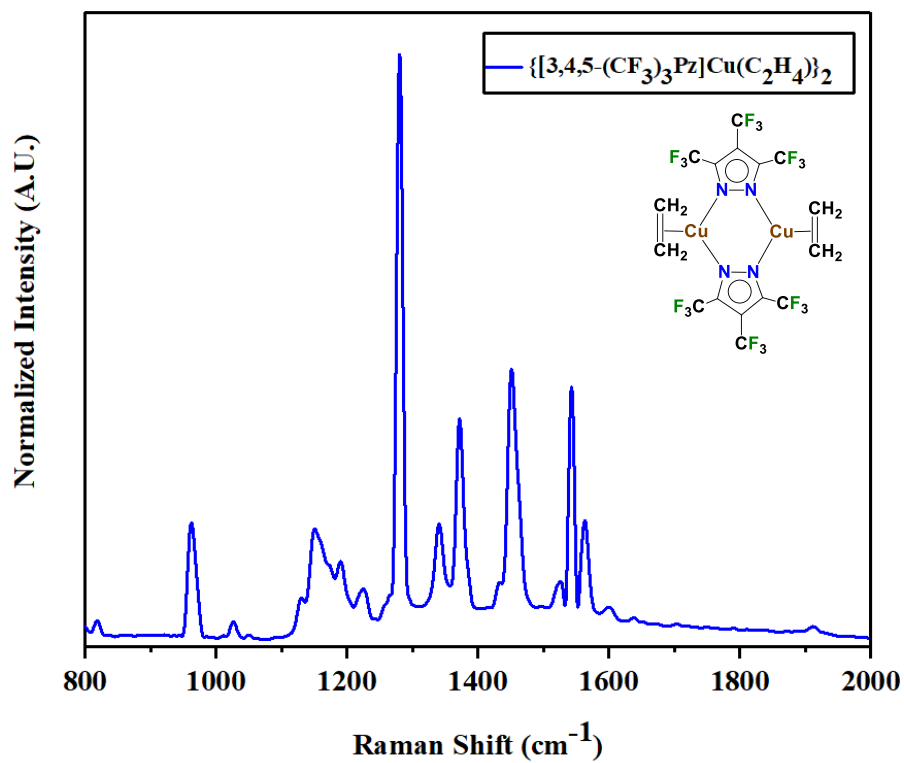
^1H NMR spectrum of $[(3,4,5\text{-(CF}_3)_3\text{Pz)Cu(C}_2\text{H}_4)]_2$ ($[\text{Cu}_2\bullet(\text{C}_2\text{H}_4)_2]$) in CDCl_3 at the $-30\text{ }^\circ\text{C}$. At lower temperature the reaction proceeds towards $[\text{Cu}_2\bullet(\text{C}_2\text{H}_4)_2]$ formation, thus signal for bound ethylene is obtained as a sharp peak at 4.90 ppm while signal for free ethylene is obtained as a broad signal at 4.51 ppm.



^{19}F NMR spectrum of $[(3,4,5\text{-(CF}_3)_3\text{Pz)Cu(C}_2\text{H}_4)]_2$ ($[\text{Cu}_2\bullet(\text{C}_2\text{H}_4)_2]$) in CDCl_3 at the $-30\text{ }^\circ\text{C}$. At lower temperature, the reaction proceed towards $[\text{Cu}_2\bullet(\text{C}_2\text{H}_4)_2]$ formation. Sharp peaks at -54.87 ppm and -59.30 ppm corresponds to $[\text{Cu}_2\bullet(\text{C}_2\text{H}_4)_2]$ while peaks at -55.11 ppm and -60.17 ppm corresponds to $[\text{Cu}_3]$.



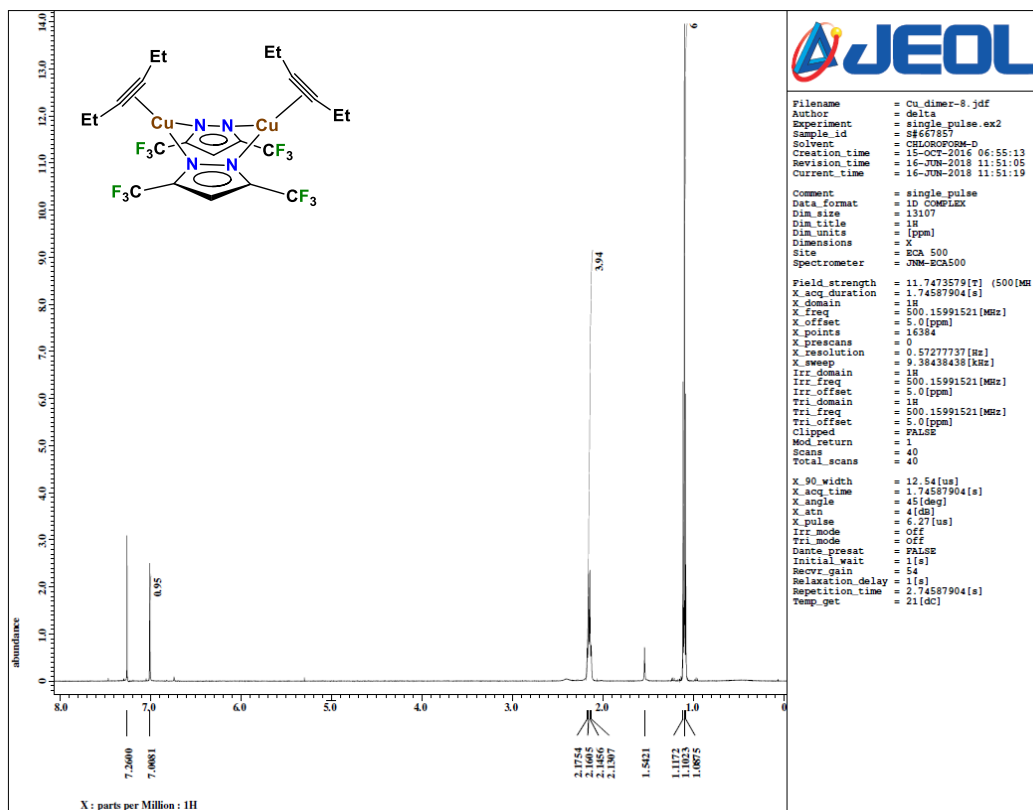
Raman spectrum of solid $[(3,4,5-(\text{CF}_3)_3\text{Pz})\text{Cu}]_3$ ($[\text{Cu}_3]$)



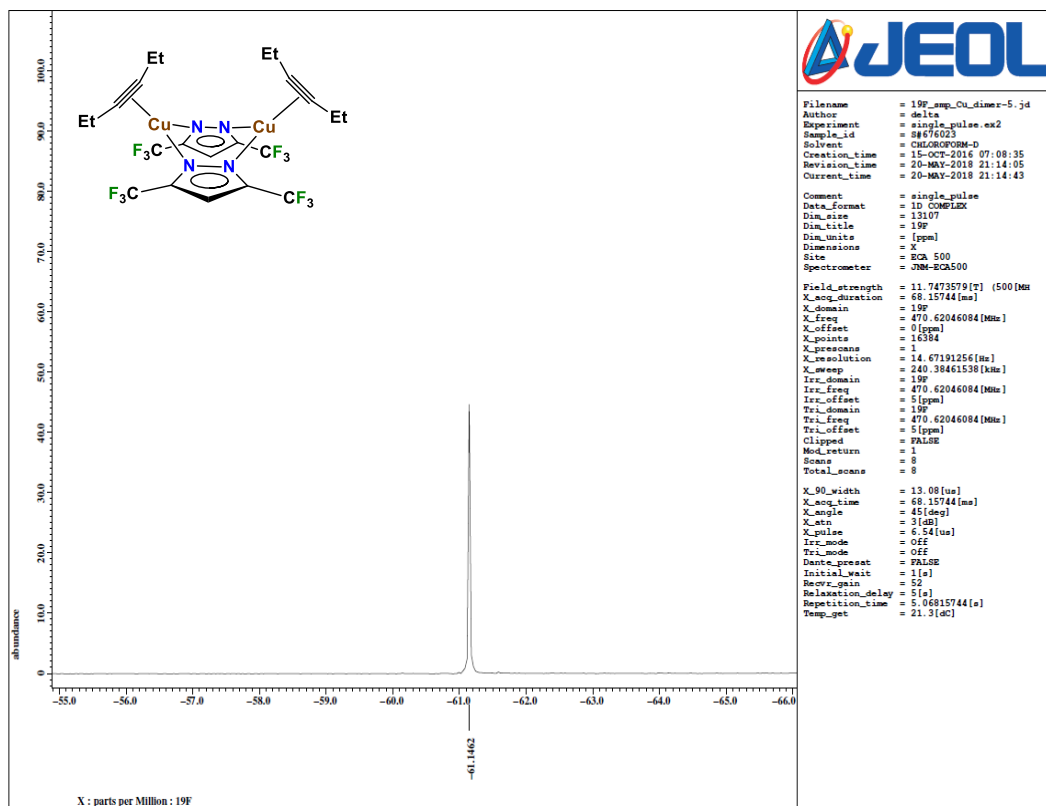
Raman spectrum of solid $[(3,4,5-(\text{CF}_3)_3\text{Pz})\text{Cu}(\text{C}_2\text{H}_4)]_2$ ($[\text{Cu}\bullet(\text{C}_2\text{H}_4)]_2$)

Appendix B

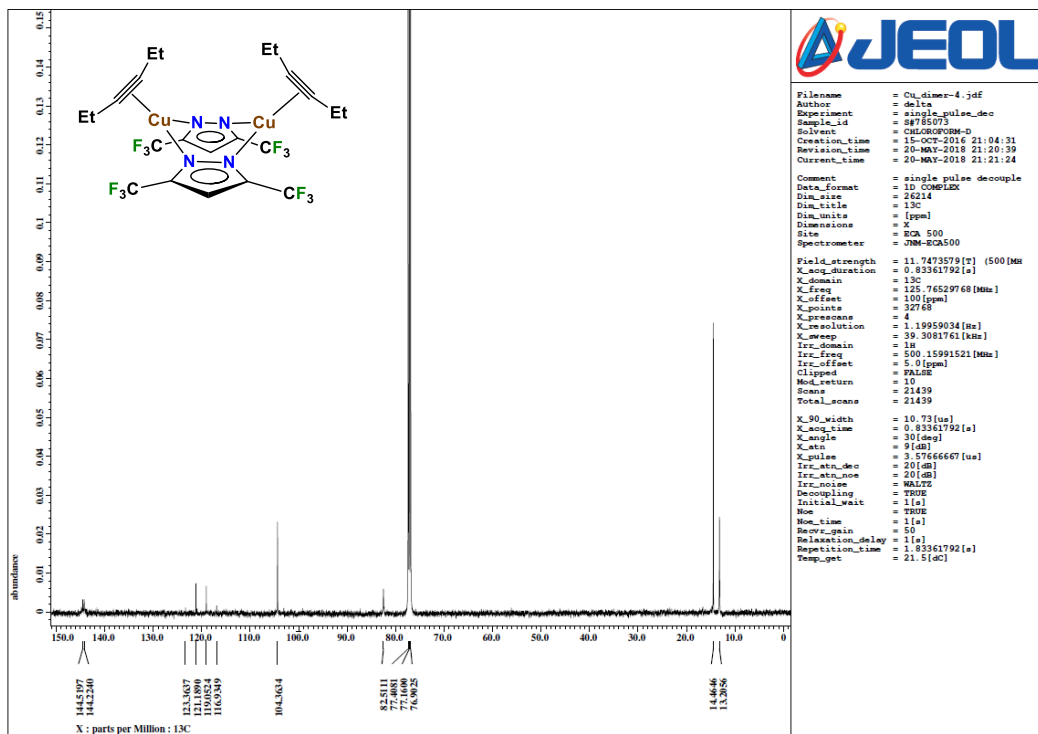
Spectroscopic data of Part 3.1 from chapter 3



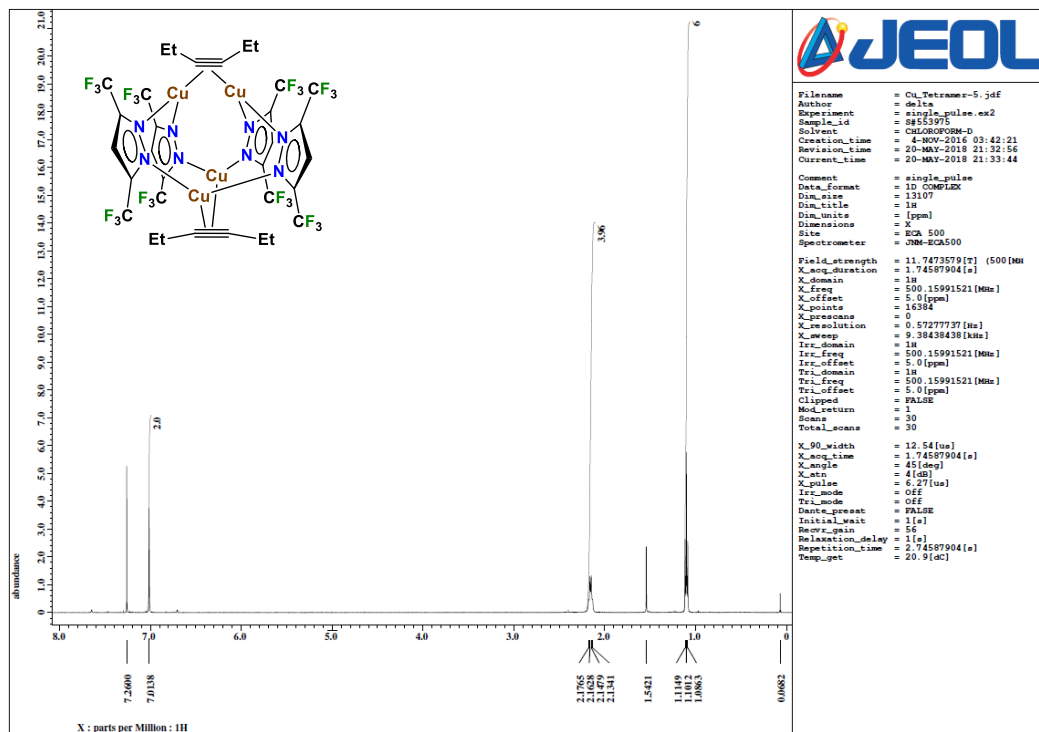
^1H NMR spectrum of $\text{Cu}_2(\mu\text{-}[3,5\text{-}(\text{CF}_3)_2\text{Pz}])_2(\text{EtC}\equiv\text{CEt})_2$ (**1**) in CDCl_3 at the room temperature.



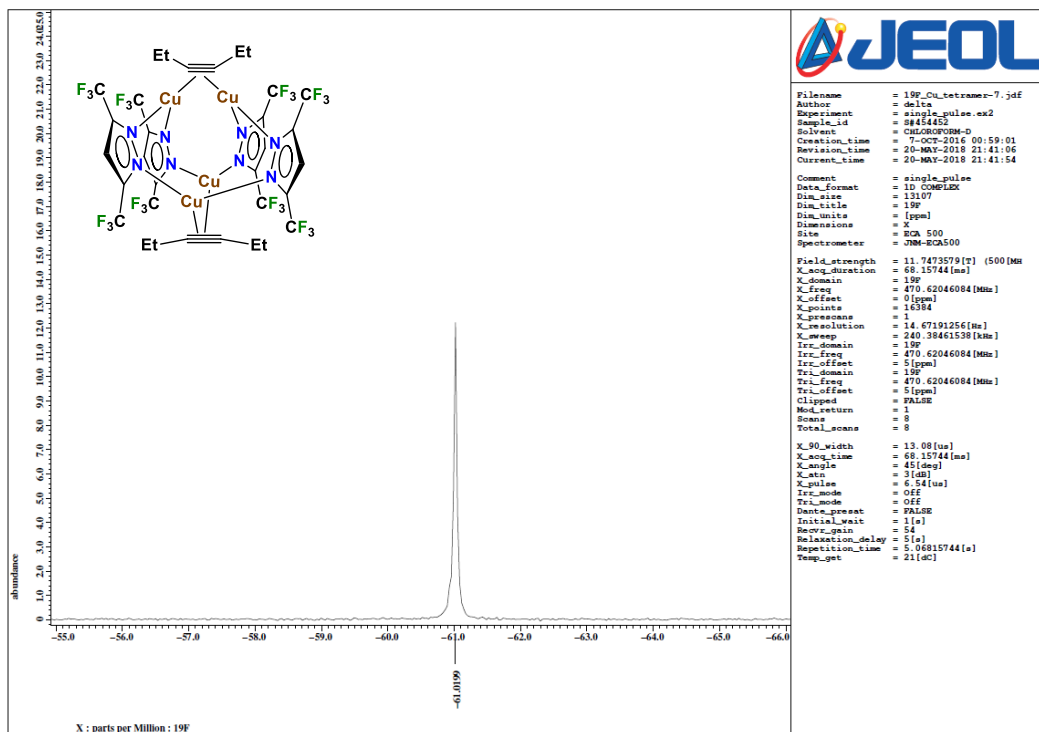
^{19}F NMR spectrum of $\text{Cu}_2(\mu\text{-}[3,5\text{-}(\text{CF}_3)_2\text{Pz}])_2(\text{EtC}\equiv\text{CEt})_2$ (**1**) in CDCl_3 at the room temperature.



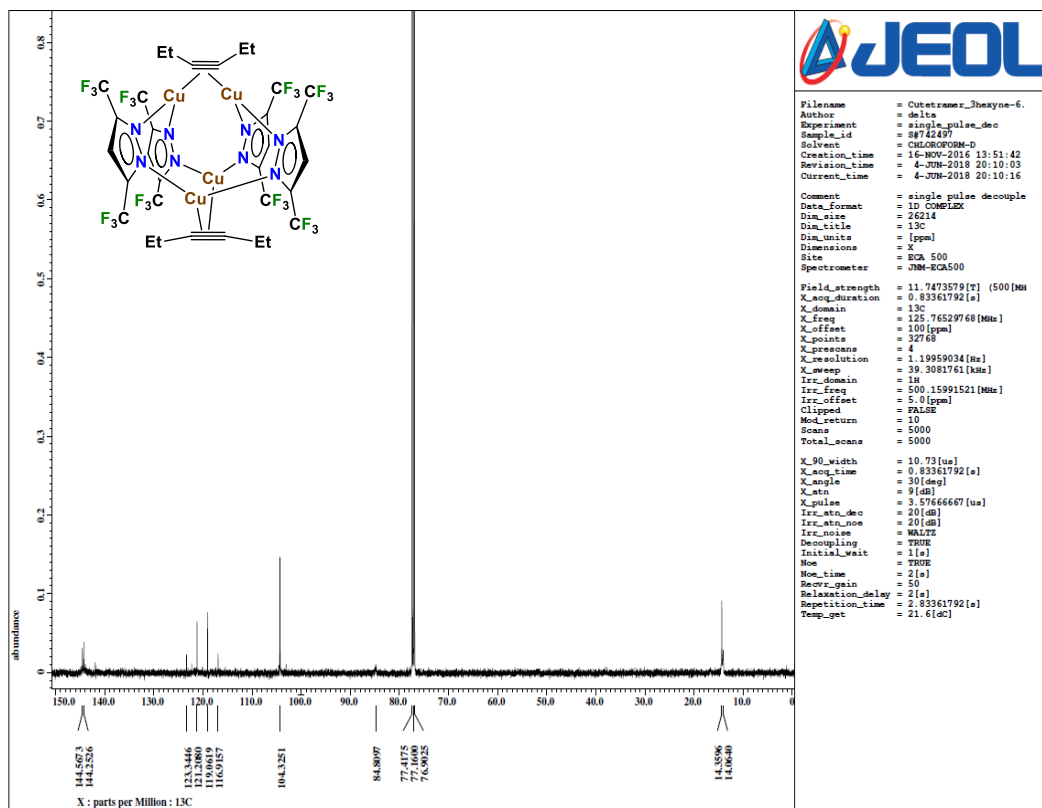
$^{13}\text{C}\{^1\text{H}\}$ NMR spectrum of $\text{Cu}_2(\mu\text{-}[3,5\text{-}(\text{CF}_3)_2\text{Pz}])_2(\text{EtC}\equiv\text{CEt})_2$ (**1**) in CDCl_3 at the room temperature.



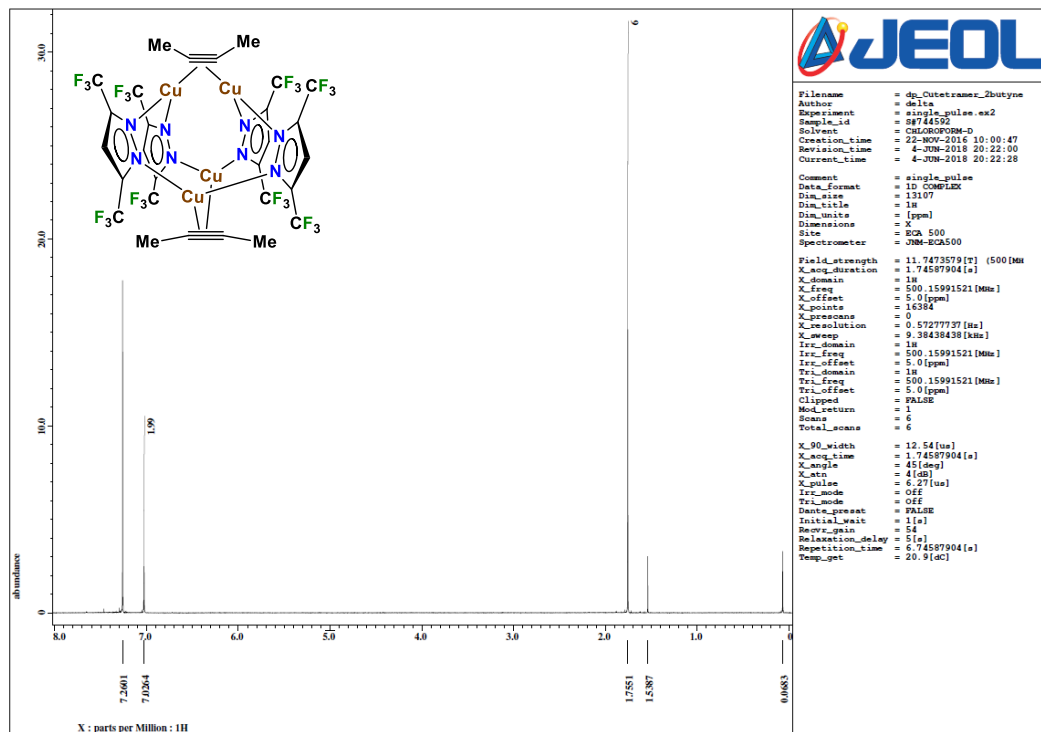
^1H NMR spectrum of $\text{Cu}_4(\mu\text{-}[3,5\text{-}(\text{CF}_3)_2\text{Pz}])_4(\mu\text{-EtC}\equiv\text{CEt})_2$ (**2**) in CDCl_3 at the room temperature.



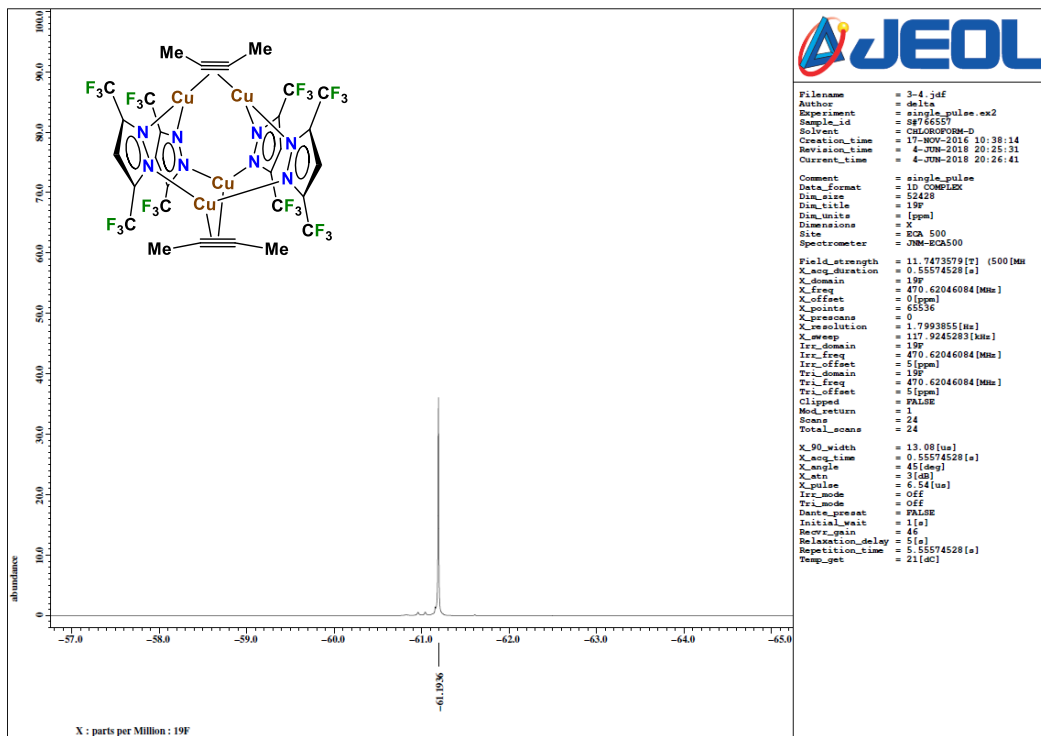
^{19}F NMR spectrum of $\text{Cu}_4(\mu\text{-[3,5-(CF}_3)_2\text{Pz]})_4(\mu\text{-EtC}\equiv\text{CEt})_2$ (2) in CDCl_3 at the room temperature.



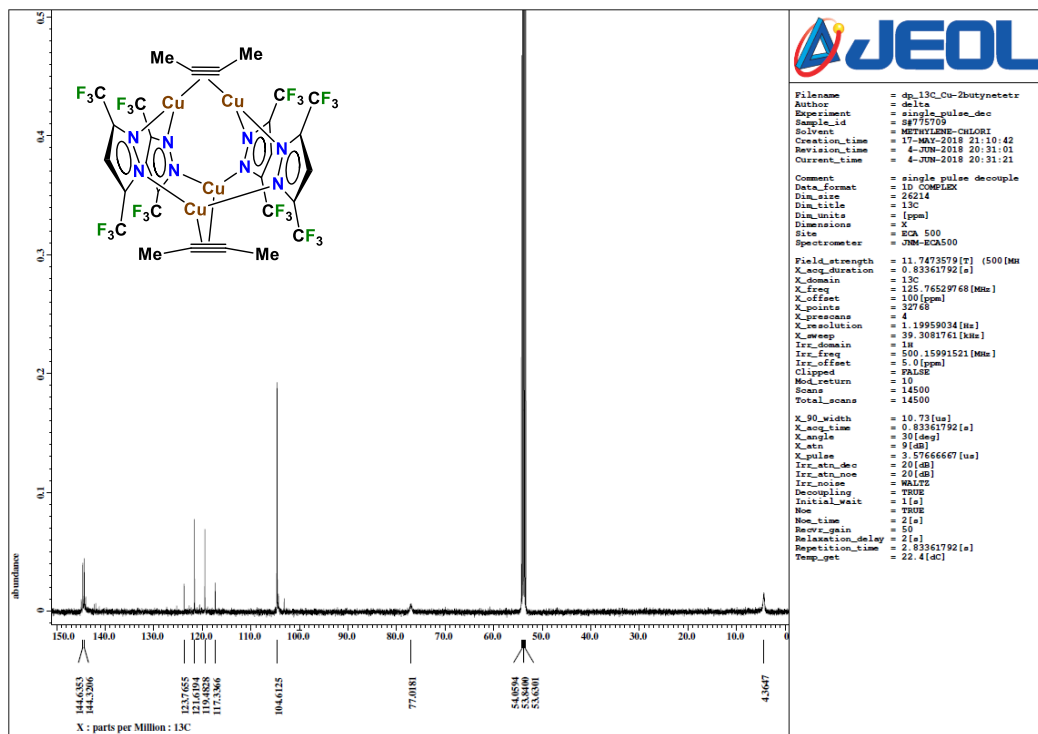
$^{13}\text{C}\{^1\text{H}\}$ NMR spectrum of $\text{Cu}_4(\mu\text{-[3,5-(CF}_3)_2\text{Pz]}_4)(\mu\text{-EtC}\equiv\text{CEt})_2$ (**2**) in CDCl_3 at the room temperature.



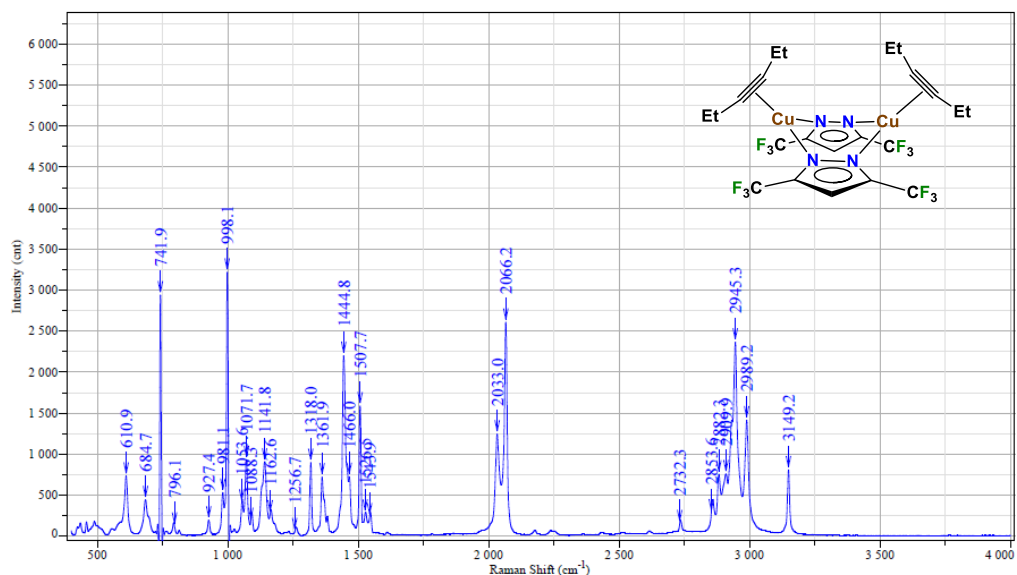
^1H NMR spectrum of $\text{Cu}_4(\mu\text{-}[3,5\text{-}(\text{CF}_3)_2\text{Pz}])_4(\mu\text{-MeC}\equiv\text{CMe})_2$ (**3**) in CDCl_3 at the room temperature.



^{19}F NMR spectrum of $\text{Cu}_4(\mu\text{-}[3,5\text{-}(\text{CF}_3)_2\text{Pz}])_4(\mu\text{-MeC}\equiv\text{CMe})_2$ (**3**) in CDCl_3 at the room temperature.

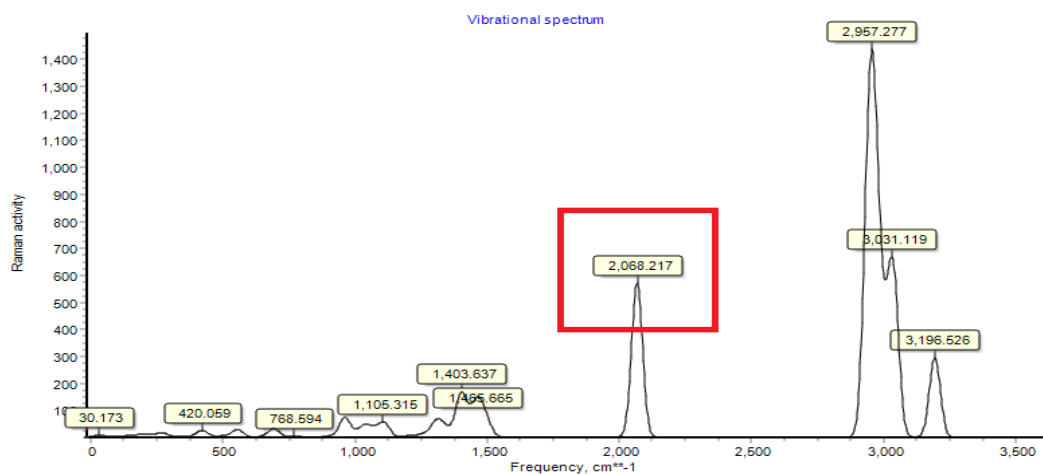


$^{13}\text{C}\{^1\text{H}\}$ NMR spectrum of $\text{Cu}_4(\mu\text{-}[3,5\text{-}(\text{CF}_3)_2\text{Pz}])_4(\mu\text{-MeC}\equiv\text{CMe})_2$ (**3**) in CD_2Cl_2 at the room temperature.

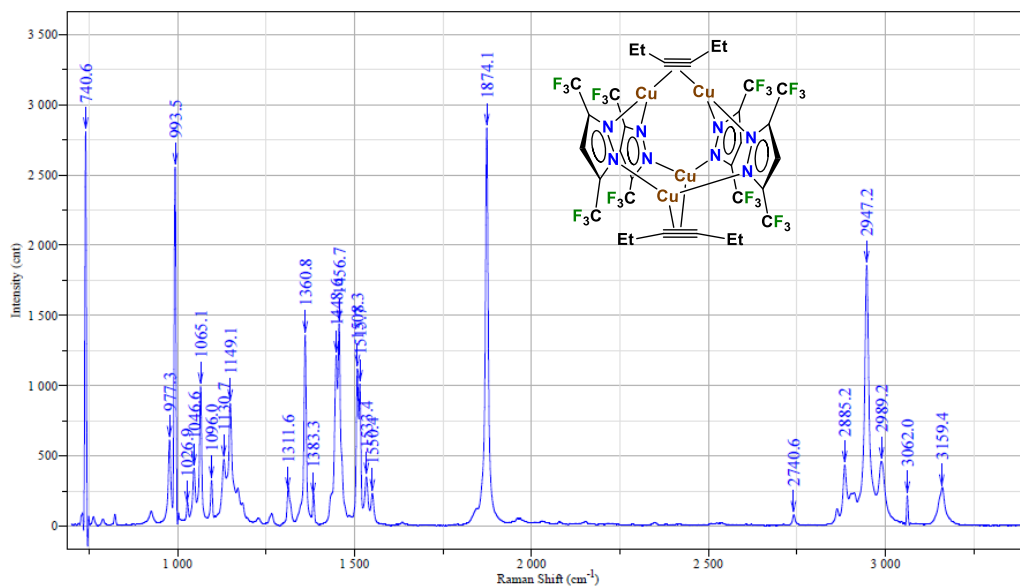


Exposition	10	Slit	100
Accumulation	5 x 6	Operator	Parasar
Laser	632.817	Sample	3,5(CF3)2PzCu-3hexynedi
Spectro	Multi	Remark	
Hole	200	Power	

HORIBAJOBIN YVON

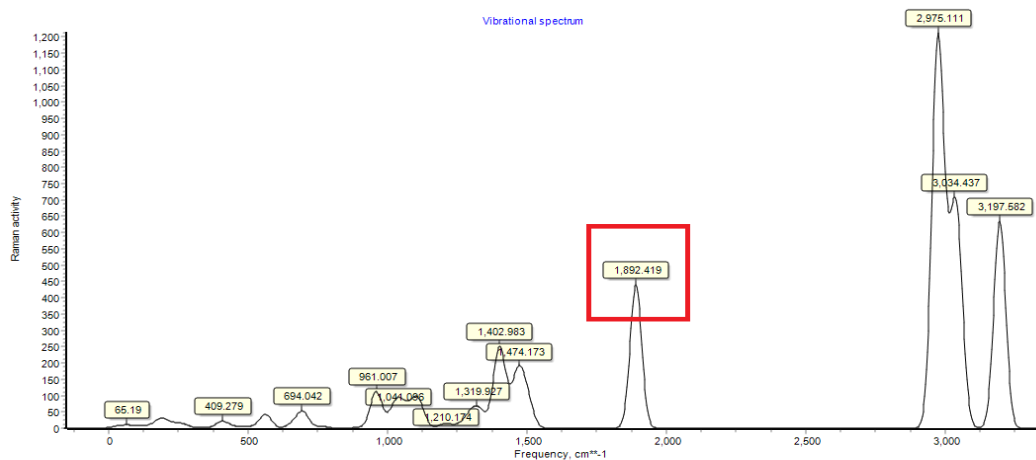


Raman spectrum of solid $\text{Cu}_2(\mu\text{-}[3,5\text{-}(\text{CF}_3)_2\text{Pz}])_2(\text{EtC}\equiv\text{CEt})_2$ (1) (Experimental-top, Computational-bottom); $\text{C}\equiv\text{C}$ triple bond frequency of 3-hexyne is given in the red square.

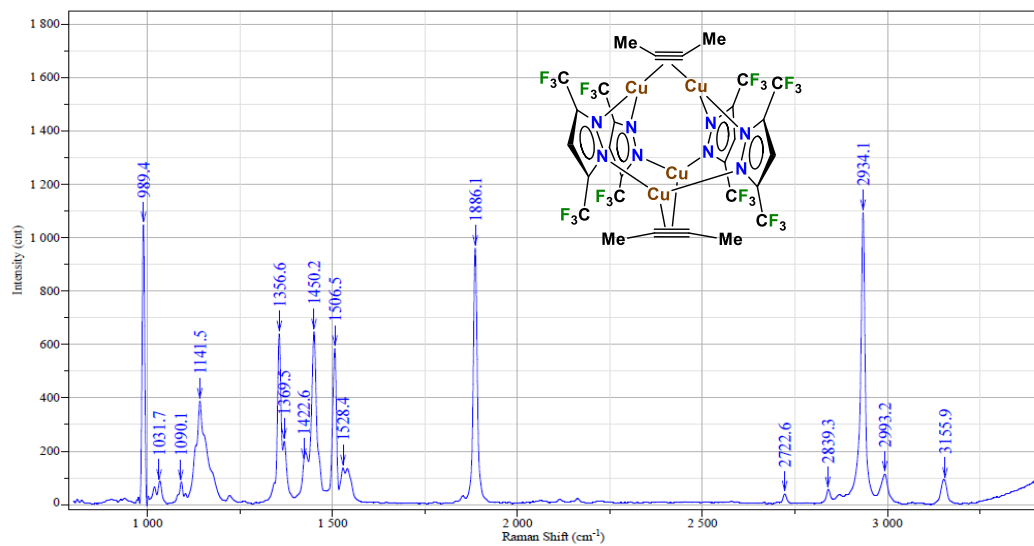


Exposition	10	Slit	100
Accumulation	10 x 4	Operator	Parasar
Laser	632.817	Sample	3,5(CF ₃) ₂ Pz ₂ Cu-3hexynetetra
Spectro	Multi	Remark	
Hole	200	Power	

HORIBA JOBIN YVON

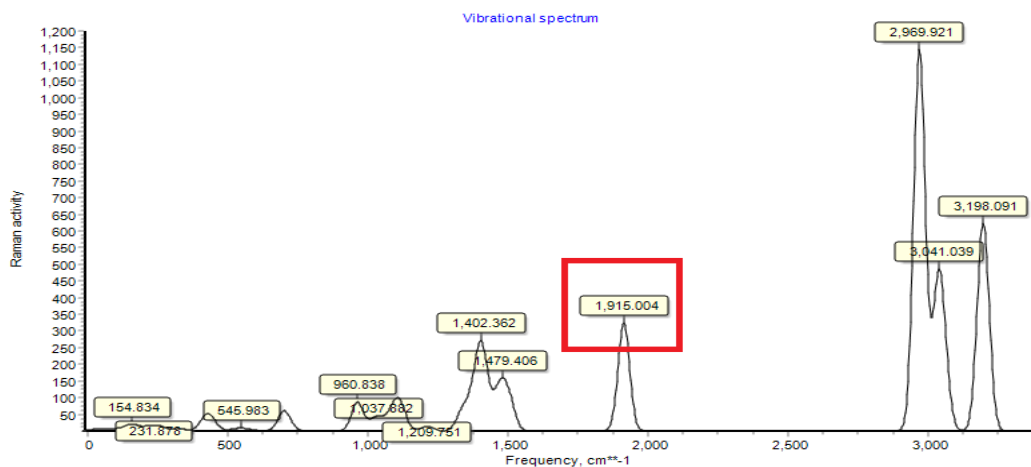


Raman spectrum of solid $\text{Cu}_4(\mu\text{-}[3,5\text{-(CF}_3)_2\text{Pz}])_4(\mu\text{-EtC}\equiv\text{CEt})_2$ (**2**).
(Experimental-top, Computational-bottom); C≡C triple bond frequency of 3-hexyne is given in the red square.



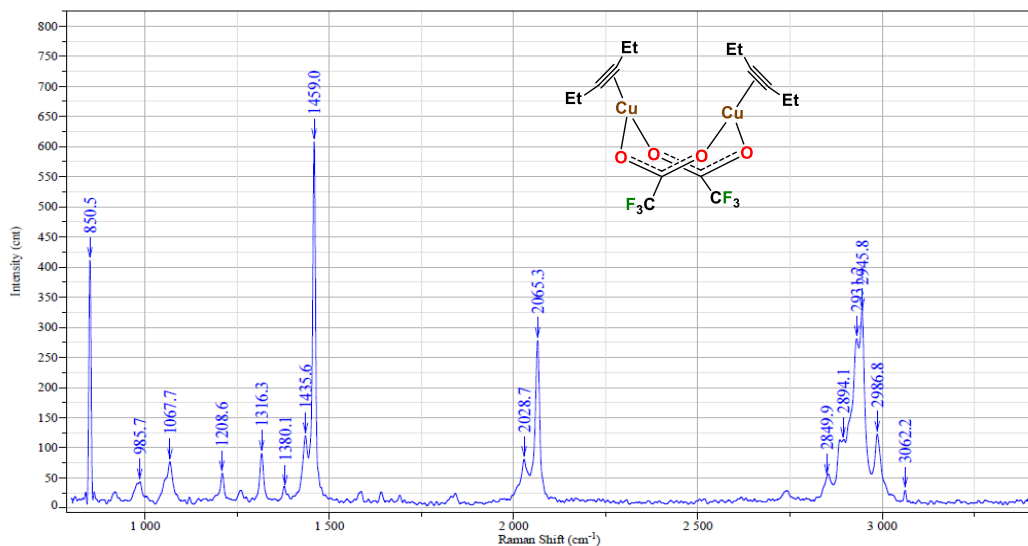
Exposition	10	Slit	100
Accumulation	10 x 4	Operator	Parasar
Laser	632.817	Sample	cu3_2butyne_tetramer
Spectro	Multi	Remark	
Hole	200	Power	

HORIBA JOBIN YVON



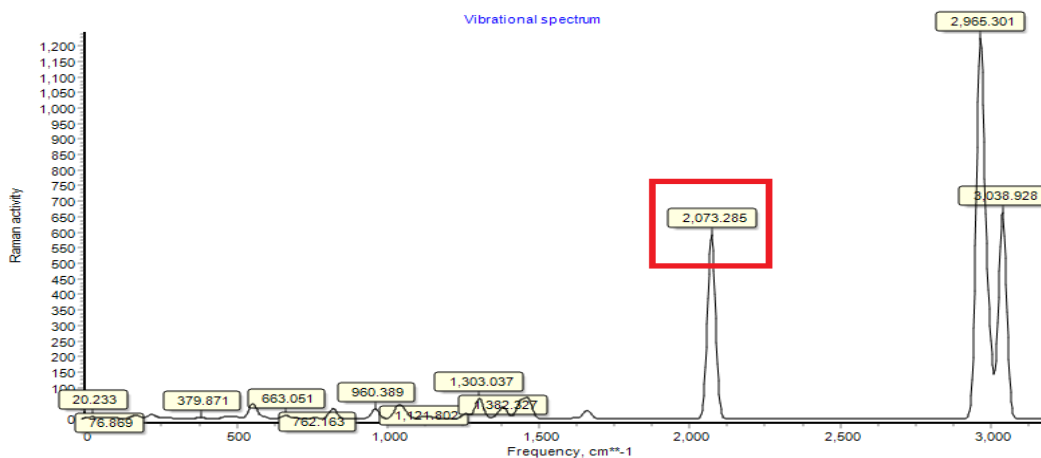
Raman spectrum of solid $\text{Cu}_4(\mu\text{-}[3,5\text{-}(\text{CF}_3)_2\text{Pz}]_4(\mu\text{-MeC}\equiv\text{CMe})_2$ (3).

(Experimental-top, Computational-bottom); $\text{C}\equiv\text{C}$ triple bond frequency of 2-butyne is given in the red square.

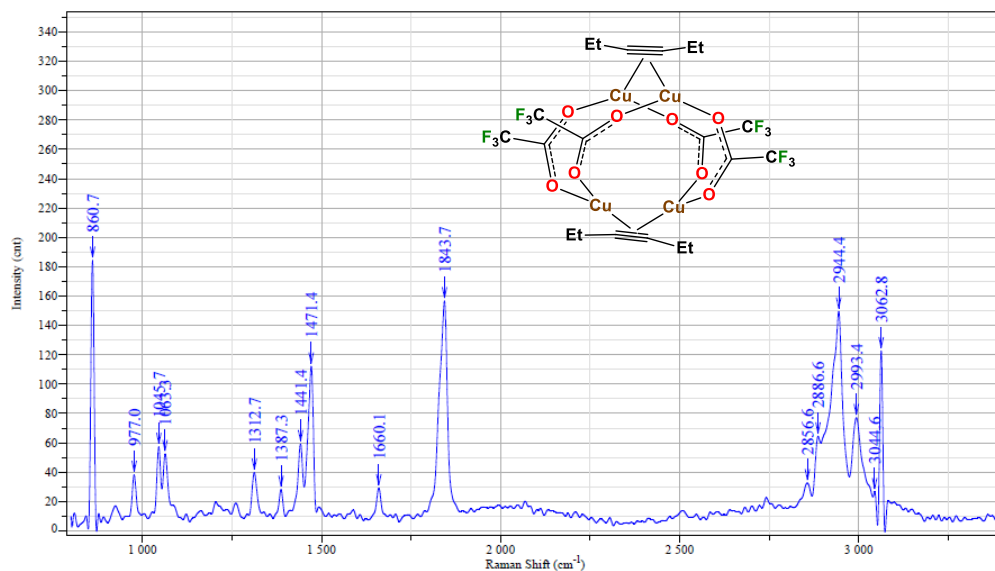


Exposition	1	Slit	100
Accumulation	1 x 4	Operator	Parasar
Laser	632.817	Sample	Cutrifluoroacetate3hexyne.c
Spectro	Multi	Remark	
Hole	200	Power	

HORIBA JOBIN YVON

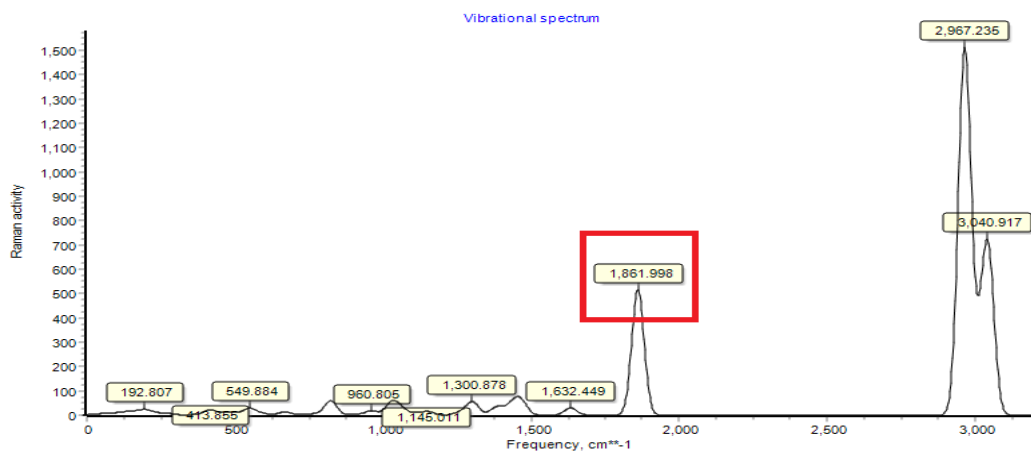


Raman spectrum of solid $\text{Cu}_2(\mu\text{-CF}_3\text{CO}_2)_2(\text{EtC}\equiv\text{CEt})_2$ (**4**). (Experimental-top, Computational-bottom); $\text{C}\equiv\text{C}$ triple bond frequency of 3-hexyne is given in the red square.

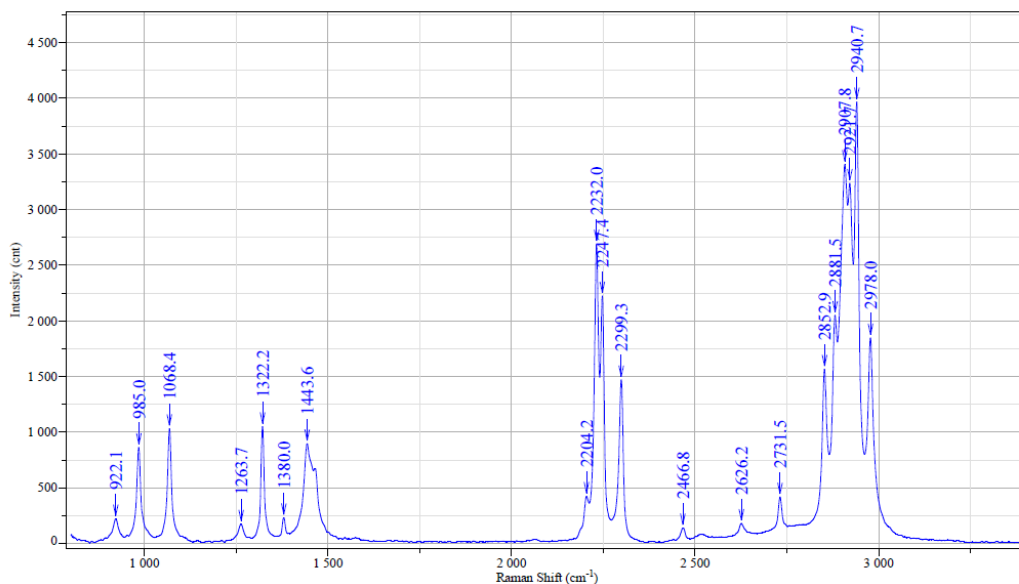


Exposition	10	Slit	100
Accumulation	5 x 4	Operator	Parasar
Laser	632.817	Sample	Cutrifluoroacetate3hexyne_t
Spectro	Multi	Remark	
Hole	200	Power	

HORIBA JOBIN YVON

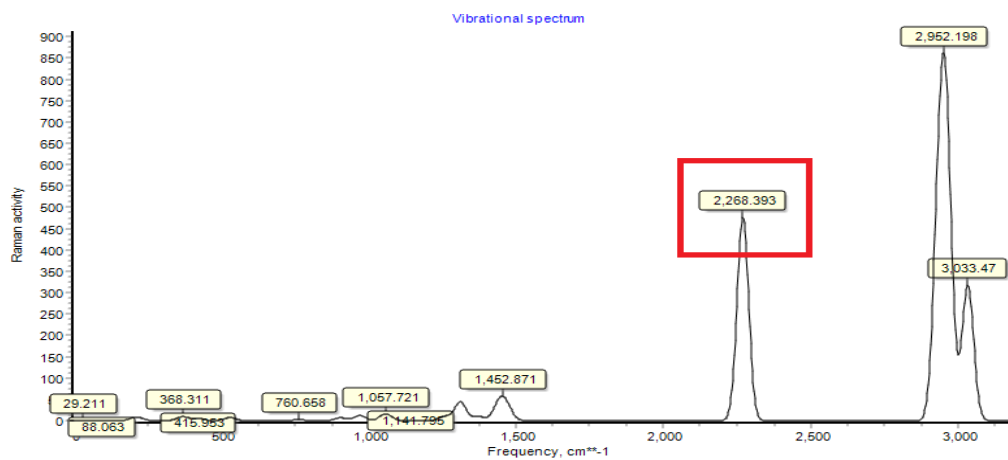


Raman spectrum of solid $\text{Cu}_4(\mu\text{-CF}_3\text{CO}_2)_4(\mu\text{-EtC}\equiv\text{CEt})_2$ (5). (Experimental-top, Computational-bottom); $\text{C}\equiv\text{C}$ triple bond frequency of 3-hexyne is given in the red square.

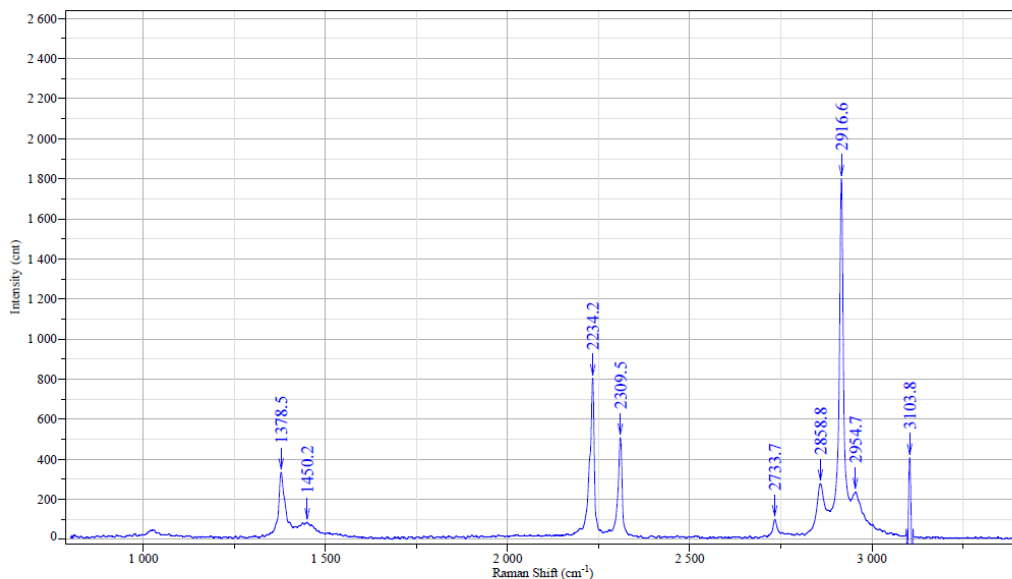


Exposition	5	Slit	100
Accumulation	5 x 4	Operator	Parasar
Laser	632.817	Sample	3-hexyne
Spectro	Multi	Remark	
Hole	200	Power	

HORIBA JOBIN YVON

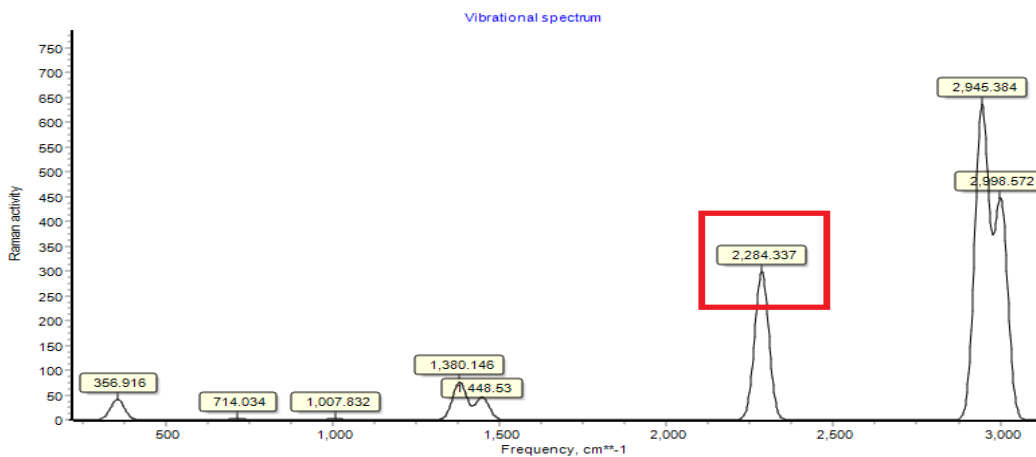


Raman spectrum of neat 3-hexyne at room temperature (Experimental-top, Computational-bottom). The assignment of $\text{C}\equiv\text{C}$ bands were based on literature reports.¹²⁷ $\text{C}\equiv\text{C}$ triple bond frequency of 3-hexyne is given in the red square.

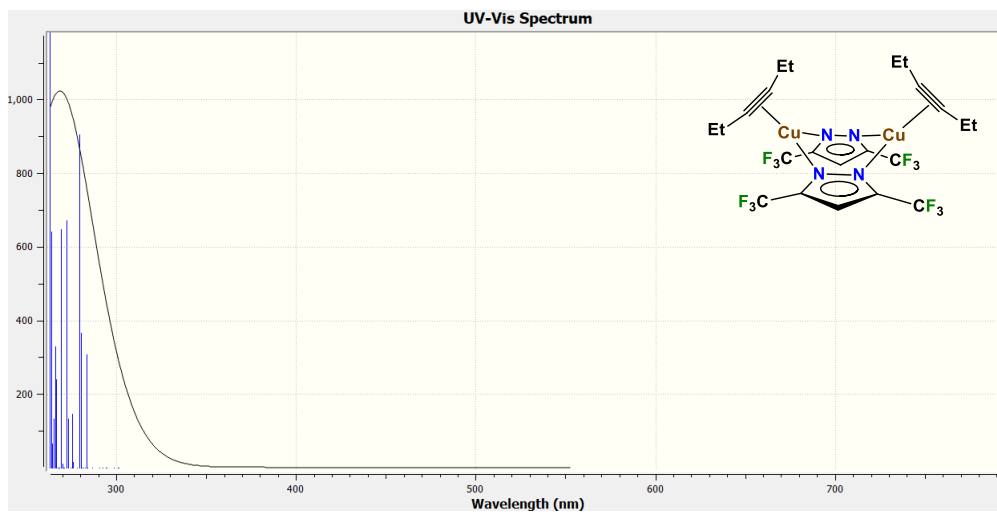


Exposition	1	Slit	100
Accumulation	1 x 4	Operator	Parasar
Laser	632.817	Sample	2-butyne
Spectro	Multi	Remark	
Hole	200	Power	

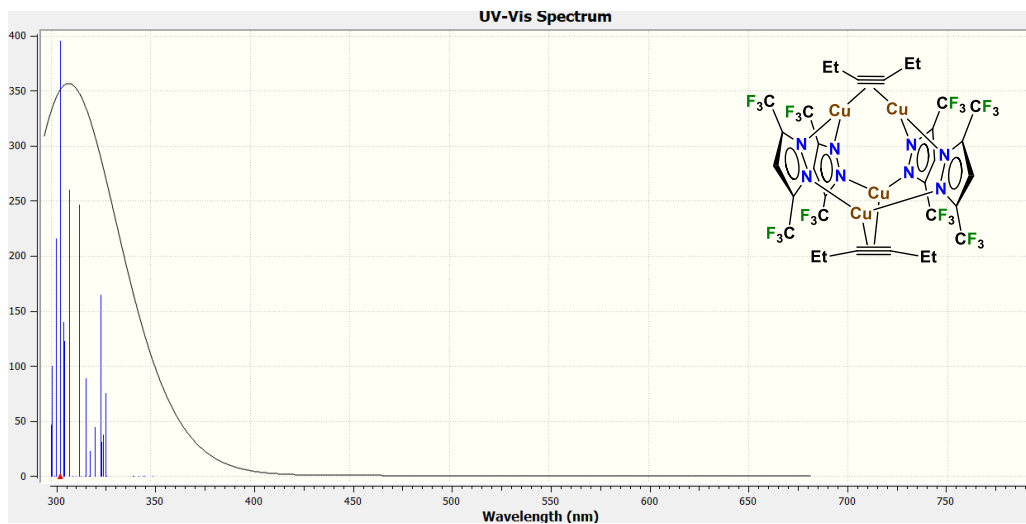
HORIBA JOBIN YVON



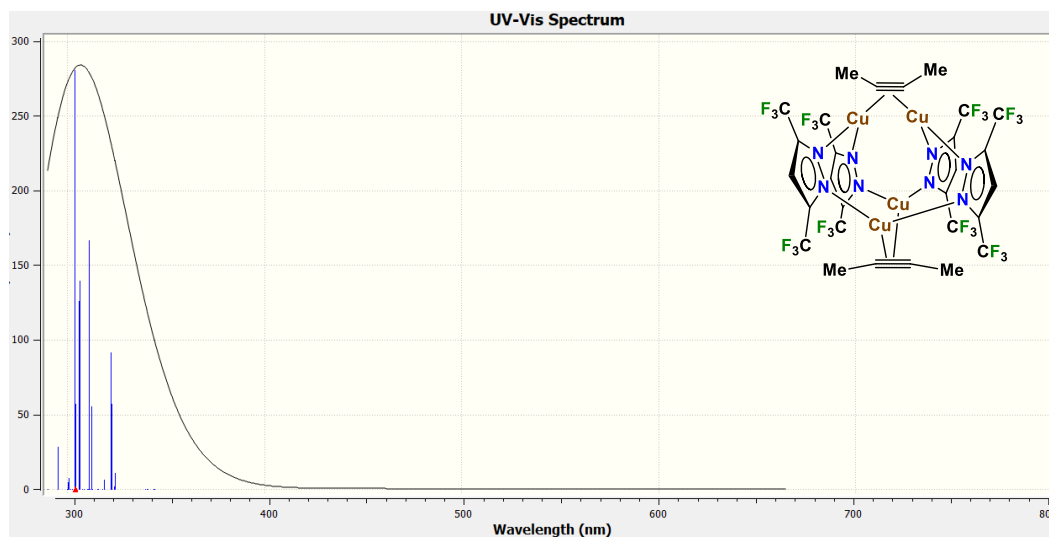
Raman spectrum of 2-butyne neat sample at room temperature (Experimental-top, Computational-bottom). The assignment of C≡C band was based on literature reports.³⁴⁵ C≡C triple bond frequency of 2-butyne is given in the red square.



Calculated electronic spectrum with spin-allowed (singlet-to-singlet, $S_0 \rightarrow S_n$) excitation energies (vertical lines) and oscillator strengths for the dinuclear complex $\text{Cu}_2(\mu\text{-[3,5-(CF}_3)_2\text{Pz]})_2(\text{EtC}\equiv\text{CEt})_2$ (1) in the gas phase.

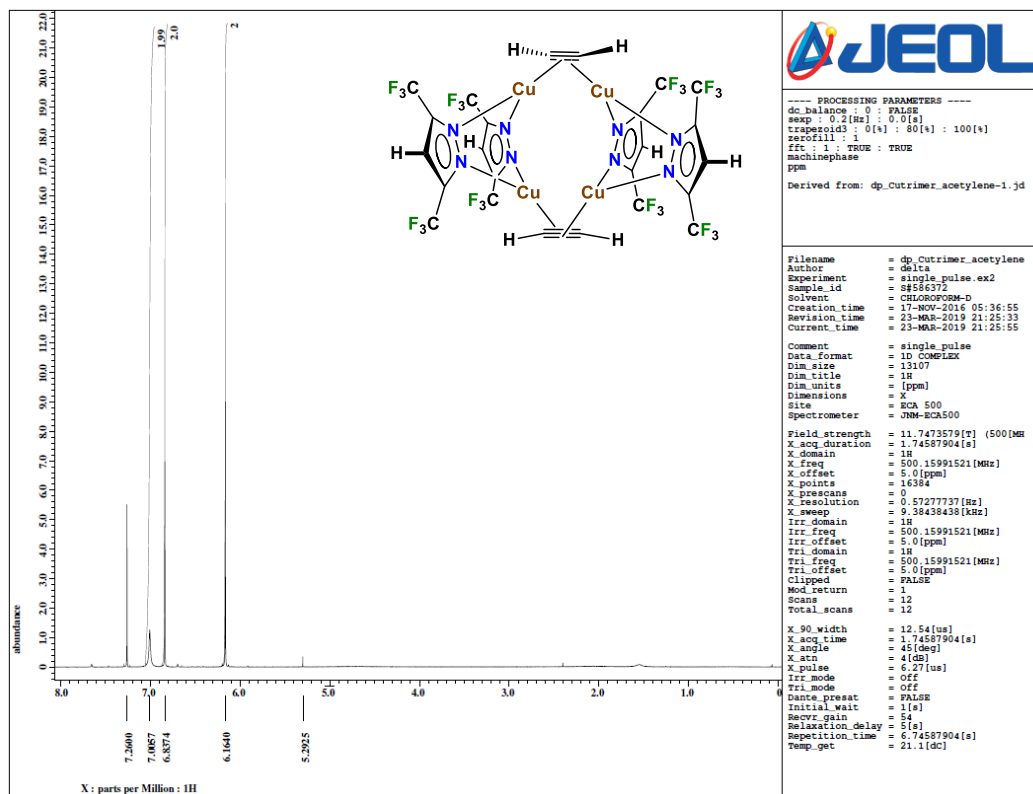


Calculated electronic spectrum with spin-allowed (singlet-to-singlet, $S_0 \rightarrow S_n$) excitation energies (vertical lines) and oscillator strengths for the tetranuclear complex $\text{Cu}_4(\mu\text{-[3,5-(CF}_3)_2\text{Pz]})_4(\mu\text{-EtC}\equiv\text{CEt})_2$ (2) in the gas phase.

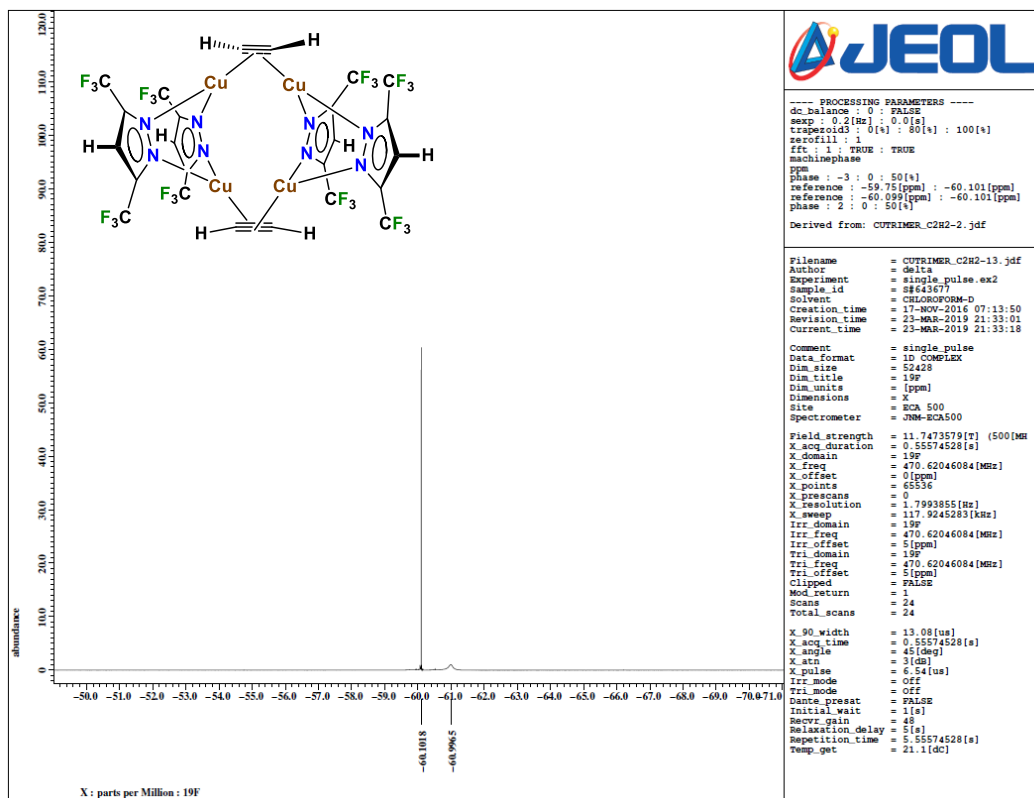


Calculated electronic spectrum with spin-allowed (singlet-to-singlet, $S_0 \rightarrow S_n$) excitation energies (vertical lines) and oscillator strengths for the tetranuclear complex $\text{Cu}_4(\mu\text{-[3,5-(CF}_3)_2\text{Pz]})_4(\mu\text{-MeC}\equiv\text{CMe})_2$ (**3**) in the gas phase.

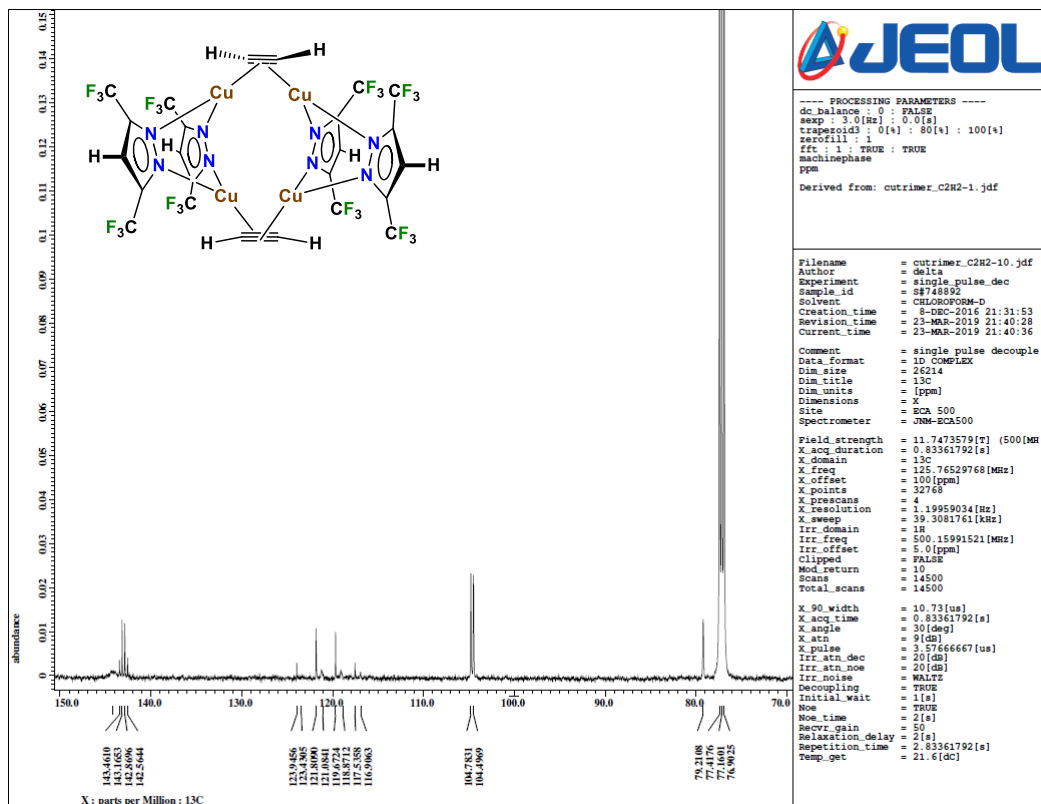
Spectroscopic data of Part 3.2 from chapter 3



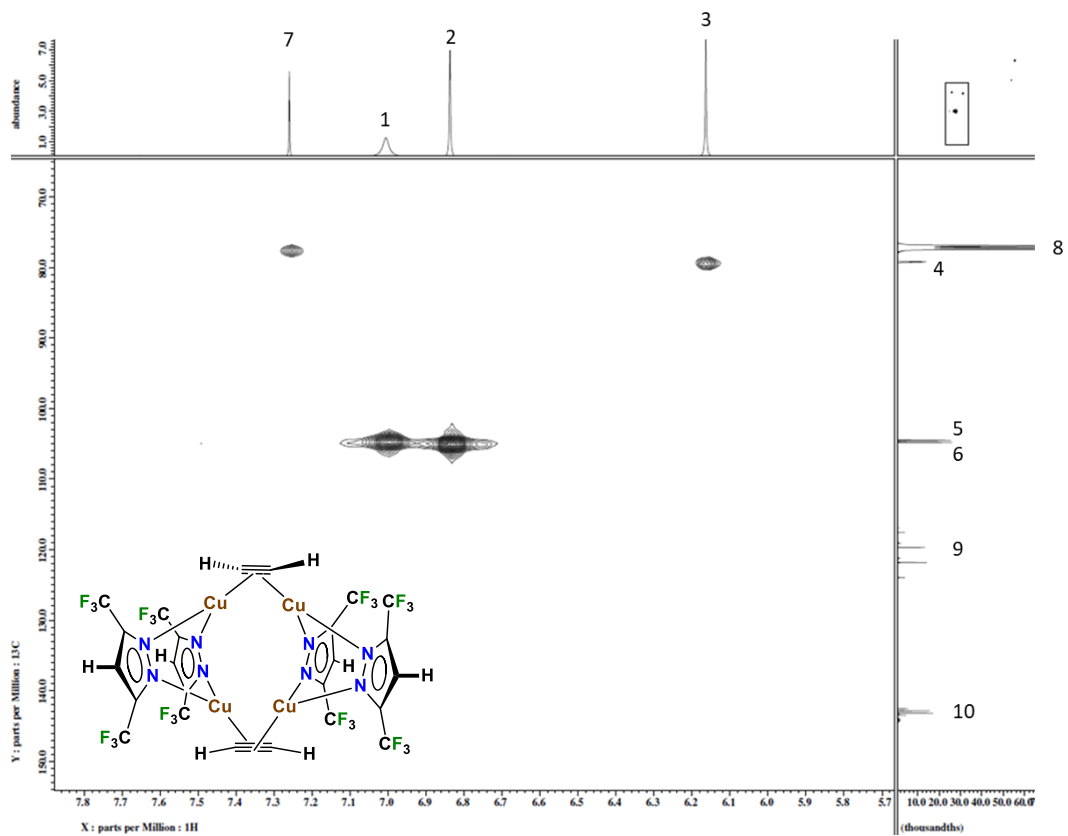
^1H NMR spectrum of $\text{Cu}_4(\mu\text{-}[3,5\text{-}(\text{CF}_3)_2\text{Pz}])_4(\mu\text{-HC}\equiv\text{CH})_2$ (**4**) in CDCl_3 at room temperature.



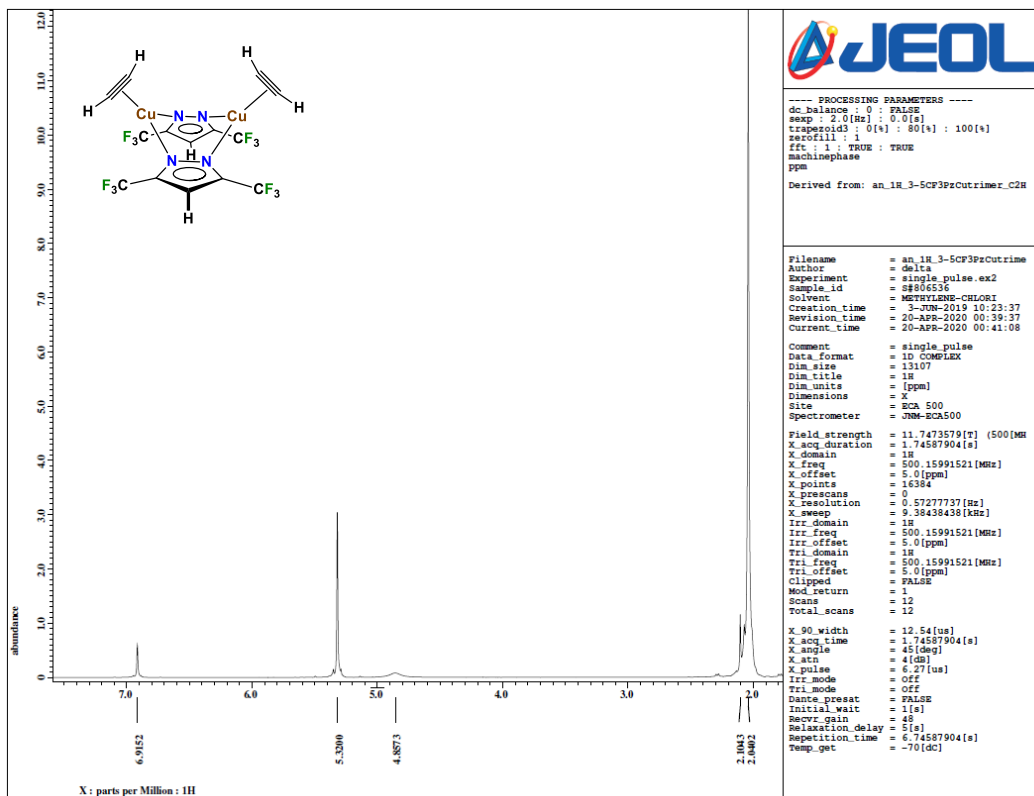
^{19}F NMR spectrum of $\text{Cu}_4(\mu\text{-}[3,5\text{-}(\text{CF}_3)_2\text{Pz}])_4(\mu\text{-HC}\equiv\text{CH})_2$ (**4**) in CDCl_3 at room temperature



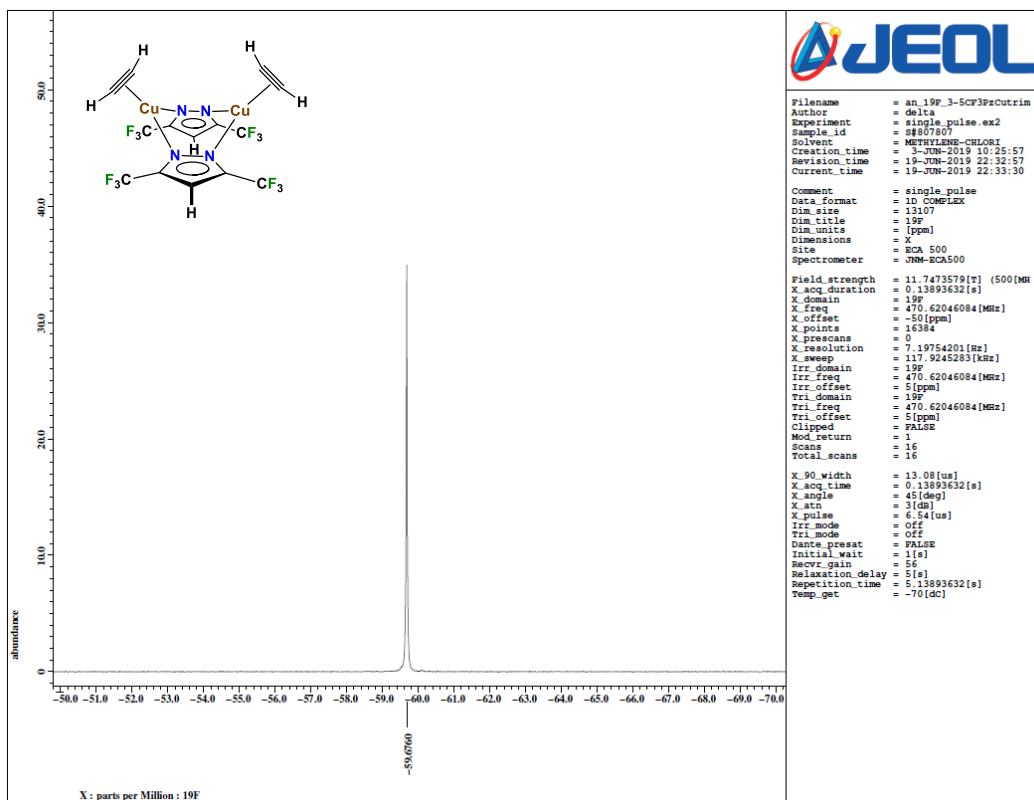
$^{13}\text{C}\{^1\text{H}\}$ NMR spectrum of $\text{Cu}_4(\mu\text{-[3,5-(CF}_3)_2\text{Pz]}_4)(\mu\text{-HC}\equiv\text{CH})_2$ (**4**) in CDCl_3 at room temperature.



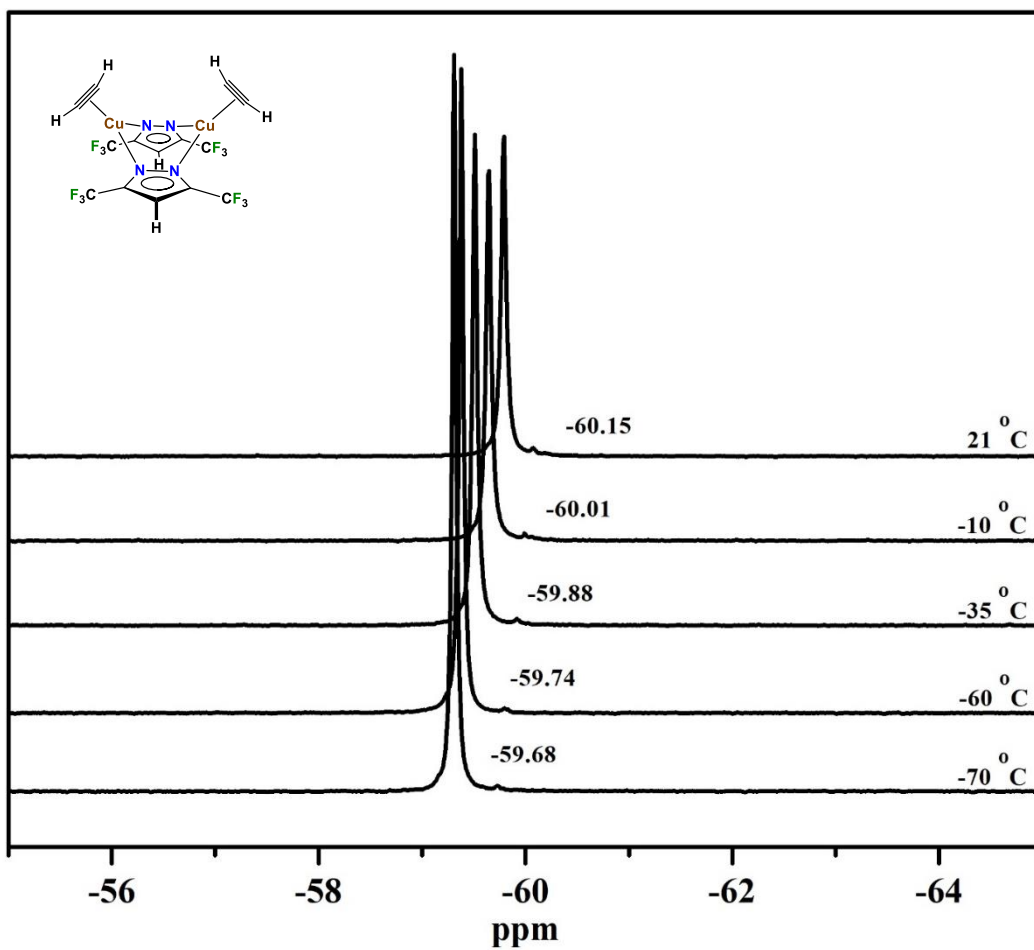
HMQC NMR spectrum of $\text{Cu}_4(\mu\text{-}[3,5\text{-}(\text{CF}_3)_2\text{Pz}])_4(\mu\text{-HC}\equiv\text{CH})_2$ (**4**) in CDCl_3 at room temperature.



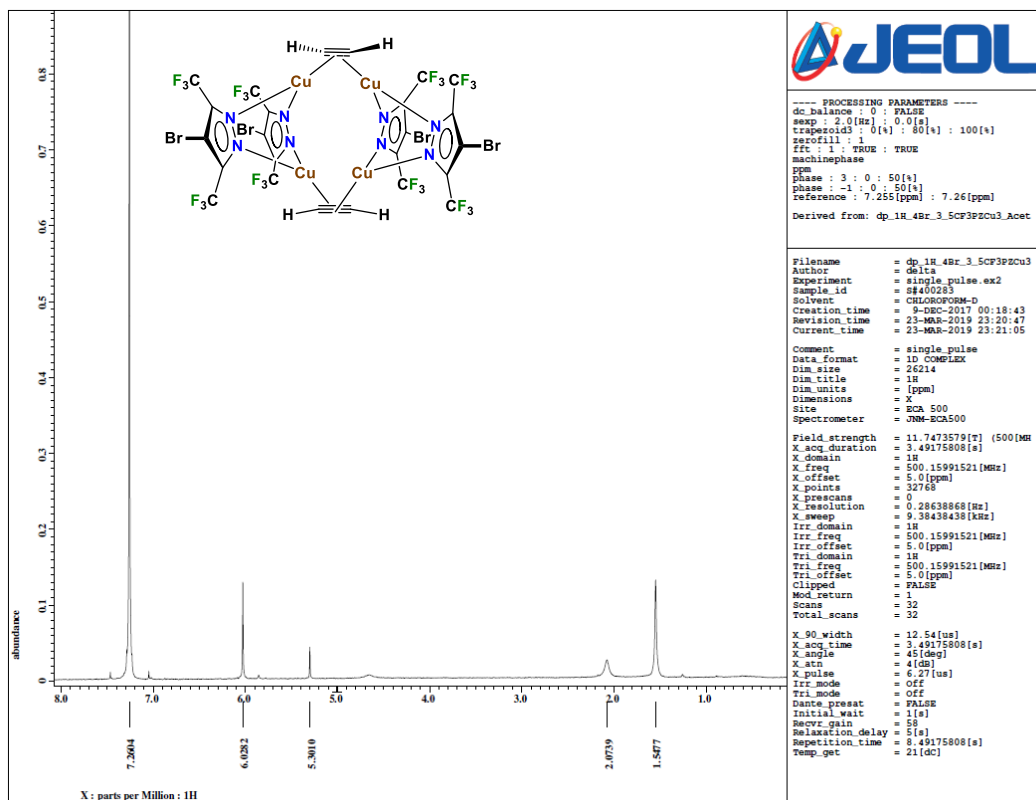
^1H NMR spectrum of $\text{Cu}_2(\mu\text{-}[3,5\text{-}(\text{CF}_3)_2\text{Pz}])_2(\text{HC}\equiv\text{CH})_2$ (**5**) with excess acetylene in CD_2Cl_2 at -70°C .



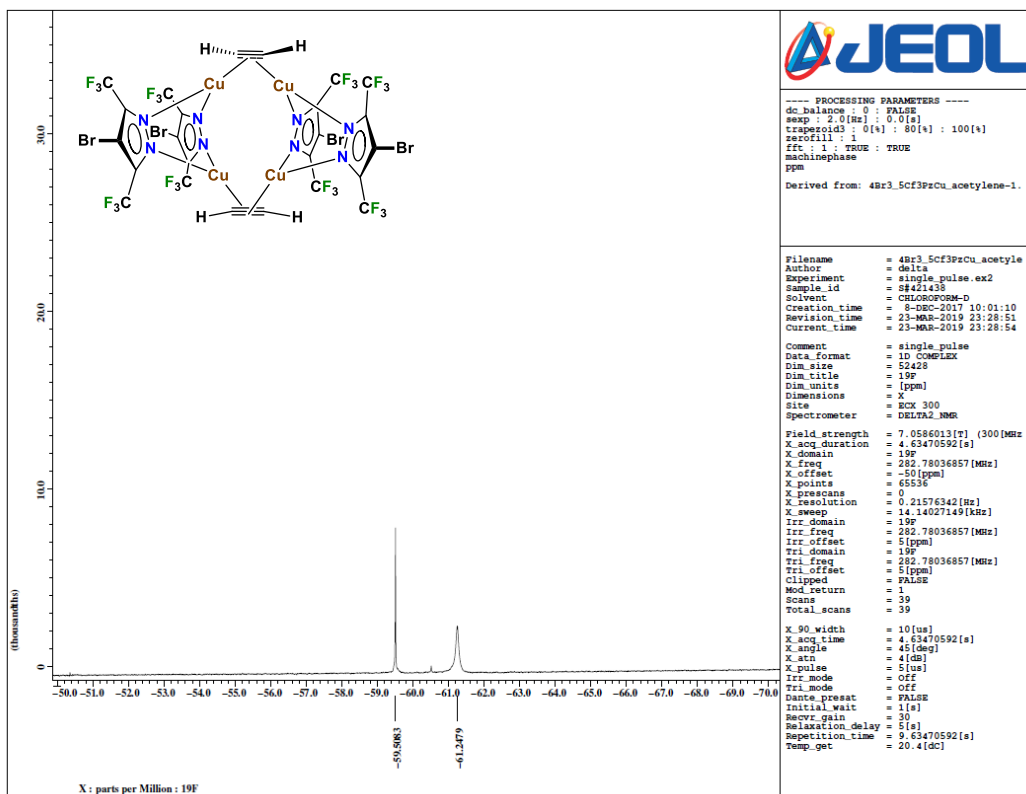
^{19}F NMR spectrum of $\text{Cu}_2(\mu\text{-}[3,5\text{-}(\text{CF}_3)_2\text{Pz}])_2(\text{HC}\equiv\text{CH})_2$ (**5**) with excess acetylene in CD_2Cl_2 at -70°C



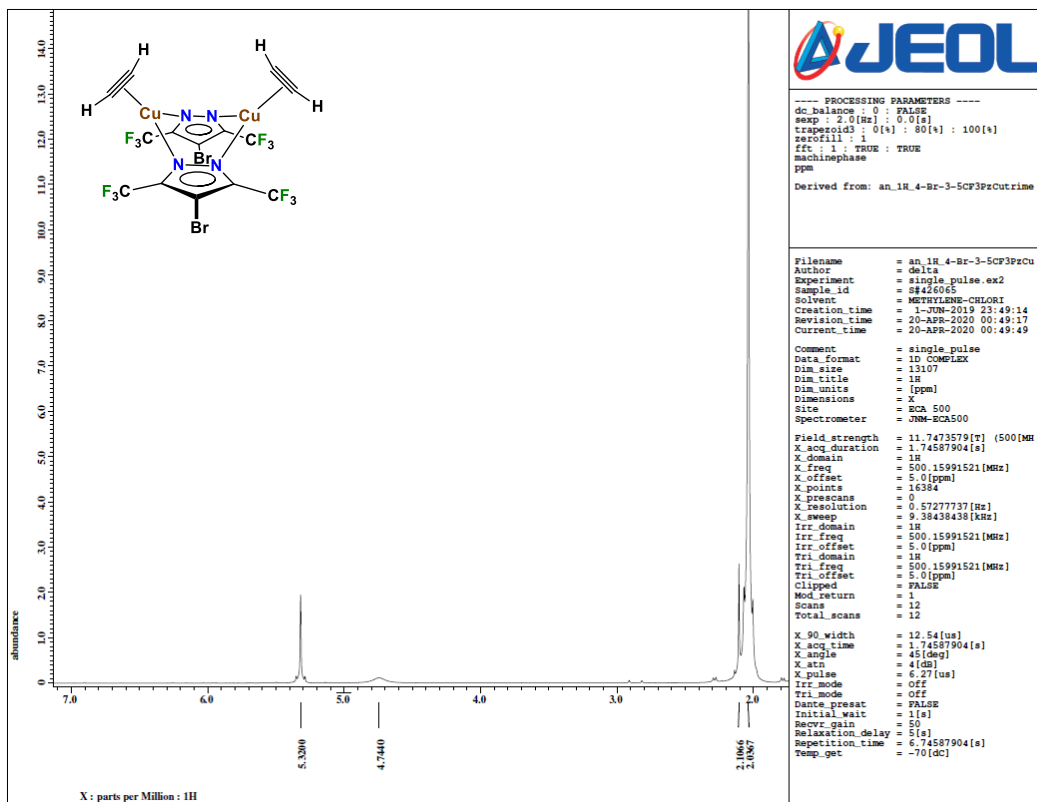
¹⁹F NMR spectra of Cu₂(μ-[3,5-(CF₃)₂Pz])₂(HC≡CH)₂ (**5**) (in CD₂Cl₂) in presence of excess acetylene at various temperatures. Peak at -59.68 ppm (-70 °C) is the signal corresponding to **5**.



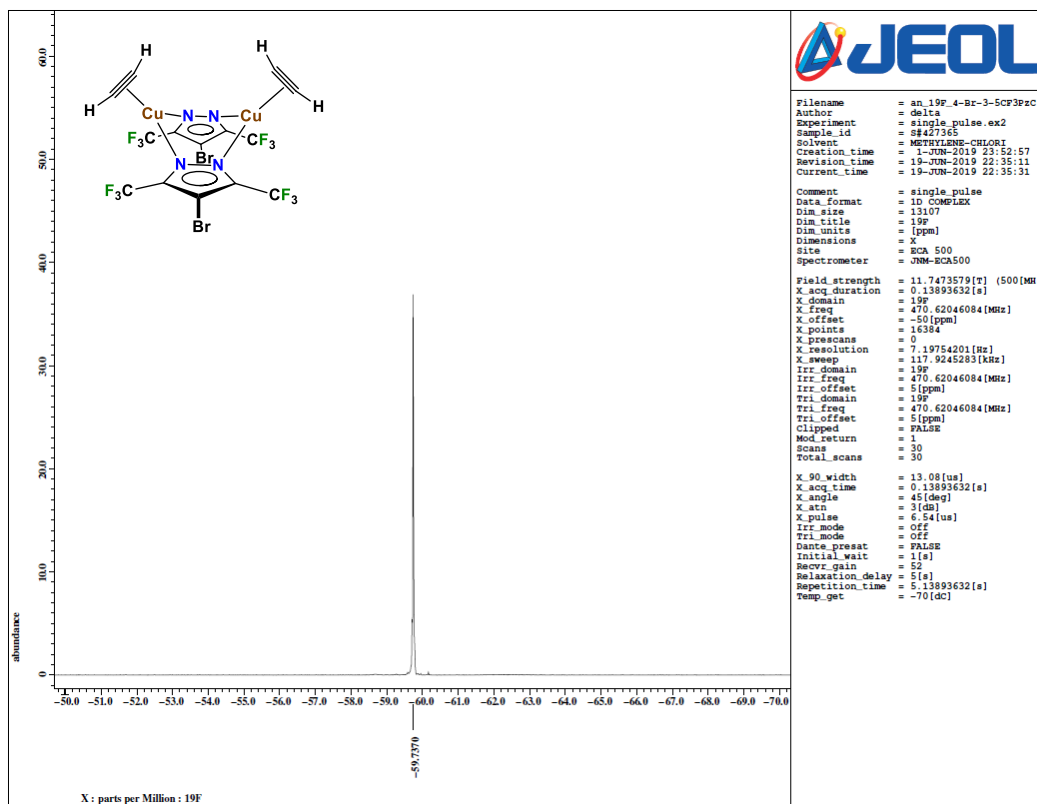
^1H NMR spectrum of $\text{Cu}_4(\mu\text{-[4-Br-3,5-(CF}_3)_2\text{Pz]})_4(\mu\text{-HC}\equiv\text{CH})_2$ (6) in CDCl_3 at room temperature. This spectrum also shows presence of free acetylene resulting from the disproportionation of $\text{Cu}_4(\mu\text{-[4-Br-3,5-(CF}_3)_2\text{Pz]})_4(\mu\text{-HC}\equiv\text{CH})_2$ to $\{\mu\text{-[4-Br-3,5-(CF}_3)_2\text{Pz]Cu}\}_3$ and free acetylene. Peak at 6.03 ppm is the signal corresponding to coordinated acetylene while 2.07 ppm peak is the signal of free acetylene.



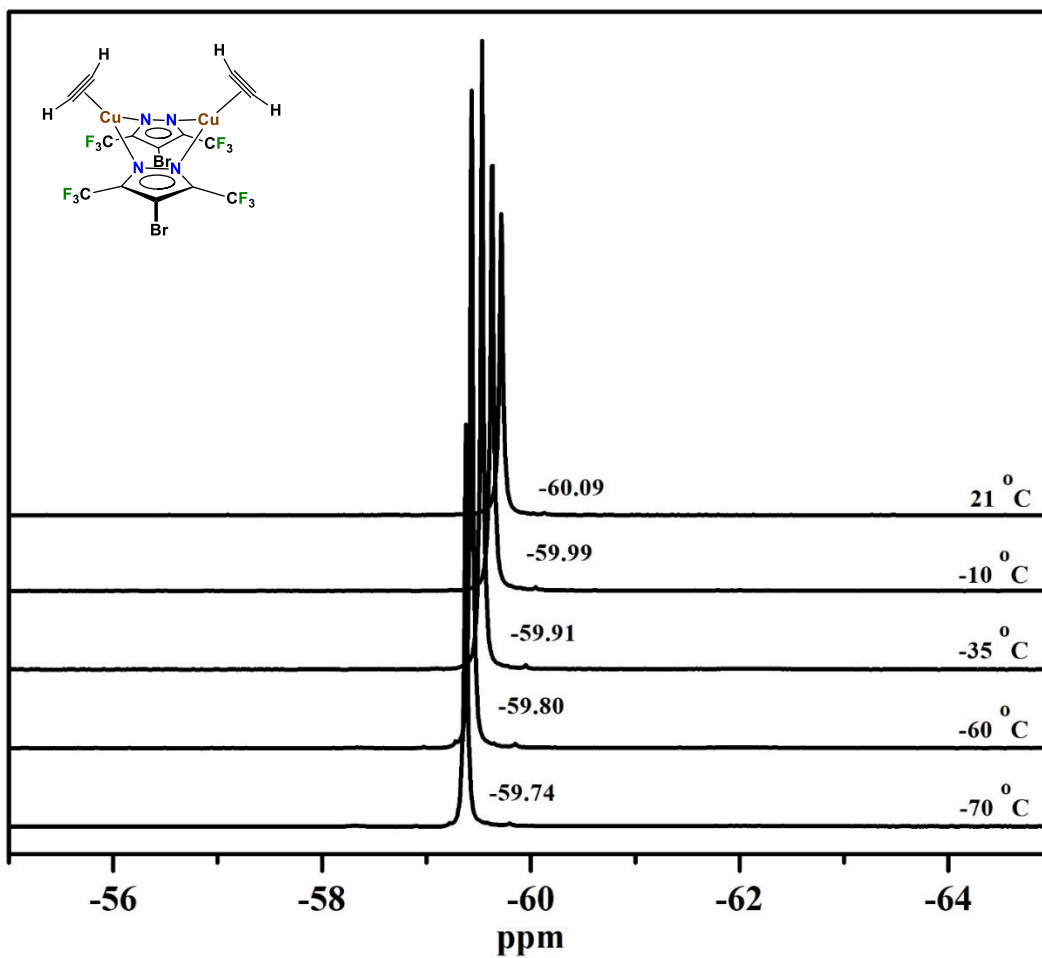
^{19}F NMR spectrum of $\text{Cu}_4(\mu\text{-[4-Br-3,5-(CF}_3)_2\text{Pz]})_4(\mu\text{-HC}\equiv\text{CH})_2$ (**6**) in CDCl_3 at room temperature. This spectrum also shows presence of $\{\mu\text{-[4-Br-3,5-(CF}_3)_2\text{Pz]Cu}\}_3$ resulting from the disproportionation of $\text{Cu}_4(\mu\text{-[4-Br-3,5-(CF}_3)_2\text{Pz]})_4(\mu\text{-HC}\equiv\text{CH})_2$ to $\{\mu\text{-[4-Br-3,5-(CF}_3)_2\text{Pz]Cu}\}_3$ and free acetylene. Peak at -59.5 ppm corresponds to $\text{Cu}_4(\mu\text{-[4-Br-3,5-(CF}_3)_2\text{Pz]})_4(\mu\text{-HC}\equiv\text{CH})_2$ while peak at -61.2 ppm corresponds to $\{\mu\text{-[4-Br-3,5-(CF}_3)_2\text{Pz]Cu}\}_3$.



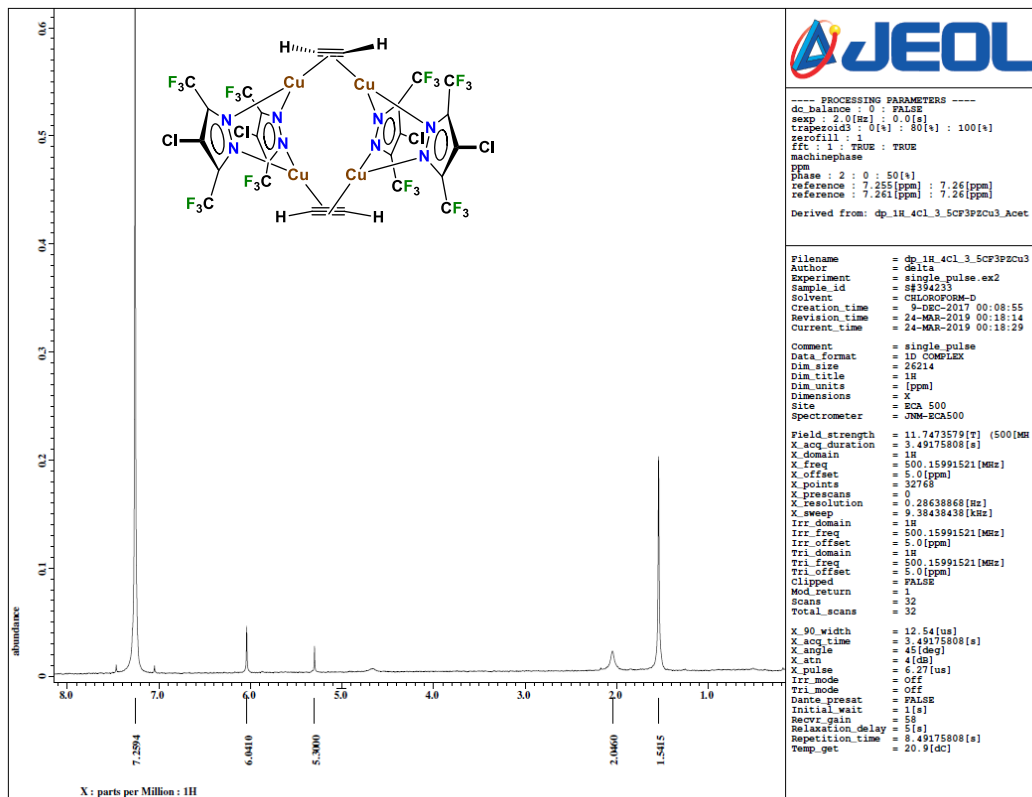
$^1\text{H NMR}$ spectrum of $\text{Cu}_2(\mu\text{-[4-Br-3,5-(CF}_3)_2\text{Pz]})_2(\text{HC}\equiv\text{CH})_2$ (**8**) with excess acetylene in CD_2Cl_2 at $-70\text{ }^\circ\text{C}$.



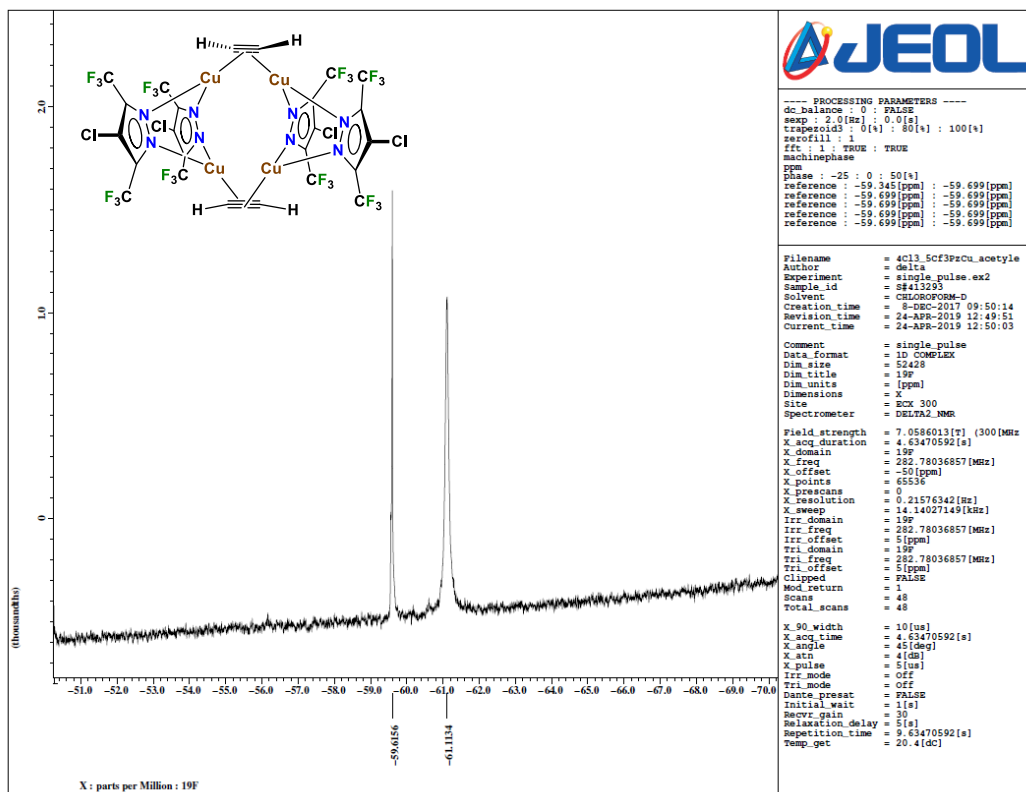
^{19}F NMR spectrum of $\text{Cu}_2(\mu\text{-[4-Br-3,5-(CF}_3)_2\text{Pz]})_2(\text{HC}\equiv\text{CH})_2$ (8) with excess acetylene in CD_2Cl_2 at -70°C



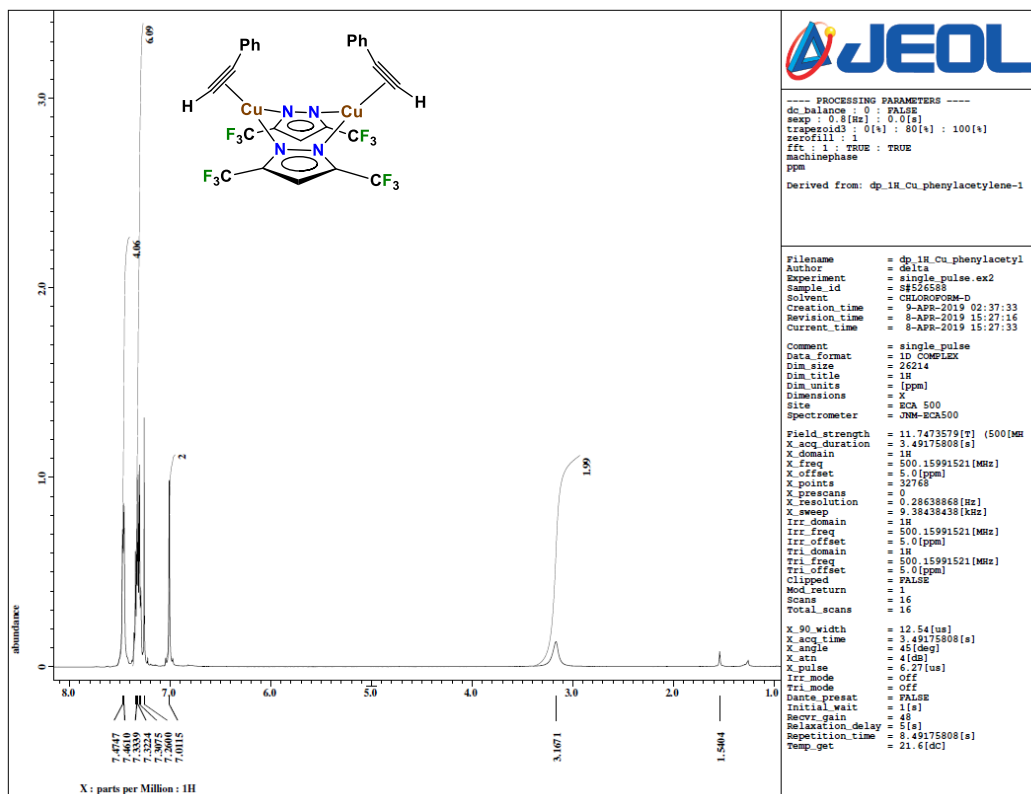
^{19}F NMR spectra of $\text{Cu}_2(\mu\text{-[4-Br-3,5-(CF}_3)_2\text{Pz]})_2(\text{HC}\equiv\text{CH})_2$ (**8**) (in CD_2Cl_2) in presence of excess acetylene at various temperatures. Peak at -59.74 ppm (-70 $^\circ\text{C}$) is the signal corresponding to **8**.



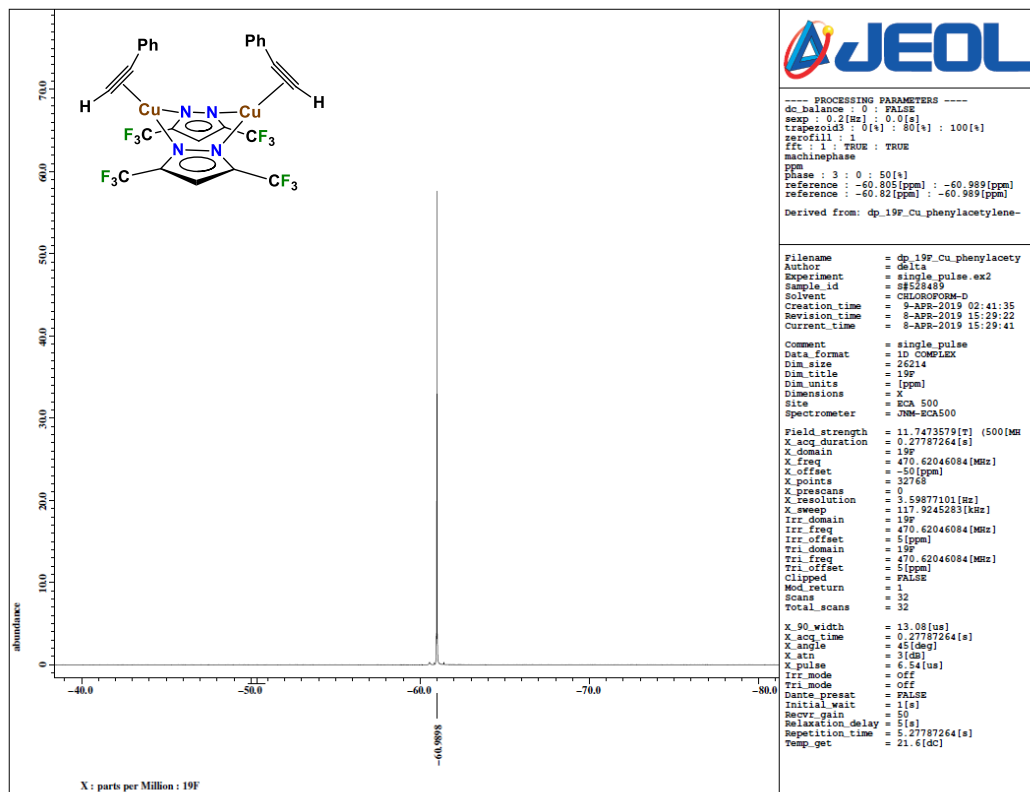
^1H NMR spectrum of $\text{Cu}_4(\mu\text{-[4-Cl-3,5-(CF}_3)_2\text{Pz]})_4(\mu\text{-HC}\equiv\text{CH})_2$ (**7**) in CDCl_3 at room temperature. This spectrum also shows presence of free acetylene resulting from the disproportionation of $\text{Cu}_4(\mu\text{-[4-Cl-3,5-(CF}_3)_2\text{Pz]})_4(\mu\text{-HC}\equiv\text{CH})_2$ to $\{\mu\text{-[4-Cl-3,5-(CF}_3)_2\text{Pz]Cu}\}_3$ and free acetylene. Peak at 6.04 ppm is the signal corresponding to coordinated acetylene while 2.05 ppm peak is the signal of free acetylene.



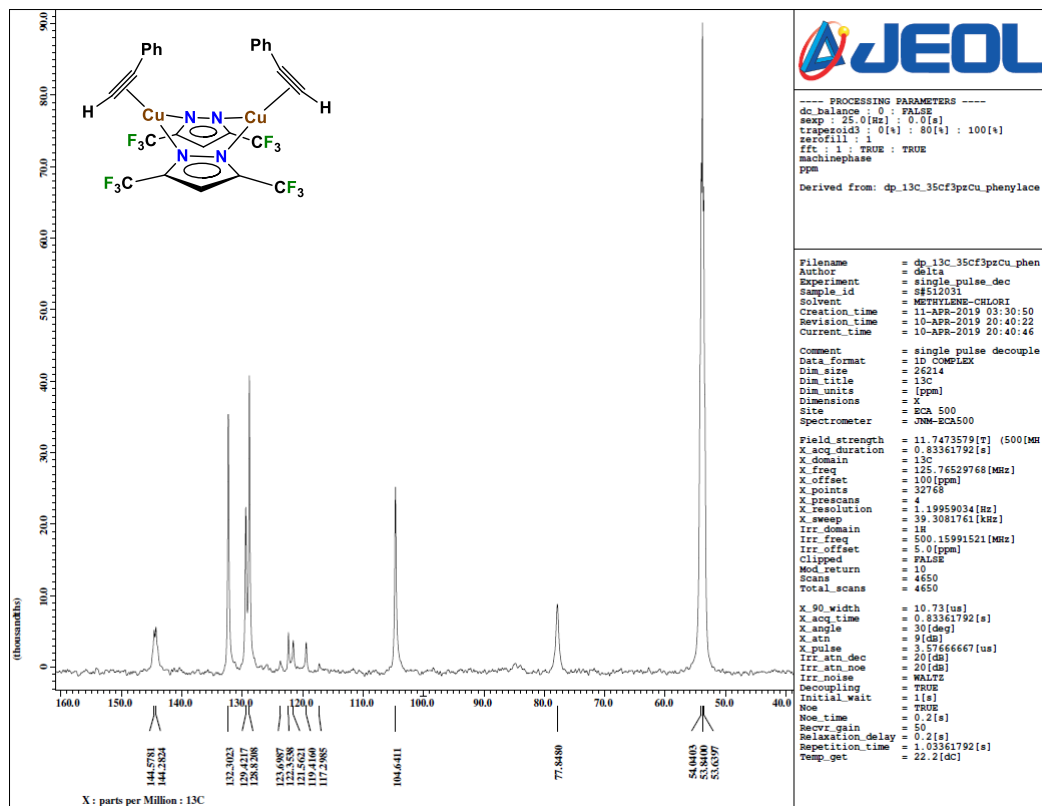
^{19}F NMR spectrum of $\text{Cu}_4(\mu\text{-[4-Cl-3,5-(CF}_3)_2\text{Pz]})_4(\mu\text{-HC}\equiv\text{CH})_2$ (**7**) in CDCl_3 at room temperature. This spectrum also shows presence of $\{\mu\text{-[4-Cl-3,5-(CF}_3)_2\text{Pz]Cu}\}_3$ resulting from the disproportionation of $\text{Cu}_4(\mu\text{-[4-Cl-3,5-(CF}_3)_2\text{Pz]})_4(\mu\text{-HC}\equiv\text{CH})_2$ to $\{\mu\text{-[4-Cl-3,5-(CF}_3)_2\text{Pz]Cu}\}_3$ and free acetylene. Peak at -59.6 ppm corresponds to $\text{Cu}_4(\mu\text{-[4-Cl-3,5-(CF}_3)_2\text{Pz]})_4(\mu\text{-HC}\equiv\text{CH})_2$ while peak at -61.1 ppm corresponds to $\{\mu\text{-[4-CL-3,5-(CF}_3)_2\text{Pz]Cu}\}_3$.



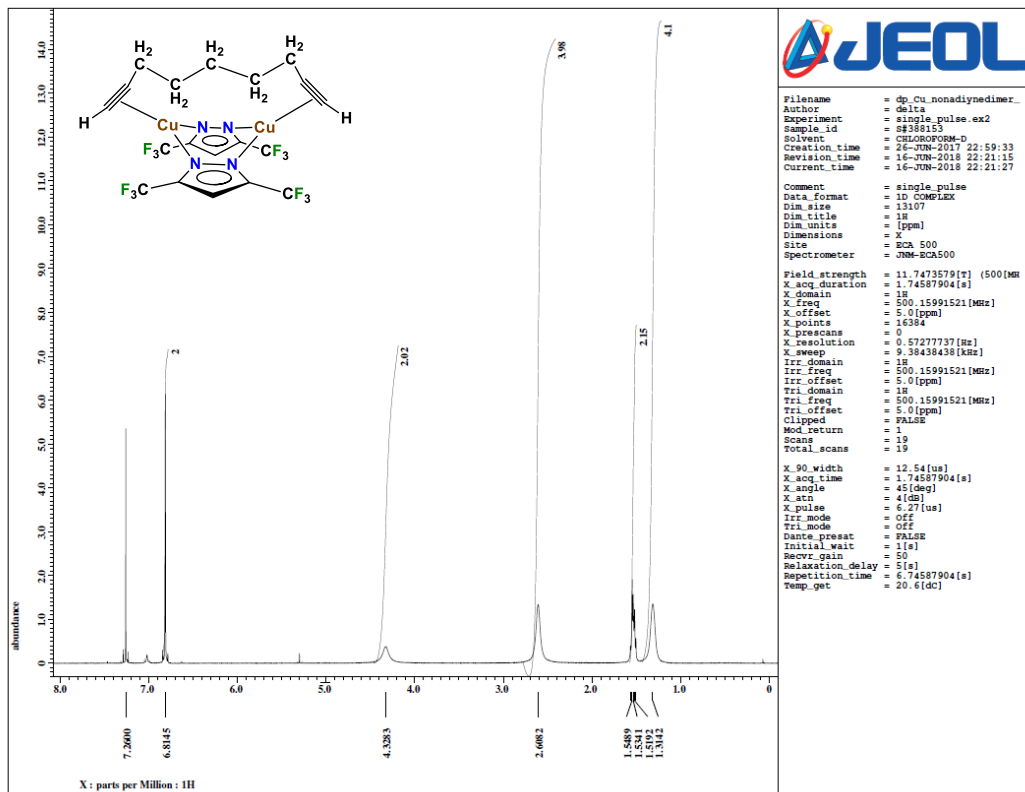
^1H NMR spectrum of $\text{Cu}_2(\mu\text{-[3,5-(CF}_3)_2\text{Pz]})_2(\text{HC}\equiv\text{CPh})_2$ (**9**) in CDCl_3 at room temperature.



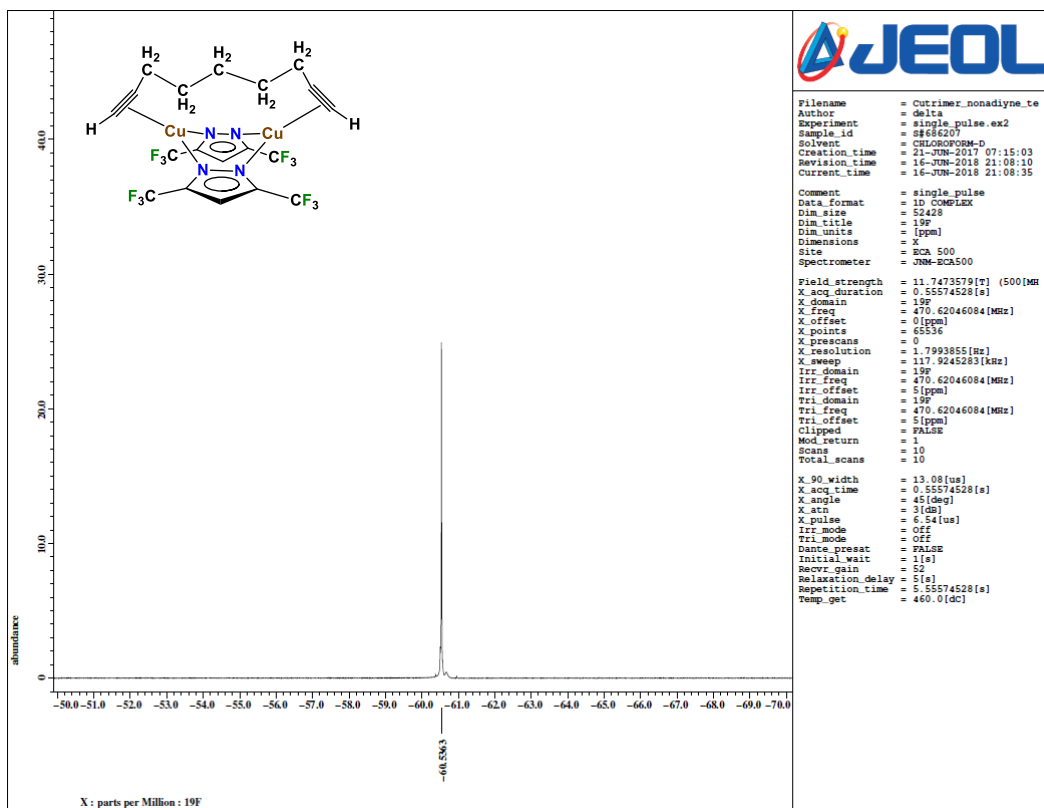
^{19}F NMR spectrum of $\text{Cu}_2(\mu\text{-[3,5-(CF}_3)_2\text{Pz]})_2(\text{HC}\equiv\text{CPh})_2$ (**9**) in CDCl_3 at room temperature.



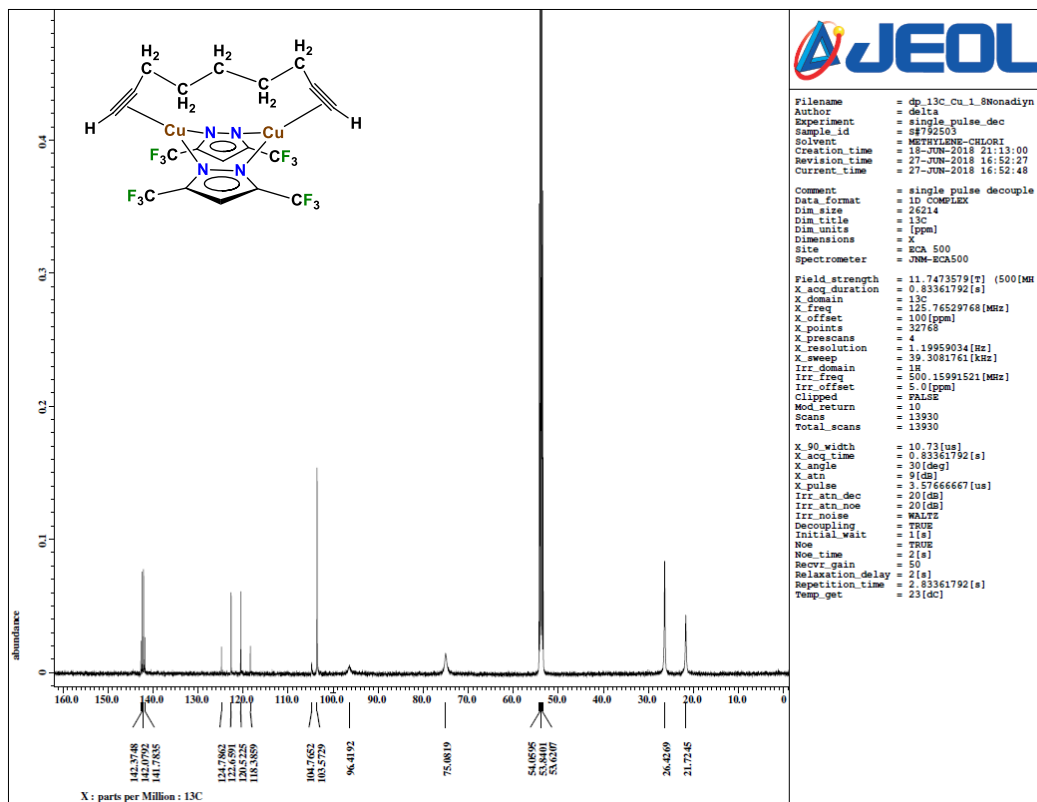
$^{13}\text{C}\{^1\text{H}\}$ NMR spectrum of $\text{Cu}_2(\mu\text{-}[3,5\text{-}(\text{CF}_3)_2\text{Pz}])_2(\text{HC}\equiv\text{CPh})_2$ (9) in CD_2Cl_2 at room temperature.



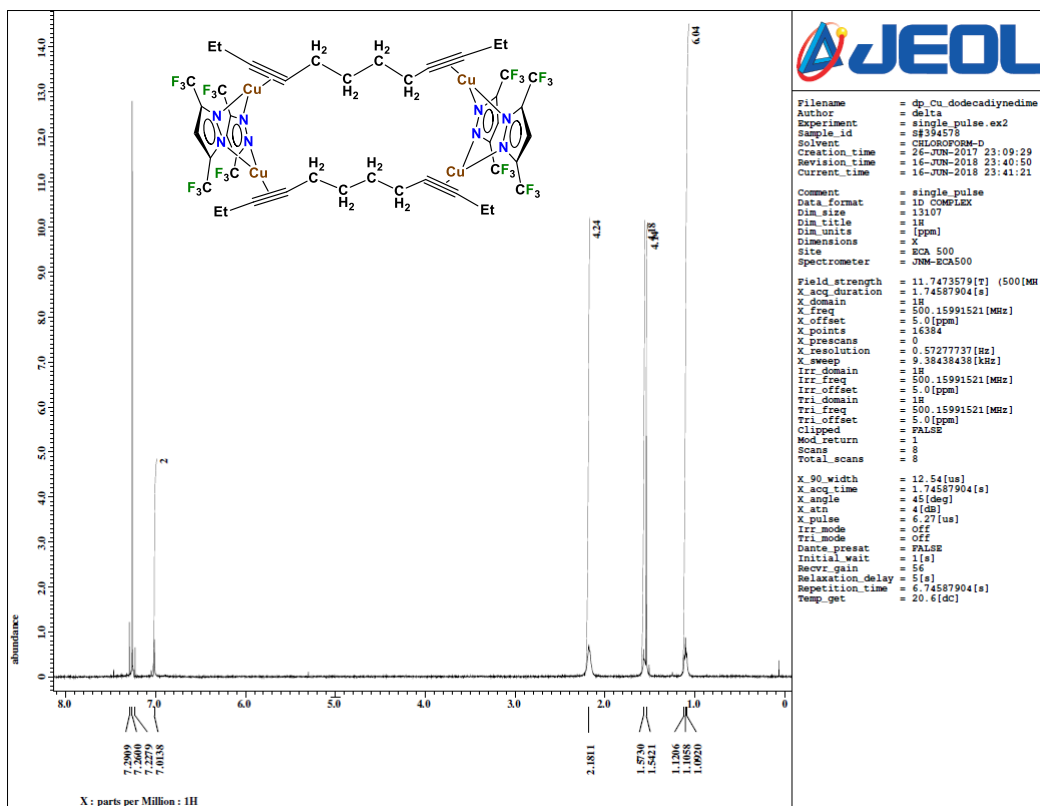
¹H NMR spectrum of $\text{Cu}_2(\mu\text{-[3,5-(CF}_3)_2\text{Pz]})_2(\text{HC}\equiv\text{C}(\text{CH}_2)_5\text{C}\equiv\text{CH})$ (10) in CDCl_3 at room temperature.



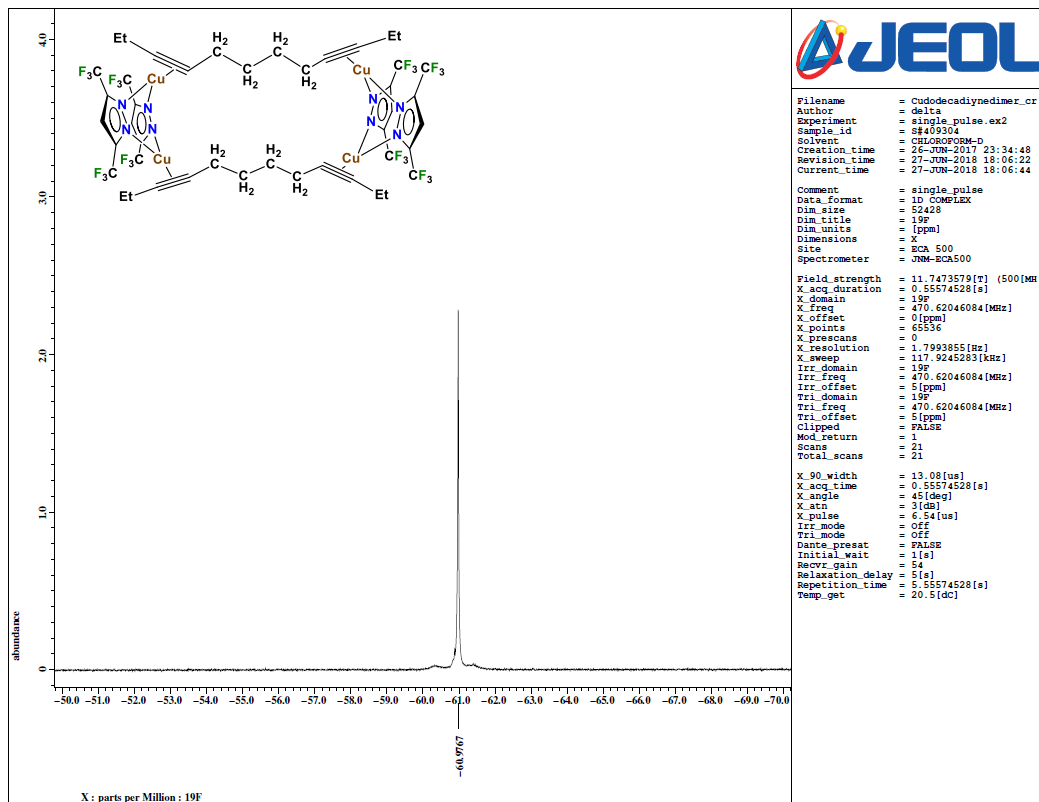
^{19}F NMR spectrum of $\text{Cu}_2(\mu\text{-}[3,5\text{-}(\text{CF}_3)_2\text{Pz}]_2)(\text{HC}\equiv\text{C}(\text{CH}_2)_5\text{C}\equiv\text{CH})$ (**10**) in CDCl_3 at room temperature.



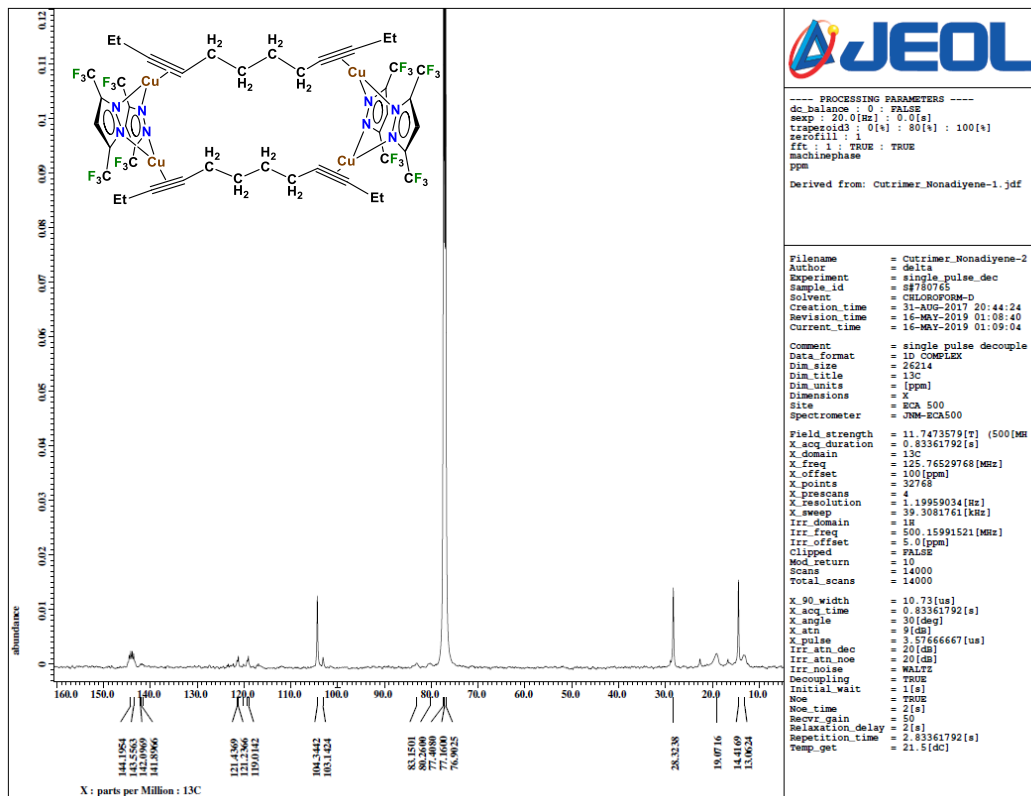
$^{13}\text{C}\{^1\text{H}\}$ NMR spectrum of $\text{Cu}_2(\mu\text{-}[3,5\text{-}(\text{CF}_3)_2\text{Pz}])_2(\text{HC}\equiv\text{C}(\text{CH}_2)_5\text{C}\equiv\text{CH})$ (10) in CD_2Cl_2 at room temperature.



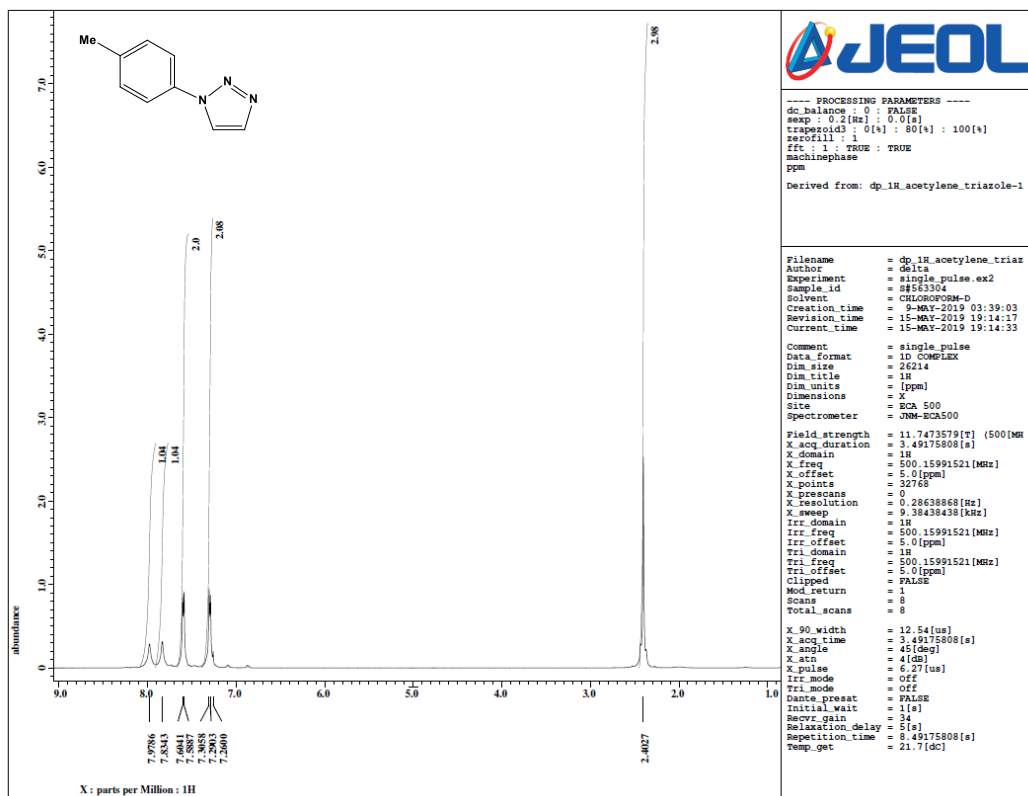
^1H NMR spectrum of $\text{Cu}_4(\mu\text{-}[3,5\text{-}(\text{CF}_3)_2\text{Pz}])_4(\text{C}_2\text{H}_5\text{C}\equiv\text{C}(\text{CH}_2)_4\text{C}\equiv\text{CC}_2\text{H}_5)_2$ (**12**) in CDCl_3 at room temperature.



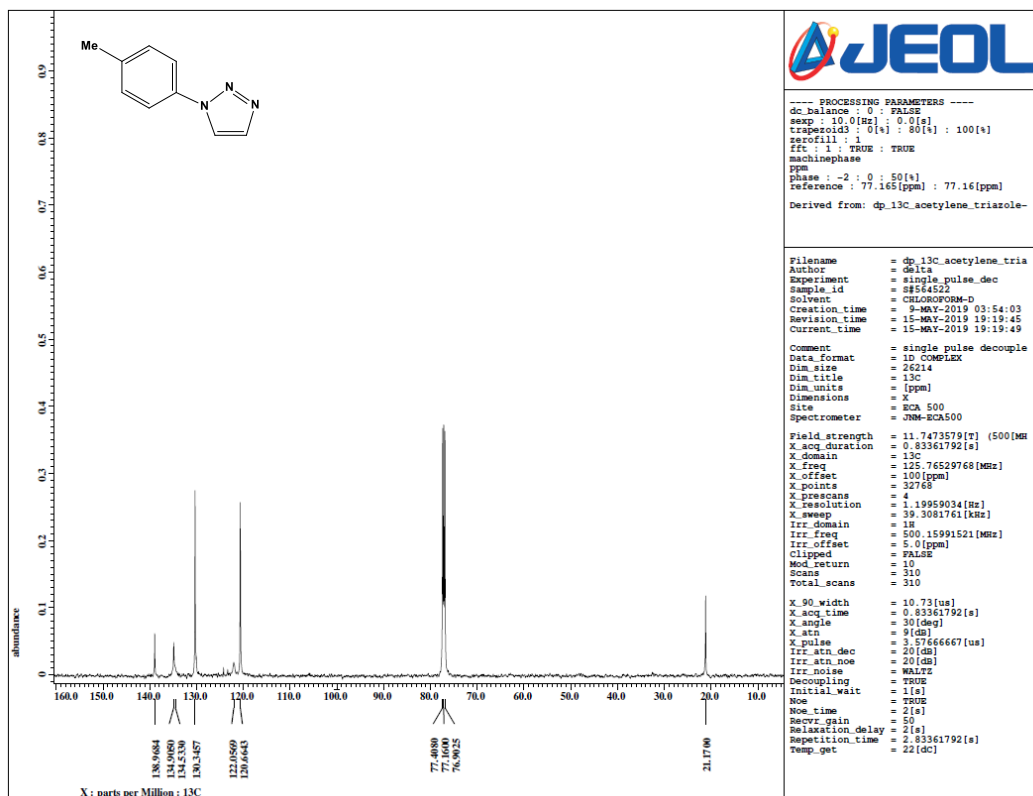
^{19}F NMR spectrum of $\text{Cu}_4(\mu\text{-}[3,5\text{-}(\text{CF}_3)_2\text{Pz}])_4(\text{C}_2\text{H}_5\text{C}\equiv\text{C}(\text{CH}_2)_4\text{C}\equiv\text{CC}_2\text{H}_5)_2$ (**12**) in CDCl_3 at room temperature.



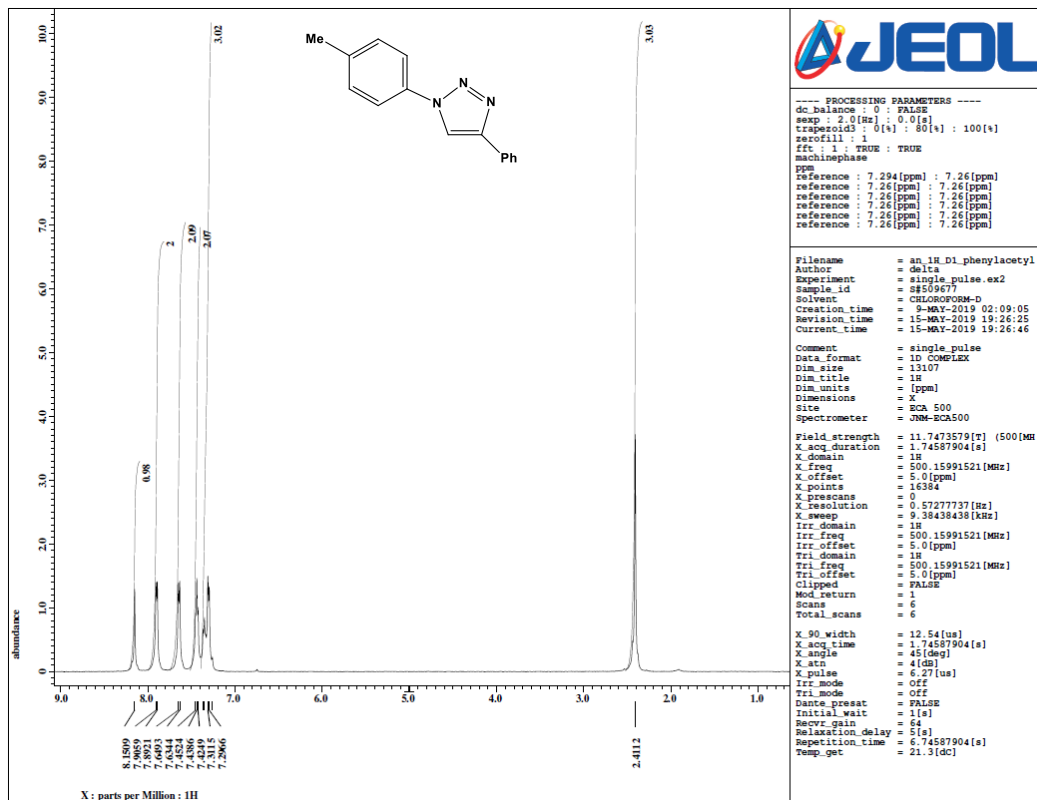
$^{13}\text{C}\{^1\text{H}\}$ NMR spectrum of $\text{Cu}_4(\mu\text{-}[3,5\text{-}(\text{CF}_3)_2\text{Pz}])_4(\text{C}_2\text{H}_5\text{C}\equiv\text{C}(\text{CH}_2)_4\text{C}\equiv\text{CC}_2\text{H}_5)_2$ (12) in CDCl_3 at room temperature.



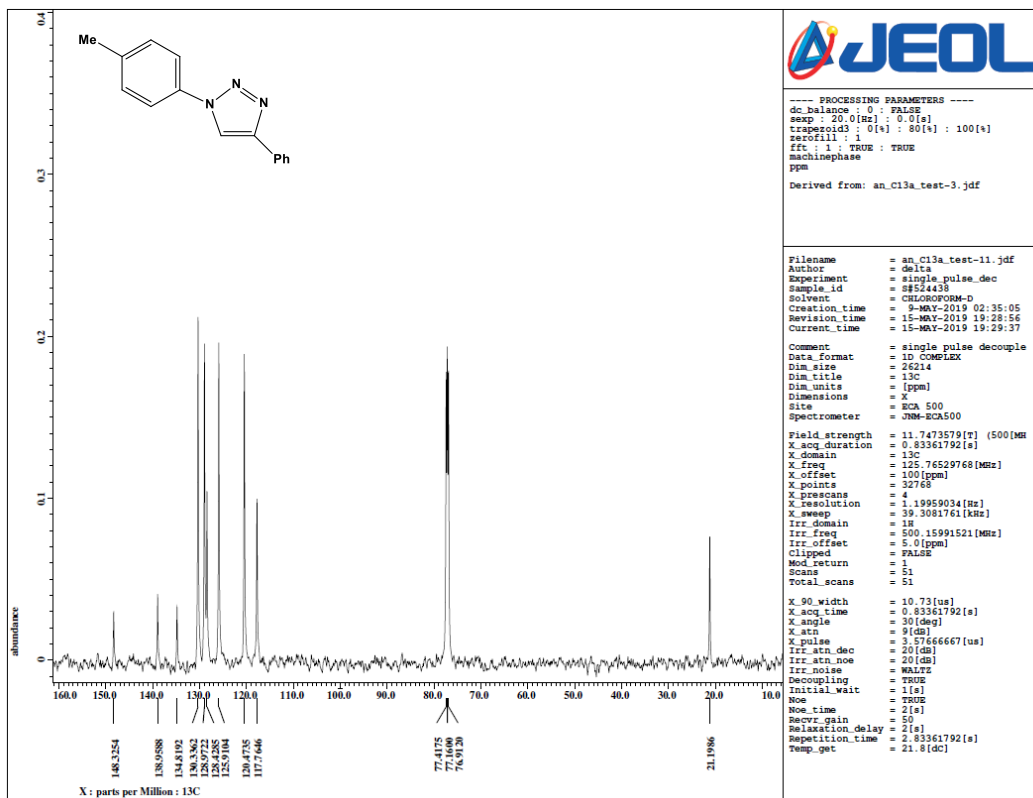
^1H NMR spectrum of 1-*p*-Tolyl-1*H*-1,2,3-triazole in CDCl_3 at the room temperature.



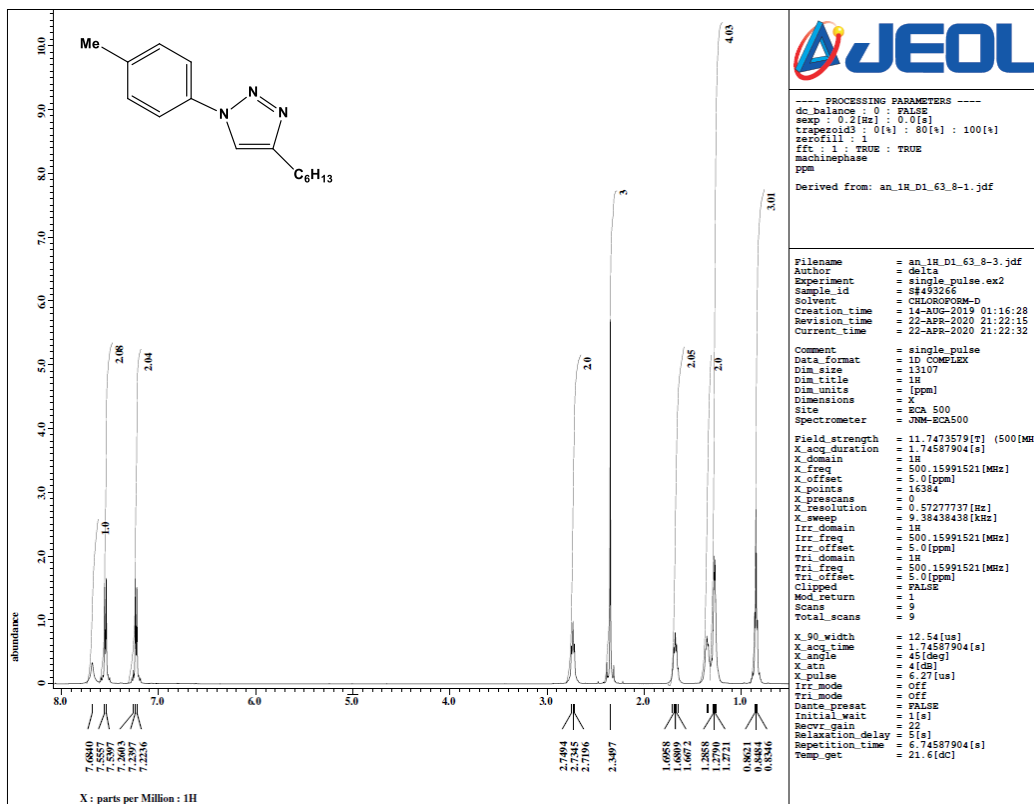
$^{13}\text{C}\{^1\text{H}\}$ NMR spectrum of 1-*p*-Tolyl-1*H*-1,2,3-triazole in CDCl_3 at the room temperature.



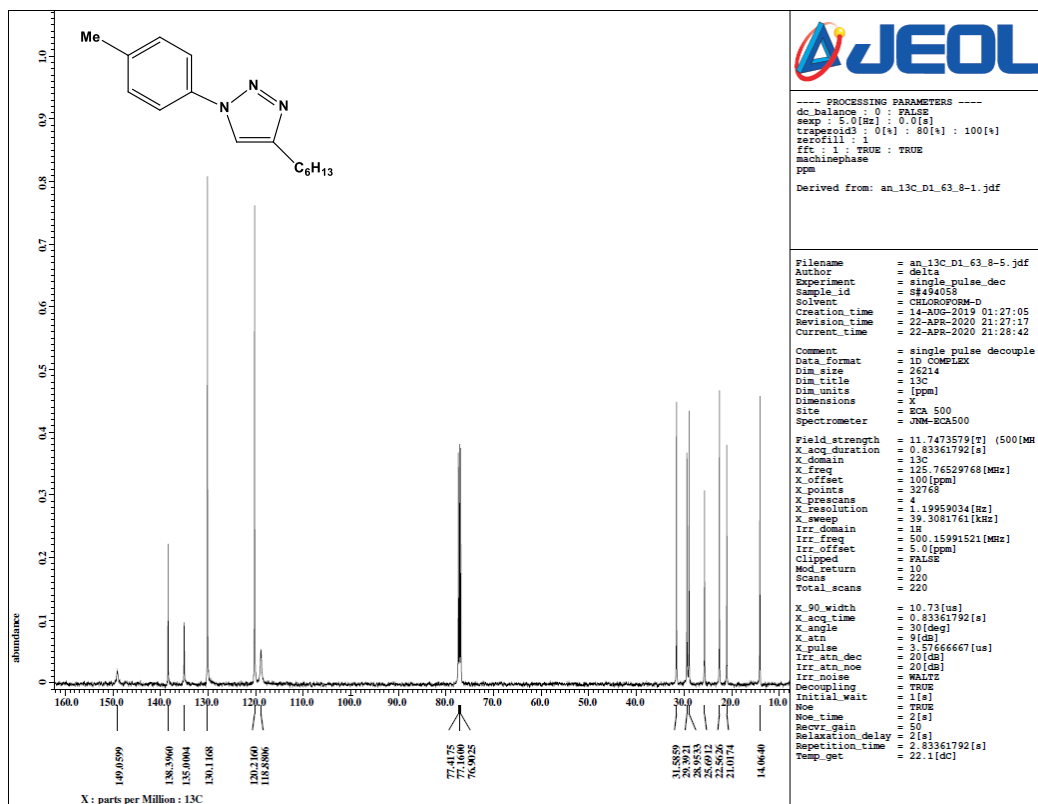
^1H NMR spectrum of 1-*p*-Tolyl-4-phenyl-1*H*-1,2,3-triazole in CDCl_3 at the room temperature.



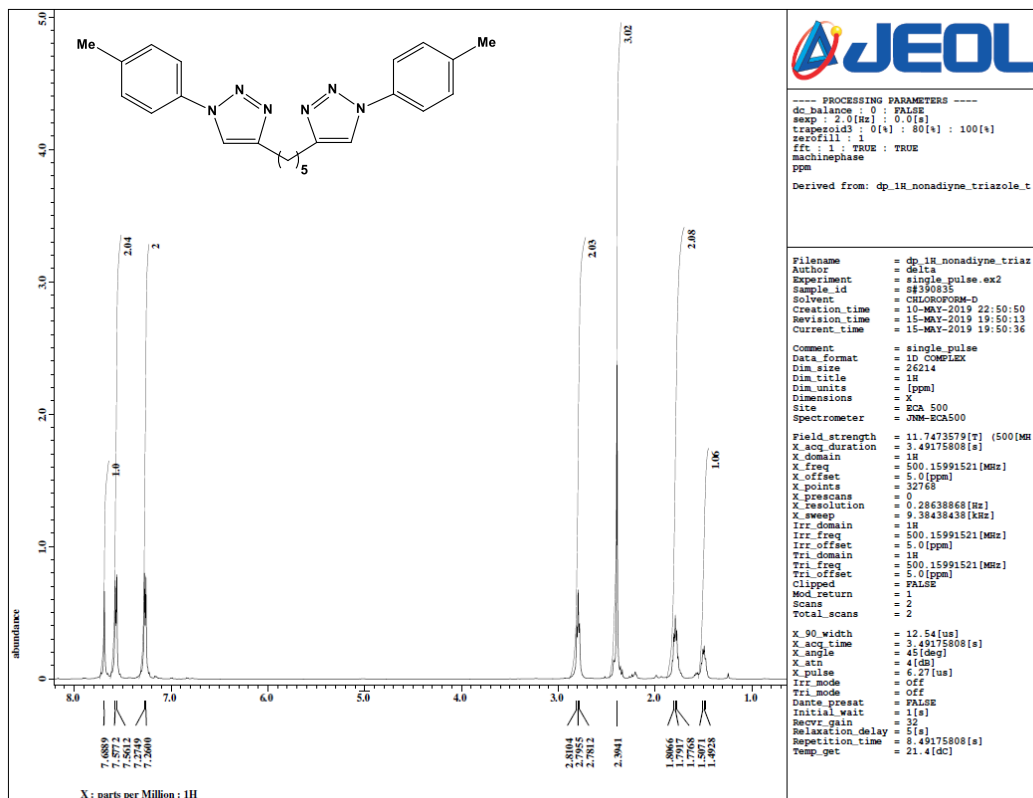
$^{13}\text{C}\{^1\text{H}\}$ NMR spectrum of 1-*p*-Tolyl-4-phenyl-1*H*-1,2,3-triazole in CDCl_3 at the room temperature.



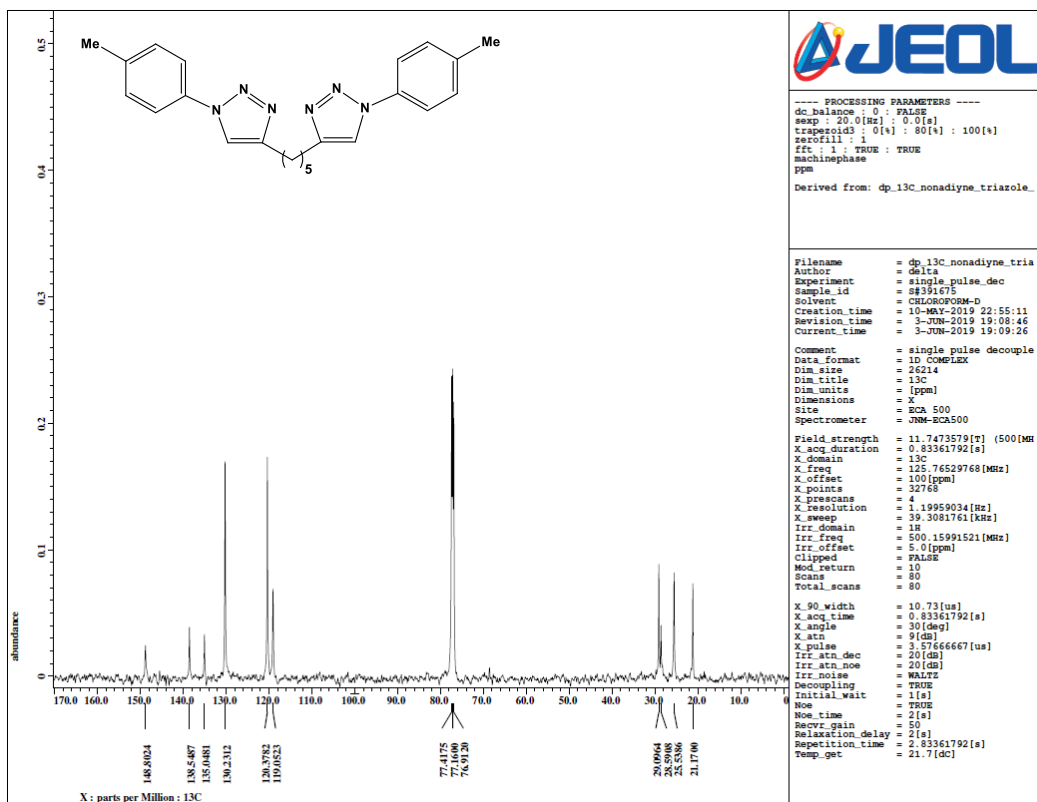
^1H NMR spectrum of 4-hexyl-1-(*p*-tolyl)-1*H*-1,2,3-triazole in CDCl_3 at room temperature.



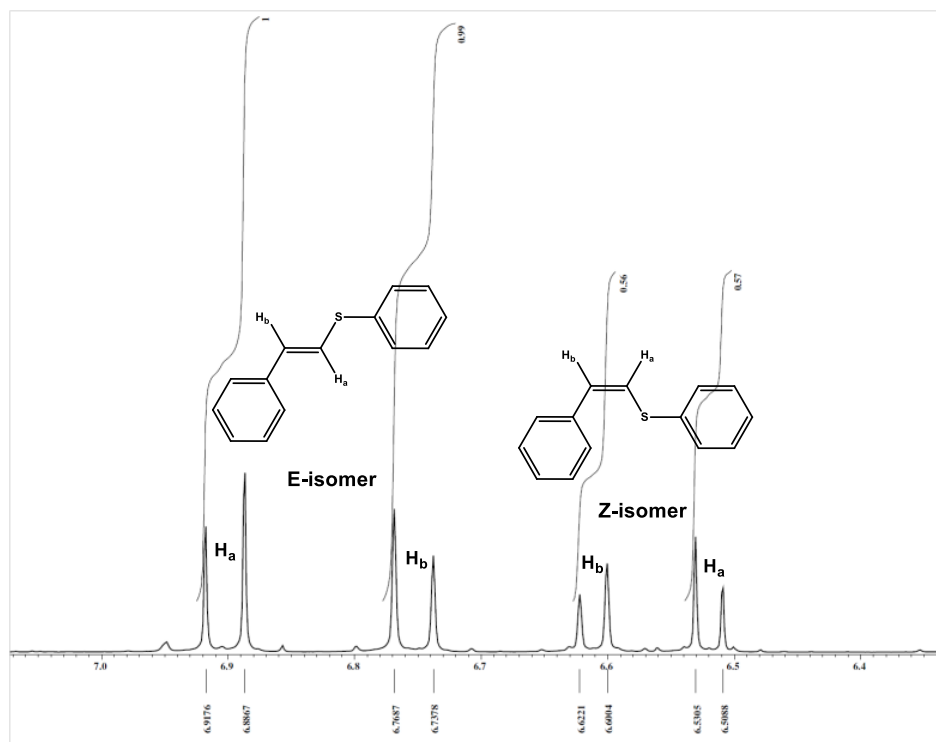
$^{13}\text{C}\{^1\text{H}\}$ NMR spectrum of 4-hexyl-1-(*p*-tolyl)-1*H*-1,2,3-triazole in CDCl_3 at the room temperature.



^1H NMR spectrum of 1-*p*-tolyl-4-(5-(1-*p*-tolyl-1*H*-1,2,3-triazol-4-yl)pentyl)-1*H*-1,2,3-triazole in CDCl_3 at the room temperature.

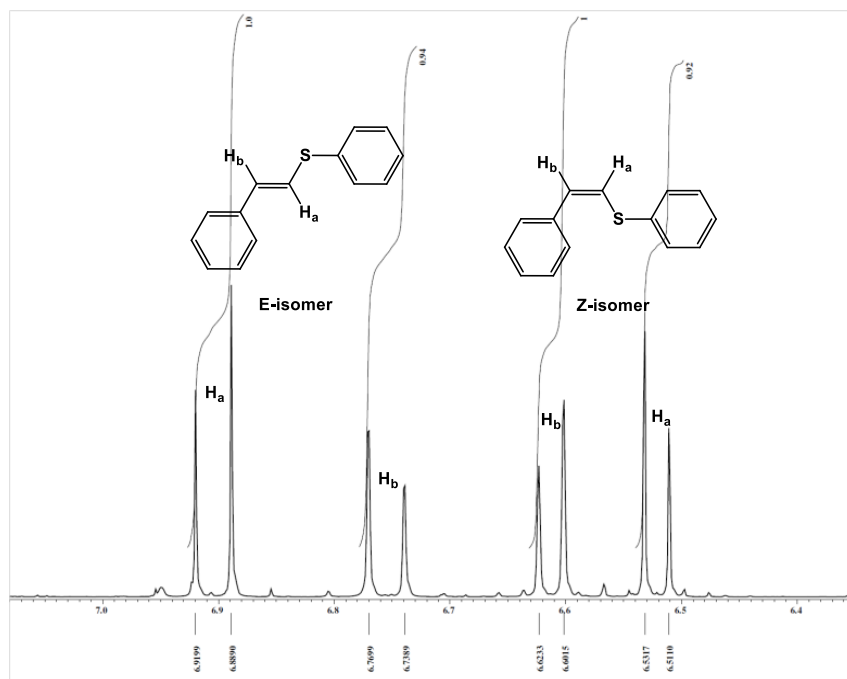


$^{13}\text{C}\{^1\text{H}\}$ NMR spectrum of 1-*p*-tolyl-4-(5-(1-*p*-tolyl-1*H*-1,2,3-triazol-4-yl)pentyl)-1*H*-1,2,3-triazole in CDCl_3 at the room temperature.



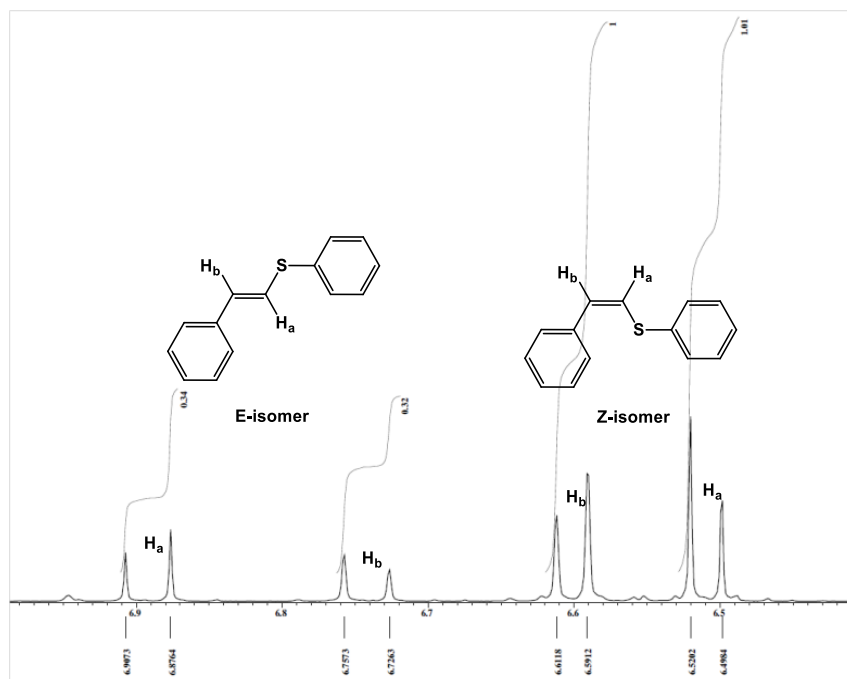
¹H NMR spectrum of Phenyl(styryl)sulfane in CDCl₃ at the room temperature.

Entry 1 CO₂ atm. Isolated as light yellow oil in 70% yield, E/Z ratio: 63:37.



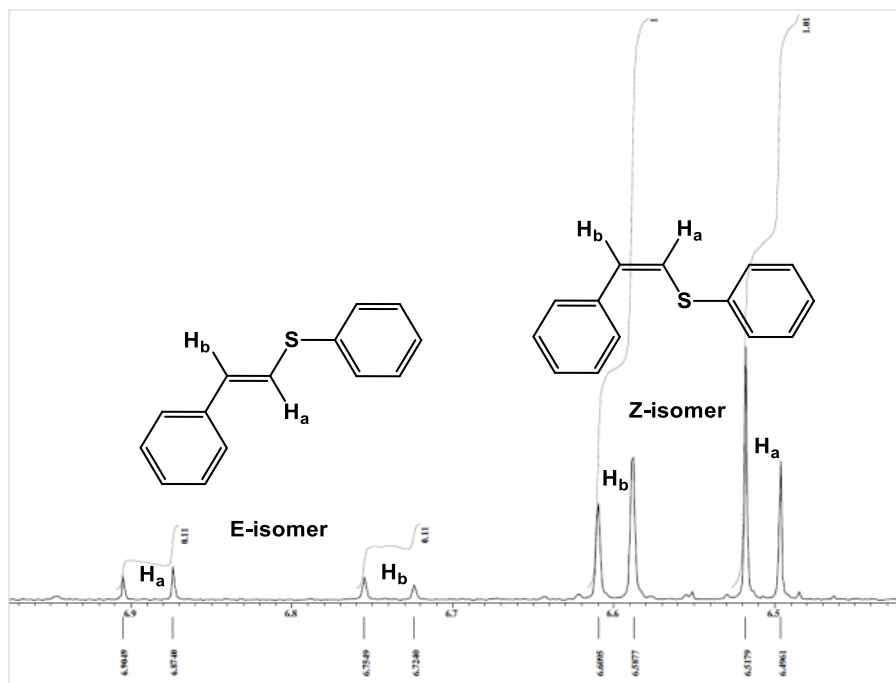
¹H NMR spectrum of Phenyl(styryl)sulfane in CDCl₃ at the room temperature.

Entry 1 N₂ atm. Isolated as light yellow oil in 56% yield, E/Z ratio: 50:50.



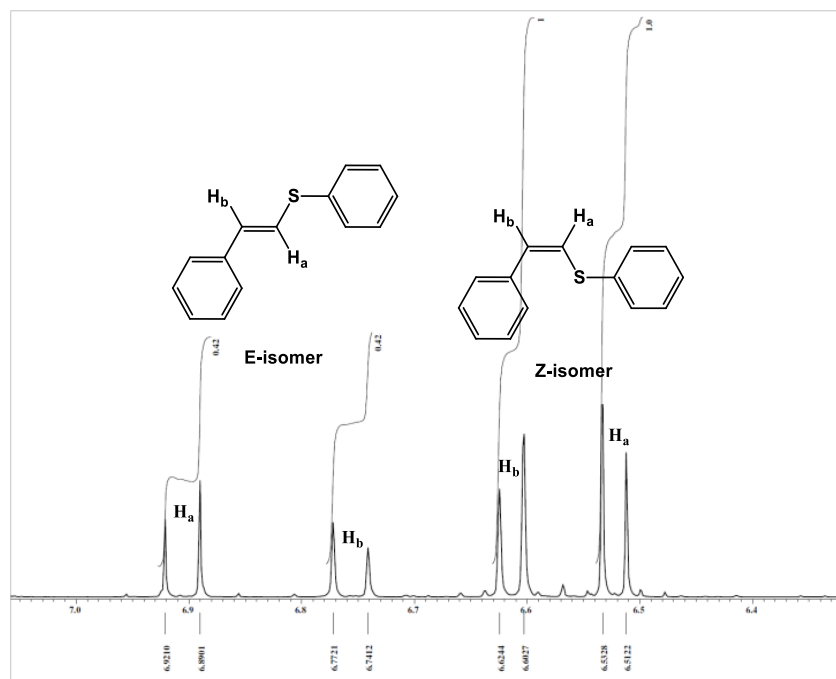
¹H NMR spectrum of Phenyl(styryl)sulfane in CDCl₃ at the room temperature.

Entry 3 CO₂ atm. Isolated as light yellow oil in 65% yield, E/Z ratio: 26:74.



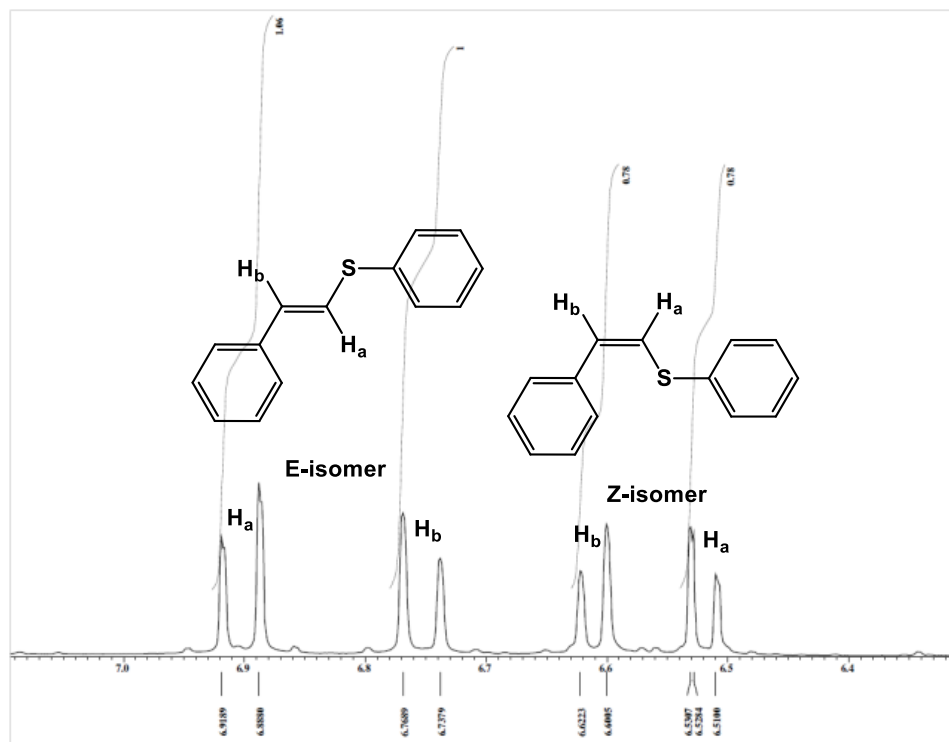
¹H NMR spectrum of Phenyl(styryl)sulfane in CDCl₃ at the room temperature.

Entry 3 N₂ atm. Isolated as light yellow oil in 48% yield, E/Z ratio: 10:90.



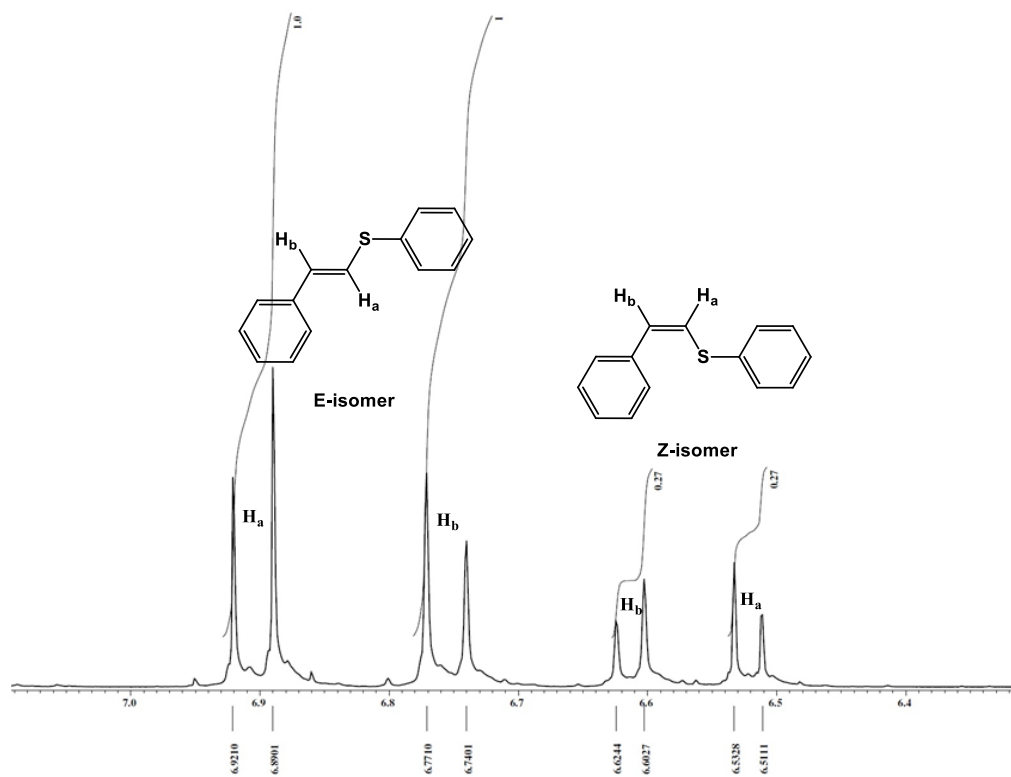
¹H NMR spectrum of Phenyl(styryl)sulfane in CDCl₃ at the room temperature.

Entry 4 CO₂ atm. Isolated as light yellow oil in 78% yield, E/Z ratio: 30:70.



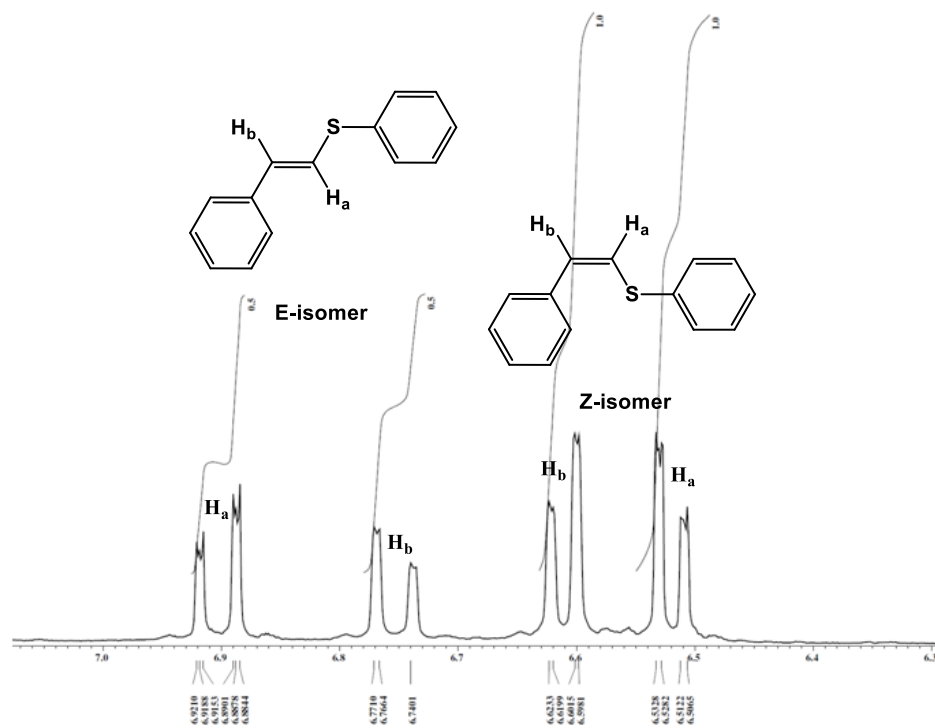
¹H NMR spectrum of Phenyl(styryl)sulfane in CDCl₃ at the room temperature.

Entry 4 N₂ atm. Isolated as light yellow oil in 62% yield, E/Z ratio: 56:44.



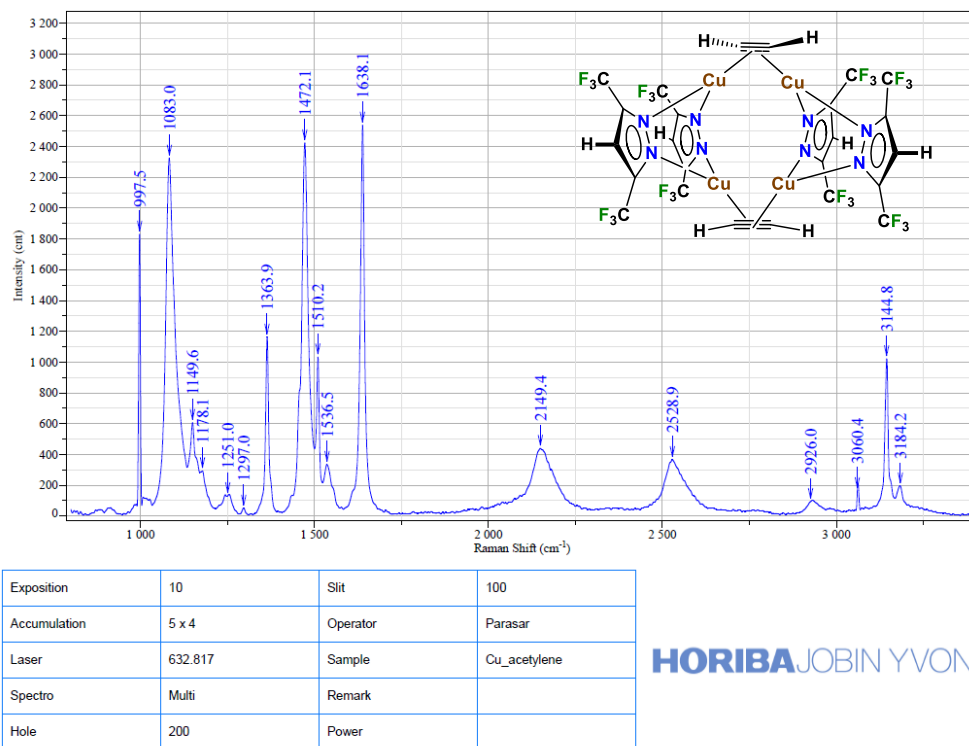
¹H NMR spectrum of Phenyl(styryl)sulfane in CDCl₃ at the room temperature.

Entry 5 CO₂ atm. Isolated as light yellow oil in 90% yield, E/Z ratio: 78:22

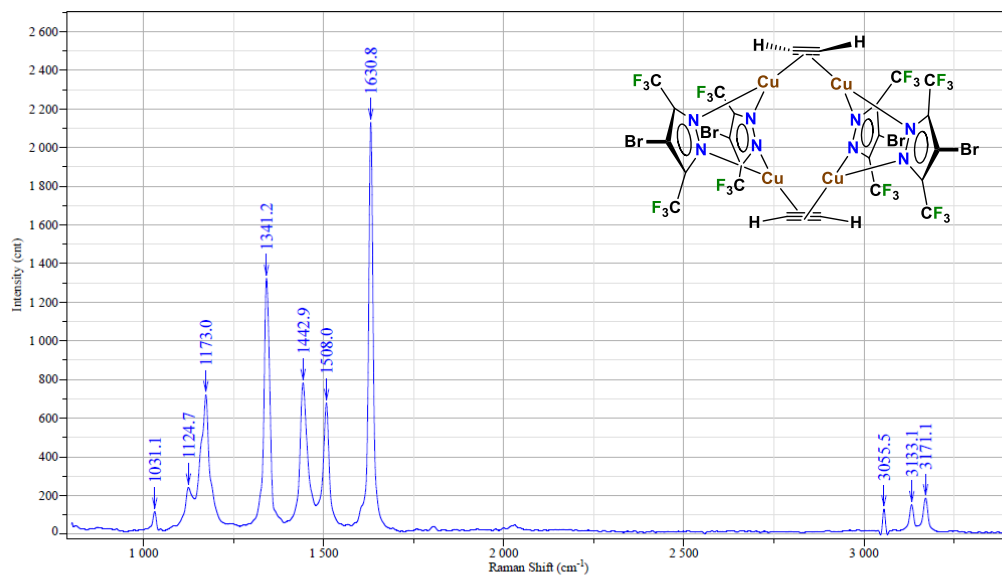


¹H NMR spectrum of Phenyl(styryl)sulfane in CDCl₃ at the room temperature.

Entry 5 N₂ atm. Isolated as light yellow oil in 81% yield, E/Z ratio: 34:66.



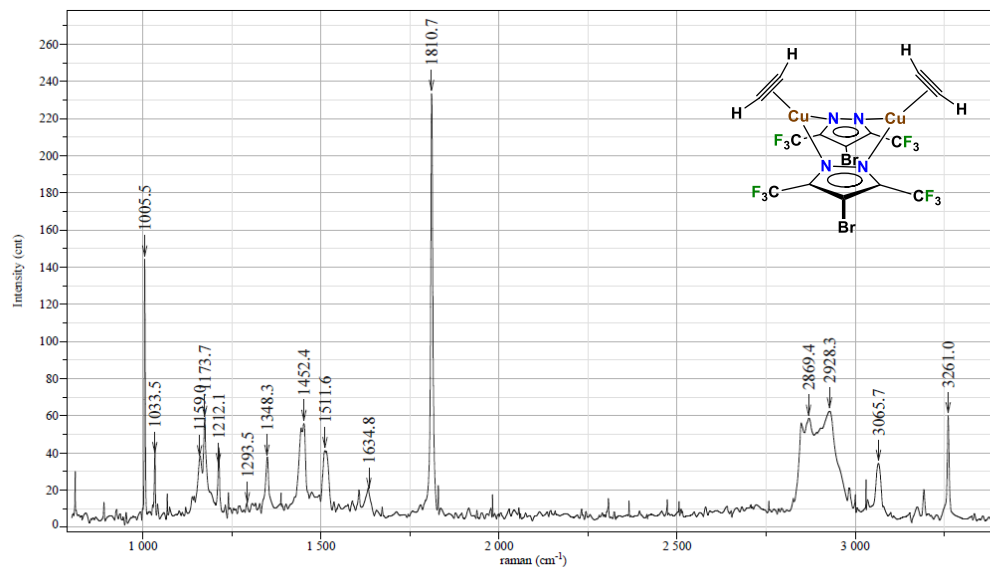
Raman spectrum of solid $\text{Cu}_4(\mu\text{-}[3,5\text{-}(\text{CF}_3)_2\text{Pz}]_4)(\mu\text{-HC}\equiv\text{CH})_2$ (**4**)



Exposition	10	Slit	100
Accumulation	5 x 4	Operator	Parasar
Laser	632.817	Sample	4Br3,5(CF3)2PZCu3_acetylide
Spectro	Multi	Remark	
Hole	200	Power	

HORIBAJOBIN YVON

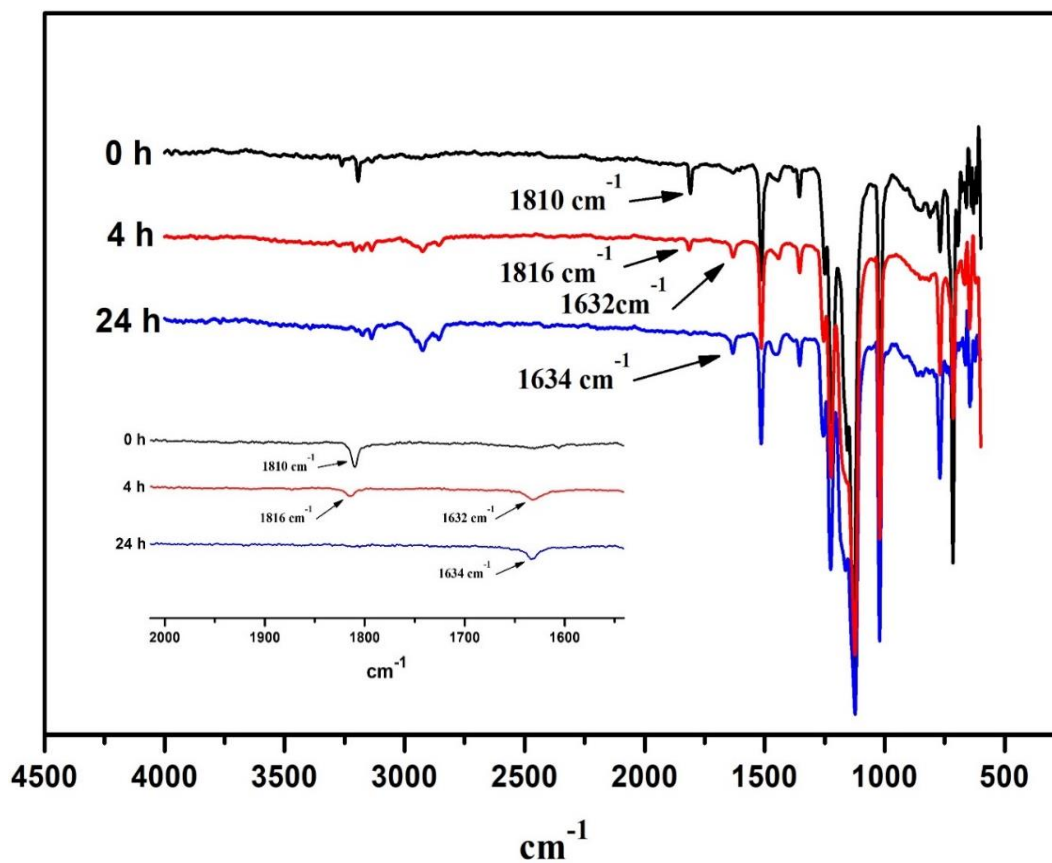
Raman spectrum of solid $\text{Cu}_4(\mu\text{-[4-Br-3,5-(CF}_3)_2\text{Pz]})_4(\mu\text{-HC}\equiv\text{CH})_2$ (**6**)



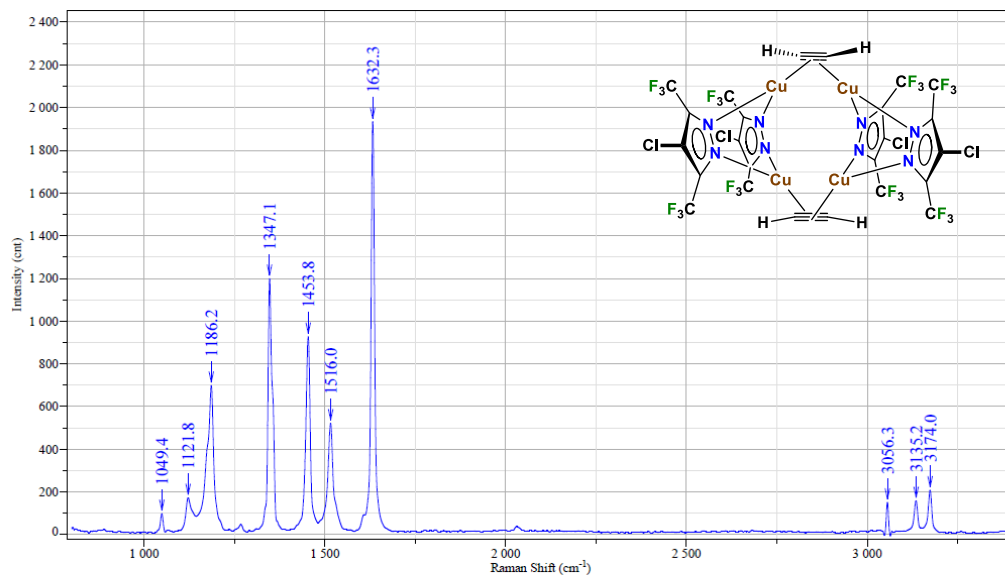
Exposition	5	Slit	100
Accumulation	10 x 4	Operator	
Laser	632.817	Sample	
Spectro	Multi	Remark	
Hole	200	Power	

HORIBA JOBIN YVON

Raman spectrum of solid $\text{Cu}_2(\mu\text{-[4-Br-3,5-(CF}_3)_2\text{Pz]})_2(\text{HC}\equiv\text{CH})_2$ (**8**)



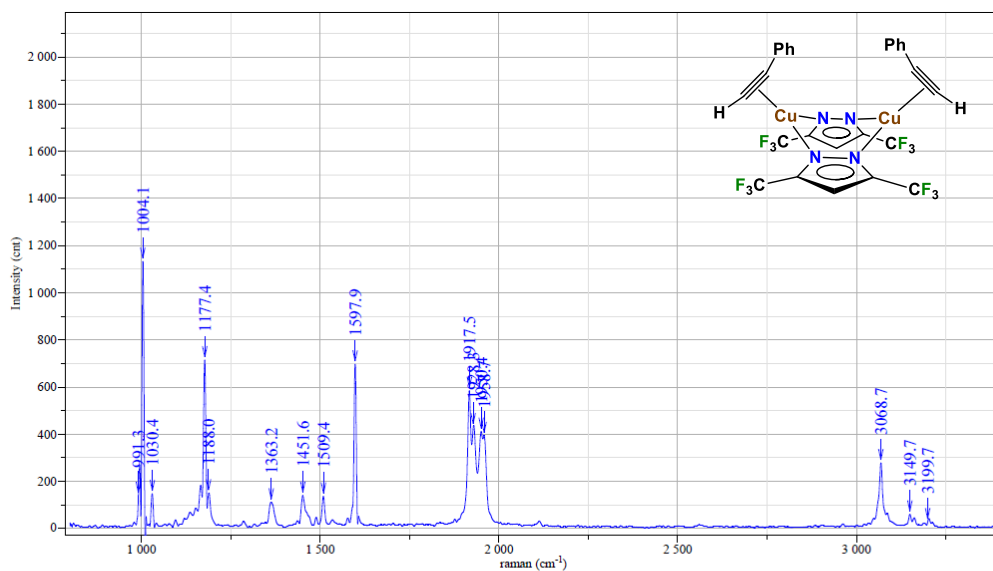
IR spectra of $\text{Cu}_2(\mu\text{-[4-Br-3,5-(CF}_3)_2\text{Pz]})_2(\text{HC}\equiv\text{CH})_2$ (**8**), and the products resulting from its decomposition with the loss of acetylene at room temperature, in open to air, and the likely formation of $\text{Cu}_4(\mu\text{-[4-Br-3,5-(CF}_3)_2\text{Pz]})_4(\mu\text{-HC}\equiv\text{CH})_2$ (**6**). The peaks at 1810 cm^{-1} and 1634 cm^{-1} correspond to complexes **8** and **6**.



Exposition	10	Slit	100
Accumulation	5 x 4	Operator	Parasar
Laser	632.817	Sample	4Cl3,5(CF3)2PZCu3_acetylide
Spectro	Multi	Remark	
Hole	200	Power	

HORIBAJOBIN YVON

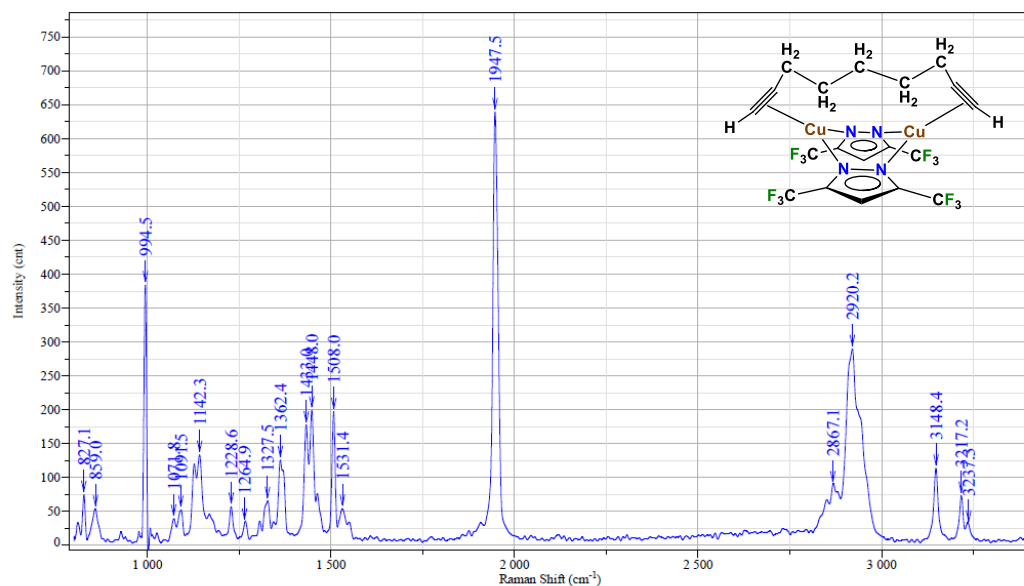
Raman spectrum of solid $\text{Cu}_4(\mu\text{-[4-Cl-3,5-(CF}_3)_2\text{Pz]})_4(\mu\text{-HC}\equiv\text{CH})_2$ (**7**)



Exposition	5	Slit	100
Accumulation	5 x 4	Operator	
Laser	632.817	Sample	
Spectro	Multi	Remark	
Hole	200	Power	

HORIBA JOBIN YVON

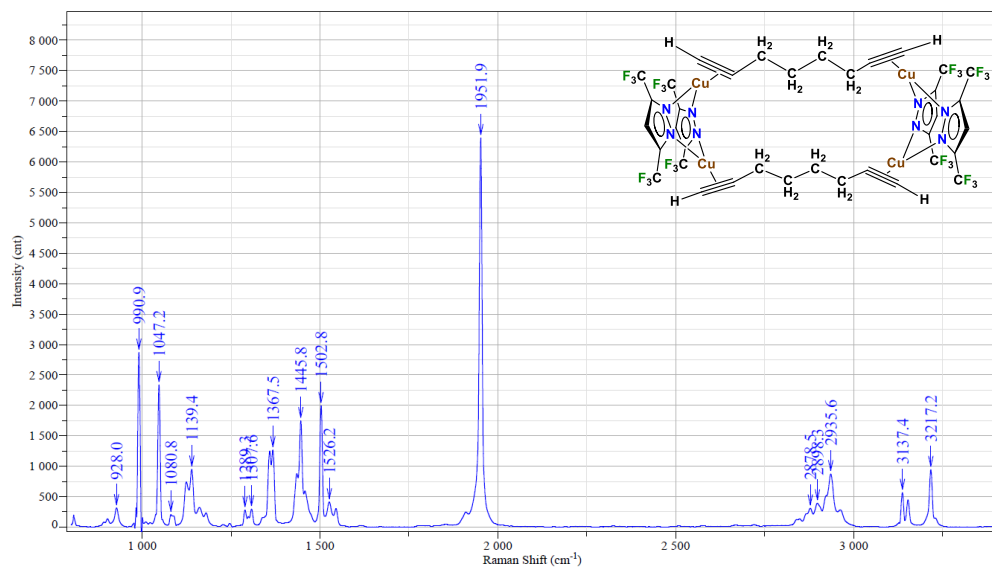
Raman spectrum of solid $\text{Cu}_2(\mu\text{-[3,5-(CF}_3)_2\text{Pz]})_2(\text{HC}\equiv\text{CPh})_2$ (**9**)



Exposition	5	Slit	100
Accumulation	5 x 4	Operator	Parasar
Laser	632.817	Sample	Cu_1,9Nonadiyne_2:3
Spectro	Multi	Remark	
Hole	200	Power	

HORIBA JOBIN YVON

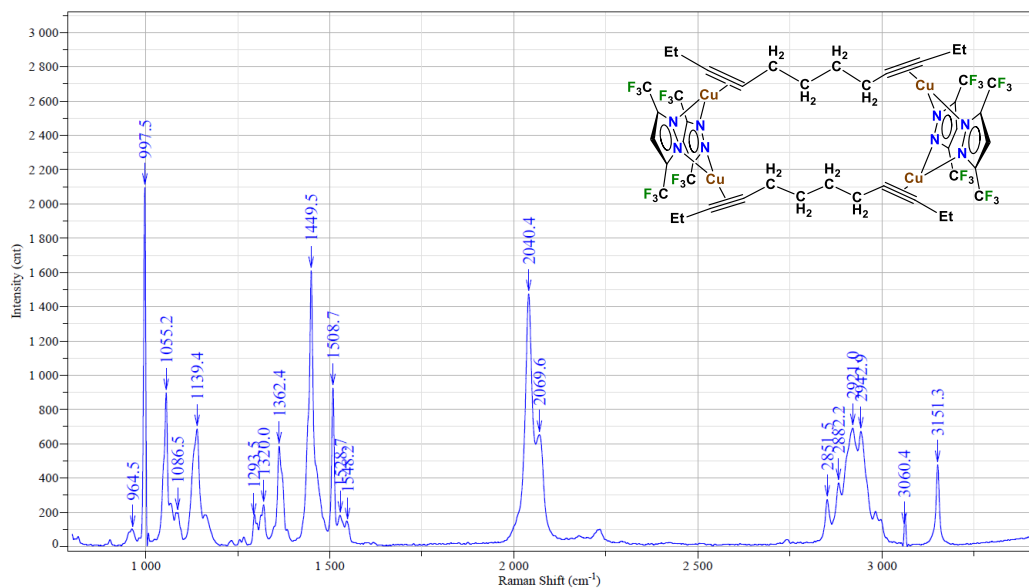
Raman spectrum of solid $\text{Cu}_2(\mu\text{-}[3,5\text{-(CF}_3)_2\text{Pz}])_2(\text{HC}\equiv\text{C}(\text{CH}_2)_5\text{C}\equiv\text{CH})$ (**10**)



Exposition	10	Slit	100
Accumulation	10 x 4	Operator	Parasar
Laser	632.817	Sample	Cu ₃ _1,7-Octadiyne
Spectro	Multi	Remark	
Hole	200	Power	

HORIBAJOBIN YVON

Raman spectrum of solid $\text{Cu}_4(\mu\text{-}[3,5\text{-}(\text{CF}_3)_2\text{Pz}])_4(\text{HC}\equiv\text{C}(\text{CH}_2)_4\text{C}\equiv\text{CH})_2$ (**11**)



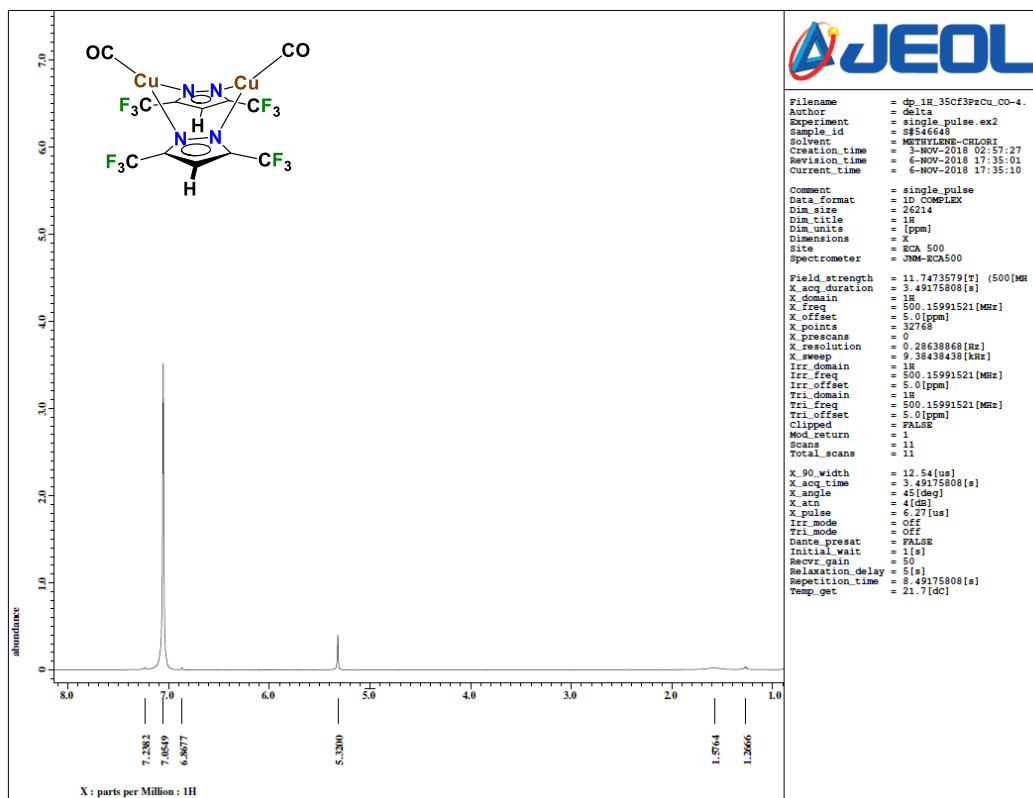
Exposition	10	Slit	100
Accumulation	5 x 4	Operator	Parasar
Laser	632.817	Sample	Cu_Dodecadiene
Spectro	Multi	Remark	
Hole	200	Power	

HORIBA JOBIN YVON

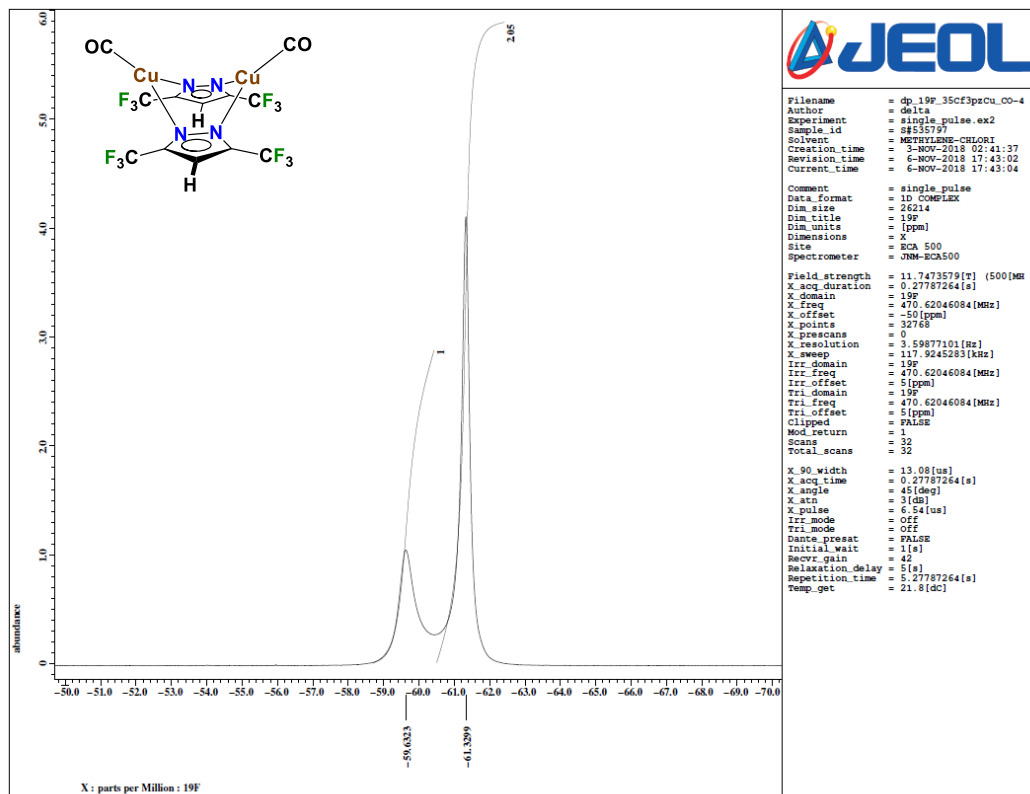
Raman spectrum of solid $\text{Cu}_4(\mu\text{-}[3,5\text{-}(\text{CF}_3)_2\text{Pz}])_4(\text{C}_2\text{H}_5\text{C}\equiv\text{C}(\text{CH}_2)_4\text{C}\equiv\text{CC}_2\text{H}_5)_2$ (**12**)

Appendix C

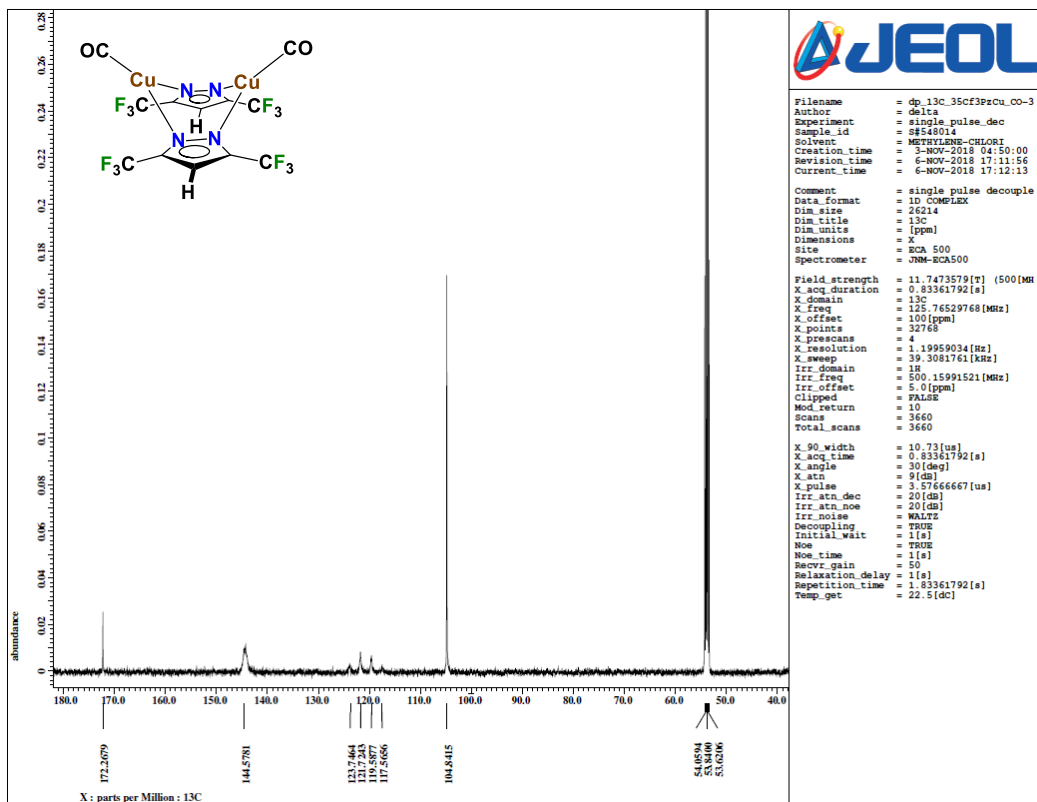
Spectroscopic data of chapter 4



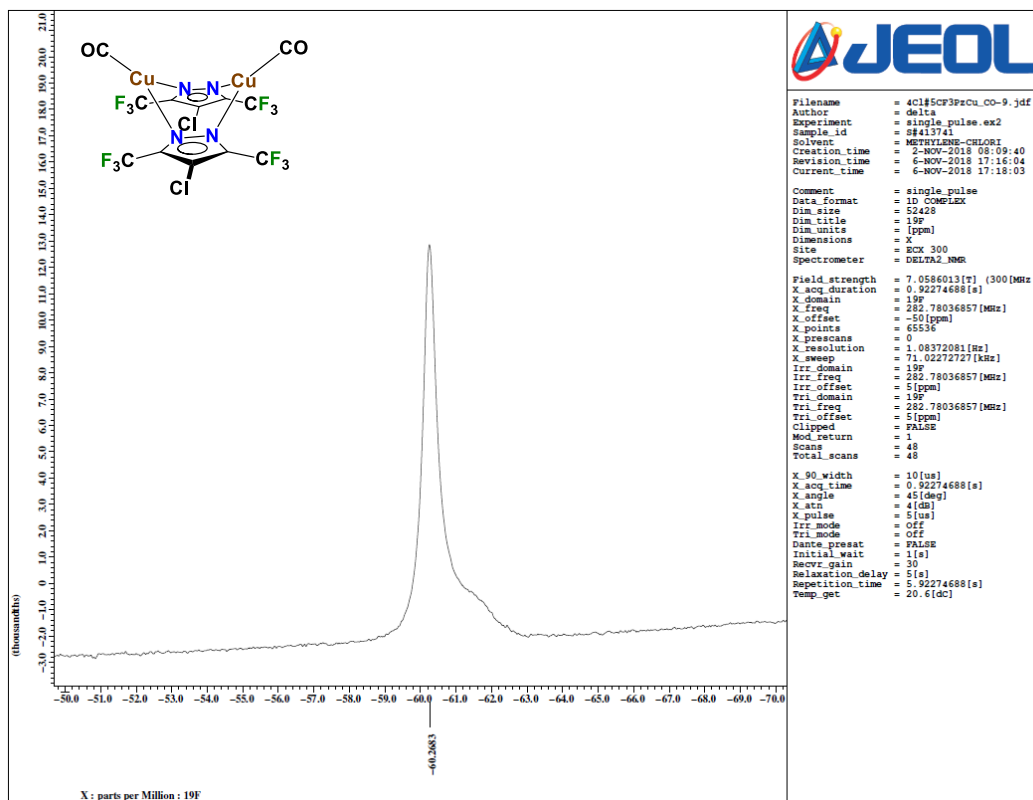
1H NMR spectrum of $\{ [3,5-(CF_3)_2Pz]Cu(CO) \}_2$ (**5**) in CD_2Cl_2 at room temperature.



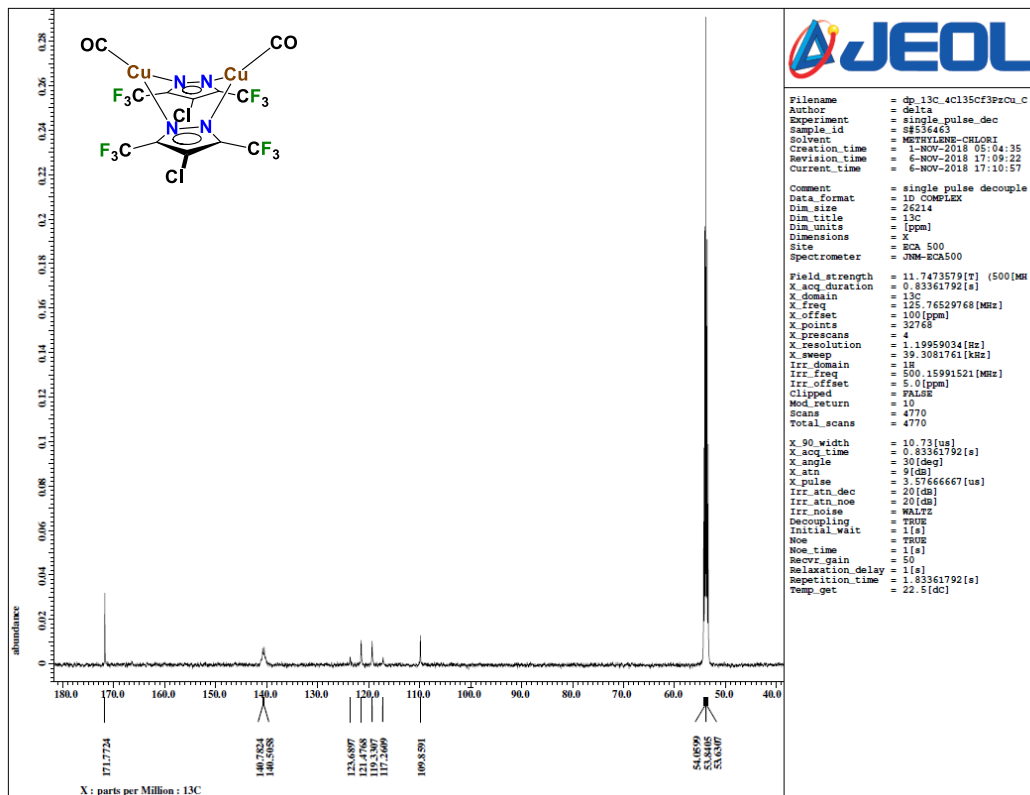
¹⁹F NMR spectrum of $\{[3,5-(CF_3)_2Pz]Cu(CO)\}_2$ (**5**) in CD_2Cl_2 at room temperature. This spectrum also shows presence of $\{[3,5-(CF_3)_2Pz]Cu\}_3$ generated from the disproportionation of $\{[3,5-(CF_3)_2Pz]Cu(CO)\}_2$ to $\{[3,5-(CF_3)_2Pz]Cu\}_3$ and free CO. Peak at -59.63 ppm is the signal corresponding to $\{[3,5-(CF_3)_2Pz]Cu(CO)\}_2$ while peak at -61.33 ppm corresponds to $\{[3,5-(CF_3)_2Pz]Cu\}_3$.



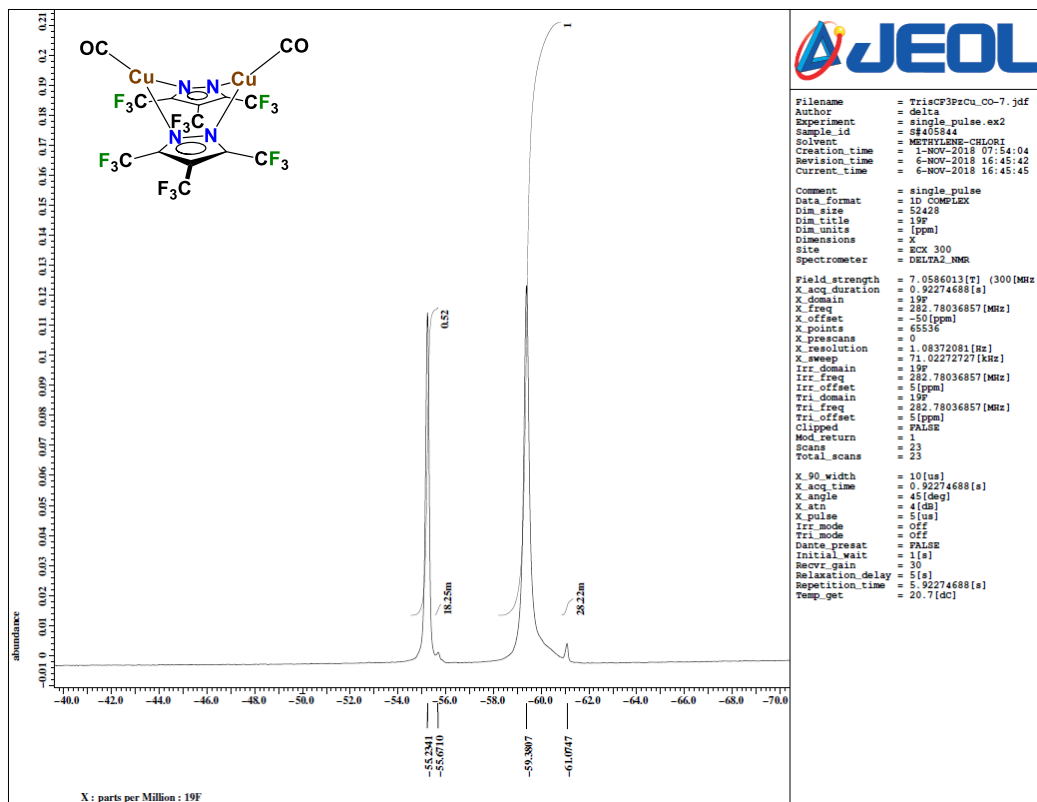
$^{13}\text{C}\{^1\text{H}\}$ NMR spectrum of $\{[3,5-(\text{CF}_3)_2\text{Pz}]\text{Cu}(\text{CO})\}_2$ (**5**) in CD_2Cl_2 at room temperature.



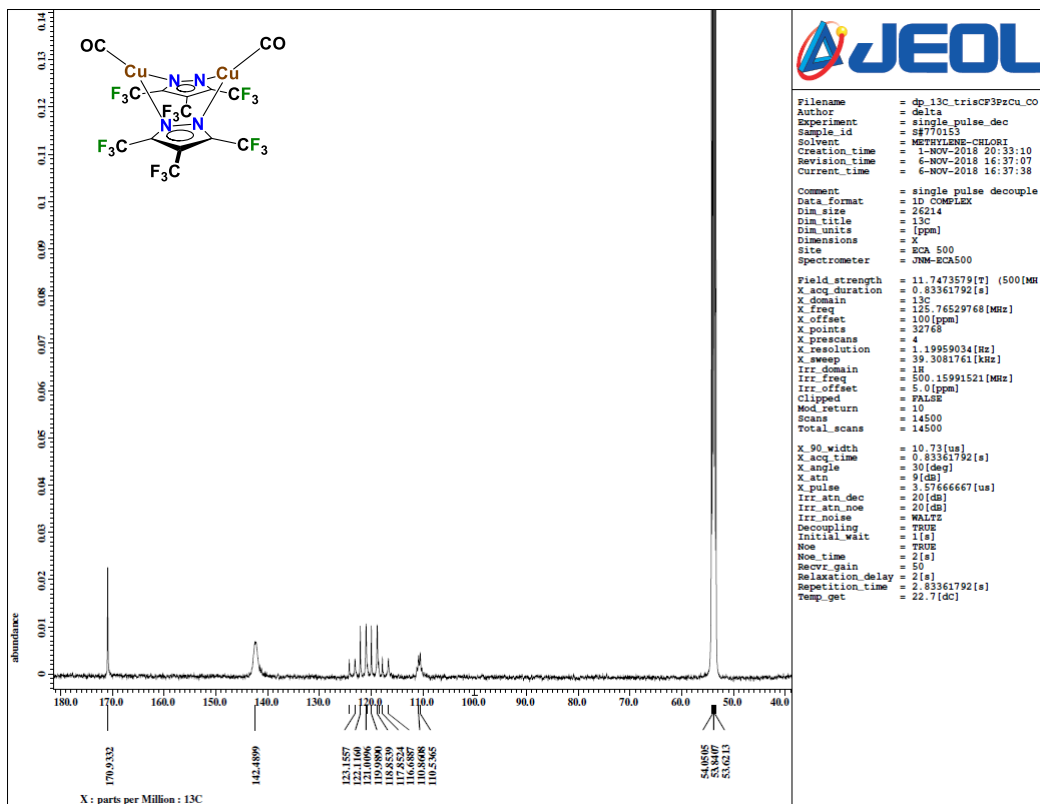
^{19}F NMR spectrum of $\{[4\text{-Cl-3,5-(CF}_3)_2\text{Pz}]_2\text{Cu(CO)}\}_2$ (6) in CD_2Cl_2 at room temperature.



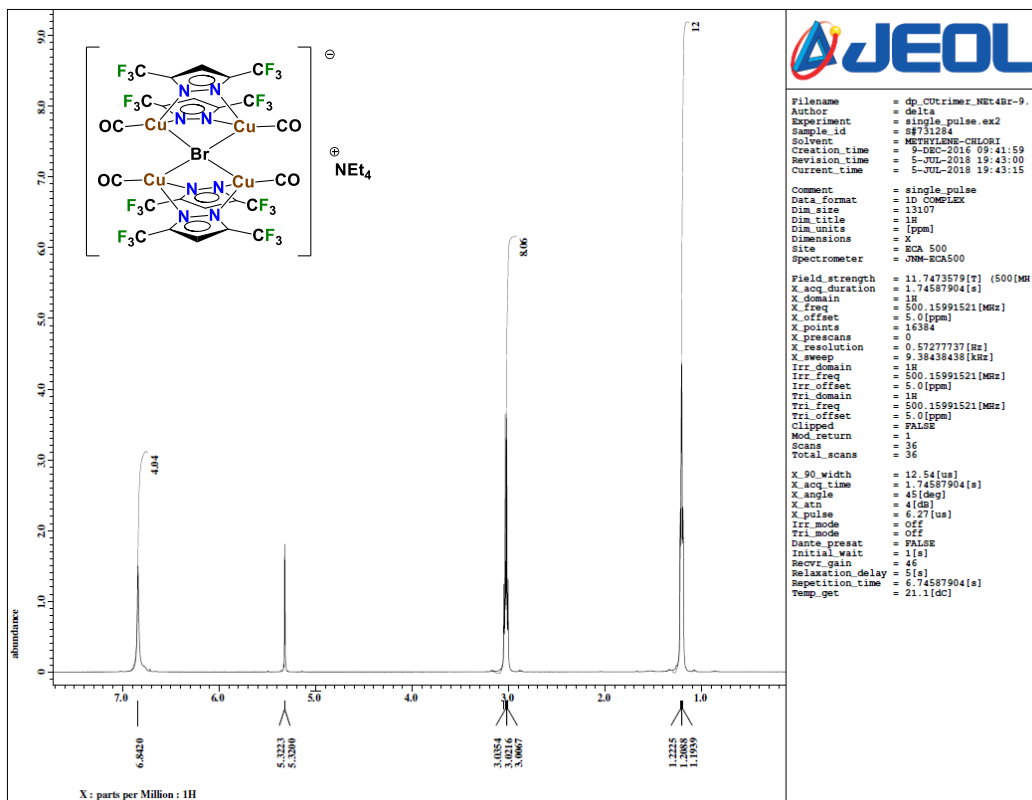
$^{13}\text{C}\{^1\text{H}\}$ NMR spectrum of $\{[4\text{-Cl-3,5-(CF}_3)_2\text{Pz}]_2\text{Cu(CO)}_2\}$ (6) in CD_2Cl_2 at room temperature.



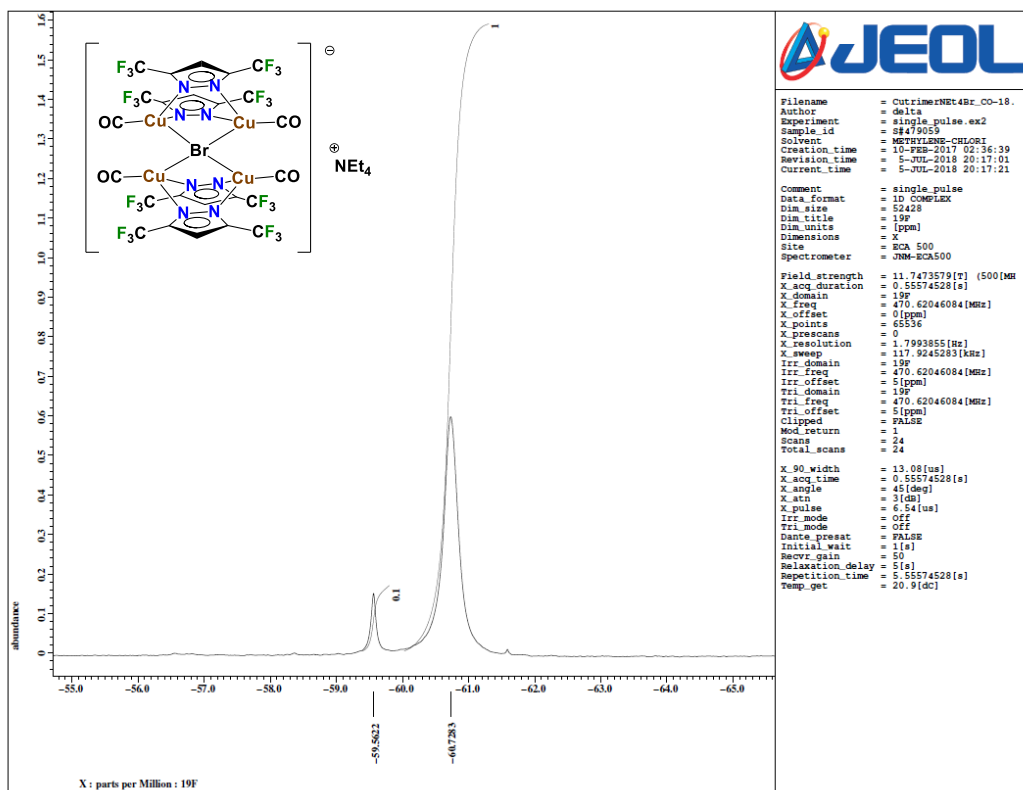
^{19}F NMR spectrum of $\{[3,4,5-(CF_3)_3Pz]Cu(CO)_2\}_2$ (**7**) in CD_2Cl_2 at room temperature. This spectrum also shows presence of $\{[3,4,5-(CF_3)_3Pz]Cu\}_3$ generated from the disproportionation of $\{[3,4,5-(CF_3)_3Pz]Cu(CO)_2\}_2$ to $\{[3,4,5-(CF_3)_3Pz]Cu\}_3$ and free CO. Peaks at -55.23 and -59.38 ppm are the signals corresponding to $\{[3,4,5-(CF_3)_3Pz]Cu(CO)_2\}_2$ while peaks at -55.67 and -61.07 ppm corresponds to $\{[3,4,5-(CF_3)_3Pz]Cu\}_3$.



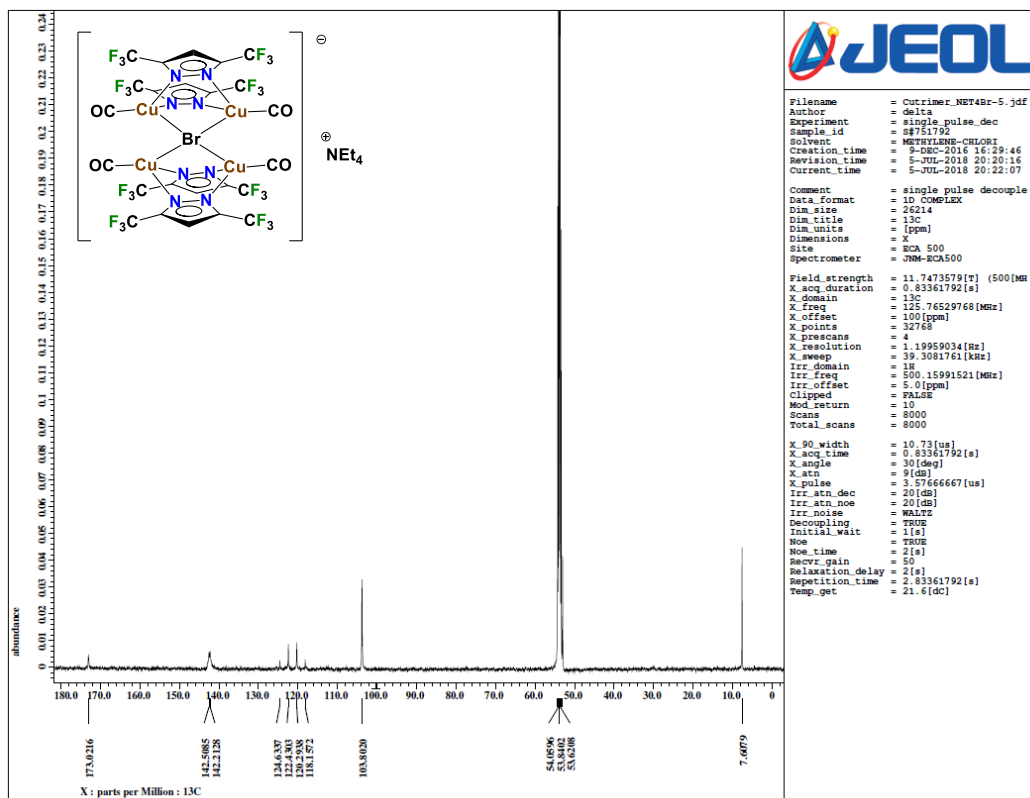
$^{13}\text{C}\{^1\text{H}\}$ NMR spectrum of $\{[3,4,5-(\text{CF}_3)_3\text{Pz}]\text{Cu}(\text{CO})\}_2$ (**7**) in CD_2Cl_2 at room temperature. This spectrum also shows presence of minor amount of $\{[3,4,5-(\text{CF}_3)_3\text{Pz}]\text{Cu}\}_3$ generated from the disproportionation of $\{[3,4,5-(\text{CF}_3)_3\text{Pz}]\text{Cu}(\text{CO})\}_2$ to $\{[3,4,5-(\text{CF}_3)_3\text{Pz}]\text{Cu}\}_3$ and free CO.



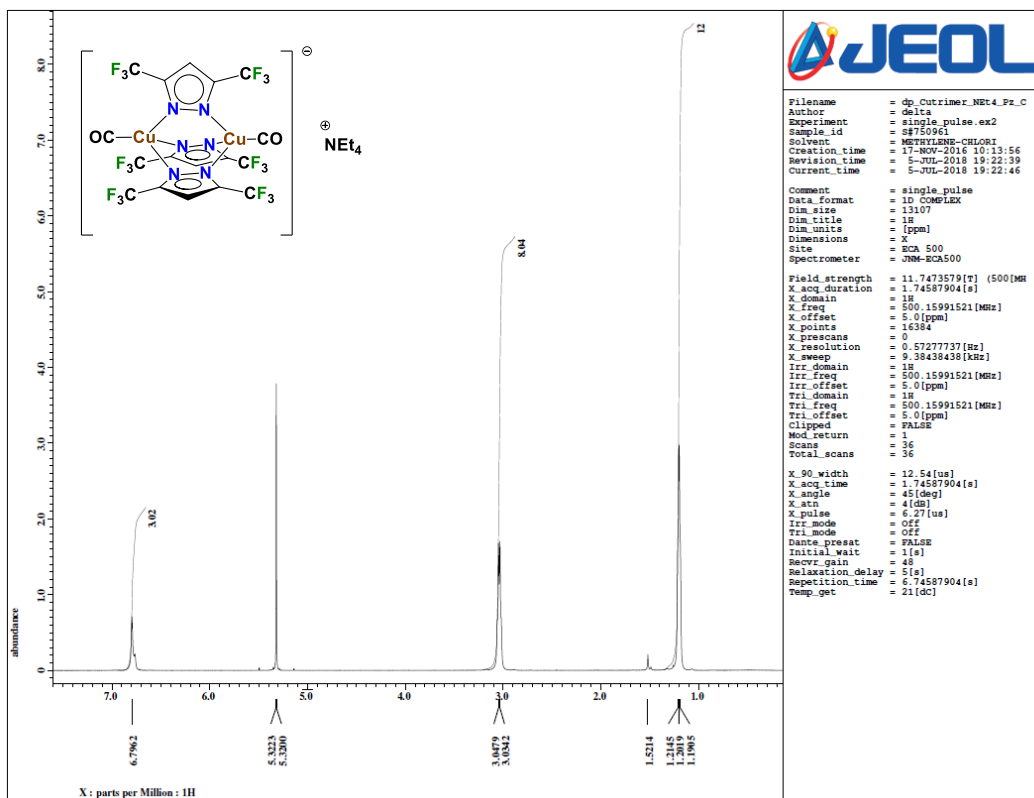
¹H NMR spectrum of [NEt₄][{[3,5-(CF₃)₂Pz]Cu(CO)}₄(μ₄-Br)] (**8**) in CD₂Cl₂ at the room temperature.



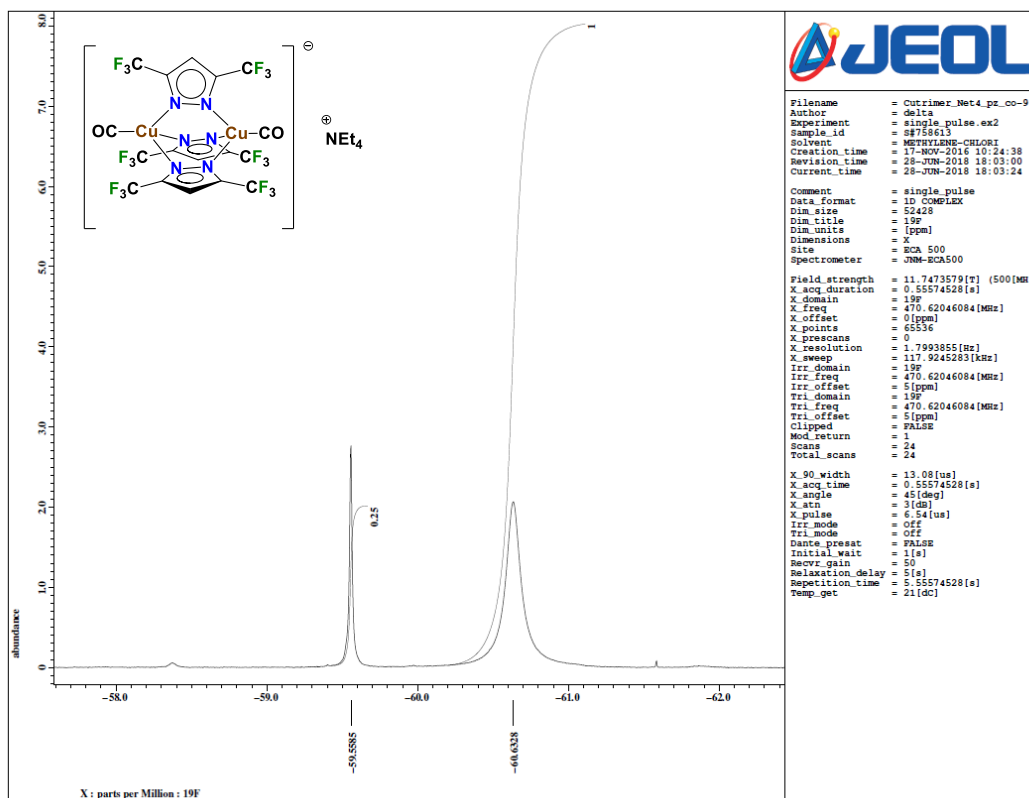
^{19}F NMR spectrum of $[\text{NEt}_4][\{[3,5\text{-(CF}_3)_2\text{Pz]Cu(CO)}\}_4(\mu_4\text{-Br)}]$ (**8**) in CD_2Cl_2 at the room temperature.



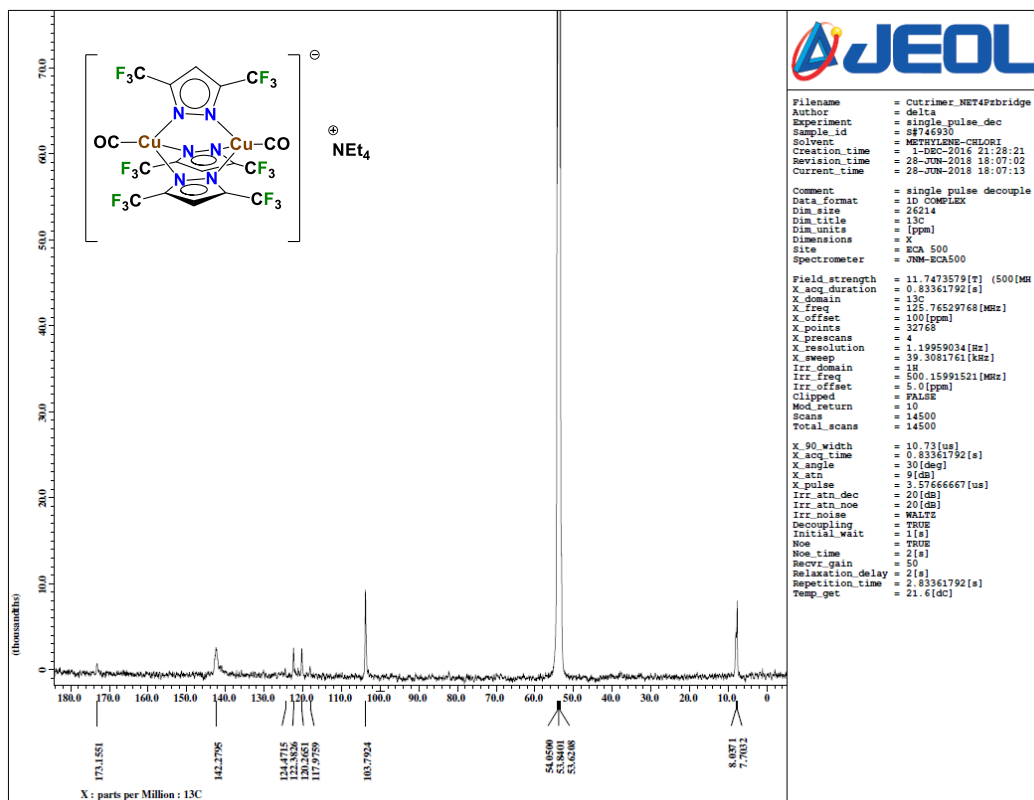
$^{13}\text{C}\{^1\text{H}\}$ NMR spectrum of $[\text{NEt}_4][\{[3,5\text{-(CF}_3)_2\text{Pz]Cu(CO)}\}_4(\mu_4\text{-Br})]$ (8) in CD_2Cl_2 at the room temperature.



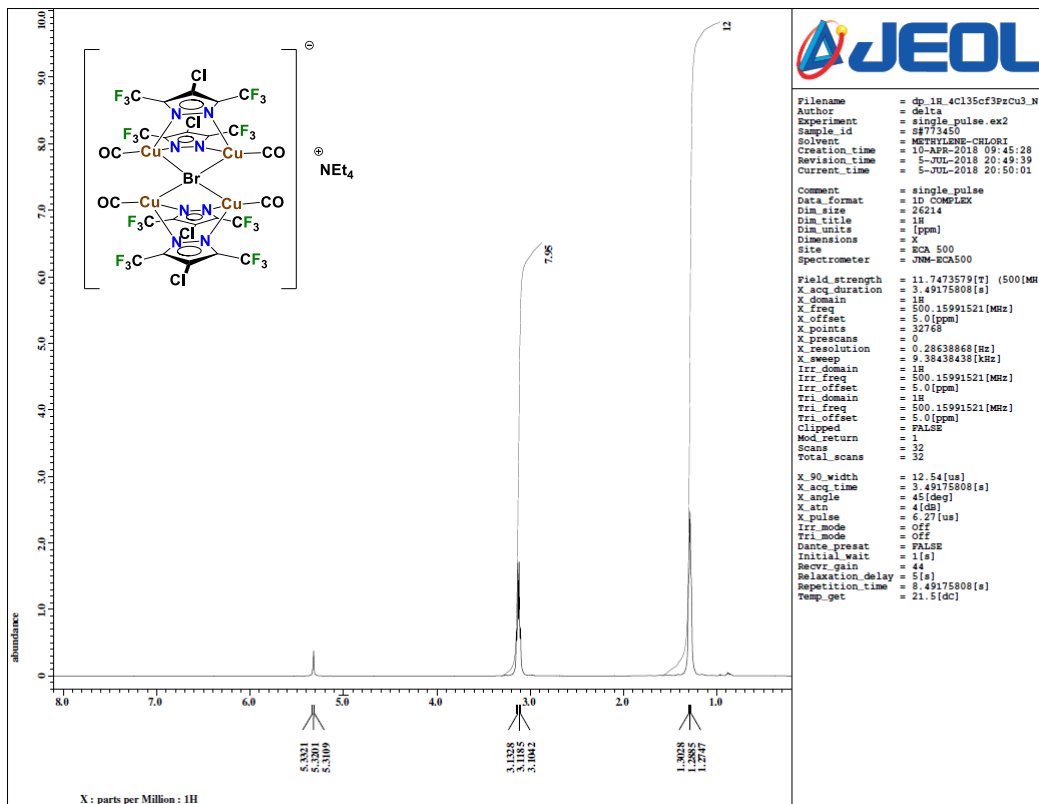
^1H NMR spectrum of $[\text{NEt}_4][\text{3,5-(CF}_3)_2\text{Pz}]_3\text{Cu}_2(\text{CO})_2$ (**9**) in CD_2Cl_2 at the room temperature.



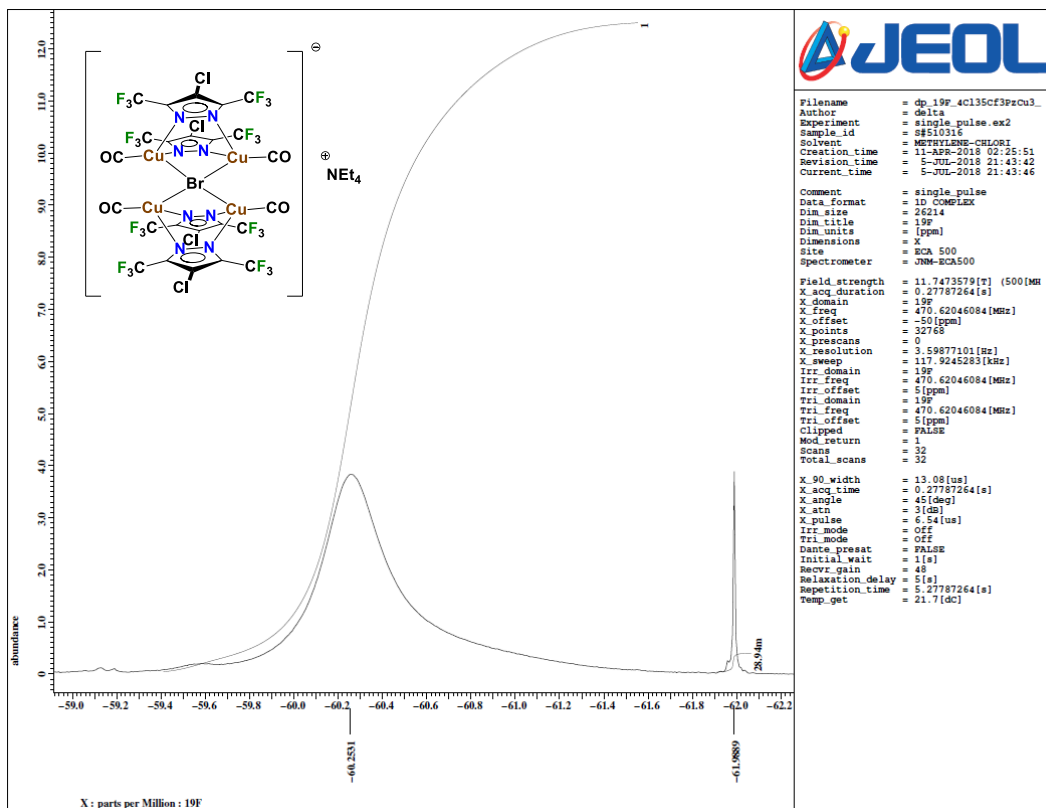
^{19}F NMR spectrum of $[NEt_4][\{3,5-(CF_3)_2Pz\}_3Cu_2(CO)_2]$ (**9**) in CD_2Cl_2 at the room temperature.



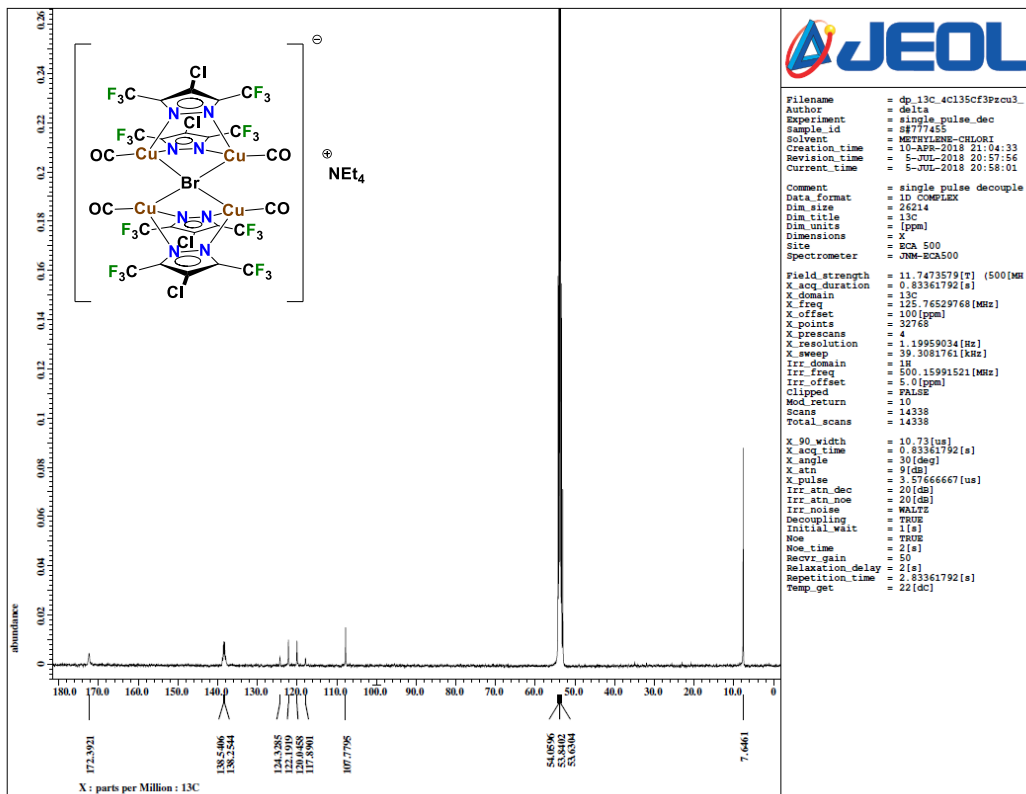
$^{13}\text{C}\{^1\text{H}\}$ NMR spectrum of $[\text{NEt}_4][\{[3,5-(\text{CF}_3)_2\text{Pz}]_3\text{Cu}_2(\text{CO})_2\}]$ (**9**) in CD_2Cl_2 at the room temperature.



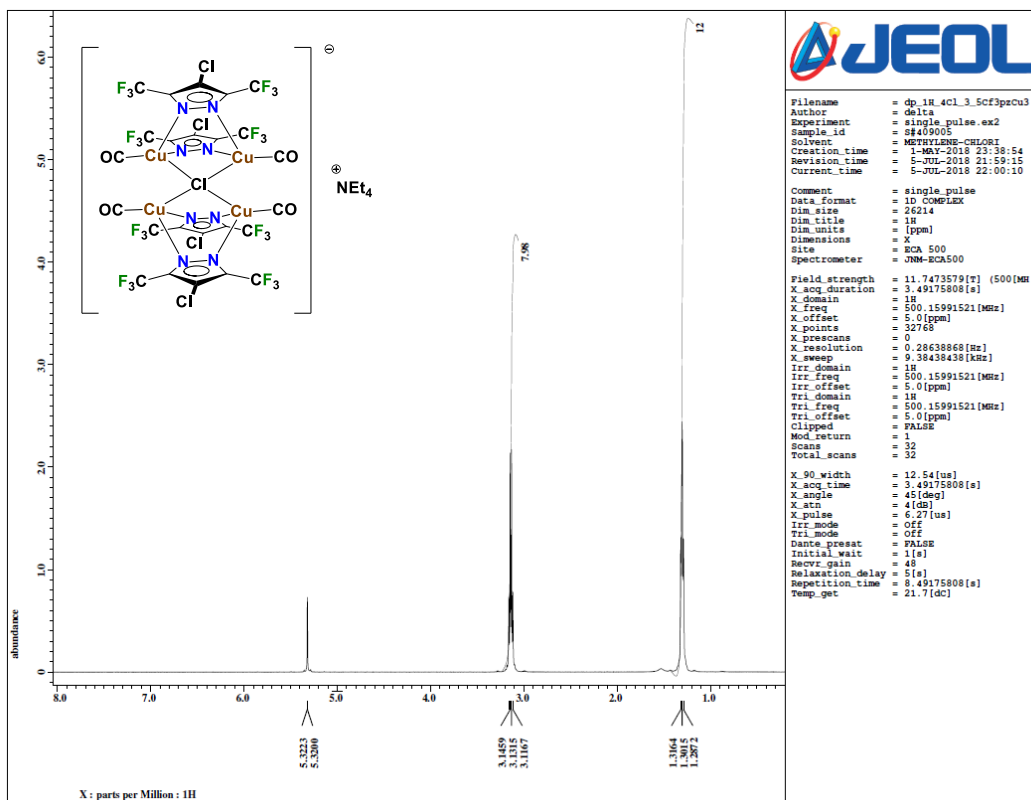
^1H NMR spectrum of $[\text{NEt}_4][\{[4\text{-Cl-3,5-(CF}_3)_2\text{Pz]Cu(CO)}\}_4(\mu_4\text{-Br})]$ (**10**) in CD_2Cl_2 at the room temperature.



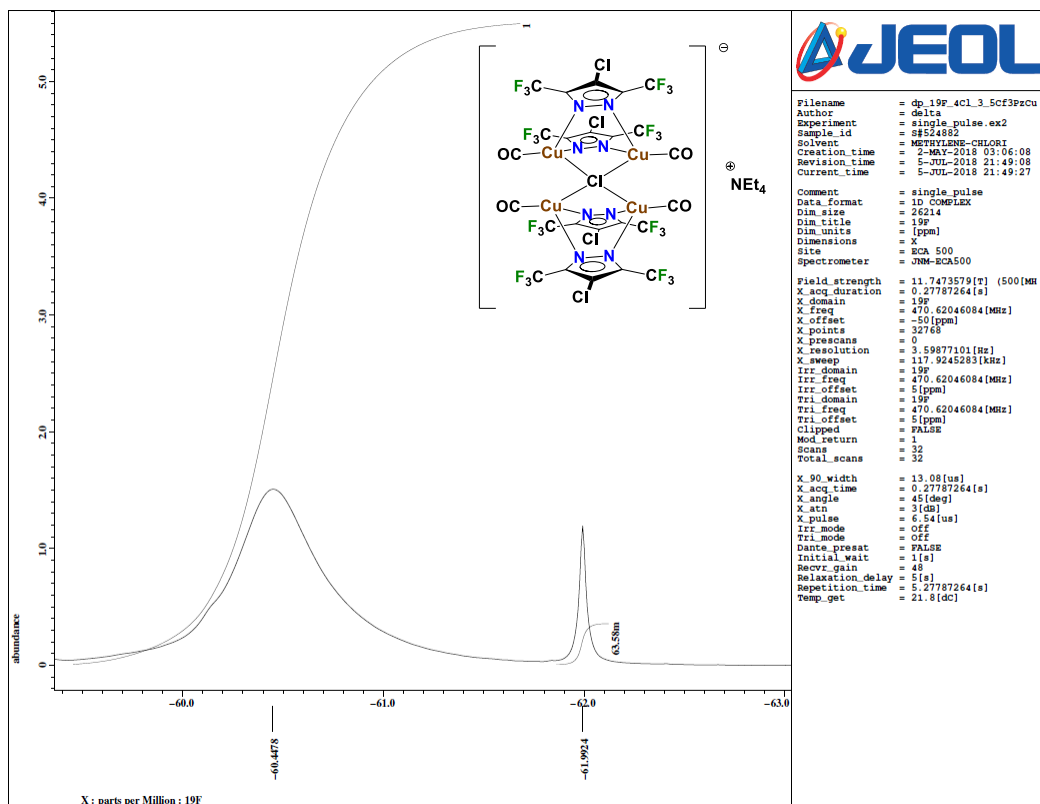
^{19}F NMR spectrum of $[\text{NEt}_4][\{[4\text{-Cl-3,5-(CF}_3)_2\text{Pz]Cu(CO)}\}_4(\mu_4\text{-Br})]$ (**10**) in CD_2Cl_2 at the room temperature.



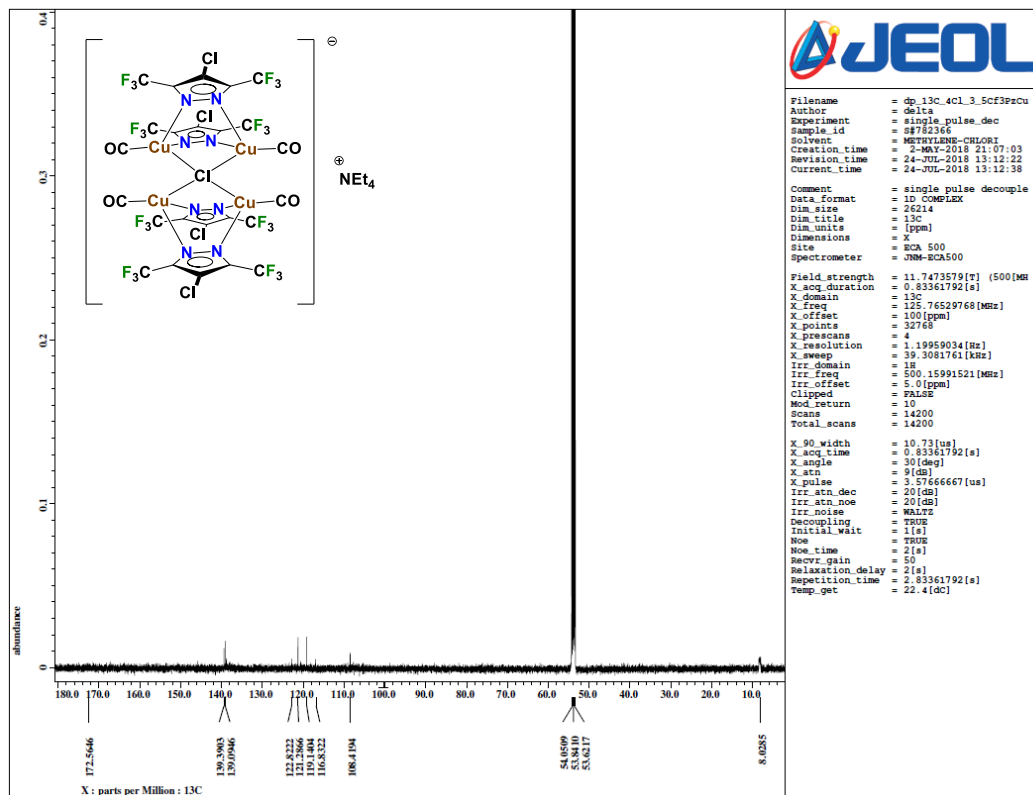
$^{13}\text{C}\{^1\text{H}\}$ NMR spectrum of $[\text{NEt}_4][\{[4\text{-Cl-3,5-(CF}_3)_2\text{Pz]Cu(CO)}\}_4(\mu_4\text{-Br})]$ (10) in CD_2Cl_2 at the room temperature.



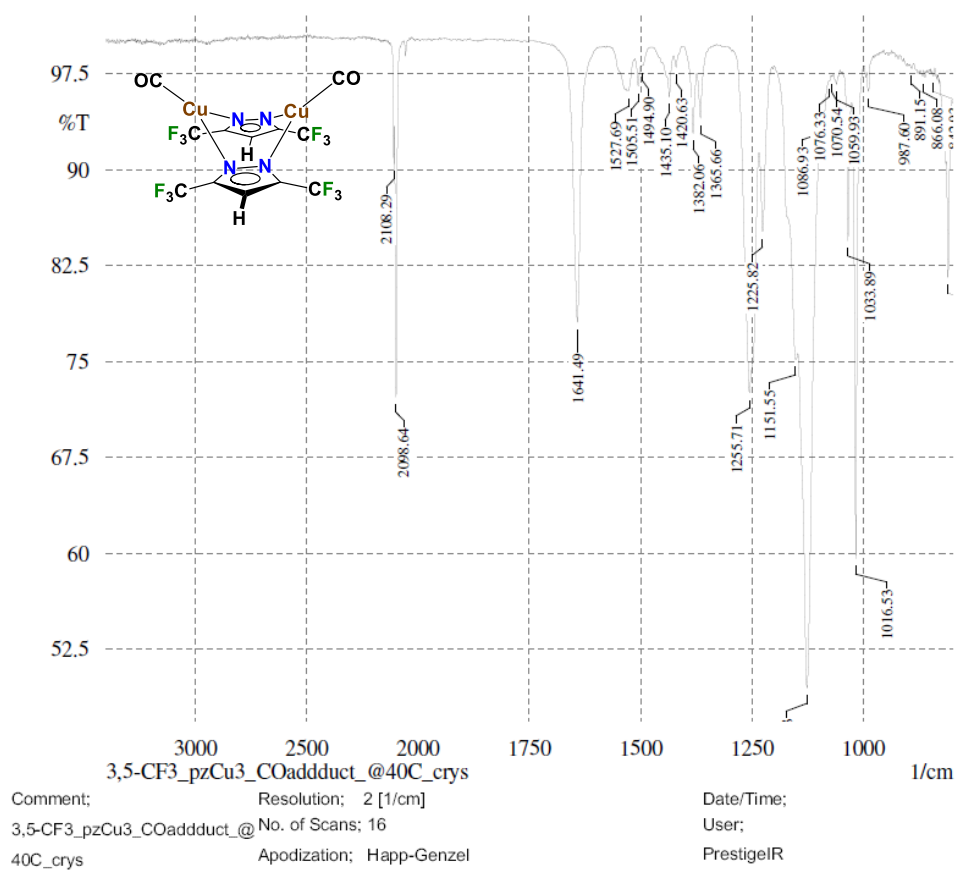
¹H NMR spectrum of [NEt₄][{[4-Cl-3,5-(CF₃)₂Pz]Cu(CO)}₄(μ₄-Cl)] (**11**) in CD₂Cl₂ at the room temperature.



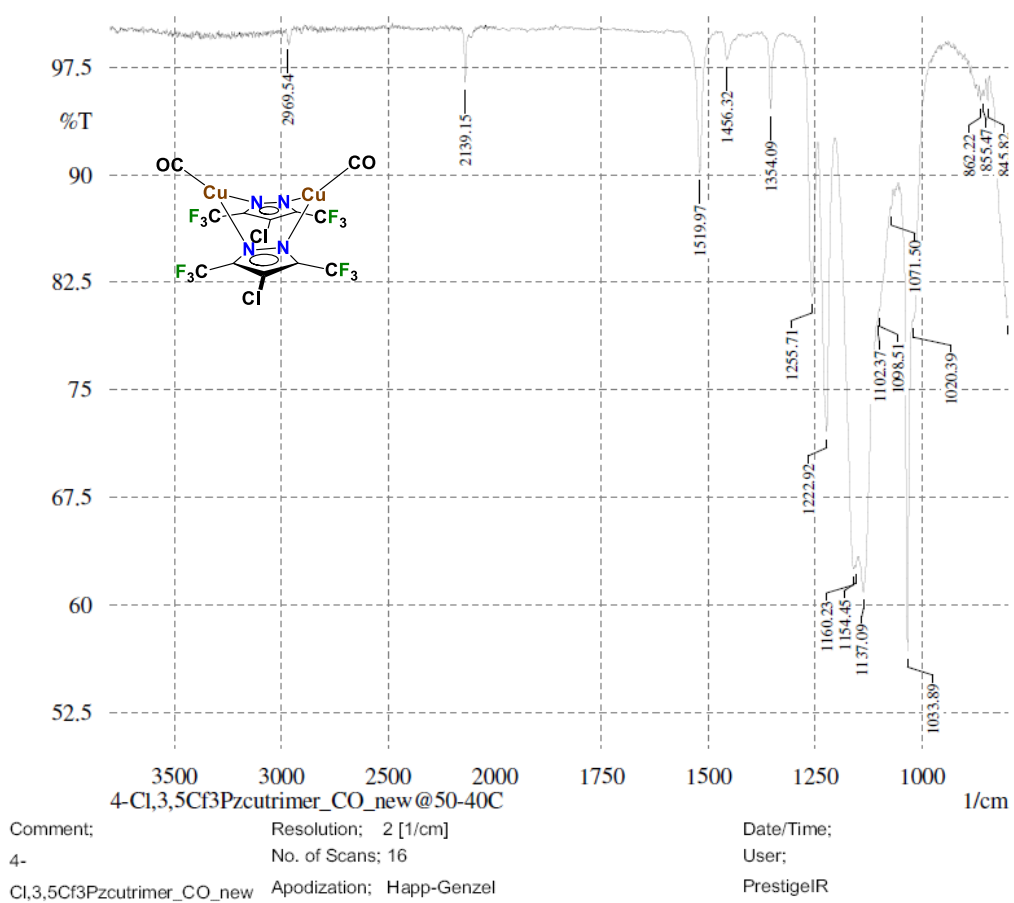
¹⁹F NMR spectrum of [NEt₄][{[4-Cl-3,5-(CF₃)₂Pz]Cu(CO)}₄(μ₄-Cl)] (**11**) in CD₂Cl₂ at the room temperature.



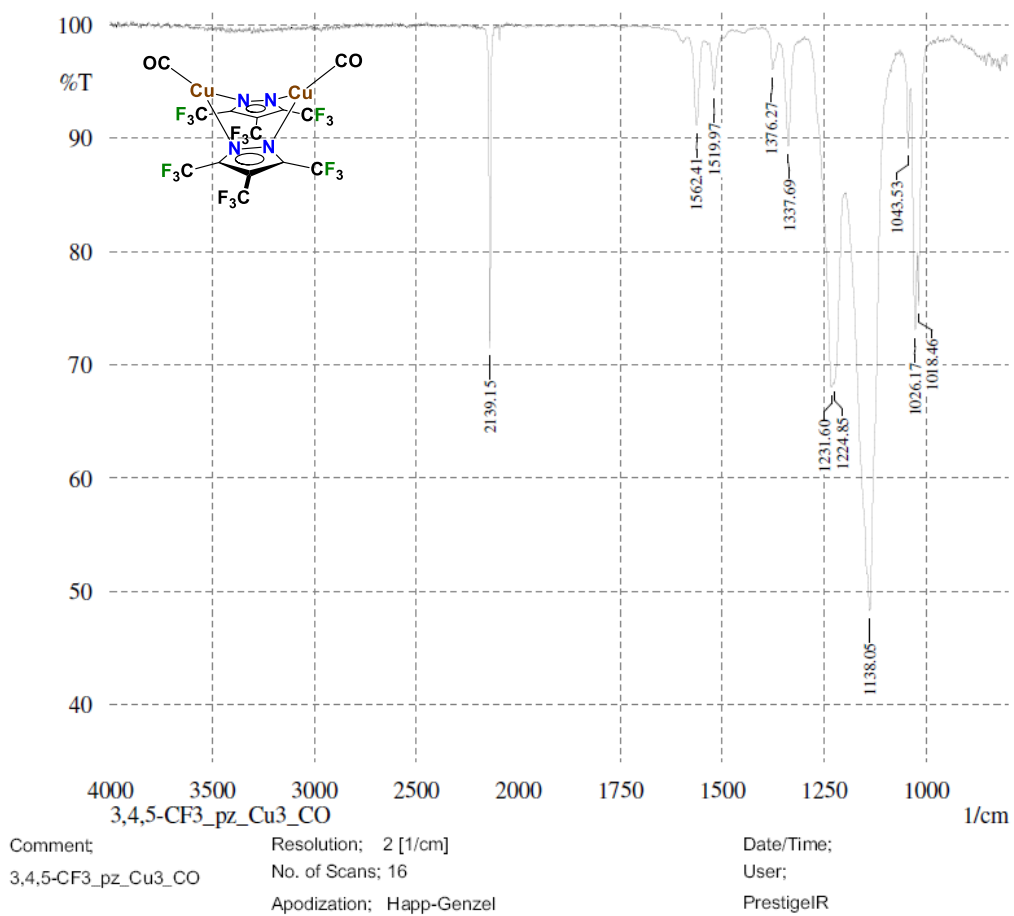
$^{13}\text{C}\{^1\text{H}\}$ NMR spectrum of $[\text{NEt}_4][\{\text{[4-Cl-3,5-(CF}_3)_2\text{Pz]Cu(CO)}\}_4(\mu_4\text{-Cl})]$ (**11**) in CD_2Cl_2 at the room temperature.



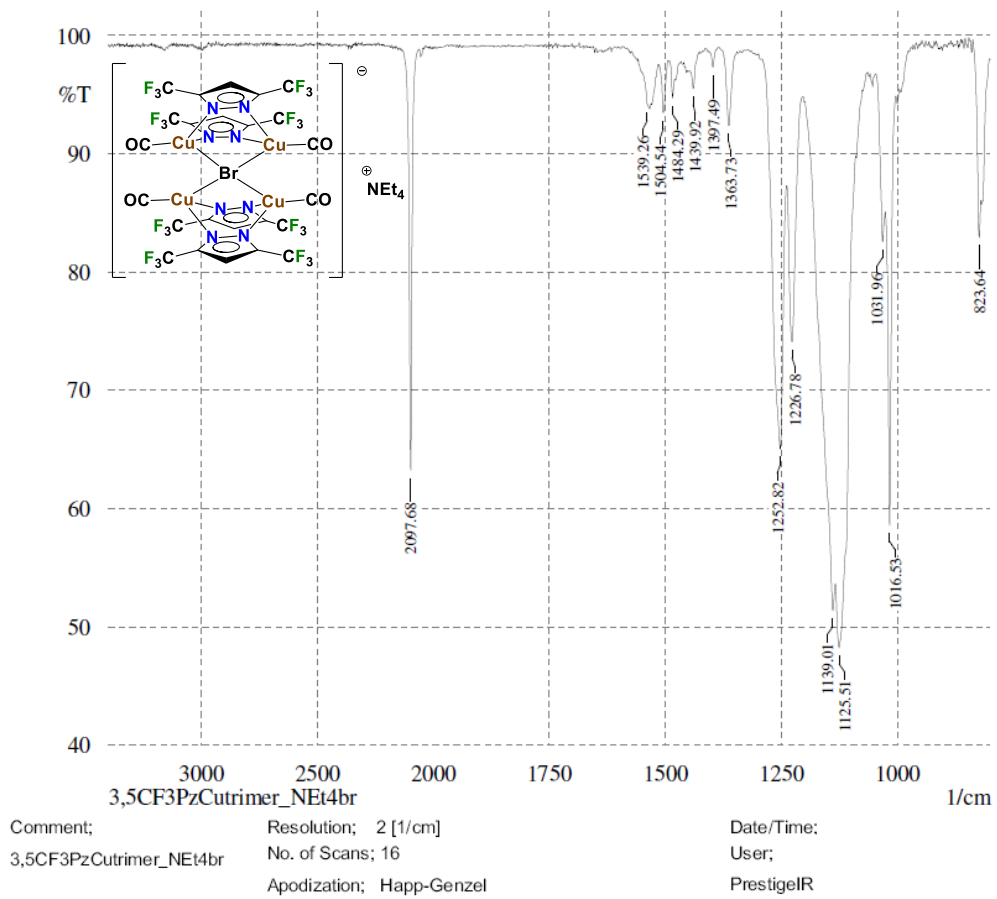
Infrared spectrum of solid {[3,5-(CF₃)₂Pz]Cu(CO)}₂ (**5**)



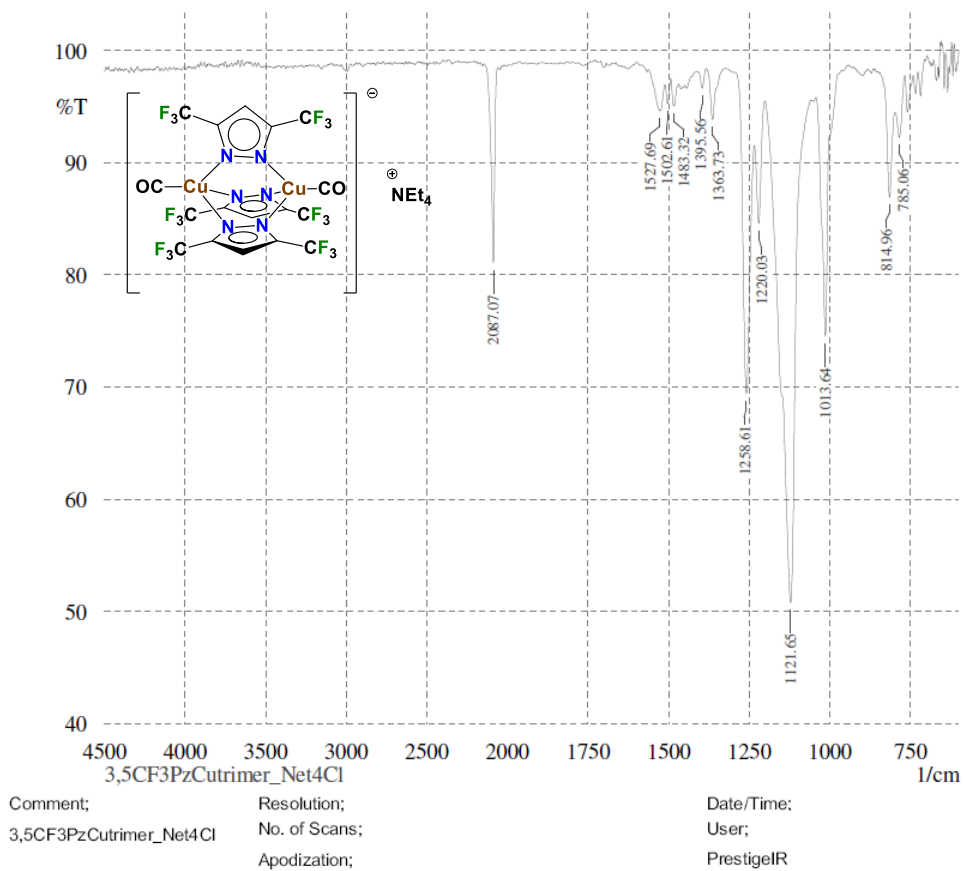
Infrared spectrum of solid $\{[4\text{-Cl-}3,5\text{-(CF}_3)_2\text{Pz]Cu(CO)}_2\}_2$ (**6**)



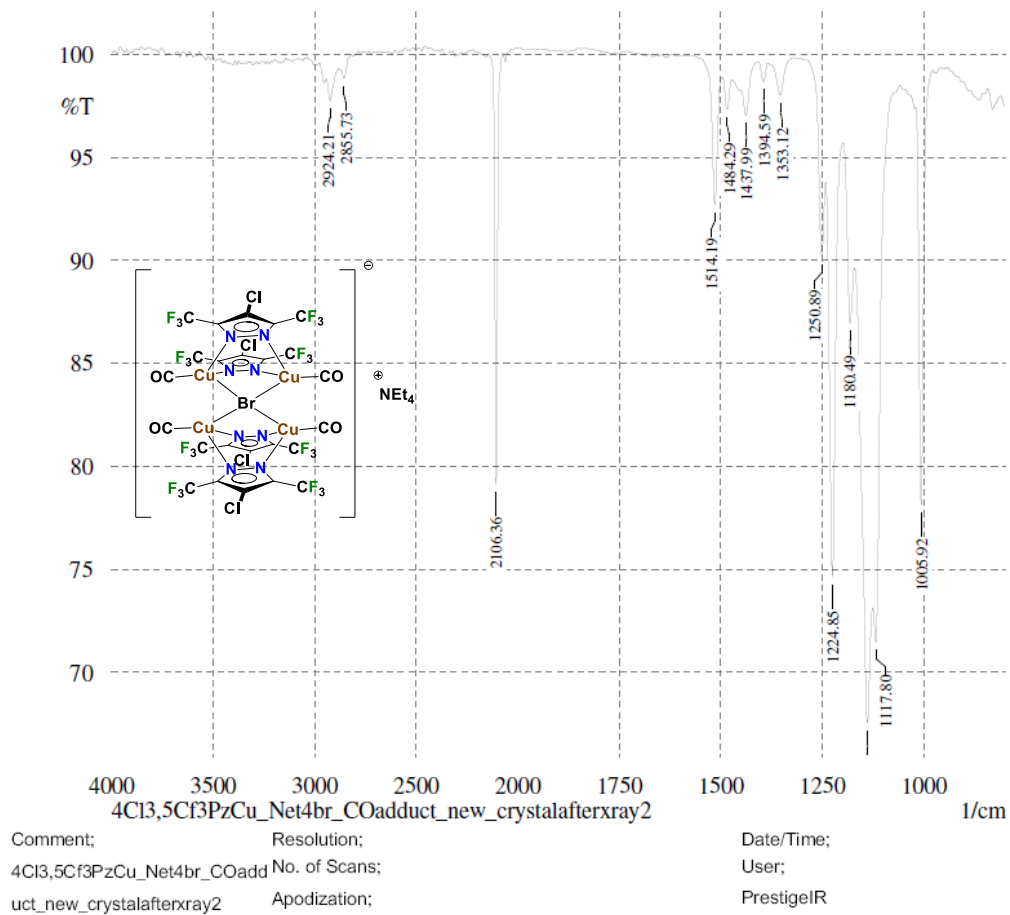
Infrared spectrum of solid {[3,4,5-(CF₃)₃Pz]Cu(CO)}₂ (**7**)



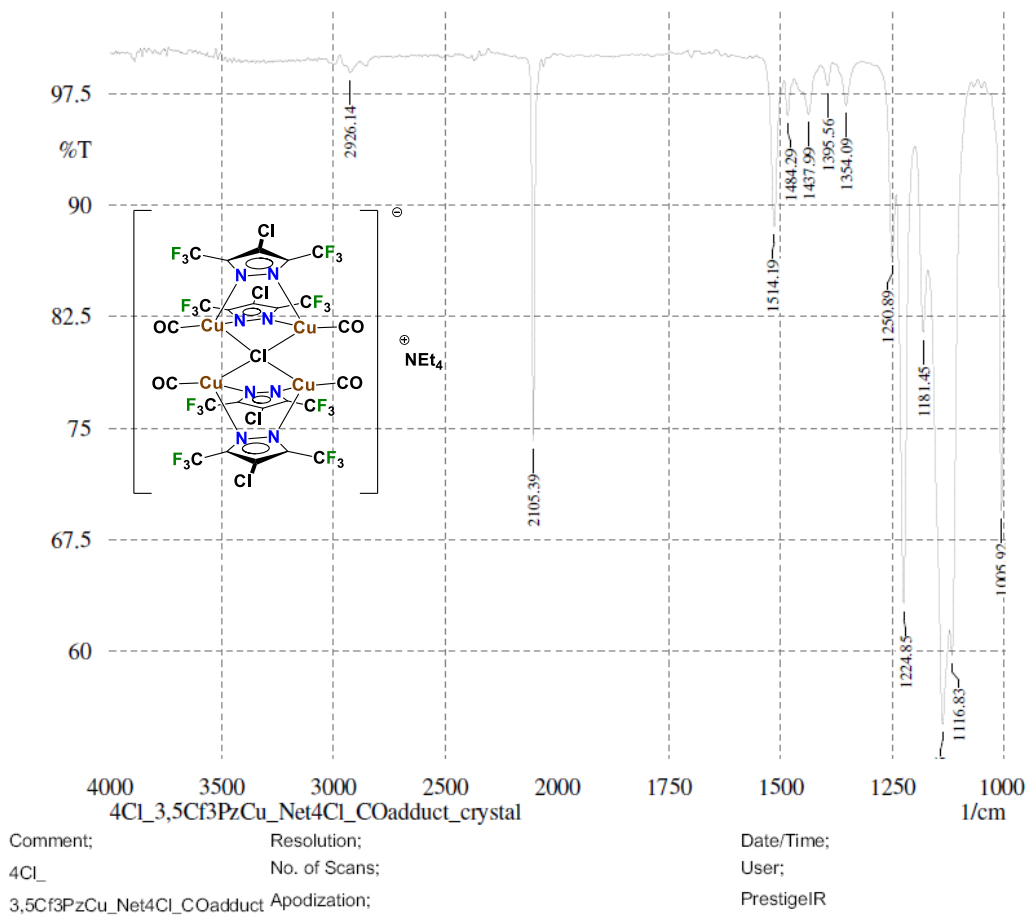
Infrared spectrum of solid $[\text{NEt}_4][\{[3,5\text{-(CF}_3)_2\text{Pz]Cu(CO)}\}_4(\mu_4\text{-Br})]$ (**8**)



Infrared spectrum of solid $[\text{NEt}_4][\{[3,5\text{-(CF}_3)_2\text{Pz}]_3\text{Cu}_2(\text{CO})_2\}]$ (**9**)



Infrared spectrum of solid $[\text{NEt}_4][\{[4\text{-Cl-3,5-(CF}_3)_2\text{Pz]Cu(CO)}\}_4(\mu_4\text{-Br})]$ (**10**)



Infrared spectrum of solid $[\text{NEt}_4][\{[4\text{-Cl-3,5-(CF}_3)_2\text{Pz]Cu(CO)}\}_4(\mu_4\text{-Cl})]$ (11)

References

- (1) Tejel, C.; Villoro, J. M.; Ciriano, M. A.; López, J. A.; Eguizá, E.; Lahoz, F. J.; Bakhmutov, V. I.; Oro, L. A. *Organometallics* **1996**, *15*(13), 2967-2978.
- (2) Grünebaum, M.; Buchheit, A.; Günther, C.; Wiemhöfer, H. D. *Tetrahedron Lett.* **2016**, *57* (14), 1555-1559.
- (3) La Monica, G. and Ardizzoia, G. A. *Prog. Inorg. Chem.* **1997**, *46*, 151-212.
- (4) Halcrow, M.A. *Dalt. Trans.* **2009**, *12*, 2059-2073.
- (5) Ardizzoia, G. A.; La Monica, G.; Liu, C. W. and Fackler Jr., J. P. Pyrazolato Copper(I) Complexes. In *Inorganic syntheses* **1997**, *31*, 299-302.
- (6) Ardizzoia, G. A.; Cenini, S.; La Monica, G.; Masciocchi, N.; Maspero, A.; Moret, M. *Inorg. Chem.* **1998**, *37* (17), 4284-4292.
- (7) Rasika Dias, H. V.; Polach, S. A.; Wang, Z. *J. Fluor. Chem.* **2000**, *103* (2), 163-169.
- (8) Yang, G. and Raptis, R.G. *Inorganica Chim. Acta* **2003**, *352*, 98-104.
- (9) Murray, H. H.; Raptis, R. G.; Fackler Jr. J. P. *Inorg. Chem.* **1988**, *27* (1), 26-33.
- (10) Omary, M. A.; Rawashdeh-Omary, M. A.; Diyabalanage, H. V. K.; Dias, H. V. R. *Inorg. Chem.* **2003**, *42* (26), 8612-8614.
- (11) Maspero, A.; Giovenzana, G. B.; Monticelli, D.; Tagliapietra, S.; Palmisano, G.; Penoni, A. *J. Fluor. Chem.* **2012**, *139*, 53-57.
- (12) Bönemann, H. *Angew. Chem. Int. Ed.* **1985**, *24* (4), 248-262.
- (13) Chang, C. K. and Ebina, F. *Chem. Commun.* **1981**, *15*, 778-779.
- (14) Dias, H. V. R.; Lu, H.; Kim, H.; Polach, S. A.; Goh, T. K. H. H.; Browning, R. G.; Lovely, C. J. *Organometallics* **2002**, *21* (7), 1466-1473.
- (15) Dias, H. V. R.; Diyabalanage, H. V. K.; Eldabaja, M. G.; Elbjeirami, O.; Rawashdeh-Omary, M. A.; Omary, M. A. *J. Am. Chem. Soc.* **2005**, *127* (20), 7489-7501.
- (16) Chi, Y.; Lay, E.; Chou, T. Y.; Song, Y. H.; Carty, A. J. *Chem. Vap. Depos.* **2005**, *11* (4), 206-212.
- (17) Ehlert, M. K.; Rettig, S. J.; Storr, A.; Thompson, R. C.; Trotter, J. *Can. J.*

- Chem.* **1990**, 68 (8), 1444-1449.
- (18) Fujisawa, K.; Ishikawa, Y.; Miyashita, Y.; Okamoto, K. *Chem. Lett.* **2004**, 33 (1), 66-67.
- (19) Maspero, A.; Brenna, S.; Galli, S.; Penona, A. *J. Organomet. Chem.* **2003**, 672 (1-2), 123-129.
- (20) Hettiarachchi, C. V.; Rawashdeh-Omary, M. A.; Korir, D.; Kohistani, J.; Yousufuddin, M.; Dias, H. V. R. *Inorg. Chem.* **2013**, 52 (23), 13576-13583.
- (21) Kishimura, A.; Yamashita, T.; Aida, T. *J. Am. Chem. Soc.* **2005**, 127 (1), 179-183.
- (22) Lintang, H. O.; Kinbara, K.; Tanaka, K.; Yamashita, T.; Aida, T. *Angew. Chem. Int. Ed.* **2010**, 49 (25), 4241-4245.
- (23) Omary, M. A.; Rawashdeh-Omary, M. A.; Gonser, M. W. A.; Elbjeirami, O.; Grimes, T.; Cundari, T. R.; Diyabalanage, H. V. K.; Palehepitiya Gamage, C. S.; Dias, H. V. R. *Inorg. Chem.* **2005**, 44 (23), 8200-8210.
- (24) Jahnke, A. C.; Pröpper, K.; Bronner, C.; Teichgräber, J.; Dechert, S.; John, M.; Wenger, O. S.; Meyer, F. *J. Am. Chem. Soc.* **2012**, 134 (6), 2938-2941.
- (25) Dias, H. V. R.; Palehepitiya Gamage, C. S.; Keltner, J.; Diyabalanage, H. V. K.; Omari, I.; Eyobo, Y.; Dias, N. R.; Roehr, N.; McKinney, L.; Poth, T. *Inorg. Chem.* **2007**, 46 (8), 2979-2987.
- (26) Tsupreva, V. N.; Titov, A. A.; Filippov, O. A.; Bilyachenko, A. N.; Smol'yakov, A. F.; Dolgushin, F. M.; Agapkin, D. V.; Godovikov, I. A.; Epstein, L. M.; Shubina, E. S. *Inorg. Chem.* **2011**, 50 (8), 3325-3331.
- (27) Krishantha, D. M. M.; Palehepitiya Gamage, C. S.; Schelly, Z. A.; Dias, H. V. R. *Inorg. Chem.* **2008**, 47 (16), 7065-7067.
- (28) den Boer, D.; Krikorian, M.; Esser, B.; Swager, T. M. *J. Phys. Chem. C* **2013**, 117 (16), 8290-8298.
- (29) Richey, S. A. Dissertation thesis titled- Coinage Metal Complexes of Fluorinated Pyrazole Based Ligands, University of Texas at Arlington, **2002**.
- (30) (a) Dias, H.V.R; Diyabalanage, H; Jayaratna, N.B.; Shaw, D.; Hettiarachchi, H.V.; and Parasar, D. *Eur. J. Inorg. Chem.* 2019, 31, 3638-3644.
 (b) Dias, H. V. R.; Diyabalanage, H. V. K.; Gamage, C. S. P. *Chem. Commun.* **2005**, 12, 1619-1621.
- (31) Titov, A. A.; Filippov, O. A.; Smol'Yakov, A. F.; Godovikov, I. A.;

- Shakirova, J. R.; Tunik, S. P.; Podkorytov, I. S.; Shubina, E. S. *Inorg. Chem.* **2019**, *58* (13), 8645-8656.
- (32) Gamage, C. S. Dissertation thesis titled- Computational Studies of Small Inorganic Molecules and Synthesis of Coinage Metal Pyrazolate Complexes, University of Texas at Arlington, **2007**.
- (33) Jayaratna, N. B.; Cowan, M. G.; Parasar, D.; Funke, H. H.; Reibenspies, J.; Mykhailiuk, P. K.; Artamonov, O.; Noble, R. D.; Dias, H. V. R. *Angew. Chem. Int. Ed.* **2018**, *57* (50), 16442-16446.
- (34) Sholl, D. S. and Lively, R. P. *Nature* **2016**, 435-437.
- (35) Motelica, A.; Bruinsma, O. S. L.; Kreiter, R.; den Exter, M.; Vente, J. F. *Ind. Eng. Chem. Res.* **2012**, *51*, 6977-6986.
- (36) Faiz, R. and Li, K. *Chem. Eng. Sci.* **2012**, *73*, 261-284.
- (37) Azhin, M.; Kaghazchi, T.; Rahmani, M. *J. Ind. Eng. Chem.* **2008**, *14* (5), 622-638.
- (38) Grande, C. A.; Poplow, F.; Rodrigues, A. E. *Sep. Sci. Technol.* **2010**, *45* (9), 1252-1259.
- (39) Rege, S. U.; Padin, J.; Yang, R. T. *AIChE J.* **1998**, *44* (4), 799-809.
- (40) Berger, A. H. and Bhowan, A. S. *Energy Procedia.* **2011**, *4*, 562-567.
- (41) Bereciartua, P. J.; Cantín, Á.; Corma, A.; Jordá, J. L.; Palomino, M.; Rey, F.; Valencia, S.; Corcoran, E. W.; Kortunov, P.; Ravikovitch, P. I.; Burton, A.; Yoon, C.; Wang, Y.; Paur, C.; Guzman, J.; Bishop, A. R.; Casty, G. L. *Science* **2017**, *358* (6366), 1068-1071.
- (42) Wang, K. and Stiefel, E. I. *Science* **2001**, *291* (5501), 10-109.
- (43) Cadiou, A.; Adil, K.; Bhatt, P. M.; Belmabkhout, Y.; Eddaoudi, M. *Science* **2016**, *353* (6295), 13-140.
- (44) Bachman, J. E.; Smith, Z. P.; Li, T.; Xu, T.; Long, J. R. *Nat. Mater.* **2016**, *15* (8), 845-849.
- (45) Koh, D. Y.; McCool, B. A.; Deckman, H. W.; Lively, R. P. *Science* **2016**, *353* (6301), 804-807.
- (46) Cui, X.; Chen, K.; Xing, H.; Yang, Q.; Krishna, R.; Bao, Z.; Wu, H.; Zhou, W.; Dong, X.; Han, Y.; Li, B.; Ren, Q.; Zaworotko, M.J.; Chen, B. *Science* **2016**, *353* (6295), 141-144.

- (47) Yang, R. T.; London, B.; Singapore, D.; Wellington, S. T. *Gas Separation by Adsorption Processes* **1987**.
- (48) Seo, S.; Simoni, L. D.; Ma, M.; DeSilva, M. A.; Huang, Y.; Stadtherr, M. A.; Brennecke, J. F. *Energy and Fuels* **2014**, *28* (9), 5968-5977.
- (49) Eisinger, R. S. and Keller, G. E. *Energy and Fuels* **2014**, *28* (11), 7070-7078.
- (50) Nijem, N.; Wu, H.; Canepa, P.; Marti, A.; Balkus, K. J.; Thonhauser, T.; Li, J.; Chabal, Y. J. *J. Am. Chem. Soc.* **2012**, *134* (37), 15201-15204.
- (51) Mason, J. A.; Oktawiec, J.; Taylor, M. K.; Hudson, M. R.; Rodriguez, J.; Bachman, J. E.; Gonzalez, I.; Cervellino, A.; Guagliardi, A.; Brown, C. M.; Llewellyn, P.L.; Masciocchi, N.; Long, J.R. *Nature* **2015**, *527*, 357-361.
- (52) Slobodyanyuk, E. Y.; Artamonov, O. S.; Shishkin, O. V.; Mykhailiuk, P. K. *Eur. J. Org. Chem.* **2014**, *2014* (12), 2487-2495.
- (53) Dias, H. V. R.; Diyabalanage, H. V. K.; Rawashdeh-Omary, M. A.; Franzman, M. A.; Omary, M. A. *J. Am. Chem. Soc.* **2003**, *125* (40), 12072-12073.
- (54) Thompson, J. S.; Swiatek, R. M. *Inorg. Chem.* **1985**, *24* (1), 110-113.
- (55) Klimovica, K.; Kirschbaum, K.; Daugulis, O. *Organometallics* **2016**, *35* (17), 2938-2943.
- (56) Wang, F.; Kusaka, S.; Hijikata, Y.; Hosono, N.; Kitagawa, S. *ACS Appl. Mater. Interfaces* **2017**, *9* (39), 33455-33460.
- (57) Schick, C. *Anal Bioanal Chem* **2009**, *395*, 1589-1611.
- (58) Jayaratna, N. B.; Gerus, I. I.; Mironets, R. V.; Mykhailiuk, P. K.; Yousufuddin, M.; Dias, H. V. R. *Inorg. Chem.* **2013**, *52* (4), 1691-1693.
- (59) Berger, R.; Resnati, G.; Metrangolo, P.; Weber, E.; Hulliger, J. *Chemical Society Reviews*. **2011**, *7*, 3496-3508.
- (60) Owen, M. J.; Kobayashi, H. *Macromol. Symp.* **1994**, *82* (1), 115-123.
- (61) Yang, C.; Wang, X.; Omary, M. A. *J. Am. Chem. Soc.* **2007**, *129* (50), 15454-15455.
- (62) Seo, J.; Bonneau, C.; Matsuda, R.; Takata, M.; Kitagawa, S. *J. Am. Chem. Soc.* **2011**, *133* (23), 9005-9013.
- (63) Coudert, F. X.; Jeffroy, M.; Fuchs, A. H.; Boutin, A.; Mellot-Draznieks, C. *J. Am. Chem. Soc.* **2008**, *130* (43), 14294-14302.

- (64) Lee, W. R.; Jo, H.; Yang, L. M.; Lee, H.; Ryu, D. W.; Lim, K. S.; Song, J. H.; Min, D. Y.; Han, S. S.; Seo, J. G.; Park, Y. K.; Moon, D.; Hong, C. S. *Chem. Sci.* **2015**, *6* (7), 3697-3705.
- (65) McDonald, T. M.; Mason, J. A.; Kong, X.; Bloch, E. D.; Gygi, D.; Dani, A.; Crocellà, V.; Giordanino, F.; Odoh, S. O.; Drisdell, W. S.; Vlasisavljevich, B.; Dzubak, A. L.; Poloni, R.; Schnell, S. K.; Planas, N.; Lee, K.; Pascal, T.; Wan, L. F.; Prendergast, D.; Neaton, J. B.; Smit, B.; Kortright, J. B.; Gagliardi, L.; Bordiga, S.; Reimer, J. A.; Long, J. R. *Nature* **2015**, *519* (7543), 303-308.
- (66) Maji, T. K.; Mostafa, G.; Matsuda, R.; Kitagawa, S. *J. Am. Chem. Soc.* **2005**, *127* (49), 17152-17153.
- (67) Triguero, C.; Coudert, F. X.; Boutin, A.; Fuchs, A. H.; Neimark, A. V. *J. Phys. Chem. Lett.* **2011**, *2* (16), 2033-2037.
- (68) Coudert, F. X.; Mellot-Draznieks, C.; Fuchs, A. H.; Boutin, A. *J. Am. Chem. Soc.* **2009**, *131* (32), 11329-11331.
- (69) Kondo, A.; Noguchi, H.; Carlucci, L.; Proserpio, D. M.; Ciani, G.; Kajiro, H.; Ohba, T.; Kanoh, H.; Kaneko, K. *J. Am. Chem. Soc.* **2007**, *129* (41), 12362-12363.
- (70) Goto, M.; Furukawa, M.; Miyamoto, J.; Kanoh, H.; Kaneko, K. *Langmuir* **2007**, *23* (10), 5264-5266.
- (71) Cowan, M. G.; McDanel, W. M.; Funke, H. H.; Kohno, Y.; Gin, D. L.; Noble, R. D. *Angew. Chem. Int. Ed.* **2015**, *127* (19), 5832-5835.
- (72) Merkel, T. C.; Blanc, R.; Ciobanu, I.; Firat, B.; Suwarlim, A.; Zeid, J. *J. Memb. Sci.* **2013**, *447*, 177-189.
- (73) Parasar, D.; Almotawa, R. M.; Jayaratna, N. B.; Ceylan, Y. S.; Cundari, T. R.; Omary, M. A.; Dias, H. V. R. *Organometallics* **2018**, *37* (21), 4105-4118.
- (74) Zhang, J. P.; Zhang, Y. B.; Lin, J. Bin; Chen, X. M. *Chem. Rev.* **2012**, 1001-1033.
- (75) Kishimura, A.; Yamashita, T.; Yamaguchi, K.; Aida, T. *Nat. Mater.* **2005**, *4* (7), 546-549.
- (76) Zangrando, E.; Casanova, M.; Alessio, E. *Chem. Rev.* **2008**, *108* (12), 4979-5013.
- (77) Rawashdeh-Omary, M. A. *Comments Inorg. Chem.* **2012**, *33* (3-4), 88-101.

- (78) Singh, K.; Long, J. R.; Stavropoulos, P. *J. Am. Chem. Soc.* **1997**, *119* (12), 2942-2943.
- (79) Yam, V. W. W.; Au, V. K. M.; Leung, S. Y. L. *Chem. Rev.* **2015**, 7589-7728.
- (80) Grimes, T.; Omary, M. A.; Dias, H. V. R.; Cundari, T. R. *J. Phys. Chem. A* **2006**, *110* (17), 5823-5830.
- (81) Vorontsov, I. I.; Kovalevsky, A. Y.; Chen, Y. S.; Graber, T.; Gembicky, M.; Novozhilova, I. V.; Omary, M. A.; Coppens, P. *Phys. Rev. Lett.* **2005**, *94* (19), 193003.
- (82) Hu, B.; Gahungu, G.; Zhang, J. *J. Phys. Chem. A* **2007**, *111* (23), 4965-4973.
- (83) Tekarli, S. M.; Cundari, T. R.; Omary, M. A. *J. Am. Chem. Soc.* **2008**, *130* (5), 1669-1675.
- (84) Galassi, R.; Ghimire, M. M.; Otten, B. M.; Ricci, S.; McDougald, R. N.; Almotawa, R. M.; Alhmoud, D.; Ivy, J. F.; Rawashdeh, A. M. M.; Nesterov, V. N.; Reinheimer, E. W.; Daniels, L. M.; Burini, A.; Omary, M. A. *Proc. Natl. Acad. Sci. USA*. **2017**, *114* (26), E5042-E5051.
- (85) Hou, L.; Shi, W. J.; Wang, Y. Y.; Wang, H. H.; Cui, L.; Chen, P. X.; Shi, Q. *Z. Inorg. Chem.* **2011**, *50* (1), 261-270.
- (86) Mathivathanan, L.; Torres-King, J.; Primera-Pedrozo, J. N.; García-Ricard, O. J.; Hernández-Maldonado, A. J.; Santana, J. A.; Raptis, R. G. *Cryst. Growth Des.* **2013**, *13* (6), 2628-2635.
- (87) Titov, A. A.; Filippov, O. A.; Epstein, L. M.; Belkova, N. V.; Shubina, E. S. *Inorganica Chimica Acta*. **2018**, 22-35.
- (88) Xiao, Q.; Zheng, J.; Li, M.; Zhan, S. Z.; Wang, J. H.; Li, D. *Inorg. Chem.* **2014**, *53* (21), 11604-11615.
- (89) Tu, B.; Pang, Q.; Xu, H.; Li, X.; Wang, Y.; Ma, Z.; Weng, L.; Li, Q. *J. Am. Chem. Soc.* **2017**, *139* (23), 7998-8007.
- (90) Ghazalli, N. F., Yuliati, L., Endud, S., Shamsuddin, M., & Lintang, H. O. *Adv. Mat. Res.* **2014**, 970, 44-47.
- (91) Gong, F.; Wang, Q.; Chen, J.; Yang, Z.; Liu, M.; Li, S.; Yang, G.. *Inorg. Chem.* **2010**, *49* (4), 1658-1666.
- (92) He, J.; Yin, Y. G.; Wu, T.; Li, D.; Huang, X. C. *Chem. Commun.* **2006**, 27, 2845-2847.
- (93) Jayaratna, N. B.; Hettiarachchi, C. V.; Yousufuddin, M.; Rasika Dias, H. V.

New J. Chem. **2015**, 39 (7), 5092-5095.

- (94) Titov, A. A.; Smol'yakov, A. F.; Filippov, O. A.; Godovikov, I. A.; Muratov, D. A.; Dolgushin, F. M.; Epstein, L. M.; Shubina, E. S. *Cryst. Growth Des.* **2017**, 17 (12), 6770-6779.
- (95) Xu, C.; Baum, T.; Wang, Z. Pyrazolate Copper Complexes, and MOCVD of Copper Using Same. US Patent. **2002**.
- (96) Zhan, S. Z.; Li, M.; Zheng, J.; Wang, Q. J.; Ng, S. W.; Li, D. *Inorg. Chem.* **2017**, 56 (21), 13446-13455.
- (97) Zhang, J. X.; He, J.; Yin, Y. G.; Hu, M. H.; Li, D.; Huang, X. C. *Inorg. Chem.* **2008**, 47 (9), 3471-3473.
- (98) Casarin, M.; Corvaja, C.; Di Nicola, C.; Falcomer, D.; Franco, L.; Monari, M.; Pandolfo, L.; Pettinari, C.; Piccinelli, F.; Tagliatesta, P. *Inorg. Chem.* **2004**, 43 (19), 5865-5876.
- (99) Veronelli, M.; Kindermann, N.; Dechert, S.; Meyer, S.; Meyer, F. *Inorg. Chem.* **2014**, 53 (4), 2333-2341.
- (100) Jayaratna, N. B.; Olmstead, M. M.; Kharisov, B. I.; Dias, H. V. R. *Inorg. Chem.* **2016**, 55 (17), 8277-8280.
- (101) Kivi, C. E. and Song, D. *Dalt. Trans.* **2016**, 45, 17087-17090.
- (102) Meycr, F.; Jacobi, A.; Zsolnai, L. *Chem. Ber.* **1997**, 130 (10), 1441-1447.
- (103) Reger, D. L.; Huff, M. F. *Organometallics* **1990**, 9 (10), 2807-2810.
- (104) Amblard, F.; Cho, J. H.; Schinazi, R. F. *Chem. Rev.* **2009**, 109 (9), 4207-4220.
- (105) Moses, J. E. and Moorhouse, A. D. *Chem. Soc. Rev.* **2007**, 36 (8), 1249-1262.
- (106) Kolb, H. C.; Sharpless, K. B. *Drug Discovery Today* **2003**, 1128-1137.
- (107) Kolb, H. C.; Finn, M. G.; Sharpless, K. B. *Angew. Chem. Int. Ed.* **2001**, 40 (11), 2004-2021.
- (108) Pérez, P. J.; Brookhart, M.; Templeton, J. L. *Organometallics* **1993**, 12 (2), 261-262.
- (109) Martín, C.; Sierra, M.; Alvarez, E.; Belderrain, T. R.; Pérez, P. J. *Dalt. Trans.* **2012**, 41 (17), 5319-5325.
- (110) Chen, L.; Leslie, D.; Coleman, M. G.; Mack, J. *Chem. Sci.* **2018**, 9 (20),

4650-4661.

- (111) Doppelt, P.; Baum, T. H. *J. Organomet. Chem.* **1996**, *517* (1-2), 53-62.
- (112) Jain, A.; Kudas, T. T.; Chi, K. M.; Hampden-Smith, M. J.; Farr, J. D.; Paffett, M. F. *Chem. of Mat.* **1991**, 995-997.
- (113) Lang, H.; Köhler, K.; Bau, S. *Coord. Chem. Rev.*, **1995**, *143*, 113-168.
- (114) Lang, H.; Jakob, A.; Milde, B. *Organometallics* **2012**, *31* (22), 7661-7693.
- (115) El-Sagheer, A. H.; Brown, T. *Chem. Soc. Rev.* **2010**, *4*, 1388-1405.
- (116) Baum, T. H. and Larson, C. E. *Chem. Mater.* **1992**, *4* (2), 365-369.
- (117) Allen, F. H. *Acta Crystallogr. Sect. B Struct. Sci.* **2002**, *58* (3 Part 1), 380-388.
- (118) Villacorta, G. M.; Gibson, D.; Williams, I. D.; Lippard, S. J. *J. Am. Chem. Soc.* **1985**, *107* (23), 6732-6734.
- (119) Villacorta, G. M.; Gibson, D.; Williams, I. D.; Whang, E.; Lippard, S. J. *Organometallics* **1987**, *6* (11), 2426-2431.
- (120) Reger, D. L.; Huff, M. F.; Wolfe, T. A.; Adams, R. D. *Organometallics* **1989**, *8* (3), 848-850.
- (121) Kumar, S. and Mandon, D. *Inorg. Chem.* **2015**, *54* (15), 7481-7491.
- (122) Aalten, H. L.; van Koten, G.; Riethorst, E.; Stam, C. H. *Inorg. Chem.* **1989**, *28* (22), 4140-4146.
- (123) Olbrich, F.; Behrens, U.; Groeger, G.; Weiss, E. *J. Organomet. Chem.* **1993**, *448*, C10-C12.
- (124) Köhler, K.; Eichhorn, J.; Meyer, F.; Vidovic, D. *Organometallics* **2003**, *22* (22), 4426-4432.
- (125) Oguadinma, P. O.; Schaper, F. *Organometallics* **2009**, *28* (23), 6721-6731.
- (126) Rasika Dias, H. V.; Flores, J. A.; Wu, J.; Kroll, P. *J. Am. Chem. Soc.* **2009**, *131* (31), 11249-11255.
- (127) Crowder, G.A. and Blankenship, P. *J. Mol. Struct.* **1987**, *156*, 147-150.
- (128) Boese, R.; Bläser, D.; Latz, R.; Bäumen, A. *Acta Crystallogr. Sect. C Cryst. Struct. Commun.* **1999**, *55* (3), IUC9900016.
- (129) Bondi, A. *J. Phys. Chem.* **1964**, *68* (3), 441-451.

- (130) Alvarez, S. *Dalt. Trans.* **2013**, 42 (24), 8617-8636.
- (131) Batsanov, S. S. *Inorg. Mater.* **2001**, 37 (9), 871-885.
- (132) Carvajal, M. A.; Alvarez, S.; Novoa, J. J. *Chem. A Eur. J.* **2004**, 10 (9), 2117-2132.
- (133) Otten, B. M.; Melançon, K. M.; Omary, M. A. *Comm. on Inorg. Chem.* **2018**, 38 (1), 1-35.
- (134) Cotton, F. A.; Feng, X.; Matusz, M.; Poli, R. *J. Am. Chem. Soc.* **1988**, 110 (21), 7077-7083.
- (135) Lavalley, J. C.; Saussey, J.; Lamotte, J. *Spectrochim. Acta, Part A* **1979**, 35A, 695-700.
- (136) Dewar, M. J. S. *Bull. Soc. Chim. Fr.* **1951**, C71-9.
- (137) Chatt, J.; Duncanson, L. A. *J. Chem. Soc.* **1953**, 2939-2947.
- (138) Chatt, J.; Duncanson, L. A.; Venanzi, L. M. *J. Chem. Soc.* **1955**, 4456-4460.
- (139) Uoyama, H.; Goushi, K.; Shizu, K.; Nomura, H.; Adachi, C. *Nature* **2012**, 492, 234-241.
- (140) Linfoot, C. L.; Leitzl, M. J.; Richardson, P.; Rausch, A. F.; Chepelin, O.; White, F. J.; Yersin, H.; Robertson, N. *Inorg. Chem.* **2014**, 53 (20), 10854-10861.
- (141) Hofbeck, T.; Monkowius, U.; Yersin, H. *J. Am. Chem. Soc.* **2015**, 137 (1), 399-404.
- (142) Arvapally, R. K.; Sinha, P.; Hettiarachchi, S. R.; Coker, N. L.; Bedel, C. E.; Patterson, H. H.; Elder, R. C.; Wilson, A. K.; Omary, M. A. *J. Phys. Chem. C* **2007**, 111 (28), 10689-10699.
- (143) Parasar, D.; Ponduru, T. T.; Noonikara-Poyil, A.; Jayaratna, N. B.; Dias, H. V. R. *Dalt. Trans.* **2019**, 48 (42), 15782-15794.
- (144) Cariati, E.; Lucenti, E.; Botta, C.; Giovanella, U.; Marinotto, D.; Righetto, S. *Coord. Chem. Rev.* **2016**, 306, 566-614.
- (145) Zhang, J. P. and Kitagawa, S. *J. Am. Chem. Soc.* **2008**, 130 (3), 907-917.
- (146) Enomoto, M.; Kishimura, A.; Aida, T. *J. Am. Chem. Soc.* **2001**, 123 (23), 5608-5609.
- (147) Raptis, R. G. and Fackler, J. P. *Inorg. Chem.* **1988**, 27 (23), 4179-4182.

- (148) Fujisawa, K.; Ishikawa, Y.; Miyashita, Y.; Okamoto, K. I. *Inorganica Chim. Acta* **2010**, *363* (12), 2977-2989.
- (149) Parasar, D.; Jayaratna, N. B.; Muñoz-Castro, A.; Conway, A. E.; Mykhailiuk, P. K.; Dias, H. V. R. *Dalt. Trans.* **2019**, *48* (19), 6358-6371.
- (150) Di Nicola, C.; Karabach, Y. Y.; Kirillov, A. M.; Monari, M.; Pandolfo, L.; Pettinari, C.; Pombeiro, A. J. L. *Inorg. Chem.* **2007**, *46* (1), 221-230.
- (151) Ardizzoia, G. A.; Angaroni, M. A.; La Monica, G.; Cariati, F.; Cenini, S.; Moret, M.; Masciocchi, N. *Inorg. Chem.* **1991**, *30* (23), 4347-4353.
- (152) Wang, L.; Guo, B.; Li, H. X.; Li, Q.; Li, H. Y.; Lang, J. P. *Dalt. Trans.* **2013**, *42* (44), 15570-15580.
- (153) Grzywa, M.; Geßner, C.; Bredenkötter, B.; Denysenko, D.; Van Leusen, J.; Kögerler, P.; Klemm, E.; Volkmer, D. *Dalt. Trans.* **2014**, *43* (44), 16846-16856.
- (154) Pandolfo, L. and Pettinari, C. *Cryst. Eng. Comm.* **2017**, *13*, 1701-1720.
- (155) Colombo, V.; Galli, S.; Choi, H. J.; Han, G. D.; Maspero, A.; Palmisano, G.; Masciocchi, N.; Long, J. R. *Chem. Sci.* **2011**, *2* (7), 1311-1319.
- (156) Grzywa, M.; Denysenko, D.; Schaller, A.; Kalytta-Mewes, A.; Volkmer, D. *Cryst. Eng. Comm.* **2016**, *18* (40), 7883-7893.
- (157) Alonso, F.; Beletskaya, I. P.; Yus, M. *Chem. Rev.* **2004**, *104* (6), 3079-3159.
- (158) Kolb, H. C.; Finn, M. G.; Sharpless, K. B. *Angew. Chem. Int. Ed.* **2001**, *40* (11), 2004-2021.
- (159) Díaz-Requejo, M. M.; Mairena, M. A.; Belderrain, T. R.; Nicasio, M. C.; Trofimenko, S.; Pérez, P. J. *Chem. Commun.* **2001**, *1* (18), 1804-1805.
- (160) Hamada, T.; Ye, X.; Stahl, S. S. *J. Am. Chem. Soc.* **2008**, *130* (3), 833-835.
- (161) Manjolinho, F.; Arndt, M.; Gooßen, K.; Gooßen, L. J. *ACS Catalysis* **2012**, *2* (9), 2014-2021.
- (162) Ye, M. C.; Zhou, J.; Tang, Y. *J. Org. Chem.* **2006**, *71* (9), 3576-3582.
- (163) Yu, D. and Zhang, Y. *Nat. Acad. Sci. USA* **2010**, *107*, 20184-20189.
- (164) Hay, A. S. *J. Org. Chem.* **1962**, *27*, 3320-3321.
- (165) Siemsen, P.; Livingston, R. C.; Diederich, F. *Angew. Chem. Int. Ed.* **2000**, *39* (15), 2632-2657.

- (166) Adeleke, A. F.; Brown, A. P. N.; Cheng, L. J.; Mosleh, K. A. M.; Cordier, C. J. *Synthesis* **2017**, 49 (4), 790-801.
- (167) Su, L.; Dong, J.; Liu, L.; Sun, M.; Qiu, R.; Zhou, Y.; Yin, S. F. *J. Am. Chem. Soc.* **2016**, 138 (38), 12348-12351.
- (168) Buschbeck, R.; Low, P. J.; Lang, H. *Coord. Chem. Rev.* **2011**, 255 (1-2), 241-272.
- (169) Trotaş, I. T.; Zimmermann, T.; Schüth, F. *Chem. Rev.* **2014**, 114 (3), 1761-1782.
- (170) Martín, C.; Muñoz-Molina, J. M.; Locati, A.; Alvarez, E.; Maseras, F.; Belderrain, T. R.; Pérez, P. J. *Organometallics* **2010**, 29 (16), 3481-3489.
- (171) Titov, A. A.; Larionov, V. A.; Smol'yakov, A. F.; Godovikova, M. I.; Titova, E. M.; Maleev, V. I.; Shubina, E. S. *Chem. Commun.* **2019**, 55 (3), 290-293.
- (172) Hyman, M. R. and Arp, D. J. *Appl. Environ. Microbiol.* **1987**, 53 (2), 298-303.
- (173) Fast, H.; Welsh, H. L. *J. Mol. Spectrosc.* **1972**, 41 (1), 203-221.
- (174) Bauer, H.; Faust, J.; Froböse, R.; Füssel, J.; Krüerke, U.; Kunz, M.; Somer, H. M. *Cu Organocopper Compounds*; Springer Berlin Heidelberg, 1987; pp 1-101.
- (175) Jardine, F. H. *Adv. Inorg. Chem. Radiochem. Acad. Press* **1975**, 17, 115-163.
- (176) Thompson, J. S.; Whitney, J. F. *J. Am. Chem. Soc.* **1983**, 105 (16), 5488-5490.
- (177) Thompson, J. S.; Whitney, J. F. *Inorg. Chem.* **1984**, 23 (18), 2813-2819.
- (178) Munakata, M.; Kitagawa, S.; Kawada, I.; Maekawa, M.; Shimono, H. *J. Chem. Soc. Dalt. Trans.* **1992**, 14, 2225-2230.
- (179) Mykhalchenko, B. M.; Myskiv, M. G. and Davydov, V. N. *Zh. Neorg. Khim. Chem. Soc. Dalt. Trans.* **1992**, 14, 2225-2230.
- (179) Mykhalchenko, B. M.; Myskiv, M. G. and Akselrud, L. G. *Koord. Khim.* **1993**, 19, 722-726.
- (181) Osechkin, S. I.; Myskiv, M. G. et al. *Met. Khim.* **1991**, 4, 997-1003.
- (182) Wieder, N. L.; Carroll, P. J.; Berry, D. H. *Organometallics* **2011**, 30 (8), 2125-2136.

- (183) Iwashita, Y.; Tamura, F.; Nakamura, A. *Inorg. Chem.* **1969**, 8 (5), 1179-1183.
- (184) Tachiyama, T.; Yoshida, M.; Aoyagi, T.; Fukuzumi, S. *Appl. Organomet. Chem.* **2008**, 22 (4), 205-210.
- (185) Dias, H. V. R.; Richey, S. A.; Diyabalanage, H. V. K.; Thankamani, J. *Organometallic* **2005**, 690, 1913-1922.
- (186) Martín, C.; Sierra, M.; Alvarez, E.; Belderrain, T. R.; Pérez, P. J. *Dalt. Trans.* **2012**, 41 (7), 5319-5325.
- (187) Lorber, C. Y.; Youinou, M.T.; Kress, J.; Osborn, J. A. *Polyhedron*. **2000**, 19, 1693-1698
- (188) Lang, H.; Köhler, K.; Blau, S. *Coord. Chem. Rev.* **1995**, 143 (C), 113–168.
- (189) Das, A.; Dash, C.; Celik, M. A.; Yousufuddin, M.; Frenking, G.; Dias, H. V. R. *Organometallics* **2013**, 32 (11), 3135-3144.
- (190) Das, A.; Dash, C.; Yousufuddin, M.; Dias, H. V. R. *Organometallics* **2014**, 33 (7), 1644-1650.
- (191) Tornøe, C. W.; Christensen, C.; Meldal, M. *J. Org. Chem.* **2002**, 67 (9), 3057-3064.
- (192) Rostovtsev, V. and Green, L. *Angew. Chem. Int. Ed.* **2002**, 41 (14), 2596-2599.
- (193) Wang, C.; Ikhlef, D.; Kahlal, S.; Saillard, J. Y.; Astruc, D.. *Coord. Chem. Rev.* **2016**, 316, 1-20.
- (194) Wu, L. Y.; Xie, Y. X.; Chen, Z. S.; Niu, Y. N.; Liang, Y. M. *Synlett* **2009**, 2009 (9), 1453-1456.
- (195) Creary, X.; Anderson, A.; Brophy, C.; Crowell, F.; Funk, Z. *J. Org. Chem.* **2012**, 77 (19), 8756-8761.
- (196) Wang, Z. L.; Tang, R. Y.; Luo, P. S.; Deng, C. L.; Zhong, P.; Li, J. H. *Tetrahedron* **2008**, 64 (47), 10670-10675.
- (197) Nurhanna Riduan, S.; Ying, J. Y.; Zhang, Y. *Org. Lett.* **2012**, 14 (7), 1780-1783.
- (198) Yang, Y.; Rioux, R. M. *Green Chem.* **2014**, 16 (8), 3916-3925.
- (199) Orlov, N. V. *ChemistryOpen Rev.* **2015**, 4, 682-697.

- (200) Trostyanskaya, I. G. and Beletskaya, I. P. *Synlett* **2012**, 4, 535-540.
- (201) Dondoni, A. and Marra, A. *Eur. J Org. Chem.* **2014**, 2014 (19), 3955-3969.
- (202) Bruce, M. I. *J. Organometallic Chem.* **1972**, 44 (2), 209-226.
- (203) Pike, R. D. *Organometallics* **2012**, 31 (22), 7647-7660.
- (204) Hieber, W. *Adv. Organomet. Chem.* **1970**, 8 (C), 1-28.
- (205) Dias, H. V. R. and Lovely, C. J. *Chem. Rev.* **2008**, 108 (8), 3223-3238.
- (206) Xu, Q. *Coord. Chem. Rev.* **2002**, 231, 83-108.
- (207) Pasquali, M. and Floriani, C. *Copper Coord. Chem.: Biochem. Inorg. Perspect.* **1983**, 311-330.
- (208) Pasquali, M.; Floriani, C.; Gaetani-Manfredotti, A. *Inorg. Chem.* **1981**, 20 (10), 3382-3388.
- (209) Caulton, K. G.; Davies, G.; Holt, E. M. *Polyhedron* **1990**, 9 (19), 2319-2351.
- (210) Kim, E.; Chufán, E. E.; Kamaraj, K.; Karlin, K. D. *Chem. Rev.* **2004**, 104 (2), 1077-1133.
- (211) Dell'Amico, D. B.; Alessio, R.; Calderazzo, F.; Pina, F. Della; Englert, U.; Pampaloni, G.; Passarelli, V. *Dalt. Trans.* **2000**, 13, 2067-2075.
- (212) Scott, A. F.; Wilkening, L. L.; Rubin, B. *Inorg. Chem.* **1969**, 8 (11), 2533-2534.
- (213) Bruce, M. I. and Ostazewski, A. P. *J. Chem. Soc. Chem. Commun.* **1972**, 0 (20), 1124-1125.
- (214) Churchill, M. R.; Deboer, B. G.; Rotella, F. J.; Salah, O. M. A.; Bruce, M. I. *Inorg. Chem.* **1975**, 14 (9), 2051-2056.
- (215) Pierantozzi, R. *Kirk-Othmer Encyclopedia of Chemical Tech.* **2000**.
- (216) Allgood, H. Y. *Fert. Sci. Technol. Ser.* **1974**, 2, 289-309.
- (217) Capracotta, M. D.; Sullivan, R. M.; Martin, J. D. *J. Am. Chem. Soc.* **2006**, 128 (41), 13463-13473.
- (218) Haase, D. J. and Walker, D. G. *Chem. Eng. Progr.* **1974**, 70, 74-77.
- (219) Hogendoorn, J. A.; van Swaij, W. P. M.; Versteeg, G. F. *Chem. Eng. J. Biochem. Eng. J.* **1995**, 59 (3), 243-252.
- (220) Zhang, Z.; Wang, S. S.; Song, R.; Cao, T.; Luo, L.; Chen, X.; Gao, Y.; Lu,

- J.; Li, W. X.; Huang, W. *Nat. Commun.* **2017**, 8 (1), 1-10.
- (221) Xia, G. G.; Yin, Y. G.; Willis, W. S.; Wang, J. Y.; Suib, S. L. *J. Catal.* **1999**, 185 (1), 91-105.
- (222) Xie, X.; Li, Y.; Liu, Z. Q.; Haruta, M.; Shen, W. *Nature* **2009**, 458 (7239), 746-749.
- (223) Gokhale, A. A.; Dumesic, J. A.; Mavrikakis, M. *J. Am. Chem. Soc.* **2008**, 130 (4), 1402-1414.
- (224) Grabow, L. C. and Mavrikakis, M. *ACS Catal.* **2011**, 1 (4), 365-384.
- (225) Li, Y.; Fu, Q.; Flytzani-Stephanopoulos, M. *Appl. Catal. B Environ.* **2000**, 27 (3), 179-191.
- (226) Behrens, M.; Studt, F.; Kasatkin, I.; Kühn, S.; Hävecker, M.; Abild-Pedersen, F.; Zander, S.; Girgsdies, F.; Kurr, P.; Knief, B. L.; Tovar, M.; Fischer, R. W.; Norskov, J. K.; Schlogl, R. *Science* **2012**, 336 (6083), 893-897.
- (227) Bart, J. C. J.; Sneed, R. P. A. *Catal. Today* **1987**, 2 (1), 1-124.
- (228) Waugh, K. C. *Catal. Today* **1992**, 15 (1), 51-75.
- (229) Davies, B. J. V.; Šarić, M.; Figueiredo, M. C.; Schjødt, N. C.; Dahl, S.; Moses, P. G.; Escudero-Escribano, M.; Arenz, M.; Rossmeisl, J. *ACS Catal.* **2019**, 9 (2), 859-866.
- (230) Souma, Y.; Iyoda, J.; and Sano, H. *Bull. Chem. Soc. Jpn* **1976**, 49 (11), 3291-3295.
- (231) Souma, Y. and Sano, H. *Bull. Chem. Soc. Jap.* **1973**, 46 (10), 3237-3240.
- (232) Souma, Y. and Sano, H. *J. Org. Chem.* **1973**, 38 (20), 3633-3635.
- (233) Cheng, L.; Zhong, Y.; Ni, Z.; Du, H.; Jin, F.; Rong, Q.; Han, W. *RSC Adv.* **2014**, 4 (83), 44312-44316.
- (234) Saegusa, T.; Kobayashi, S.; Hirota, K.; Ito, Y. *Tetrahedron Lett.* **1966**, 7 (49), 6125-6129.
- (235) Li, Y.; Dong, K.; Zhu, F.; Wang, Z.; Wu, X. F. *Angew. Chem. Int. Ed.* **2016**, 55 (25), 7227-7230.
- (236) Raab, V.; Merz, M.; Sundermeyer, J. *J. Mol. Catal. A Chem.* **2001**, 175 (1-2), 51-63.
- (237) Zhang, H.; Li, J.; Cheng, M. J.; Lu, Q. *ACS Catal.* **2019**, 9 (1), 49-65.

- (238) Imai, S.; Fujisawa, K.; Kobayashi, T.; Shirasawa, N.; Fujii, H.; Yoshimura, T.; Kitajima, N.; Moro-oka, Y. *Inorg. Chem.* **1998**, *37* (12), 3066-3070.
- (239) Iwamoto, M. and Hoshino, Y. *Inorg. Chem.* **1996**, *35* (24), 6918-6921.
- (240) Meyer, F.; Chen, Y. M.; Armentrout, P. B. *J. Am. Chem. Soc.* **1995**, *117* (14), 4071-4081.
- (241) Zecchina, A.; Bordiga, S.; Palomino, G. T.; Scarano, D.; Lamberti, C.; Salvalaggio, M. *J. Phys. Chem. B* **1999**, *103* (19), 3833-3844.
- (242) Borovkov, V.Y.; Jiang, M. and Fu, Y. *J. Phys. Chem. B* **1999**, *103* (24), 5010-5019.
- (243) Rondelez, Y.; Sénèque, O.; Rager, M.; Duprat, A. F.; Reinaud, O. *Eur. J. Chem.* **2000**, *6* (22), 4218-4226.
- (244) Shiraishi, N. and Nishikimi, M. *FEBS Lett.* **2002**, *511* (1-3), 118-122.
- (245) Fry, H. C.; Scaltrito, D. V.; Karlin, K. D.; Meyer, G. J. *J. Am. Chem. Soc.* **2003**, *125* (39), 11866-11871.
- (246) Laitar, D. S.; Mathison, C. J. N.; Davis, W. M.; Sadighi, J. P. *Inorg. Chem.* **2003**, *42* (23), 7354-7356.
- (247) Fujisawa, K.; Ono, T.; Ishikawa, Y.; Amir, N.; Miyashita, Y.; Okamoto, K. I.; Lehnert, N. *Inorg. Chem.* **2006**, *45* (4), 1698-1713.
- (248) Liang, F. P.; Qin, S. N.; Jiang, C. F.; Zhang, Z.; Chen, Z. L. *Organometallics* **2007**, *26* (19), 4839-4842.
- (249) Fianchini, M.; Cundari, T. R.; DeYonker, N. J.; Dias, H. V. R. *J. Chem. Soc. Dalt. Trans.* **2009**, *12*, 2085-2087.
- (250) Shanmugam, M.; Wilcoxon, J.; Habel-Rodriguez, D.; Cutsail, G. E.; Kirk, M. L.; Hoffman, B. M.; Hille, R. *J. Am. Chem. Soc.* **2013**, *135* (47), 17775-17782.
- (251) Davó-Quñonero, A.; Navlani-García, M.; Lozano-Castelló, D.; Bueno-López, A.; Anderson, J. A. *ACS Catal.* **2016**, *6* (3), 1723-1731.
- (252) Einarsdóttir, Ó.; Dyer, R. B.; Lemon, D. D.; Killough, P. M.; Stephan, H.; Hubig, M.; Atherton, S. J.; López-Garriga, J. J.; Palmer, G.; Woodruff, W. H. *Biochemistry* **1993**, *32*, 12013-12024
- (253) Kujime, M.; Kurahashi, T.; Tomura, M.; Fujii, H. *Inorg. Chem.* **2007**, *46* (2), 541-551.

- (254) Kitajima, N.; Fujisawa, K.; Fujimoto, C.; Moro-oka, Y *J. Am. Chem. Soc.* **1992**, *114* (4), 1277-1291.
- (255) Solomon, E. I.; Heppner, D. E.; Johnston, E. M.; Ginsbach, J. W.; Cirera, J.; Qayyum, M.; Kieber-Emmons, M. T.; Kjaergaard, C. H.; Hadt, R. G.; Tian, L. *Chem. Rev.* *2014*, **2014**, *114*, 3659-3853.
- (256) Rasika Dias, H. V.; Lu, H. L. *Inorg. Chem.* **1995**, *34* (21), 5380-5382.
- (257) Lupinetti, A. J.; Strauss, S. H. and Frenking, G. *Prog. Inorg. Chem.* **2001**, 1-112.
- (258) Dias, H. V. R.; Lu, H. L.; Kim, H. J.; Polach, S. A.; Goh, T. K. H. H.; Greg Browning, R.; Lovely, C. J. *Organometallics* **2002**, *21* (7), 1466-1473.
- (259) Rasika Dias, H. V.; Greg Browning, R.; Richey, S. A.; Lovely, C. J. *Organometallics* **2004**, *23* (6), 1200-1202.
- (260) Rangan, K.; Fianchini, M.; Singh, S.; Dias, H. V. R. *Inorganica Chim. Acta* **2009**, *362* (12), 4347-4352.
- (261) Krishnamoorthy, P.; Browning, R. G.; Singh, S.; Sivappa, R.; Lovely, C. J.; Dias, H. V. R. *Chem. Commun.* **2007**, *7*, 731-733.
- (262) Gava, R.; Olmos, A.; Noverges, B.; Varea, T.; Álvarez, E.; Belderrain, T. R.; Caballero, A.; Asensio, G.; Pérez, P. J. *ACS Catal.* **2015**, *5* (6), 3726-3730.
- (263) Singh, K.; Long, J. R.; Stavropoulos, P. *Inorg. Chem.* **1998**, *37* (5), 1073-1079.
- (264) Ardizzoia, G. A.; Monica, G. La; Beccalli, E. M.; Masciocchi, N.; Moret, M. *Inorg. Chem.* **1992**, *31* (13), 2706-2711.
- (265) Fritzsche, J.; Grzywa, M.; Denysenko, D.; Bor, V.; Senkovska, I.; Kaskel, S. and Volkmer, D. *Dalt. Trans.* **2017**, *46*, 6745-6755.
- (266) Dias, H. V. R.; Goh, T. K. *Polyhedron* **2004**, *23* (2-3), 273-282.
- (267) Groom, C. R.; Bruno, I. J.; Lightfoot, M. P.; Ward, S. C. The Cambridge Structural Database. *Acta Crystallogr. Sect. B Struct. Sci. Cryst. Eng. Mater.* **2016**, *72* (2), 171-179.
- (268) Hill, L. M. R.; Gherman, B. F.; Aboelella, N. W.; Cramer, C. J.; Tolman, W. B. *Dalt. Trans.* **2006**, *41*, 4944-4953.
- (269) Dias, H. V. R.; Singh, S.; Flores, J. A. *Inorg. Chem.* **2006**, *45* (22), 8859-8861.

- (270) Huse, K.; Wölper, C.; Schulz, S. *Eur. J. Inorg. Chem.* **2018**, 2018 (30), 3472-3480.
- (271) Dias, H. V. R. and Singh, S. *Inorg. Chem.* **2004**, 43 (19), 5786-5788.
- (272) Green, O.; Gandhi, B. A.; Burstyn, J. N. *Inorg. Chem.* **2009**, 48 (13), 5704-5714.
- (273) Pasquali, M.; Gaetani-Manfredotti, A.; Floriani, C. *Inorg. Chem.* **1980**, 19 (5), 1191-1197.
- (274) Villacorta, G. M. and Lippard, S. J. *Inorg. Chem.* **1987**, 26 (22), 3672-3676.
- (275) Ziegler, T. and Rauk, A. *Theor. Chim. Acta* **1977**, 46 (1), 1-10.
- (276) Pan, S.; Zhao, L.; Dias, H. V. R.; Frenking, G. *Inorg. Chem.* **2018**, 57 (13), 7780-7791.
- (277) Frenking, G. and Shaik, S. *The Chemical Bond: Fundamental Aspects of Chemical Bonding* **2014**, 1-411.
- (278) Mitoraj, M. P.; Parafiniuk, M.; Srebro, M.; Handzlik, M.; Buczek, A.; Michalak, A. *J. Molecular Modeling* **2011**, 17, 2337-2352.
- (279) Pampaloni, G.; Pelosos, R.; Belletti, D.; Graiff, C.; Tiripicchio, A. *Organometallics* **2007**, 26 (17), 4278-4286.
- (280) Mohamed, A. A.; Ricci, S.; Burini, A.; Galassi, R.; Santini, C.; Chiarella, G. M.; Melgarejo, D. Y.; Fackler, J. P. *Inorg. Chem.* **2011**, 50 (3), 1014-1020.
- (281) Altmann, P. J.; Pöthig, A. *Chem. Commun.* **2016**, 52 (58), 9089-9092.
- (282) Rasika Dias, H. V.; Jin, W.; Kim, H. J.; Lu, H. L. *Inorg. Chem.* **1996**, 35 (8), 2317-2328.
- (283) Van Dijkman, T. F.; Siegler, M. A.; Bouwman, E. *Dalt. Trans.* **2015**, 44 (48), 21109-21123.
- (284) Ebrahimpour, P.; Cushion, M.; Haddow, M. F.; Hallett, A. J.; Wass, D. F. *Dalt. Trans.* **2010**, 39 (45), 10910-10919.
- (285) Ponce-Vargas, M.; Muñoz-Castro, A. *Phys. Chem. Chem. Phys.* **2014**, 16 (26), 13103-13111.
- (286) Yu, C.; Cowan, M. G.; Noble, R. D.; Zhang, W. *Chem. Commun.* **2014**, 50 (43), 5745-5747.
- (287) McDanel, W. M.; Cowan, M. G.; Carlisle, T. K.; Swanson, A. K.; Noble, R.

- D.; Gin, D. L. *Polymer* **2014**, *55* (16), 3305-3313.
- (288) Thomas, J.; John, J.; Parekh, N.; Dehaen, W. *Angew. Chem. Int. Ed.* **2014**, *126* (38), 10319-10323.
- (289) Krause, L.; Herbst-Irmer, R.; Sheldrick, G. M.; Stalke, D. *J. Appl. Crystallogr.* **2015**, *48* (1), 3-10.
- (290) Sheldrick, G. M. *Acta Crystallogr. Sect. A Found. Adv.* **2015**, *71*, 3-8.
- (291) Sheldrick, G. M. *Acta Crystallogr. Sect. C Struct. Chem.* **2015**, *71*, 3-8.
- (292) Dolomanov, O. V.; Bourhis, L. J.; Gildea, R. J.; Howard, J. A. K.; Puschmann, H. *J. Appl. Cryst.* **2009**, *42* (2), 339-341.
- (293) Bruker, DIFFRAC.EVA Version 4.2 User Manual. Bruker AXS: Karlsruhe, G. **2016**.
- (294) Wang, F.; Kusaka, S.; Hijikata, Y.; Hosono, N.; Kitagawa, S. *ACS Appl. Mater. Interfaces* **2017**, *9*, 33455-33460.
- (295) Duan, X.; Wang, H.; Ji, Z.; Cui, Y.; Yang, Y.; Qian, G. *Mater. Lett.* **2017**, *196* (196), 112-114.
- (296) Campbell, C.; Ferreira-Rangel, C. A.; Fischer, M.; Gomes, J. R. B.; Jorge, M. *J. Phys. Chem. C* **2017**, *121* (1), 441-458.
- (297) Amino, S.; Arguelles, E.; Diñ, W. A.; Okada, M.; Kasai, H. *Phys. Chem. Chem. Phys.* **2016**, *18*, 23621-23627.
- (298) Verma, G.; Kumar, S.; Pham, T.; Niu, Z.; Wojtas, L.; Perman, J. A.; Chen, Y.-S.; Ma, S. *Crystal Growth and Design* **2017**, *17*, 2711-2717.
- (299) Gammage, M. D.; Stauffer, S.; Henkelman, G.; Becker, M. F.; Keto, J. W.; Kovar, D. *Surf. Sci.* **2016**, *653*, 66-70.
- (300) Farmanzadeh, D.; Abdollahi, T. *Appl. Surf. Sci.* **2016**, *385*, 241-248.
- (301) Yan, Y.; Juríček, M.; Coudert, F. X.; Vermeulen, N. A.; Grunder, S.; Dailly, A.; Lewis, W.; Blake, A. J.; Stoddart, J. F.; Schröder, M. *J. Am. Chem. Soc.* **2016**, *138* (10), 3371-3381.
- (302) Hähnel, T.; Kalies, G.; Krishna, R.; Möllmer, J.; Hofmann, J.; Kobalz, M.; Krautscheid, H. *Microporous Mesoporous Mater.* **2016**, *224* (224), 392-399.
- (303) Martins, V. F. D.; Ribeiro, A. M.; Ferreira, A.; Lee, U. H.; Hwang, Y. K.; Chang, J. S.; Loureiro, J. M.; Rodrigues, A. E. *Sep. Purif. Technol.* **2015**, *149*, 445-456.

- (304) Bondarchuk, S. V. and Minaev, B. F. *RSC Adv.* **2015**, 5 (15), 11558-11569.
- (305) Makino, T.; Okada, M.; Kokalj, A. *J. Phys. Chem. C* **2014**, 118 (47), 27436-27448.
- (306) Liu, K.; Li, B.; Li, Y.; Li, X.; Yang, F.; Zeng, G.; Peng, Y.; Zhang, Z.; Li, G.; Shi, Z.; et al. *Chem. Commun.* **2014**, 50 (39), 5031-5033.
- (307) Denysenko, D.; Grzywa, M.; Jelic, J.; Reuter, K.; Volkmer, D. *Angew. Chemie Int. Ed.* **2014**, 53 (23), 5832-5836.
- (308) Hanke, F.; Dyer, M. S.; Björk, J.; Persson, M.; Dyer, M. *J. Phys. Condens. Matter* **2012**, 42, 424217-424225.
- (309) Kravchuk, T.; Venugopal, V.; Vattuone, L.; Burkholder, L.; Tysoe, W. T.; Smerieri, M.; Rocca, M. *J. Phys. Chem. C* **2009**, 113 (49), 20881-20889.
- (310) Rejmak, P.; Mitoraj, M.; Broclawik, E. *Phys. Chem. Chem. Phys.* **2010**, 12, 2321-2330.
- (311) Watson, G. W.; Wells, R. P. K.; Willock, D. J.; Hutchings, G. J. *Surf. Sci.* **2000**, 459 (1), 93-103.
- (312) Linke, R.; Becker, C.; Pelster, T.; Tanemural, M.; Wandelt, K. *Surface Science* **1997**, 377-379, 655-658.
- (313) Kubota, J.; Kondo, J. N.; Domen, K.; Hirose, C. *J. Phys. Chem.* **1994**, 98 (31), 7653-7656.
- (314) Graham, A. P.; Bertino, M. F.; Hofmann, F.; Toennies, J. P. *J. Chem. Soc. Faraday Trans.* **1996**, 92 (23), 4749-4757.
- (315) Cen, P. L. *AIChE J.* **1990**, 36 (5), 789-793.
- (316) Huang, Y. *J. Catal.* **1980**, 61 (2), 461-476.
- (317) Li, B.; Zhang, Y.; Krishna, R.; Yao, K.; Han, Y.; Wu, Z.; Ma, D.; Shi, Z.; Pham, T.; Space, B.; et al. *J. Am. Chem. Soc.* **2014**, 136 (24), 8654-8660.
- (318) Mofarahi, M. and Salehi, S. M. *Adsorption* **2013**, 19 (1), 101-110.
- (319) Choudhary, V. R.; Mayadevi, S.; Singh, A. P. *J. Chem. Soc. Faraday Trans.* **1995**, 91 (17), 2935-2944.
- (320) Weston, M. H.; Colón, Y. J.; Bae, Y. S.; Garibay, S. J.; Snurr, R. Q.; Farha, O. K.; Hupp, J. T.; Nguyen, S. T. *J. Mater. Chem. A* **2014**, 2 (2), 299-302.
- (321) He, Y.; Krishna, R.; Chen, B. *Energy Environ. Sci.* **2012**, 5 (10), 9107-9120.

- (322) Bloch, E. D.; Queen, W. L.; Krishna, R.; Zdrozny, J. M.; Brown, C. M.; Long, J. R. *Science*. **2012**, *335* (6076), 1606-1610.
- (323) Li, P.; He, Y.; Arman, H. D.; Krishna, R.; Wang, H.; Weng, L.; Chen, B. *Chem. Commun.* **2014**, *50* (86), 13081-13084.
- (324) Frisch, M. J. T., G. W.; Schlegel, H. B.; Scuseria, G. E.; Robb, M. A.; Cheeseman, J. R.; Scalmani, G.; Barone, V.; Mennucci, B.; Petersson, G. A.; Nakatsuji, H.; Caricato, M.; Li, X.; Hratchian, H. P.; Izmaylov, A. F.; Bloino, J.; Zheng, G.; Sonnenberg, D. J. *Gaussian, Inc. Wallingford, CT* **2009**.
- (325) McLean, A. D. and Chandler, G. S. *J. Chem. Phys.* **1980**, *72* (10), 5639-5648.
- (326) Krishnan, R.; Binkley, J. S.; Seeger, R.; Pople, J. A. *J. Chem. Phys* **1980**, *72* (1), 650-655.
- (327) Kazi, A. B.; Rasika Dias, H. V.; Tekarli, S. M.; Morello, G. R.; Cundari, T. R. *Organometallics* **2009**, *28* (6), 1826-1831.
- (328) Dias, H. V. R.; Fianchini, M.; Cundari, T. R.; Campana, C. F. *Angew. Chem. Int. Ed.* **2008**, *47* (3), 556-559.
- (329) Fianchini, M.; Campana, C. F.; Chilukuri, B.; Cundari, T. R.; Petricek, V.; Dias, H. V. R. *Organometallics* **2013**, *32* (10), 3034-3041.
- (330) Ullrich, C. A.; Yang, Z. H. *Brazilian Journal of Physics.* **2014**, *44*(1), 154-188.
- (331) Gooßen, L. J.; Rodríguez, N.; Manjolinho, F.; Lange, P. P. *Adv. Synth. Catal.* **2010**, *352* (17), 2913-2917.
- (332) Dingyi, Y. and Yugen, Z. *Green Chem.* **2011**, *13* (5), 1275-1279.
- (333) Wang, D.; Li, J.; Li, N.; Gao, T.; Hou, S.; Chen, B. *Green Chem.* **2010**, *12*, 45-48.
- (334) Yin, W.; He, C.; Chen, M.; Zhang, H.; Lei, A. *Org. Lett.* **2009**, *11*, 709-712.
- (335) Song, R. J.; Deng, C. L.; Xie, Y. X.; Li, J. H. *Tetrahedron Lett.* **2007**, *48* (44), 784-7848.
- (336) Meng, X.; Xu, X.; Gao, T.; Chen, B. *European J. Org. Chem.* **2010**, *2010* (28), 5409-5414.
- (337) te Velde, G.; Bickelhaupt, F. M.; Baerends, E. J.; Fonseca Guerra, C.; van Gisbergen, S. J. A.; Snijders, J. G.; Ziegler, T. *J. Comput. Chem.* **2001**, *22* (9), 931-967.

- (338) Wolff, S. K.; Ziegler, T.; Van Lenthe, E.; Baerends, E. J. *J. Chem. Phys.* **1999**, *110* (16), 7689-7698.
- (339) Becke, A. D. *Phys. Rev. A* **1988**, *38* (6), 3098-3100.
- (340) Perdew, J. P. and Wang, Y. *Physical Rev. B.* **1986**, *33*(12), 8800-8802.
- (341) Grimme, S. *J. Comput. Chem.* **2006**, *27* (15), 1787-1799.
- (342) Johnson, E. R. and Becke, A. D. *J. Chem. Phys.* **2005**, *123*, 024101-1-7.
- (343) Versluis, L.; Ziegler, T. *J. of Chemical Physics.* **1988**, 322-328.
- (344) Zhang, Y.; Wu, A.; Xu, X.; Yan, Y. *Chem. Phys. Lett.* **2006**, *421* (4-6), 383-388.
- (345) Butler, I. S. and Newbury, M. L. *Spectrochim. Acta Part A Mol. Spectrosc.* **1980**, *36* (5), 453-458.

Biographical Information

Devaborniny Parasar was born in Jorhat, Assam, India. She completed her high school education from Don Bosco High School in 2007, higher secondary education from Assam Rifles Nodal School in 2009, and joined Jorhat Institute of Science and Technology for her Bachelors. She received her B.Sc in Chemistry (Major) in 2012. She joined Tezpur University and pursued her M.Sc in Nanoscience and Technology (2012-2014). She joined the Ph.D graduate program in Chemistry at The University of Texas at Arlington in Fall, 2015.